Civilian Radioactive Waste Management System
Management and Operating Contractor

TOTAL SYSTEM PERFORMANCE ASSESSMENT - 1995:

AN EVALUATION OF THE POTENTIAL
YUCCA MOUNTAIN REPOSITORY

B00000000-01717-2200-00136, Rev. 01

November, 1995

Prepared by: _Joel Atkins_   Date: __11/10/95__
Joel E. Atkins

Prepared by: _(signature)_   Date: __11/10/95__
Joon H. Lee

Prepared by: _(signature) for_   Date: __11/10/95__
Suresh Lingineni

Prepared by: _(signature)_   Date: __11/10/95__
Srikanta Mishra

Prepared by: _Jerry A. McNeish_   Date: __11/10/95__
Jerry A. McNeish

Prepared by: _(signature)_   Date: __11/10/95__
David C. Sassani

Prepared by: _S. David Sevougian_   Date: __11/10/95__
S. David Sevougian

Reviewed by: _(signature)_   Date: __11/10/95__
Robert W. Andrews, Manager
Performance Assessment & Modeling

Approved by: _(signature)_   Date: __11/10/95__
Jean L. Younker, Manager of
Suitability and Licensing Operations

**Civilian Radioactive Waste Management System
Management and Operating Contractor**

TOTAL SYSTEM PERFORMANCE ASSESSMENT - 1995:

**AN EVALUATION OF THE POTENTIAL
YUCCA MOUNTAIN REPOSITORY**

B00000000-01717-2200-00136, Rev. 01

November 1995

Prepared for:

U.S. Department of Energy
Yucca Mountain Site Characterization Project
P.O. Box 98608
Las Vegas, Nevada 89193-8608

Prepared by:

TRW
101 Convention Center Drive
Suite P-110
Las Vegas, Nevada 89109-2006

Under Contract Number
DE-AC01-91RW00134

DISCLAIMER

ACKNOWLEDGEMENTS

Table of Contents

Table of Contents (Continued)

List of Tables

List of Figures

List of Figures (Continued)

EXECUTIVE SUMMARY

*Robert W. Andrews, S. David Sevougian, Joon H. Lee, Srikanta Mishra
and Jerry A. McNeish*

ES.1 INTRODUCTION

The U.S. Department of Energy (DOE) is currently investigating the feasibility of permanently disposing the nation's commercial high-level radioactive wastes (in the form of spent fuel from the over 100 electric power-generating nuclear reactors across the U.S.) and a portion of the defense high-level radioactive wastes (currently stored at federal facilities around the country) in the unsaturated tuffaceous rocks at Yucca Mountain, Nevada. Quantitative predictions based on the most current understanding of the processes and parameters potentially affecting the long-term behavior of the disposal system are used to assess the ability of the site and its associated engineered designs to meet regulatory objectives set forward by the U.S. Nuclear Regulatory Commission (NRC) and the U.S. Environmental Protection Agency (EPA).

The evaluation of the ability of the overall system to meet the performance objectives specified in the applicable regulatory standards has been termed total system performance assessment (TSPA). Total system performance assessments require the explicit quantification of the relevant processes and process interactions. In addition to providing a quantitative basis for evaluating the suitability of the site to meet regulatory objectives, such assessments are useful to help define the most significant processes, the information gaps and uncertainties regarding these processes and the corresponding parameters, and therefore the additional information required in order to have a more robust and defensible assessment of the overall performance.

Total system performance assessments explicitly acknowledge the uncertainty in the process models and parameters and strive to evaluate the impact of this uncertainty on the overall performance. The aim of any total system performance assessment is to be as complete and reasonably conservative as possible and to assure that the descriptions of the predictive models and parameters are sufficient to ascertain their accuracy.

Total system performance assessments evolve with time. As additional site and design information is generated, performance assessment analyses can be revised to become more representative of the expected conditions and remove some of the conservative assumptions necessitated by the incompleteness of site and design data. Previous iterations of total system performance assessment of the Yucca Mountain site and associated engineered barriers have been conducted in 1991 and 1993. These analyses have been documented in Barnard et al. (1992), Eslinger et al. (1992), Wilson et al. (1994) and Andrews et al. (1994).

ES.2 OBJECTIVES

The overall philosophy of any assessment of total system performance is (1) to use models and parameters which are as representative as current information allows for those processes that may affect the predicted behavior of the system and (2) to predict the responses of the natural and engineered components of the system that are expected to result from the emplacement of wastes in the potential repository. In those cases where representative information is not available or

is very uncertain, bounding or conservative assumptions must be made, in order that the predicted performance is demonstrably worse than would be the case if more optimistic assumptions were included in the analyses. The performance assessment process requires the explicit treatment of uncertainty and variability of natural phenomena. The impact of the uncertainty is directly evaluated in the assessments themselves due to the stochastic nature of the analyses. In addition to evaluating the overall performance of the total system of engineered and natural barriers working in concert, an important objective of any predictive performance assessment modeling is to identify the significance of the current uncertainty in processes, models, and parameters on the performance. Those components that are most significant and which are uncertain are therefore identified as warranting additional information. This provides direct input to the site characterization and design programs to assist in prioritizing the necessary testing to develop more robust and defensible performance assessments.

The specific goals of the current iteration of total system performance assessment are to (1) utilize what are believed to be more representative conceptual models that build upon the assumptions employed in TSPA-1993, in particular for the treatment of the engineered barrier system including the waste package, (2) incorporate more recent design information since the completion of TSPA-1993, (3) utilize the most recent site information and models (where available) acknowledging their uncertainty and variability, and (4) evaluate the engineered barrier system release performance measure as well as alternative measures of total system performance (cumulative release and peak dose over different time periods).

Given the universe of potential issues that may be incorporated in any TSPA, it is necessary to limit the analyses to those components and processes that have been determined from previous analyses to be most significant or address particular concerns that may be raised by regulatory or technical oversight groups. In the present TSPA iteration, advantage has been made of the recommendations made in the most recent TSPA analyses documented in Wilson et al. (1994) and Andrews et al. (1994), namely, the need to develop and apply more representative models of (1) drift-scale thermal-hydrologic environment to provide more reasonable estimates of relative humidity and temperature adjacent to the waste packages, since these control the initiation and rate of humid-air and aqueous corrosion processes; (2) waste-package degradation, including the effects of variable near-field environments and the temporal degradation history of the waste packages, since this controls the time period during which the radionuclides are contained; (3) near-field unsaturated-zone aqueous flux, since this controls the percentage of waste packages potentially subjected to advective-flux release from the EBS; and (4) unsaturated-zone flow and transport, including the potential effects of fracture-matrix interaction, since this controls the advective travel time from the repository horizon to the water table. In addition to identifying the most significant issues, the earlier iterations of TSPA have also been used to eliminate some processes from consideration in the current analyses, including (1) disruptive events such as volcanism and human intrusion due to their insignificant effect on post-closure performance, and (2) gaseous-phase transport in the unsaturated zone because the gaseous-phase transport rate to the atmosphere is so much faster than the degradation rate of the waste package.

Where appropriate, the current TSPA iteration has incorporated revised design and site information, new since completion of TSPA-1993, to enhance the representativeness of the analyses. Design information that has been revised includes the thermal load, possible alternative backfills, the degradation model for corrosion of the mild-steel corrosion-allowance material, and

the effects of cathodic protection of the corrosion-resistant material. Site information that has been revised since the completion of TSPA-1993 includes estimates of the spatial variability of surficial infiltration, alternative conceptual representations of the distribution of surficial infiltration at the depth of the potential repository horizon, alternative conceptual representations of fracture/matrix flow and radionuclide transport, and modified geochemical information such as radionuclide solubilities and retardation potential.

Although several alternative measures of performance could be evaluated to quantify the ability of the site and associated engineering barriers to isolate radioactive wastes from the biosphere over the extended periods of time that pose the greatest environmental and health risks, the present analyses focus on two measures of total system performance, namely, the cumulative release of radionuclides at the accessible environment boundary normalized to the limits presented in Table 1 of 40 CFR Part 191, and the maximum dose to an individual using groundwater from a well in the tuff aquifer at the accessible-environment boundary. For consistency, the definition of the "accessible environment" in both instances is assumed to correspond to a location 5 kilometers down the saturated zone hydraulic gradient from the edge of the potential repository.

While integrated release or peak dose are accepted as being appropriate total system performance measures of long-term safety associated with the containment and isolation of radioactive wastes, the NRC has promulgated additional requirements on three subsystems. These subsystems include the waste package itself, the engineered barrier system, and the geosphere. The first two of these subsystems are directly quantified in the definition of the source term used in the total system performance assessment analyses. Therefore, predictions of the performance of these engineered barrier components are also addressed in this TSPA iteration.

ES.3 INFORMATION FLOW IN THE CURRENT TSPA

Total system performance assessments bring together all relevant components of the waste containment and isolation system that potentially affect the release of radionuclides to the accessible environment and the corresponding concentration and dose associated with the release. The individual components of the analyses are indicated on the schematic flow diagram illustrated in Figure ES.3-1. Each of the bubbles of the influence diagram corresponds to a process-level model which in turn is based on direct laboratory or field data that have been synthesized using either empirical relationships or a numerical relationship describing the process of interest. The key attributes of the multiple barriers associated with waste disposal in the unsaturated zone at Yucca Mountain are presented in Figure ES.3-2.

The flow of information in any assessment of total system performance goes from (1) the test data and corresponding interpretation and documentation of these data, to (2) the use of process-level models to synthesize the available test data and other soft information into a consistent representation of the relevant processes affecting waste isolation and containment, to (3) the abstraction of results from these process-level models in the form of response surfaces, table look-ups or other functional relationships for use in the total system performance assessment software, and finally, to (4) the total system performance assessments themselves. The information flow used in TSPA-1995 is depicted in Figure ES.3-3.

In many cases the information derived from laboratory or *in-situ* testing is used directly in the analyses rather than going through the process-level model and abstraction steps. Examples of this include the alteration/dissolution rate of the waste form, the solubility of individual radionuclides, and radionuclide sorption values all of which are derived from laboratory experiments. In many other instances, however, predictive models are required to provide results that can be abstracted for input to the TSPA analysis. Examples of these include unsaturated and saturated-zone flow, drift-scale thermal hydrology, and waste-package degradation. In these instances, the results from the process-level model simulations are used to define the relationship between the "known" parameters, including their corresponding uncertainty and spatial variability, and the required results used as input to the TSPA calculations. The abstraction process is required for these analyses because it is not possible to efficiently imbed the process model itself into the total system performance predictions and make the repetitive simulations required of the probabilistic analyses.

The abstracted models and parameter distributions derived from process-level models or other information sources are input to the total system performance assessment model RIP (Repository Integration Program). RIP was developed by Golder Associates Inc. (GAI) in order to evaluate the performance of a potential radioactive waste disposal facility at Yucca Mountain (Miller et al., 1992) and has subsequently been applied to a wide variety of proposed radioactive waste disposal facilities both in the U.S. and internationally. RIP allows for the stochastic prediction of total system or subsystem performance caused by the uncertainty and variability in the input distributions.

ES.4   SUMMARY OF SITE AND DESIGN DESCRIPTIONS

Yucca Mountain is located in the Southern Great Basin, about 140 km northwest of Las Vegas in the state of Nevada (Figure ES.4-1). The Great Basin is characterized topographically by north-trending mountain ranges separated by alluvium-filled valleys.   Structurally, Yucca Mountain is a complex of north- to northwest-trending fault-delineated ridges. The potential repository is proposed to be constructed within Yucca Crest which is bounded to the west by the Solitario Canyon Fault and to the east by the Bow Ridge Fault and is transected by the Ghost Dance Fault (Figure ES.4-2).

Hydrologically, the Great Basin is characterized as an arid to semi-arid region. Precipitation in the vicinity of Yucca Mountain is approximately 170 mm/yr, with an estimated potential evapotranspiration of about 1000 mm/yr. Consequently, most of the precipitation is returned to the atmosphere and only a small residual remains to infiltrate into the unsaturated zone. Net infiltration is believed to be extremely variable over Yucca Mountain due to variations in soil cover, topographic controls and vegetation patterns (Flint and Flint, 1994).

Stratigraphically, the unsaturated zone beneath Yucca Crest consists of a layered sequence of tuffs deposited from volcanic eruptions which occurred about 10 million years ago. The tuffs range from porous, nonwelded ash-flow, ash-fall and reworked/bedded tuff deposits to massive, welded ash-flow and ash-fall rocks. The four major hydrogeologic units from the surface to the water table consist of the following:

- <u>Tiva Canyon welded (TCw) unit</u>: consisting of moderately- to densely-welded tuffs characterized by low matrix porosity, low matrix saturated hydraulic conductivity, and high fracture density.

- <u>Paintbrush nonwelded (PTn) unit</u>: consisting of partially-welded to nonwelded tuffs characterized by high matrix porosity, high matrix saturated hydraulic conductivity, and low fracture density.

- <u>Topopah Spring welded (TSw) unit</u>: consisting of welded tuffs characterized by low matrix porosity, low matrix saturated hydraulic conductivity, and high fracture density. The basal vitrophyre of the Topopah Spring member (TSv) is generally identified as a subunit because of its lower porosity compared to TSw.

- <u>Calico Hills nonwelded (CHn) unit</u>: consisting of moderately-welded to nonwelded tuffs of the Topopah Spring member underlying the basal vitrophyre and other partially-welded to nonwelded tuffs located below the Calico Hills formation (i.e., Prow Pass, Bullfrog and Tram members of the Crater Flat Unit). Portions of the lower Topopah Spring member are vitrified, and zeolitic alteration appears in both the lower part of the Topopah Spring member and in the tuffaceous beds of the Calico Hills, leading to a further division of this unit into vitric (CHnv) and zeolitic (CHnz) subunits. The fracture density is similar in both zones, and the porosity of the vitric tuffs is marginally higher than that of the zeolitic tuffs. However, the matrix saturated hydraulic conductivity of the CHnv is roughly two orders of magnitude higher than that of the CHnz.

A conceptual design of the potential repository at Yucca Mountain has been described in the Site Characterization Plan (DOE, 1988) and has been revised to take into account the possibility of alternative areal mass loads as well as the decision to use a tunnel boring machine for the excavation of the emplacement drifts (M&O, 1994c). Two alternative areal mass-load ranges have been proposed for the potential repository, a "low" thermal load of between 20 and 40 metric tons of uranium (MTU) per acre and a "high" thermal load of between 80 and 100 MTU/acre. Two areal mass loads have been investigated in TSPA-1995, 25 MTU/acre and 83 MTU/acre. The total amount of radioactive waste to be emplaced in the potential repository consists of 63,000 MTU of spent nuclear fuel and 7,000 MTU of defense high-level waste.

In the current design concept of waste disposal containers for the potential repository at Yucca Mountain, two or three layers of different metals, depending on thermal load, have been proposed for the containment of spent nuclear fuel (SF) and vitrified defense high-level waste (DHLW). For spent fuel in the high thermal load case, a corrosion-allowance material (CAM) such as mild steel has been proposed as the outer containment barrier, and a corrosion-resistant material (CRM) such as Inconel 825 (Alloy 825) has been proposed as the inner containment barrier. For the low thermal load case, a moderately corrosion resistant material (MCRM) such as Monel 400 has been added as an additional containment barrier on top of the two-layer containment barrier design used for the high thermal load case. Since adequate models for predicting the performance of the moderately corrosion resistant materials (Monel 400 and 70/30 copper-nickel alloy) are not available, it has been recommended that this potential containment barrier not be included in any waste package performance analysis (Doering, 1995). Thus, in TSPA-1995, all waste containers for spent fuel and defense high-level waste are assumed to have the same

design, viz., a corrosion-resistant inner barrier of Alloy 825 and a corrosion-allowance outer barrier of carbon steel. The stainless-steel shell of the multi-purpose canister (MPC) and the DHLW pour canister are not considered as barriers to waste-package degradation in the current TSPA iteration.

For a typical large MPC, containing 21 pressurized-water-reactor (PWR), or 40 boiling-water-reactor (BWR), fuel assemblies, the dimensions of the waste container are about 5.7 m long and about 1.8 m in diameter. The thickness of the inner barrier for both the large MPC and DHLW waste containers is 20 mm; the thickness of the outer barrier for the large MPC waste container is 100 mm, and for the DHLW waste container 50 mm.

The adoption of the MPC waste package concept has necessitated the use of in-drift emplacement as the preferred emplacement option based a number of factors including operational considerations, ease of retrieval, safety, and flexibility. A schematic cross section of a centered in-drift package (CIDP) is illustrated in Figure ES.4-3.

The potential use of backfill as a capillary barrier and thermal management tool has been advocated in recent studies of near-field thermohydrologic environments (Buscheck et al., 1995). This iteration of TSPA therefore considers both backfill and no backfill options in evaluating waste package/EBS and total system performance.

ES.5 AMBIENT AND THERMALLY-PERTURBED FLOW MODELS AND ABSTRACTIONS

The total system simulator employed for TSPA-1995 does not explicitly include hydrologic and thermohydrologic process models describing the redistribution of moisture and heat following waste emplacement. However, information concerning the velocity and flux through the unsaturated zone is required for EBS and geosphere transport calculations. In addition, information concerning near-field temperature, saturation and relative humidity is required for waste package degradation and EBS release calculations. TSPA-1995 assumes that thermal effects have dissipated prior to the onset of EBS/geosphere transport, thus facilitating the use of ambient models of unsaturated flow for post-closure performance predictions.

ES.5.1 Conceptual Hydrologic Model

The conceptual model of unsaturated zone hydrology at Yucca Mountain utilized in the present TSPA analyses is shown schematically in Figure ES.5-1. This model provides a qualitative description of how moisture is assumed to be distributed within the unsaturated zone. A part of the precipitation received at the ground surface (q_{ppt}) enters the unsaturated zone as infiltration flux, q_{inf}. After moving vertically and/or laterally through the Tiva Canyon welded (TCw) and the Paintbrush nonwelded (PTn) units, this flux is modified to a percolation flux, q_{perc}, at the proposed repository horizon within the Topopah Springs welded (TSw) unit. At the scale of the repository block (~ 1 km), the "average" percolation flux is distributed (for each hydrostratigraphic unit) between the fractures and matrix blocks as q_{frac} and q_{mat}, respectively, depending on the hydrologic properties of the unit. At the scale of individual drifts (~ 10 m), the "average" percolation flux over the repository horizon is re-distributed across each drift as $q_{perc,i}$, reflecting the underlying local spatial variability in material properties. Each local percolation flux is

further partitioned into a component entering the drifts via dripping fractures ($q_{drip,i}$) and a component retained by the intact rock matrix surrounding the drift ($q_{mat,i}$).

ES.5.2 Site-Scale Unsaturated Flow Model and Abstractions

A suite of simulations was performed with the LBL-USGS site-scale unsaturated flow model (Wittwer et al., 1995) to incorporate the effects of: (i) uncertainty in the assumed infiltration scenarios, (ii) the impact of uncertain and/or spatially variable matrix hydrologic properties, and (iii) conceptualizations of fracture-matrix flow using both equilibrium and non-equilibrium assumptions. The simulations were also used to develop abstractions of unsaturated hydrology in the form of functional relationships between the key dependent variables (i.e., pore velocity and percent of total flux in fractures/matrix for each hydrogeologic unit) and the primary independent variable (i.e., infiltration rate). A NW-SE cross-section (Figure ES.5-2) extracted from the LBL-USGS model was used as the basis for these simulations. Detailed calculations were carried out using the one-dimensional column denoted as Column 153 (located in the center of the proposed repository block) assuming the pervasiveness of vertical flow.

Two infiltration scenarios were postulated based on the infiltration map of Flint and Flint (1994). For the "low" infiltration scenario, the surficial infiltration over the footprint of the potential repository (~0.02 mm/yr) was assumed to be invariant with depth due to predominantly 1-D vertical flow. For the "high" infiltration scenario, the areally-weighted average flux (~ 1.2 mm/yr) over the site-scale model domain was assumed to be uniformly distributed over the potential repository horizon due to significant lateral diversion. Hydrologic simulations were carried out for six discrete cases consistent with the above scenarios, i.e., at 0.01, 0.02, 0.05 mm/yr for the "low" range, and at 0.5, 1.0 and 2.0 mm/yr for the "high" range.

The hydrogeologic database developed by Schenker et al. (1995) was used as the source for matrix and fracture properties. In order to account for the uncertainty/variability in matrix hydrologic properties, ten random sets of values for porosity, saturated conductivity and the two van Genuchten parameters were generated. The properties for the hydrogeologic units above the potential repository horizon (TCw, PTn) were kept fixed at their expected values, and fracture properties were treated as constants for all the units.

The LBL-USGS model conceptualizes the fractured units as equivalent continua with specified threshold saturations for triggering liquid flow in fractures. A key assumption of the equivalent continuum model (ECM) is that liquid flow in the fractures is initiated only after bulk-liquid saturation exceeds a threshold value corresponding to full saturation of the matrix. A relaxation of this assumption, as proposed by Xiang et al. (1995), allows fracture flow to commence whenever the matrix liquid saturation is greater than or equal to a "satiated" matrix saturation.

Steady-state simulations were carried out to develop hydrologic abstractions for: the cases described above (i.e., six infiltration rates, ten sets of material properties, and two fracture-flow initiation rules) by treating matrix pore velocity, v_{mat}, and fractional fracture flux, f_{frac}, along Column 153 as the two performance measures. For each of the four hydrostratigraphic units below the potential repository horizon (TSw, TSv, CHnv, CHnz), ranges for v_{mat} and f_{frac} were tabulated as a function of the infiltration rate—an example for the TSw unit being shown in Figure ES.5-3. The ranges in this figure reflect the effects of uncertainty in material properties

and the fracture-flow initiation rule, and provide a simple approach for propagating uncertainty from the detailed process model to the RIP TSPA model.

Within RIP, infiltration rate is treated as a stochastic parameter. For a given sampled value of infiltration rate, the information such as that presented in Figure ES.5-3 is used to determine the appropriate minimum and maximum values for v_{mat} (or f_{frac}). Treating these as the lower and upper bounds for a uniform distribution, a second sampling would then provide the corresponding value for v_{mat} (or f_{frac}) for input into the geosphere transport module of RIP.

ES.5.3 Stochastic Drift-Scale Fracture Flow Model and Abstractions

As discussed previously, the dynamics of flow at the drift scale are influenced by the spatial variability in percolation flux and in material properties (e.g., saturated hydraulic conductivity). The stochastic fracture flow model developed for TSPA-1995 assumes that the infiltration flux (or "average" percolation flux at the repository horizon) is distributed log-normally into a series of local percolation fluxes, corresponding to each waste package "catchment area". This local percolation flux, denoted as $q_{perc,i}$ in Figure ES.5-1, is then partitioned between a "dripping" fracture intercepting the drift, and the rock matrix surrounding the drift, depending on the local spatially variable saturated matrix conductivity, also sampled from a log-normal distribution.

This methodology allows the development of functional relationships between the number of (and flux through) dripping fractures and the imposed infiltration rate, as shown in Figure ES.5-4. Such information is then used in RIP to predict advective release from the EBS.

ES.5.4 Drift-Scale Thermohydrologic Model and Abstractions

A drift-scale thermohydrologic model was developed to provide descriptions of the thermally-perturbed near-field environment (e.g., temperature, saturation, relative humidity). These variables are required inputs for waste-package degradation modeling and analyses of diffusive release from the EBS. The model assumes a two-dimensional geometry in a plane orthogonal to the emplacement drift and extending from the ground surface to the water table. The modeled domain represents a "unit cell" between adjacent waste packages and adjacent drifts. The model geometry is discretized into a two-dimensional mesh near the waste package which gradually transitions into essentially one-dimensional elements in the far-field. The unsaturated zone stratigraphy is taken to be identical to that of Column 153 shown in Figure ES.5-2.

Thermohydrologic simulations were carried out for areal mass loadings of 25 and 83 MTU/acre, using waste stream characteristics typical of a 21-PWR waste package containing 30-year fuel with an initial heat output of 0.98 kW/MTU. Simulations included cases with and without a "gravel"-type backfill, and for infiltration rates of 0.05 and 0.3 mm/yr. Abstracted results consisted of temporal variations in: (i) waste package surface temperature, (ii) average liquid saturation within drift, and (iii) relative humidity at the surface of the waste package. The latter was calculated by equating the absolute humidity at the waste package surface to that at the dry-out front. These attributes of the perturbed near-field environment were also abstracted from another drift-scale model developed by Buscheck et al. (1995) to provide a range of expected post-emplacement conditions for the waste package and the engineered barrier system. This was done in view of the uncertainty in backfill thermohydrologic characteristics and the conceptual

uncertainty associated with quantifying heat-driven liquid and vapor flow at sub-residual saturation (and the corresponding calculation of relative humidities).

Figure ES.5-5 shows an example comparison of temperature and relative humidities for the 83 MTU/acre case with 0.05 mm/yr infiltration (this study), and for the 80 MTU/acre case with 0 mm/yr infiltration (Buscheck et al.). Note that the two alternative models yield considerably different results, especially for the case with backfill. The impact of these differences on radionuclide release and dose at the accessible environment are discussed in Section ES.8.

ES.6 SUMMARY OF WASTE-PACKAGE DEGRADATION MODELS AND PREDICTED RESULTS

Given that the waste packages must "fail" (i.e., be breached to an extent that the mobile water present in the near field environment can enter the package and any dissolved radionuclides can be transported out of the package) before any dissolution of the waste form can occur, an important first step in total system performance assessment is the prediction of waste package degradation. The degradation rate of the waste package is dependent on (1) the waste package design (in particular the material(s) used in the waste package fabrication and the thickness of these material(s)), (2) the repository design (in particular the thermal load, the presence of backfill, and the size of the emplacement drifts), (3) the near-field thermohydrologic regime in the drifts adjacent to the waste package surface (in particular the temperature and relative humidity), and (4) the degradation characteristics of the waste package materials (including the criteria for corrosion initiation and the rate of corrosion as a function of the near field thermohydrologic environment). Information from each of these topics is required as input to the waste package degradation model to predict the time-rate of "failure" of the waste packages.

ES.6.1 Waste-Package Degradation Models

A detailed stochastic waste-package performance simulation model has been developed for TSPA-1995. The stochastic simulation model incorporates the following five individual corrosion models: (1) humid-air general corrosion model (including uncertainty) for the carbon steel corrosion-allowance outer barrier; (2) stochastic humid-air pitting corrosion model for the carbon steel outer barrier; (3) aqueous general corrosion model (including uncertainty) for the carbon steel outer barrier; (4) stochastic aqueous pitting corrosion model for the carbon steel outer barrier; and (5) aqueous pitting corrosion model (including pit growth rate distribution) for the Alloy 825 corrosion-resistant inner barrier. The uncertainties in the individual corrosion models were incorporated to capture the variability in the corrosion degradation among waste packages and among pits in the same waste package.

Humid-Air Corrosion Models for the Corrosion-Allowance Outer Barrier

Humid-air general corrosion and pitting corrosion models (including their uncertainties) for the corrosion-allowance (carbon steel) outer barrier were developed using a total of 166 atmospheric corrosion data points (up to 16 years of exposure time) for a suite of cast iron and carbon steel which are known to have corrosion behaviors similar to the candidate carbon steel. The collected data are from various exposure conditions in tropical, rural, urban, and industrial testing sites. The atmospheric corrosion data incorporate the effects of pollutants such as SO_2 and other

chemicals in the atmosphere that interact with test specimens. The data also embed any effects of salts that may form on the surface of the corroding specimen due to cyclic wetting and drying.

The humid-air general corrosion model for the outer barrier was developed as a function of exposure time, relative humidity, temperature, and sulfur-dioxide content in air. The corrosion data used, and the model prediction with its uncertainties ($\pm$ 2 standard deviations), are shown in Figure ES.6-1. The input parameters (15 °C, 84% R.H., and 90 μg SO_2/m^3) for the model-prediction in the figure are the averages of the data set. In the waste-package degradation simulation, sulfur-dioxide content in the potential repository is assumed to be negligible.

Pitting corrosion of corrosion-allowance material is commonly represented with a pitting factor that is defined as the ratio of the maximum pit depth to the general corrosion depth at a given exposure time. Accordingly, the pitting factor has been utilized in the development of the stochastic pitting corrosion model for the corrosion-allowance barrier in a humid-air condition. The pitting factor was assumed to be normally distributed with a mean at 4 and a standard deviation of 1. In addition, the pitting factor was constrained to be greater than or equal to 1, i.e. with the pitting factor equal to 1, the pit depth is equal to the general corrosion depth. The pitting factor was sampled randomly and used as a multiplier to the general corrosion depth.

Aqueous Corrosion Models for the Corrosion-Allowance Outer Barrier

The aqueous general corrosion model for the corrosion-allowance outer barrier was developed as a function of exposure time and temperature. In the model development, "long-term" corrosion data (up to 16 years) in polluted river water and in tropical lake water were used to determine parameter values for the corrosion reaction term and time-dependence term. The data include the potential effects of various chemical species dissolved and of microbial activity in the waters. Parameter values for the temperature-dependence terms were determined from a set of short-term corrosion data for temperatures from 5 to 90 °C. The current model has an improved representation for the temperature dependence of aqueous corrosion of the corrosion-allowance outer-barrier material compared to the aqueous corrosion model used in TSPA-1993 (Andrews, et al., 1994). The aqueous pitting corrosion of the outer barrier was modeled using the same approach as in the humid-air pitting corrosion of the outer barrier.

Aqueous Pitting Corrosion Model for the Corrosion-Resistant Inner Barrier

Since there has been no new development or improvement over the pitting corrosion model for the Alloy 825 inner barrier used in TSPA-1993 (Andrews, et al., 1994), the same pitting model was utilized in the development of the stochastic waste-package degradation model in TSPA-1995. The elicitation provides a range of time-independent pit growth rates in aqueous conditions at 70 and 100 °C, and the pit-growth-rate ranges are presented as median, 95th-percentile, and 5th-percentile growth rates. For the pit-growth-rate ranges at other temperatures, these values were extrapolated as a function of temperature in an Arrhenius-type functional form. In the stochastic waste-package degradation simulation model, pit growth rates for the Alloy 825 inner barrier were sampled randomly within the 95th and 5th percentile pit-growth-rate ranges given in the elicitation.

ES.6.2 Approach to Stochastic Waste-Package Degradation Simulation

A flowchart that illustrates the approach to stochastic waste-package degradation simulation is shown in Figure ES.6-2. The approaches and assumptions made for the waste-package degradation modeling are discussed below. The temperature and relative-humidity profiles at the waste-package surface are incorporated into the stochastic waste-package degradation simulation model as a lookup table.

The initial post-closure near-field environment of the potential repository will be hot and dry, and following the peak temperature period, the near-field environment would cool down gradually. Thus, the waste containers are expected to undergo humid-air corrosion initially at elevated temperatures, but the corrosion mode would gradually shift to aqueous corrosion as the near-field environment continues to cool down to lower temperature and more humid conditions. It was assumed that both humid-air general corrosion and humid-air pitting corrosion of the carbon-steel outer barrier initiate at a threshold relative humidity (R.H.) that is uniformly distributed between 65% and 75%, and that both aqueous general corrosion and aqueous pitting corrosion of the outer barrier initiate at a threshold R.H. that is uniformly distributed between 85% and 95%. The Alloy 825 corrosion-resistant inner-barrier material was assumed to be subjected to aqueous pitting corrosion only (not to general corrosion). When pits reach the inner barrier through the outer barrier, aqueous conditions are assumed.

In the post-closure repository, about 10,000 waste packages will be spread over the repository area, and a local corrosion environment in one part of the repository may be different from that in another part. This variability of the local corrosion environment is referred to here as waste-package-to-waste-package variability. Also, since a waste container has a relatively large surface area (37.26 m^2), the general corrosion rate on one part of the waste package may be different from that on another part of the waste package. This variability in corrosion rate on a waste package is referred to here as pit-to-pit variability. The uncertainties in the humid-air and aqueous general corrosion models for the outer barrier and those in the aqueous pitting corrosion model for the inner barrier were utilized to account for the variability among waste packages and the variability among pits.

It is generally agreed that in the current waste-package design, some degree of cathodic protection of the Alloy 825 corrosion-resistant inner barrier will be provided by the carbon-steel outer barrier. An expert elicitation was provided to account for the cathodic protection of the corrosion-resistant inner barrier in the waste package (McCright, 1995). The elicitation suggests the pitting corrosion of the inner barrier be delayed until the thickness of the carbon-steel outer barrier is reduced by 75%.

The simulation module provides as output the "failure" time for each waste package, which corresponds to the time for the initiation of waste-form alteration (or radionuclide mobilization) inside the waste package. "Failure" of a waste package is defined as having at least one pit completely penetrated through all package barriers. The simulation module also provides the pitting history of a "failed" waste package in terms of the number of pit penetrations as a function of time. The total number of pit penetrations at a given time gives the area on the waste package that is available for transport of mobilized radionuclides through the waste package. The waste package "failure" time and subsequent pitting history are fed into the EBS transport model.

ES.6.3 Summary of Major Waste-Package Degradation Results

Within the scope of assumptions employed in the simulations, the corrosion modes considered, and the near-field conditions from the drift-scale thermohydrologic model, the results of the waste package performance analyses show that the current waste-package design appears to meet the "controlled design assumption" requirement on waste-package performance, which is currently defined as having less than 1% of waste packages breached at 1,000 years (M&O, 1995c). Breach of a waste package is defined here as having at least one pit penetration. Since a quantitative definition of the substantially complete containment requirement, as referred to in the NRC subsystem requirement (10 CFR 60.113), has not been decided, the (tentative) "controlled design assumption" requirement has been employed throughout the analyses of the waste-package degradation simulations in this study.

Another important finding is the significant impact on waste-package performance of cathodic protection of the corrosion-resistant Alloy 825 inner barrier by the corrosion-allowance carbon-steel outer barrier. The impacts of cathodic protection on waste-package performance are shown in Figure ES.6-3, in which the simulation results for the case of 83 MTU/acre, no backfill, high infiltration rate (0.3 mm/yr), and cathodic protection are compared to the corresponding case without cathodic protection. The time for the initiation of waste-package failure is delayed significantly from about 2,200 years without cathodic protection to about 8,000 years with cathodic protection. The waste-package failure rate is also significantly lowered. Also shown in the figure is the fraction of waste packages with their outer barrier thickness reduced by 75%.

Currently, alternative thermohydrologic models are being used by M&O Performance Assessment Group and Lawrence Livermore National Laboratory (Buscheck, et al., 1995; hereafter referred to as Buscheck's model). Using the temperature and humidity profiles at the waste-package surface from Buscheck's model, a series of simulations were conducted for waste-package performance in the different near-field environments for the four cases, and the results were compared to those from a "similar" case in this study. The near-field conditions calculated with Buscheck's model are generally hotter and drier than those for "similar" cases in this study, and these resulted in fewer waste package failures and slower degradation.

In Figure ES.6-4, the simulation results for the case of 24 MTU/acre, without backfill and no infiltration (from Buscheck's model) are compared to those for the case of 25 MTU/acre, without backfill and high infiltration (from this study). The time for the initiation of waste-package failure for the two cases are comparable, both cases being at about 2,000 years. However, the waste-package failure rate for the case with Buscheck's model is significantly lower than for the case based on this study. Differences of the predicted waste-package performance between the two thermohydrologic models are more significant in the corresponding thermal loading cases with backfill.

The differences caused by alternative thermohydrologic models are even more pronounced in the high thermal loading cases (i.e., 83 MTU/acre cases with and without backfill in this study vs 80 MTU/acre cases with and without backfill from Buscheck's model). Shown in Figure ES.6-5 is the comparison of the waste-package failure results for the case of 80 MTU/acre, without backfill and no infiltration (from Buscheck's model) to those for the case of 83 MTU/acre, without backfill and high infiltration rate (from this study). There is a significant difference in

the time for the initiation of waste-package failures between the two cases. The initiation time for the case from Buscheck's model is about 50,000 years, whereas it is about 2,000 years for the case from this study. Also, the waste-package failure rates from Buscheck's model are significantly lower than those from this study. The impacts of these differences on peak dose at the accessible environment are discussed in Section ES.8.

ES.7 SUMMARY OF EBS RELEASE MODELS AND PREDICTED RESULTS

ES.7.1 EBS Release Models

Figure ES.7-1 shows a sketch of the major EBS processes and parameters leading to release from the EBS. The thermohydrologic drift-scale modeling analyses provide waste-package surface temperature and relative humidity (which are used in the waste-package degradation modeling), and liquid saturation of the gravel invert (which is used in calculation of the diffusion coefficient for diffusive release of radionuclides). The waste-package degradation modeling results provide the time to first pit penetration of the waste container, and subsequent degradation or pitting of the waste container. The waste form in the nominal case was assumed to be exposed upon first pit penetration, due to immediate cladding failure. No detailed cladding failure modeling was conducted in TSPA-1995, although limited sensitivity analyses were conducted using a simple cladding model.

The near-field environmental conditions affect such processes as the waste-form dissolution, the solubility of the radionuclides in the aqueous phase in contact with the waste form, and the magnitude of both the advective and diffusive components of transport from the waste-form surface through the degraded waste package and the in-drift materials into the host rock. Waste-form dissolution rates have been derived from empirical fits to data obtained from laboratory experiments under a range of environmental conditions. Radionuclide solubilities have also been derived from empirical fits to data obtained from laboratory experiments under a range of thermal and chemical conditions. The advective flux component of radionuclide transport is derived from the distribution of local percolation flux in excess of the saturated hydraulic conductivity of the host rock. The diffusive flux component of radionuclide transport is derived from the hydrologic conditions in the drift materials as calculated in thermohydrologic modeling for TSPA-1995.

Three alternative EBS-release conceptual models were evaluated (Figure ES.7-2). First, for the conceptual model of advective and diffusive release from both the waste package and EBS (the "drips-on-waste-form" model), after a waste package has "failed" (i.e., the initial pit has penetrated the inner corrosion-resistant layer), it is assumed that the near-field environmental conditions (i.e., the temperature, humidity, liquid saturation, and the presence of drips) occurring outside of the waste package are immediately transferred to the inside of the waste package. These environmental conditions, combined with information on the behavior of the waste form and other engineered barriers under these environmental conditions, are required in the prediction of radionuclide releases from the engineered barriers to the host rock. In this model, advective release occurs at a rate proportional to the flow of dripping water in the drift, and diffusive release occurs at a rate proportional to the number of pits penetrating the waste container.

A second EBS-release conceptual model (the "drips-on-waste-container" model) is presumed to be more realistic than the first model, and takes more credit for a partially intact waste container.

This model assumes only diffusive releases through the waste container, because of corrosion products filling the corrosion pits and blocking advective flow into the waste container. Near-field environmental conditions (except for dripping flow) were assumed present inside the waste container immediately after the first pit. The model still assumes both advective and diffusive release from the EBS.

A third EBS release conceptual model was developed to evaluate the potential benefits associated with the emplacement of a so-called Richards' or capillary barrier, in which the backfill is designed to conduct any advective flux (i.e., drips) away from the waste package and underlying invert materials due to the capillary-pressure differences across unconsolidated materials of different grain size. Only diffusive releases from both the waste package and EBS were allowed to occur in this model.

ES.7.2   EBS Release Results

The analyses of the waste-package/EBS performance evaluated the release of radionuclides from the EBS for several scenarios with the NRC peak-release-rate standard in mind. The analyses considered the effects on the EBS peak release rate of three alternative corrosion-initiation models, two alternative thermal loads, two different infiltration-rate ranges, various backfill conditions, alternative cladding-performance models, alternative thermohydrologic models, and alternative EBS-release models. Eight radionuclides were selected for the analyses—those with a maximum release rate that exceeded 0.1% of the NRC total-release-rate limit. These radionuclides, ^{14}C, ^{135}Cs, ^{59}Ni, ^{237}Np, ^{210}Pb, ^{226}Ra, ^{79}Se, and ^{99}Tc, were all considered in the analyses that evaluated the importance of the various parameters and conceptual models listed above. EBS release rates were calculated as a function of time for simulations that used the expected values of the stochastic distributions of the various model parameters.

The analyses demonstrate the significance of the rate of percolation or dripping on the waste containers to the predicted release (Figure ES.7-3). Generally, the influence of infiltration was more significant than the alternate corrosion-initiation criteria (i.e., temperature and R.H. vs. R.H. only) in terms of causing radionuclides to exceed the NRC total-release-rate limit. However, when cathodic protection was considered in the corrosion-degradation model, the initial release from the EBS to the host rock was delayed until after 10,000 years and the peak release rate at that time was predicted to be reduced by about a factor of 10. As expected, using a simple cladding failure model, the EBS release was correspondingly decreased when the percent of cladding failure decreased. The Buscheck thermohydrologic conceptual model produced significantly less EBS release than the thermohydrologic model used in this study, due to lower waste-package failure rates caused by higher temperatures and lower relative humidities. The higher thermal load cases produced higher releases than the corresponding lower thermal load cases for all simulations performed.

The effects of alternative EBS-release models on the EBS release rate was significant (Figure ES.7-4). Comparing the "drips-on-waste-container" EBS-release model, which assumed only diffusive release through the perforations in "failed" waste containers, to the more conservative "drips-on-waste-form" EBS-release model, which allows advective flow through the perforations, the former yielded release rates for most nuclides that are within their NRC limit. The implication is that the "partially failed" waste containers by pitting corrosion should still be able

to perform as a potentially important barrier to radionuclide release, and EBS transport models that incorporate more realism need to be considered. Assuming a capillary-barrier effect (i.e., no advective flux through the EBS), the EBS peak release rate showed an additional decrease of several orders of magnitude.

The key model parameters contributing to EBS peak release were identified using regression analysis for the 25 and 83 MTU/acre, no backfill, and high infiltration cases. ^{99}Tc solubility, infiltration or percolation rate, and spent fuel dissolution rate were identified as the three most important parameters contributing to EBS peak release.

ES.8 SUMMARY OF GEOSPHERE TRANSPORT MODELS AND PREDICTED RELEASES AND DOSES AT THE ACCESSIBLE ENVIRONMENT

ES.8.1 Geosphere Transport Models

<u>Unsaturated-Zone Transport</u>

Those radionuclides released from the engineered barrier system are available for transport through the geosphere to the accessible environment. The travel time of radionuclides in the geosphere is a function of both physical and chemical processes between the fluid and the rock, and in the best possible scenario, this time delay between release from the EBS and arrival at the accessible environment would be long enough to allow the bulk of the radionuclide mass to decay to insignificant levels of radioactivity.

Travel time to the accessible environment is a function of the percolation flux distribution in the unsaturated zone and the advective flux distribution in the saturated zone, as well as the conceptual representation of hydrostratigraphy along the along the likely ground-water flow paths between the repository and the accessible environment (Figure ES.8-1). The percolation flux distribution within the Topopah Spring hydrostratigraphic unit (and other UZ units below it) is a function of the infiltration rate and the conceptual model for ground-water flow in the unsaturated zone. In particular, the key conceptual uncertainty in the transport of radionuclides through the geosphere at Yucca Mountain is the possible presence of fracture flow and transport which might, if fracture pathways existed and were continuous and interconnected, lead to the formation of so-called "fast" paths. However, "fast paths" *per se* are more of a concern with regard to the groundwater travel-time requirement than the peak dose at the accessible environment. This is because the latter is caused by the arrival of the bulk of the radionuclide mass, which is a result of combined fracture/matrix flow, whereas the former is due to the arrival of the initial part of the breakthrough curve through the fast paths.

At the time of the TSPA-1995 simulations, the Yucca Mountain process-level aqueous-transport model (Robinson et al., 1995) had not been completed. Thus, unlike the TSPA-1995 UZ flow model (discussed above), which is based on abstracted process-level model results, the TSPA transport model is incorporated directly into the RIP TSPA model. It is partly based on the abstractions from the process-level flow model (i.e., the matrix and fracture velocity fields and the partitioning of volumetric flow between fractures and matrix), but also includes a fracture-matrix interaction model (to represent intra-unit fracture connectivity and matrix imbibition) and a radionuclide retardation model (to represent chemical interaction between the matrix and pore

water), neither of which is based on process-level transport modeling (although the chemical retardation model is based on LANL experiments on whole tuff samples).

To simulate particle transport in the RIP TSPA model, velocity fields for both fracture and matrix transport are required. These steady-state fields come from simulations with process-level models. From these simulations, which use the equivalent continuum model (ECM), two families of curves (v_{mat} vs. q_{inf} and f_{frac} vs. q_{inf}) were generated for each hydrogeologic unit (where v_{mat} is the matrix velocity and f_{frac} is the fraction of the total percolation flux within the fractures). The range in uncertainty of v_{mat} or f_{frac} for any given q_{inf} was determined by a range in material properties, fracture/matrix coupling, and vertical spatial variability. According to this method, the infiltration rate, q_{inf}, is the primary independent variable for geosphere transport in the aqueous phase. In particular, during a stochastic simulation, RIP will sample from a q_{inf} distribution (either over the "high" infiltration range, 0.5–2.0 mm/yr, or over the "low" infiltration range, 0.01–0.05 mm/yr) to determine the q_{inf} at repository closure (i.e., the initial q_{inf}). For this value of q_{inf}, there will be stochastic distributions of v_{mat} and f_{frac} (as functions of depth or pathway), which are described by the minimum and maximum values of the given parameter at that q_{inf}. Random uniform sampling between these minimum and maximum values is used to determine a stochastic initial v_{mat} and f_{frac} for a given realization, as illustrated in Figure ES.8-2. During any given simulation (realization), q_{inf} may change due to climatic variations, and thus, f_{frac} and v_{mat} will be time dependent.

Because of the lack of an appropriate process-level model, fracture/matrix interaction in the geosphere, for example, fracture connectivity, imbibition, and matrix diffusion, is simulated directly in the TSPA model by a Markovian process algorithm that randomly transitions particles between fracture and matrix modes. The magnitude of this transition "rate" (which is not really a rate, but rather the inverse of the random travel length in a fracture or in the matrix), λ, determines the strength of the fracture/matrix coupling. For TSPA-1995, the "default" particle-transition rate for the Markovian dispersion process between fracture and matrix is set equal to the inverse of the pathway length, h. This means that on average a radionuclide particle will travel the length of the pathway (e.g., through the TSw) within a fracture, before transitioning to the matrix-flow mode or vice-versa. For a slug input through a single pathway (i.e., one hydrogeologic unit), this will result in some smearing of the two peaks (fracture and matrix) in the breakthrough curve, but will retain much of the bimodal character of the breakthrough curve. Two sensitivity cases for fracture/matrix coupling were considered: $\lambda = 1/(0.1h)$, which represents strong fracture/matrix coupling, i.e., a reduction of transport through fractures, and $\lambda = 1/(100h)$, which represents weak fracture/matrix coupling, i.e., much weaker than the $\lambda = 1/h$ "default" case (see Figure ES.8-3).

In TSPA-1995, all rock/water interactions that can serve to retard the transport of radionuclides are modeled with a simple, equilibrium (infinite capacity), distribution-coefficient (K_d) model. Whole rock distribution functions (K_d's) have been used based on laboratory-derived data and the "minimum K_d concept" (Meijer, 1992). These distribution coefficients are related to the chemical nature of the individual hydrostratigraphic unit, and are classified according to vitric, devitrified, and zeolitic (Meijer, 1995). In addition, for TSPA-1995, K_d distributions in the saturated zone are different from those in the unsaturated zone, with the main difference due to the effect of ionic strength of the groundwater in the different domains.

Saturated-Zone Transport

The saturated-zone flux affects the arrival time of radionuclides at the accessible-environment boundary as well as the degree of mixing and dilution in the ground water of the tuff aquifer prior to its extraction and use. Since process-level modeling of saturated-zone flow and transport has not changed appreciably since the completion of TSPA-1993, the same abstraction and basis thereof used in the previous TSPA iteration (Andrews et al., 1994) is also used in the current analyses. The entire flux distribution incorporates the effects of large-scale spatial heterogeneity of aquifer properties. Small-scale heterogeneity is included through the use of dispersion in the solution of the one-dimensional advection-dispersion equation. Because of the one-dimensional nature of the solution algorithm, only longitudinal dispersion is simulated, i.e., there is no transverse dispersion. This is conservative when considering predictions of peak concentration or peak dose.

The actual distribution for q_{SZ} (Darcy velocity in the saturated zone) used in TSPA-1995 is a log-normal distribution with a mean of 2.0 m/yr, a median of 1.1 m/yr, and a standard deviation of 0.4859. Based on this distribution, both TSPA-1993 and TSPA-1995 indicate that the saturated zone is not a significant geosphere barrier compared to the unsaturated zone, as far as time delay of the breakthrough to the accessible environment. The saturated zone's greatest importance lies in its dilution effect.

Climate Change

Given the long time frames of potential interest in total system performance assessment (up to 1,000,000 years), it is likely that the atmospheric conditions will change with a resulting change in climate, especially precipitation and net evapotranspiration. Therefore, the potential effects of climate change are important to consider. Climate-change effects are abstracted directly into the current total system performance assessment. It is reasonable to postulate that increased precipitation would result in an increase in percolation flux and a rise in the water table, although the degree of correlation and the time lag between changes in surficial processes and the subsurface effects are uncertain. Both of these effects are included in TSPA-1995, although the water-table rise is only considered as a sensitivity case.

Biosphere/Dose Modeling

Although only engineered barrier and natural barrier (i.e., geosphere) models and parameters are required in the prediction of cumulative releases of radionuclides at the accessible-environment boundary, the calculation of dose requires the definition of the potentially exposed population(s) and the potential biosphere pathways by which individuals may be exposed to any radionuclides released. In the current total system performance assessment it is assumed that the peak individual dose corresponds to an individual taking drinking water from the tuff aquifer (2 liters/day). It is also assumed that this "maximally-exposed" individual is located at the point on the accessible-environment boundary that corresponds to the peak of the radionuclide concentration within the tuff aquifer. Mixing volumes are based on a fixed cross-sectional area of flow in the saturated zone, with the horizontal mixing being given by the width of the potential repository and the vertical mixing by a well with a 50 m saturated-zone interval. Dose

conversion factors, which convert radionuclide concentrations to doses, have been derived from published values used by the U.S. Environmental Protection Agency (EPA, 1988).

Treatment of Gaseous-Phase Radionuclides, ^{14}C

For TSPA-1995, geosphere transport of radionuclides in the gaseous phase of the unsaturated zone is not considered (except in one limiting sensitivity case). The primary radionuclide to be transported in the gas (air) phase in the geosphere would be ^{14}C. However, given the recent recommendations of the NAS (National Research Council, 1995) on protection of the global population, the risk from gaseous release of ^{14}C is negligible. Therefore, TSPA-1995 assumes that the ^{14}C released from the inventory is dissolved in the aqueous phase once it reaches the geosphere (i.e., the top of the TSw), and is then transported by the aqueous phase to the accessible environment. Since this is a conservative assumption with respect to computing dose at the accessible environment (although it has little effect, since ^{237}Np, ^{99}Tc, and ^{129}I doses are much higher than those from ^{14}C), there is one sensitivity analysis that computes aqueous dose at the accessible environment assuming ^{14}C is directly released to the atmosphere, i.e., it never enters the aqueous phase and therefore does not contribute to dose exposure in a water well at the accessible environment.

ES.8.2 Predicted Radionuclide Release and Dose at the Accessible Environment

This section of the executive summary discusses predicted radionuclide release and radiation dose at the accessible-environment boundary, 5 km from the repository footprint boundary (Figure ES.8-1). Inherent in the nature of any such prediction is its uncertain or stochastic nature. This statistical behavior is captured by plots of the complementary cumulative distribution function (CCDF) of a particular performance measure over the time period of interest, either 10,000 or 1,000,000 years. (Note: CCDF = 1 – CDF, where CDF is the cumulative distribution function.) The performance measure for radionuclide release (in Curies) is the total (i.e., the sum of all radionuclides) cumulative release over 10,000 years, normalized to the Table 1 values in 40 CFR Part 191. The performance measure for radiation dose (in rem/yr) is the total (i.e., the sum of all radionuclides) peak dose to a person (the "maximally exposed individual") at the accessible environment using the tuff aquifer for his or her drinking water (2 liters/day), calculated over both 10,000 years and 1,000,000 years. The 1,000,000-year time frame for peak dose is the one suggested in the recent report by the National Research Council (1995). These peak doses should not be compared to the average dose a member of the "critical" population may be exposed to over the time period of interest. The average dose is expected to be more than an order of magnitude less than the peak dose to the maximally-exposed individual.

The expected value of a statistical distribution is one of the most important parameters used to characterize the behavior of the distribution. Thus, besides showing CCDFs that represent the entire range of the various parameter distributions, expected-value time histories ("breakthrough curves") are also shown for the radionuclides with the highest release rates or doses at the accessible environment. An expected-value release-rate history is the breakthrough curve for rate-of-release of radioactivity (Ci/yr) at the accessible environment for a single realization that uses the expected values for all stochastic parameters. Similarly, an expected-value dose history is the breakthrough curve for dose exposure (rem/yr) at the accessible environment for a single realization that uses the expected values for all stochastic parameters.

The effect of model and parameter uncertainty on predicted results is evaluated by a number of sensitivity analyses. Alternative repository designs and alternative scenarios for natural-system behavior are considered, including (1) low and high water-infiltration rates through the unsaturated zone (0.01–0.05 mm/yr and 0.5–2.0 mm/yr); (2) low and high thermal load (25 MTU/acre and 83 MTU/acre); (3) alternative thermohydrologic models for the near-field environment (one developed in this study, referred to as the Lingineni model vs. one developed by LLNL, referred to as the Buscheck model); (4) three waste-package-degradation (corrosion-initiation) models (relative-humidity controlled, temperature and relative-humidity controlled, and temperature and relative-humidity controlled with cathodic protection); (5) five conceptual models of EBS transport and water movement (drips directly on waste form, drips on waste package but not on waste form, no drips or capillary-barrier effect, no drips and aqueous EBS transport of ^{129}I and ^{36}Cl, and no drips and aqueous EBS transport of ^{129}I and ^{36}Cl plus ^{14}C transport directly to atmosphere—the "diffusion-only" model); (6) fracture/matrix interaction in the geosphere (the effect of intra-unit fracture connectivity within a given hydrogeologic unit); and (7) climate change (with and without water table rise).

In addition to CCDFs and expected-value time histories, evaluation of repository performance using linear regression analysis provides an explanation for the degree of the variance in the performance measures (total peak dose or cumulative release) that can be explained by one or more of the model parameters. This type of analysis can indicate where to focus future efforts in gathering more data to substantiate physical models. It can also indicate what repository design elements are most important, e.g., waste-package design or backfill design.

10,000-year Cumulative Releases

Although all of the sensitivity analyses mentioned above were carried out for the 10,000-year time frame, a number of combinations of repository design and natural system behavior resulted in no releases at the accessible environment up to 10,000 years postclosure. These included the following: (i) low infiltration range (0.01 – 0.05 mm/yr), (ii) cathodic protection of the waste-package, (iii) Buscheck 80 MTU/acre thermal load with and without backfill and Buscheck 24 MTU/acre thermal load with backfill, and (iv) matrix-flow-only (zero fracture flow) in the unsaturated zone. Thus for these cases, there are no CCDFs or expected-value breakthrough curves to be shown.

Two cases that do result in releases to the accessible environment are the two thermal loads modeled with the Lingineni thermohydrologic model, 83 MTU/acre and 25 MTU/acre, with a gravel backfill, at the high infiltration range (0.5–2.0 mm/yr). Normalized total cumulative releases for these two thermal loads are shown in Figure ES.8-4, where the shaded area in the figure represents the Table-1 release limits in 40 CFR Part 191. Although not specifically indicated in this figure, the radionuclides with greatest releases to the accessible environment during the 10,000-year time frame are ^{99}Tc, ^{14}C, ^{129}I, and ^{36}Cl. All of these are nonsorbing nuclides, i.e., $K_d = 0$ in the geosphere.

As indicated by Figure ES.8-4, and because of the fact that the two thermal loads generate similar temperature and relative humidities in the near field, the release at the accessible environment is about the same for 83 MTU/acre compared to 25 MTU/acre. However, as discussed above, this conclusion is not valid when using the Buscheck thermohydrologic model,

which produces very different releases over the 10,000-year time period at high versus low thermal load. This points to the need to better substantiate and test the thermohydrologic process-level models used for TSPA predictions.

<u>10,000-year Total Peak Dose</u>

Figure ES.8-5 shows 100-realization CCDFs of predicted total peak dose at the accessible environment during the first 10,000 years. All of these cases were modeled using the thermohydrologic results (temperatures, humidities, and saturations) for the Lingineni 83 MTU/acre case with gravel backfill. The particular curves shown in this plot represent a comparison of alternative conceptual models of water movement and radionuclide transport in the EBS. These models are (1) fractures dripping directly onto the waste-form, i.e., directly on the spent fuel and DHLW glass; (2) fractures dripping on the corroding metal waste containers, but not directly on the waste form; (3) no dripping fractures (the so-called capillary-barrier effect); (4) no dripping fractures and also aqueous (rather than gaseous) transport of ^{129}I and ^{36}Cl; and (5) no dripping fractures and also aqueous transport of ^{129}I and ^{36}Cl plus direct shunting of ^{14}C to the atmosphere (i.e., ^{14}C does not travel to the accessible environment in the aqueous phase, so it has no effect on aqueous dose). The last model is also called the "diffusion-only" model, since in this model any radionuclide transport to the accessible environment must result from pure diffusive transport through the aqueous phase in the EBS. This mode of transport is so slow that no radionuclides reach the accessible environment in 10,000 years, so no curve is present on the plot. The basis for the fourth model is that, although the first three models conservatively assume that ^{129}I and ^{36}Cl traverse the EBS in the gas phase, it is quite possible, due to the high reactivity of I_2 and Cl_2, that they may dissolve in the aqueous phase before being transported across the EBS.

These various transport models are listed above in order of conservatism, with the first model (i.e., the "drips-on-waste-form") being the most conservative (i.e., most pessimistic) regarding repository performance. The dose curve for this model in Figure ES.8-5 corresponds to the cumulative release curve labeled "83 MTU/acre, backfill" in Figure ES.8-4. The CCDFs in Figure ES.8-5 indicate that over 10,000 years, different models of EBS transport yield somewhat different peak doses. For example, the capillary barrier model reduces doses by about 50%, while the capillary barrier combined with aqueous transport of ^{129}I and ^{36}Cl reduces peak doses by about a factor of 20. However, since the ultimate peak of the radionuclide breakthrough curves is far from reaching the accessible environment after 10,000 years (i.e., only the leading edge of the curve has broken through), the effect of these various models is much less than it is at 1,000,000 years (see next section).

Linear regression analysis was used to determine the most influential model parameters. Over the 10,000-year time frame the top two parameters are the matrix velocity in the CHnv and the mean percolation flux in the unsaturated zone (which is assumed to be equal to the infiltration rate, q_{inf}). This ranking is not unexpected. In particular, the peak concentrations of the radionuclides never reach the accessible environment during 10,000 years and variability in q_{inf} translates directly to a shifting in time of the initial portion of the breakthrough curve. However, since this is the steeply rising portion of the breakthrough curve(s) regardless of the value of q_{inf} (for $q_{inf} = 0.5-2.0$ mm/yr), there is a very strong dependence on q_{inf}. The strong dependence on

matrix velocity in the CHnv is also not unexpected because the CHnv is the formation with the highest value of saturated matrix conductivity, K_{sat}, and therefore the lowest value of flow in fractures. Therefore, it tends to control connected fracture flow throughout the mountain, as noted in the Calico Hills System Study (M&O, 1995d); and without fracture flow, no releases can reach the accessible environment in 10,000 years.

1,000,000-year Total Peak Dose

In their recent report to Congress, the National Research Council (1995) has concluded that "...there is no scientific basis for limiting the time period of the individual-risk standard to 10,000 years... (and) that compliance assessment be conducted for the time when the greatest risk occurs, within the limits imposed by long-term predictability of both the geologic environment and the distribution of local and global populations." Based on geologic considerations, they also state that "the ultimate restriction on time scale ... is on the order of 1,000,000 years at Yucca Mountain." For these reasons, we have conducted performance assessments to predict dose and peak dose over a 1,000,000-year time frame. These are presented here as various sensitivity analyses that examine the effect of various natural system parameters and various repository designs.

Alternative Infiltration Rates. Figure ES.8-6 shows the history of dose exposure from ^{129}I and ^{237}Np to the maximally exposed individual at the accessible environment (5 km from the repository boundary) over the 1,000,000 year time frame for the 83 MTU/acre thermal load, with backfill, and using a climate-change model that is based on a cyclical variation of the infiltration rate, q_{inf}. ^{129}I is one of the two highest-dose radionuclides that is nonsorbing in the geosphere (the other is ^{99}Tc), while ^{237}Np is the highest-dose nonsorbing nuclide (and also the highest-dose nuclide, period). The dose histories for these two radionuclides are for the two different infiltration-rate scenarios, i.e., 0.03 mm/yr versus 1.25 mm/yr. For the high infiltration case, ^{237}Np at late times, and ^{99}Tc and ^{129}I at early times, produce the highest dose exposure at the accessible environment. (The same is true for a 25 MTU/acre thermal load). For the low infiltration case ^{129}I dominates the dose exposure at all times.

One major point of Figure ES.8-6 is to examine the differences between the high and low infiltration scenarios. First of all, the long-lived, sorbing nuclides, such as ^{237}Np, do not have significant releases for low UZ infiltration fluxes over the 1,000,000-year time frame. Second, the periods of highest releases (and doses) for nonsorbing nuclides, such as ^{129}I and ^{99}Tc, are spread out over a much broader time interval for the low-q_{inf} case compared to the high-q_{inf} case, and have a much lower peak.

Alternative Thermohydrologic Models. 100-realization CCDFs of the 1,000,000-year total peak dose to the maximally exposed individual are presented in Figure ES.8-7 for the two alternative near-field thermohydrologic models, at the low and high infiltration ranges. Within the RIP TSPA simulator, the relative humidities, temperatures, and water saturations for these two thermohydrologic models are coupled to the dripping-fracture EBS transport model and the far-field geosphere transport model. The Buscheck model has much later and more spread-out package failure times than the Lingineni model, which are a result of a considerably lower relative-humidity history. However, Figure ES.8-7 demonstrates that even large changes in

ES-21

relative humidity and temperature in the near field do not greatly affect the ultimate peak dose during the 1,000,000-year time frame. In particular, the high-thermal-load Lingineni model only gives about 2 to 3 times greater peak doses over the entire sampled range of stochastic variables than the Buscheck model. So, although the Buscheck model delays the appearance of the peak dose at the accessible environment by tens- to hundreds-of-thousands of years (not shown on these plots), it does not reduce the peak very much over the long time span of 1,000,000 years. Another result was that backfill in either thermohydrologic model (and the resulting changes in humidity, temperature, and saturation) had a negligible effect on 1,000,000-year total peak dose (although it could serve to significantly delay initial arrivals at the accessible environment). However, this conclusion is predicated on the assumption that backfill does not alter the EBS transport model. If EBS transport were assumed to be different for backfill versus no-backfill (e.g., if drips on the waste-package were assumed for the no-backfill scenario, but not assumed for the backfill scenario), then the results are significantly different, as discussed below.

Alternative Conceptual Models for EBS Transport. Similarly to Figure ES.8-5 for 10,000-year total peak dose, Figure ES.8-8 examines the effect of alternative EBS transport models on 1,000,000-year total peak dose at the accessible environment. These five models manifest much larger differences in peak dose over 1,000,000 years than 10,000 years because the peak of the breakthrough curve for ^{237}Np reaches the accessible environment over that long time frame. The 100-realization, total-peak-dose CCDFs in Figure ES.8-8 are for the case of 83 MTU/acre, with backfill, over the high infiltration range, with a cyclical-q_{inf} climate model. The total peak dose is reduced by about a factor of about 25 for the "drips-on-waste-container" compared to the "drips-on-waste-form" model, because of a large reduction in ^{237}Np dose, resulting from its slow diffusion through the corrosion pits in the waste container before it is able to interact with dripping flow in the EBS. The no-drip (or capillary-barrier-effect) model does not show much additional reduction in dose compared to the "drips-on-waste-container" model because of the contribution from gaseous ^{129}I. The fourth model, which combines the "capillary barrier" with aqueous EBS transport of ^{129}I and ^{36}Cl, reduces the peak doses by about an additional factor of about 200 for the entire range of the CCDF. In this case, the only nuclide that is able to traverse the EBS rapidly is ^{14}C in the gaseous phase, which is then assumed to enter the aqueous phase in the geosphere, from whence it is transported through the unsaturated and saturated zones to the accessible environment. The final model, which eliminates ^{14}C as a contributor to peak dose at the accessible environment (by assuming it is transported in the gaseous phase to the atmosphere), leaves only diffusively transported aqueous-phase nuclides across the EBS. This results in an additional reduction by a factor of more than 10^4 in peak dose over the 1,000,000-year time frame, compared to the fourth model. In summary, these various EBS transport models point to the importance of estimating the amount of dripping flow in the EBS, and to the advantages of constructing a barrier to such flow.

Fracture/Matrix Interaction in the Geosphere. Figure ES.8-9 shows the effect of fracture/matrix interaction on the ultimate peak dose at the accessible environment during the first 1,000,000 years. At one extreme is matrix flow only, i.e., no water flow in fractures. At the other extreme is highly connected intra-unit fracture flow [$\lambda=1/(100h)$], such that radionuclides remain within the fractures of each unit for the entire time spent traveling through the unit (and similarly for nuclides traveling within the matrix), i.e., there is very little interaction between fractures and matrix. The only interaction between fractures and matrix is at the hydrogeologic-unit boundaries, where matrix flow leaving the base of a given unit can enter the fractures of the next

lower unit and fracture flow from the base of the unit can enter the matrix of the next lower unit. Figure ES.8-9 indicates that fracture/matrix interaction does not significantly affect peak doses over the long time frame of 1,000,000 years. Although strong fracture/matrix coupling (such as in matrix diffusion) can significantly delay initial breakthrough (not shown by the CCDFs), it does not delay it enough to affect the peak dose very much over the 1,000,000-year time span.

Most Important Model Parameters During 1,000,000-Year Time Frame

One important difference between repository performance over the 1,000,000-year time frame compared to the 10,000-year time frame is which physical parameters are most influential. For 10,000 years it is mainly percolation rate in the unsaturated zone (or, equivalently, infiltration rate, q_{inf}) and fracture/matrix flow in the CHnv, but for the 1,000,000-year time frame, dilution in the saturated zone (i.e., the saturated-zone fluid flux, q_{SZ}) is apparently the most important parameter. This is demonstrated by Figures ES.8-10 and ES.8-11. Figure ES.8-10 shows scatter plots of 1,000,000-year peak dose vs. q_{SZ} over the high and low q_{inf} ranges. Clear linear trends are apparent. Figure ES.8-11 shows the result of two linear regression analyses for the high q_{inf} case: (1) ln(dose) vs. ln(x) and (2) ln(dose) vs. x, where x is a subset of the stochastic parameters that were expected to be the most important. For each analysis, the five most important independent parameters are shown in Figure ES.8-11, as well as the amount of the variability they explain. For example, consider the ln(dose) vs. ln(x) transformation, which explains the results much better than the ln(dose) vs. x transformation. In particular, q_{SZ} is the most important parameter, and by itself explains 48% of the variance in the results, assuming a ln-ln relationship (whereas, it only explains 23% of the variance by itself for the ln-linear relationship). The second most important parameter is q_{inf}, and in combination with q_{SZ}, they explain 65% of the variability when using a ln-ln fit.

An explanation of the different rankings for 1,000,000 years versus 10,000 years is that the breakthrough of the dose peak has generally occurred within the 1,000,000-year time period, so that the only model parameter of importance is how much the waste mass has been diluted (or how much it has decayed); whereas, for 10,000 years only the leading edge of the breakthrough curve has arrived at the accessible environment, so a change in an important UZ parameter can significantly shift this steeply rising portion of the breakthrough curve.

In TSPA-1995 some of the stochastic distributions for parameters have been eliminated and replaced with sensitivity analyses, which are conducted for only three or four values of the given parameter. Thus, the linear regression analysis does not include such parameters in the importance rankings, even though they could be more important than the ranked parameters. An example is the fracture/matrix particle transition parameter, λ. A more important example is q_{inf}, which is equivalent in TSPA-1995 to the mean UZ percolation flux at repository depth. In particular, q_{inf} has been separated into two ranges, or sensitivity cases. Within each range, we have included q_{inf} in the stepwise linear regression, but its importance has been much reduced compared to if we had constructed 100-realization CCDFs over the entire q_{inf} range from 0.01–2.0 mm/yr. Thus, q_{SZ} is the #1 ranked parameter. However, if stepwise linear regression is performed over the entire range, then q_{inf} becomes the #1 ranked parameter and q_{SZ} becomes the #2 ranked parameter. This is shown in Figure ES.8-12, which is a scatter plot of 1,000,000-year peak dose versus q_{inf}, over the entire range 0.01–2.0 mm/yr, and also in Figure ES.8-13, which show the importance rankings for a linear regression analysis over this entire q_{inf} range.

It should be noted that it is actually the ratio of q_{inf} (i.e., q_{UZ}) to q_{SZ} that determines dilution in the saturated zone, so this again points out that over the 1,000,000-year time frame, it is primarily dilution that controls peak dose at the accessible environment—at least according to the current models and data incorporated into TSPA-1995.

Subsystem Performance

Another important aspect of the TSPA analysis is to determine the ability of various *parts* of the system, both engineered and natural, to contain or retard the transport of the waste. To evaluate the containment capability of these various subsystems, cumulative (but not normalized) expected-value releases were calculated for a particular case (83 MTU/acre, with backfill, "high" q_{inf} = 1.25 mm/yr initially, and cyclical q_{inf} due to climate change) at various times (10,000, 100,000, and 1,000,000 years) at the following locations:

1. From the engineered barrier system (EBS),
2. From the base of the repository-level formation (TSw),
3. From the base of the unsaturated zone (PPn), and
4. At the accessible environment (AE).

Results are presented in Figure ES.8-14 for ^{237}Np release. Generally, the saturated zone does not act as a significant containment barrier as evidenced by the releases being similar at the base of the unsaturated zone and at the AE. However, the individual natural barriers, and combinations thereof, in the unsaturated zone provide additional reduction of radioactivity compared to the EBS, up to and slightly beyond 1,000,000 years. The natural barriers have a much greater effect at earlier times because the bulk of the ^{237}Np is still in the unsaturated zone; however, by 1,000,000 years, the natural barrier system only reduces ^{237}Np releases by about a factor of 1.5 compared to the EBS, since a large portion of the ^{237}Np has traveled to the accessible environment.

This comparison of subsystem performance demonstrates that the natural barriers are less effectual as time increases, and one must rely on dilution or effective EBS containment to reduce doses at the accessible environment. However, given the many conservative assumptions in TSPA-1995, neither of these may be necessary, since doses may already be at a very low level.

ES.8.3   Summary of Predicted Repository Performance

10,000-year Predicted Performance

The following are general conclusions concerning 10,000-year repository performance, based on the sensitivity analyses completed in TSPA-1995:

(1)   10,000-year total peak dose, due mainly to ^{99}Tc and ^{129}I, is most sensitive to the following model parameters: matrix velocity in the CHnv and percolation flux in the unsaturated zone;

(2)   Over 10,000 years there are zero releases to the accessible environment for the following cases: (i) low infiltration range (0.01 – 0.05 mm/yr), (ii) cathodic protection of the waste-

package, (iii) Buscheck 80 MTU/acre thermal load with and without backfill and Buscheck 24 MTU/acre thermal load with backfill, and (iv) matrix-flow-only (zero fracture flow) in the unsaturated zone;

(3)   Depending on the conceptual model of intra-unit fracture connectivity, fracture/matrix interaction can significantly affect peak dose and cumulative release during the first 10,000 years after repository closure;

(4)   Depending on the conceptual model for radionuclide transport across the EBS (viz., if ^{129}I and ^{36}Cl are assumed to be in the aqueous phase and/or ^{14}C is supposed not to contribute to peak dose since it is dispersed in the atmosphere), a "capillary barrier" that prevents drips (i.e., advective flow) from contacting the waste packages can reduce 10,000-year peak doses at the accessible environment by at least a factor of 20 or more (and up to many orders-of-magnitude if only diffusive releases are possible through the EBS).

1,000,000-year Predicted Performance

The following general conclusions can be drawn about 1,000,000-year repository performance from the sensitivity analyses completed in TSPA-1995:

(1)   1,000,000-year total peak dose, due mainly to ^{129}I over the low infiltration range ($q_{inf} =$ 0.01–0.05 mm/yr) and to ^{237}Np over the high infiltration range ($q_{inf} = 0.5-2.0$ mm/yr), is most sensitive to the following model parameters: (i) dilution in the saturated zone (or equivalently, the saturated-zone bulk Darcy flux, q_{SZ}), and (ii) percolation flux in the unsaturated zone (where the mean UZ percolation flux equals the average infiltration flux, q_{inf}—both averaged over the repository area);

(2)   1,000,000-year total peak dose may be greatly reduced by a barrier that intercepts dripping water on the waste packages (the capillary-barrier effect), i.e., for aqueous-phase radionuclides, pure diffusion (no advection) through the WP/EBS produces extremely low doses at the accessible environment (reduced by a factor of 10^8 compared to dripping flow on the waste form);

(3)   Low intra-unit fracture connectivity in the unsaturated zone (i.e., high transition rate between the fracture and matrix in the RIP model) can significantly delay the breakthrough of peak doses to the accessible environment, but only slightly reduces the ultimate peak dose that occurs during the entire 1,000,000-year time frame after repository closure (a similar conclusion applies to matrix diffusion);

(4)   Alternative thermal loads, alternative thermohydrologic models for the near-field, and alternative corrosion-initiation models (including cathodic protection) do not have a very large effect on the total peak dose that occurs during the 1,000,000-year time span (a factor of three is about the largest effect);

(5)   Over 1,000,000 years, climate change with water table rise can increase peak dose at the accessible environment by a factor of about 2 to 10 compared to no change in climate;

climate change without water table rise (varying infiltration rate only) falls in between these two extremes.

ES.9 EFFECT OF CONSERVATISM ON PREDICTED RESULTS

A large number of sensitivity and uncertainty analyses have been performed during the course of this iteration of total system performance assessment. Such analyses are always an important component of any performance assessment. They provide an important means to gain insights into those components, processes, models, and parameters which most significantly affect the predicted waste containment and isolation over the time periods of interest.

While many useful insights have been reached on the basis of the sensitivity analyses performed, it is also instructive to step back and examine in a more qualitative fashion the implications of some of the assumptions made in the development of the total system performance assessment. The implications may be in the direction of improving the predicted performance (when the conservative assumptions are relaxed) or in the direction of degrading the predicted performance (when the nonconservative assumptions are tightened).

The question of the significance of nonconservative assumptions may be posed as follows: What components, processes, models, or parameters could, with some reasonable likelihood, be sufficiently different from the assumptions made in the current TSPA iteration, such that the predicted releases or doses could be greater than those presented? The primary factor which could cause a significant increase in the predicted releases or doses at the accessible environment is the unsaturated-zone percolation flux. Significantly greater percolation flux values (on the order of 10 mm/yr) would be expected to increase the percentage of waste packages experiencing advective release from the EBS and the magnitude of that advective release if no hydraulically-engineered barrier (such as a capillary barrier or drip shield) were emplaced in the drifts. At some percolation flux, the limiting factor on the predicted release from the EBS would be the dissolution rate of the waste form itself, which in the present analyses is quite conservative. Although increasing the percolation flux also decreases the advective travel time in the unsaturated zone and therefore increases the possible release of key radionuclides to the accessible environment, the travel time factor does not appreciably affect the peak dose because the dominant dose contributor is always ^{237}Np (at the higher percolation flux values) and it is released eventually anyway.

An additional factor that may increase the dose above the values predicted is the assumed value for the dose conversion factor. This factor, which converts from mass concentration to radiation dose, has been derived from an EPA reference, but it is possible that revised biosphere modeling of ingestion pathways and bio-concentration factors may affect the conversion factor. It is recommended that the EPA delineate this conversion ratio as part of their rulemaking process, assuming they accept the notion of dose- or risk-based total system performance.

Given that it is neptunium which generally controls the predicted peak dose at the higher percolation flux values (it may be iodine or technetium at lower percolation flux values), the solubility of this radionuclide plays a significant role. The assumed solubility value of this nuclide is already considered to be at the conservative end of the expected range. Therefore increasing this value substantially is not believed reasonable. In addition, even if the value were

increased, one would quickly reach a point where the dissolution rate would control the release of this radionuclide (assuming a significant advective release component through the EBS).

Finally, colloidal transport of radionuclides has not been considered in the present TSPA analyses. Although natural- and/or radio-colloids may be formed in the waste package environment, their stability and mobility is uncertain. For those nuclides that may exist as a colloidal phase and that are also stable and mobile, their transport to the accessible environment may be significantly enhanced if the colloidal matter does not sorb onto the rock. In such a scenario, albeit unlikely, the peak concentration of some key dose-producing radionuclides (especially plutonium) may be significantly increased, which would correspondingly increase the predicted total peak dose.

The question of the significance of conservative assumptions may be posed as follows: What components, processes, models, or parameters could, with some reasonable likelihood, be sufficiently different from the assumptions made in the current TSPA iteration, such that the predicted releases or doses could be less than those presented? In answering this question, virtually every element of the total system is a candidate for discussion. A large number of conservative assumptions have been made that would tend to significantly impact the predicted long-term release or dose if the assumptions were relaxed or if the nonconservative end of the parameter space was considered. For example, when considering the lowest percolation fluxes, the peak dose is reduced by a factor of about 100, even when the release of ^{129}I from the EBS is assumed to be in the gaseous phase. Assuming that the ^{129}I is released in the aqueous phase would reduce the peak dose by an additional factor of about 100. Low average percolation fluxes have two very positive effects, namely reducing the EBS release rate (because the advective component of the release is reduced) and increasing the travel time (because the propensity for fracture flow and transport is reduced and the matrix velocities are lower).

Limiting the available inventory by either extending the lifetime of a certain fraction of the waste packages or incorporating the potential contribution of cladding has a positive effect on the predicted performance. Therefore, although the time of waste-package failure may not be so important in peak dose calculations (even in the most optimal degradation model some packages have failed by 100,000 years), the fact that only a small fraction of the packages have failed for certain assumptions is still important.

An important conservatism that significantly affects the predicted peak dose is the determination of the amount of mixing due to dilution and dispersion in the saturated zone. For the present analyses, the only dispersive mixing assumed to occur is in the vertical plane to a depth of 50 m below the top of the water table. Transverse dispersion would not be considered significant over the 5 km distance to the accessible environment. Also, longitudinal dispersion has a minimal effect when considering essentially a constant source term. However, if one considers the mixing possible between the repository and the ultimate point of ground-water discharge (whether 30 km down-gradient in the Amargosa Valley or 80 km down-gradient at Franklin Lake Playa), then significant reductions in the peak concentrations and doses would result.

In those cases where the neptunium release dominates the peak dose, the neptunium solubility plays a key role. It has been suggested that the neptunium solubilities used in the TSPA analyses are based on experiments that represent metastable equilibrium concentrations and that the actual

equilibrium concentration may be several orders of magnitude lower. If this were the case, neptunium would be replaced by either technetium or iodine as the peak dose contributor and would result in a lower predicted peak dose by about an order of magnitude.

ES.10 CONCLUSIONS AND RECOMMENDATIONS

When considering a 10,000-year total system performance measure, there are many EBS and natural-barrier system factors that affect the predicted results. Under certain conceptual assumptions, the engineered barriers by themselves can provide complete containment of the radionuclides for the entire 10,000-year time period. Similarly, for cases when the percolation flux distribution is at the lower end of the possible range of likely values, the natural barrier by itself can provide complete isolation of the radionuclides from the accessible environment for the entire 10,000-year time period. This is the definition of redundant barriers.

For cases when the most conservative estimates of both EBS and natural barrier performance are considered, i.e., those cases which produce some non-zero integrated release to the accessible environment over 10,000 years, several factors are important. The predominant factor is the percolation flux distribution. This distribution not only affects the likelihood of there being advective flux (i.e., dripping) through the EBS, but it also affects the magnitude of the advective release from the EBS, the distribution of radionuclide transport between the fractures and matrix in the unsaturated zone and the average matrix velocity through the unsaturated zone. That is, for given conservative assumptions regarding the waste-package degradation model, the percolation flux distribution controls the 10,000-year cumulative release. This is the same conclusion reached in TSPA-1991 (Barnard et al., 1992) and TSPA-1993 (Wilson et al., 1994 and Andrews et al., 1994). It is worthwhile to point out that the radionuclides of interest over the 10,000-year time period are highly soluble nuclides with little or no sorption such as ^{99}Tc, ^{129}I, and ^{14}C. Slightly sorbed nuclides such as ^{237}Np can be released in small quantities over 10,000 years in cases of high percolation flux. For the parameter distributions used in the present analyses (which may be subject to change upon evaluation of the controlling phase of the nuclide), highly sorbed and low-solubility nuclides, such as plutonium, americium, and curium, are not transported appreciable distances through the EBS or host rock in 10,000 years.

While the predicted peak dose over a 10,000-year time period is dependent on numerous factors, in extending the time to 1,000,000 years only a few factors dominate the predicted response. In general, factors which tend to delay the arrival of the peak concentration at the accessible environment are found to be less significant. This is a direct result of the extremely long time period considered and the long half-lives of some of the key radionuclides that always contribute to the predicted peak dose (notably ^{99}Tc with a 200,000-year half-life, ^{237}Np with a 2,000,000-year half-life, and ^{129}I with a 20,000,000-year half-life). Even for the low end of the assumed percolation flux distribution and even assuming the optimal conceptual representation of fracture-matrix flow and transport, the above radionuclides are either not sorbed at all (^{99}Tc and ^{129}I) or are only slightly sorbed (^{237}Np), and they generally tend to break through to the accessible-environment boundary within 1,000,000 years. In addition, even with the most optimal waste-package degradation model assumptions, a certain fraction of waste packages would be degraded within the 1,000,000-year period. In sum, although a combination of waste package and site performance can contribute to containing and isolating radioactive wastes within the Yucca Mountain area for some tens to even hundreds of thousands of years, it is unlikely that such

barriers can be reasonably shown to delay the above radionuclides sufficiently to preclude their release over a 1,000,000-year time period.

While delay itself does not contribute appreciably to the prediction of long term doses, dispersion and dilution are still significant processes. Dispersion in this case is the result of both geosphere and EBS processes. Dispersion tends to spread out the release of the radionuclides over time and therefore reduce the peak concentration and peak dose. Geosphere dispersion is enhanced by increasing the matrix diffusion or decreasing the mean fracture-flow length (in cases where fracture transport is active) or increasing the vertical, lateral, and/or longitudinal dispersion in the saturated zone. The dispersive effects in the saturated zone are enhanced as the distance between the repository and the assumed user of the tuff aquifer increases. This effect has significant ramifications with respect to the definition of where the average member of the critical population proposed in the recent NAS recommendations resides. If the critical group is located in the Amargosa Valley, some 25 km down gradient from the present "accessible environment" as defined in 40 CFR Part 191, the increased geosphere dispersion may be expected to reduce the peak concentration and peak dose by more than one order of magnitude.

Dispersive-type effects within the engineered barrier system are extremely important in reducing the predicted peak concentration and dose in the geosphere. Spreading of releases from the EBS can occur as a result of (1) a wide distribution of waste-package failure times, (2) an extremely low alteration/dissolution rate or (3) diffusion-dominated releases through the package and EBS. The first two factors are generally insufficient to significantly decrease the peak release rate over the range of values considered in this TSPA iteration. However, diffusion-dominated releases from the EBS can significantly reduce the peak release rate. Such diffusion-dominated releases occur when either a low percolation flux distribution is assumed (in which case only a small percent of the packages experience advective release) or a very efficient capillary barrier in the backfill is considered. In both cases, the diffusion through the waste package and other EBS materials is a highly nonlinear function of the in-drift liquid saturation (generally very low for all thermal loads except when advective flow into the drift occurs), as well as the effective surface area through which diffusion occurs (which in turn is controlled by the waste-package degradation model).

Confidently demonstrating that diffusive release is the dominant transport mechanism in the EBS is key to reducing the predicted long term dose to individuals or critical groups. It is not at all coincidental that virtually every other high-level radioactive waste disposal program around the world that has published results of total system performance has incorporated a diffusive barrier in their engineered barrier design (see Neall et al., 1995). In other countries the diffusive barrier is a bentonite or bentonite-sand mixture, because these programs have focussed on crystalline host rocks within the saturated zone. An equivalent barrier (in the sense of maximizing the possibility of diffusive only releases from the EBS) in an unsaturated hydrologic environment such as Yucca Mountain is a crushed rock with low capillary suction.

In addition to spreading out the release of radionuclides from the source term, dilution in the saturated zone also significantly affects the predicted peak dose at the accessible environment boundary over the 1,000,000-year time period. This dilution can occur by the mixing of different ground-water sources either naturally along the flow path between the repository and the user of the tuff aquifer (or other ground-water sources that are supplied by the tuff aquifer) or by the

user tapping alternative sources of water for consumption (i.e., by slotting the well over different isolated hydrostratigraphic units). Although alternative dilution scenarios are likely, quantitative descriptions of these scenarios are beyond the scope of the present document. Assuming that the EPA accepts the NAS recommendations of protecting individuals of critical groups as an appropriate environmental standard that should be applied to Yucca Mountain, additional analyses of regional ground-water flow patterns should be conducted. It is relevant to point out that saturated-zone mixing issues are not important for the cumulative release performance measure and are less significant at shorter distances between the potential repository and the defined location of the critical group.

Throughout the assessment of the individual components included in the overall TSPA analyses, an over-arching theme comes back again and again as being the driving factor impacting the predicted results. Simply stated, it is the amount of water present in the natural and engineered systems and the magnitude of aqueous flux through these systems that controls the overall predicted performance. The following discussion details the significance of water to the overall performance of the system. First, the degradation of the waste package is controlled by the relative humidity of the near field environment—at low relative humidities there is virtually no corrosion of the corrosion-allowance material. Second, once the waste packages have failed, the rate of dissolution of the waste form is dependent on the presence of liquid water in direct contact with the spent fuel. Third, the concentration of the radionuclides dissolved in this liquid water is dependent on the volume of water in contact with the spent fuel and the solubility of the radionuclides in that water. Fourth, transport of any dissolved radionuclides through the failed waste packages and other materials in the engineered barrier system (such as the invert upon which the packages are placed or any backfill or packing placed around the waste packages) is controlled by the presence of liquid water on the grain boundaries, which affects the diffusive transport component, and by the presence of dripping water through the drifts, which control the advective transport component. Fifth, those radionuclides which are transported through the drifts to the host rock may be advectively transported through the unsaturated zone to the water table, with the rate of transport being directly related to the aqueous percolation flux distribution. Sixth, those radionuclides which reach the water table are expected to be transported laterally through the saturated zone to the ultimate discharge of the ground water or to a potential user of the water between the potential repository and the ultimate discharge location. Seventh, within the saturated zone, the dissolved radionuclides would be diluted and dispersed due to small scale velocity heterogeneity of the ground-water flow regime. Finally, if an individual does extract ground water from the tuff aquifer, the particular use of that water will affect the pathways by which any dissolved radionuclides in the ground water may by consumed by that individual. In summary, the amount of water present at all points along the system, from the drift to the saturated zone, controls the ultimate release of radionuclides to the accessible environment and the corresponding dose attributed to those radionuclides. Therefore, information on the distribution of the amount and rate of water movement through the various scales relevant to the prediction of post-closure performance, remains the key need to enhance the representativeness of future iterations of TSPA.
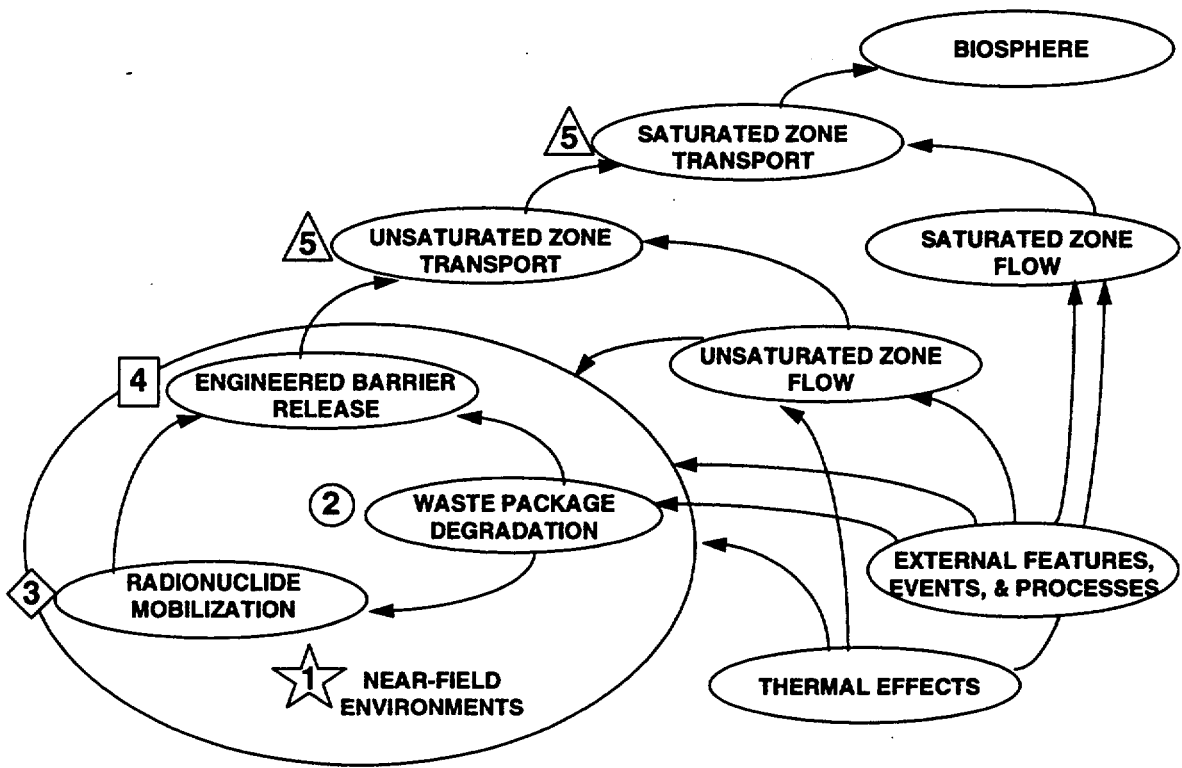
Figure ES.3-1   Process Model Influence Diagram Used in Total System Performance
                       Assessment
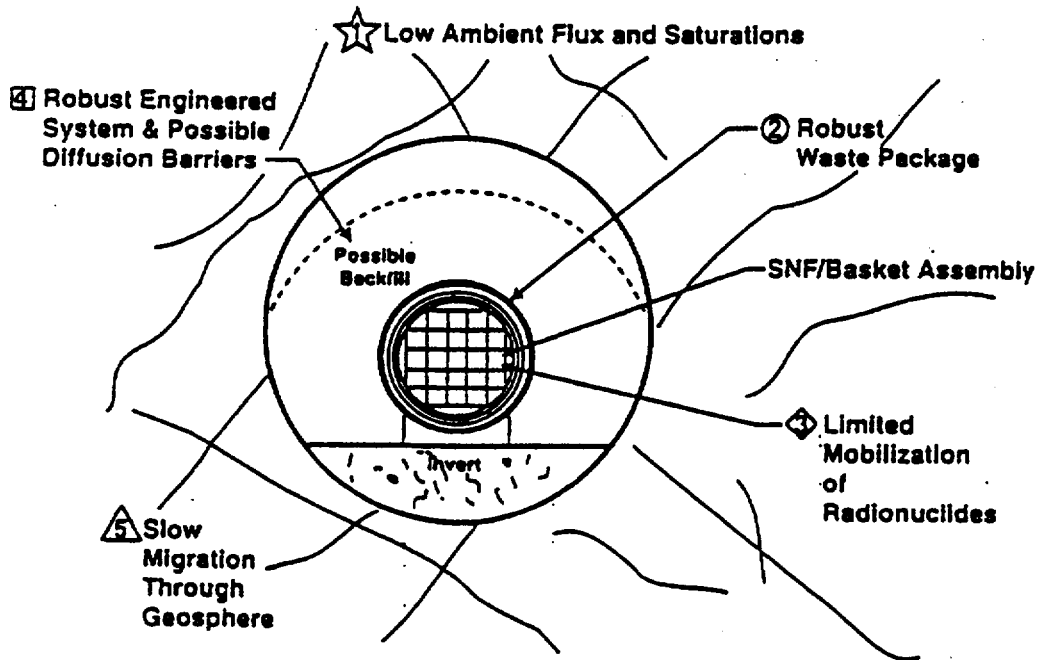
Figure ES.3-2   Engineered Barrier System Components

Information

Site Biosphere → 8

Site Geology → 7

Site Hydrology → 6

Site Geochemistry → 5

Repository Design → 4

Waste Package Design → 3

Material Properties → 2

Waste Form Properties → 1

Process-Level Model

7 → 6 → Saturated Zone Flow Model

7 → 6 → Unsaturated Zone Flow Model

7 → 6 → 4 → Drift-Scale Thermo-Hydrologic Model

B

3 → 2 → Waste Package Degradation Model

Process Level Model Abstractions

Response surface of saturated zone flux → E

Response surface of unsaturated zone flux
- fracture flux
- matrix flux
→ D

Response surface of drift-scale flux
- % packages with drips
- advective flux in drips
→ C

Response surface of
- temperature
- humidity
- liquid saturation
→ B

Response surface of
- first pit
- pit distribution
→ A

Total System Performance Assessment

Dose

8

Geosphere Cumulative Release

D E 5 6 7

EBS Release Rate

B C 5 4 3 2 1

Waste Package Lifetime

A

Figure ES.3-3   Information Flow Diagram for TSPA-1995
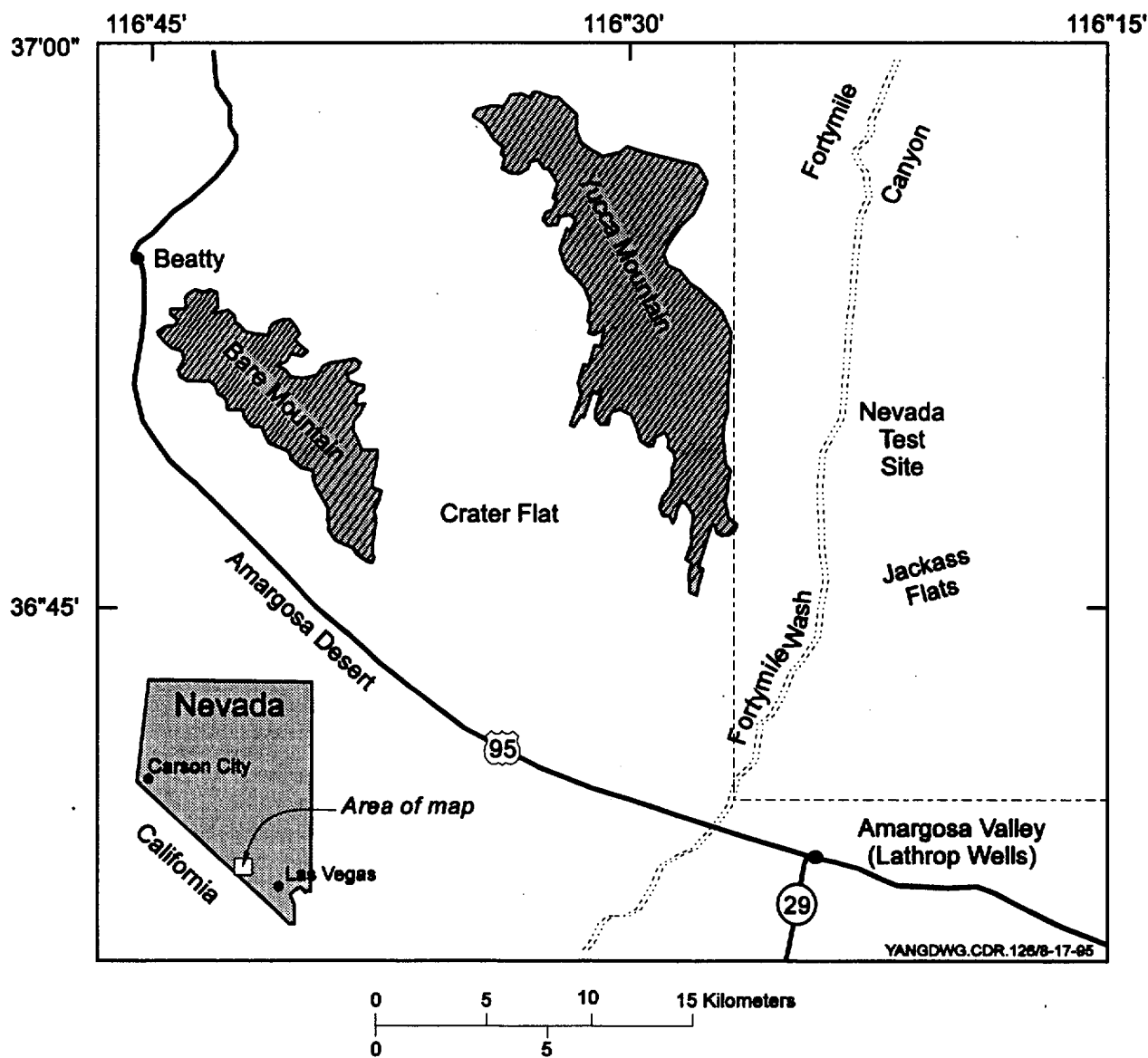
Figure ES.4-1   Location of the Yucca Mountain Area (modified from Montazer and Wilson, 1984)
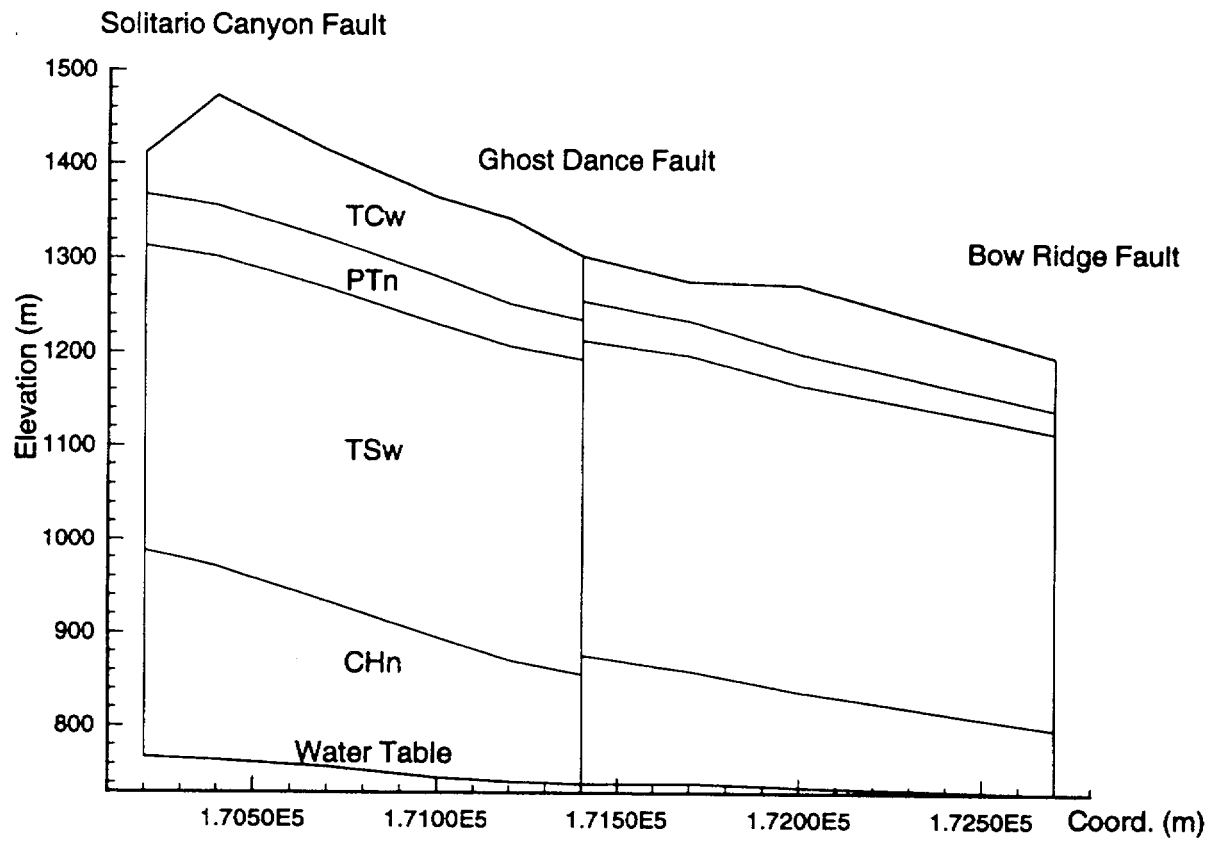
Figure ES.4-2   Geologic Cross-Section through the Potential Repository at Yucca Mountain (from Wittwer et al., 1995)
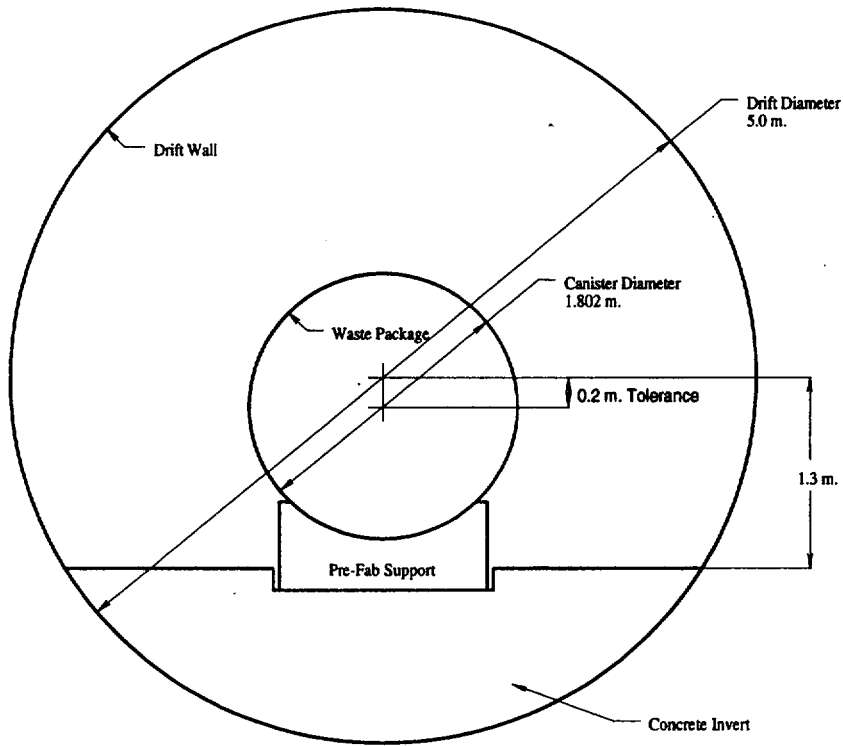
Figure ES.4-3   Emplacement drift design for the CIDP option (after M&O, 1995f)
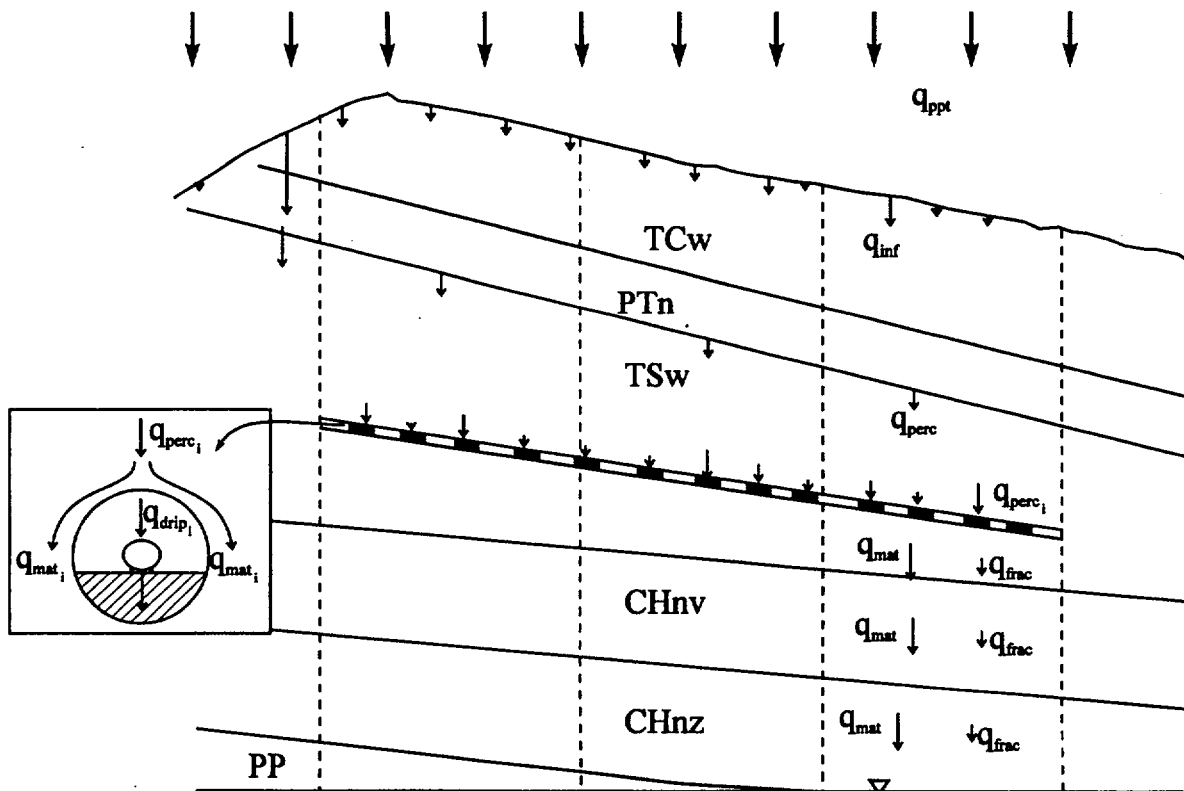
Figure ES.5-1   Conceptual model of unsaturated zone hydrology at Yucca Mountain as utilized in TSPA-1995.

LBL/USGS Site Scale Model, 2D Cross Section
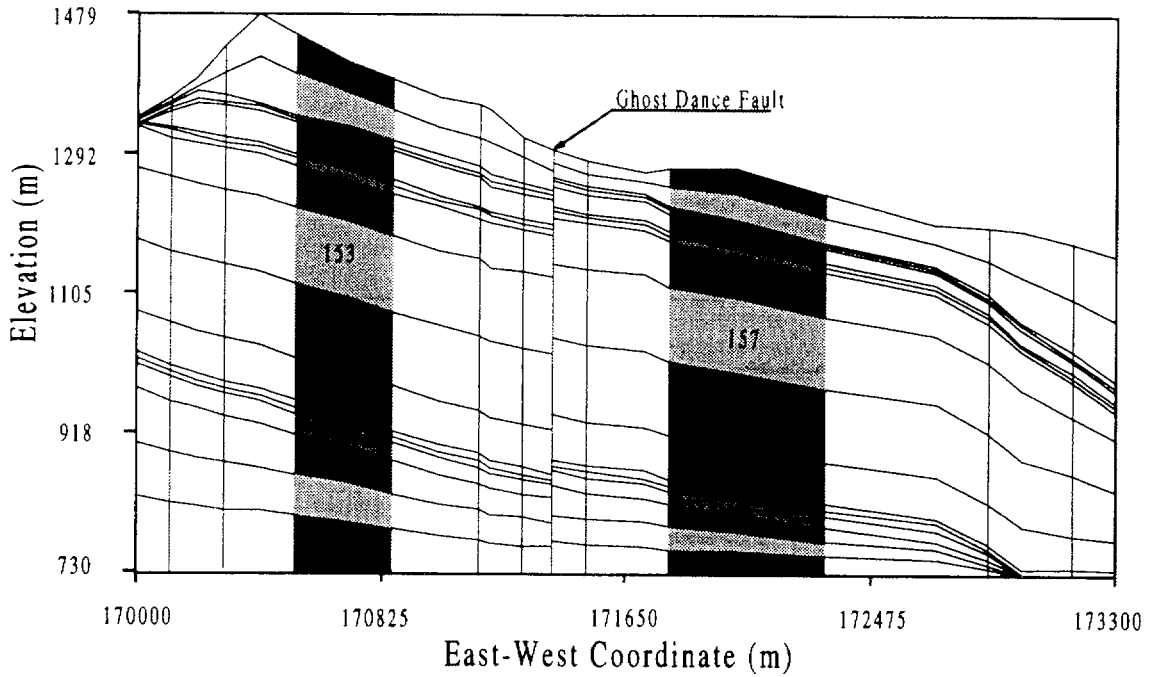
Figure ES.5-2   NW-SE cross-section extracted from the LBL-USGS site-scale model and used for hydrologic abstractions.
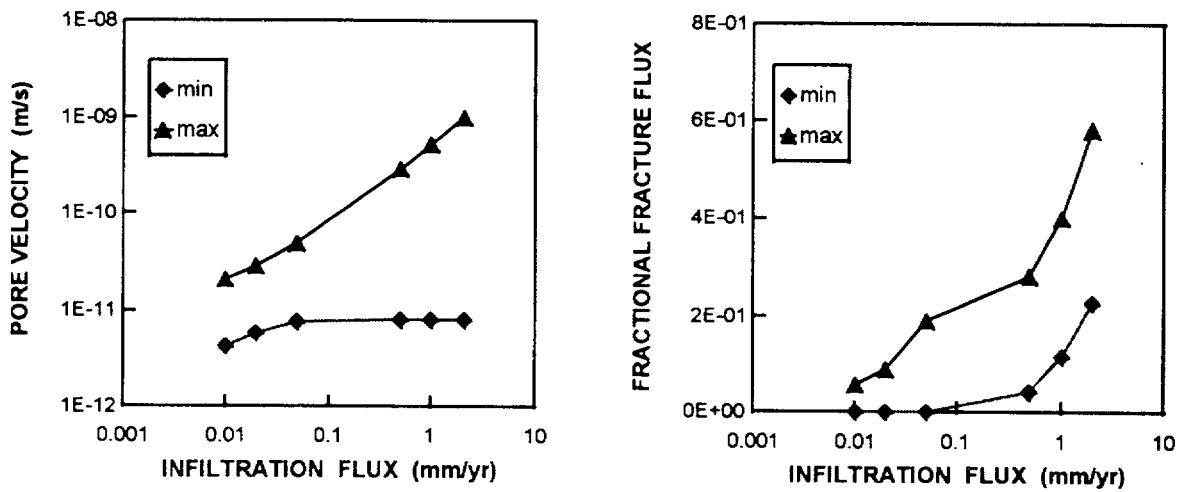
Figure ES.5-3   Abstractions of matrix pore velocity and fractional fracture flow as a function of infiltration rate for TSw.
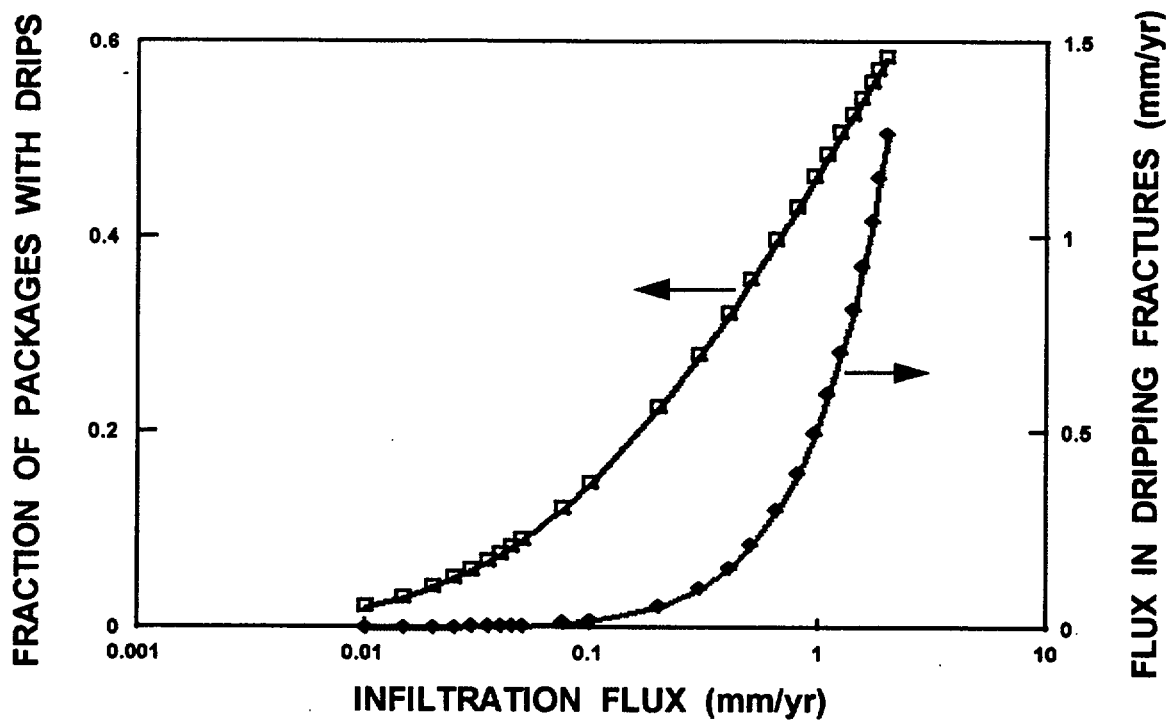
Figure ES.5-4   Drift-scale abstractions of the number of (and flux through) dripping fractures as a function of infiltration rate
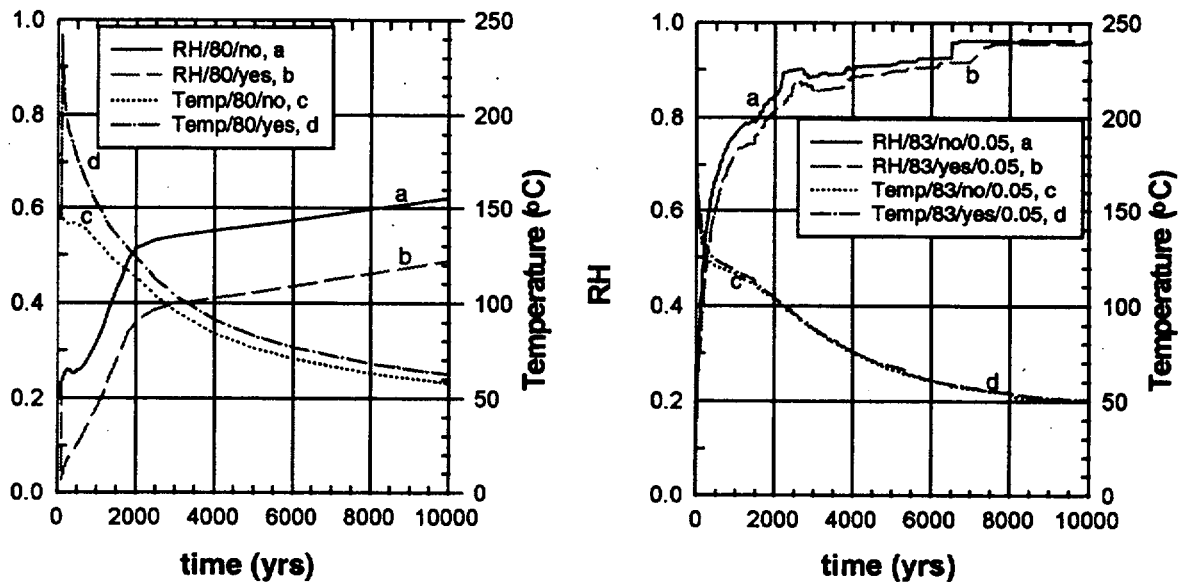
Figure ES.5-5   Comparison of temperature and relative humidities for the 83 MTU/acre, 0.05 mm/yr infiltration (this study), and for the 80 MTU/acre, 0 mm/yr infiltration (Buscheck et al., 1995).

General Corrosion of CAM in Humid Air
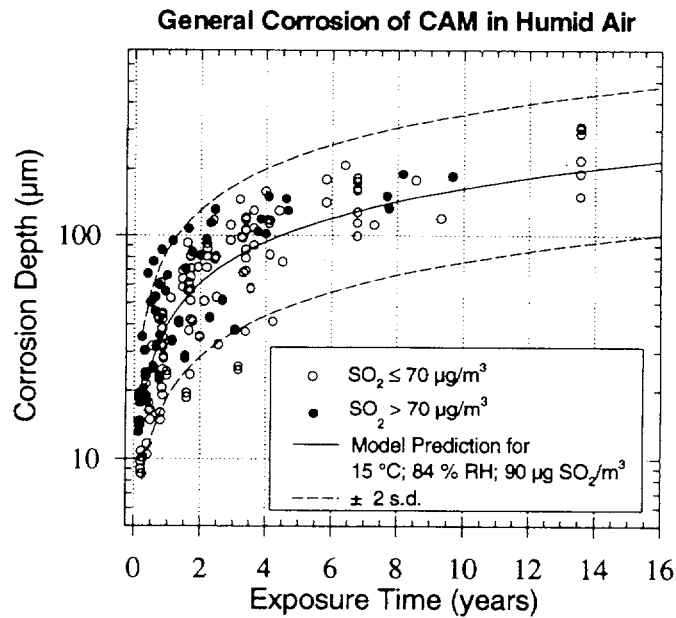
Figure ES.6-1 — Atmospheric general corrosion data used and the model estimate with its uncertainty for corrosion-allowance barrier material.

Approach to Stochastic Waste Package Degradation Simulation
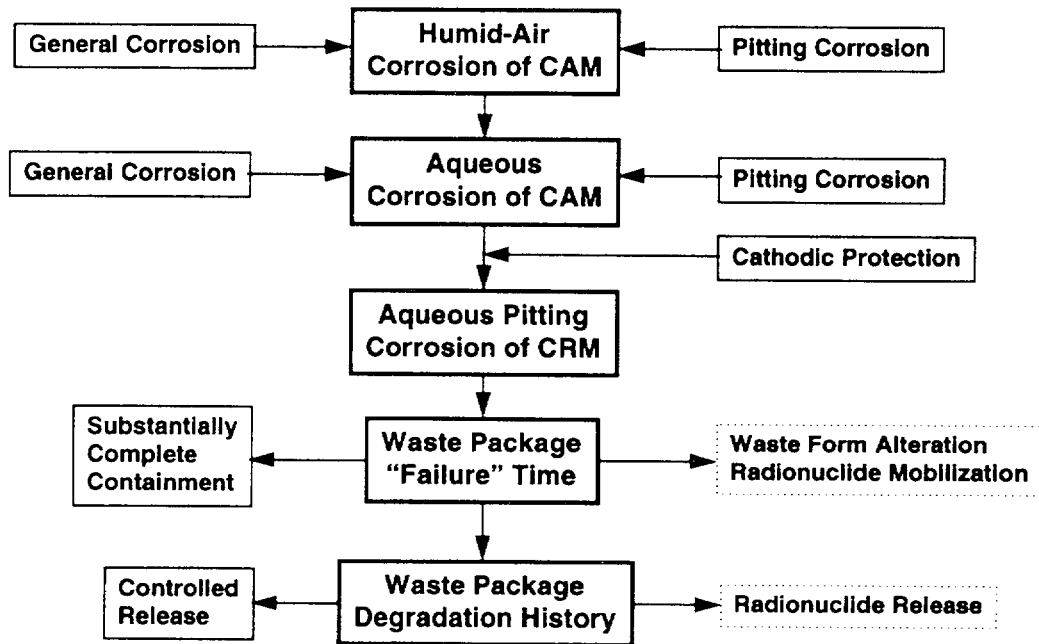
Figure ES.6-2 — Flowchart illustrating the approach to stochastic waste package degradation simulation.

Waste Package Performance vs Cathodic Protection

Legend:
- Without Cathodic Protection
- Outer Barrier Thickness Reduced by 75 %
- With Cathodic Protection

Axes: Cumulative Fraction of Failed WPs (vertical, 0.0 to 1.0); Exposure Time (years) (horizontal, 10^3 to 10^5)
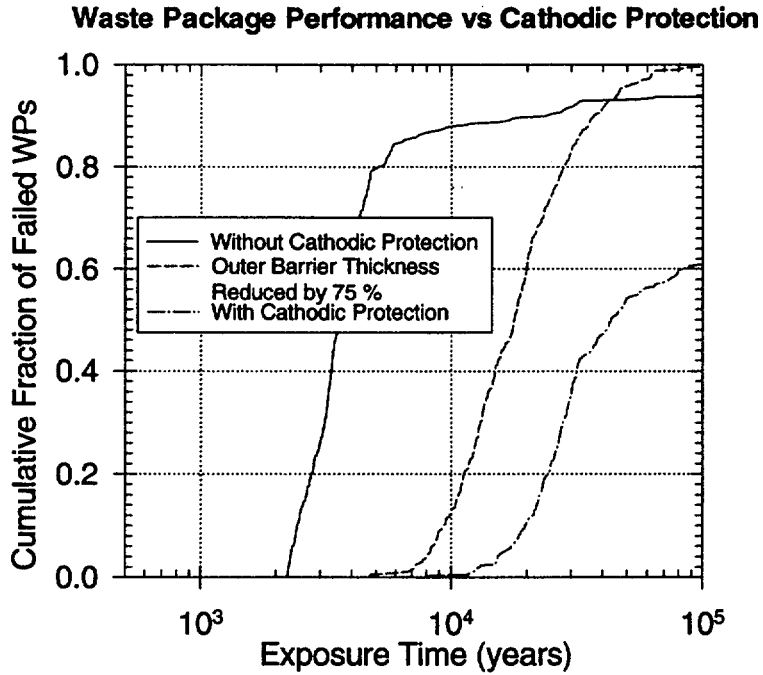
Figure ES.6-3   Comparison of waste package failure history with cathodic protection to that without cathodic protection for the case of 83 MTU/acre, without backfill and high infiltration rate.

Waste Package Perormance vs Alternative T-H Models

Legend:
- This Study
- Buscheck's Model

Axes: Cumulative Fraction of Failed WPs (vertical, 0.0 to 1.0); Exposure Time (years) (horizontal, 10^3 to 10^6)
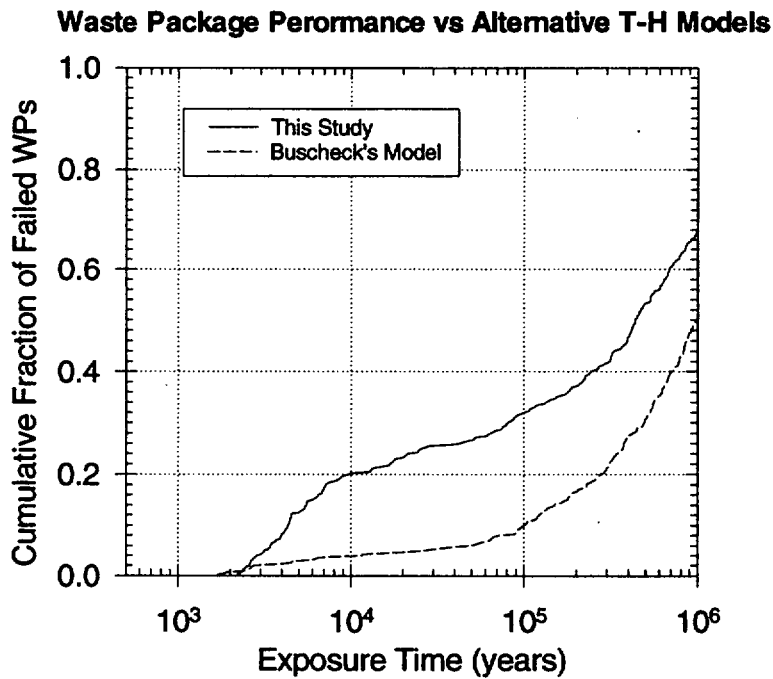
Figure ES.6-4   Comparison of waste package failure history for the case from Buscheck's model (24 MTU/acre, without backfill and no infiltration) to that for the case from this study (25 MTU/acre, without backfill and high infiltration rate).

Waste Package Performance vs Alternative T-H Models
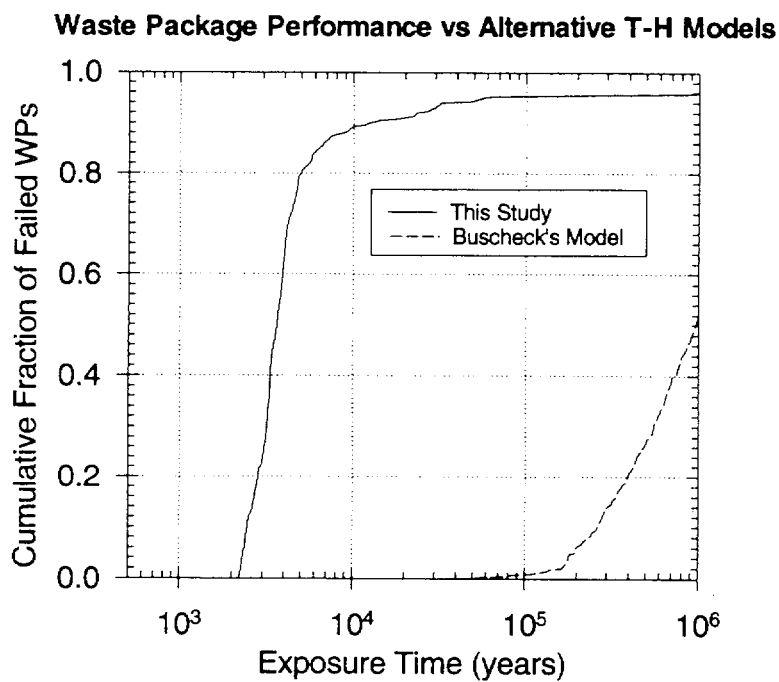
Figure ES.6-5   Comparison of waste package failure history for the case from Buscheck's model (80 MTU/acre, without backfill and no infiltration) to that for the case from this study (83 MTU/acre, without backfill and high infiltration rate).
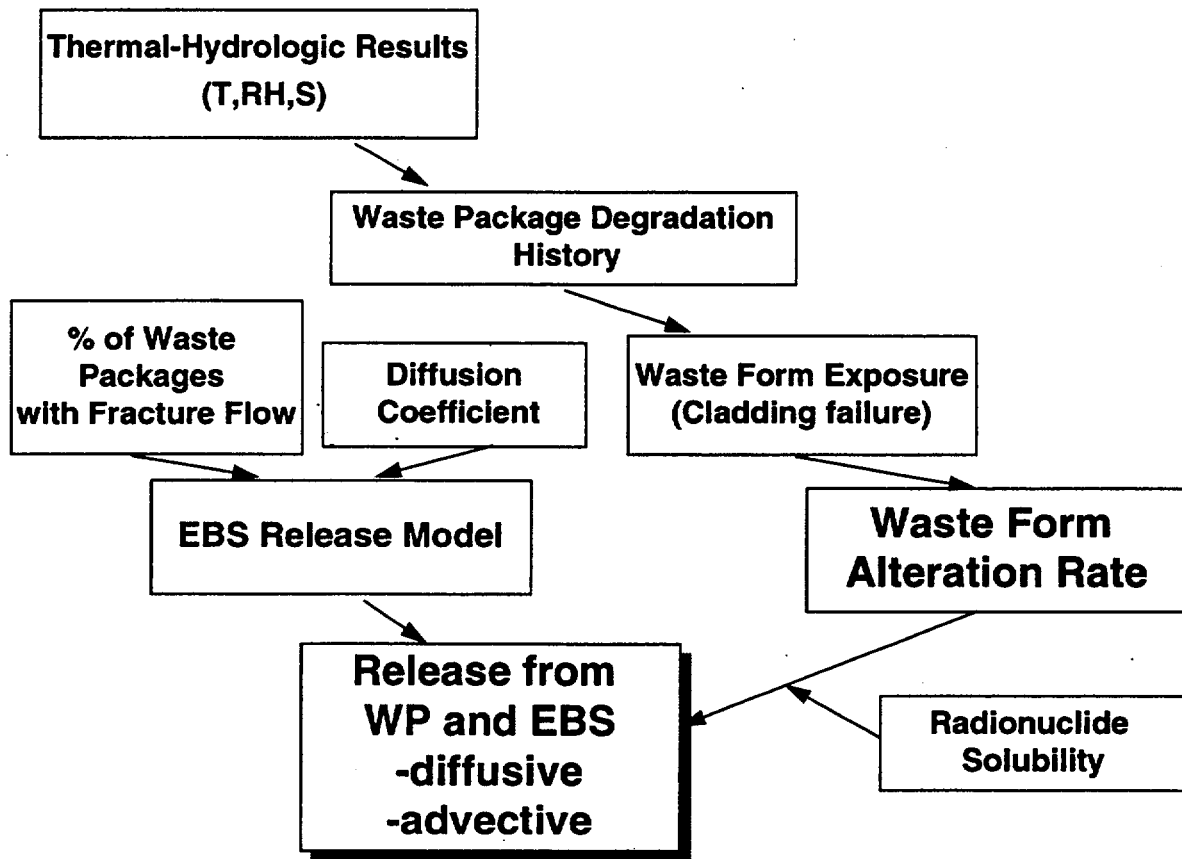
Figure ES.7-1   Engineered Barrier System Processes

**Model for Diffusive and Advective Release
from Waste Container and EBS**

Radionuclide Release
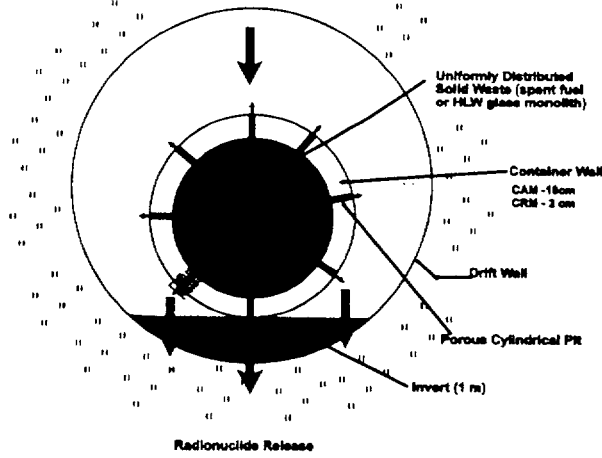
**Model for Diffusive Release from Waste Container
and Diffusive/Advective Release from EBS**

Radionuclide Release
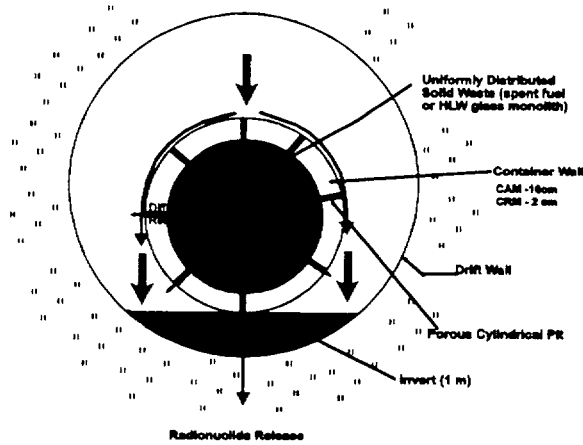
**Model for Only Diffusive Release from
Waste Container and EBS (capillary barrier effect)**

Radionuclide Release
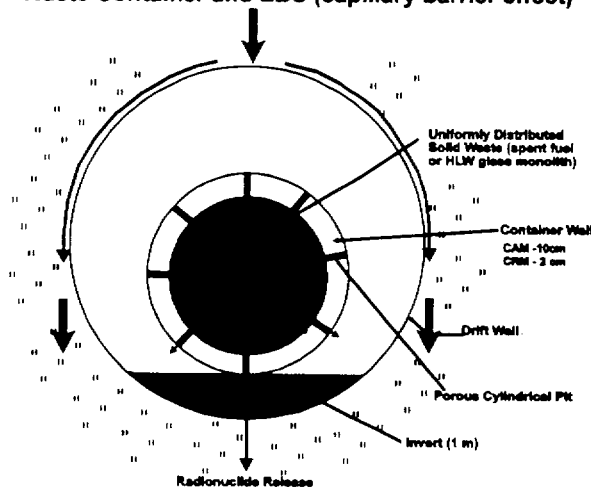
Figure ES.7-2   EBS Release Conceptual Models.
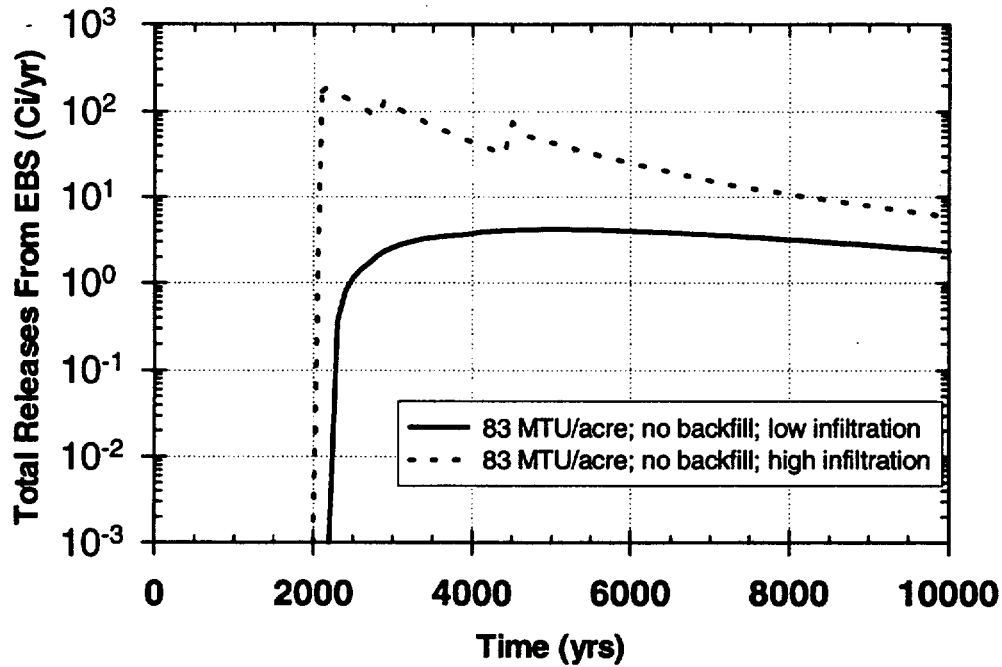
Figure ES.7-3   Predicted EBS ^{99}Tc Release Rate History: Sensitivity to Infiltration
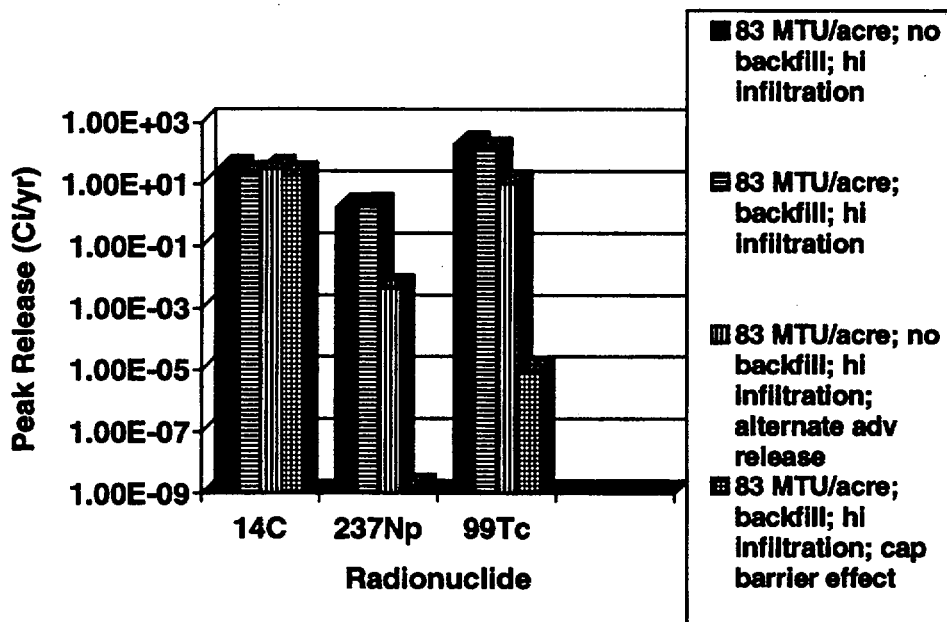
Figure ES.7-4   Predicted EBS Peak Release Rate: EBS Release Model Comparison.

Schematic of Natural Barriers

UZ percolation at repository horizon

N ←

Repository Plan View

TSw

TSv

CHv

CHz

PPn

Unsaturated-
Zone
Transport

Saturated-
Zone
Transport

Measure
Cumulative Release (Ci)
and
Peak Dose (rem/yr)
at

water well

SZ

Saturated-
Zone
Transport

Accessible
Environment
(5 km)
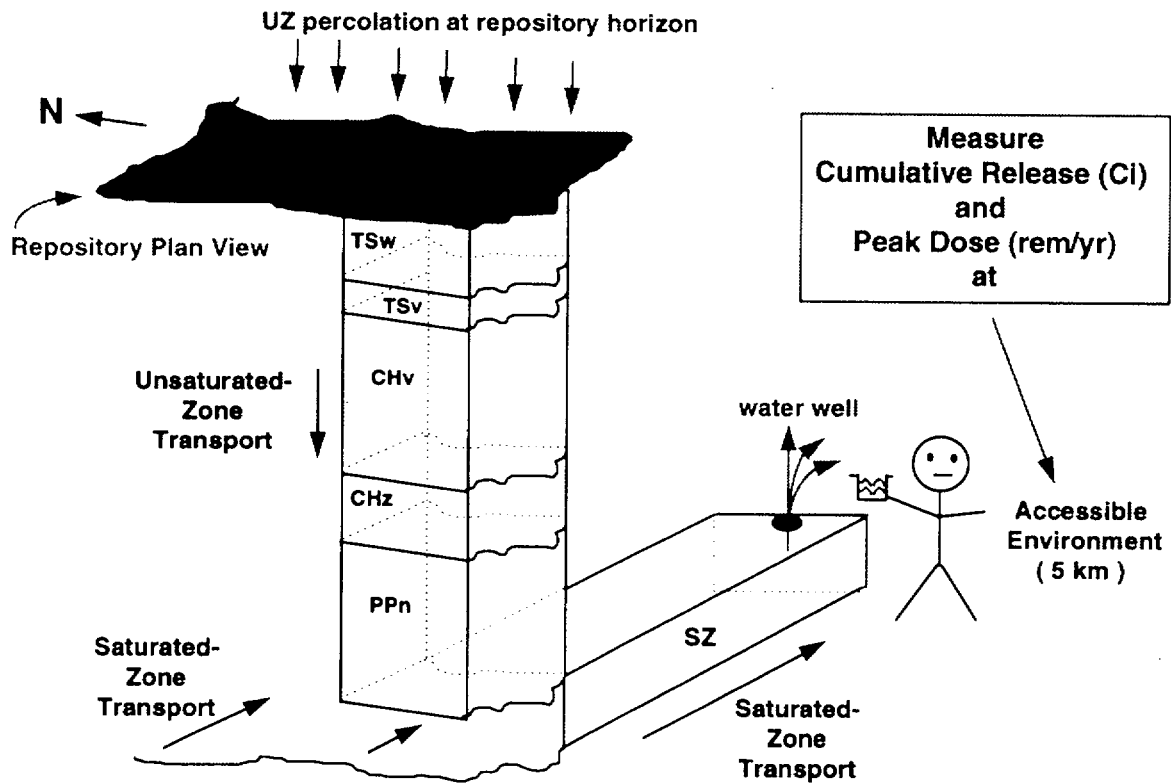
Figure ES.8-1   Schematic of Natural Barriers.

How Much?
(Fractional-Fracture-Flow Process-Level Abstraction)

TSw

TSv

CHnv

CHnz/
PPn

CHnz
Fractional
Fracture
Flux, f

f_{max}

$f_{sampled}$

f_{min}

Sampled q_{inf}

Infiltration Rate, q_{inf}

$$\frac{f_{sampled} - f_{min}}{f_{max} - f_{min}} = U(0,1)$$
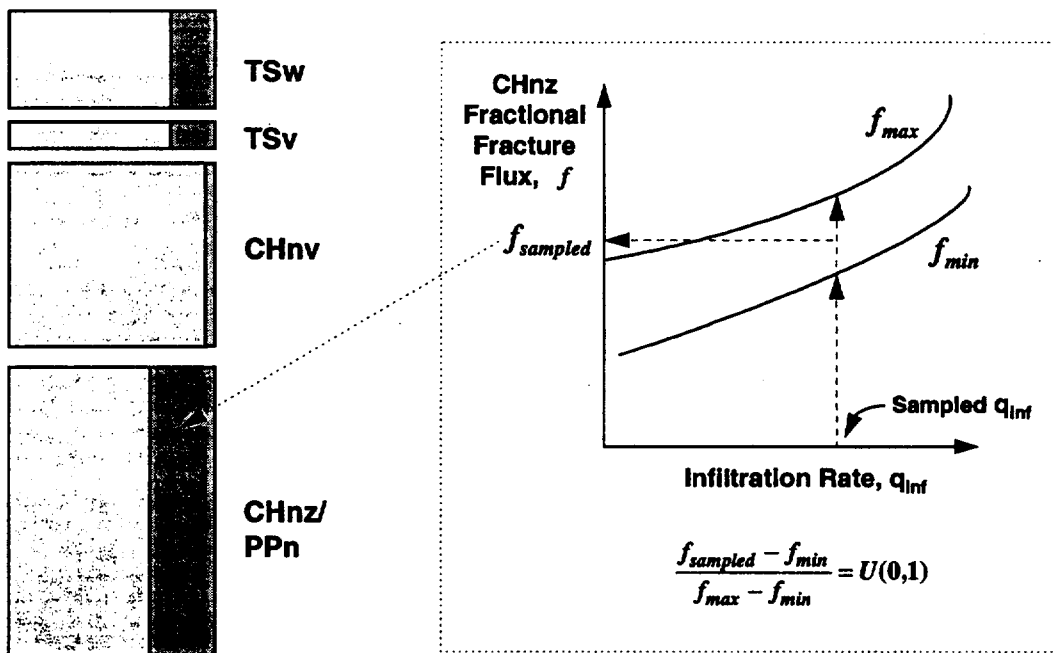
How Fast?
(Matrix-Velocity-Field Process-Level Abstraction)

TSw

TSv

CHnv

CHnz/
PPn

CHnv
Matrix
Velocity

v_{max}

$v_{sampled}$

v_{min}

Sampled q_{inf}

Infiltration Rate, q_{inf}

$$\frac{\log_{10} v_{sampled} - \log_{10} v_{min}}{\log_{10} v_{max} - \log_{10} v_{min}} = 1 - U(0,1)$$
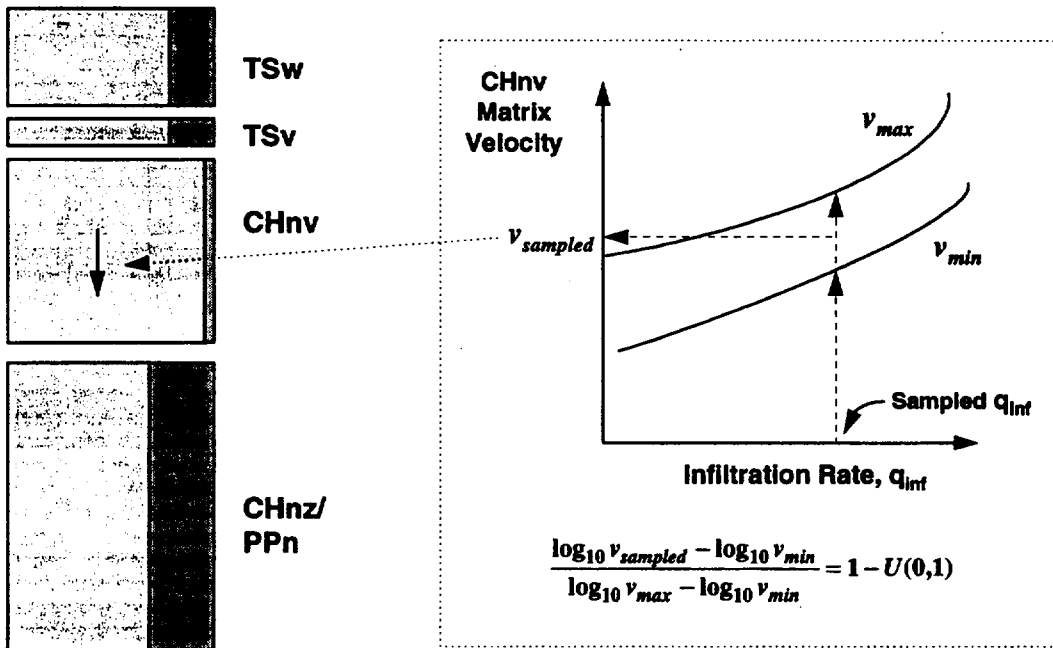
Figure ES.8-2   Schematic of proposed abstraction methodology for determining velocity and fraction of fracture flow as a function of infiltration flux, q_{inf}.

(Intra-unit Fracture Connectivity: TSPA Abstraction)

- Average path length in fracture or in matrix before transitioning is equal 1/λ, where λ is the transition rate:

$$\lambda = \frac{1}{(0.1)L} \qquad \lambda = \frac{1}{L} \qquad \lambda = \frac{1}{(100)L}$$

random travel length in fracture, $l = -\frac{1}{\lambda}\ln[U(0,1)]$

particle transition rate, $\lambda = \frac{1}{l_{avg}}$
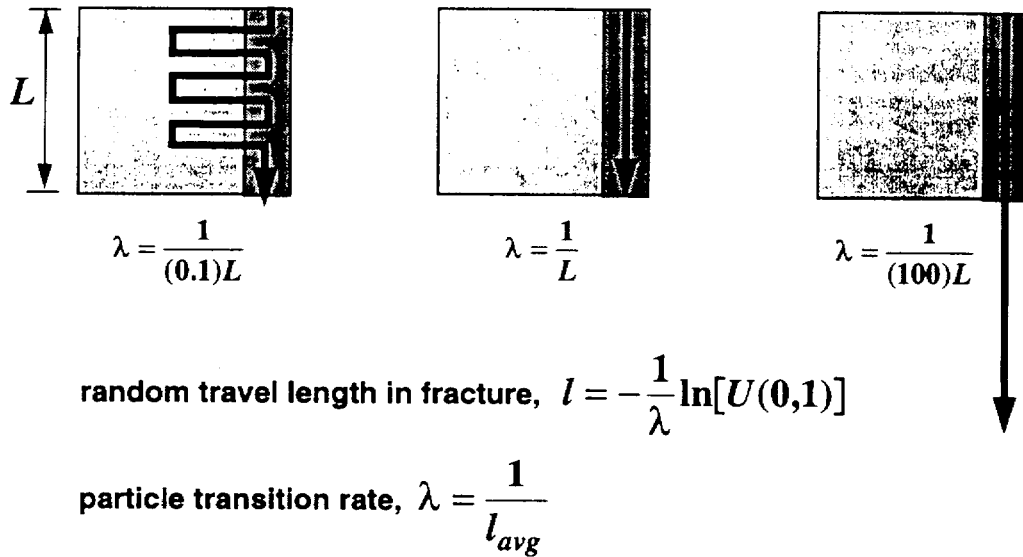
Figure ES.8-3   Schematic of fracture/matrix interaction in RIP: Markovian-particle-transitioning process to represent intra-unit fracture connectivity.

10,000-yr Total Releases
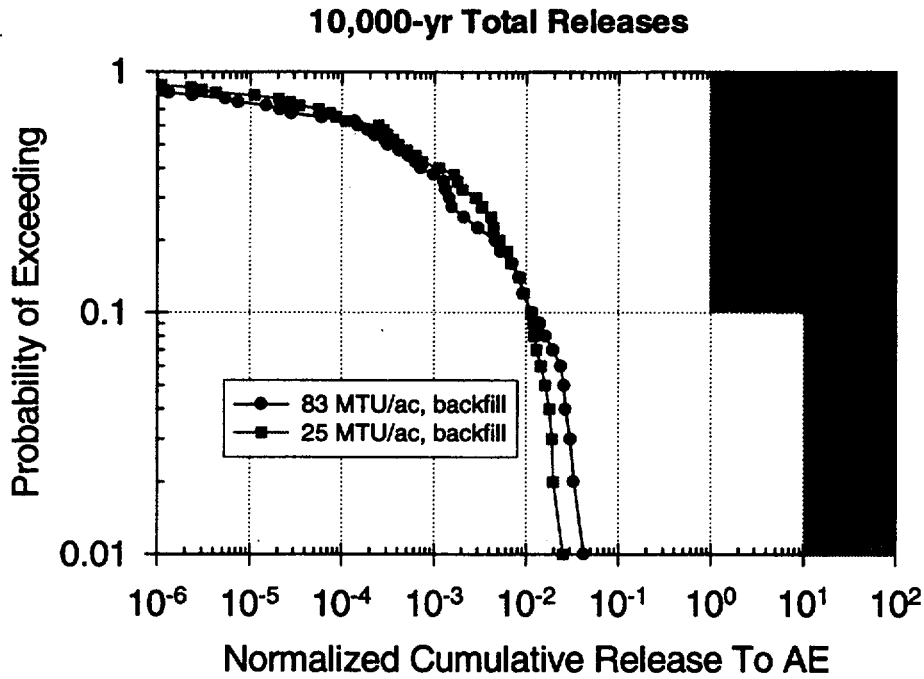
Figure ES.8-4   CCDF of Total Normalized Cumulative Release: 10,000 years, 83 MTU/acre and 25 MTU/acre, backfill, high infiltration range.

10,000-yr Total Peak Dose
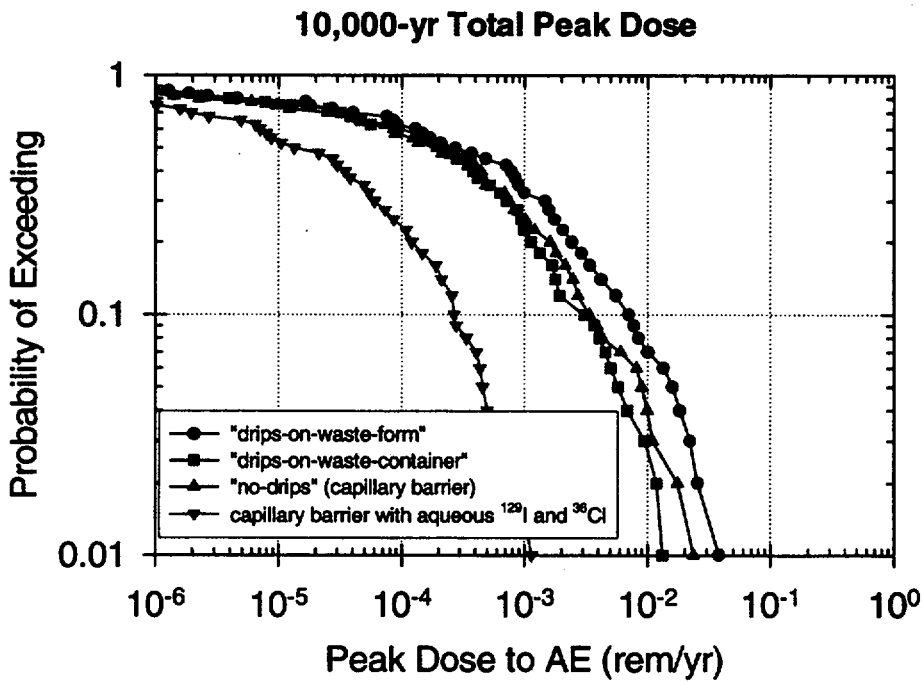
Figure ES.8-5   Comparison of EBS transport models. CCDF of Total Peak Dose: 10,000 years, 83 MTU/acre, backfill, high infiltration range.

1,000,000-yr Expected-Value Dose History
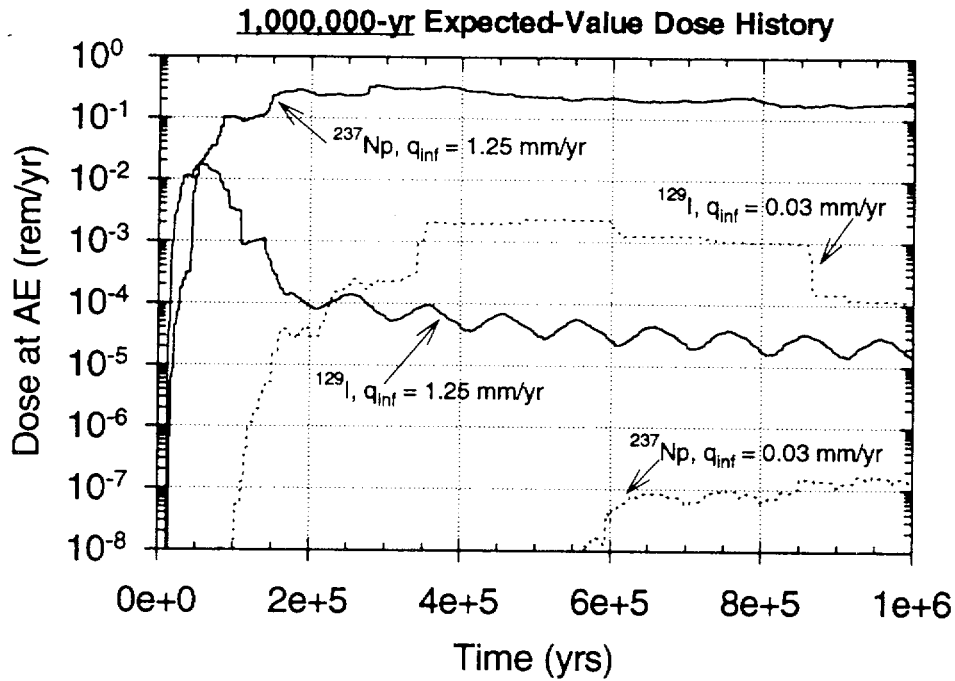
Figure ES.8-6   Expected-value dose history for ^{99}Tc and ^{237}Np. 1,000,000 years, Infiltration Rate Comparison: "high" (q_{inf} = 1.25 mm/yr) versus "low" (q_{inf} = 0.03 mm/yr) infiltration, 83 MTU/acre, backfill, cyclical-q_{inf} climate model.

1,000,000-yr Total Peak Dose
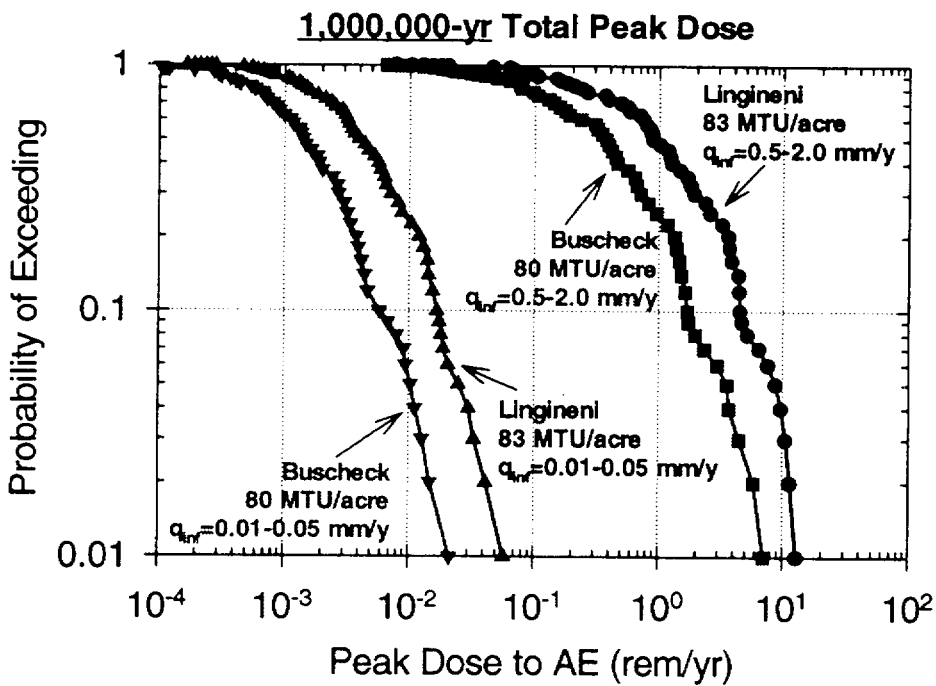
Figure ES.8-7   CCDF of Total Peak Dose: 1,000,000 years, Lingineni 83 MTU/acre and Buscheck 80 MTU/acre thermohydrologic models, <u>backfill</u>, high and low infiltration (q_{inf}) ranges, cyclical-q_{inf} climate model.

1,000,000-yr Total Peak Dose
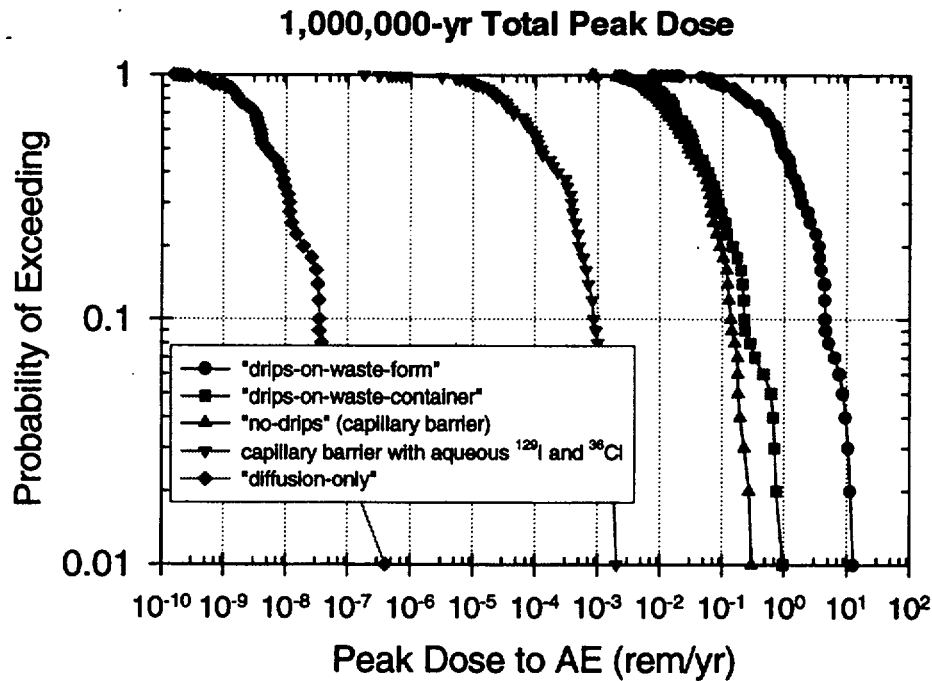
Figure ES.8-8   Comparison of EBS transport models. CCDF of Total Peak Dose: 1,000,000 years, 83 MTU/acre, high infiltration range, cyclical-q_{inf} climate model.

1,000,000-yr Total Peak Dose
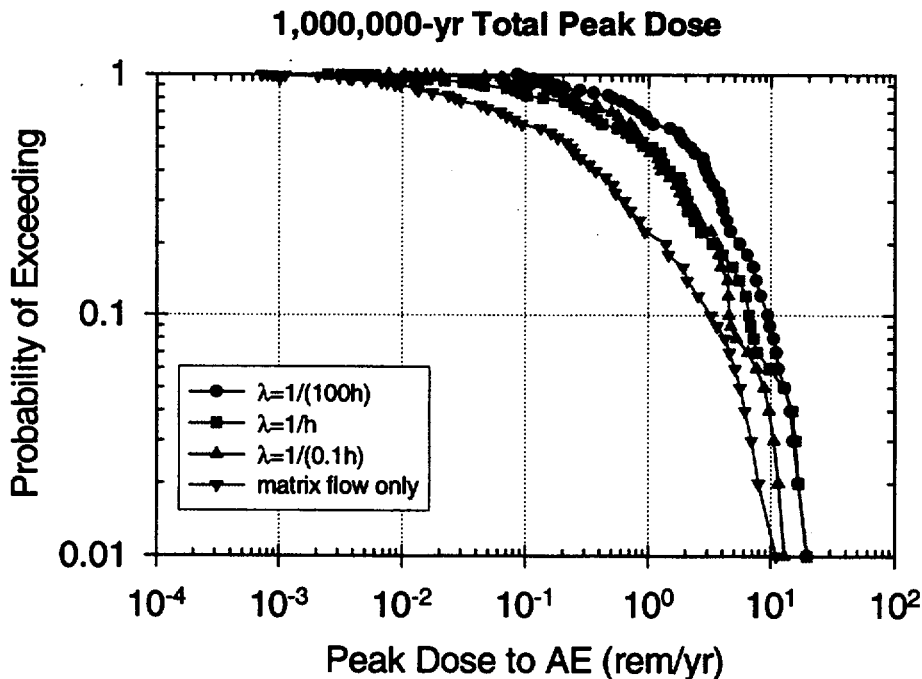
Figure ES.8-9   Comparison of intra-unit fracture connectivity parameter: $\lambda=1/(100h)$ vs. $\lambda=1/h$ vs. $\lambda=1/(0.1h)$ vs. matrix-flow-only (no fractures), where h = pathway length in each unit. CCDF of Total Peak Dose: 1,000,000 years, 83 MTU/acre, backfill, high infiltration range, cyclical-q_{inf} climate model.

high q_{inf} **range (0.5 - 2.0 mm/yr)**   **low** q_{inf} **range (0.01 - 0.05 mm/yr)**
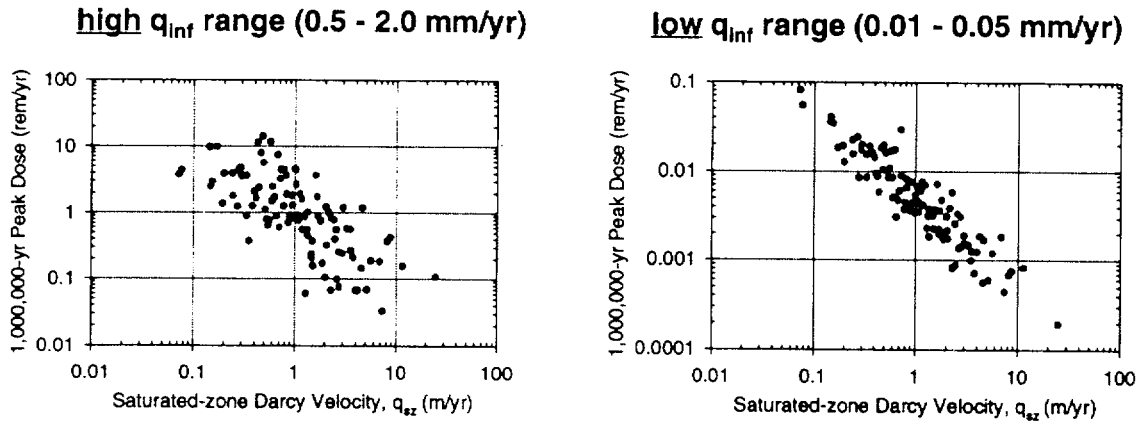
Figure ES.8-10   Sensitivity of 1,000,000-year Total Peak Dose to saturated-zone flux distribution, q_{sz}, for 83 MTU/acre, gravel backfill, climatic variation of q_{inf}.

high q_{inf} range (0.5 - 2.0 mm/yr)

Performance Measure	ln (P.M.) vs. x		ln (P.M.) vs. ln (x)	
	Rank Importance	% of variance explained	Rank Importance	% of variance explained
$U_{cli}(1,3)$	3	53	4	81
$Np\ K_d$ (TSv, CHnv)				
q_{sz}	1	23	1	48
f_{frac} CHnz				
v_{mat} CHnz				
q_{inf} (UZ)	2	45	2	65
f_{frac} TSv	5	62		
v_{mat} TSv			5	85
f_{frac} TSw			3	75
v_{mat} TSw	4	60		

Figure ES.8-11   Stepwise linear regression analysis for 1,000,000-year Total Peak Dose, high infiltration range (0.5-2.0 mm/yr), 83 MTU/acre, gravel backfill, climatic variation of q_{inf}.
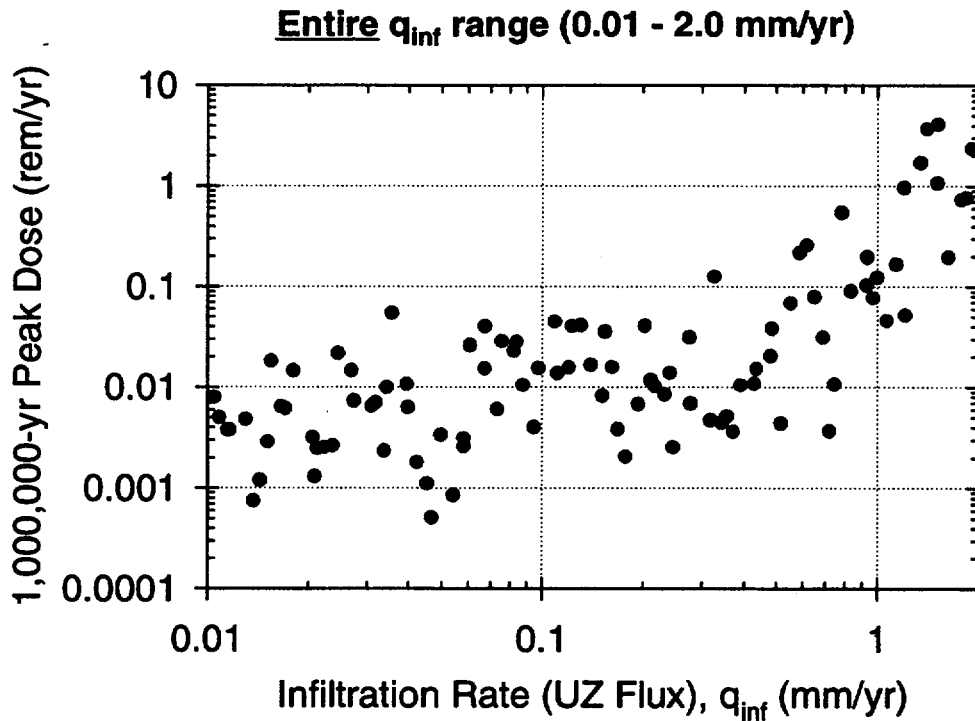
Figure ES.8-12   Sensitivity of 1,000,000-year Total Peak Dose to initial infiltration-rate distribution, q_{inf}, over broad infiltration range (0.01-2.0 mm/yr), 83 MTU/acre, gravel backfill, climatic variation of q_{inf}

Entire q_{inf} range (0.01 - 2.0 mm/yr)

Performance Measure	ln (P.M.) vs. x		ln (P.M.) vs. ln (x)	
	Rank Importance	% of variance explained	Rank Importance	% of variance explained
$U_{cli}(1,3)$	3	78	5	88
$Np\ K_d$ (TSv, CHnv)	4	80		
q_{sz}	2	75	2	74
f_{frac} CHnz				
v_{mat} CHnz				
q_{inf} (UZ)	1	64	1	50
f_{frac} TSv				
v_{mat} TSv				
f_{frac} TSw	5	81		
v_{mat} TSw			4	86
WP f_{drip}			3	83

Figure ES.8-13   Stepwise linear regression analysis for 1,000,000-year Total Peak Dose, broad infiltration range (0.01-2.0 mm/yr), 83 MTU/acre, gravel backfill, climatic variation of q_{inf}.

83YH Subsystem Releases: ^{237}Np

Release (Ci) vs Time (yrs)

Legend:
- from EBS
- from TSw
- to SZ
- AE
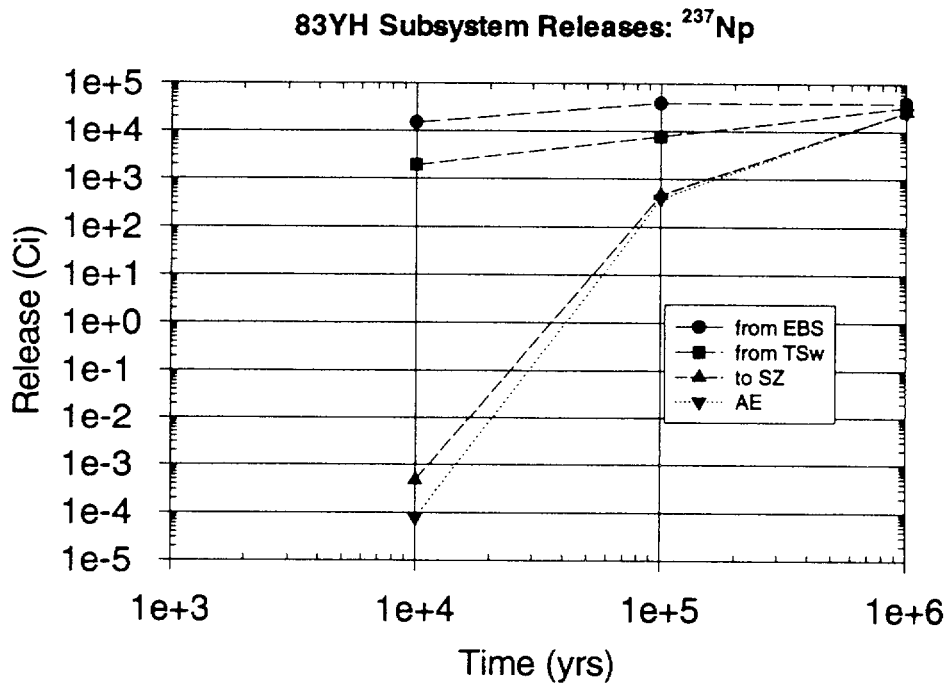
Figure ES.8-14   Subsystem total release for ^{237}Np. Expected-value release at 10,000, 100,000 and 1,000,000 years for 83 MTU/acre, backfill, high infiltration (q_{inf} = 1.25 mm/yr), no climate change, with decay.

1. INTRODUCTION

Robert W. Andrews

1.1 BACKGROUND

As required by the Nuclear Waste Policy Act, as amended, the U.S. Department of Energy (DOE) is investigating the feasibility of permanently disposing the nation's commercial high-level radioactive wastes (currently in the form of spent fuel at over 100 electric power-generating nuclear reactors) and a portion of the defense high-level radioactive wastes (currently stored at federal facilities) in the unsaturated tuffaceous rocks at Yucca Mountain, Nevada. Over the past decade, detailed investigations of the site and preliminary designs of the facility and waste packages have been undertaken by DOE contractors. These activities are aimed at evaluating the suitability of the site and the adequacy of the engineered barriers to meet regulatory standards set by the U.S. Environmental Protection Agency (EPA) and the U.S. Nuclear Regulatory Commission (NRC) to protect the public from the potentially harmful effects of ionizing radiation.

Quantitative predictions based on the most current understanding of the processes and parameters potentially affecting the long-term behavior of the disposal system are used to assess the ability of the site and engineered barriers to meet the regulatory standards. These predictions are termed performance assessments. It is the goal of performance assessment to evaluate all relevant features, events and processes that may affect the ability of the site and engineered barriers to meet the regulatory standards for containing and isolating the wastes from the biosphere.

The evaluation of the ability of the overall system to meet the regulatory standards has been termed total system performance assessment (TSPA). These analyses are distinct from the evaluation of individual components of the system (such as the period of containment associated with waste package "lifetime", the release of radionuclides from the engineered barrier system, or the isolation ability of the geologic barrier as embodied in the ground-water travel time requirement). Total system performance assessments require the explicit quantification of the relevant features, events and processes and their interactions. In addition to providing a quantitative basis for evaluating the suitability of the site to meet regulatory standards for the overall system, such assessments are useful at early stages of an investigation program to help identify the most significant processes and the information gaps and uncertainties regarding these processes and their parameters. This is essential for defining the additional information required assuring a defensible assessment of the overall system performance.

Total system performance assessment relies largely on simulations with a computer code that links mathematical models of the important features, events and processes for computing overall system performance. Because of the uncertainty in the processes and parameters, the computer code is run repeatedly with different model assumptions and parameter values in order to estimate the range of possible model outputs for the expected ranges of process and parameter uncertainty. Because of the many processes to be simulated, the many parameters involved, and the need for repeated simulations, the individual process models in a total system performance assessment code have to be simplified mathematically in order to be executed in a reasonable amount of time

and at a reasonable cost. These simplifications (also called abstractions), however, are based on more detailed models for each process that have their basis in field and laboratory tests and that can be validated with field and laboratory measurements. In total system performance assessments, both detailed process-level codes and the overall total system performance assessment code are run. The outputs of the individual process-level codes provide inputs to the total system performance assessment code, while the latter predicts overall system performance with the associated uncertainties.

Total system performance assessments explicitly acknowledge the uncertainty in the processes, models and parameters and strive to evaluate the impact of this uncertainty on meeting the overall system performance standards. A significant portion of this uncertainty is a result of the variability in site properties over the domain being considered. The effect of this uncertainty on total system performance is evaluated with a variety of sensitivity analysis techniques depending on the nature of the uncertainty in the process or parameter. In some cases, discrete sensitivity analyses are conducted, while in other cases, the sensitivity analyses are embodied directly in the stochastic simulation. In either instance, the sensitivity analyses provide useful insights that may assist managers in the prioritization of testing and design activities.

Total system performance assessments are one component of the suitability evaluation (and ultimately, licensing, if the site is found suitable) of the Yucca Mountain site and associated engineered barriers. Another component is the fundamental scientific and engineering basis for the models and parameters used in the TSPA analyses. In the overall framework, the technical underpinnings of the abstracted models used in performance assessment are based on field and laboratory tests that are interpreted, synthesized and incorporated into detailed process-level models. With respect to meeting regulatory standards, the importance of a particular model or parameter can only be evaluated quantitatively within the context of performance assessment; i.e., significance is defined with respect to the impact on performance. Conversely, the reliability or confidence in a particular model of a site or engineered component can only be ascertained with respect to the ability of the process-level model to adequately reproduce the observed conditions. Therefore, the performance assessment and site characterization/engineering-design functions progress in an iterative fashion. In each iteration, performance assessment (1) uses the most representative (and/or demonstrably conservative[1]) process level models or abstractions in order to define the most significant processes and components, and (2) site-characterization/engineering-design conducts, interprets and synthesizes test information into process-level models to increase the confidence in those models and parameters that are most significant to performance.

1.2   SCOPE OF THE CURRENT TOTAL SYSTEM PERFORMANCE ASSESSMENT

Prior to initiating an iteration of total system performance assessment, it is important to place the effort into the context of the rest of the Project's understanding of the important issues affecting the suitability of the potential site and the range of possible engineering designs. A goal of any performance assessment is to be as complete and reasonably conservative as possible, with the

---

[1]Conservative as used in this report implies that the particular model or parameter, when used in a quantitative performance assessment, leads to a prediction of poorer overall performance.

descriptions of the predictive models and parameters being sufficient for the reader to easily ascertain their technical basis. The descriptions should point to the need for additional interpretation and/or synthesis so that the basis for the model can be demonstrably shown to be conservative.

Each set of analyses of total system performance is associated with some basic objectives that define the scope of the work performed. These objectives may be broadly stated as (1) attempting to incorporate reasonably conservative representations of the relevant processes and parameters affecting total system performance, (2) evaluating a range of alternative conceptual models and parameters to explicitly address the uncertainty and variability in the current understanding and the significance of this uncertainty on the predicted performance, (3) focussing the analyses on those components of the waste containment and isolation system that are most sensitive (i.e., small changes in the model or parameter have a relatively large affect on the predicted response of the overall system) and/or most transparent (i.e., those models or parameters which are easiest to confidently demonstrate their validity for the intended purpose of predicting long term performance), and (4) evaluating the long-term performance of the engineered and site barriers using a range of possible measures of "safety" (including cumulative radionuclide releases, peak concentrations or doses, or other measures of risk to the public). Each of these general objectives is relevant to the analyses performed as part of the current iteration of total system performance.

The focus of the current total system performance assessment is on those components of the system that have been determined by previous analyses (e.g., TSPA-1993: see Wilson et al., 1994; Andrews et al., 1994) to be most significant in the predicted containment and isolation of radioactive wastes from the biosphere. Therefore, the current focus is on the engineered components of the system and on the near-field environment in which these engineered components reside. Consequently, this assessment includes (1) drift-scale thermohydrologic analyses to predict the temperature and humidity environments in the vicinity of the waste package (as these control the initiation and rate of humid air and aqueous corrosion processes) and the liquid saturation within the materials placed in the drift (as this controls the diffusive release through these materials), (2) degradation analyses of waste package localized corrosion (as this controls the time period during which the radionuclides are contained within the waste package and the effective diffusion through partially "failed" waste packages), and (3) analyses of near-field unsaturated-zone aqueous flux (as this defines the magnitude of the advective flux and controls the percentage of waste packages potentially exposed to advective flux releases).

An underlying premise in the current total system performance assessment is to be as realistic as possible, acknowledging that in many instances conservative and/or bounding assumptions are required. These bounding assessments are required when process-level models are absent or are unsubstantiated by site- or design-specific relevant observations. Increased realism is incorporated in TSPA-1995 in the drift-scale thermohydrologic analyses and the container degradation analyses for corrosion-allowance materials in a humid air environment, among others. Bounding assessments are employed to describe the cathodic protection provided by corrosion allowance material, the model for corrosion-resistant material degradation, the degradation of cladding, and the relationship between fracture and matrix flow. In each bounding assessment, sensitivity analyses are conducted to evaluate the significance of the uncertainty in the model and

1-3

the associated parameters (i.e, the potential benefit to overall performance if it could be confidently demonstrated that the conservative/bounding assumption could be replaced by a more realistic approximation).

An important issue in any performance assessment is the issue of how to best represent the uncertainty in the existing understanding of the processes affecting overall performance, as well as distinguishing between uncertainty and variability in individual parameters within the models used to describe these processes. Approximately 10,000 waste packages are currently planned for disposal in the potential repository at Yucca Mountain. These waste packages would be spread over an area of about 10,000,000 m^2. Over the spatial scale of interest, the geologic and hydrogeologic properties of significance are expected to be highly variable and it is assumed that the observed distribution in properties is representative of what might be expected at any particular location (e.g., at any of the 10,000 waste package emplacement locations). Given the large number of waste packages and the variability in material properties and local-scale environmental conditions different waste package degradation rates are expected from package to package. Additionally, given the size of each waste package, on the order of 25 to 40 m^2 the micro-environment and material property is expected to vary from location to location on each package, with the range in this variability being determined by the range in observed degradation rates on similar materials under a range of undetermined micro-environmental conditions. Whether, and how, a model or parameter is treated as uncertain or variable (or both) is discussed in the technical details of the model implementation.

All total system performance assessments strive to be as complete as reasonably possible and to include all relevant processes and parameters that may conceivably affect the overall performance of the site and engineered barriers. In the current assessments, the focus is on the engineered components and the near-field environmental conditions (in particular the thermohydrologic conditions) that affect the performance of the engineered components. Less emphasis is placed on the externally-initiated natural phenomena (such as seismic and volcanic events and tectonic processes) that may disrupt the repository if they occur. Such scenario analyses have been considered in several earlier analyses, including those conducted by Sandia National Laboratories (Barnard et al., 1992; Wilson et al., 1994), as well as those conducted by Risk Engineering, Inc. for the Electric Power Research Institute (McGuire et al., 1990 and 1992), and by the Nuclear Regulatory Commission (NRC, 1995). In all of these instances, the probability-weighted releases associated with externally-initiated natural events and processes have been insignificant in comparison to the range of releases caused by repository-induced processes. When a complete total system performance assessment is submitted for regulatory review, however, the performance-related consequences of all significant features, events and processes (collectively referred to as FEPs) will have to be addressed either quantitatively or screened based on conservative estimates of the probability or potential effects of such FEPs on components of the waste isolation and disposal system.

Many processes that may affect repository performance are complexly coupled to one another. Examples of these couplings include (1) the thermo-mechanical response of the rock mass adjacent to emplacement drifts caused by the transfer of heat away from the waste packages and the coupling of this response through a change in bulk permeability with the near-field hydrology, (2) the thermo-chemical response of the rock mass and the coupling of the resultant dissolution/precipitation reactions with the bulk permeability and therefore the near-field

1-4

hydrology, and (3) the chemical response caused by the interaction of the ambient mineralogy and aqueous geochemistry with the introduced anthropogenic materials placed in the drifts. Although these couplings could be incorporated into predictions of system performance, their effects are probably insignificant, primarily because the variability in ambient (i.e., unperturbed by the presence of the drifts) hydrogeologic and geochemical properties accounted for in the analyses already encompasses the changes induced by the coupled processes. As a result, these complex process couplings are not included explicitly in this iteration of total system performance assessment.

1.3   OBJECTIVES OF THE CURRENT TOTAL SYSTEM PERFORMANCE ASSESSMENT

Several analyses of the overall system performance of the Yucca Mountain site and associated engineered barriers have been conducted by DOE contractors over the past several years. The most recently completed iteration of total system performance assessments is documented in Wilson et al., (1994) and Andrews et al., (1994). Other studies have built upon these documents by conducting sensitivity analyses addressing particular technical issues associated with the earlier analyses. For example, M&O (1994a) evaluated the effect of drift-scale thermohydrologic conditions on the degradation of waste packages, the release of radionuclides from the engineered barrier system to the host rock, the radionuclide release to the accessible environment, and the radiation doses to maximally-exposed individual. M&O (1994a) also examined the peak release rate from the engineered barrier system for a range of alternative thermal loads. In addition, analyses were performed with alternative unsaturated- zone flow and transport conceptual models and parameter values in support of the systems study that evaluated options for characterizing the Calico Hills hydrogeologic unit (M&O, 1995d).

The specific goals of the current iteration of total system performance assessment are to (1) utilize what are believed to be more representative conceptual models that build upon the assumptions employed in TSPA-1993, in particular for the treatment of the engineered barrier system including the waste package, (2) incorporate more recent design information since the completion of TSPA-1993, (3) utilize the most recent site information and models (where available) acknowledging their uncertainty and variability, and (4) evaluate the engineered barrier system release performance measure as well as alternative measures of total system performance (cumulative release and peak dose over different time periods)[2], and the correlation between these measures of performance. Each of these goals is discussed in the following paragraphs.

In the concluding comments of TSPA-1993 (Andrews et al., 1994), the need to use more representative process-level models and to incorporate their corresponding abstractions into the total system code was noted in order to increase the realism of the analyses. In particular, the

---

[2]Alternative time periods have been proposed by various regulatory bodies in different countries concerned with the ultimate disposal of high-level radioactive wastes containing very long-lived radionuclides. A recently completed study commissioned by the National Academy of Sciences (NAS, 1995) has recommended a time corresponding to the arrival of the peak dose to average members of a critical group, where this time may be several tens to hundreds of thousands of years.

definition of the very near field (drift-scale) thermohydrologic environment and the effect of this environment on the initiation and rate of aqueous corrosion was identified as a key uncertainty warranting additional predictive ability. Towards this end, the present TSPA iteration includes drift-scale thermohydrologic analyses with response surfaces that were fit to the temperature, relative humidity and liquid saturations in the drift materials. In addition, TSPA-1993 identified the degradation models of both the corrosion-allowance and corrosion-resistant waste package materials as requiring more technical substantiation from either direct laboratory measurements or analog observations. Although TSPA-1995 revises the model of localized corrosion of the corrosion-allowance material substantially (with the bases being developed from empirical fits to observations of corrosion of similar materials under similar environments), it employs the same model used in TSPA-1993 for the corrosion-resistant layer due to a lack of any specific information on this material since then. Finally, it was noted in TSPA-1993 that the process-model understanding of localized advective flow in the unsaturated zone needed to be substantiated. Although there is no better indication of the potential for localized advective flux than existed then, TSPA-1995 includes additional process model analyses in order to try to quantify the likelihood and amount of localized advective flux.

Both the repository and waste package designs have evolved since the completion of TSPA-1993. The bases for repository and waste package designs used in this iteration of total system performance assessment have been derived from the conceptual design information documented in the Conceptual Design Assumption Report (M&O, 1995c). Alternative designs continue to be developed and evaluated by the design organizations of the M&O with respect to their cost and schedule impacts. One of the purposes of performance assessment in general, and this iteration of total system performance assessment in particular, is to evaluate the performance implications of some representative subset of the alternative designs that are being explored. For example, the current TSPA iteration uses both a high and a low thermal load, evaluates the implications of using backfill or not (with or without the use of the backfill as a capillary barrier). The previous iteration of TSPA documented in Andrews et al., (1994) examined the effects of alternative waste package material thicknesses for both the outer corrosion allowance layer and the inner corrosion resistant layer. Many factors go into the decision of the final design of any waste repository and the associated waste packages that are independent of their consequences on performance. Trade-off studies between cost, constructability, and performance are required to define the optimum design. The design decisions of significance to post-closure performance include the thermal load, the presence or absence of backfill, the use of ventilation during the pre-closure performance monitoring period, the drift size, the number of fuel assemblies within each waste package, and the thickness and materials selected for the waste package corrosion-allowance and corrosion-resistant layers. In TSPA-1995, only the first two of these issues were directly evaluated in the analyses.

Significant advances have been made in the site characterization program since the completion of TSPA-1993. In particular, preliminary estimates of surficial infiltration rates based on observed steady-state matrix water contents, assumed matrix characteristic curves, and assumed hydraulic gradients have been generated by Flint and Flint (1994). Also, analyses incorporating the potential effect of fracture-initiated infiltration have recently been presented by Flint (1995).

In addition, the preliminary site-scale unsaturated zone flow model[3] which aims to synthesize all available hydrogeologic information into a self-consistent representation of the average unsaturated-zone flow regime, has recently been published by Wittwer et al., (1995). Additional characterization efforts have been focused on reducing the uncertainty in some of the key geochemical parameters, including the solubility of neptunium, as well as providing more representative estimates of radionuclide retardation. These new site data are considered in the current TSPA.

The unsaturated-zone aqueous flow system is a critical component of any assessment of system performance. Two aspects of the flow system are important: on one hand, the distribution of volumetric flux through the unsaturated zone in general, and the magnitude of the localized percolation flux in the vicinity of the potential repository drifts in particular, are important as they significantly affect the near-field hydrologic environment and ultimately the releases from the engineered barrier system; on the other hand, the distribution of advective velocities (along with other transport processes such as matrix diffusion and retardation) significantly affects the rate of release of radionuclides to the saturated zone. Therefore the distribution of localized unsaturated-zone flow pathways that might have high advective velocities (i.e., be "fast" paths) is a significant consideration in the overall performance assessment. Recently interpreted isotopic evidence for ground-water residence times in the unsaturated zone at Yucca Mountain (Kwicklis, 1994; Fabryka-Martin, 1995) indicate the potential for "fast" paths through the unsaturated zone. Although these data and interpretations are ambiguous (i.e., alternative interpretations of the same information yield the possibility that there are no "fast" paths in the aqueous phase in the unsaturated zone), the potential for "fast" advective paths caused by, among other aspects, localized increases in the percolation flux, needs to be accommodated in the total system performance assessment. The approach taken in the current TSPA iteration to address the issue of localized percolation fluxes and "fast" paths is discussed in Chapter 7.

A number of different measures of system and subsystem performance have been postulated by various regulatory agencies. The degree to which any of these performance measures, if they were met, would ensure adequate protection of human health and the environment over the time period the radioactive wastes could pose the most severe hazard, is a societal issue beyond the scope of the present document. An important aspect of performance assessment is to quantify the expected performance using different measures of "safety" (and the corresponding uncertainty in the expected performance) and to determine the relationship, if any, between the different measures. It is not inconceivable, for example, to have a "poor" predicted performance of a particular subsystem, such as defined by the peak release rate from the engineered barrier system, while the total system performance as defined by the peak dose to a maximally-exposed individual is well below the levels of concern to society. In the present performance assessment, the waste package lifetime (as defined by the time the first localized pit penetrates the multi-layer waste package), the peak EBS release rate, the cumulative release at the edge of the accessible environment (assumed to be 5 km down gradient from the potential repository), and the peak dose to the maximally exposed individual located at the accessible environment boundary are all evaluated.

---

[3] The preliminary site-scale unsaturated-zone transport model has been documented concurrently with the completion of this TSPA-1995 report (Robinson et al, 1995).

1.4 ANALYSIS COMPONENTS AND INFORMATION FLOW IN THE CURRENT TOTAL SYSTEM PERFORMANCE ASSESSMENT

1.4.1 System and Analysis Components

Total system performance assessments bring together all relevant components of the waste containment and isolation system that potentially affect the release of radionuclides to the accessible environment and the corresponding radionuclide concentration and radiation dose associated with the release. The individual components of the analyses are indicated on the schematic flow diagram illustrated in Figure 1.4-1. Each of the bubbles of the influence diagram corresponds to a process-level model, which in turn is based on direct laboratory or field data that have been synthesized using either an empirical relationship (as in the case of observations of generalized corrosion rates of corrosion allowance materials, waste form alteration/dissolution rates, and radionuclide solubilities among others) or a numerical relationship describing the process of interest. The general flow of information between the different model domains is illustrated in Figure 1.4-2. In this depiction, the boundary conditions of one domain are provided by the output from the preceding domain. For example, the repository-scale percolation flux (q) is derived from the results of the site-scale unsaturated- zone flow model. Similarly, the source term for radionuclide transport in the unsaturated zone is provided by the calculated release from the engineered barrier system. Other parameters that are transferred between domains include the temperature (T), liquid water saturation (Sw), chemical composition (C), and mechanical stress (σ).

A sketch of the multiple barriers associated with waste disposal in the unsaturated zone at Yucca Mountain is presented in Figure 1.4-3. The engineered barrier components contributing to waste isolation and containment are illustrated in Figure 1.4-4. All of the above figures serve to orient the reader towards the many components and the corresponding processes, models and parameters required to construct a comprehensive total system performance assessment that aims to capture the relevant aspects that influence the predicted performance.

1.4.2 Analysis Hierarchy

Performance assessments for underground repository systems typically consist of several levels of analyses, ranging from the detailed representation of individual processes to analyses of the entire waste disposal system. This model hierarchy is shown in Figure 1.4-5. The base of the pyramid corresponds to independent phenomenological modeling of processes acting within the engineered or the geologic components of the system. The top of the pyramid corresponds to the abstracted representation of processes that are used to evaluate the effects of various scenarios on total system performance.

For each detailed process/conceptual model, there exists a corresponding, albeit abstracted, version for the purposes of total system performance assessment. The need for abstracted (i.e., simplified) models originates from the complexities inherent in total system assessments due to the coupling between various processes/sub-systems, parameter and model uncertainties, spatial and temporal variabilities, and multiplicity of designs and future scenarios. The use of probabilistic performance assessments to evaluate regulatory compliance of complex systems within current computational capabilities also necessitates some degree of simplification within

the abstracted models. Codell and Sagar (1995) discuss various approaches for model abstraction currently being used by the performance assessment community, viz., (1) intuitive simplification, (2) equivalent parameters, (3) direct propagation of variability and uncertainty, (4) integration, (5) dimensional analysis, and (6) empirical models based on full models.

For the purposes of TSPA-1995, the word *abstraction* is used to connote the development of a simplified/idealized process model (with appropriately defined inputs) that reproduces/bounds the results of an underlying detailed process model. The inputs for the abstracted model can be a subset of those required for the detailed process model. Alternatively, intermediate results from the detailed process model can be analyzed to develop "response functions" which can then be used as inputs to the abstracted model. In either case, it is necessary to demonstrate that predictions of both the detailed process model and the abstracted model are reasonably similar.

The assessment of total system performance is based on results derived from process-level models which in turn are based on direct observations or interpretations of laboratory and/or field tests. The flow of information used in the current TSPA iteration from "data" to process-level models (where applicable), to abstractions of process-level models (where applicable), and finally to the total system performance assessment itself, is illustrated in Figure 1.4-6. This figure will be revisited at the beginning of each chapter to orient the reader as to the topics of the particular chapter.

1.4.3   Information Flow

The flow of information in any assessment of total system performance starts from test data and the corresponding interpretation and documentation of these data, the use of process-level models to synthesize the available test data and other information into a consistent representation of the relevant processes affecting waste isolation and containment, the abstraction of results from these process-level models in the form of response surfaces, table look-ups or other functional relationships for use in the total system performance assessment software, and finally, the total system performance assessments themselves. In many cases the information derived from field and laboratory testing is used directly in the analyses rather than going through the process-level model and abstraction steps. Examples of information derived from laboratory experiments include alteration/dissolution rates of the waste form, solubility of individual radionuclides, and radionuclide sorption values. Examples of information derived directly or indirectly from field measurements include hydrogeologic unit thicknesses and surficial infiltration rates. In many other instances, however, predictive models are required to provide results that can become input to the TSPA analysis. Examples of these include unsaturated- and saturated-zone flow, drift-scale thermal hydrology, and waste package degradation. In these instances, the results from the process-level model simulations are used to define the relationship between the "known" parameters, including their corresponding uncertainty and spatial variability, and the required results used as input to the TSPA calculations. The detailed process modeling is required for these analyses because it is not possible to either (1) simplify the process model sufficiently for meaningful predictions in the total system code or (2) efficiently imbed the coupled process model itself into the total system performance code and make the repetitive simulations required of the probabilistic analyses.

It is important to bear in mind that the TSPA calculations are conducted in a probabilistic or stochastic fashion in order to attempt to capture the uncertainty and variability in the processes and the corresponding parameters so that the significance of this uncertainty on the predicted performance can be evaluated. Performance assessments attempt to explicitly include uncertainty and variability in the analyses through the use of parameter distributions covering the range of observed or inferred conditions.

1.4.4 Regulatory Implications

Although several alternative measures of performance could be evaluated to quantify the ability of the site and associated engineered barriers to isolate radioactive wastes from the biosphere over the extended periods of time that the wastes pose the greatest environmental and health risks, the present analyses focus on two measures of total system performance. These performance measures are (1) the cumulative release of radionuclides at the accessible environment boundary normalized to the limits presented in Table 1 of 40 CFR Part 191, and (2) the maximum radiation dose to an individual[4] using groundwater derived from a well into the tuff

---

[4] It is important to point out that the potentially exposed population defined by the "critical group" mentioned in the National Academy of Sciences (NAS) recommended standard for high-level radioactive waste disposal at Yucca Mountain, is based on existing land and water use patterns in the vicinity of the Yucca Mountain potential repository site. At present the closest members of the public are about 20 kilometers from the potential repository. Individuals that are downgradient from the site rely on water primarily derived from the alluvial aquifer, not the tuff aquifer. The correlation between the calculated peak individual doses evaluated in this total system performance assessment, the peak individual doses presented previously in TSPA-1993 (Wilson et al., 1994; Andrews et al., 1994), and the analyses conducted in support of the Calico Hills Systems Study (M&O, 1995d)) should not be construed to represent the peak dose associated with the average individual of a "critical" population. The NAS committee has recommended that the definition of the "critical" population be developed as part of the EPA rulemaking process in repromulgating the environmental standards applicable to the Yucca Mountain potential repository site. Although performance assessment could be used to evaluate the effect of alternative definitions of this "critical" population, such analyses are beyond the scope of the present document due to the short time available between the release of the NAS recommendations on August 1, 1995, and the due date of the draft TSPA-1995 documentation of August 31, 1995. It is recommended that (1) alternative biospheres utilizing the concept of a "critical" population be defined, (2) alternative saturated-zone travel paths and associated mixing, dilution, and lateral and transverse dispersion be analyzed and (3) the assumptions and results be compared with the present analyses. When this comparison is completed, the reader should have a better understanding of how different definitions of the biosphere affect the absolute value of the predicted peak dose. Until such time, great care should be used in interpreting the peak dose of the maximally-exposed individual of the current analyses. They should not be interpreted on the basis of the NAS recommended biosphere. Additional comments regarding the potential significance of the NAS recommendations are presented in the concluding remarks of this document (Chapter 10).

aquifer at the accessible environment boundary. For consistency, the definition of the "accessible environment" in both instances is assumed to correspond to a location in the saturated zone, five kilometers downgradient from the edge of the potential repository.

In addition to the analysis of alternative measures of total system performance, these predictions can be made over a range of times following closure of the repository. In order to provide a comparison to the remanded EPA standard presented in 40 CFR Part 191, the normalized cumulative release is calculated over the first 10,000 years after waste emplacement. Given the EPA direction to evaluate the cumulative release over 10,000 years, this same time period has been chosen to evaluate the peak individual dose (this is consistent with the revised EPA standard in 40 CFR Part 191 that is only applicable to the Waste Isolation Pilot Plant). Also in this study, analyses of peak individual dose have been extended to 1,000,000 years to predict the time of occurrence of the maximum dose. This time period was mentioned in the NAS recommendations on applicable Yucca Mountain environmental standards. NAS based this time period on earlier performance assessment calculations (Wilson et al., 1994; Andrews et al., 1994), which showed that the predicted peak doses occurred several tens to hundreds of thousands of years following waste emplacement (with the predicted time of occurrence of the peak depending primarily on the advective flux within the unsaturated zone). Because this time period is generally sufficient to ensure the arrival of the most significant radionuclide peaks given virtually all reasonable estimates of advective flux except for the lowest possible values, it appears to be adequate for the relative comparison of peak dose or risk.

While integrated release or peak dose (or other surrogates of these performance measures such as cumulative population dose, peak concentration, peak individual risk or health effects) are generally accepted as being appropriate total system performance measures of long-term safety associated with the containment and isolation of radioactive wastes, the NRC has promulgated additional requirements on three subsystems. These subsystems include (1) the waste package itself [substantially complete containment, 10 CFR 60.113(a)(1)(ii)(A)], (2) the engineered barrier system [maximum release rate, 10 CFR 60.113(a)(1)(ii)(B)], and (3) the geosphere [ground-water travel time, 10 CFR 60.113(a)(2)]. The first two of these subsystems are directly quantified in the definition of the source term used in the total system performance assessment. In fact, they are prerequisites to the calculation of releases and doses at the accessible environment, with the waste package containment having to be breached and radionuclides released from the engineered barrier (the cladding, the waste form, the waste package itself and the materials placed under or around the waste package) before any transport in the geosphere occurs. Therefore, predictions of the performance of these engineered barrier components are also addressed in this document (Chapter 5 for substantially complete containment and Chapter 8 for peak release rate from the EBS). The ground-water travel time performance measure could be evaluated as a component of the total system performance assessment, but separate analyses of this geosphere subsystem requirement precluded the need to include these in this document. The interested reader is referred to Arnold et al., (1995) for a discussion of preliminary analyses of ground-water travel time.

1.4.5   Waste Package Processes

Given that the waste packages must "fail" (i.e., be breached to an extent that the mobile water present in the near field environment can ingress into the package and any dissolved

radionuclides can be transported out of the package) before any dissolution of the waste form can occur, an important first step in total system performance assessment is the prediction of waste package degradation. The degradation rate of the waste package is dependent on (1) the waste package design (in particular, the material(s) used in the waste package fabrication and the thickness of these material(s)), (2) the repository design (in particular, the thermal load, the presence and nature of backfill, and the size of the emplacement drifts), (3) the near-field thermohydrologic regime in the drifts adjacent to the waste package surface (in particular, the temperature and relative humidity), and (4) the degradation characteristics of the waste package materials (including the criteria for corrosion initiation and the rate of corrosion as a function of the near-field thermohydrologic environment). Information from each of these topics is required as input to the waste package degradation model to predict the time-rate of "failure" of the waste packages. Brief descriptions of the current repository and waste package designs are presented in Chapter 3. The predicted near-field thermohydrologic response using a drift-scale model is presented in Chapter 4. The bases for the material properties used in the prediction of waste package degradation, as well as the results associated with this prediction, are presented in Chapter 5.

As with every process that affects the total performance of the repository system (including both the engineered and natural components), the prediction of waste package degradation uses a stochastic representation. Employing such an assumption acknowledges that each of the approximately 10,000 waste packages is not exactly the same. It would be unreasonable to expect that they would be the same given, among other things, that the waste packages would be fabricated over approximately a 30-year time period. However, the stochastic assumption is made that the range of predicted material behavior of all waste packages is encompassed by the range in observed material characteristics. Similarly, it is unreasonable to assume that all environments encountered by the 10,000 waste packages are identical, either initially or as the system evolves under the applied thermal load. Again, the stochastic approximation attempts to capture this package to package variability due to the heterogeneity of the natural system as well as the heterogeneity of the local thermohydrologic perturbation. Also, for the waste package degradation model described in Chapter 5, localized corrosion of the surface of the waste package is considered to be the dominant degradation mechanism. Observations of corrosion over a range of materials indicate that localized corrosion is highly variable, i.e., it may be more rapid in some locations than others along the surface of the metal. This variability is again treated in the analysis presented in Chapter 5 as a stochastic process. Combining all these stochastic representations causes a distribution of waste package "failures" as well as a distribution of the amount of each waste package that is degraded as a function of time. It is worthwhile to point out that if these processes were not treated as being stochastic, then all waste packages would "fail" at exactly the same time and the radionuclide release rate over time would be exactly the same from all waste packages. Treating the processes as stochastic leads to a fraction of the waste packages "failing" earlier while another fraction will "fail" later and to radionuclide release rates that vary between waste package groups.

Once the waste packages have "failed" (i.e., the initial pit has penetrated the inner corrosion-resistant layer), it is assumed that the environmental conditions (in particular the temperature, humidity, liquid saturation (if any) and the presence of drips (if any)) occurring outside of the waste package are immediately transferred to the inside of the waste package. It is these

environmental conditions, combined with information on the behavior of the waste form and other engineered barriers under these environmental conditions, that are required in the prediction of radionuclide releases from the engineered barriers to the host rock.

1.4.6   Near-Field Environment

The thermohydrologic conditions inside the package and within the materials placed in the drift are derived from response surface fits to the results from the drift-scale thermohydrologic process model. The predicted thermohydrologic response in the vicinity of the drift-emplaced waste packages is dependent on a number of repository and waste package design issues, notably the areal mass loading of the waste packages in the repository, the line loading of the waste packages along the drift, the size of the drift, the use of backfill around the waste package, the use of ventilation prior to closure of the repository, the number of waste packages (or equivalently, the mass loading of each waste package), the age of waste at emplacement, and the average burn-up of the fuel. It is not possible to incorporate this many degrees of freedom in the current TSPA iteration. With the exception of the thermal load emplaced in the repository (both average areal mass loading and line loading of the drift) and the use of backfill within the drift, the other design related parameters are fixed at their best-estimate values from the Controlled Design Assumptions Report (M&O, 1995c). These assumptions are discussed in Chapter 4. Two areal mass loads are used in the present total system performance assessment, a "high" value corresponding to 83 MTU/acre and a "low" value corresponding to 25 MTU/acre.

In addition to the design-related factors affecting the predicted drift-scale thermohydrologic response, a number of hydrogeologic conceptual model and parameter uncertainties also exist. These include the conceptual representation of fracture-matrix flow, the hydrologic characteristic curves for the Topopah Spring Tuff host rock, the characteristic curves for the emplaced backfill (if present) and invert materials, the thermal characteristics of the backfill (if present) and invert materials, the amount of percolation flux (which also affects the liquid saturation in the host rock prior to emplacement of the heat-generating waste), and finally the magnitude of the bulk permeability of the host rock. In addition to being uncertain, each of these factors is likely to be variable from location to location within the potential repository block due to the heterogeneity of the hydrogeologic environment and the engineered emplacement of any drift-emplaced materials. To account for this uncertainty and/or variability, a number of process-level model realizations are conducted to evaluate the range in the thermohydrologic response; the key model parameters are the applied percolation flux and the thermal properties of the in-drift materials. The sensitivity of the predicted waste package degradation times and engineered barrier system releases to this uncertainty is evaluated in the results that are presented in Chapters 5 and 8, respectively.

The geochemical environment inside the waste package is assumed to be analogous to the ambient aqueous geochemistry inferred to exist in the Topopah Spring Tuff host rock. This neglects any geochemical perturbation likely to occur as a result of the varying thermohydrologic regime, as well as the interaction of the pore fluids with the introduced materials placed in the drift (not the least of which is the thick iron-based corrosion-allowance outer layer of the waste package). The likelihood and magnitude of localized advective flux (i.e., drips) into and through the in-drift materials is predicted by a stochastic representation of the distribution of percolation flux and saturated hydraulic conductivity of the host rock (both of which are assumed to be log-

normally distributed) in the vicinity of the in-drift emplaced waste packages . The localized advective flux is then represented by a response surface.

1.4.7   Waste Form Processes

The near-field environmental conditions affect such processes as the waste form dissolution, the solubility of the radionuclides in the aqueous phase in contact with the waste form, and the magnitude of both the advective and diffusive components of transport from the waste form surface through the degraded waste package and the in-drift materials into the host rock. Waste form dissolution rates are derived from empirical fits to data collected in laboratory experiments conducted under a range of environmental conditions (primarily different temperature and geochemistry environments although hydrologic conditions are also being investigated). The empirical fits include the uncertainty in the fitting parameters but do not include any stochastic effects (i.e., variability associated with different waste form samples). Radionuclide solubilities are also derived from empirical fits to data obtained from laboratory experiments for a range of thermal and chemical conditions. Uncertainty in the fitting parameters reflects the uncertainty in the experimental data only and does not account for uncertainty in the stability of the controlling phase (i.e., conceptual uncertainty) or the variability associated with a range of local geochemical environments.

The advective flux component of radionuclide transport is derived from the distribution of local percolation flux in excess of the saturated hydraulic conductivity of the host rock. This is a stochastic parameter that is directly correlated with the average percolation flux. The diffusive flux component of radionuclide transport is derived from the hydrologic conditions in the drift materials. For cases with an advective flux component, the diffusion coefficient is derived from laboratory-observed values of diffusion through coarse-grained materials. For cases with no advective flux, the diffusion coefficient is derived from an empirical fit of laboratory observed values as a function of liquid saturation. This empirical fit includes the uncertainty in the fit to the laboratory values, but does not include potential stochastic effects associated with material heterogeneity. Sensitivity analyses are conducted to evaluate the potential benefits associated with the emplacement of a so-called Richard's or capillary barrier, in which the backfill is designed to conduct (or "wick") any advective flux (i.e., drips) away from the waste package and underlying invert materials due to the capillary pressure (or matric potential) differences across unconsolidated materials of different grain-size.

An important component in the determination of radionuclide releases from the engineered barrier system to the host rock is the percent of the waste form surface that is exposed to the environmental conditions inside the waste package and the percent of the exposed waste form surface that is in contact with liquid water. The first component is related to the degradation of the cladding and any expansion of the waste form caused by thermal-chemical alteration. The second component is related to the amount and distribution of liquid water present in the waste package as a function of time. Both of these issues are difficult to predict rigorously. Sensitivity analyses are conducted to evaluate the potential contribution to total system performance associated with cladding performance.

1.4.8   Radionuclide Transport Processes

The radionuclides released from the engineered barrier system are available for transport in the geosphere to the accessible environment. The geosphere provides for both a physical and chemical delay for radionuclides to reach the accessible environment. This delay is a function of (1) the percolation flux distribution in the unsaturated zone, (2) the advective flux distribution in the saturated zone, and (3) the conceptual representation of transport in the hydrogeologic layers along the likely ground-water travel path between the repository and the accessible environment. The percolation flux distribution within the Topopah Spring hydrogeologic unit is a function of the surficial infiltration rate and the conceptual model for ground-water flow in the unsaturated zone. The infiltration rate is a complex function of many near-surface hydrologic factors including (1) precipitation timing, intensity, and duration (including snowmelt), (2) surficial slope orientation and angle, (3) surficial geology, and (4) surficial vegetation.

For the present total system performance assessment, an infiltration distribution based on inferences made by Flint and Flint (1994) is employed. Two conceptual representations of the distribution of these infiltration rates to the percolation flux within the Topopah Spring hydrogeologic unit are considered. In one instance, the surficial infiltration over the footprint of the repository is assumed to be invariant with depth, i.e., there is an insignificant amount of lateral diversion of areally distributed infiltration. This assumption is consistent with the existing version of the unsaturated-zone hydrology model (Wittwer et al., 1995). An alternative conceptual representation is that the areally variable infiltration rate (which ranges from about 0.02 mm/yr to over 10 mm/yr) is uniformly distributed across the Topopah Spring hydrogeologic unit due to significant lateral diversion within the basal vitrophyre of the Tiva Canyon hydrogeologic unit or within the Paintbrush hydrogeologic unit. In this case, the areally-weighted average infiltration rate is used to define the percolation flux. This model is consistent with small-scale flow models tested by Kwicklis (1994).

The key conceptual uncertainty in the transport of radionuclides through the geosphere at Yucca Mountain is the possible presence of fracture flow and transport which might, if fracture pathways existed and were continuous and interconnected, lead to the formation of so-called "fast" paths. Although the magnitude and distribution of percolation flux may also be considered a conceptual uncertainty, in the present analyses this flux is treated as a parameter. Therefore the conceptual uncertainty is embodied in the two parameter distributions. The likelihood and magnitude of any fracture flow is a function of the average percolation flux and the spatial distribution of hydrologic characteristics of the unsaturated media. In order to develop a representative distribution of fracture flow, a series of one- and two-dimensional process-level analyses are conducted over a range of possible unsaturated zone hydrologic characteristics. The results are then abstracted for use in the total system performance assessment by fitting a response surface through the results, with each hydrogeologic layer having different distributions because of their differing hydrologic properties. Because the resulting probability and magnitude of fracture flow are highly dependent on the average percolation flux, the principal dependency used in the TSPA analyses is a correlation with percolation flux.

The conceptual model for fracture transport is dependent on the mean travel path length through fractures before the dissolved constituents can transition into the matrix. This length corresponds physically to the average fracture length combined with the degree of interconnectedness of the

fracture network. A range of mean flow path lengths is studied in the sensitivity analyses of this total system performance assessment. In addition, alternative conceptual representations, including the effects of radionuclide retardation along fracture walls and matrix diffusion from the fractures into the rock matrix, are investigated.

Geosphere transport is also affected by the potential for radionuclide sorption on the mineral grains in the rock matrix. Whole rock distribution functions (k_d's) are used based on laboratory-derived data and the "minimum k_d concept" (Meijer, 1992) for the highly-sorbed radionuclides. These distribution coefficients are related to the individual hydrogeologic unit. Although the actual retardation within any particular unit is expected to be spatially variable due to mineralogic heterogeneity and perhaps local geochemical variability, this stochastic effect is not considered in the current total system performance assessment. The use of the "minimum" k_d value (i..e, most conservative from a release or peak dose perspective) obviates the need to account for the spatial variability explicitly.

The advective flux distribution in the saturated zone used in TSPA-1995 is the same as that employed in TSPA-1993. The entire flux distribution incorporates the effects of the considered large-scale spatial heterogeneity of aquifer properties. Small-scale heterogeneity is included through the use of dispersion in the solution of the one-dimensional advective-dispersive equation. Because of the one-dimensional nature of the solution algorithm, only longitudinal dispersion is simulated, i.e., there is no transverse dispersion. This is conservative when considering predictions of peak concentration or peak dose.

1.4.9 Future Climates

Given the long time frames of potential interest in total system performance (up to 1,000,000 years), it is likely that the atmospheric conditions will change with a resulting change in climate, especially precipitation and net evapotranspiration. Therefore, the potential effects of climate change are important to consider. Although a range of estimates exist on the possible changes in precipitation in the Yucca Mountain region over the next 10,000 years, at present no process model results of the potential effects of precipitation changes on (1) net infiltration and percolation flux in the unsaturated zone or on (2) the elevation of the water table and advective flux in the saturated zone are available. It is rational to postulate that increased precipitation would result in an increase in percolation flux and a rise in the water table, although the degree of correlation and the time lag between changes in surficial processes and the subsurface effects are uncertain. For simplicity it is assumed in the current total system performance assessment that changes in precipitation are immediately transferred through the unsaturated zone to the water table and that there is a linear relationship between precipitation and infiltration rate (and therefore percolation flux) and the magnitude of the water table rise.

1.4.10 Radiation Dose Calculation

Although only engineered barrier and natural barrier (i.e., geosphere) models and parameters are required in the prediction of cumulative releases of radionuclides at the accessible environment boundary, the calculation of radiation dose requires the definition of the potentially exposed population(s) and the potential biosphere pathways by which individuals may be exposed to any radionuclides released. In the current total system performance assessment it is assumed that an

individual receives the peak dose by taking all his or her drinking water from the tuff aquifer. It is also assumed that this individual is located at the point on the accessible environment boundary which corresponds to the peak of the radionuclide concentration within the tuff aquifer. Mixing volumes are based on a fixed cross-sectional area of flow in the saturated zone, with the horizontal mixing being given by the width of the potential repository and the vertical mixing assuming a well with a 50-m saturated-zone interval. Dose conversion factors, which convert radionuclide concentrations to radiation doses, are derived from published values of the U.S. Environmental Protection Agency (EPA, 1988).

1.5   REPOSITORY INTEGRATION PROGRAM (RIP)

The total system performance of a potential radioactive waste repository at the Yucca Mountain site is computed with the computer program RIP (Repository Integration Program) in conjunction with detailed process-level models. This subsection describes RIP, while the detailed process models are identified and described in later chapters of this document. RIP was specifically developed by Golder Associates Inc. (GAI) in order to evaluate the performance of a potential radioactive waste disposal facility at Yucca Mountain (Miller et al., 1992; Golder Associates, 1993) and has subsequently been applied to a wide variety of proposed radioactive waste disposal facilities both in the U.S. and abroad. Most recently, RIP has been applied to the WIPP site in New Mexico (Golder Associates, 1994a; Golder Associates, 1995a) and to evaluating alternative disposal options for low-level waste for the State of New York (Golder Associates, 1995b). RIP is fully documented in a Theory Manual and User's Guide (Golder Associates, 1994) and has a context-sensitive online help utility. The program has recently been formally verified consistent with ASME NQA-1 and ISO-9000 standards (Golder Associates, 1995c).

The major features of the four component models of RIP (see Figure 1.5-1) that comprise the performance assessment model are (1) waste package behavior and radionuclide release component model, (2) radionuclide transport pathways component model, (3) disruptive events model, and (4) biosphere dose/risk model. These models are summarized briefly below.

The *waste package behavior and radionuclide release component model* input requirements are descriptions of the radionuclide inventories in the waste packages, a description of near field environmental conditions (which may be defined as temporally and spatially variable), and subjective estimates of high-level parameters describing container failure, matrix alteration/dissolution, and radionuclide mass transfer. The waste package component model can simulate two layers of containment (e.g., outer package and zircalloy cladding). Waste package failure rates, along with matrix alteration/dissolution rates, are used to compute the rate at which radionuclides are *exposed*. Once exposed, RIP computes the rate of *mass transfer* out of and away from the waste package. Parameters describing waste package failure and radionuclide exposure and mass transfer can be described as a function of near-field environmental conditions. The output from this component (for each system realization) consists of time histories of release for each radionuclide from the waste packages, and acts as the input for the transport pathways component.

The *radionuclide transport pathways component* model simulates radionuclide transport through the near and far field in a probabilistic mode. The RIP model uses a phenomenological approach that attempts to describe rather than explain the transport system. The resulting transport

algorithm is based on a network of user defined *pathways*. The geosphere and biocell pathways reflect the major features of the hydrologic system and the biosphere, and are conduits through which transport occurs. The pathways may be used for both flow balance and radionuclide transport purposes, and may account for either gas or liquid phase transport. The purpose of a pathway is to represent large-scale heterogeneity of the hydrologic system, such as geologic structures and formation-scale hydrostratigraphy.

Geosphere pathways may be subdivided into *flow modes*, which address heterogeneity at the local scale (e.g., flow in rock matrix, flow in fractures). The flow modes are primarily distinguished from one another based on flow velocity in the mode, although retardation parameters may also differ between flow modes.

The transport of radionuclides along a geosphere pathway is based on a *breakthrough curve*, which is calculated as a cumulative probability distribution for radionuclide travel times along the pathway. The breakthrough curve combines the effects of all flow modes and retardation on the radionuclide travel time, and determines the expected proportion of mass that has traversed the pathway by any specified time. The breakthrough curve is computed based on a Markov process algorithm for exchange between different flow modes.

The third performance assessment component model represents *disruptive events*. Disruptive events are defined as discrete occurrences that have some quantifiable effect on the processes described by the other two component models. Examples of disruptive events include volcanism, faulting, and human intrusion. The user first identifies all significant events (i.e., events that are both credible and consequential). Having done so, each event is assigned a rate of occurrence and, if desired, one or more descriptor parameters, which define the characteristics and magnitude of the event (e.g., length of a volcanic dike). Descriptor parameters may be described stochastically. Event occurrences are simulated as Poisson processes.

The user defines probability distributions for the event consequences (which may be functions of event descriptors). A consequence may take the form of a number of discrete responses (e.g., disrupting a number of waste packages, moving radionuclides from some waste packages directly to the accessible environment). It is also possible for an event to directly modify parameters defined in the other two component models, and this capability can be used to specify long-term consequences (e.g., raising the water table or opening a new pathway).

The fourth performance assessment component model describes the fate and effect of radionuclides in the biosphere. The *biosphere dose/risk model* allows the user to define *dose receptors* in the system. Receptors receive radiation doses from specified geosphere (e.g., a water supply aquifer) or biosphere (e.g., a pond, or flora and fauna) pathways. Concentrations in these pathways are converted to radiation doses (or cancer risks) based on user-defined conversion factors.

1.6 ORGANIZATION OF THE CURRENT TOTAL SYSTEM PERFORMANCE ASSESSMENT DOCUMENT

Following this introductory chapter, Chapter 2 describes the Yucca Mountain site in general and the geohydrologic and geochemical attributes of the site that are significant with respect to the prediction of total system performance. The information presented in Chapter 2 is used as input to the development and substantiation of the process-level models that simulate the aqueous flow and transport in the unsaturated zone. Information on the saturated zone is only briefly presented because little additional analyses have been conducted since TSPA-1993 to better define this component of geosphere. Chapter 2 summarizes the current conceptual representation of flow in the unsaturated zone and describes the basis for the infiltration rates used in the current iteration of TSPA. In addition, this chapter describes the potential natural changes that may occur and their possible effects on the repository system.

Chapter 3 describes the current repository and waste package designs which have been used in the current total system performance assessment. The emphasis is on changes in understanding or designs since the last TSPA iteration in 1993. Within this chapter, the general layout of the potential repository is described, including the proposed alternative thermal loading cases. This chapter also describes the alternative waste package emplacement and backfill options proposed for the repository drifts. The radionuclide inventory associated with both the spent fuel containers and the high-level waste canisters within each waste package are also presented in this chapter.

Chapter 4 presents the conceptual representation used to predict the drift-scale thermal hydrology resulting from a range of alternative repository designs. In particular, two thermal loads, with and without the presence of backfill above and around the waste packages have been considered. In addition, due to the uncertainty in the ambient percolation flux, the thermohydrologic analyses have considered both a "low" percolation flux (0.05 mm/yr) and a "high" percolation flux (0.3 mm/yr). Although higher percolation fluxes are conceivable, the numerical algorithm used in the prediction of the thermohydrologic response had numerical convergence problems at higher percolation fluxes. In order to address some conceptual uncertainties, alternative drift-scale thermohydrologic analyses are also presented in Chapter 4.

Chapter 5 presents the conceptual representation and the associated parameters used for the evaluation of waste package degradation. A range of predictions of waste package "failures", based on a range of alternative conceptual assumptions, is presented in this chapter. These predictions use the thermohydrologic results described in Chapter 4.

Chapter 6 presents the abstraction of models and other parameters required in the prediction of engineered barrier system releases. The processes that are described in this chapter include waste form alteration/dissolution, solubility constraints on the concentration of dissolved radionuclide species, the potential existence of colloids to increase the mobile component of radionuclides in the aqueous phase, the effective diffusion of radionuclides through the degraded waste package and other engineered materials, and the potential for advective transport in the presence of localized flow intersecting the drift. This chapter presents the abstraction of laboratory-derived information for use in the prediction of releases from the engineered barrier system.

Chapter 7 presents the technical basis for the abstraction of unsaturated- and saturated-zone advective fluxes for the different hydrostratigraphic layers at Yucca Mountain. The response surface fits to the process-model results are presented in this chapter. Both site-scale and repository-scale unsaturated zone hydrology abstractions are presented in this chapter.

Chapter 8 presents the predicted results of radionuclide releases from the engineered barrier system to the host rock for a range of alternative conceptual representations and sampled parameter distributions. These results provide the source term for geosphere transport. The results are presented as both cumulative releases and peak release rates, with the latter being compared to the NRC release rate limits specified in 10 CFR 60.113(a)(1)(ii)(B).

Chapter 9 presents the predicted results of radionuclide releases at the accessible environment boundary and the peak individual doses attributed to these releases. The cumulative releases are normalized to the Table 1 values in 40 CFR Part 191 (the remanded environmental standard). The peak individual doses presented in this chapter are attributed to an individual at the accessible environment using the tuff aquifer for all of his or her drinking water and are calculated over a 10,000-yr and 1,000,000-yr time period. *[Note, these peak doses should not be compared to the average dose to which a member of the "critical" population may be exposed over the time periods of interest. The average dose is expected to be some orders of magnitude less than the peak dose to the maximally-exposed individual.]* In order to evaluate the significance of the predicted results to uncertainties in models and parameters, a number of sensitivity analyses are described in this chapter.

Chapter 10 presents a summary of the major results of this iteration of total system performance assessment and the potential implications of these results to current site characterization and design activities. In addition, the need to substantiate process-level model assumptions and the requirements of process-level models are discussed in this chapter.

Important Components of TSPA-1995 Analyses
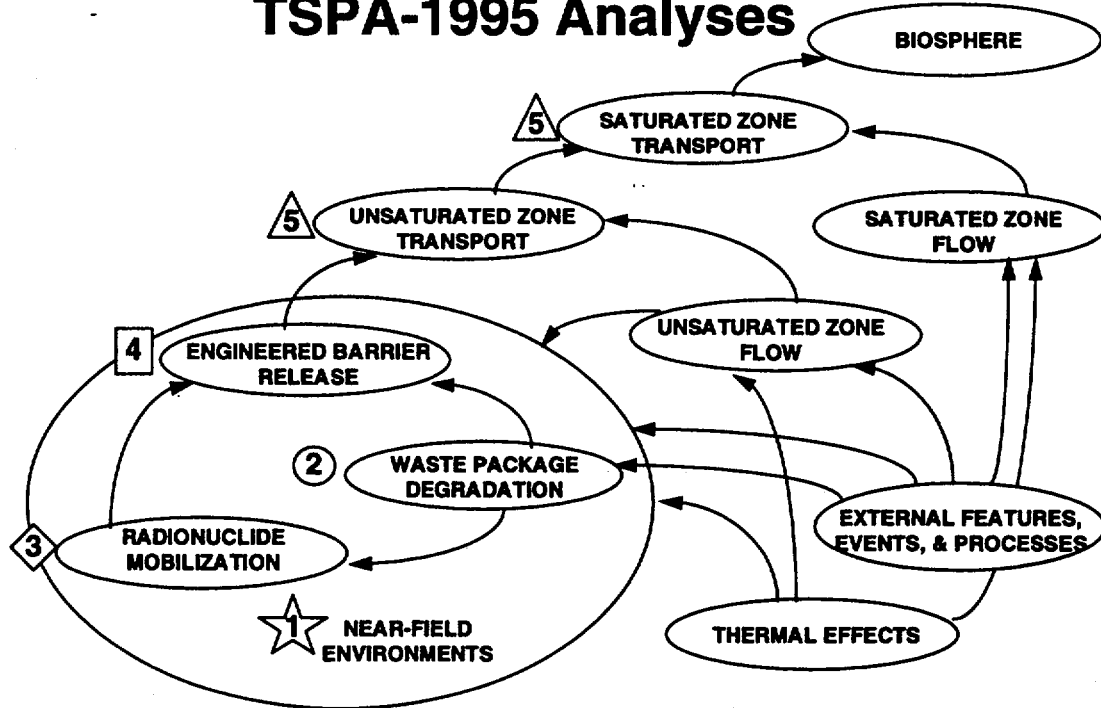
Figure 1.4-1 Process Model Influence Diagram Used in Total System Performance Assessment.

- • Dry Desert Environment
  - • Unsaturated Overburden
    - • Repository Host Rock
      - • Engineered Barriers
        - • Waste Package
          - • Waste Form
            - • Unsaturated Rock
              - • Saturated Rock
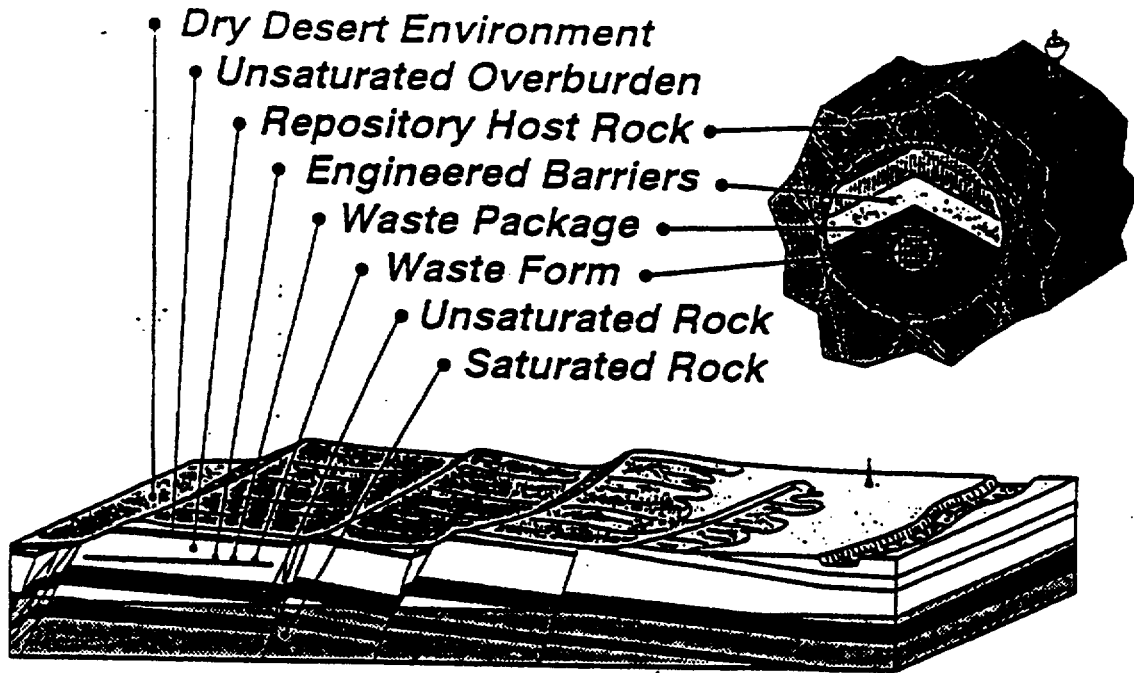
Figure 1.4-2   Schematic of Information Transfer Between Domains.

Information Transfer Between Domains
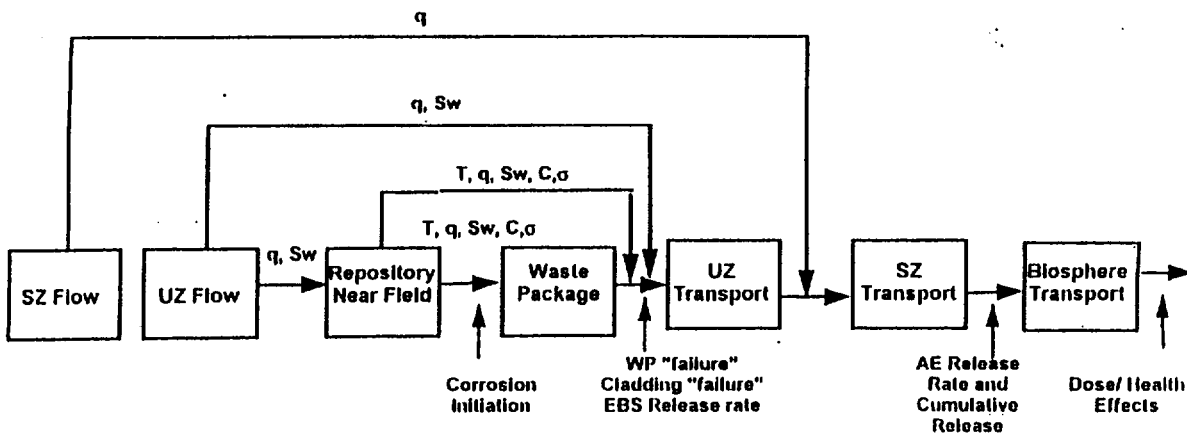
Figure 1.4-3   Schematic Depiction of the Barriers to Radionuclide Migration at the Potential Yucca Mountain Repository.

Top-Level Strategy for Waste Isolation

☆ **Low Ambient Flux and Saturations**

④ **Robust Engineered System & Possible Diffusion Barriers**

② **Robust Waste Package**

Possible Backfill

SNF/Basket Assembly

Invert

③ **Limited Mobilization of Radionuclides**

⑤ **Slow Migration Through Geosphere**
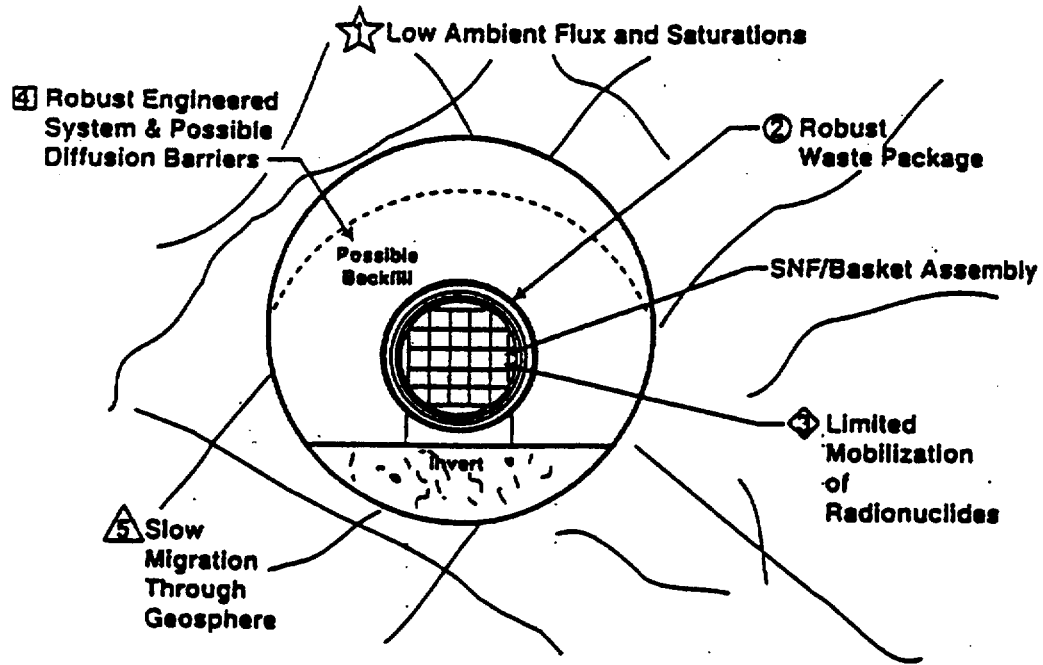
Figure 1.4-4   Engineered Barrier System Components.

MODEL HIERARCHY

Simplest representation of processes
- Probabilistic modeling
- Contains all important features of lower-level models

Intermediate complexity
- Contains all important features of lower-level models
- Integrates process models pertinent to the domains involved
- Evaluation of process uncertainty

Most detailed
- Understanding of phenomena as completely as possible
- Evaluation of parameter uncertainty

Total System Model

Subsystem Models

Process Modelss

Conceptual Models

Figure 1.4-5   Levels of Models Used to Evaluate MGDS Performance.

INFORMATION

- Site Biosphere → 8
- Site Geology → 7
- Site Hydrology → 6
- Site Geochemistry → 5
- Repository Design → 4
- Waste Package Design → 3
- Material Properties → 2
- Waste Form Properties → 1

PROCESS-LEVEL MODEL

- 7 →, 6 → Saturated Zone Flow Model
- 7 →, 6 → Unsaturated Zone Flow Model
- 7 →, 6 →, 4 →, 3 → Drift-Scale Thermo-Hydrologic Model
- 3 →, 2 → Waste Package Degradation Model

PROCESS-LEVEL MODEL ABSTRACTIONS

- Response surface of saturated zone flux → E
- Response surface of unsaturated zone flux
  - fracture flux
  - matrix flux → D
- Response surface of drift-scale flux
  - % packages with drips
  - advective flux in drips → C
- Response surface of
  - temperature
  - humidity
  - liquid saturation → B
- Response surface of
  - first pit
  - pit distribution → A

TOTAL SYSTEM PERFORMANCE ASSESMENT

- Biosphere Transport -Dose
  - ↑ 8
- Geosphere Transport -Cumulative Release
  - D E 5 6 7
- EBS Transport -Release Rate
  - B C 5 4 3 2 1
- Waste Package Degradation -Containment
  - A

Figure 1.4-6   Information Flow Diagram for TSPA-1995.

1-25
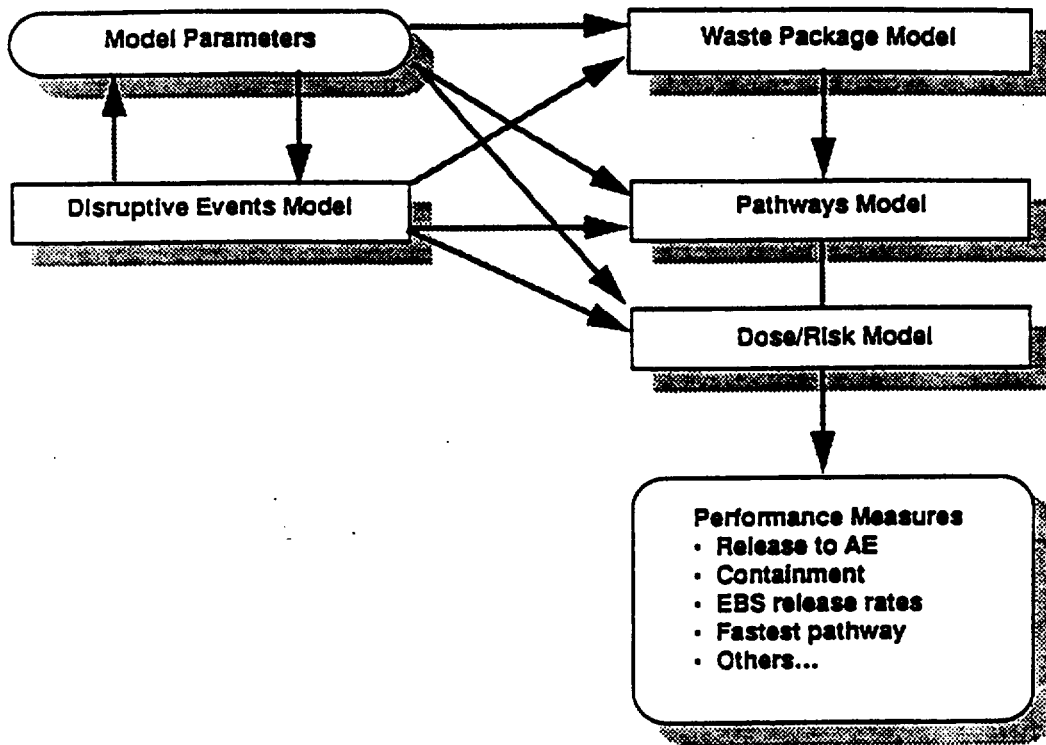
Figure 1.5-1   RIP Total System Performance Assessment Model Components.

2. SITE DESCRIPTION

Srikanta Mishra, James O. Duguid

2.1 INTRODUCTION

The geologic setting at Yucca Mountain provides the framework within which all relevant processes affecting the long-term containment and isolation of radioactive wastes are active. It provides the boundary conditions for the engineered components of the system and defines those aspects of the geosphere barrier which retard and spread the arrival of dissolved nuclides at the accessible environment boundary. Although several excellent summaries of the natural environment exist for the interested reader to gain an understanding of the Yucca Mountain area and its surroundings (most notably the Early Site Suitability Evaluation (Younker et al., 1992) and the License Application Annotated Outline (DOE, 1995)), the salient aspects of the geosphere affecting long-term performance are briefly described in the present chapter.

The information in the present chapter is used as input to the development and substantiation of the process-level models describing aqueous flow and transport in the unsaturated zone, as illustrated in Figure 2.1-1. Information on the saturated zone is presented only briefly because few additional analyses have been conducted since TSPA-1993 to better define this component of the waste isolation system. Section 2.2 discusses the basic geologic framework of the Yucca Mountain area. Section 2.3 presents the hydrostratigraphy of the unsaturated zone. Section 2.4 summarizes the available information regarding matrix and fracture hydrologic characteristics for the unsaturated media at Yucca Mountain. Section 2.5 briefly summarizes the conceptual model for saturated-zone flow. Section 2.6 summarizes the current conceptual representation of flow in the unsaturated zone and describes the basis for the infiltration rates used in the current iteration of TSPA. Finally, Section 2.7 describes the potential natural changes that may occur and their possible effect on the repository system.

The geo-hydrologic descriptions in Sections 2.2 - 2.4 are based primarily on the works of Montazer and Wilson (1984), Schenker et al., (1995) and Wittwer et al., (1995), as well as the review by Hoxie (1989). In addition to providing a geologic frame-of-reference for the proposed repository site, this information is used to develop the one-dimensional stratigraphy for radionuclide transport calculations implemented in RIP and to provide the parametric bases for the supporting thermo-hydrologic simulations presented in Chapter 7.

2.2 GEO-ENVIRONMENTAL FRAMEWORK

Yucca Mountain is located in the Southern Great Basin, about 140 km northwest of Las Vegas in the state of Nevada (Figure 2.2-1). The Great Basin of Nevada and Utah is a broad, arid-to-semiarid region characterized topographically by linear, usually north-trending mountain ranges separated by deep alluvium-filled valleys. The mountain ranges are typically tilted fault blocks that are delineated by mountain-front normal faults on which considerable vertical displacement has occurred.

Precipitation in the vicinity of Yucca Mountain is approximately 170 mm/yr, whereas potential evapotranspiration is estimated to be about 1000 mm/yr (Hevesi et al., 1993). Consequently,

most of the precipitation received at the surface is returned to the atmosphere, leaving only a small residual to infiltrate into the unsaturated zone. Net infiltration into Yucca Mountain is believed to be extremely variable spatially due to variations in soil cover, and associated differences in the impact of evapotranspiration rates, retention time, topographic controls, and fracture exposure on the infiltration process (Flint and Flint, 1994).

Structurally, Yucca Mountain is a complex of north- to northwest-trending, parallel to subparallel, generally fault-delineated ridges (Figure 2.2-2). The potential repository is proposed to be constructed within Yucca Crest, a major ridge that attains an elevation of more than 1,500 m above sea level and more than 300 m above the adjacent valley floors. Yucca Crest is bounded on the west by a steep escarpment defined by the trace of the Solitario Canyon fault, which is a west-dipping normal fault with vertical displacements ranging between 70 m and 300 m. To the west and north, Yucca Crest is bounded by a plexus of west-dipping normal faults and, possibly, a few northwest-trending strike-slip faults. Although the block is transected by the Ghost Dance Fault, a west-dipping, north-trending normal fault on which about 25 m of vertical displacement has occurred, Yucca Crest is a relatively undisturbed structural block that is tilted 5° to 8° to the east.

Stratigraphically, the unsaturated zone beneath Yucca Crest consists of a layered sequence of tuffs deposited from volcanic eruptions which occurred about 10 million years ago. Tuff is a siliceous rock composed of compacted, indurated volcanic ash. The compaction depends upon the temperature and pressure within the original deposit and, in general, is described by the degree of "welding" of the resultant tuff. The tuffs range from porous, nonwelded ash-flow, ash-fall, and reworked/bedded tuff deposit to massive, highly brittle, welded ash-flow and ash-fall rocks depending on their depositional mechanisms and cooling history.

The formal geologic stratigraphy for Yucca Mountain is shown in Figure 2.2-3 (Scott and Bonk, 1984; Montazer and Wilson, 1984). The basis for this lithostratigraphic subdivision is genetic. Specifically, the first-order nomenclature (e.g., Paintbrush group) is used for deposits interpreted to be of common petrogenetic character, perhaps indicating eruption from the same magma chamber. Secondary sub-divisions (e.g., Tiva Canyon member), commonly designated as cooling units for the welded ash-flow tuffs, are used for rocks produced by single/multi-stage eruptive cycles. The boundaries between the deposits of these major eruptive events possibly represent extended periods of relative quiescence, which may have produced relatively thin intervals of reworked (bedded) deposits or unreworked ash-fall tuffs.

Measurements of ground-water compositions from the saturated zone indicate that the fluids within the tuffaceous units (as represented by samples from well J-13) are predominantly dilute sodium-bicarbonate fluids with high concentrations of aqueous silica (Benson et al., 1983; Ogard and Kerrisk, 1984; Kerrisk, 1987). Generally, the saturated-zone fluids have pHs in the range of 7-8 (but have been measured as low as 6.7 or as high as 9.4), and contain the cations Ca^{2+}, K^+, and Mg^{2+}, and the anions SO_4^{2-}, Cl^-, F^-, and NO_3^- in order of decreasing concentration. The ground water from the deep Paleozoic carbonate aquifer (sampled from well UE-25p#1) is more highly concentrated with respect to all these constituents except aqueous silica and is characterized by pH values slightly lower than 7 (Ogard and Kerrisk, 1984; Kerrisk, 1987). The saturated-zone water analyses suggest that these fluids are, in general, relatively oxidized, but a few samples may indicate reducing conditions at depth (Ogard and Kerrisk, 1984).

Measurements of the organic content of the saturated-zone fluids are below 1 ppm (Means et al., 1983).

Analysis of water compositions from the unsaturated-zone tuffaceous rocks (Yang et al., 1988, 1990; Peters et al., 1992) indicates that the water samples have pH values in the range of 6.4 to 7.5 and that some constituents (i.e., Ca^{2+}, K^+, Mg^{2+}, SO_4^{2-}, Cl^-, and dissolved silica) are more concentrated than found in samples from the saturated-zone tuffaceous aquifer. However, the average HCO_3^- content measured in 83 water samples extracted from unsaturated-zone, non-welded tuff was lower than that for the saturated-zone samples (Peters et al., 1992). Some of this variability may be caused by the extraction techniques used to remove water from unsaturated samples (Peters et al., 1992). No analyses of the dissolved organic content have been given in the studies of the unsaturated-zone fluid compositions. Because of the intimate contact between the unsaturated-zone fluids and the pore gases in the rock, these ground waters are relatively oxidizing.

2.3   HYDROSTRATIGRAPHY

As shown in Figure 2.2-3, the lithostratigraphic units may be regrouped into four major hydrogeologic units based largely on the degree of welding (Montazer and Wilson, 1984). This delineation results in a sequence of welded, fractured and low matrix porosity/permeability rocks alternating with nonwelded, poorly fractured, high matrix porosity/permeability rocks, viz.:

- Tiva Canyon welded (TCw) unit: consisting of the moderately- to densely-welded zones of the Tiva Canyon geologic member. This unit is characterized by low matrix porosity (~10%), low matrix saturated hydraulic conductivity (~10^{-11} m/s), and high fracture density (10-20 fractures/m^3).

- Paintbrush nonwelded (PTn) unit: consisting of the lower partially-welded to nonwelded zones of the Tiva Canyon geologic member, partially-welded to nonwelded Yucca Mountain and Pah Canyon members, the porous interlayers of bedded tuffs, and the upper partially-welded to nonwelded part of the Topopah Spring member. This unit is characterized by high matrix porosity (~40%), high matrix saturated hydraulic conductivity (~10^{-7} m/s), and low fracture density (~1 fracture/m^3).

- Topopah Spring welded (TSw) unit: consisting of the welded zones of the Topopah Spring member. This unit is characterized by low matrix porosity (~10%), low matrix saturated hydraulic conductivity (~10^{-11} m/s), and high fracture density (8-40 fractures/m^3). The basal vitrophyre of the Topopah Spring member (TSv) is generally identified as a subunit because of its lower porosity compared to TSw.

- Calico Hills nonwelded (CHn) unit: consisting of the moderately-welded to nonwelded zones of the Topopah Spring member underlying the basal vitrophyre, the partially-welded to nonwelded tuffs of the Calico Hills formation, and other partially-welded to nonwelded tuffs located below the Calico Hills formation (i.e., Prow Pass, Bullfrog and Tram members of the Crater Flat Unit). Portions of the lower Topopah Spring member are vitrified, and zeolitic alteration appears in both the lower part of the Topopah Spring member and in the tuffaceous beds of the Calico Hills, leading to a further division of this

unit _ into vitric (CHnv) and zeolitic (CHnz) subunits. The fracture density (2-3 fractures/m^3) is similar in both zones, and the porosity of the vitric tuffs (~30%) is marginally higher than that of the zeolitic tuffs. However, matrix saturated hydraulic conductivity of CHnv (~10^{-9} m/s) is roughly two orders of magnitude higher than that of CHnz.

A 3-D hydrostratigraphic model was developed by Wittwer et al., (1995) to provide the framework for the LBL-USGS site-scale model of the unsaturated hydrologic system at Yucca Mountain. Lithologic logs from 34 boreholes, as identified in Figure 2.3-1, were used to define the spatial distribution of the four major hydrogeologic units. Figures 2.3-2 through 2.3-6 show: (i) an isopach map for TCw, (ii) an isopach map for PTn, (iii) an isopach map for TSw, (iv) an isopach map for CHn, and (v) a contour map for the water table. Based on the above information, a northwest-southeast cross-section through the potential repository at Yucca Mountain is shown in Figure 2.3-7.

Although stratigraphic information is also available from such sources as (i) the USGS lithostratigraphic model (Buesch et al., 1995), (ii) a stochastic lithologic model developed in support of SNL's TSPA-1993 activities (Schenker et al., 1995), and (iii) the thermo-mechanical stratigraphic model of Ortiz et al., (1985), the hydrostratigraphic model from Wittwer et al., (1995) was chosen for this study because of the following reasons:

- The latest lithostratigraphic information from the USGS geologic framework model (Buesch et al., 1995) has already been incorporated into the LBL-USGS model.

- A preliminary version of the LBL-USGS site-scale model has been used for performing hydrologic sensitivity analyses and developing hydrologic abstractions in support of this study (Xiang et al., 1995).

- The LBL-USGS model also provides the framework for the site-scale unsaturated-zone transport model being developed at LANL, which will be used as the basis for abstractions of coupled flow and transport in subsequent TSPAs.

2.4 MATRIX/FRACTURE HYDROLOGIC PROPERTIES

The LBL-USGS site-scale model uses a 'best-guess' hydrologic parameter set (Wittwer et al., 1995). An alternative, and more comprehensive, set of material properties has been developed by Schenker et al., (1995) in support of Sandia National Laboratory's total system performance assessments (TSPA-1993) for the potential repository at Yucca Mountain (Wilson et al., 1994). This database, which includes the latest available information from ongoing site-characterization activities, consists of ranges and summary statistics associated with matrix and fracture properties for the hydrogeologic units at Yucca Mountain, and is more amenable to uncertainty propagation studies. Therefore, this more comprehensive data set is used as the basis for the unsaturated-flow calculations carried out in support of TSPA-1995. The following paragraphs briefly summarize the information available for the various parameters.

- Matrix bulk density (ρ_b): Rock bulk-density data are derived from core samples taken from various boreholes, i.e., UE-25a-4/5/6/7, UE-25p#1, USW UZ-13, USW GU-3, USW

G-4, UZN-54, UZN-55, USW H-1, UE-25b#1, J-13, USW G-2, UE-25a#1, USW GU-3/G-3, USW G-1, UE-25a#3, USW UZ-7; as well as from samples taken from surface transects. Summary statistics of these data for each hydrogeologic unit are presented in Table 2.4-1. These statistics include measurements over the entire range of water saturation, from 0 to 1.

- Matrix porosity (ϕ): Porosity data are derived from core samples taken from various boreholes, i.e., UE-25a-4/5/6/7, UE-25a#1, UE-25p#1, USW GU-3, USW G-4, UZN-54, UZN-55, USW H-1, UE-25b#1, USW GU-3/G-3, USW UZ-7; as well as from samples taken from surface transects. Summary statistics of these data for each hydrogeologic unit are presented in Table 2.4-2.

- Matrix saturated hydraulic conductivity (K_{sat}): Saturated hydraulic conductivity data are derived from core samples taken from boreholes USW G-1, UE-25c#1, UE-25a#1, UE-25a#6, USW G-4, USW H-1, and UE-25b#1. Because saturated conductivity is commonly found to be log-normally distributed (Gelhar, 1993), summary statistics of the log-transformed data for each hydrogeologic unit are presented in Table 2.4-3.

- Matrix capillary retention properties: The functional form of van Genuchten (1980) is used to describe the retention function, i.e., the relationship between capillary-pressure head (h) and liquid saturation (S). The van Genuchten (VG) model has the form:

$$S = S_r + (1-S_r) \, [1 + |\alpha h|^\beta]^{1/\beta - 1} \qquad (2.4\text{-}1)$$

where α is the VG air-entry parameter, β is the VG pore-size distribution parameter, and S_r is the residual liquid saturation. These parameters have been determined by fitting the VG equation to retention functions measured in core samples taken from boreholes USW G-1, USW GU-3, UE-25a#1, UE-25a#6, USW G-4, and other samples taken from surface transects. Because α and β are commonly found to be log-normally distributed (e.g., Wang and Narasimhan, 1993), summary statistics of the log-transformed data for α and β, for each hydrogeologic unit, are presented in Table 2.4-4 and Table 2.4-5, respectively.

The residual saturation, S_r, is known to be an ill-determined fitting parameter (van Genuchten and Nielsen, 1985), and hence, the arithmetic average for each hydrogeologic unit is used as a surrogate representative value. Following Schenker et al., (1995), these values have been determined to be as follows: TCw - 0.021, PTn - 0.154, TSw - 0.045, TSv - 0.118, CHnv - 0.097 and CHnz - 0.121.

- Bulk rock permeability (K_{bulk}): Bulk saturated hydraulic-conductivity and air-permeability data are derived from pump tests and/or barometric-pumping data in boreholes USW G-4, USW H-1, USW H-3, USW H-4, UE-25b#1, UE-25p#1, J-13, USW UZ-1, UE-25a#4 and UZ-16. In some cases, permeability values for units with sparse measurements have been inferred from measured permeability values of lithologically similar units (Schenker et al., 1995). The bulk permeability represents the transmissive potential of the combined matrix-fracture system in general, and the permeability to vapor migration through the fracture network, in particular. However, given the paucity of bulk-permeability data it was decided to use only the geometric-mean value, rather than a statistical distribution, for

characterizing bulk permeability of various hydrogeologic units. These values are tabulated in Table 2.4-6.

- **Fracture hydrologic properties**: Based on fracture-density frequency data available from boreholes USW G-1, USW GU-3, USW G-4, UE-25a#1, as well as the bulk-rock permeability information described above, Schenker et al., (1995) derived such fracture properties as spacing, porosity, VG air-entry parameter, aperture, angle/orientation, and saturated hydraulic conductivity for each hydrogeologic unit. Given the uncertainty associated with such derived parameters (in as much as geometric fracture density is commonly found to be weakly correlated with hydraulic properties), it was decided to use a single set of values to characterize fracture properties for all units. These values, which are similar to the ones recommended for the fractures by Klavetter and Peters (1986), are also presented in Table 2.4-6.

2.5 REGIONAL HYDROGEOLOGY AND GROUND-WATER USE

2.5.1 Regional Hydrogeology

The regional ground-water flow system in the vicinity of the Yucca Mountain site encompasses several topographic basins and ground-water basins. Interbasin flow is common and important with respect to the total volume of water transferred within the system boundaries. The lengths of regional ground-water flow paths are relatively large when compared to those of "local" flow systems (Mifflin and Hess, 1979). The Hydrologic Study Area is defined as that portion of the regional-flow system that is of interest in defining the potential transport path to ground-water users downgradient from a repository at Yucca Mountain (Figure 2.5-1). The study area consists of three ground-water sub-basins; Oasis Valley, Alkali Flat/Furnace Creek Ranch, and Ash Meadows (Figure 2.5-1). Also shown on Figure 2.5-1 are the State-of-Nevada hydrographic areas used by the State Engineer as a basis for estimation of perennial ground-water yield. A summary for estimates of annual ground-water inflow, recharge, and outflow of these hydrographic areas is given in Table 2.5-1.

Figure 2.5-2 shows the major inflows and outflows of the three ground-water sub-basins in the hydrogeologic study area. The flow southward from Yucca Mountain in the Alkali Flat/Furnace Creek Ranch sub-basin is about 8 acre-ft/yr (10,000 m^3/yr) based on the outflow from the Jackass Flat and Buckboard Mesa hydrographic areas (Table 2.5-1). The northwestward flow from the Amargosa Desert sub-basin is about 20 acre-ft/yr (25,000 m^3/yr) (Table 2.5-1). These two components of flow are strongly influenced by ground-water withdrawal, and both flows are toward the location of heavy withdrawal to the south and west of the town of Amargosa Valley.

The ground-water flow from Yucca Mountain is generally south to southeast as indicated by the potentiometric surface of the ground-water table of the Amargosa Desert (Figure 2.5-3). A schematic cross section of the flow system between Yucca Mountain and Eagle Mountain is presented in Figure 2.5-4. The flow system can be generalized to consist of recharge at the higher elevations just north of Yucca Mountain, flow through the hydrogeologic units to the south and southeast, and discharge through both evapotranspiration at Franklin Lake Playa and flow into other ground-water sub-basins (i.e., Death Valley).

2.5.2 Ground-Water Use

The Yucca Mountain Site is located within the Alkali Flat/Furnace Creek Ranch sub-basin between Crater Flat and Jackass Flat and to the north of the Amargosa Desert (Figure 2.5-1). Very little ground water is withdrawn in the northern and central parts of this sub-basin. In addition, very little ground water has been appropriated to the north of Yucca Mountain (upgradient) according to information filed with the Nevada State Engineer's Office.

The major ground-water users in the area, the town of Amargosa Valley and small rural communities of the northeastern Amargosa Desert, are located in the southwestern portion of the Alkali Flat/Furnace Creek Ranch sub-basin (Figure 2.5-5). Figure 2.5-5 indicates the location of major ground-water users as areas of heavy withdrawal. Most of the water is supplied by wells; however, there has been development of some springs. Most residences rely on individual wells, while some trailer parks, public facilities, and commercial establishments are served by small, private water companies. Table 2.5-2 summarizes the public water suppliers in the area, the type of well used, and the population served. All of these wells are completed in, and produce from, the valley-fill aquifer.

Two mineral production operations are located in the Amargosa Desert. One operation, owned by the American Borate Corporation, located between Amargosa Valley, Nevada, and Death Valley Junction, California, was decommissioned in July, 1986. The facility consisted of a large mineral processing plant and a housing development for its employees (French et al., 1984). The other operation is owned by IMV Division of Floridin, Inc. and is also located between Amargosa Valley, Nevada and Death Valley Junction, California. This operation employs approximately 53 people to mine specialty clays (Nevada Bureau of Mines and Geology, 1993).

In addition to well production, a number of springs supply water to the region. The main concentration of springs is in Death Valley in the vicinity of Furnace Creek Ranch, approximately 50 to 60 km southwest of the Yucca Mountain Site (Figure 2.5-5). Many points of ground-water discharge have been identified in the Death Valley National Park in California (Winograd and Thordarson, 1975). The water supply for the National Park Service facilities is derived principally from three groups of springs: Travertine Springs, Texas Springs, and Nevares Springs (French et al., 1984). The population served by this water supply varies during the year. From October through April, approximately 800 persons live in the area on a semipermanent basis, and an additional 2,000 persons live in the area as visitors. From May through September, the number of semipermanent residents decreases, and there are few visitors (French et al., 1984).

Water use within the Alkali Flat/Furnace Creek Ranch sub-basin occurs primarily in the Amargosa Desert (shown as hydrographic area 230 in Figure 2.5-1). The perennial yield to this hydrographic area is estimated to be 2.96×10^7 m^3/yr (French et al., 1984). An estimated 2.10×10^7 m^3/yr of this total is naturally discharged from springs and seeps in the Ash Meadows area (French et al., 1984), and nearly 10,000 acre-ft/yr (1.23×10^7 m^3/yr) is artificially discharged from wells in the Amargosa Valley (Coache, 1986). Thus, an overdraft of 3.70×10^6 m^3/yr currently exists. Water levels in wells drilled in the valley-fill aquifer declined an average of 3.75 m between 1963 and 1984 (Nichols and Akers, 1985). Total appropriations in 1985 were over 8.64×10^7 m^3/yr. If these rights to appropriate water were exercised, rapid depletion of the valley-fill aquifer would result.

Crater Flat (hydrographic area 229 in Figure 2.5-1) is currently overdrawn because of an appropriation made to Saga Exploration, Inc. for the development of the Sterling Mine, a gold deposit, located on the east side of Bare Mountain. The mine uses its own well for its heap-leach operation and relies on municipal water for its potable water. The mine employs approximately 40 individuals, and is expected to be in operation until 1997 or 1998. Although an overdraft exists, no protective measures will be taken because the water has been appropriated for mining, which is considered a preferred use under the Nevada Revised Statutes. Under these Nevada statutes, overdrafts for mining are allowable for periods not to exceed five years.

2.6 UNSATURATED ZONE HYDROLOGY

2.6.1 Flow Dynamics

The ground-water-flow regime through the partially-saturated tuffaceous rocks at Yucca Mountain is controlled by the hydrologic characteristics, including the heterogeneity and spatial variability, of the hydrostratigraphic units identified in Section 2.3. Because of the large disparity in capillary suction between fracture and matrix, pore water in the unsaturated zone is bound mostly in the matrix. Average annual precipitation at Yucca Mountain is estimated to be approximately 170 millimeters per year, of which only a very small fraction becomes net infiltration. Precipitation occurs during a few intense storms. Surface runoff is infrequent and of short duration, and no perennial streams exist in the area. Water infiltrates principally into the Tiva Canyon welded (TCw) unit, but also into the Paintbrush nonwelded (PTn) unit and Topopah Spring welded (TSw) unit where they are exposed at the land surface.

The qualitative description of the unsaturated-zone flow dynamics presented here is based on the conceptual hydrologic flow model of Montazer and Wilson (1984), and is shown schematically in Figure 2.6-1. Eastward lateral flow occurs within the PTn unit and above its upper contact. The lateral flow is intercepted by structural features, which transmit most of the infiltrated water vertically to the water table. Percolation through the matrix occurs principally vertically in the welded units and both laterally and vertically in the nonwelded units. Fracture flow is predominant in the TCw unit during intense pulses of infiltration and is insignificant in the TSw unit except near the upper contact and near structural features. Temporary development of perched water bodies is possible within and above the nonwelded units near structural features. This water drains into the structural flow paths and much of it travels directly to the water table.

2.6.2 Infiltration Pattern and Rate

The overall flow regime and the distribution of percolation flux (i.e., the flux that passes the root zone and is no longer susceptible to evapotranspiration processes) is controlled by the infiltration rate through the surficial layers. Quantification of the infiltration rate at arid sites has been the focus of numerous scientific investigations over the past decade. An excellent review of infiltration studies associated with arid hydrology is found in Scanlon (1995). Such investigations have intensified due to both the desire to develop ground-water resources in these environments and the effort to evaluate these environments for the potential disposal of wastes. In the United States potential waste-disposal sites in arid environments have been investigated in Texas (the potential West Texas low-level radioactive waste-disposal facility at Eagle Flat), California (the potential Ward Valley low-level radioactive waste-disposal facility), and Nevada (the Greater

Confinement Area in Beatty and the potential repository for high-level radioactive waste at Yucca Mountain). In each of these instances, understanding and bounding the possible infiltration rate has been a key component of the scientific investigations into the suitability of the planned facility.

Because no direct observations of infiltration are possible, infiltration rate is always a derived parameter. In general, infiltration rate is obtained from other observations or inferred from process-level models which attempt to capture the relevant factors and quantify the effect of these factors on the net infiltration. An analogous situation exists in saturated-zone investigations where the advective flux is not directly measured (with the possible exception of point measurement of borehole dilution), but is inferred from potentiometric observations and hydrogeologic properties. Numerous variables affect the prediction of the net infiltration rate of water in arid climates. These variables include (1) surficial soil texture, including the possible existence of preferential pathways such as fractures or root tubules, (2) vegetation, (3) topography, and (4) climate, including the timing, intensity and duration of precipitation events (Scanlon, 1995). Greater infiltration rates are associated with coarse-grained surficial soils, areas with bare soil instead of vegetated soil (with the exception that preferential flow may occur along plant-root systems), topographic lows where water may pond intermittently, and precipitation events in the winter (due to a lower potential for evapotranspiration) (Scanlon, 1995).

The general factors identified above are directly applicable to the quantification of net infiltration over the surface of the Yucca Mountain area and are the focus of ongoing scientific investigations. The recent status of the Yucca Mountain Site Characterization Project Office studies on shallow infiltration measurements and their interpretations have been summarized by Flint (1995). The key variables noted by Flint in the estimation of total infiltration include: (1) the depth of the alluvial cover overlying the bedrock, (2) the hydrologic characteristics of the bedrock including matrix porosity and fracture intensity and connectivity, (3) the topographic position providing differences in radiation load, slope, runoff and run-on, and (4) the time of the precipitation events.

Although revised estimates of the spatial distribution of infiltration over the Yucca Mountain area and the associated uncertainty and variability in these estimates are expected to be provided to the Project early in Fiscal Year 1996, the existing interpretations are based on assumed matrix-driven flow processes. The present interpretations (documented in Flint and Flint, 1994) utilize quasi-steady-state soil-moisture profiles developed from neutron logs in approximately 100 shallow boreholes combined with laboratory-derived moisture retention curves. These characteristics curves relate moisture content to effective permeability using an assumed unit hydraulic gradient. By combining these observations and assumptions, it is possible to infer the magnitude of infiltration.

Due to the highly nonlinear nature of the characteristic curves at low liquid saturations, extrapolation of effective permeability is very uncertain in this region. This uncertainty is compounded by the large spatial variability and/or uncertainty in the properties of the tested samples (see Section 2.4). Based on the above approximations, Flint and Flint (1994) generated a matrix infiltration map (reproduced as Figure 2.6-2) defining the spatial distribution of estimated infiltration rates primarily based on the outcropping lithologic unit. This map only partially includes the potential effects of slope and soil cover, which would be expected to modify substantially this distribution (especially in areas of steep slope such as along the western

escarpment of Yucca Crest to the east of the Solitario Canyon fault). This distribution of infiltration rates has been incorporated in the site-scale model of the unsaturated zone recently documented in Wittwer et al (1995). Revisions to this model based on revised estimates of the infiltration rate are expected in Fiscal Year 1996 and should be available in time for inclusion in the next iteration of total system performance assessment.

In order to test the sensitivity of the total system performance to uncertainties in the ambient infiltration rate (and the resulting percolation flux) a series of process-level calculations have been conducted covering a range of values. The process-model results and corresponding abstractions are presented in Chapter 7.

2.7 POTENTIAL NATURAL CHANGES TO THE AMBIENT GEO-ENVIRONMENT

2.7.1 Climatic Effects

The ambient hydrologic conditions in the Yucca Mountain region are characterized by extremely low precipitation (generally concentrated in the winter months) and very high potential evapotranspiration rates (concentrated in the summer months). Numerous ongoing studies sponsored by the DOE and NRC have indicated that the climate has remained essentially uniform over the past several thousand years and may change to a slightly wetter and cooler period over the next 10,000 years. The general effects of such a potential climate change on the net infiltration amount are uncertain because of the complex interrelation between precipitation and vegetation (e.g, increased precipitation yields the potential for increased infiltration, but the presumed increase in transpiration due to the presence of more vegetation may offset that increase). However, observations at Rainier Mesa suggest that for increased precipitation levels, there is a significant increase in net infiltration (this observation does not account for the fact that the topography at Rainier Mesa is much flatter than at Yucca Mountain). In summary, there is little quantitative information on the direct (i.e, infiltration-rate change) or indirect (i.e., water-table rise) effects potentially associated with climate change. [Note: A major deliverable on this topic is expected to be completed by the end of Fiscal Year 1996.]

2.7.2 Volcanic Effects

Two tasks are planned to support the inclusion of volcanism effects into TSPA-1995. The first includes: (1) simulation modeling of the probability of magmatic intersection of specified areas (area of the potential repository, controlled area, and surrounding areas of the Yucca Mountain region), (2) assessment of spatial models of the distribution of basaltic volcanic centers, and (3) review of published volcanism probability models by the State of Nevada. The second task is modeling, using the RIP code, the radiological releases associated with direct penetration of a repository by basalt magma that subsequently erupts at the surface. The scope and objectives of these tasks are described below.

As part of the first task described above, spatial simulation modeling has been conducted using the FRACMAN computer code to estimate the probability of magmatic disruption for specific areas associated with the Yucca Mountain site. The simulation uses the set of alternative spatial and structural models described in the volcanism status report (Crowe et al., 1995). For each spatial and structural model, simulations have been run using three sets of feeder systems for

basaltic volcanic centers. These sets are: (1) simple linear feeder dikes, (2) linear feeder dikes with associated plug-like intrusive masses (conduit plug, radial and concentric dikes), and (3) linear feeder dikes with associated plugs and sill-like intrusions. The dimensions of the basalt feeder systems have been developed from literature references and from analog studies of eroded basalt centers. The orientations of the basalt feeder systems have been established using constraints from the local stress field, orientation of basalt centers and cone alignments, and predictions/observations of the spatial geometry imposed by individual spatial or structural models. The simulations record the number of penetrations of specified areas, the probability of penetration, the projected area of penetration, and the projected volume of penetration. Data from these simulations have been used to refine the disruption ratio of the variable E2 in estimating the occurrence probability of magmatic disruption of the repository and associated areas. These data will be used to revise the probabilistic-volcanic-hazard assessments of Crowe et al. (1995). A second application of the results from simulation modeling would be as input for studies of the subsurface effects of magmatic disruption of the potential repository.

A review of published models for the spatial distribution of volcanic centers in the Yucca Mountain region has been conducted (Crowe et al., 1995). This review assesses the strengths and weaknesses of existing models, emphasizing stationary and nonstationary distribution models, and also evaluate ranges of alternative distribution models that could be applied to the record of Plio-Quaternary volcanic centers in the Yucca Mountain region. The review is emphasizes the impact of different spatial distribution models on probabilistic volcanic hazard assessment.

A brief review by the State of Nevada of published probability models has been completed, emphasizing assessment of homogeneous and nonhomogeneous models and the application of methods of Bayesian statistics to probabilistic volcanic hazard assessment.

If the occurrence probability of direct disruption of a repository by future volcanic activity is $< 10^{-8}$ yr^{-1}, the risk of future volcanism would be judged not to be a disqualifying issue. The most current estimates of the occurrence probability for direct disruption of the potential repository are about 1-3 x 10^{-8} yr^{-1} (Crowe et al., 1995). After the conclusion of the Los Alamos volcanism task, DOE was advised that release calculations will need to include estimates for eruptive releases from direct magmatic penetration of the potential repository (pending possible changes in 40 CFR Part 191). The purpose of this task is to initiate that work, building on volcanism studies completed as part of performance assessments.

Volcanic scenarios have been developed for: (1) the geometry of basaltic feeder systems, (2) the induced changes in the rocks immediately surrounding basaltic feeder systems, (3) the incorporation of radioactive waste in magma, and (4) the dispersal of that waste in basaltic eruptions. Parameters identified from these scenarios are used as inputs into the RIP computer code to assess the changes in the nominal-case releases for a potential repository system at Yucca Mountain. The eruption simulations have been used to identify the most critical input parameters. These parameters will be reassessed through ongoing scientific investigations and the refined parameters will be used in future computer simulations of cumulative releases. The goal of this iterative work is to assess the significance of future volcanic events on the long-term performance of a repository. If eruptive releases are insignificant with respect to the base case repository performance, studies of the eruptive effects will be terminated and future work will focus on the subsurface effects of future volcanism (perturbation of the repository system). If the eruptive

releases are significant with respect to nominal-case performance, enhanced studies of eruption dynamics will be conducted to constrain more carefully the predictions of total radiological releases and to clarify the mechanisms of dispersal of radioactive waste in basaltic eruptions.

2.7.3 Tectonic Effects

Gauthier et al. (1995) recently presented an evaluation of the effects of potential seismic activity on the release of radionuclides from a potential repository at Yucca Mountain. Future seismic events were predicted using data from seismic hazard analysis conducted for the Exploratory Studies Facility (ESF). Several phenomenological models were developed, including rockfall in unbackfilled emplacement drifts, container damage caused by fault displacement within the repository, and flow-path change caused by changes in strain. Total system release over a 10,000 year period was evaluated using the total system simulator TSA (Wilson et al., 1994) with a composite-porosity flow model (relatively large-scale, regular percolation), as well as the weeps model (episodic pulses of flow in locally saturated fractures). For the composite-porosity model, seismic events showed little effect on total-system release, whereas for the weeps model, container damage and flow-path changes cause over an order of magnitude increase in releases. In separate calculations using more realistic representations of faulting, water-table rise caused by seismically induced changes was found to be insufficient to reach a potential repository.

These calculations suggest that the consequences of potential seismic activity on total-system performance (i.e., release to accessible environment) are negligible.

Table 2.4-1. Summary Statistics for Matrix Bulk Density (ρ_b)

UNIT	Number of samples	E(x) (kg/m^3)	SD(x)	Minimum (kg/m^3)	Maximum (kg/m^3)
TCw	380	2285	114.2	1410	2420
PTn	268	1419	279.5	850	2420
TSw	750	2247	134.8	1360	2710
TSv	59	2308	60.0	2090	2400
CHnv	199	1737	290.1	1050	2280
CHnz	198	1746	192.1	1300	2230

Table 2.4-2. Summary Statistics for Matrix Porosity (ϕ)

Unit	Number of samples	E(x)	SD(x)	Minimum	Maximum
TCw	290	0.087	0.055	0.033	0.450
PTn	205	0.421	0.104	0.132	0.650
TSw	300	0.139	0.057	0.004	0.480
TSv	26	0.065	0.043	0.014	0.177
CHnv	117	0.331	0.090	0.097	0.510
CHnz	127	0.306	0.064	0.141	0.470

Table 2.4-3. Summary Statistics for Matrix Saturated Conductivity (K_{sat})

UNIT	Number of samples	E(x)[1] (m/s)	SD(x)[2]	Minimum (m/s)	Maximum (m/s)
TCw	14	1.3E-11	1.07	7.0E-13	4.8E-09
PTn	12	1.1E-08	2.40	2.9E-12	2.4E-06
TSw	66	2.0E-11	0.90	3.1E-13	5.2E-09
TSv	7	1.0E-11	0.68	1.5E-12	6.9E-11
CHnv	44	1.0E-09	1.03	5.1E-13	2.9E-07
CHnz	51	1.6E-11	1.00	2.4E-14	3.1E-09

[1] Geometric Mean
[2] Standard deviation of $\log_{10}(K_{sat})$

Table 2.4-4. Summary Statistics for Matrix VG Air-Entry Parameter (α)

UNIT	Number of samples	E(x)[1] (1/m)	SD(x)[2]	Minimum (1/m)	Maximum (1/m)
TCw	19	0.0081	0.68	0.0003	0.1338
PTn	43	0.0735	0.72	0.0104	1.6690
TSw	51	0.0130	0.50	0.0021	0.4224
TSv	10	0.0024	0.44	0.0002	0.0077
CHnv	24	0.0227	0.50	0.0054	0.3752
CHnz	50	0.0054	0.62	0.0004	0.2355

[1] Geometric mean
[2] Standard deviation of $\log_{10}(\alpha)$

Table 2.4-5. Summary Statistics for Matrix VG Pore-Size Distribution Parameter (β)

UNIT	Number of samples	E(x)[1]	SD(x)[2]	Minimum	Maximum
TCw	19	1.607	0.053	1.349	2.085
PTn	43	2.223	0.225	1.187	11.80
TSw	51	1.710	0.122	1.155	5.363
TSv	10	2.234	0.188	1.377	4.473
CHnv	24	2.361	0.229	1.249	9.888
CHnz	50	1.671	0.120	1.184	5.914

[1] Geometric mean
[2] Standard deviation of $\log_{10}(\beta)$

Table 2.4-6. Bulk Permeability and Fracture Hydrologic Properties

Parameter	Value
Bulk permeability, K_{bulk} (m/s)	1.8 E-5 (TCw, TSw, TSv) 5.4 E-6 (PTn, CHnv) 1.2 E-6 (CHnz)
Porosity, ϕ (-)	1.00E-3
VG air-entry parameter, α (1/m)	10
VG pore-size distribution parameter, β (-)	5
Residual saturation, S_r (-)	0

Table 2.5-1. Summary Estimates of Annual Ground-Water Inflow, Recharge, and Outflow in thousands of acre-feet per year

Unit	Sub-surface Inflow	Local Recharge	Sub-Surface Outflow	Source of Estimates
Amargosa Desert	20	2	20	Walker and Eakin, 1963
Crater Flat	2	0	2	Rush, 1970; Rush et al., 1971
Emigrant	0	3	3	Rush, 1970; Rush et al., 1971
Indian Springs	22	10	32	Rush, 1970; Rush et al., 1971
Jackass Flat and Buckboard Mesa	6	2	8	Rush, 1970; Rush et al., 1971
Mercury and Rock	33	0	33	Rush, 1970; Rush et al., 1971
Pahrump	0	42	18	Harrill, 1986
Three Lakes	5	8	13	Rush, 1970; Rush et al., 1971
Tikaboo	6	6	12	Rush, 1970; Winograd and Friedman, 1972
Yucca and Frenchman Flats	32	1	33	Rush, 1970; Rush et al., 1971

Table 2.5-2. Public Water Suppliers in the Community of Amargosa Valley, for wells located in the southern portion of the Alkali Flat/Furnace Creek Ranch sub-basin and in the southwestern portion of the Ash Meadows sub-basin

Supplier	Type	Population Served
American Borate Trailer Park	Community	300
Amargosa Water Company (IMV)	Community	45
Embrey's Trailer Park	Community	45
Mountain View Apartments and Shopping Center	Community	75
Amargosa Elementary School	Single User	a
Amargosa Senior Citizen's Center	Single User	a
Coach House Bar	Single User	a
Roadside Park 801NY	Single User	a
Water-N-Hole	Single User	a

[a] In general these systems serve a transient population of at least 25 persons per day.

INFORMATION

Site Biosphere → 8

Site Geology → 7

Site Hydrology → 6

Site Geochemistry → 5

Repository Design → 4

Waste Package Design → 3

Material Properties → 2

Waste Form Properties → 1

PROCESS-LEVEL MODEL

7 → 6 → Saturated Zone Flow Model

7 → 6 → Unsaturated Zone Flow Model

7 → 6 → 4 → 3 → Drift-Scale Thermo-Hydrologic Model

3 → 2 → Waste Package Degradation Model

PROCESS LEVEL MODEL ABSTRACTIONS

Response surface of saturated zone flux → E

Response surface of unsaturated zone flux
- fracture flux
- matrix flux → D

Response surface of drift-scale flux
- % packages with drips
- advective flux in drips → C

Response surface of
- temperature
- humidity
- liquid saturation → B

Response surface of
- first pit
- pit distribution → A

TOTAL SYSTEM PERFORMANCE ASSESMENT

Biosphere Transport -Dose

8

Geosphere Transport -Cumulative Release

D E 5 6 7

EBS Transport -Release Rate

B C 5 4 3 2 1

Waste Package Degradation - Containment

A

Figure 2.1-1   Relationship of Chapter 2 to the Overall Information Flow Diagram for TSPA 1995 (Figure 1.4-6)
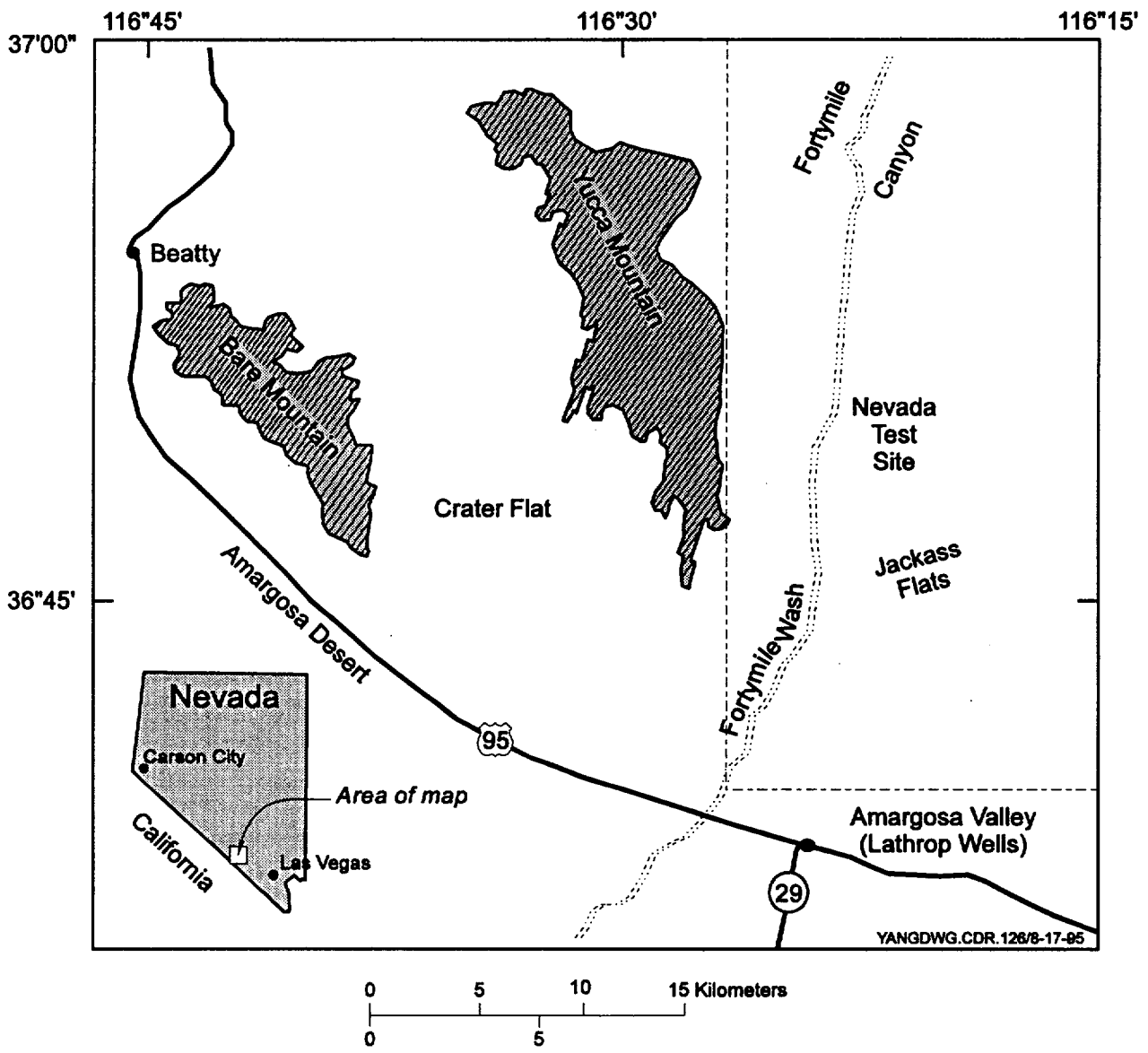
Figure 2.2-1 Location of the Yucca Mountain Area (modified from Montazer and Wilson, 1984)

Figure 2.2-2 Geologic map of Yucca Mountain (from Hoxie, 1989)

GEOLOGICAL UNIT		LITHOLOGY	HYDRO-GEOLOGICAL UNIT
PAINTBRUSH GROUP	Tiva Canyon Member	densely welded tuff moderately welded tuff	TIVA CANYON
		partially welded tuff nonwelded tuff bedded tuff	PAINTBRUSH
	Yucca Mountain Member	non- to moder. welded tuff bedded tuff	
	Pah Canyon Member	non- to moder. welded tuff bedded tuff	
	Topopah Spring member	non- to partially welded tuff	
		moder. to densely welded tuff densely welded tuff basal vitrophyre	TOPOPAH SPRING
		moder. to partially welded tuff	
CALICO HILLS FORMATION		bedded tuff non- to partially welded tuff	
CRATER FLAT GRP.	Prow Pass Member	non-to partially welded tuff bedded tuff	CALICO HILLS
	Bullfrog Member	non- to densely welded tuff bedded tuff	
	Tram Member	non- moder. to welded tuff	

Figure 2.2-3   Lithology of Major Stratigraphic Units at Yucca Mountain (after Montazer and Wilson, 1984)
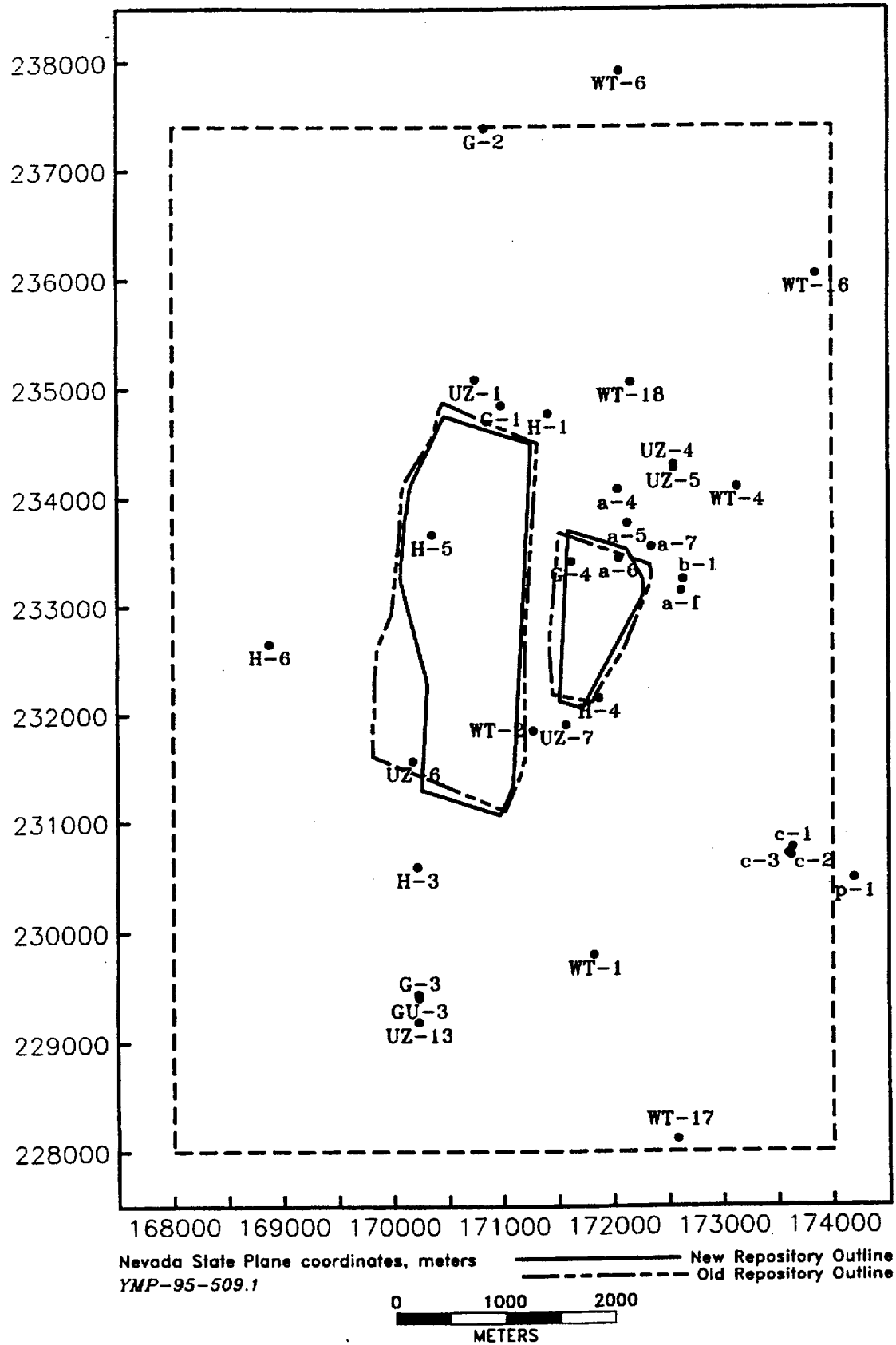
Figure 2.3-1   Borehole Locations in the Yucca Mountain Region
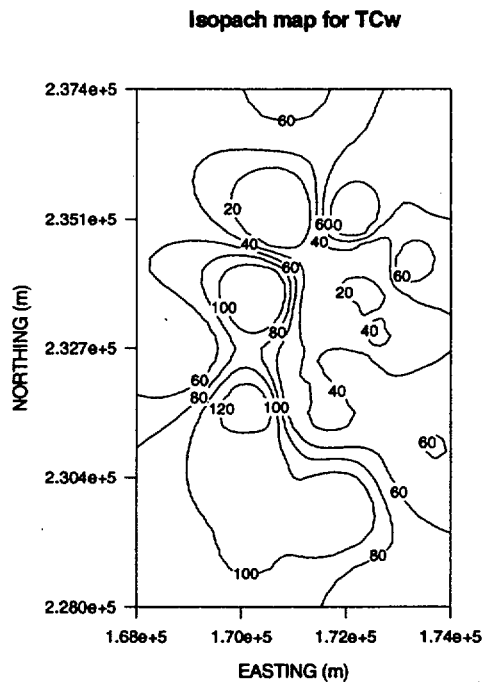
Isopach map for TCw

Figure 2.3-2   Isopach Map for Tiva Canyon welded (TCw) Unit (Contours in meters)
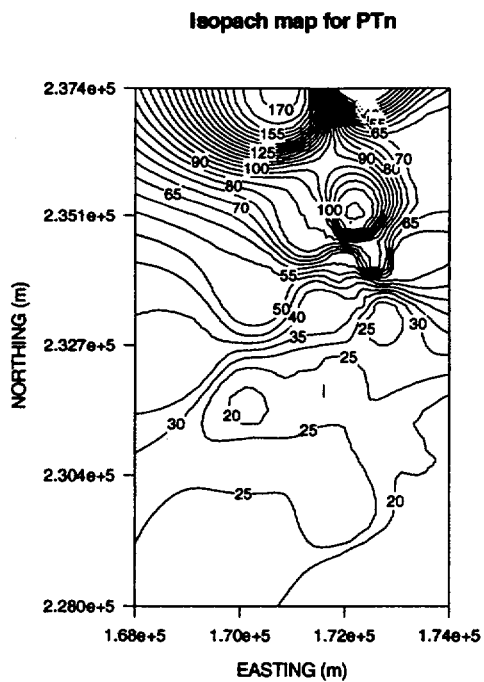
Isopach map for PTn

Figure 2.3-3   Isopach Map of Paintbrush nonwelded (PTn) Unit (Contours in meters)
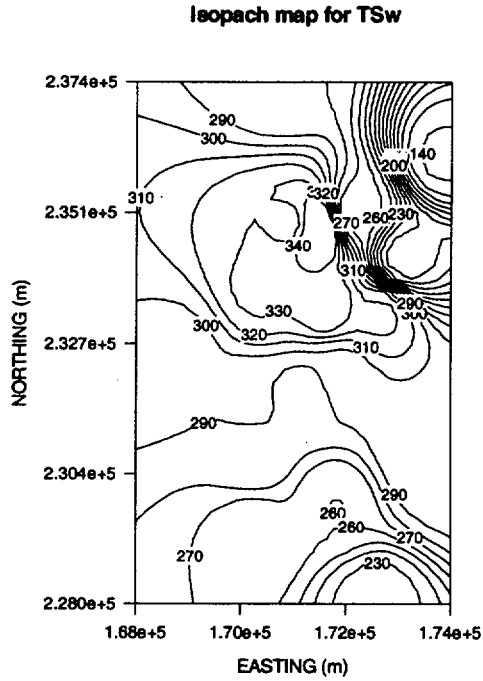
Isopach map for TSw

Figure 2.3-4   Isopach Map of Topopah Spring welded (TSw) unit (Contours in meters)
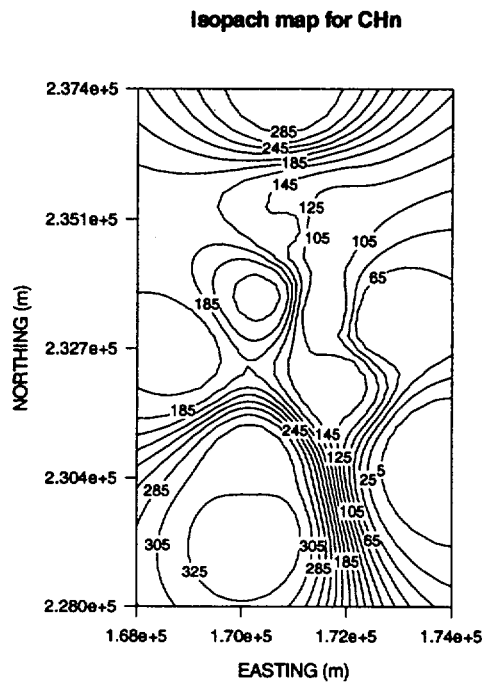
Isopach map for CHn

Figure 2.3-5   Isopach Map for Calico Hills nonwelded (CHn) unit (Contours in meters)
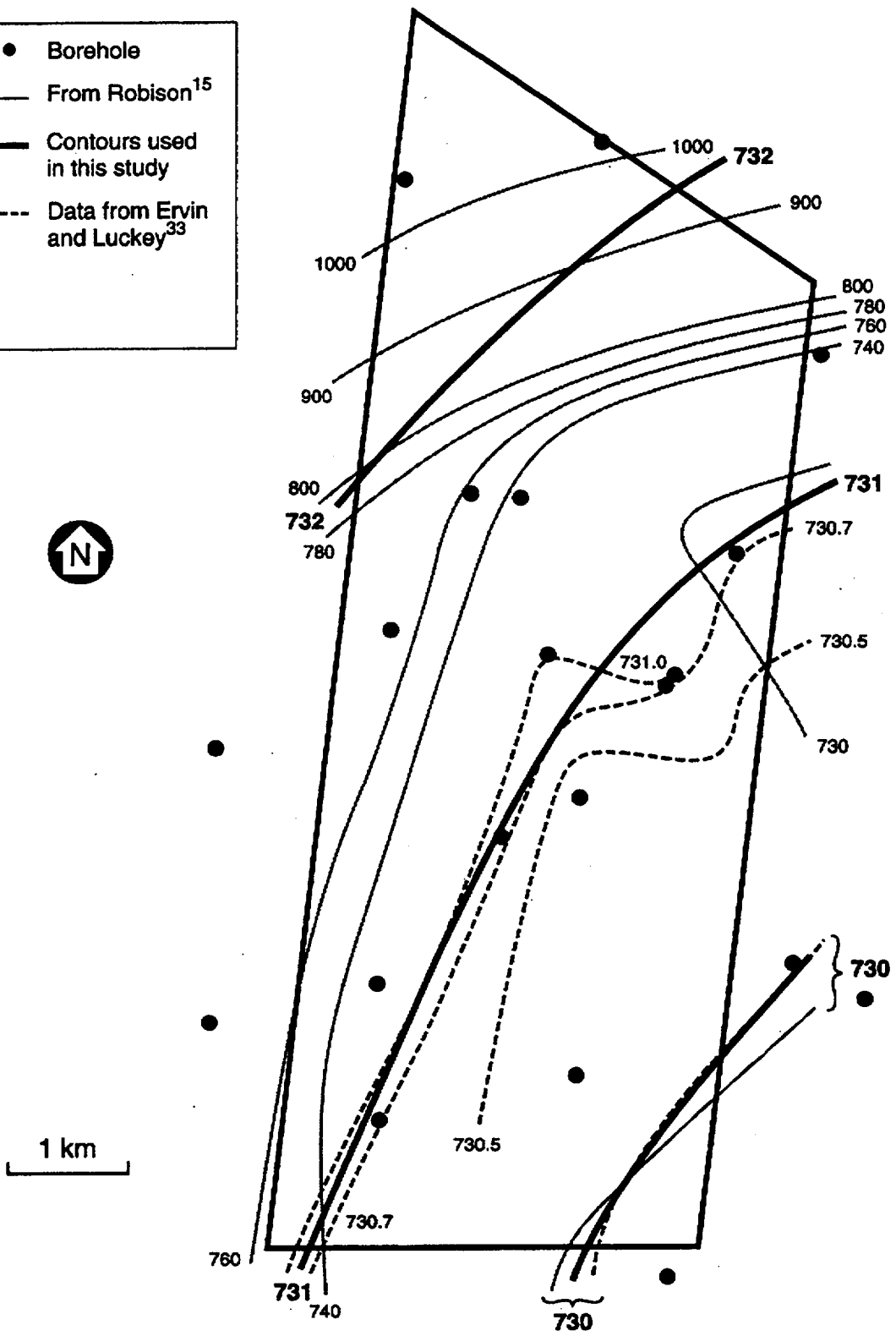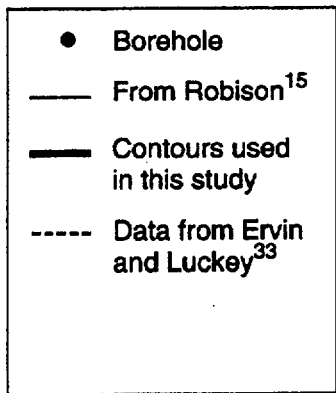
Figure 2.3-6   Contour Map of Water Table at Yucca Mountain (from Wittwer et al., 1995)
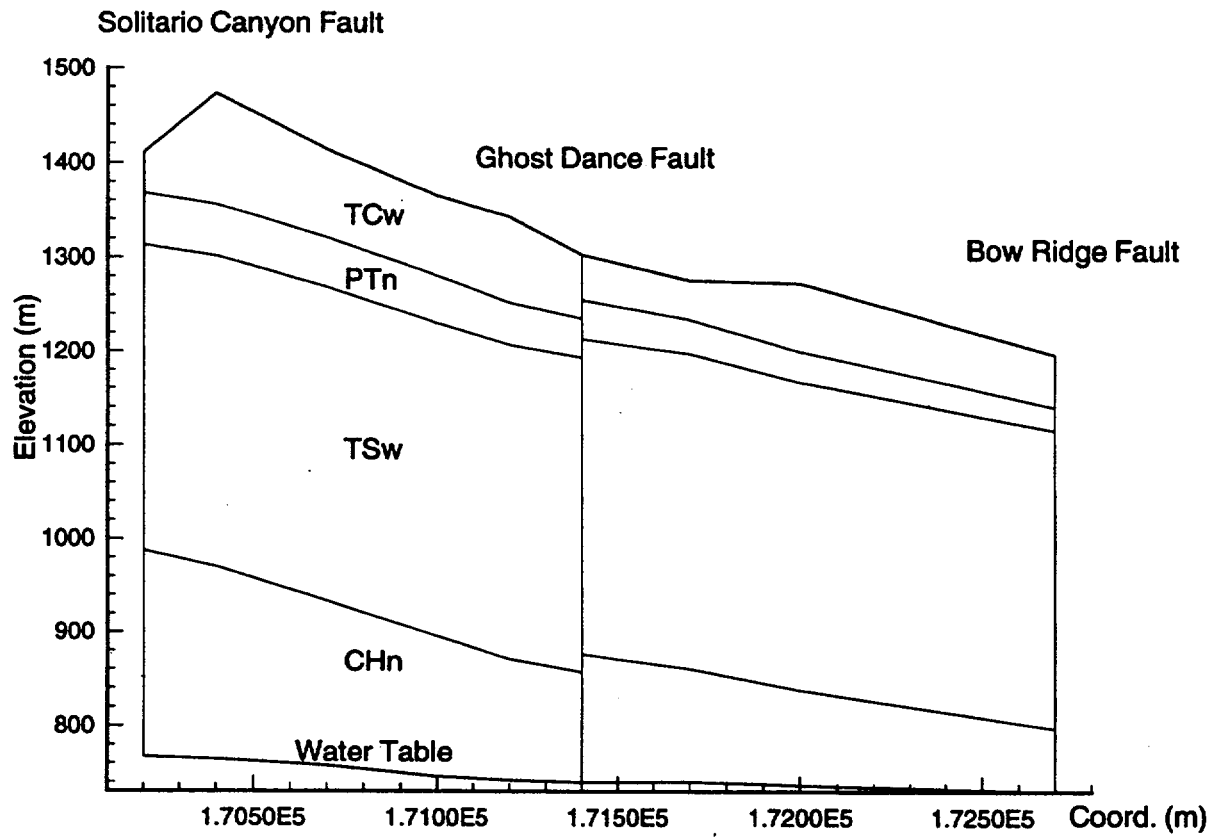
Figure 2.3-7   Geologic Cross-Section through the Potential Repository at Yucca
Mountain (from Wittwer et al., 1995)
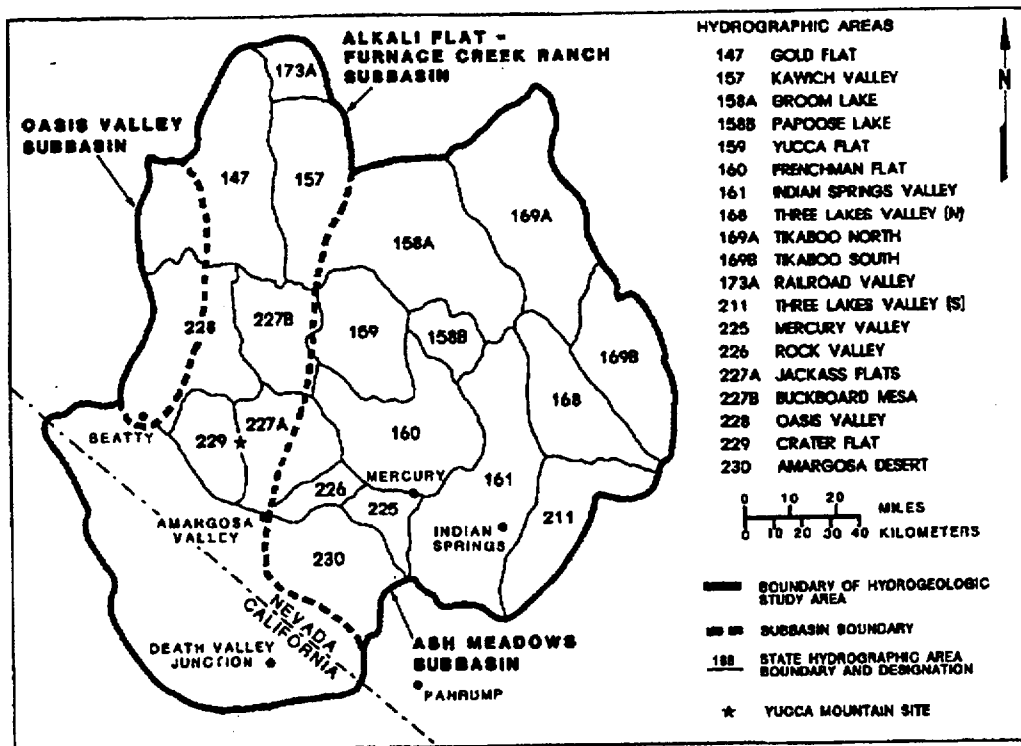
Figure 2.5-1 State of Nevada Hydrographic Areas Within the Yucca Mountain Hydrogeologic Study Area
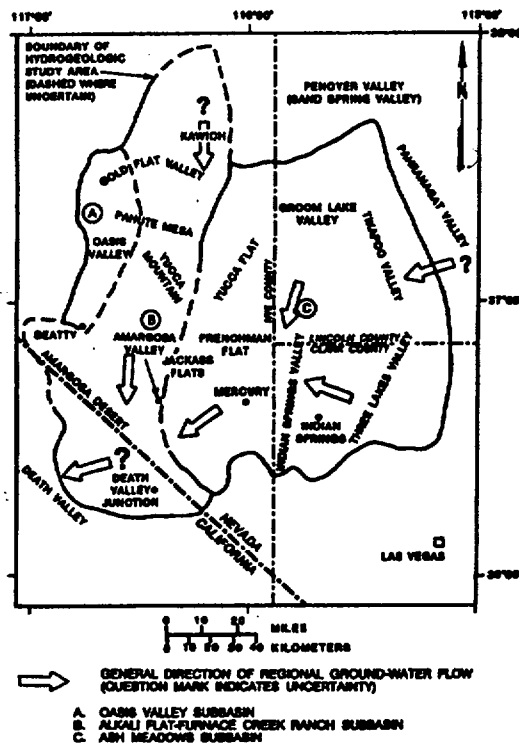
Figure 2.5-2 Hydrogeologic Study Area Showing Major Inflows and Outflows Across Subbasin Boundaries. Modified from Rush (1970), Blankennagel and Weir (1973), Winograd and Thordarson (1975), Dudley and Larson (1976), Waddell (1982), and Waddell et al., (1984)

2-27
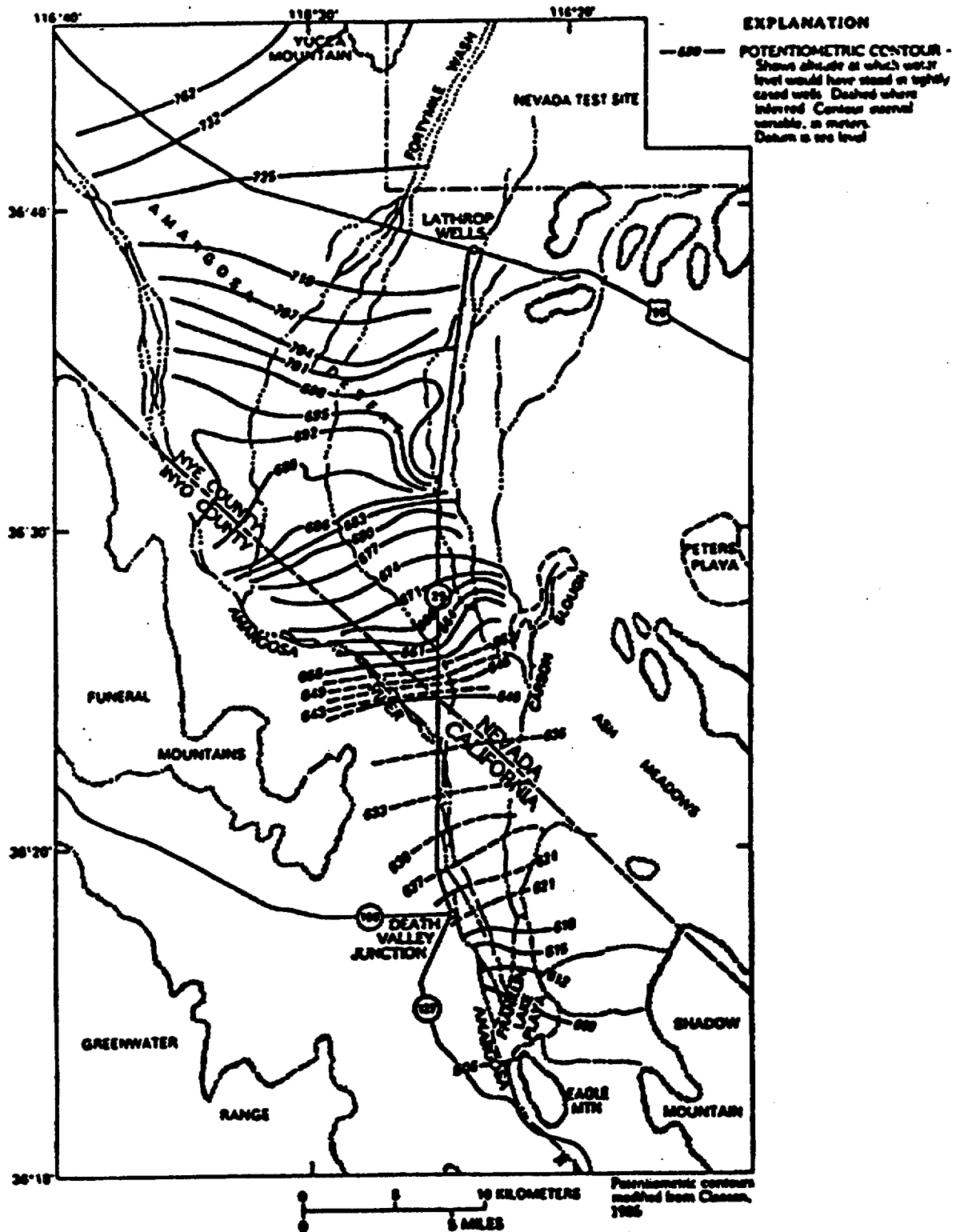
Figure 2.5-3   Potentiometric Surface of the Ground-Water Table Down Gradient from Yucca Mountain (modified from Claassen, 1985)

NORTH

SOUTH

B

B

YUCCA MOUNTAIN

AMARGOSA FARMS

EAGLE MOUNTAIN

LARGE HYDRAULIC
GRADIENT

DESIGN
REPOSITORY

EVAPOTRANSPIRATION

UPWARD LEAKAGE (?)

THROUGH
FLOW TOWARD
DEATH VALLEY

NOT TO SCALE

EXPLANATION

Playa sediments

Undifferentiated Tertiary rocks

Tertiary carbonate rocks

Tertiary volcanic rocks

Undifferentiated Paleozoic rocks

Paleozoic carbonate aquifer (?)

Possible fault

Inferred contact

General direction of
ground-water flow

Water table

Figure 2.5-4   Idealized Geohydrologic Cross Section from Yucca Mountain to Eagle Mountain (After Czarnecki, 1989)
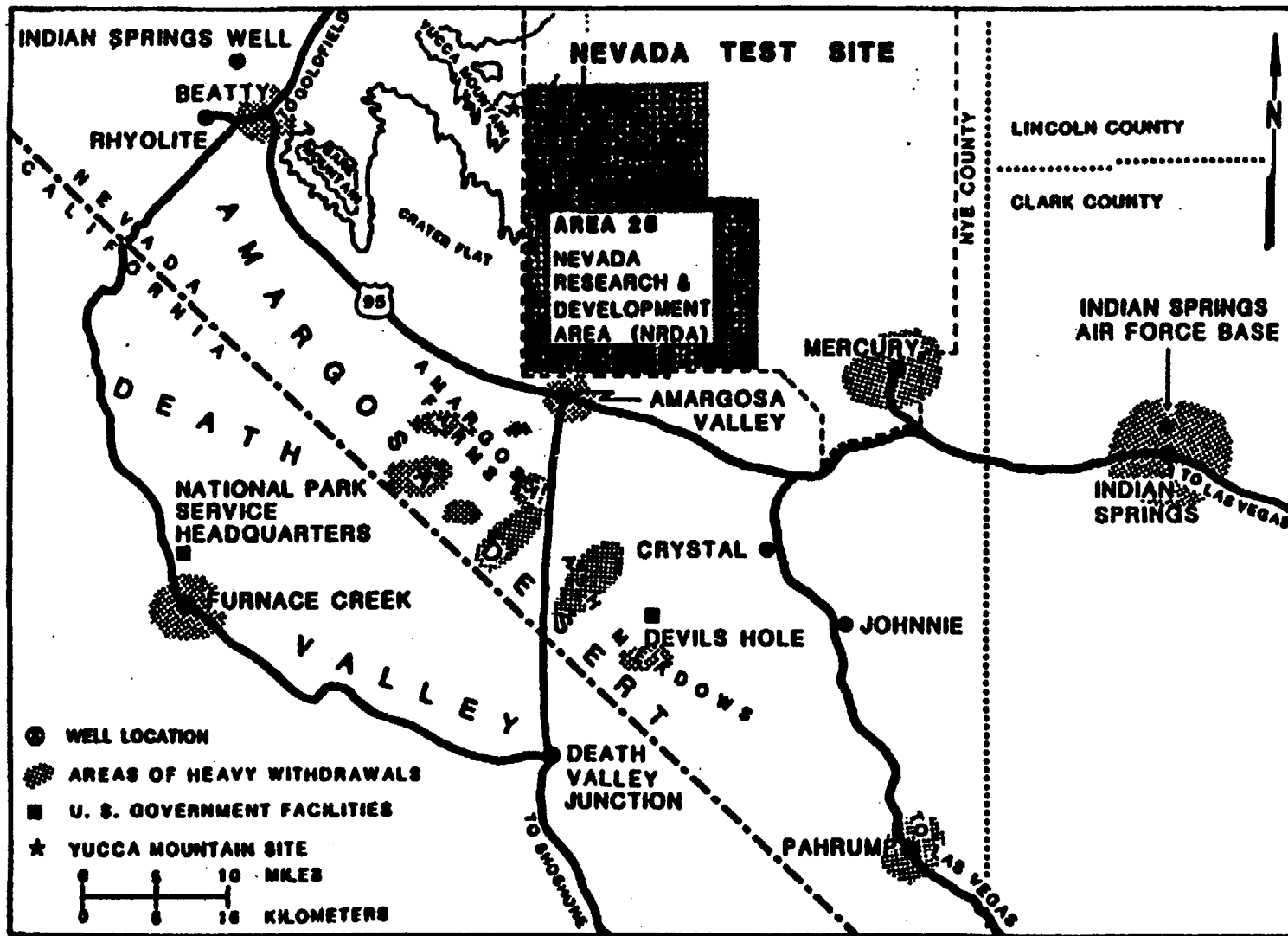
Figure 2.5-5   Map Showing Areas of Heavy Ground-Water Withdrawal Down Gradient FromYucca Mountain (modified from French et al., 1984)

NOT TO SCALE

EXPLANATION

A ALLUVIUM

TC TIVA CANYON WELDED UNIT

P PAINTBRUSH NONWELDED UNIT

TS TOPOPAH SPRING WELDED UNIT

CH CALICO HILLS NONWELDED UNIT

CF CRATER FLAT UNIT

⟶ DIRECTION OF LIQUID FLOW

⟶ DIRECTION OF VAPOR MOVEMENT

▽ PERCHED WATER
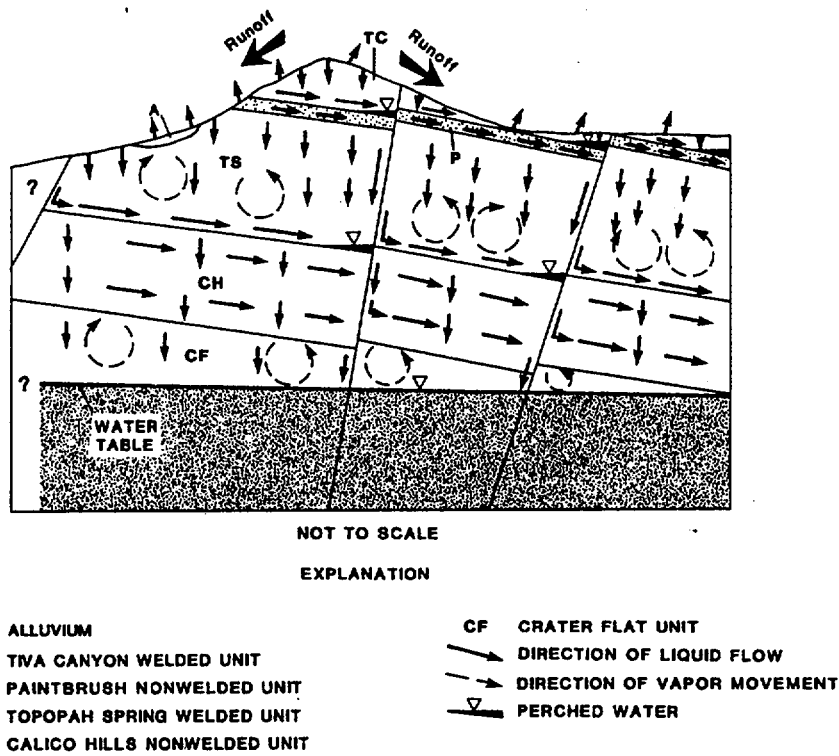
Figure 2.6-1 Generalized Section Across Yucca Mountain Showing Flow Regime Under Baseline Conditions

Flux in mm/year

■ Tiva Mod. Welded 0.22

☐ Tiva Welded 0.02

▦ PTn 13.40

■ Topopah Welded 0.08

☐ Rainier Mesa 0.60
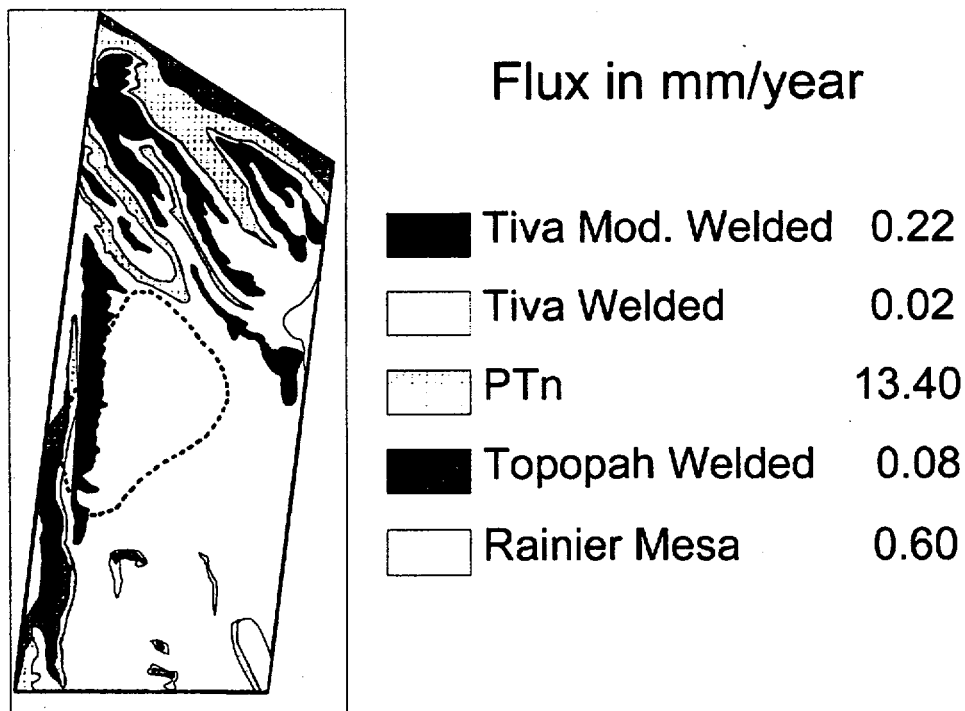
Figure 2.6-2 Spatial Distribution of Ambient Matrix Driven Infiltration Rates (derived from Flint and Flint, 1994)

2-31

3. REPOSITORY AND WASTE PACKAGE DESCRIPTION

Srikanta Mishra, Joon H. Lee, Jerry A. McNeish

3.1 INTRODUCTION

Determination of total system performance requires definition of the planned engineered components of the system that are proposed to be constructed for the disposal of the radioactive wastes. Complete definition of all the engineered components is not possible at this time as many factors, including cost and constructability, must be factored into the final design. However, in order to provide a consistent basis for design, analysis (including performance assessment) and cost/schedule evaluations, a Controlled Design Assumption document has been compiled (M&O, 1995c).

The information presented in the current chapter describes the repository and drift design options used to evaluate drift-scale thermal hydrology, and the waste package design options used to evaluate waste package degradation (Figure 3.1-1). Section 3.2 describes the general layout of the potential repository. Section 3.3 presents alternative thermal loading designs that have been proposed. Section 3.4 presents the repository layouts proposed to accommodate the different thermal loads. Section 3.5 presents the current waste package design options consistent with the Multi-Purpose Container (MPC) concept. Section 3.6 presents alternative waste package emplacement and backfill options proposed for the repository drifts. Section 3.7 presents the radionuclide inventory associated with both the spent fuel containers and the high-level waste canisters within each waste package. Finally, Section 3.8 describes the hydrostratigraphy associated with repository layouts for the two different thermal loads examined in this TSPA.

3.2 GENERAL LAYOUT CONSIDERATIONS

A conceptual design of a potential, high-level nuclear waste repository at Yucca Mountain is described in Chapter 6 of the Site Characterization Plan (SCP) (DOE, 1988) and is based on evaluations presented in the Site Characterization Plan - Conceptual Design Report (SCP-CDR) (SNL, 1987). This conceptual design consists of a series of emplacement panels approximately rectangular in shape and extending from the outer main drift to the perimeter of the repository (Figure 3.2-1). Three main drifts traversing the length of the repository provide access to the emplacement panels, with panel-access drifts leading from the main drifts to the emplacement drifts within the panels.

Subsequently, several programmatic decisions have necessitated modifications to the SCP-CDR emplacement concept. These include: (i) the construction of the Exploratory Studies Facility (ESF) and the need to develop an ESF-repository interface, (ii) the decision to use a Tunnel Boring Machine (TBM) for constructing the repository in lieu of the primarily drill-and-blast method proposed in the SCP-CDR, and (iii) the possibility of emplacing waste packages at a lower (or higher) areal mass loading than the SCP-CDR design. Motivated by such concerns, new conceptual layouts were developed using the following key criteria (M&O, 1993b):

- Provide a layout that provides for logical development and waste emplacement schemes, and is compatible with the TBM-based repository concept.

- Locate the emplacement horizon within the unsaturated zone and at least 200 m below the ground surface.

- Locate the waste emplacement horizon within the lithophysae-poor section of the Topopah Spring welded (TSw) unit.

- Locate and orient emplacement areas, to the extent practicable, to avoid major identifiable faults and fracture systems, consistent with achieving relatively continuous disposal areas and a workable layout.

Six potential emplacement areas were identified using these and other operational (i.e., ventilation, drainage, etc.) criteria, and are shown in Figure 3.2-2. The general characteristics as well as bounding conditions which formed the bases for the configurations shown in this figure are discussed elsewhere (M&O, 1994c). The individual emplacement area available for each of the potential emplacement areas is given in Table 3.2-1.

3.3 THERMAL LOADING ISSUES

Thermal loading refers to the spatial density at which waste packages (WP) are emplaced within the repository, and is typically characterized by two common measures: (i) the areal power density (APD), which relates the average initial heat generated by WPs at the time of emplacement to the two-dimensional area occupied by WPs in the subsurface, and (ii) the areal mass loading (AML), which relates the amount of waste expressed in metric tons of uranium (MTU) to the emplacement area. The SCP designs, as well as subsequent analyses of thermal/thermohydrologic/thermo-mechanical behavior, have used the APD concept, with the thermal loading expressed in kW/acre. A major shortcoming of this approach is that it cannot address the wide variability in the thermal characteristics of the waste stream. Using a constant emplacement drift spacing and spacing the WPs within the drift according to their initial heat output (APD) would result in non-uniform thermal conditions within the repository after a relatively short period of time because of the variability in waste stream characteristics. These considerations have led recent work to use the AML concept, with the thermal loading expressed in MTU/acre. The AML approach recognizes that WP heat output will be nearly the same after several hundred years for packages containing the same amount of waste. Thus, package spacings based on MTU content will provide more uniform thermal conditions over the long-term performance period.

The original thermal loading strategy for the potential repository at Yucca Mountain, as described in the SCP (DOE, 1988), involved emplacement of 63,000 MTU of spent nuclear fuel (SNF) and 7,000 MTU of defense high-level waste within the primary area - resulting in an areal power density of 57 kW/acre. Small waste packages, containing only a few SNF assemblies with low thermal output (1-3 kW), were designed for emplacement in boreholes in the floors or walls of the emplacement drifts. Since that time, a wide range of thermal loadings and thermal designs have been investigated with a view to maximizing thermohydrologic performance and/or minimizing thermohydrologic disturbance to the repository system (e.g., Buscheck and Nitao, 1992, 1993; Pruess and Tsang, 1993, 1994). Such studies led to the inclusion of thermal loads of 28 kW/acre and 114 kW/acre, in addition to the SCP value of 57 kW/acre, in previous evaluations of total system performance for Yucca Mountain (Andrews et al., 1994).

No decisions have been made as yet regarding the final thermal loading for the proposed repository at Yucca Mountain. These decisions have been deferred until such time as results from laboratory and in-situ thermal tests (and performance confirmation testing) are available to provide greater confidence to the understanding of thermohydrologic phenomena and more defensible bases to their predictions using numerical models (M&O, 1995e). In the interim, engineering design is proceeding under the assumption that *"Surface, subsurface and waste package/EBS designs will be robust and flexible and will accommodate a range of thermal loads from about 20 to about 100 MTU/acre"* (M&O, 1995c, Key Assumption 019). Within the framework of this general guideline, design/analyses are being carried out for two cases:

- 'Low' Thermal Load (~20-40 MTU/acre): For these conditions, it is postulated that the hydrology of the host rock will not be significantly disturbed from its ambient state. A low loading can be achieved using either wide spacing of WPs with moderately spaced drifts (the minimal disturbance, MD, concept), or with WPs spaced close together in widely-spaced drifts (the localized disturbance, LD, concept). The MD option minimizes near-field temperatures, while the LD option minimizes thermal influences on the overall hydrologic system. The low thermal loading option requires emplacement of wastes beyond the primary emplacement area (in optional areas A through D as shown in Figure 3.2-2) to meet the statutory capacity requirements as specified in the Nuclear Waste Policy Act Amendment of 1987.

- 'High' Thermal Load (~80-100 MTU/acre): At a sufficiently high thermal load, it is hypothesized that water will be vaporized and driven away from the vicinity of the waste packages, resulting in dry conditions for extended periods of time (the extended dry, ED, concept), and hence, improved waste containment and isolation. This option would allow the statutory capacity requirements to be met by emplacing wastes in the upper block of the primary emplacement area alone (Figure 3.2-2).

TSPA-1995 focusses on these two thermal loading scenarios, i.e., the low thermal loading case (~20-40 MTU acre) and the high thermal loading case (~80-100 MTU/acre). In order to integrate the various design, performance assessment and systems analysis calculations related to thermal loading, it has been suggested that the values of 25 MTU/acre and 83 MTU/acre be taken as common points of reference (Saterlie, 1994). These two values have therefore been used as representative 'point designs' for low and high thermal loading, respectively, in this study.

Note that for the reference waste stream used in TSPA-1995 (Section 4.2.5), the conversion factor between areal mass loading (MTU/acre) and areal power density (kW/acre) is ~1 kW/MTU.

3.4   LAYOUTS FOR 25 AND 83 MTU/ACRE

The layouts for waste emplacement are developed for 63,000 MTU of spent nuclear fuel, assuming that the heat generation from defense high-level wastes is negligible. For the 25 MTU/acre case, this requires an area of approximately 2520 acres - which is 7% less than the cumulative area of the six emplacement panels identified in Table 3.2-1. A further examination of the emplacement panels reveals that Optional Area A is located over the region of potentially large hydraulic gradient (Ervin et al., 1994) and also has a relatively short travel distance to the water table. Eliminating Optional Area A from consideration reduces the cumulative area to

2535 acres --which satisfies the areal requirements for the 25 MTU/acre case, and also minimizes the potential for any adverse impact of the large hydraulic gradient on waste isolation. Figure 3.4-1 shows the corresponding spatial distribution of wastes over the five emplacement areas.

The high thermal loading (83 MTU/acre) case requires an area of approximately 760 acres, and can be accommodated within the upper emplacement block of the Primary Area. The corresponding spatial distribution of wastes is shown in Figure 3.4-2. Note that both of these layouts (25 and 83 MTU/acre) are essentially similar to those presented in M&O (1994c), with the exception that Optional Area A has been excluded for the low thermal loading case because of the reasons described above.

3.5 WASTE PACKAGE DESIGN

The waste package (WP) as defined in 10 CFR Part 60.2 includes the waste form and any containers, shielding, packing and other absorbent materials immediately surrounding an individual waste container (NRC, 1993). The NRC regulations define the engineered barrier system (EBS) as the waste packages and the underground facility. The waste package and engineered barrier system components have been discussed briefly in Section 1.4 with the schematic diagram for the components shown in Figure 1.4-4. Except for the waste disposal container and the invert, specifics of the design of other Waste Package and EBS components are in their early stages (Stahl, 1995).

In the current design concept of waste disposal containers for the potential repository at Yucca Mountain, two or three layers of different metals, depending on thermal load, have been proposed for the disposal containment barriers for spent nuclear fuel (SF) and vitrified defense high-level waste (DHLW). According to the recent Controlled Design Assumption (CDA) Document (M&O, 1995c), a corrosion-allowance material (CAM) such as mild steel has been proposed as the outer containment barrier, and a corrosion-resistant material (CRM) such as Inconel 825 (Alloy 825) has been proposed as the inner containment barrier for the spent fuel waste disposal container and for a high thermal load case. For the low thermal load case, a moderately corrosion resistant material (MCRM) such as Monel 400 has been added as an additional containment barrier on top of the two-layer containment barrier design for a high thermal load case. Addition of MCRM in a low thermal load case was prompted by the possibility of microbiologically influenced corrosion (MIC). For the DHLW waste container design for both thermal load cases, CAM is replaced with another candidate MCRM (70/30 copper-nickel alloy).

Additional details on the dimensions of the waste disposal containers were provided in a recent M&O document (Doering, 1995). The dimensions of the waste container for a typical large multi-purpose canister (MPC) for 21 pressurized water reactor (PWR) or 40 boiling water reactor (BWR) fuel assemblies are given in Table 3.5-1 along with those of the waste container for four DHLW pour canisters. The thickness of the inner barrier for the large MPC and DHLW waste container is 20 mm, the thickness of the outer barrier for the large MPC waste container is 100 mm, and that for DHLW waste container is 50 mm. The M&O document did not provide the specifications of the potential third (or outermost) containment barrier (Monel 400) specified in the CDA for a low thermal load case.

In the current design concept, Alloy 825 was chosen because it is highly resistant to uniform corrosion and in many environments is resistant to localized corrosion such as pitting, crevice, and stress corrosion. Carbon steel has relatively low corrosion resistance in nearly all environments; but, its corrosion rates are predictable, and its cost is low. A thick layer of carbon steel is intended to allow for the higher corrosion rate and to provide structural integrity of the waste package and radiation shielding to the outer surface of the waste package. Once penetrated, carbon steel would serve as a sacrificial anode which cathodically protects the Alloy 825 inner barrier. Moderately corrosion resistant materials have properties between corrosion resistant and corrosion allowance materials, but their corrosion behavior is largely unknown (Van Konynenburg et al., 1994).

Since adequate models for predicting the performance of the moderately corrosion resistant materials (Monel 400 and 70/30 copper-nickel alloy) are not available, it has been recommended that this potential containment barrier not be included in any waste package performance analysis (Doering, 1995). Thus, in TSPA-1995, all waste containers for spent fuel and defense high-level waste are assumed to have the same design, viz., a 20 mm thick corrosion-resistant inner barrier of Alloy 825, and a 100 mm thick corrosion-allowance outer barrier of carbon steel. Also, the stainless steel MPC shell and DHLW pour canister are not considered in this TSPA iteration.

3.6   WASTE PACKAGE EMPLACEMENT

3.6.1 Background

Three major waste emplacement concepts have been considered in previous conceptual repository design studies, i.e., vertical borehole emplacement, horizontal borehole emplacement, and in-drift emplacement. Schematic diagrams illustrating the emplacement concepts are shown in Figure 3.6-1 (DOE, 1988). The two borehole emplacement methods were developed as part of the SCP-CDR (SNL, 1987). The primary emplacement mode called for placement of waste packages in vertical boreholes drilled into the floor of emplacement drifts. The alternative consisted of placing waste packages in long horizontal boreholes drilled between adjacent drifts. In-drift emplacement was also proposed as an alternative to horizontal borehole emplacement in order to accommodate large waste packages.

The adoption of the Multi-Purpose Canister (MPC) waste package concept has lead to a re-thinking of repository emplacement modes for the following reasons:

- A typical 21 pressurized water reactor (PWR) MPC-based waste package would be 5.6 m long and 1.8 m in diameter, weigh 66 tons, contain 9 MTU and produce an average of 10 kW heat at emplacement. The SCP-based consolidated 3 PWR / 4 BWR waste package, on the other hand, would be 4.6 m long and 0.7 m in diameter, weigh 5.3 tons, contain 2.6 MTU and produce an average of 2-3 kW heat at emplacement. Emplacement of the large-diameter, high heat output MPC-based waste packages would not be appropriate in boreholes because thermal design goals associated with canister centerline temperatures (<350°C) would be violated (M&O, 1994b).

- The Controlled Design Assumption document (M&O, 1995c) calls for a flexible subsurface repository design to accommodate a range of thermal loads from about 20 to

about 100 MTU/acre. The need for maintaining such design flexibility must be taken into account in developing and selecting an emplacement mode.

3.6.2 Emplacement Mode Selection

A recent M&O study (M&O, 1995f) provides a basis for the selection of a waste package emplacement mode with which to complete current repository advanced conceptual design activities. Six different modes of emplacement were described and evaluated against ten different criteria, as summarized below.

The emplacement modes evaluated included:

- *Center In-Drift* - WPs emplaced along the centerline of a TBM-excavated emplacement drift.

- *Off-Center In-Drift* - WPs emplaced off-center within the envelope of primary TBM-excavated emplacement drifts.

- *Short Parallel Alcove* - WPs emplaced in alcoves with the long axis of the alcove parallel to a primary TBM-excavated drift.

- *Short Perpendicular Alcove* - WPs emplaced in alcoves with the long axis of the alcove perpendicular to a primary TBM-excavated drift.

- *Short Angled Alcove* - WPs emplaced in alcoves excavated at a 45°C angle from the primary TBM-excavated drift.

- *Short Cross Drift* - WPs emplaced in short cross drifts between pairs of primary TBM-excavated drifts.

The criteria used to evaluate these emplacement modes included: (1) operational complexity during emplacement, (2) ease of retrieval, (3) safety, (4) flexibility to accommodate a range of thermal loads, and to adjust thermal loading, (5) potential for thermal management via ventilation, (6) constructability, (7) ability to emplace backfill, (8) inherent stability of resulting excavation, (9) relative cost, and (10) long-term performance.

The results of these evaluations showed a clear preference for in-drift modes over alcove-based modes, with little distinction between center in-drift and off-center in-drift emplacement modes (M&O, 1995f).

3.6.3 Drift Design for TSPA-1995 Analyses

This sub-section provides a brief review of the drift design used in TSPA-1995, along with related information on the issues of backfill and ventilation.

Information regarding the exact nature of emplacement (i.e., drift size, location of waste package within drift, dimensions of invert and other supporting material, etc.) is needed to develop the

geometry for the near-field thermo-hydrologic calculations described in Chapter 4. This information is also utilized in the assessment of radionuclide transfer through the engineered barrier system (EBS). In order to simplify the emplacement geometry in such model representations, the Center In-Drift On Pedestal (CIDP) option has been chosen as the basis for the analyses reported in this document.

The CIDP option, as shown schematically in Figure 3.6-2, involves placement of waste packages by a remote controlled rail-mounted gantry crane on permanent pedestals that are prepositioned in the drift. The waste package dimensions shown in the figure are typical of a 21-PWR MPC-based waste package. The drift diameter of 5 m is determined by the need to provide a reasonable operating clearance, and to provide additional space for ground support and excavation misalignment tolerance. The materials to be used in the fabrication of the emplacement pedestal have not been determined as yet. For the purposes of this study, the tunnel invert fill, as well as the support pedestal, are taken to be made of a gravel-type material similar to the backfill.

The current version of the Controlled Design Assumption document states that "*Means for retarding the escape of radionuclides from the disposal container and/or for physical protection of the waste package (e.g., backfill) will be evaluated for implementation in Waste Package and Subsurface designs*" (M&O, 1995c, Key Assumption 046). The use of a granular backfill material as a capillary barrier and a thermal management tool has also been advocated in recent studies of near-field thermohydrologic performance (Buscheck et al., 1995). On the other hand, practical considerations render the emplacement of backfill in long drifts (~1000 m), under hot conditions (~100 °C), and with unshielded waste packages, a difficult proposition. No final decision has been made with respect to the backfill issue, and the selection of likely candidates for use as backfill. This study therefore considers both backfilling and no backfilling options in evaluating Waste Package/EBS and total system performance. The characteristics of the backfill are taken to represent a gravel type material, with suitable modifications to incorporate enhancements in porosity and thermal conductivity.

Plans have been developed for ventilating the repository during the construction and waste emplacement operations (M&O, 1994b). Waste emplacement management could potentially involve continuous ventilation to maintain a constant wall rock temperature of 50 °C. This represents an extreme case that is not likely to be a realistic design option because of air flow requirements. An alternative is to focus air flow so as to minimize localized heat spikes next to emplaced waste packages, resulting in lower air quantity requirements. A third alternative is to provide ventilation only on an "as needed" basis during retrieval operations. From the perspective of near-field performance, the cumulative effects of heat removal due to ventilation is expected to be marginal for the third (and perhaps the most likely) option described above. Therefore, the effects of ventilation are not included in this analysis.

3.7   RADIONUCLIDE INVENTORY

The radionuclide inventory used in the TSPA-1995 analyses is divided into two basic components: spent fuel (PWR and BWR) and DHLW. The inventory used in the analyses is based on inventories for the PWR and BWR in the Characteristics Database (M&O, 1993c). The DHLW inventory was obtained from DOE (1987). A weighted average spent fuel inventory was determined. Screening was conducted based on contribution of the radionuclide to: (1) potential

release normalized to 40 CFR 191 Table 1 values over time periods from 1,000 to 1,000,000 years, and (2) potential average annual whole body dose over time periods from 1,000 to 1,000,000 years. This screening is explained in more detail later in the section. Spent fuel (both PWR and BWR) and DHLW are included in the inventory. Thirty-nine radionuclides for spent fuel and thirty two radionuclides for HLW are included in the analyses.

Spent Fuel: The spent fuel is composed of PWR and BWR fuel with tonnages of 40,785 MTHM and 22,210 MTHM respectively to reach a total of 63,000 MTHM. The average burnup rate for the TSPA-1995 analyses is based on a content of 64.68 percent PWR fuel and 35.32 percent BWR fuel with burnups of 39,651 MWd/MTHM and 31,186 MWd/MTHM respectively for an average burnup of 36,666 MWd/MTHM. Thirty-year-old fuel is assumed. The spent fuel inventory assumes the PWR and BWR fuel are mixed (Table 3.7-1). The metric tons of uranium (MTU) (for practical purposes the equivalent of MTHM) is calculated from the number of PWR spent fuel assemblies per container and the mass of a PWR assembly.

Defense High-Level Waste: The DHLW inventory presented in Table 3.7-2 is directly from DOE (1987). The thermal output of the DHLW is small in comparison to the spent fuel. The burnup value for DHLW is assumed to be 10,000 MWd/MTU after Golder Associates Inc. (1993). This is used only for purposes of normalization to the EPA standard. The assumption is 7,000 MTHM of DHLW in 14,000 containers. The waste is assumed to be derived from West Valley, Idaho National Energy Laboratory, Savannah River Laboratory, and Hanford Facilities.

Screening: The screening of radionuclides for inclusion in the analyses was done in two steps. The first step used the ratio of the inventory to EPA Table 1 release limits. The ratio of the weighted average spent fuel inventories of specific radionuclides to corresponding EPA Table 1 values were determined for 1,000, 10,000, 100,000, and 1,000,000 years. The fractional contribution of each isotope to release at a time of 1,000, 10,000, 100,000, and 1,000,000 years was calculated assuming a combination of delay due to waste package lifetime and retarded transport of 1,000 to 1,000,000 years. Isotopes which contributed at least a fraction of the EPA limit at any of the selected times passed this screening. The entire decay chain for daughters which contributed greater than 10^{-5} of the EPA limit at any time were also included.

The second step of the screening used dose and was based on inventories from the Characteristics Database at the same time periods. The waste form was assumed to be altered at a rate of 10^{-5} of the total inventory per year (Ci/yr). The isotopes were assumed to dissolve, as they were made available by the assumed waste form alteration rate, at the maximum solubilities according to NAS (1983), EPRI (1992), and Barnard et al., (1992). The advective, downward flux in ground water moving through the unsaturated zone was assumed to occur at 0.1 mm/yr over a cross sectional area of 33,000 m^2. On arrival at the saturated zone, the isotopes were assumed to mix in the saturated zone with a flow rate of 10,000 m^3/yr. Ingestion of 700 liters/year by a person using this ground water was assumed. The ingested dose was calculated using the maximum effective (whole body) dose conversion factor from DOE (1988), NRC (1981), or EPA (1988). The fractional contribution of each isotope to total dose at times of 1,000, 10,000, 100,000, and 1,000,000 years was determined. For radionuclides with two or more isotopes present in the waste, the solubility limit was set for the element (i.e., all isotopes) and then proportioned between the individual isotopes by the mass fraction present at the corresponding time. All isotopes contributing less than 10^{-5} of total dose at any time period were eliminated from the inventory unless they were in the

decay chain for daughters which contributed 10^{-5} of total dose at any time. The two screening steps produced the radionuclide inventory for the spent fuel shown in Table 3.7-1.

3.8 UZ PATHWAY STRATIGRAPHY

The unsaturated zone is treated as a series of vertical one-dimensional pathways in RIP. Preliminary simulations of ambient unsaturated hydrology, which indicate the pervasiveness of vertical one-dimensional flow, at least in the vicinity of the proposed repository block, are described in Chapter 7. In this section, the pathways are identified and their hydrostratigraphic descriptions presented. These pathways are overlain on the footprint of the proposed waste emplacement panels (Figure 3.2-2) and are the origination point for radionuclide transport out of the EBS and through the geosphere.

3.8.1 Pathways in Primary and Optional Areas

As noted in Section 2.3, data from 34 boreholes were used to develop the three-dimensional hydrostratigraphy for the site-scale unsaturated flow model (Wittwer et al., 1995). The region covered by this model includes the two emplacement panels in the Primary Area, i.e., the Upper Block and the Lower Block, as shown in Figure 3.2-2. Information from Wittwer et al., (1995) was thus used to define pathway stratigraphies for these two panels. Limited borehole data are available in the regions corresponding to the Optional Areas. Some preliminary stratigraphic information, based on the thermo-mechanical stratigraphic model of Ortiz et al., (1985), was developed in support of the FY/94 Thermal Loading Systems Study (M&O, 1994c). This information has been used as the basis for the pathway stratigraphies of the other three panels.

Primary Area (Upper Block)

A preliminary examination of the isopach maps of the various hydrogeologic units described in Section 2.3 revealed that there is sufficient spatial variation in formation thicknesses to warrant the subdivision of the Upper Block of the Primary Area into multiple pathways. As a first step in this process, one-dimensional stratigraphic information was extracted for the 25 vertical columns of the Wittwer et al., (1995) model falling within the Upper Block. The data consisted of the thickness of TSw, TSv, CHnv and CHnz units between the proposed repository horizon and the water table. These were then reorganized in terms of three variables: (i) depth to the water table, (ii) absolute thickness of CHn (including both vitric and zeolitic units), and (iii) percent of the pathway in CHn. Use of the two latter variables for pathway demarcation allows a grouping of areas with similar percentages of welded (or nonwelded) rocks along a vertical column between the repository and the water table.

Figure 3.8-1 shows scatter plots of: (a) the percent of the pathway in CHn vs. depth to water table, and (b) thickness of CHn vs. depth to water table. Based on these scatter plots, the columns from the Wittwer et al., (1995) model were grouped into six pathways, shown as pathways 1 to 6 in Figure 3.8-2. The boundary between pathways was established by drawing a line midway between the columns in adjacent pathways. The stratigraphy for each of these pathways was determined by averaging the thicknesses of the various units for all the columns within the pathway.

The footprint of the pathways shown in Figure 3.8-2 represents part of the required area for the low thermal loading (25 MTU/acre) layout. However, as discussed in Section 3.4, this area is adequate for the high thermal loading (83 MTU/acre) layout. The corresponding areal distribution of the pathways for the 83 MTU/acre case is shown in Figure 3.8-3.

Primary Area (Lower Block)

This emplacement area includes three columns from the Wittwer et al., (1995) model, with only modest changes in hydrogeologic unit thicknesses. A single pathway was therefore chosen to represent this region, shown as pathway 7 in Figure 3.8-2. The stratigraphy was determined, as before, by averaging the thicknesses of the various units for the three columns within this pathway. Note that this pathway is used only in the analysis of the 25 MTU/acre case.

Optional Areas

Because of limited stratigraphic information in the regions corresponding to the Optional Areas, it was decided to treat each emplacement panel as a single pathway. These are shown as pathways 8, 9, and 10 in Figure 3.8-2. Stratigraphic information for these panels has been tabulated in M&O (1994c) in terms of minimum and maximum thickness for each hydrogeologic unit. This description has been simplified to provide an average thickness for each hydrogeologic unit in the present study. Note that these pathways are used only in the analysis of the 25 MTU/acre case.

3.8.2 Comparative Statistics

The thickness of TSw, TSv, CHnv and CHnz units for each of the 10 pathways is given in Table 3.8-1. Also provided therein is the relative area occupied by the footprint of each pathway (as a percentage of the total emplacement area) for the 25 MTU/acre and the 83 MTU/acre cases. Note that the total area utilized for the 25 MTU/acre layout is 2535 acres, and for the 83 MTU/acre layout is 760 acres - assuming that 63,000 MTU are emplaced. A bar graph showing a visual comparison of the relative thickness of each pathway and its components for the 10 pathways is displayed in Figure 3.8-4.

The hydrostratigraphic division employed by Wittwer et al., (1995), as shown in Figure 3.8-4, lumps the nonwelded Prow Pass, Bullfrog and Tram Members of the Crater Flat Group - hereafter referred to as the Prow Pass nonwelded (PPn) unit - into the Calico Hills nonwelded (CHn) hydrogeologic unit. The rationale for this simplification is the similarity in the degree of welding (and hence in hydrologic properties) between these units and the overlying nonwelded vitric/zeolitic rocks of the Calico Hills formation. Although adequate for modeling water flow under ambient conditions, this strategy is inappropriate for modeling nuclide transport because of the difference in sorption properties between CHnz and PPn. Thus, a further partitioning of the CHnz unit as described in Wittwer et al., (1995) into CHnz and PPn is needed for transport modeling purposes. The relative proportion of PPn in the CHnz-PPn sequence is obtained from the 3-D thermo-mechanical stratigraphic model of Ortiz et al., (1985), and interpolated onto the pathway map shown in Figure 3.8-2. This information is also tabulated in Table 3.8-1.

Note that two complementary sources of information are used to develop the hydrostratigraphy of the pathways - the hydrogeologic model of Wittwer et al., (1995) and the thermo-mechanical model of Ortiz et al., (1985). In order to compare the consistency between the two, the ranges of thickness for the four hydrogeologic units (TSw, TSv, CHnv and CHnz) in the Primary Area (pathways 1-7) as predicted by the two models have been compared. As shown in the bar graph of Figure 3.8-5, there is good agreement between the predictions of Wittwer et al., (1995), denoted as LBL, and those of Ortiz et al., (1985), denoted as SNL.

Table 3.2-1 Available Area for Potential Emplacement Panels

Potential Emplacement Panel	Available Area	
	(m^2)	(acres)
Primary Area (Upper Block)	3,766,000	930.6
Primary Area (Lower Block)	883,000	218.2
Optional Area A	634,000	156.7
Optional Area B	1,777,000	439.1
Optional Area C	1,467,000	362.5
Optional Area D	2,369,000	585.4

Table 3.5-1 _ Dimensions of Waste Disposal Containers for A Typical Large MPC and
DHLW[1]

Parameters	Large MPC	DHLW
Capacity	21 PWR or 40 BWR Spent Fuel Assemblies	4 Pour Canisters
WP Number	6323	3259
First Layer Inner Length	4932.2	3040.0
First Layer Outer Length	5012.2	3120.0
Second Layer Inner Length	5012.2	3120.0
Second Layer Outer Length	5682.2	3680.0
First Layer Inner Diameter	1561.6	1569.0
First Layer Outer Diameter	1601.6	1609.0
Second Layer Inner Diameter	1601.6	1609.0
Second Layer Outer Diameter	1801.2	1709.0
	Thickness (mm)	
	Inner Barrier	Outer Barrier
Spent Fuel Container	20.0	99.8
DHLW	20.0	50.0

[1] Dimensions are in millimeters.

Table 3.7-1 Spent Fuel Waste Inventory

Isotope	Multi-Barrier Waste Package Design - 21 PWR (Ci/pkg) [1,2]
^{227}Ac	1.79e-4
^{241}Am	3.73e4
^{242M}Am	2.16e2
^{243}Am	2.48e2
^{14}C	1.38e1
^{36}Cl [3]	1.11e-1
^{244}Cm	1.16e4
^{245}Cm	3.36e0
^{246}Cm	6.95e-1
^{135}Cs	5.13e0
^{129}I [3]	3.43e-1
^{93M}Nb	1.82e1
^{94}Nb	8.24e0
^{59}Ni	2.36e1
^{63}Ni	3.10e3
^{237}Np	4.35e0
^{231}Pa	3.30e04
^{210}Pb	6.75e-6
^{107}Pd	1.26e0
^{238}Pu	3.05e4
^{239}Pu	3.56e3
^{240}Pu	5.26e3
^{241}Pu	3.39e5
^{242}Pu	2.01e1
^{226}Ra	2.50e-5

Table 3.7-1. Spent Fuel Waste Inventory (Continued)

Isotope	Multi-Barrier Waste Package Design - 21 PWR (Ci/pkg) [1,2]
^{228}Ra	3.10e-9
^{79}Se	4.41e0
^{151}Sm	3.53e3
^{126}Sn	8.50e0
^{99}Tc	1.40e2
^{229}Th	3.54e-6
^{230}Th	3.59e-3
^{232}Th	4.35e-9
^{233}U	7.01e-4
^{234}U	1.34e1
^{235}U	1.68e-1
^{236}U	2.72e0
^{238}U	3.07e0
^{93}Zr	2.38e1

[1]Assumes 40,785 MTU PWR with a burnup of 39,651 MWd/MTU, and 22,211 MTU BWR with a burnup of 31,186 MWd/MTU
[2]9.74 MTHM/container, 21 PWR case
[3]Carbon, Chlorine, and Iodine inventory assumed to be gaseous release

Table 3.7-2 DHLW Waste Inventory

Isotope	DHLW Inventory (Ci/pkg) [1]
^{227}Ac	6.02E-4
^{241}Am	8.65E1
^{242M}Am	2.06E-2
^{243}Am	3.67E-2
^{14}C	0
^{36}Cl	0
^{244}Cm	1.14E1
^{245}Cm	5.64E-5
^{246}Cm	6.39E-6
^{135}Cs	1.15E-1
^{129}I	1.90E-6
^{93M}Nb	5.48E-1
^{94}Nb	3.02E-5
^{59}Ni	2.70E-2
^{63}Ni	0
^{237}Np	2.83E-2
^{231}Pa	9.74E-4
^{210}Pb	2.72E-8
^{107}Pd	0
^{238}Pu	4.00E2
^{239}Pu	4.73E0
^{240}Pu	3.30E0
^{241}Pu	1.48E2
^{242}Pu	5.02E-3
^{226}Ra	9.37E-8
^{228}Ra	0

Table 3.7-2. DHLW Waste Inventory (Continued)

Isotope	DHLW Inventory (Ci/pkg) [1]
^{79}Se	9.18E-2
^{151}Sm	0
^{126}Sn	0
^{99}Tc	3.30E0
^{229}Th	1.51E-5
^{230}Th	1.24E-5
^{232}Th	1.05E-4
^{233}U	5.84E-4
^{234}U	5.00E-2
^{235}U	7.93E-5
^{236}U	4.35E-4
^{238}U	3.78E-3
^{93}Zr	7.01E-1

[1]Assumed 4 canisters per container.
Source: DOE (1987). Same inventory as DHLW inventory in TSPA-1993.

Table 3.8-1 Pathway Thicknesses and Relative Areas

Pathway	Thickness (m)				Total Thickness (m)	% PPn in CHnz	% total area (25 MTU/ac)	% total area (83 MTU/ac)
	TSw	TSv	CHnv	CHnz				
1	105	8	92	139	345	83	7.2	14.8
2	176	8	72	88	344	43	6.1	8.0
3	87	8	105	158	358	80	4.9	16.4
4	147	8	87	118	359	52	3.4	11.1
5	35	7	132	198	372	80	6.3	20.7
6	113	7	102	148	370	71	8.9	29.0
7	151	8	55	68	282	0	9.2	-
8	105	15	54	66	240	73	17.7	-
9	80	15	63	77	235	73	14.7	-
10	85	15	47	58	205	73	21.6	-
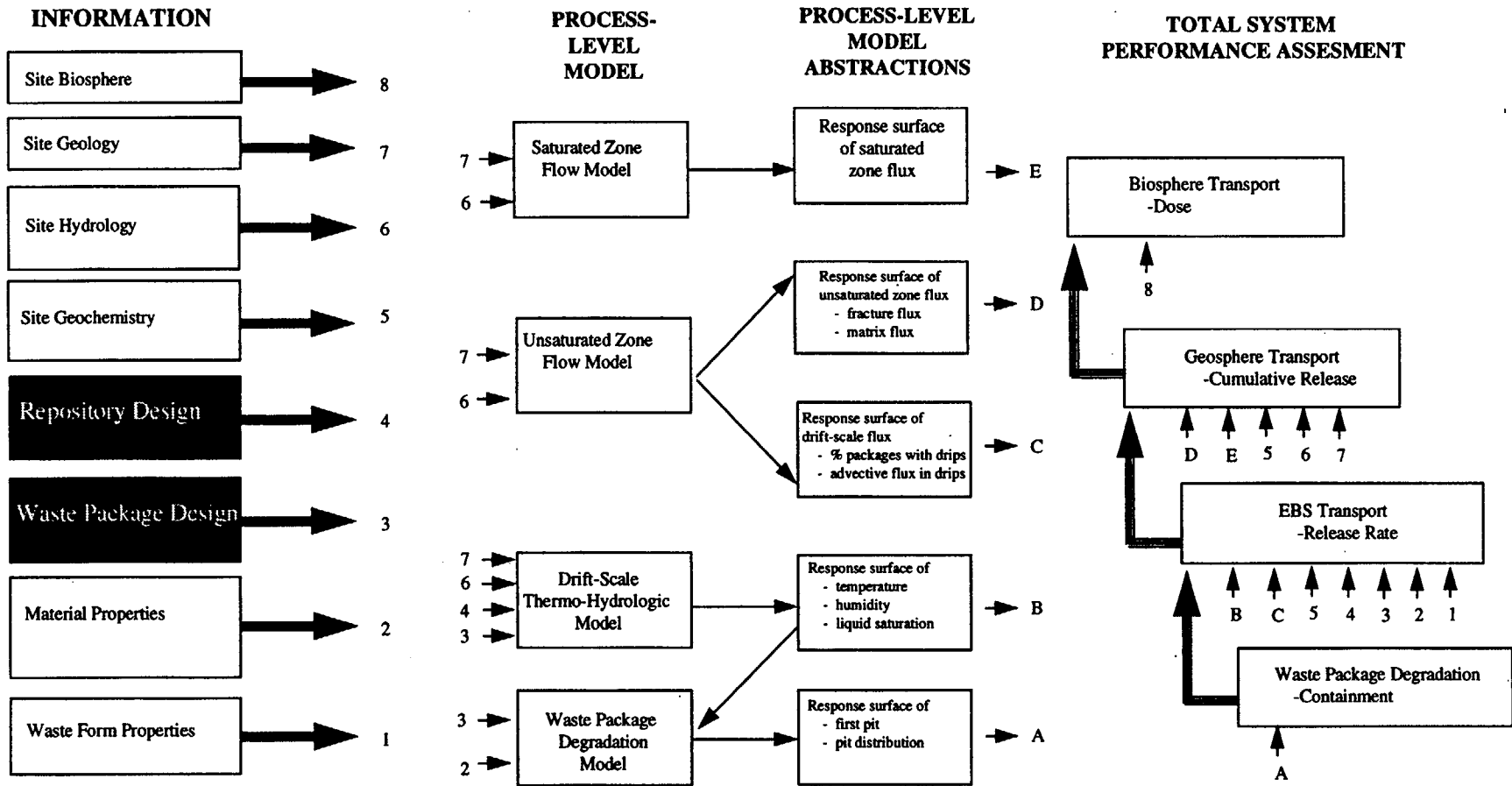
Figure 3.1-1 Relationship of Chapter 3 to the Overall Information Flow Diagram for TSPA 1995 (Figure 1.4-6)
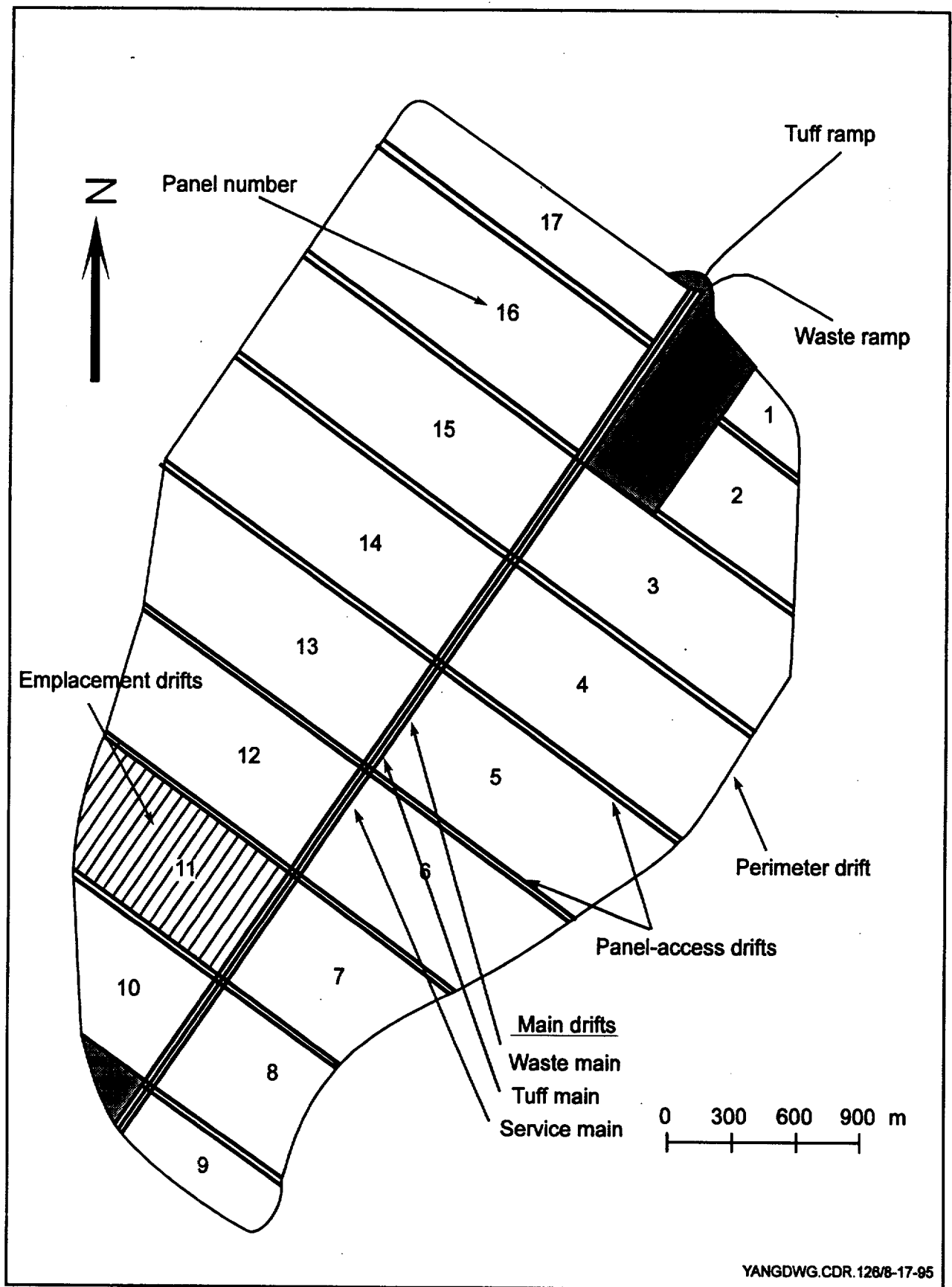
Figure 3.2-1 SCP-CDR repository layout (after DOE, 1988)
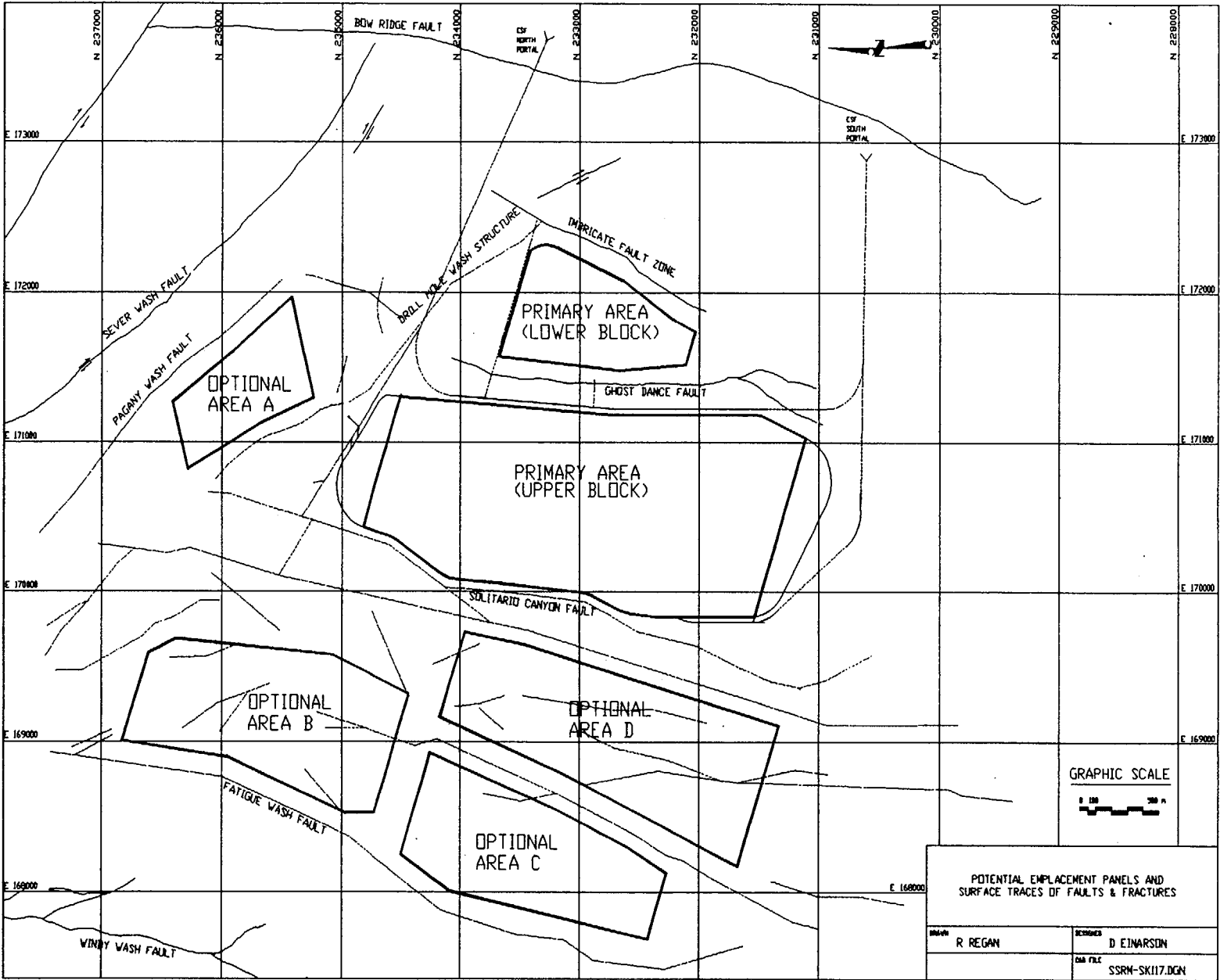
Figure 3.2-2 Potential Emplacement Panels (after M&O, 1994)

N 237000
N 236000
N 235000
N 234000
N 233000
N 232000
N 231000
N 230000
N 229000
N 228000

E 173000
E 172000
E 171000
E 170000
E 169000
E 168000

BOW RIDGE FAULT

CSF NORTH PORTAL

CSF SOUTH PORTAL

SEVER WASH FAULT

PAGANY WASH FAULT

DRILL HOLE WASH STRUCTURE

IMBRICATE FAULT ZONE

PRIMARY AREA
(LOWER BLOCK)

GHOST DANCE FAULT

OPTIONAL
AREA A

PRIMARY AREA
(UPPER BLOCK)

SOLITARIO CANYON FAULT

OPTIONAL
AREA B

OPTIONAL
AREA D

FATIGUE WASH FAULT

OPTIONAL
AREA C

WINDY WASH FAULT

GRAPHIC SCALE
0   100   500 m

POTENTIAL EMPLACEMENT PANELS AND
SURFACE TRACES OF FAULTS & FRACTURES

DRAWN R REGAN
DESIGNED D EINARSON
CAD FILE SSRM-SK117.DGN

Figure 3.4-1   25 MTU/acre Layout
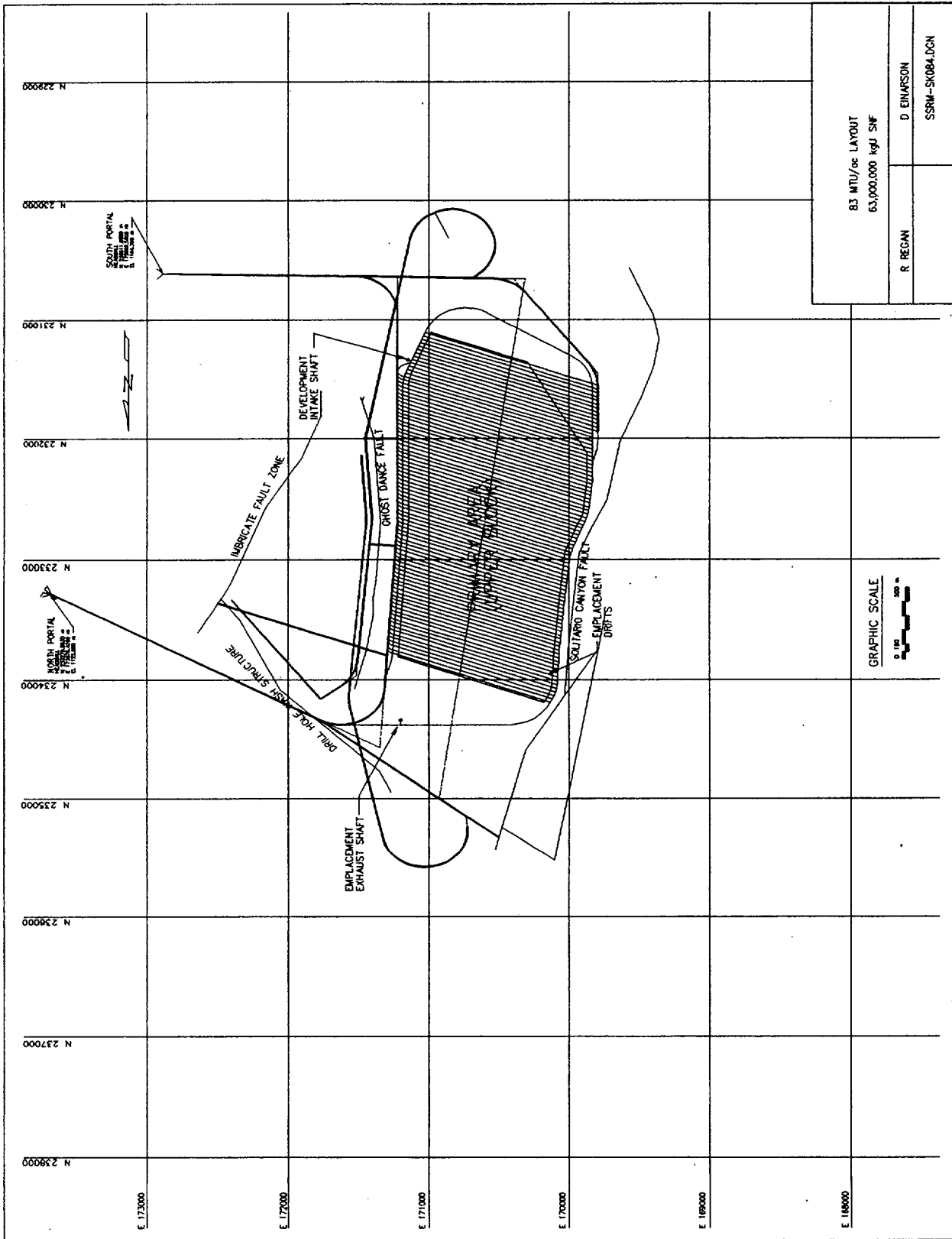
Figure 3.4-2   83 MTU/acre Layout

Vertical Borehole Emplacement

Horizontal Borehole Emplacement

In-Drift Emplacement
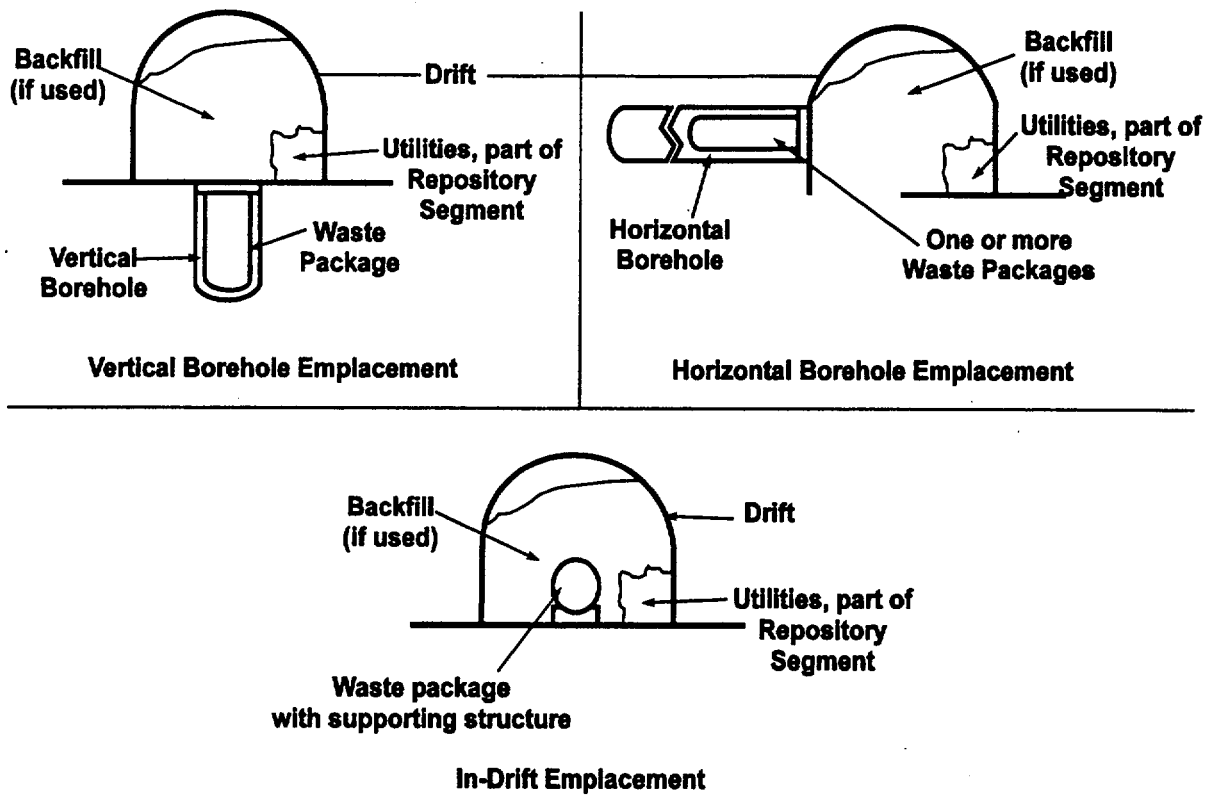
Figure 3.6-1 Borehole and in-drift emplacement concepts from SCP-CDR (DOE, 1988)
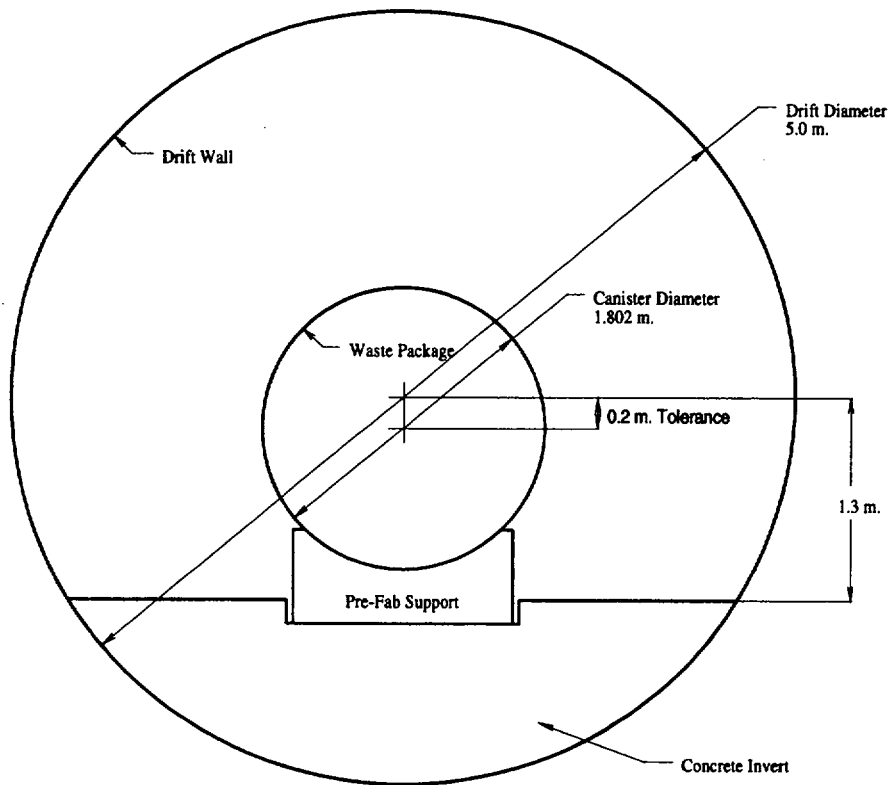
Figure 3.6-2 Emplacement drift design for the CIDP option (after M&O, 1995f)
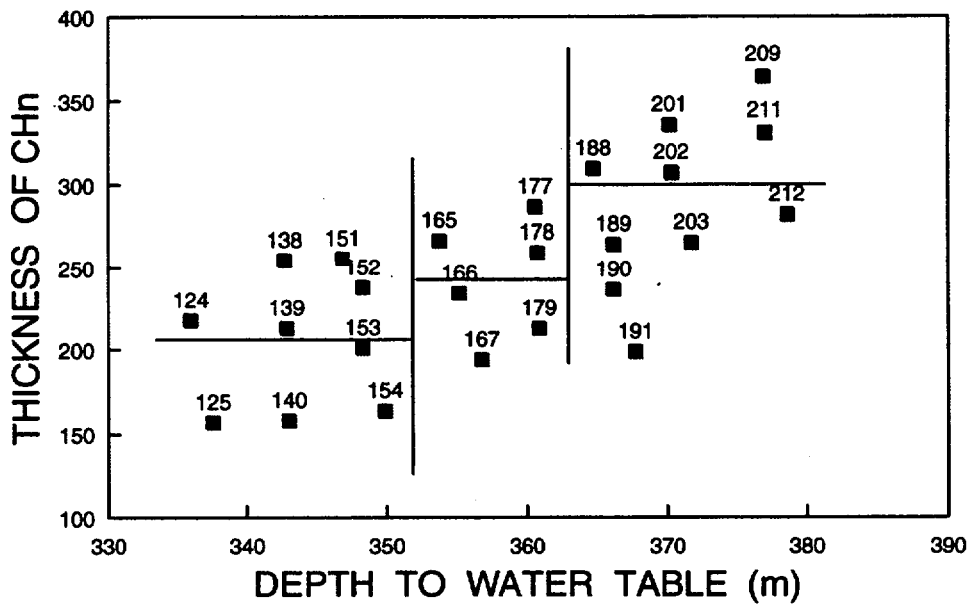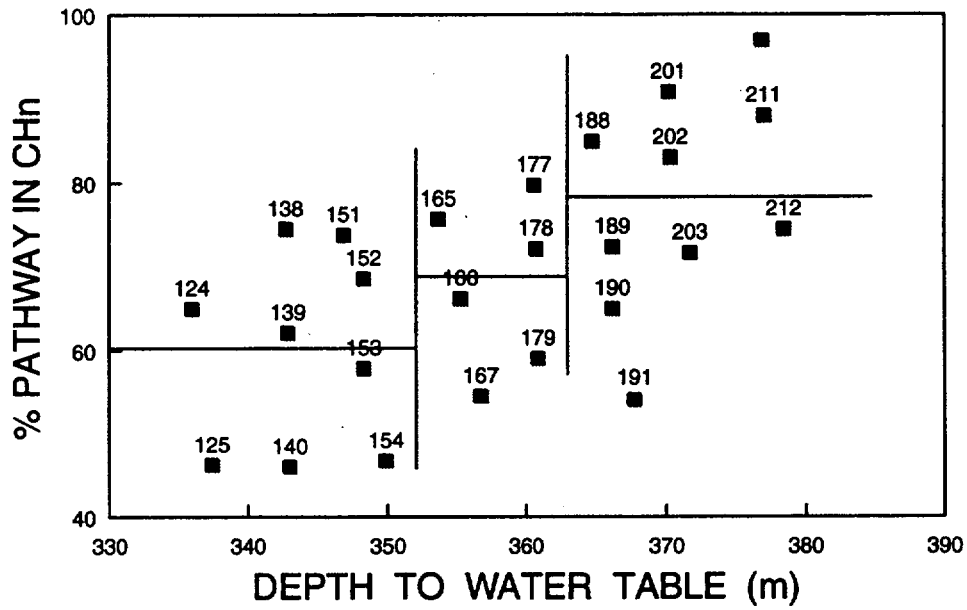
Figure 3.8-1 Subdivision of Primary Area (Upper Block) into six (6) pathways
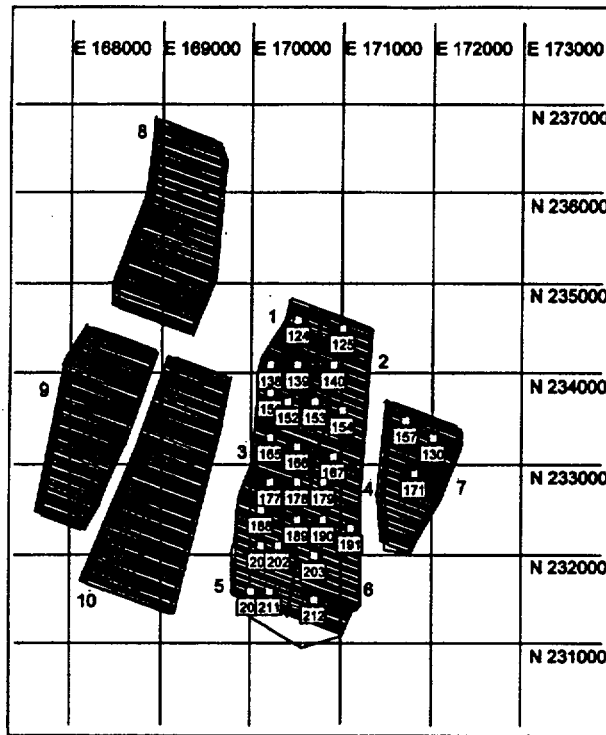
Figure 3.8-2   Pathway definition for 25 MTU/acre Case
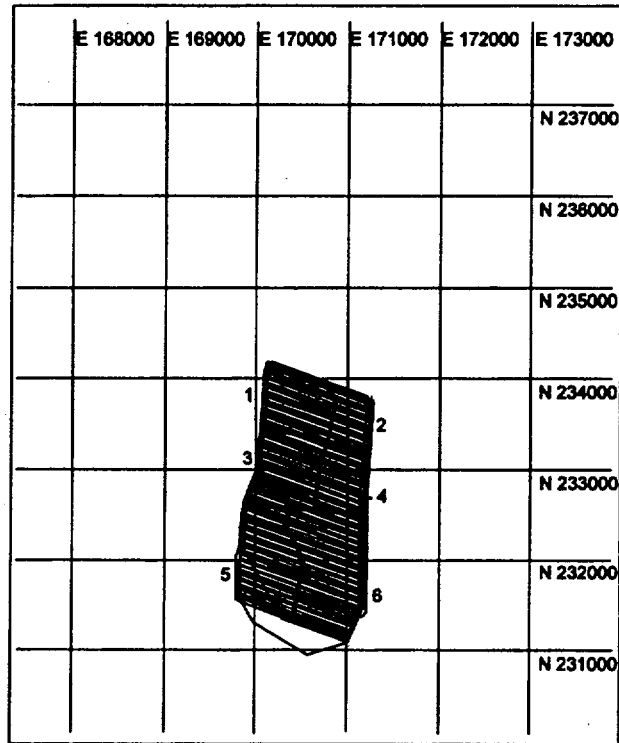
Figure 3.8-3   Pathway definition of 83 MTU/acre Case
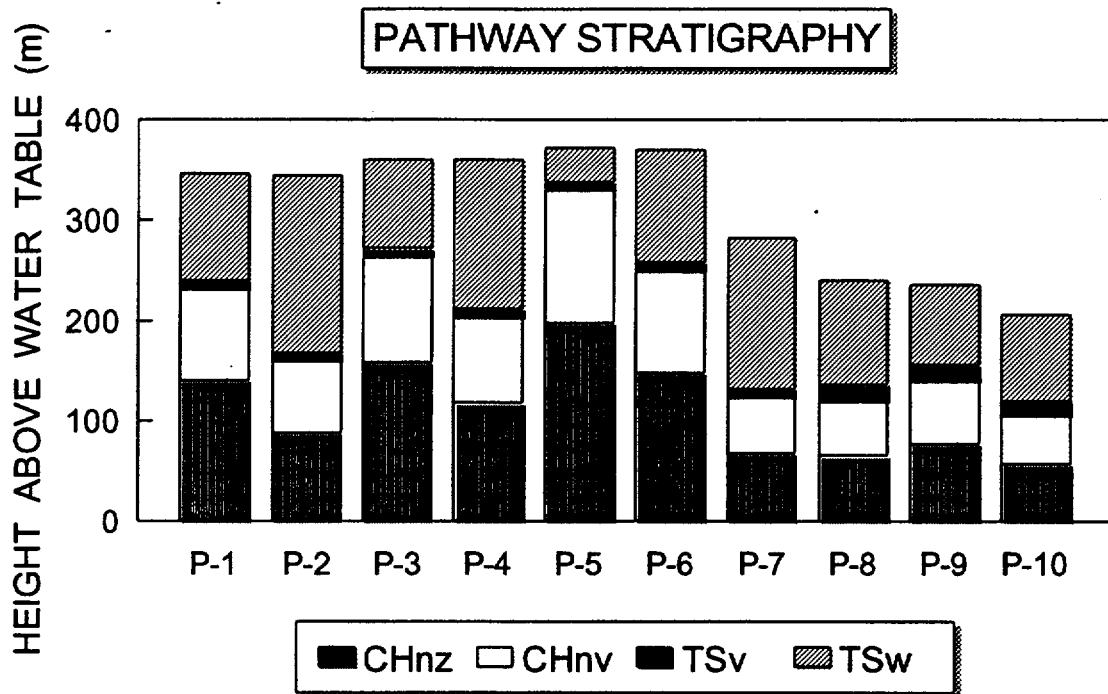
Figure 3.8-4   Relative thickness of pathways and their components
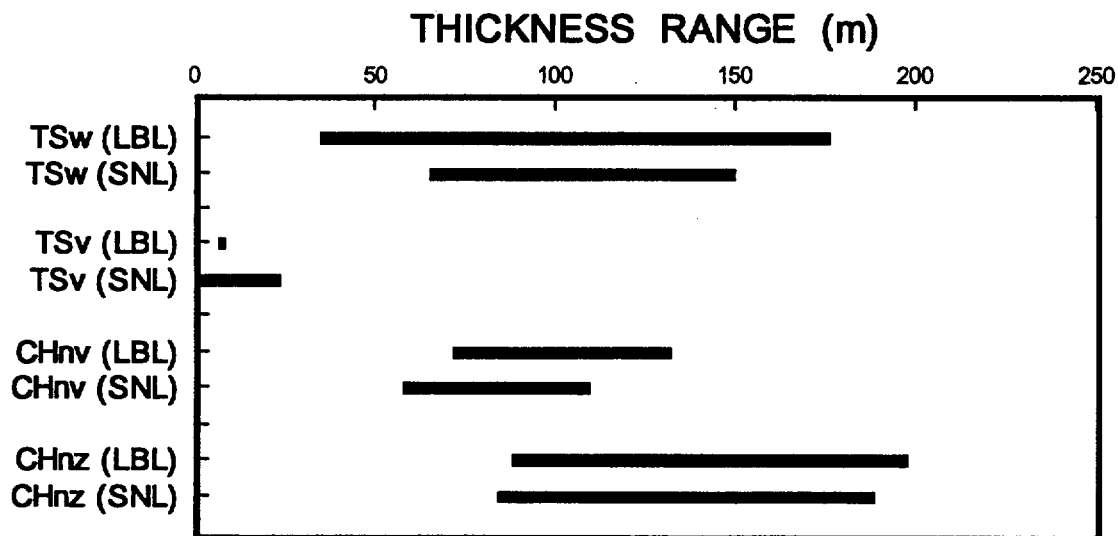
Figure 3.8-5   Comparison of thickness ranges predicted by Wittwer et al., (1995)
[LBL] and Ortiz et al., (1985) [SNL]

4. NEAR-FIELD ENVIRONMENT

Suresh Lingineni, Srikanta Mishra, Laureen R. Kennedy, Mark Reeves,
Frank Tsai, David C. Sassani

4.1   INTRODUCTION

The performance of the waste package and other components of the engineered system is affected by the environment in the vicinity of the waste packages. This environment is determined by the ambient hydrogeologic and hydrochemical conditions and the perturbation of these conditions by the emplacement of materials introduced into the drifts during construction and operation of the facility. A perturbation of central interest is the increase in temperature caused by the generation of heat from the radioactive waste itself.

Thermohydrologic perturbations to the near-field environment have a significant effect on total system performance. This is a result of: (a) the dependence of the initiation and rate of humid air and aqueous corrosion on the humidity and temperature within the drift, and (b) the effect of liquid saturation on the diffusive release of radionuclides through the waste package and drift-emplaced materials. Consequently, the primary near-field environment process-level model considered in this TSPA is the drift-scale thermal hydrology (Figure 4.1-1).

A detailed drift-scale thermohydrologic model was developed to simulate the heat transport and fluid flow caused by two different thermal loading scenarios (25 and 83 MTU/acre). Results from the drift-scale thermohydrologic analyses presented in Section 4.2 are used in subsequent corrosion modeling (Chapter 5) and repository-scale release analyses (Chapters 8 and 9).

An evaluation of the thermal effects at the edge of the repository is presented in Section 4.3. Although not used explicitly in TSPA-1995, these calculations are important in determining the cooling that may occur at the repository edge and the overall impact on the hydrologic conditions in the outer portion of the repository. Two other potential thermal couplings, mechanical and chemical, are discussed briefly in Sections 4.4 and 4.5, respectively. The thermal-mechanical effects are not explicitly included in TSPA-1995, but include such factors as rock fabric alterations that may affect repository performance. The thermal-chemical effects are included in TSPA-1995 through temperature-dependent solubilities and waste form dissolution rates.

4.2   DRIFT-SCALE THERMAL-HYDROLOGY

The near-field thermohydrologic model developed to evaluate the heat transport and fluid flow occurring in the vicinity of heat-generating waste packages is described in this section. The model simulates various processes initiated as a result of the emplacement of heat-generating waste, including: conductive and convective heat transfer; boiling and condensation; capillary adsorption and vapor pressure lowering; and thermal buoyancy driven vapor flow. All of these processes can alter the distribution and movement of heat and/or water in the vicinity of the repository and thus have a significant effect on waste package degradation, waste package failure rates and transport of radionuclides from the breached waste packages through the EBS/geosphere to the accessible environment.

The major objectives of the drift-scale thermohydrologic analyses were as follows:

- To develop a drift scale thermohydrologic model that can simulate the near-field fluid flow and heat transport processes.

- To predict temperatures and liquid saturations in the vicinity of the waste packages, for various infiltration rates, thermal loadings, and backfill scenarios.

- To provide abstractions of waste package temperatures and relative humidities near the waste packages for use in corrosion models and TSPA analyses using RIP.

The computational model chosen for performing near-field thermohydrologic simulations is the FEHM (Finite Element Heat and Mass Transfer) code developed at Los Alamos National Laboratory (Zyvoloski et al., 1995). This code is one of the multiphase, non-isothermal flow and transport codes shortlisted through a careful review of existing models from those currently used in the DOE waste management programs and those used in the recent past (Reeves et al., 1994).

4.2.1 Overview of FEHM

FEHM is a multi-dimensional heat and mass transfer code developed to simulate non-isothermal multiphase flow in porous media under saturated and unsaturated conditions (Zyvoloski, et al., 1995). The code simulates fluid flow in both gas and liquid phases under pressure, viscous, and gravity forces according to Darcy's equation. FEHM also accounts for the capillarity between liquid and gas phases as well as phase interference (relative permeability) effects. Fracture-matrix coupling can be simulated in FEHM via dual-porosity, dual-permeability or the equivalent continuum model (ECM) formulations.

Within FEHM, Kelvin's law is used to represent vapor pressure lowering due to capillary effects. Interphase equilibrium of the condensing gas component is described with standard steam tables. FEHM uses finite-element spatial discretization for both flow and transport. A Newton-Raphson technique is employed to linearize the coupled set of non-linear difference equations. FEHM solves the linearized equations for liquid pressure, temperature, and gas saturation using the minimum-residual technique, a variant of conjugate-gradient approach which is suitable for non-symmetric elements.

The original version of FEHM can simulate heat flow by conduction and convection of sensible and latent heat. During the preclosure period and/or in the case of non-backfilled drifts, the waste package will lie on a pedestal surrounded by an air-gap between the drift wall and the waste package. Under such conditions heat transfer due to radiation is expected to be the dominant mechanism of heat flow from the waste package to the drift wall. The current version of FEHM used to perform these thermohydrologic simulations has therefore been modified to account for radiative heat transfer.

4.2.2 Model Geometry

The near-field thermohydrologic model developed in this work assumes a two-dimensional geometry in a plane orthogonal to the drift and extending from ground surface to the top of the

water table (Figure 4.2-1). The modeled domain represents a unit cell within the drift, which consists of a single waste package placed inside a horizontal drift. Waste packages are assumed to be placed on pedestals lying atop an invert. The lateral width of the domain extends to the symmetry boundary between two adjacent drifts. The modeled geometry is discretized into a fine two-dimensional mesh near the waste package which gradually transitions into essentially one-dimensional grid blocks (coarse discretization in the horizontal direction) in the far-field (Figure 4.2-2). As shown in Figure 3.6-2, the diameter of the drift is 5 m and the diameter of the waste package is 1.8 m. For a given drift spacing and waste package capacity, the waste package spacing is determined from the choice of areal mass loading. Thus, the width of the model domain along the drift depends on the areal mass loading being used in a simulation.

The area inside the drift is discretized into four cylindrical layers of elements with the innermost two layers representing the waste package itself. To simplify the analysis and to reduce the total number of elements required for the discretization of model geometry, the waste package outer boundary is approximated by a dodecagon. The heat generated from the waste package is smeared over elements within the two innermost layers, and the total heat generated is distributed to each element in proportion to its area.

4.2.3 Model Assumptions

Axial Smearing of Thermal Load: As the model geometry used in this study is two-dimensional, it cannot be used to discretely represent the waste package along the drift. Thus, the heat generated from the waste package has to be smeared across the entire length of the unit cell (which is the symmetry element between adjacent drifts and adjacent waste packages). This length is usually taken to be equal to the waste package spacing. However, as the WP spacing increases, the heat smearing occurs over longer lengths, which results in underprediction of waste package temperatures. These underpredictions are greater for the lower areal mass loading case for which the waste package spacing is much greater compared to its length. The details of heat smearing effects and measures taken to minimize (or to quantify the sensitivity of) these uncertainties are discussed in Section 4.2.6.

Ventilation: The near-field thermohydrologic simulations performed for this TSPA do not account for ventilation. The heat removal from a waste package and drift wall due to ventilation depends upon the axial location of the package along the drift and also upon the design of ventilation pathways. Due to the two-dimensional nature of this model, it is not possible to accurately represent the effects of ventilation on heat and fluid flow in the near-field environment. Also, it is beyond the current capabilities of available thermohydrologic codes to simulate water or moisture transfer from the host rock into the air gap through which ventilation air is flowing. Considering these uncertainties/limitations, and realizing that neglecting ventilation would provide higher waste package surface temperatures and higher relative humidities (conservative estimates in terms of waste package performance predictions in as much as both heat and moisture removal by ventilation are not considered), ventilation effects are not included in this model.

Saturated Zone: The saturated zone is not included in the model domain. This assumption is made primarily to avoid numerical instabilities caused by oscillations in gas pressures at nodes in the neighborhood of the water table. Previous studies (Lingineni et al., 1994, Buscheck et al., 1994) have shown that the effect of including the water table is significant at late time periods

(after about 1000 years) after the thermal front reaches the water table. In the absence of the saturated zone in the model, the thermal boundary condition at the lower boundary plays an important role. This model assumes a constant prescribed temperature at the lower boundary, which is expected to remove heat from the repository at a faster rate at late time periods, thus giving rise to lower waste package temperatures at late times.

Relative Humidity: Predictions of relative humidity in the near field are performed assuming that local phase equilibrium exists at each location, and diffusional resistance and time scales for moisture transport in the rock as well as backfill are negligible. The details of these assumptions and their implications are explained in Section 4.2.7.

Fracture-Matrix Interaction: Fracture-matrix interaction is simulated using the equivalent continuum assumption. The paucity of data on geometric/hydraulic characteristics of fractures at Yucca Mountain, as well as the computational complexity associated with modeling hydrothermal behavior in a discrete fracture network, necessitates the use of such an assumption. The ECM formulation (Pruess et al., 1985) assumes capillary pressure and thermal equilibrium between the fractures and the matrix, which allows equivalent continuum properties to be derived by volume averaging of fracture and matrix characteristics. The assumption of capillary pressure continuity implies that for most cases of fracture density and permeability, the fractures will be dry so long as the matrix is not close to full liquid saturation. In other words, the ECM forces liquid movement to occur primarily within the matrix and to be controlled by the matrix permeability, whereas air/vapor movement takes place primarily in the fractures and is controlled by the fracture permeability.

4.2.4 Stratigraphy and Hydrogeologic Properties

The unsaturated zone consists of a series of variably fractured and variably welded tuffaceous rock units, with the stratigraphy taken to be that corresponding to Column 153 in the model of Wittwer et al., (1995). From the land surface down to the water table, the sequence of hydrostratigraphic units, and their corresponding thicknesses, are as follows: Tiva Canyon welded (TCw) - 94.7 m, Paintbrush nonwelded (PTn) - 52.9 m, Topopah Spring welded (TSw) - 326 m, Topopah Spring basal vitrophyre (TSv) - 8.4 m, Calico Hills non-welded vitric (CHnv) - 80.7 m, and Calico Hills non-welded zeolitic (CHnz) - 121.2 m (Figure 4.2-1). The water table is located at a depth of 683.9 m below the ground surface. The center of the potential repository horizon is located at a depth of 340.2 m below the ground surface within the TSw unit. Matrix and fracture hydraulic properties are based on data from Klavetter and Peters (1986), and are given in Tables 4.2-1 and 4.2-2. Also included therein are the hydrologic characteristics of the backfill, assuming it to be a 'gravel'-type material.

4.2.5 Thermal Properties

Thermal rock properties (shown in Table 4.2-3) correspond to those given in version 4 of the Reference Information Base (DOE, 1990). The backfill properties are assumed to be similar to that of TSw, with the thermal conductivity modified for the higher porosity of the backfill. The matrix thermal conductivity is assumed to vary with local liquid saturation with a square root dependence. The rock density, specific heat and thermal conductivity are assumed to be independent of temperature. A previous study carried out by Longenbaugh et al. (1994)

illustrated the effect of temperature dependent thermal properties on thermal predictions of a conduction based model. Their results showed that temperature-dependent thermal property models predict lower temperatures in the near-field when compared to temperature independent thermal property models. However, the major contributing factor to these differences is the term arising due to energy absorption during water evaporation. As FEHM explicitly accounts for the latent heat of vaporization of water, neglecting other temperature dependencies of thermal properties is not expected to have a major impact on the near-field thermohydrologic predictions.

4.2.6 Thermal Loading and Waste Stream Characteristics

Thermal characteristics of the emplaced spent fuel assemblies are computed assuming "Oldest Fuel First (OFF)" for a 21-PWR assembly PWR package, with an average age of 26 years, a burnup of 39 GWd/MTU and an initial heat output of 0.98 kW/MTU. The heat generated from a representative waste package is shown in Figure 4.2-3. This information, together with the drift spacing and areal mass loading, is used to determine the waste package spacing, which corresponds to the depth of the unit cell along the drift axis. Thus, for an areal mass loading of 83 MTU/acre and a nominal drift spacing of 22.5 m, the waste package spacing becomes 19 m, and for the 25 MTU/acre case with a 45 m drift spacing, it becomes 32 m.

As mentioned earlier, the two-dimensional model used in this study cannot be used to represent discretely the waste package along the drift. However, smearing the heat generated from the waste package across the entire length of the unit cell would result in an underprediction of temperatures because the unit cell is larger than the waste package. On the other hand, assuming the heat output to be concentrated only along the length of the waste package would result in overprediction of temperatures because the heat loss to the rest of the unit cell would not be taken into account. In the absence of detailed three-dimensional simulations to resolve this issue, our preliminary solution has been to use a smearing length which is larger than the waste package length, but smaller than the length of the unit cell. Thus, for the 83 MTU/acre case, a smearing length of 15 m is used for a 19 m-long unit cell, and for the 25 MTU/acre case, a smearing length of 30 m is used for the 32 m-long unit cell.

4.2.7 Initial and Boundary Conditions

Initial conditions for the model are calculated assuming an average ground surface temperature of 13°C and a water-table temperature of 27°C. Taking these two temperatures as boundary conditions, and assuming surface recharge rates of 0.05 and 0.3 mm/yr for the two alternative infiltration scenarios, a steady-state solution of the full two-phase, non-isothermal flow problem yields initial conditions for the transient simulations with repository heating.

For the steady-state calculations of initial conditions described above (as well as for the subsequent transient simulations under thermal loading) the boundary conditions are set as follows. The lateral boundaries are taken to be of the no-flow type for both heat and fluid flow. Such an assumption is representative of unit cells in the middle of the repository due to symmetry, but not very realistic for drifts close to the edges of the repository. The upper boundary is assigned a constant pressure (0.86 atm) representative of atmospheric contact. The lower boundary (water table) is taken to be at a constant (hydrostatic) pressure of 1.0 atm.

As discussed in sections 2.6 and 7.2, two infiltration scenarios were considered in TSPA-1995, i.e., a "low" infiltration rate sampled uniformly between 0.01 and 0.05 mm/yr, and a "high" infiltration rate sampled between 0.5 and 2.0 mm/yr. However, for the thermohydrologic calculations described in this section, only two discrete values of the infiltration rate were considered for computational expediency. At one extreme, the value of 0.05 mm/yr was taken to represent the low-infiltration rate scenario. At the other extreme, the value of 0.3 mm/yr was used for the high-infiltration rate scenario. Numerical difficulties prevented the use of an infiltration rate higher than 0.3 mm/yr.

4.2.8 Determination of Relative Humidity

Relative humidity near the waste package surface is an important factor in the initiation of pitting of waste package surface as well as the corrosion rates of the waste package. In the current iteration of TSPA, a direct dependence of waste package performance on the relative humidity values in the near-field environment is incorporated. However, the multi-phase flow and transport models being used in support of thermohydrologic analyses being carried out at Yucca Mountain (i.e. TOUGH2, FEHM) do not have a rigorous way of calculating relative humidities. This limitation arises due to the fact that these codes do not solve for the transport of water vapor as a species, but assume local equilibrium conditions to calculate spatial and temporal variations in water vapor concentrations. Given these limitations in the code capabilities, the methodology described below was used in calculating relative humidities in the near-field environment.

Relative humidity (RH) can be defined as the ratio of vapor pressure of water vapor (P_v) at a particular location to the saturation water vapor pressure (P_{sat}) at the temperature corresponding to that particular location (see Figure 4.2-4).

$$RH = \frac{P_v}{P_{sat}(T)} \qquad (4.2\text{-}1)$$

Thus, determination of relative humidity at a particular location requires information on both the temperature and local water vapor pressure. In the absence of explicit tracking of water vapor transport, it is a common practice to assume that local water vapor concentrations can be determined from Kelvin's law of vapor pressure lowering (Pruess, 1987). Kelvin's law relates the reduction in gas pressures due to gas-liquid interface effects, which then indirectly provides a relationship between water vapor pressure and local liquid saturation. Thus, Kelvin's law of vapor pressure lowering relates the local water vapor pressure to capillary pressure in the following functional form

$$P_v = P_{sat}(T) \exp\left[\frac{-P_c}{\rho_w TR}\right] \qquad (4.2\text{-}2)$$

where P_c is the local capillary pressure, R is the gas constant, ρ_w is the molar density of water and T is the local temperature.

Using the above relationship to determine relative humidity requires underlying assumptions that relate capillary pressure to the gas-liquid interface curvature. For example, to ensure that liquid flow ceases to exist at very low liquid saturations, it is customary to increase the capillary pressure to very high values. The exact magnitude of these high capillary pressure values is not very critical in flow calculations so long as numerical problems are avoided. However, in relative humidity calculations, unreasonably high values of capillary pressures imply that local humidity values are very low or zero, even though there is no physical basis for such result. This assumption plays an important role in the determination of relative humidity in the backfill area, because the liquid saturation levels are below or near residual saturations. The following discussion provides the methodology used in the determination of relative humidity in the near-field thermohydrologic simulations.

The main assumption in determining water vapor pressure at the waste package surface is to equate the absolute water vapor pressures at the waste package surface and at the dry-out front (Figure 4.2-4). The dry-out front can be visualized as a loci of points where non-zero liquid saturations can be encountered as one moves away from the waste package into the host rock. The validity of this assumption is based upon relative magnitudes of the characteristic time for the diffusion of water vapor from the dry-out front to the waste package surface in comparison to the time scales of simulation. Simple calculations using diffusivity of water vapor in air show that the characteristic time for diffusion is of the order of days, which justifies the above approximation. However, it still neglects the effects of any near-field thermal or pressure gradients on water vapor transport away from the package. This approach provides conservative results in terms of relative humidity predictions and waste package degradation rates, because the relative humidity values are higher than might be calculated using actual thermal or pressure gradients in the near field.

4.2.9 Drift-Scale Thermohydrologic Results

For TSPA-1995, multiple thermohydrologic simulations were conducted in order to: (a) determine transient waste package surface temperatures, water content within drift material, and relative humidity in the vicinity of waste package surface, and (b) evaluate different design options. Two thermal loads were considered, 25 and 83 MTU/acre. Also, cases with and without backfill material were considered. Simulations were carried out at two separate infiltration rates, viz. 0.05 and 0.3 mm/yr.

Temperature and Relative Humidity at Waste Package Surface

For each of the eight simulations performed with parametric variations in areal mass loading, infiltration rate and presence or absence of backfill, abstractions of waste package surface temperature and relative humidity in the vicinity of the waste package are provided as input to subsequent corrosion modeling and repository scale release analyses. Waste package surface temperatures are calculated as the average of all of the six nodal temperatures lying on the waste package surface. Relative humidity is calculated for each of the elements just outside the waste package and an average value is calculated to represent the abstracted relative humidity in the vicinity of the waste package.

Figures 4.2-5 and 4.2-6 (and 4.2-8) show the time-dependent temperatures and relative humidities predicted at the waste package surface for an areal mass loading of 83 MTU/acre, infiltration rates of 0.05 mm/yr and 0.3 mm/yr, and with and without backfill. For each of these simulations, the following general trends can be observed. Peak waste package surface temperatures are predicted to occur within 10 to 20 years after waste emplacement. In the case of backfilled drifts, there is a small increase in the waste package temperatures due to the placement of low-thermal conductivity backfill material at 100 years. Waste package surface temperatures gradually decrease to about 60°C at 10,000 years. It should be noted that these waste package surface temperatures at longer time periods (i.e. after 1,000 years) are possibly underpredicted because of the constant temperature boundary condition prescribed at the water table interface. In reality, saturated-zone temperatures increase due to heat transfer from the repository to bottom surface and further heat removal from the host rock may occur at a lower rate. At higher infiltration rates, the predicted waste package surface temperatures are lower. This is due to the fact that the ambient saturations in the host rock increase with increasing infiltration rates, and a larger amount of heat has to be utilized in the form of latent heat of vaporization during the drying out periods. Thus the surrounding rock provides a better heat sink for waste package heat removal at high infiltration rates.

Similarly, relative humidity predictions for 83 MTU/acre show the following trends. The predicted relative humidities near the waste package surface are in the range of 0.20 to 0.40 in the preclosure period and gradually increase to approximately 0.90 to 0.95 within the 10,000 year period. The relative humidities in the near-field are implicitly related to the near-field temperatures and saturations in the following manner. The relative humidity at the waste package surface is inversely proportional to its surface temperature and directly proportional to the temperature in the host rock or backfill where the dry-out front exists. Thus at later time periods, when the waste package surface temperatures are decreasing and the dry-out front is moving closer to the waste package, the relative humidities in the near-field keep increasing. For a given infiltration rate, the presence of backfill tends to reduce the relative humidities near the waste package by increasing waste package temperatures and by acting as a capillary barrier to delay the rewetting process of waste package. With an increase in infiltration rates, the dry-out region does not progress far into the host rock and thus provides a nearer source for water vapor. This effect together with lower waste package surface temperatures results in higher relative humidity predictions in the near-field.

Corresponding saturation variations in the near-field for 83 MTU/acre are shown in Figure 4.2-7. These show that at lower infiltration rates, the water within the near-field is instantly evaporated, and even at longer time levels (within 10,000 years) water is predicted to not come back into the drift. However, at higher infiltration rates, due to the high ambient saturation levels in the host rock, condensation of water is found to be significant thus allowing water to move relatively quickly toward the drift. Rewetting of the waste packages is predicted to occur within about 8,000 years. The abstractions of temperature and relative humidity predictions for 83 MTU/acre for the period of 0 to 10,000 years are shown in Figure 4.2-8.

Similar abstractions of waste package surface temperatures, saturations within the drift and relative humidities near the waste package surface for design scenarios with 25 MTU/acre areal mass loading are shown in Figures 4.2-9, 4.2-10 and 4.2-11. The general behavior of these predictions are similar to the predictions of 83 MTU/acre. However, for the case of

4-8

25 MTU/acre, a wider drift spacing is chosen so that the waste package spacing can be smaller such that the uncertainty due to heat smearing in the direction of the drift axis can be minimized. The following predictions are thus based on a drift spacing of 45 m and a waste package spacing of 32 m. A peak temperature of about 160°C is observed in the case of 25 MTU/acre, 0.05 mm/yr infiltration rate and with backfill. In the case of 25 MTU/acre, the relative humidities in the near field increased at a faster rate than that observed in 83 MTU/acre cases. This is due to the fact that for 83 MTU/acre, the waste packages remain at higher temperatures for longer period and extended dry-out forces the liquid water to move farther away from the waste package surface. However, the maximum relative humidities observed within the 10,000 year period still remain in the range of 0.90 to 0.95. Saturation variations in the near field also indicate that rewetting of waste packages only occurs in scenarios with high infiltration rates. However, due to the low thermal loading, the amount of dry-out (or reduction in liquid saturations below ambient levels) is quite small, and rewetting of the waste package occurs at very early periods. The overall abstractions of temperature and relative humidity predictions for 25 MTU/acre for the period of 0 to 10,000 years are shown in Figure 4.2-12.

Predicted drift-scale temperature and saturation distributions

The temperature and saturation distributions in the near field of the waste package at various time levels are useful in understanding the temperature gradients away from the waste package surface and movement of dry-out front in the near field. Figures 4.2-13 to 4.2-20 show two-dimensional interpolated images of temperature and liquid saturation distributions in the vicinity of the waste packages. These figures are plotted at four different time levels (10, 100, 1000 and 10000 years) and time levels are chosen on a logarithmic scale to capture both temperatures near the waste package at earlier time levels as well as dry-out front movement at late time levels. These figures correspond to four different scenarios in which areal mass loading (25 and 83 MTU/acre), infiltration rate (0.05 and 0.3 mm/yr) and backfill status (with and without backfill) are parametrically varied. Each of these figures is plotted in a half-symmetry plane, extending laterally from the centerline of the waste package to the mid-line between two adjacent drifts and extending to a distance of about 24 m above and below the waste package center.

The following general trends can be noticed from the two-dimensional images presented in Figure 4.2-13 to 4.2-20. The temperature distributions for the case of 83 MTU/acre and 0.05 mm/yr infiltration rate with backfill (Figure 4.2-13) show that at 10 years high temperatures occur near the waste package and within the drift, but thermal effects have not progressed far into the host rock. With time, the thermal front progresses into the rock, but the heat being released from the waste package is decreasing. Thus, after about 10 years, while temperatures are decreasing near the waste package, distal temperatures are rising. At very late times (after 1,000 years), the temperature distribution looks nearly uniform, and only gradual cooling continues with time.

For this case (i.e., 83 MTU/acre, backfill, and infiltration rate of 0.05 mm/yr), the ambient liquid saturations (Figure 4.2-14) are about 0.75 in the host rock and close to residual saturation levels of 0.01 within the drift. The saturation distribution at 10 years does not show much variation from the ambient levels except for a thin area around the drift where liquid saturation is slightly reduced . However, the distribution at 100 years shows that a distinct dry-out front has progressed outward from the waste package. In Figure 4.2-14, it can be seen that a region of zero liquid saturation extends about 4 m into the host rock with significant water condensation

and moisture redistribution evident outside this dry-out front. Saturation levels at 1,000 years indicate that the dry-out region has progressed further into the host rock (approximately 14 m from the drift wall). Saturation levels below and above the waste package show that dry-out is asymmetric with more dry-out below the waste package. The predicted saturation distribution at 10,000 years indicates that recondensed water has started to move back towards the drift and most of the dry-out regions have been rewetted. Average liquid saturation levels in the host rock are about 0.50, implying that hydrologic conditions have not yet returned to ambient levels.

The effect of infiltration rate variation can be noticed by comparison of Figures 4.2-13 and 4.2-14 with Figures 4.2-15 and 4.2-16. For the higher infiltration rate of 0.3 mm/yr, the ambient saturations in the host rock for are approximately 0.90 and the saturations within the backfill remain around residual saturation levels of 0.01. The general trend of a progressive dry-out front is evident for this higher infiltration case also. However, both the rate at which the dry-out front progresses into the rock and the radial extent to which complete dry-out is achieved, are much lower. This is due to the higher ambient saturations (cf. Figures 4.2-16 and 4.2-14) and lower waste package temperatures (cf. Figures 4.2-15 and 4.2-13) that are calculated for higher infiltration rates. Thus, for the 0.3 mm/yr infiltration case at the 100 years, the dry-out zone has progressed only about 3 m into the rock, and at 1,000 years, it has advanced about 8 m outward. In this case, the dry-out zone is completely gone at 10,000 years and saturations within the host rock have come back to nearly uniform values of about 0.70.

Temperature and saturation distributions shown in Figures 4.2-17 and 4.2-18 are for the case of 83 MTU/acre, 0.3 mm/yr infiltration rate and no backfill. These distributions show similar general trends as explained above for the backfilled scenario (Figures 4.2-15 and 4.2-16). The waste package surface temperatures are lower, however, the far-field values are not influenced, significantly, by the lack of backfill. The temporal variations in saturation and as position of the dry-out front, are also not significantly different from the case with backfill. Figures 4.2-19 and 4.2-20 show the temperature and saturation distributions for the case of 25 MTU/acre areal mass loading, 0.3 mm/yr infiltration rate, and backfill. Temperature gradients for this case are much lower than for the 83 MTU/acre cases and produce only minor changes to the ambient conditions. Because of this, the distributions do not show much variation in regions far from the waste package and most of the dry-out is constrained to within the drift.

4.2.10 An Alternate Drift-Scale Thermal-hydrology Model

Drift-scale models of heat and fluid flow for the proposed repository at Yucca Mountain are also being developed at Lawrence Livermore National Laboratory (LLNL) in support of waste package (WP) design related activities. Buscheck et al. (1995) describe a suite of calculations for a variety of WP-spacing and drift-spacing scenarios in their evaluation of near-field thermohydrologic performance. A selected set of simulations from that study is described in order to provide a comparison with the thermohydrologic calculations reported previously.

Model Description

The drift-scale model is based on a two-dimensional cross-section which assumes an infinite repository with uniformly spaced drifts. The model represents a symmetry element from the symmetry plane down the center of the waste package to the symmetry plane in the pillar

between neighboring drifts. The waste package has a cross-section of 1.6 m x 1.6 m and is located within an emplacement drift that is 6.0 m high and 6.0 m wide. The waste package is emplaced on a 1.2 m thick "gravel" invert within the emplacement drift. The gravel invert is also taken to be the material for backfilling the drift. Note that such a square drift/waste package model is a simplification adopted for computational convenience.

The stratigraphy and parametrization used to characterize this drift-scale model are described in Buscheck and Nitao (1993). Briefly, the ~530 m thick unsaturated zone is taken to consist of six major hydrogeologic units, viz. TCw, PTn, TSw, TSv, CHnv and CHnz. A 1000 m thick section of the saturated zone is also included in the model. Hydrologic and thermal properties of the unsaturated zone are taken from version 4 of the Reference Information Base (DOE, 1990). The saturated zone is assumed to have the properties of the welded Prow Pass (PPw) unit. Properties of the gravel invert (and of the backfill) are assumed to be similar to that of the PTn unit, albeit with a higher porosity, and correspondingly, a lower thermal conductivity.

Thermal decay characteristics are calculated by blending the heat output from the first 161 40-BWR WPs and 239 21-PWR WPs received during the first two years of repository operation, assuming an "Oldest Fuel First" scenario. This results in a typical WP containing 7.5 MTU with an average age of 26 years, a burnup of 38 GWd/MTU and an initial heat output of 0.96 kW/MTU. Simulations are carried out for thermal loads of 24 and 80 MTU/acre. For the 24 MTU/acre case, assuming a 50 m drift spacing yields a waste package spacing of 24 m. For the 80 MTU/acre case, assuming a 25 m drift spacing yields a waste package spacing of 14 m.

Results and Discussion

All calculations were performed using the V-TOUGH code (Nitao, 1989), which is LLNL's enhanced version of the TOUGH code (Pruess, 1987). V-TOUGH is a multidimensional numerical simulator capable of modeling the coupled transport of water, water vapor, air and heat in porous and fractured media. In previous benchmarking studies (Reeves et al., 1994; Lingineni et al., 1994), the TOUGH family of codes has been shown to provide essentially similar results to those obtained by the FEHM code - which is used in the thermohydrologic modeling studies described earlier. Results from four V-TOUGH simulations will be described in this section. The simulations correspond to two thermal loads (24 and 80 MTU/acre) and two backfill options (with and without backfill). These cases are similar to the FEHM calculations presented earlier, albeit for slightly different thermal loads (25 and 83 MTU/acre). Note that the LLNL calculations do not include the effects of any surficial infiltration, whereas the FEHM simulations consider infiltration rates of 0.05 and 0.3 mm/yr. For reasons of consistency, the V-TOUGH calculations are compared with the FEHM calculations corresponding to the low infiltration rate (0.05 mm/yr) case. The performance measures of interest here are the temperature and relative humidity (RH) at the surface of the waste package.

Figure 4.2-21 shows a comparison between temperature and RH predictions for the 24 MTU/acre case (Buscheck et al., 1995) and the 25 MTU/acre case (this study). The temperature predictions are in general agreement, as are the RH predictions for the no backfill case. For the case of backfill emplaced at 100 years after waste emplacement, the RH predictions of Buscheck et al. (1995) are lower than those resulting from this study. A comparison between the results of the 80 MTU/acre case (Buscheck et al., 1995) and the 83 MTU/acre case (this study) is shown in

Figure 4.2-22. As before, predictions of temperature for the no-backfill case are essentially similar for both sets of calculations. However, the results of Buscheck et al. (1995) show a significant thermal spike at the time of waste emplacement - leading to persistent higher temperatures as compared to this study. This discrepancy may be attributed to the following: (i) the use of lower value for the dry thermal conductivity of the backfill (~0.3 W/m-°K) by Buscheck et al. compared to the value used in this study (~0.6 W/m-°K), and (ii) the differences in model geometry in the two analyses. The model geometry used by Buscheck et al. (6 m square drift, 1.6 m square waste package, 1.2 m thick invert) results in a 3.2 m separation between the top of the waste package and the drift wall, as compared to a 1.6 m separation for the model used in this study (5 m diameter drift, 1.8 m diameter waste package). The combination of a larger volume of backfilled drift and a lower conductivity material results in higher temperatures predicted by Buscheck et al. (1995).

As in the case of the low-thermal loading scenario, RH predictions by Buscheck et al. (1995) for the high-thermal loading option are significantly lower than those of this study. Figure 4.2-22 shows RH values approaching a plateau of ~0.95 based on the results of this study, whereas the simulations of Buscheck et al. yield a plateau of ~0.6 and ~0.5 at 10,000 years for the no-backfill and the backfill cases, respectively. These differences are believed to be due predominantly to the methodology employed for RH calculations, as discussed below. Buscheck et al. (1995) assume that the <u>absolute humidity at the drift wall</u> is equal to that at the surface of the waste package. Thus, the RH at the waste package is obtained as the ratio of the vapor pressure at the drift wall to the saturation pressure at the waste package surface. As explained in Section 4.2.7, this study assumes that the <u>absolute humidity at the dry-out front</u> is the corresponding quantity to be equated to that at the waste package surface. Typically, the dry-out front will be located further away into the rock as compared to the drift wall, and will also have a lower temperature. Its vapor pressure will thus be lower than that prevailing at the drift-wall. Furthermore, as discussed earlier, the WP surface temperature predictions of this study are typically lower than those by Buscheck et al., with a correspondingly lower saturation pressure. The combined effect results in higher relative humidity (ratio of vapor pressure to saturation pressure) at the surface of the waste package.

The above discussion underscores the need for better definition of backfill thermohydrologic properties, as well as improvements in the methodology used to estimate relative humidity. Detailed sensitivity studies are planned to further examine the impact of various assumptions regarding backfill parameters on near-field thermohydrologic performance. In any case, the combination of various simplifying assumptions in the thermohydrologic models of this study and Buscheck et al. (1995) and the conceptual/parametric uncertainties described above, point to the need to use caution when using relative humidity to predict the initiation of corrosion in WP/EBS performance assessments.

4.3   REPOSITORY-EDGE THERMOHYDROLOGIC CALCULATIONS

4.3.1   Introduction

The near-field (drift-scale) calculations described in the previous section are based on a 2-D x-z model. In the vertical (z) direction, the model extends from the ground surface to 1000 m below the water table. Along the horizontal (x) direction, the model is centered around a typical

emplacement drift and extends to the middle of the two adjoining pillars, where symmetry boundary conditions are invoked for computational convenience. As stated above, this simplified model is more applicable at the center of the repository than at the edge, where heat transfer to the surrounding rock might produce significant edge-cooling effects (e.g., Ryder, 1993).

One approach to account for these edge effects requires embedding a locally refined mesh within a generally coarse mesh to simultaneously simulate both near- and far-field conditions. To date, however, limited software/hardware efficiency has precluded the modeling of transient heat and fluid flow in such hybrid domains. An alternative approach, which is based on the concept of scaling, is presented below. By decoupling of the drift- and repository-scale simulations, this scaling methodology seeks to enforce internal consistency in far- and near-field results and provides an efficient tool for incorporating edge effects.

4.3.2 The Scaling Concept

Consider a subdomain of the repository, which we assume can be partitioned into a 'center' and an 'edge', each with its characteristic thermohydrologic response. This implies that every point within the 'center', or the 'edge', has the same T (temperature) and/or S_{liq} (liquid saturation) vs. t (time) behavior. It is further assumed that the response of the 'edge' region is equivalent to that of the 'center' region, but for a different (lower) thermal load. In other words, the thermohydrologic response of the 'edge' region can be obtained by simulating the behavior of the 'center' region at a reduced thermal load. Because the response of the 'center' is typically obtained using a simple model with symmetry boundary conditions, this approach eliminates the need for performing detailed calculations to explicitly characterize edge effects. Note that the partitioning of the model domain into 'center' and 'edge' is for illustration purposes only, and does not preclude the use of additional zones in actual simulations.

The proposed scaling methodology consists of the following steps. Step 1 calls for far-field, two-dimensional simulations with an average heat load uniformly distributed over the repository area. Step 2 calls for one-dimensional simulations of vertical columns passing through the repository. Here the heat loading would be adjusted (scaled to an effective heat loading) by trial and error so that one-dimensional results (temperature, saturation, relative humidity) for the column optimally reproduce predictions of the two-dimensional model for the same column. Step 3 calls for detailed near-field simulations employing the effective heat loading determined in step 2 and a localized two-dimensional mesh focused around a single waste package in an emplacement drift. In what follows, we present some preliminary results related to the development of scale factors using far-field simulations are presented.

4.3.3 Model Description

A two-dimensional cross-section, adapted from the site-scale model of Wittwer et al. (1995) is shown in Figure 4.3-1. This cross-section, bounded by the Solitario Canyon Fault and the Ghost Dance Fault, includes the proposed repository horizon in the Upper Block of the Primary Emplacement Area. The model contains six major hydrostratigraphic intervals in the unsaturated zone (i.e., TCw, PTn, TSw, TSv, CHnv and CHnz), as well as 1,000 m of the saturated Prow Pass unit below the water table.

As indicated by the dots (block centers) in Figure 4.3-1, the discretization consisted of 12 vertical columns with column heights varying in accord with the surface topography. Model boundaries were characterized by atmospheric conditions at the top and deep-saturated conditions at the bottom. Although the vertical boundaries permitted no liquid or gas flows, they allowed a free exchange of heat with the external system *via* the method of Vinsome and Westerveld (1980). As implemented in TOUGH2 (Pruess, 1991), this method attaches a semi-infinite, one-dimensional thermal field to each edge block, and a semi-analytical determination of an external field employs the thermal properties of the edge block. The temperature contours of Figure 4.3-1 indicate that the method yielded realistic results, even for vertical boundaries located only 100 meters from the repository edges.

For this implementation, the heat input curve was determined for a mix of 21PWR/40BWR assemblies emplaced at an areal mass loading of 85 MTU/acre. Thermal parameters were taken from Lingineni et al. (1994), and hydrologic properties were based on data of Schenker et al. (1995) as summarized in Section 2.2. For implementation in the equivalent continuum option, fracture capillary pressures were linearized using the prescription of Tsang and Pruess (1989).

The analyses considered two different rates of infiltration (0.0 and 0.1 mm/yr) and two levels of vapor diffusion, yielding four sets of calculations. With vapor diffusivity varying in direct proportion to the factor β, one level (enhanced) assumed $\beta=1$. The other (unenhanced) assumed $\beta=\tau\phi S_g$ where τ is the tortuosity, ϕ the porosity, and S_g is the gas saturation. Citing references from soil physics literature, Tsang and Pruess (1990) discuss the basis for assuming an enhanced level of vapor diffusion. The specification of initial conditions was based on results of transient analyses representing 400,000 years. Including no heat source, four separate calculations considered both rates of infiltration and both levels of vapor diffusion.

4.3.4 Results

The combination of 0.1 mm/yr and enhanced vapor diffusivity ($\beta=1$) produced the most rapid resaturation of the dry-out zone. For brevity, the discussion presented here will be confined to this case. Figures 4.3-1 and 4.3-2 present contour plots of the two-dimensional distributions of temperature and liquid saturation at 1,000 years. Figures 4.3-3 and 4.3-4 give results for columns 6 and 11, which approximately pass through the center and edge of the repository horizon, respectively. These results indicate that at 1,000 years, resaturation of the dry-out zone is considerably more advanced at the edge than at the center of the repository. In fact, results for 10,000 years (not shown) reveal that, by this time, a small downward flow has been established in column 2 and 11 (the edges), while convergent flow toward the repository is still occurring in all interior columns.

Figures 4.3-3 and 4.3-4 present the scaled one-dimensional fits alongside two-dimensional results. Figures 4.3-4 indicates that, for the edges of the repository, the two-dimensional results were reasonably matched by the scaled one-dimensional simulations. For Column 11, the optimal (scaled) one-dimensional heat loading was found to be 58 MTU/acre. Figure 4.3-3 indicates that, within the interior, one-dimensional fits to the two-dimensional results were of lower quality. Interestingly, at the center of the repository, i.e. for Columns 6 and 7, the scaled one-dimensional heat loading had to be increased to values greater than the prescribed values of 85 MTU/acre. For Column 6, this value was found to be 92 MTU/acre.

4.3.5 Implications

As discussed earlier, the use of the 2-D drift-scale model with symmetry boundary conditions (Section 4.2) would result in optimistic predictions of the near-field thermohydrologic environment. Neglecting edge-cooling effects would mean that the waste packages emplaced near the edge of the repository would be predicted to stay hotter, and drier, for a longer period of time than might actually be the case. A separate set of calculations for the 'edge' region of the repository, using the lower (scaled) thermal loads described in the previous section, would provide more representative predictions of waste package performance.

4.4 NEAR-FIELD THERMAL-MECHANICAL CONSIDERATIONS

Thermal-mechanical response of the rock mass in the vicinity of emplacement drifts may alter the near-field hydrology. In turn, the potential changes in near-field hydrologic properties caused by thermal loading may impact repository performance. Rock fabric may be modified due to fracture creation, closure, or widening caused by temperatures above ambient geothermal conditions. Thermal-mechanical analyses may be used to assess the degree of disturbance (changes in permeability) and the extent of the thermally- and mechanically-disturbed zone for the ground-water travel time analyses.

Results of M&O (1995b) show that vertical joint apertures above and below the drifts may close due to the induced horizontal compressive stress induced by the application of thermal load to the rock mass. The M&O study also shows that horizontal joint apertures may open up to 0.2 mm in the near field due to the motion of rock blocks caused by a 111 MTU/acre thermal load. Such a disturbance may change the horizontal components of bulk permeability of the rock mass in the near field. In addition, the M&O study shows that the thermally induced stress in the near-field rock mass may exceed the rock mass strength if an 111 MTU/acre thermal load is applied. This suggests that there may be continuous joint slip in the near-field rock mass at such a thermal load.

Although no thermal-mechanical coupling has been considered in this iteration of TSPA, such processes may need to be included in subsequent TSPA iterations if significant changes in rock-mass properties (i.e., changes outside of the natural variability in rock-mass properties), are anticipated due to the emplacement of heat-generating wastes.

4.5 THERMAL-CHEMICAL EFFECTS IN THE NEAR-FIELD ENVIRONMENT

4.5.1 Introduction

In addition to the potential changes to hydrology and mechanical response of the near-field environment induced by thermal perturbations to the ambient system, the chemical evolution of the near-field geochemical environment will be impacted by these temperature changes, as well as by the masses of introduced materials which remain over geologic time in the vicinity of the potential repository horizon (West, 1988; Murphy, 1991; Glassley, 1993; Meike and Wittwer, 1993). Although the ambient geochemical system has a large capacity to moderate system geochemistry, changes to the near-field environment have the potential to affect waste-package corrosion, waste-form dissolution, radionuclide solubility limits, and transport characteristics, and

may ultimately impact the performance of a potential repository. Inclusion of such effects into Performance Assessment models relies on process-level models which quantify the detailed geochemical interactions in the near-field. The following discussion presents an overview of some of the potential effects on near-field geochemistry from introduced materials and from thermal perturbations.

4.5.2 Perturbations from Introduced Materials

During both site characterization activities and construction of a potential repository, a number of substances, which are likely to remain in the system over geologic time, will be introduced into the site. These may include a wide variety of compounds but there are three main categories that, as part of the waste package or as structural components, potentially will be abundant post-closure: steels, cementitious materials, and organic substances. Steel, containing abundant Fe, may stabilize Fe-oxide or Fe-hydroxide solids in the near field which would provide effective sorption sites for many dissolved species, and may be particularly effective in sorbing some unretarded elements such as Tc (Meijer, 1990). The dissolution of steels will liberate metal cations to the aqueous phase and the increased concentration of Fe in the fluids (which are naturally very poor in Fe), may stabilize more complex Fe-silicates. In addition, as the Fe in steel will oxidize, it will provide a sink for oxygen in the system and may generate locally reducing conditions dependent upon the rate of oxygen supply in the gas phase. Locally reducing conditions would lower solubility-limits on dissolved concentrations of many metal ions. Finally, colloids generated from steel may strongly sorb radionuclides and provide additional transport capabilities (Meike and Wittwer, 1993).

The pH of groundwater equilibrated with cement will, in general, be shifted to the extremely alkaline range of about 12-13. This pH range may not constitute a concern for accelerated waste package corrosion because of the formation of passivation films (Pourbaix, 1966). At these high pH conditions, however, dissolved elements controlled by hydroxide complexing will have increased aqueous concentrations (e.g., Aluminum—Castet et al., 1992), as may many actinides because of enhanced formation of very stable carbonate complexes (Clark et al., 1995). In addition, at such high-pH conditions, there is a large (3 to 6 orders of magnitude) increase in the capacity to dissolve silica, and thus in the potential to change the porosity and permeability of the system (Baes and Mesmer, 1976; Eikenberg, 1990; Eikenberg and Lichtner, 1992; Glassley, 1993). Because of microbial colonies feeding on organic admixtures used within concretes, acidic pH values have also been observed (Meike, 1995). As with steel, cements may generate colloids which enhance radionuclide mobility, but may also sorb dissolved species onto the immobile solids (Meike and Wittwer, 1993). Cementitious materials can provide a large source of Ca to the system phase, and therefore may effect the distribution of calcite in the near field.

The introduction of organic substances into the near field may have an impact on performance through changes in the concentrations of organic acids and organic colloids which can increase waste package corrosion, increase radionuclide solubility-limits, enhance radionuclide transport properties, and enhance silicate mineral dissolution (Choppin, 1992; Minai et al., 1992; Bennett et al., 1993; Meike and Wittwer, 1993). Such organics may also promote microbial activity which could detrimentally effect waste package corrosion (Meike 1995). In addition, organic substances can take part in oxidation/reduction reactions and, therefore, may contribute to the generation of locally reducing conditions.

4.5.3 Perturbations from Thermal Effects

As temperature increases, a number of changes may impact the geochemical behavior of the near-field environment. Mineral stabilities and phase equilibria are temperature dependent, and the rates at which reactions occur will generally increase at higher temperatures. Both continuous reactions such as the progressive dehydration or shift in cation composition of a solid phase, and discontinuous reactions such as the disappearance of a phase outside of its stability range, will occur as temperature increases (Glassley, 1993; Murphy, 1993). The higher temperatures in the near field, may result in regions where attainment of thermochemical equilibrium can be assumed (Glassley, 1993). Mineral transformation reactions, as well as precipitation/dissolution reactions will cause changes in porosity and permeability of the system as temperature increases and will result in a change in both the type and distribution of minerals in the near field (Glassley, 1993). This has ramifications for the hydrologic properties of the system as well as the near-field transport properties.

In addition to changes in the natural phases, introduced substances such as cementitious materials will undergo phase transformations which will include dehydration reactions as fluids are expelled from pores and from mineral structures (Bruton et al., 1993a, 1993b; Meike et al., 1994). Model results suggest that calcite precipitation will occur at higher temperatures and will be limited only by the Ca supply (Murphy, 1993), this could mean that Ca supplied from near-field cementitious materials may enhance the abundance of calcite precipitated (and retardation of CO_2) in close proximity to the potential repository. The increased temperatures will vaporize much of the water in the near field as an above-boiling zone forms in the very near field (Glassley, 1993). This transition will increase the capacity of the system to transport moisture as volatiles and will result in precipitation of all dissolved solids from boiling fluids in the near field. Reprecipitation of water in cooler regions above the potential repository horizon will dissolve new material which could be transported through fractures back down into the boiling zone with subsequent boiling and phase precipitation. This refluxing could result in the presence of soluble salts in the Near-field environment and could produce porosity and permeability changes that may impact the near-field hydrology (Glassley, 1993).

Table 4.2-1 Matrix Hydraulic Properties

Rock Unit Type	Porosity	Permeability (m²)	Residual Saturation	Van Genuchten Parameters		
				1/α (Pa)	β	λ=1-1/β
TCw	0.0870	9.7e-19	0.002	1.19e6	1.558	0.36
PTn	0.4210	3.9e-14	0.100	6.54e5	6.872	0.85
TSw	0.1390	1.9e-18	0.080	1.73e6	1.798	0.44
TSv	0.0650	1.9e-18	0.080	1.73e6	1.798	0.44
CHnv	0.3310	2.7e-14	0.041	6.13e5	3.861	0.74
CHnz	0.3060	2.0e-18	0.110	3.19e6	1.602	0.38
Backfill	0.5000	3.9e-14	0.010	9.04e4	3.333	0.70

Table 4.2-2 Fracture Hydraulic Properties

Rock Unit Type	Permeability (m²)	Residual Saturation	Van Genuchten Parameters		
			1/α (Pa)	β	λ=1-1/β
TCw	3.9e-12	0.04	7.66e4	4.230	0.7636
PTn	3.9e-13	0.04	7.66e4	4.230	0.7636
TSw	3.9e-12	0.04	7.66e4	4.230	0.7636
TSv	3.9e-12	0.04	7.66e4	4.230	0.7636
CHnv	3.9e-13	0.04	7.66e4	4.230	0.7636
CHnz	3.9e-12	0.04	7.66e4	4.230	0.7636
Backfill	3.9e-12	0.04	7.66e4	4.230	0.7636

Table 4.2-3 Matrix Thermal Properties

Thermohydrologic Unit	Thermal Conductivity (dry) (W/m-K)	Density (dry) (kg/m^3)	Specific Heat (dry) (J/kg-K)
TCw	1.69	2580	728
PTn	0.61	2580	422
TSw	2.10	2580	840
TSv	1.28	2580	948
CHnv	0.84	2580	488
CHnz	1.42	2580	526
Backfill	0.6	2580	840

INFORMATION

Site Biosphere → 8

Site Geology → 7

Site Hydrology → 6

Site Geochemistry → 5

Repository Design → 4

Waste Package Design → 3

Material Properties → 2

Waste Form Properties → 1

4-20

PROCESS-LEVEL MODEL

7 → 6 → Saturated Zone Flow Model

7 → 6 → Unsaturated Zone Flow Model

7 → 6 → 4 → 3 → Drift-Scale Thermo-Hydrologic Model

3 → 2 → Waste Package Degradation Model

PROCESS-LEVEL MODEL ABSTRACTIONS

Response surface of saturated zone flux → E

Response surface of unsaturated zone flux
- fracture flux
- matrix flux → D

Response surface of drift-scale flux
- % packages with drips
- advective flux in drips → C

Response surface of
- temperature
- humidity
- liquid saturation → B

Response surface of
- first pit
- pit distribution → A

TOTAL SYSTEM PERFORMANCE ASSESMENT

Biosphere Transport -Dose

8

Geosphere Transport -Cumulative Release

D E 5 6 7

EBS Transport -Release Rate

B C 5 4 3 2 1

Waste Package Degradation -Containment

A

Figure 4.1-1   Relationship of Chapter 4 to the Overall Information Flow Diagram for TSPA 1995 (Figure 1.4-6)

684 m.

TCw

589 m.

PTn

536 m.

TSw

344 m.

210 m.

TSv

202 m.

CHnv

121 m.

CHnz

0 m.   Water Table
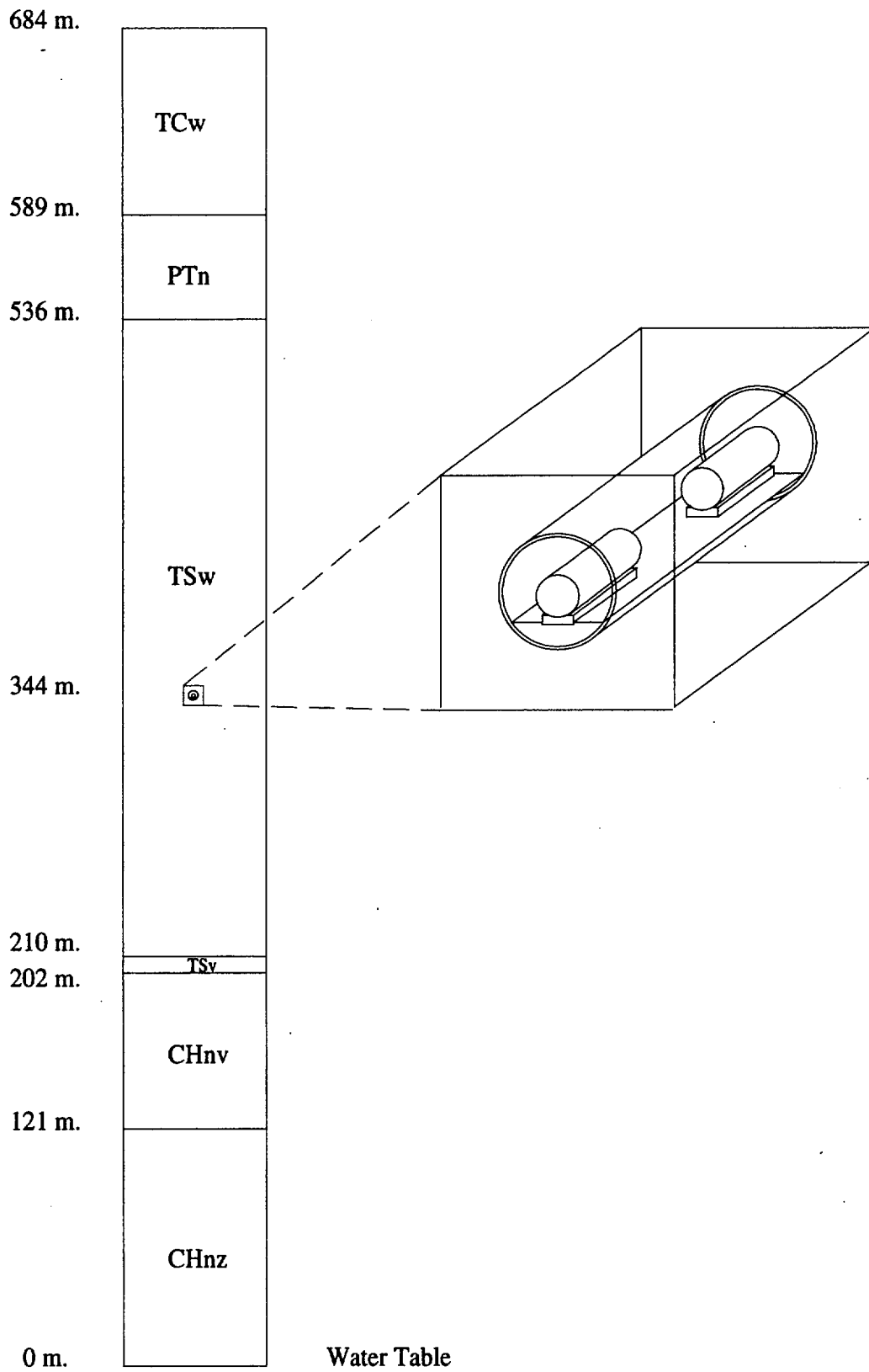
Figure 4.2-1   Near-Field Thermal-Hydrologic Conceptual Model
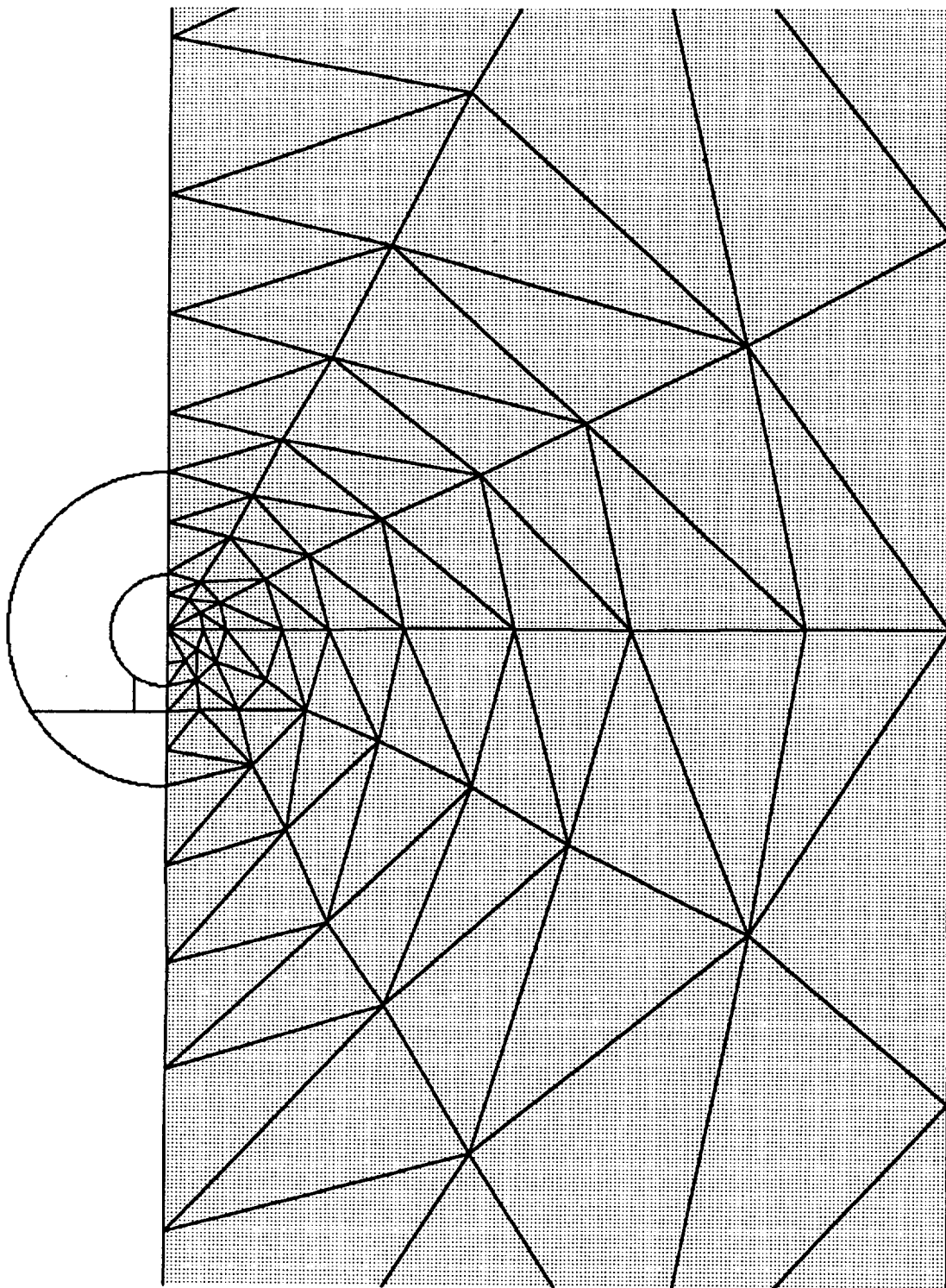
Figure 4.2-2 Finite-Element Mesh Used for Drift Scale Thermal-Hydrologic
Simulations
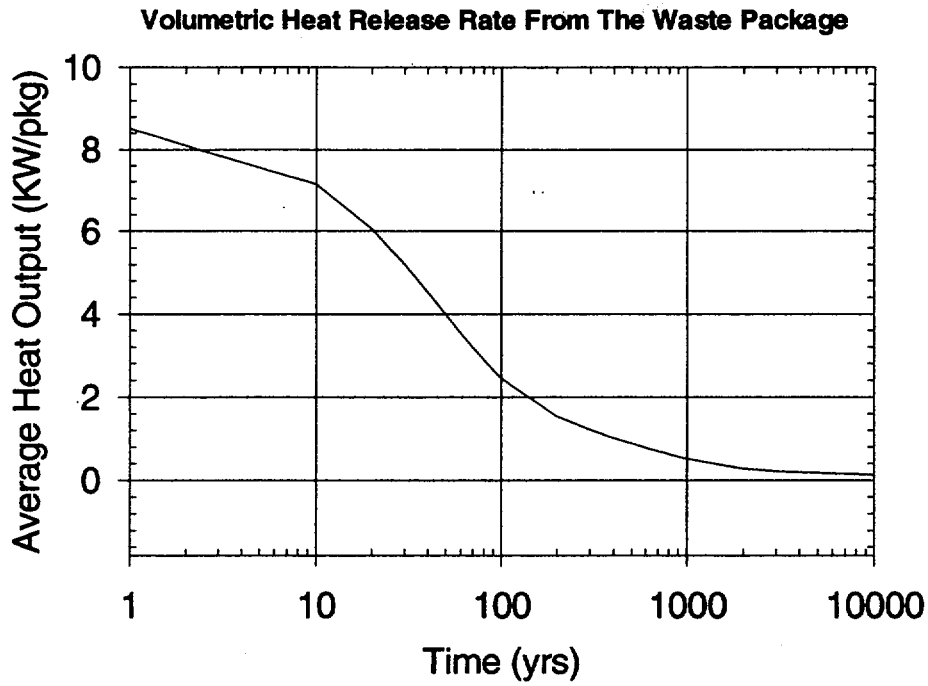
Figure 4.2-3   Heat Generation Rates of an Average Waste Package
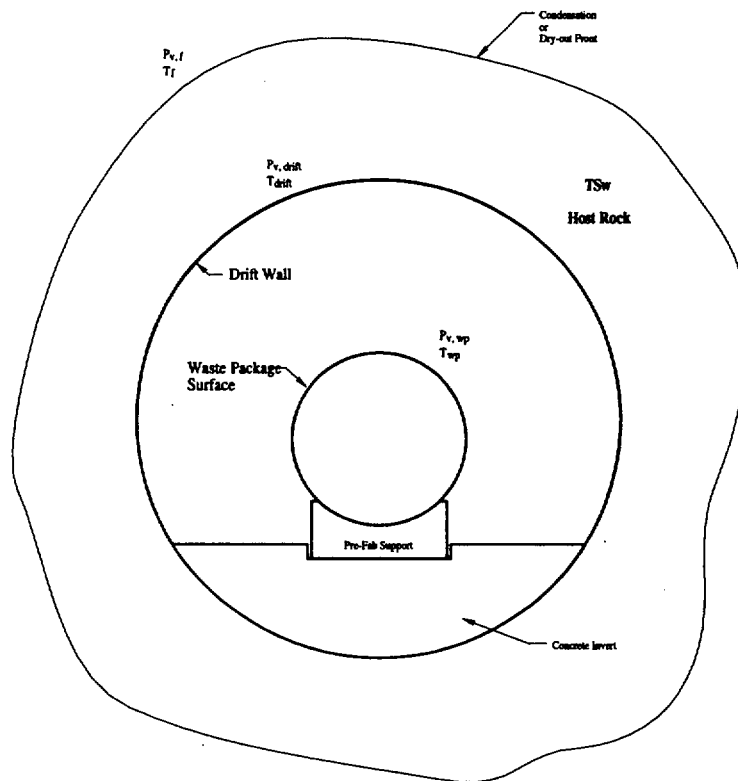
Figure 4.2-4   Conceptual View of Relative Humidity Determination Module
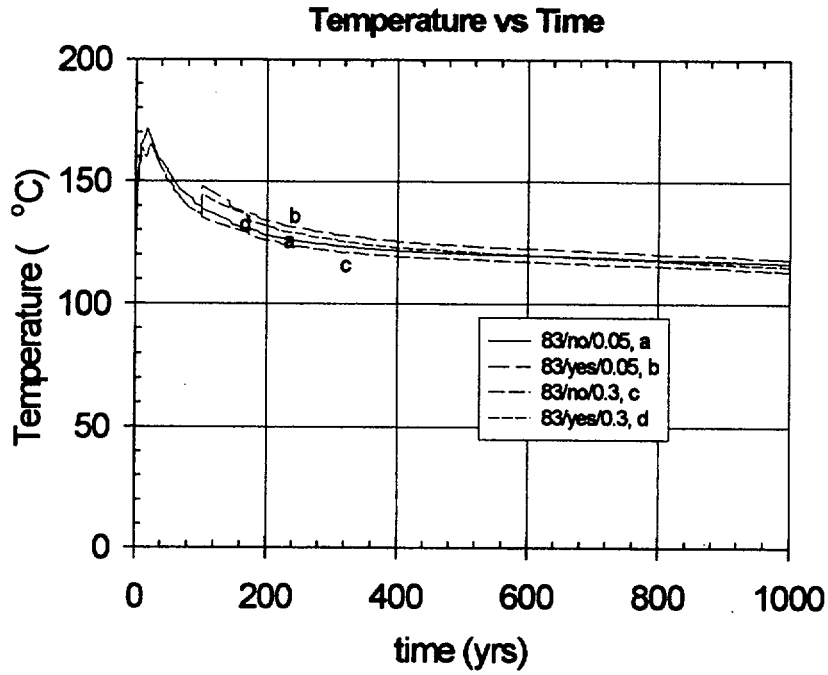
Figure 4.2-5   Waste Package Surface Temperature Predictions for 83 MTU/acre
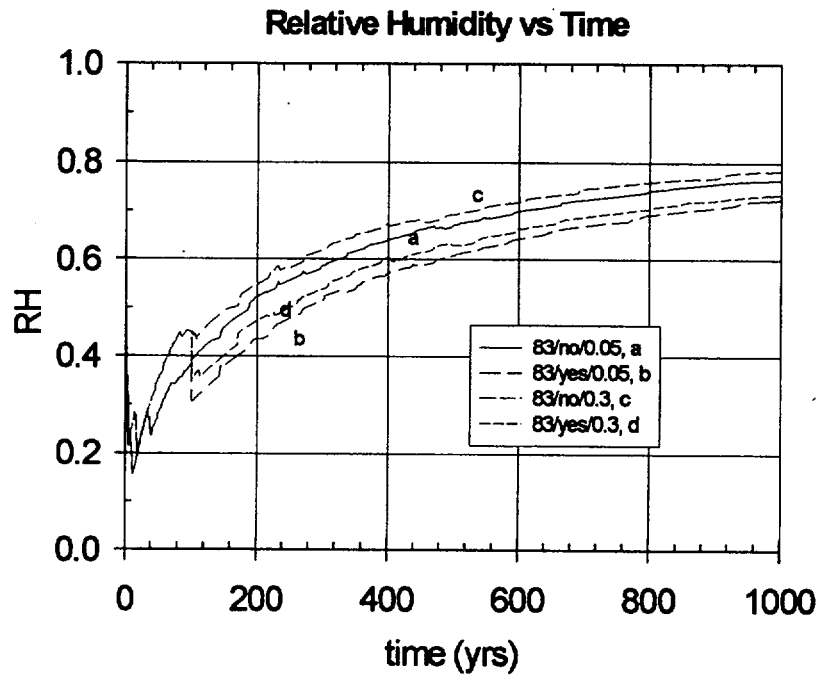
Figure 4.2-6   Relative Humidity Predictions for 83 MTU/acre Case
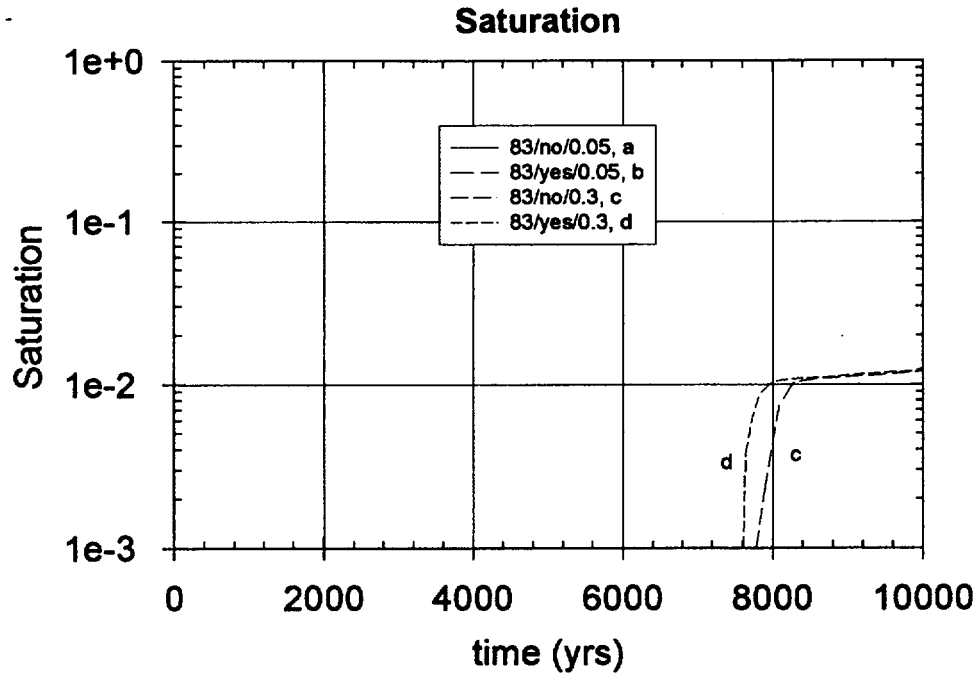
Saturation

Figure 4.2-7   Predictions of Liquid Saturation within Drift for 83 MTU/acre Case

RH, temperature vs time
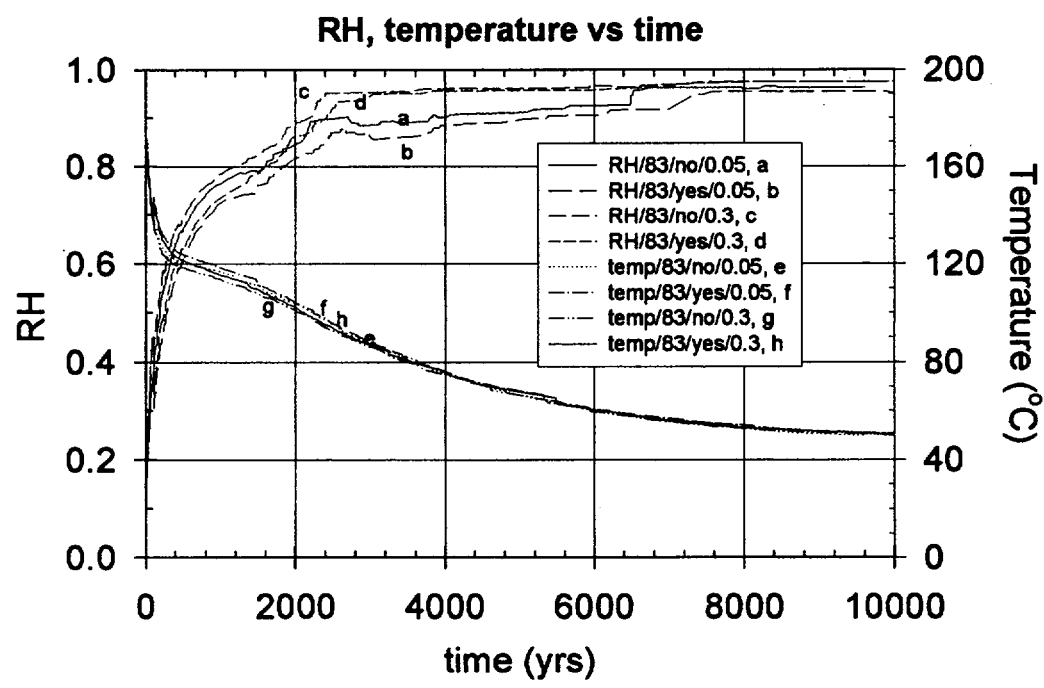
Figure 4.2-8   Abstractions of Temperatures and Relative Humidities for 10,000 years
(83 MTU/acre Case)
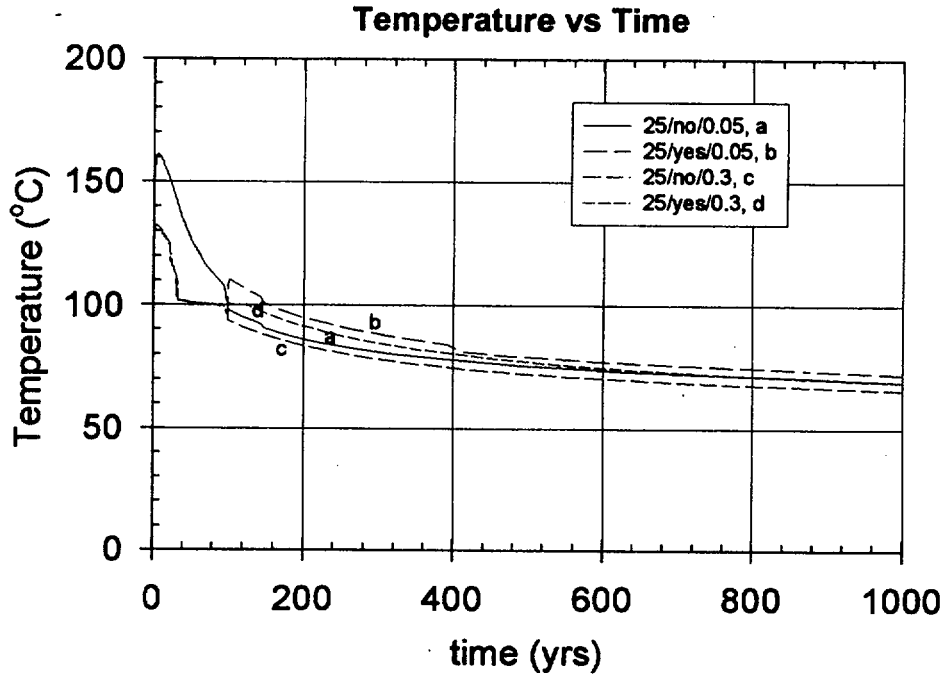
Figure 4.2-9   Waste Package Surface Temperature Predictions for 25 MTU/acre Case
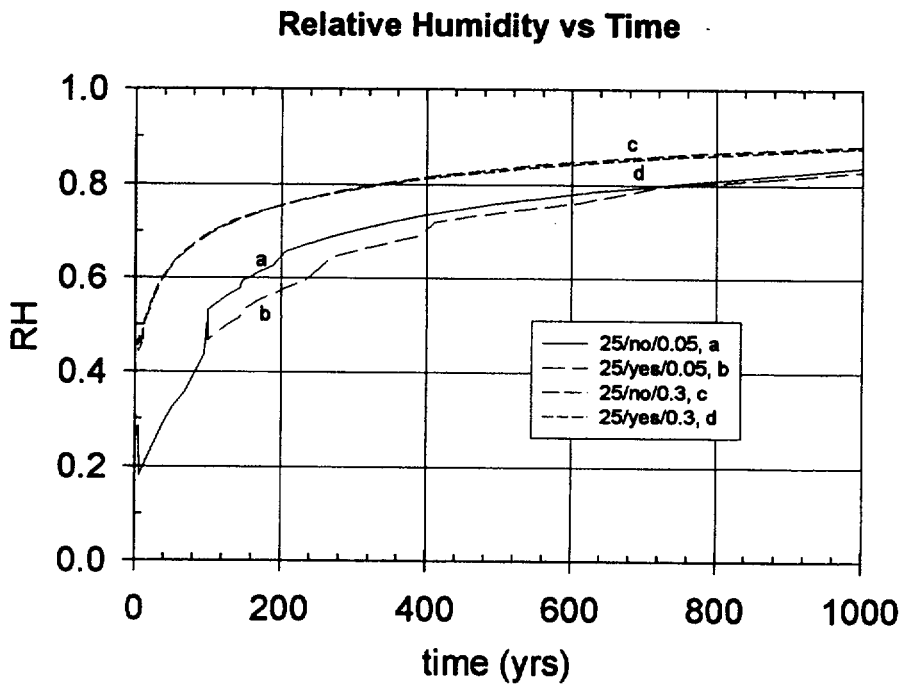
Figure 4.2-10 Relative Humidity Predictions for 25 MTU/acre Case

4-26
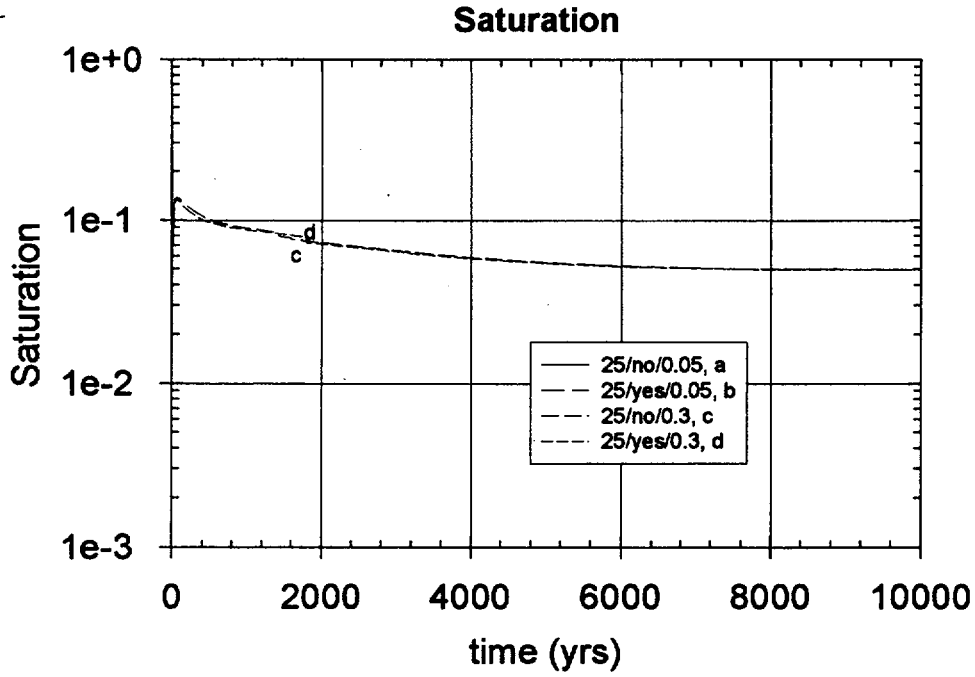
Saturation

Figure 4.2-11 Predictions of Liquid Saturation within Backfill for 25 MTU/acre Case

RH, temperature vs time
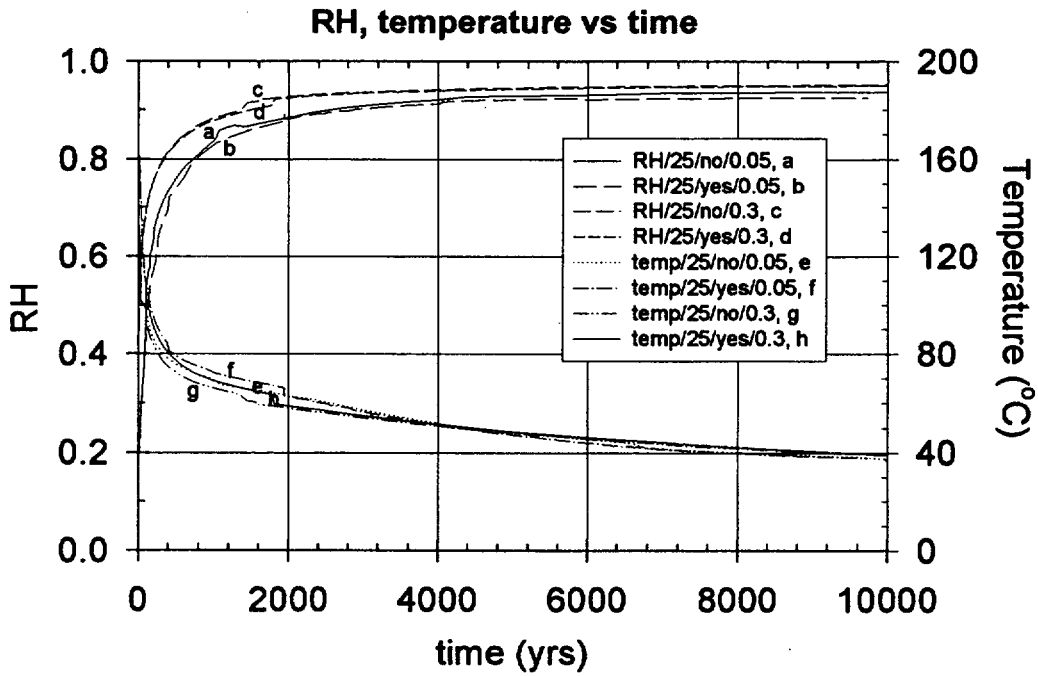
Figure 4.2-12 Abstractions of Temperatures and Relative Humidities for 10,000 years
(25 MTU/acre Case)
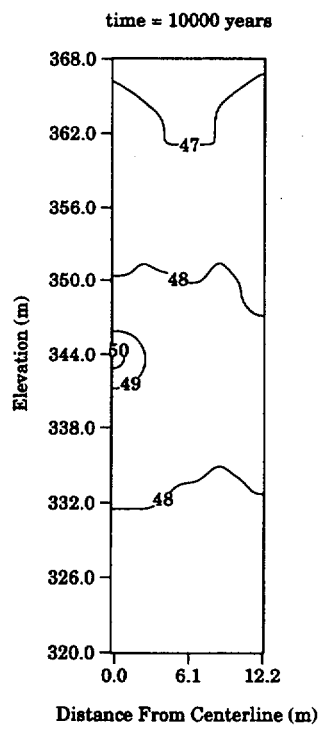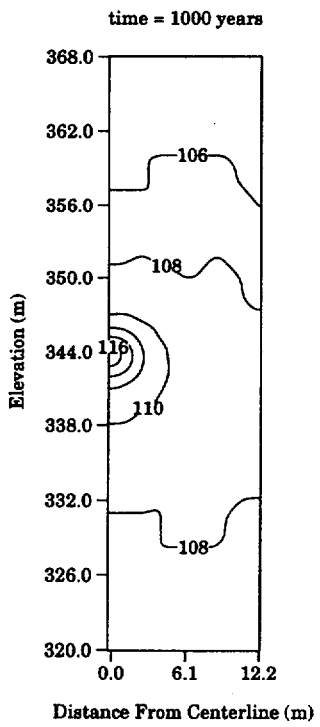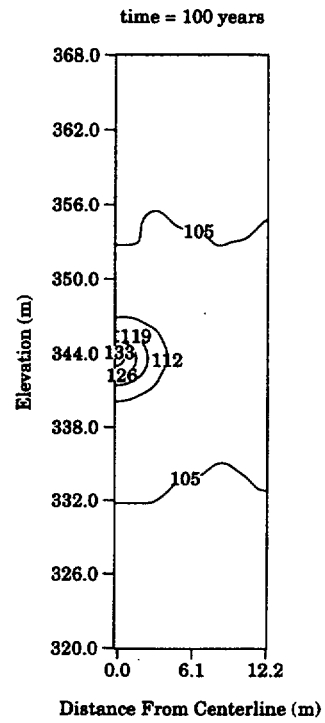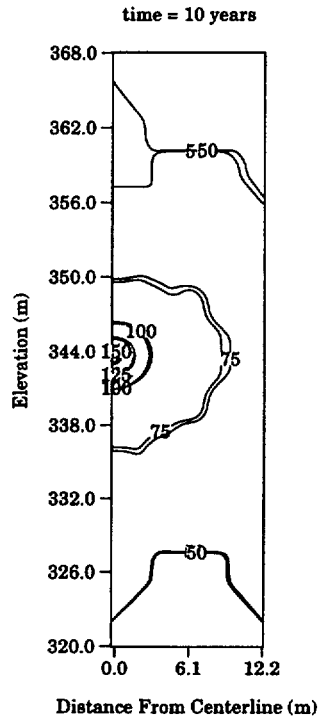
Figure 4.2-13 Predicted Temperature Distribution for 83 MTU/acre, with Backfill, Infiltration = 0.05 mm/year

time = 10 years

time = 100 years

time = 1000 years

time = 10000 years
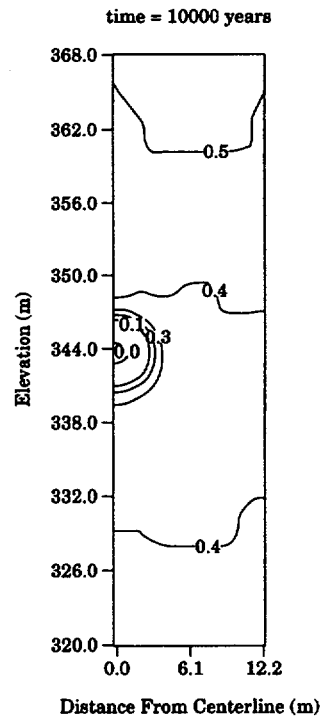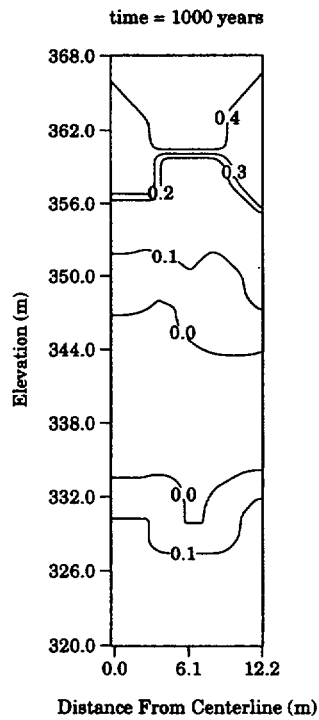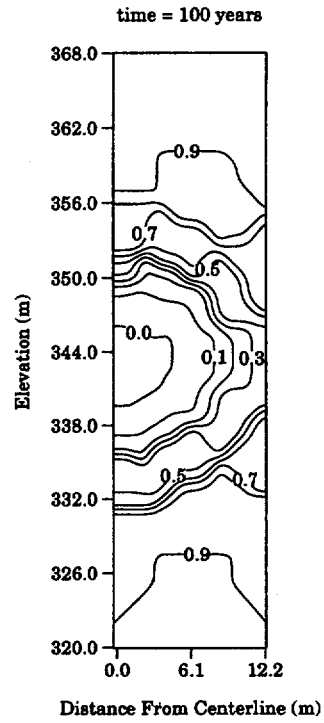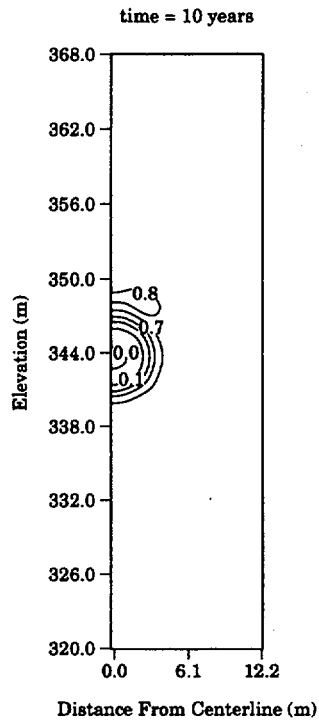
Figure 4.2-14 Predicted Saturation Distribution for 83 MTU/acre, with Backfill,
Infiltration = 0.05 mm/year
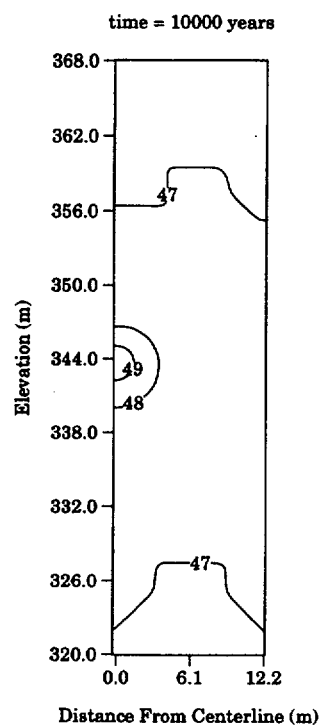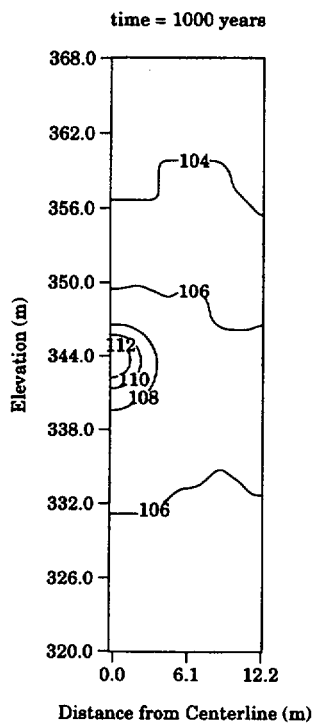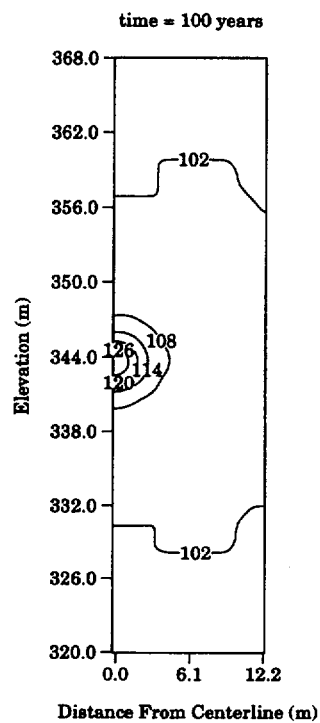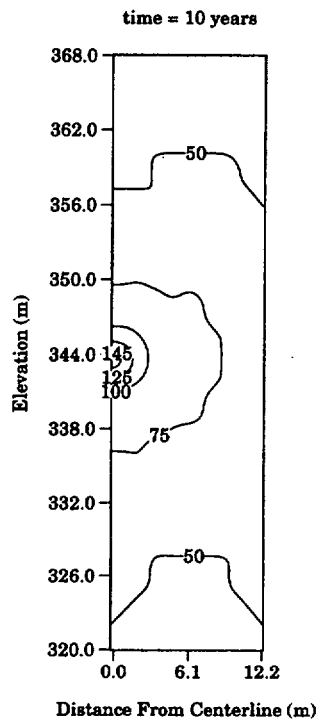
Figure 4.2-15 Predicted Temperature Distribution for 83 MTU/acre, with Backfill,
Infiltration = 0.3 mm/year
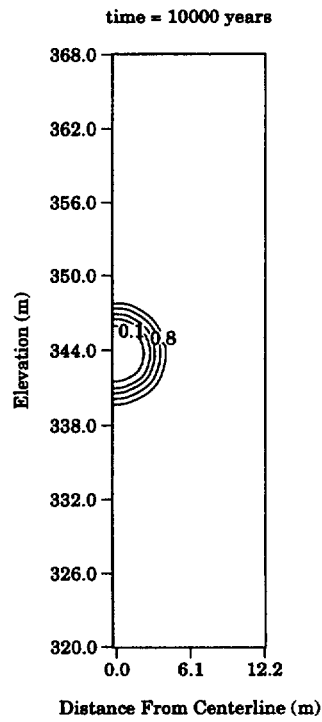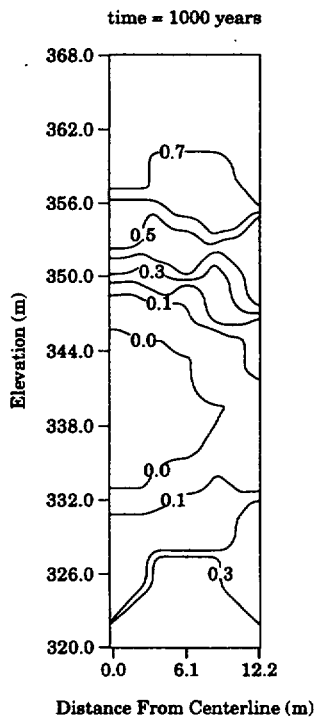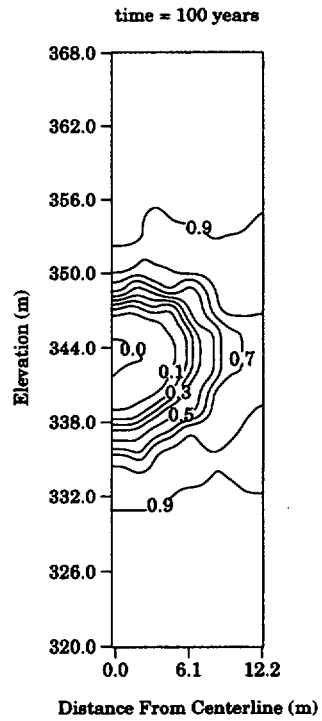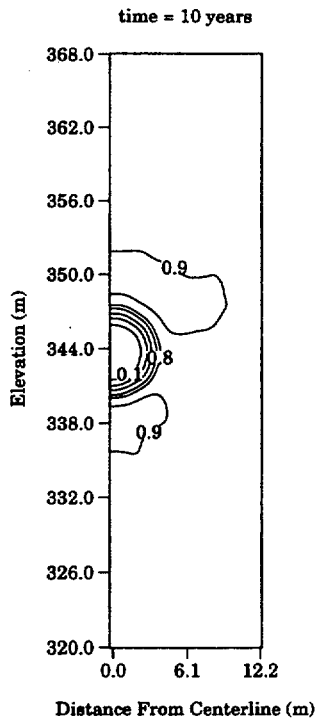
Figure 4.2-16 Predicted Saturation Distribution for 83 MTU/acre, with Backfill,
Infiltration = 0.3 mm/year
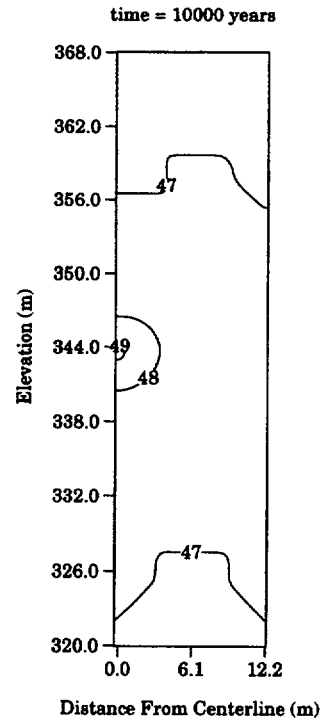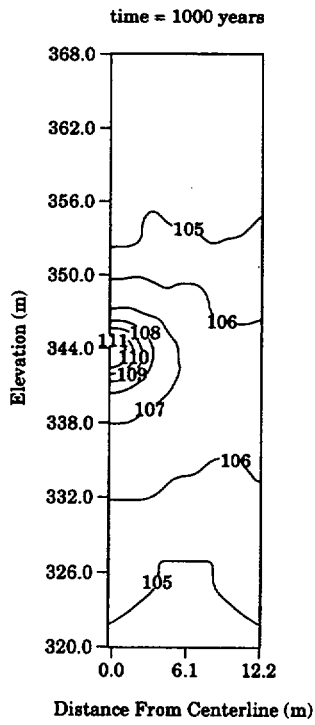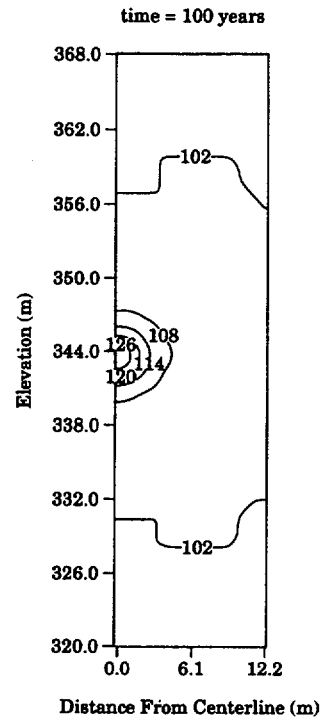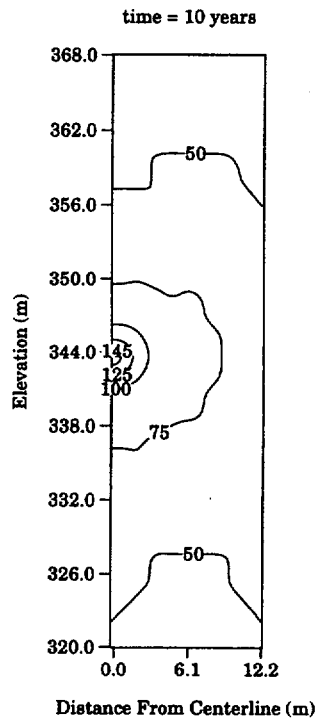
Figure 4.2-17 Predicted Temperature Distribution for 83 MTU/acre, No Backfill,
Infiltration = 0.3 mm/year
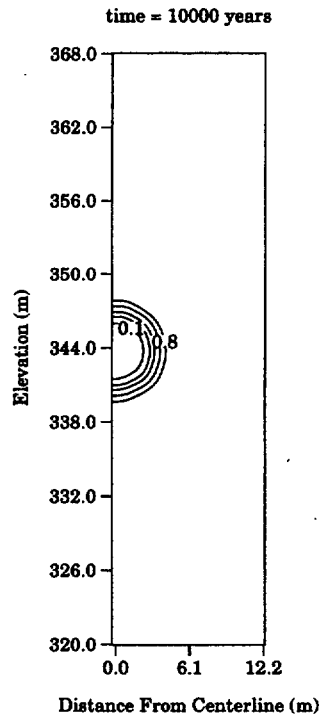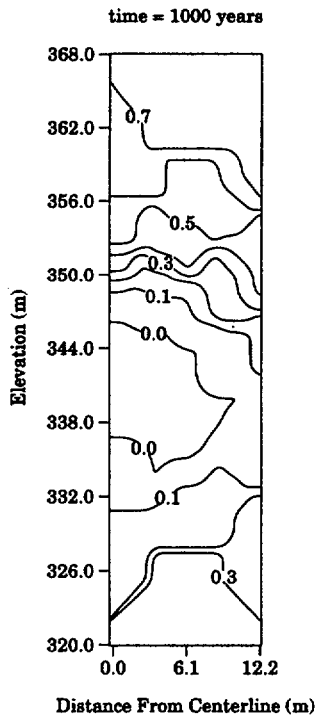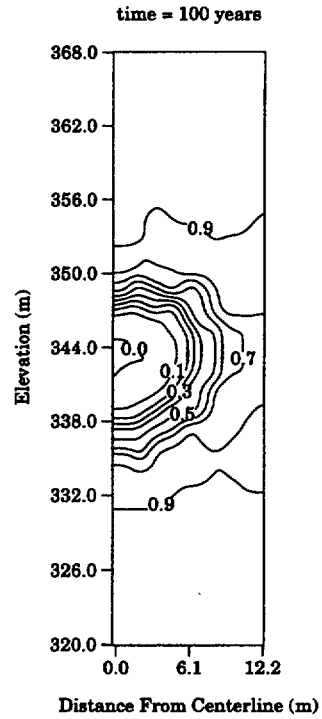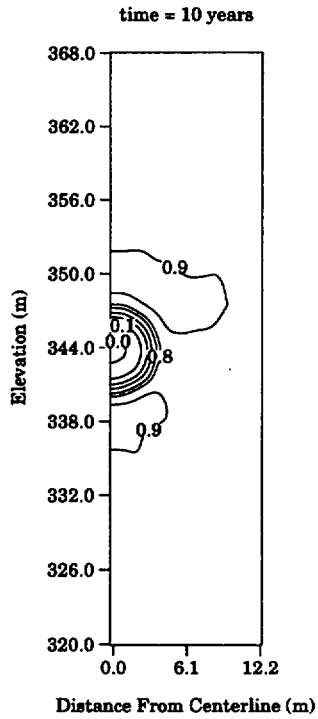
Figure 4.2-18 Predicted Saturation Distribution for 83 MTU/acre, No Backfill,
Infiltration = 0.3 mm/year
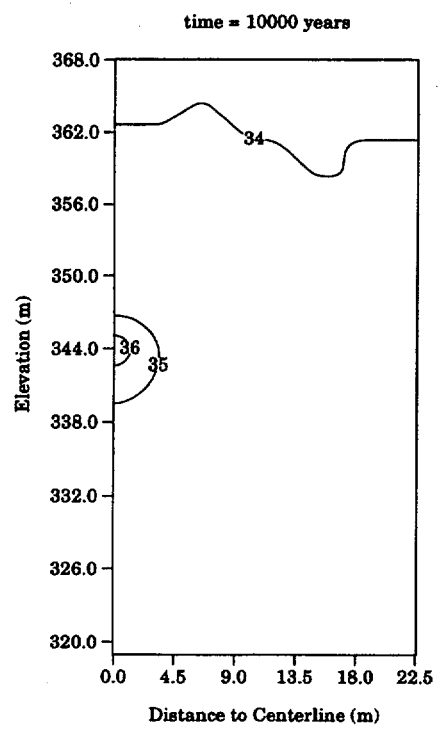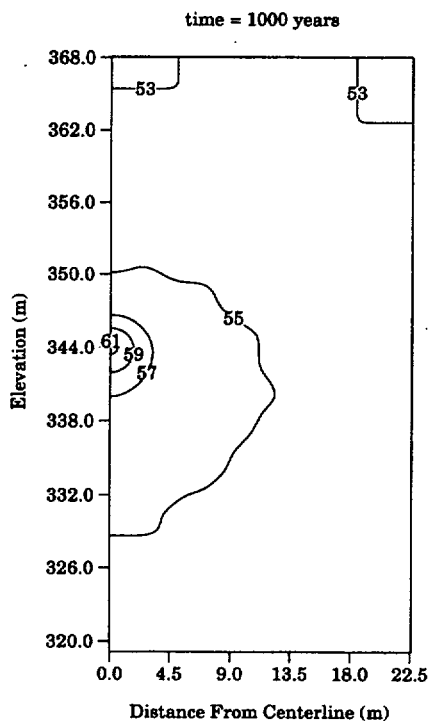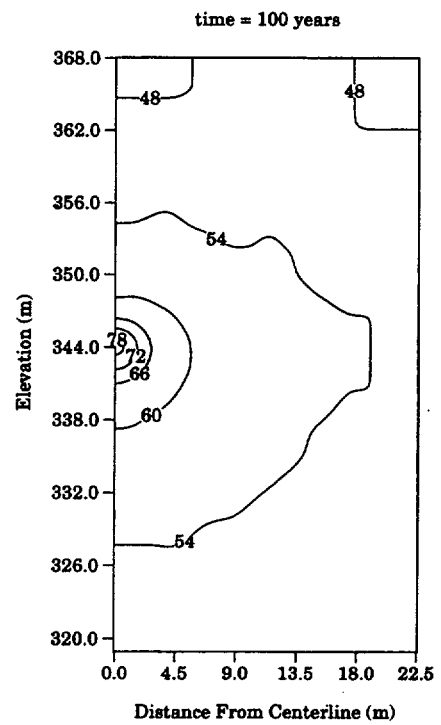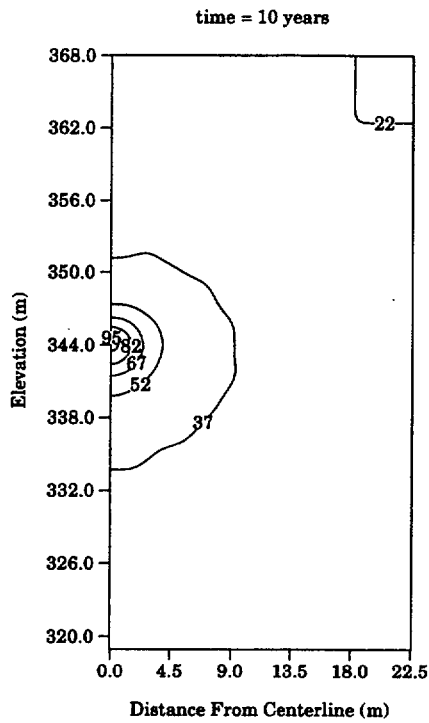
Figure 4.2-19 Predicted Temperature Distribution for 25 MTU/acre, with Backfill,
Infiltration = 0.3 mm/year
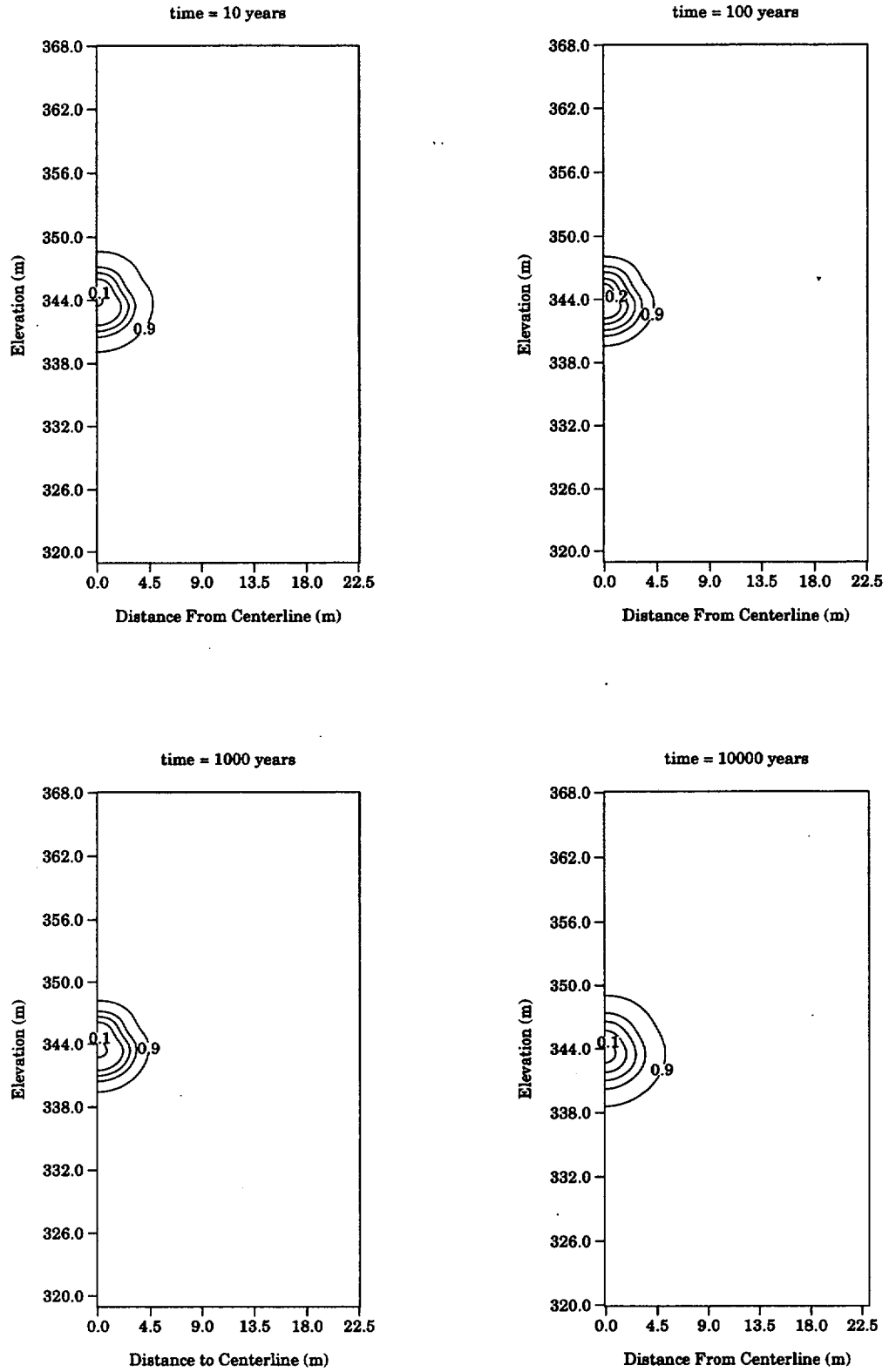
Figure 4.2-20 Predicted Saturation Distribution for 25 MTU/acre, with Backfill,
              Infiltration = 0.3 mm/year

4-35
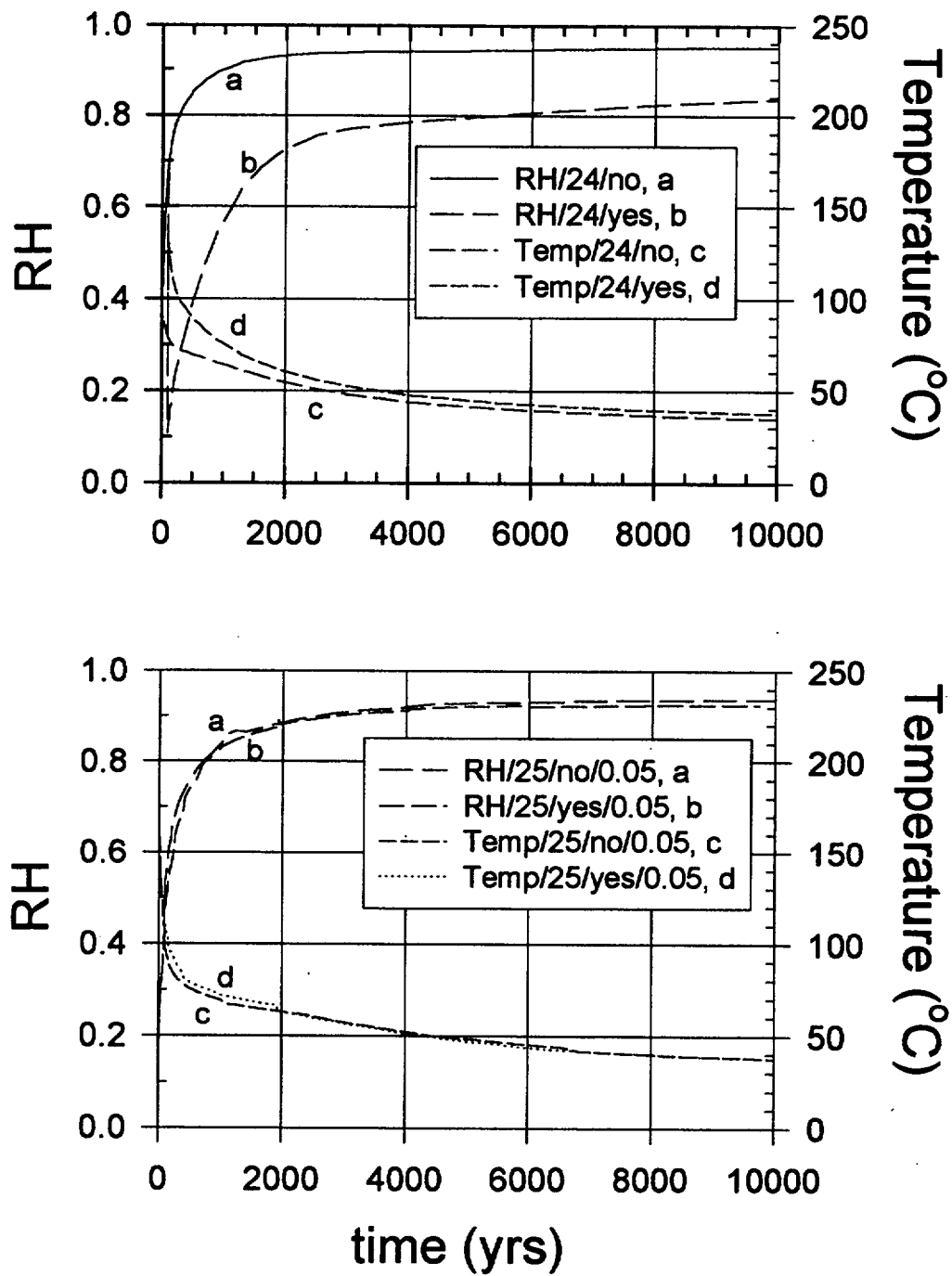
Figure 4.2-21 Comparison of RH and temperature predictions from Buscheck et al. (24 MTU/acre) and this study (25 MTU/acre).
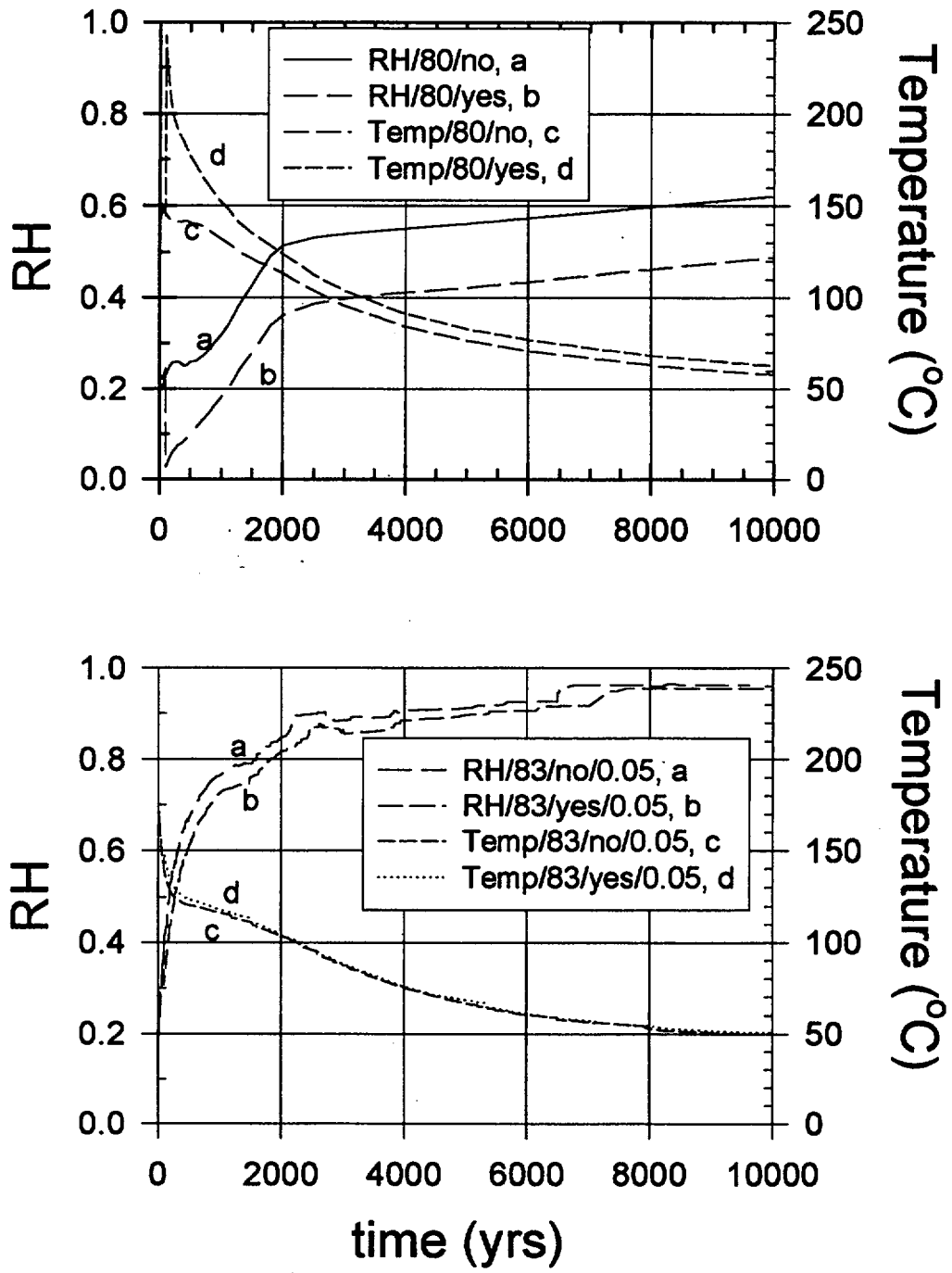
Figure 4.2-22 Comparison of RH and temperature predictions from Buscheck et al. (80 MTU/acre) and this study (83 MTU/acre).
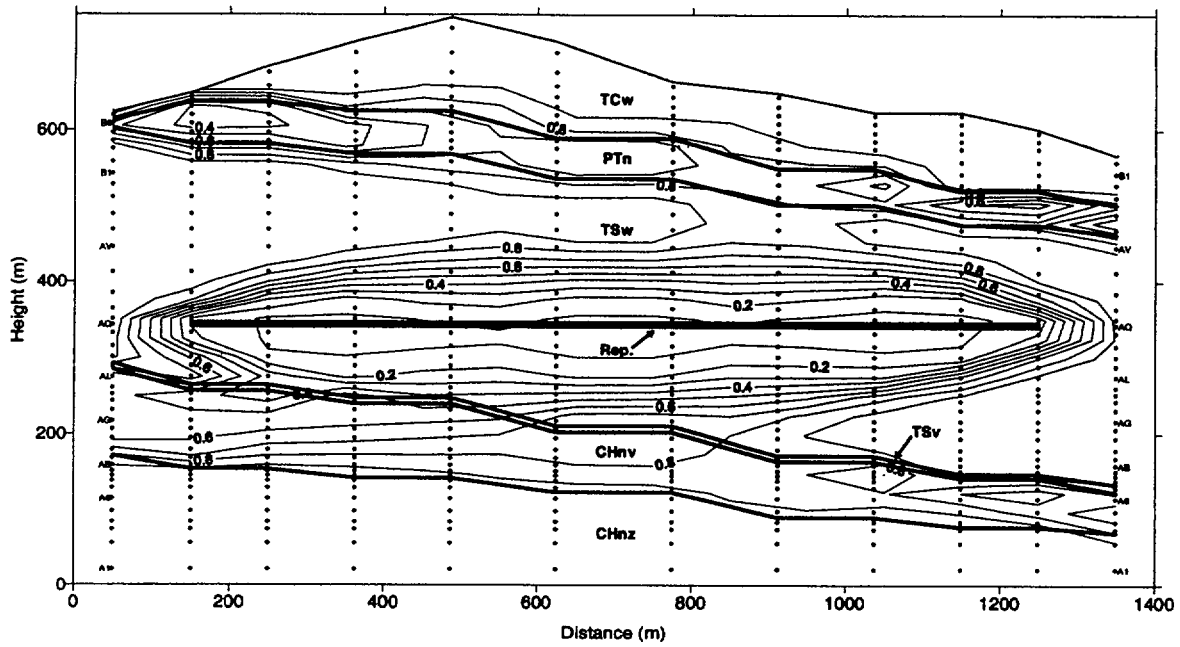
Figure 4.3-1 Temperature Contours at 1,000 Years for an Infiltration Rate of 0.1
mm/year and Enhanced Vapor Diffusivity
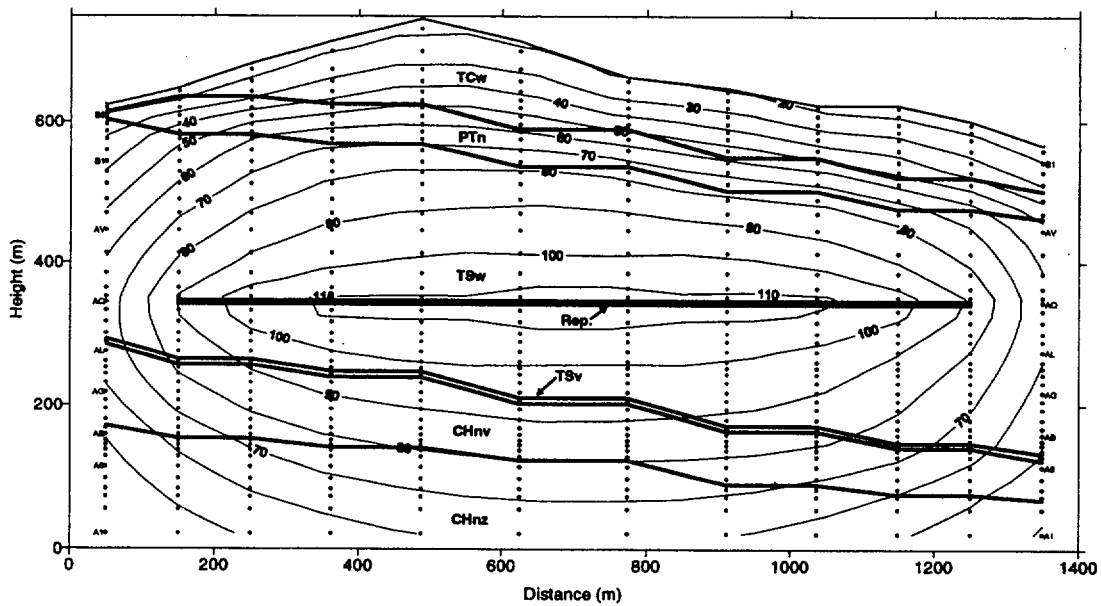
Figure 4.3-2 Liquid Saturation contours at 1,000 years for an Infiltration Rate of 0.1
mm/year and Enhanced Vapor Diffusivity
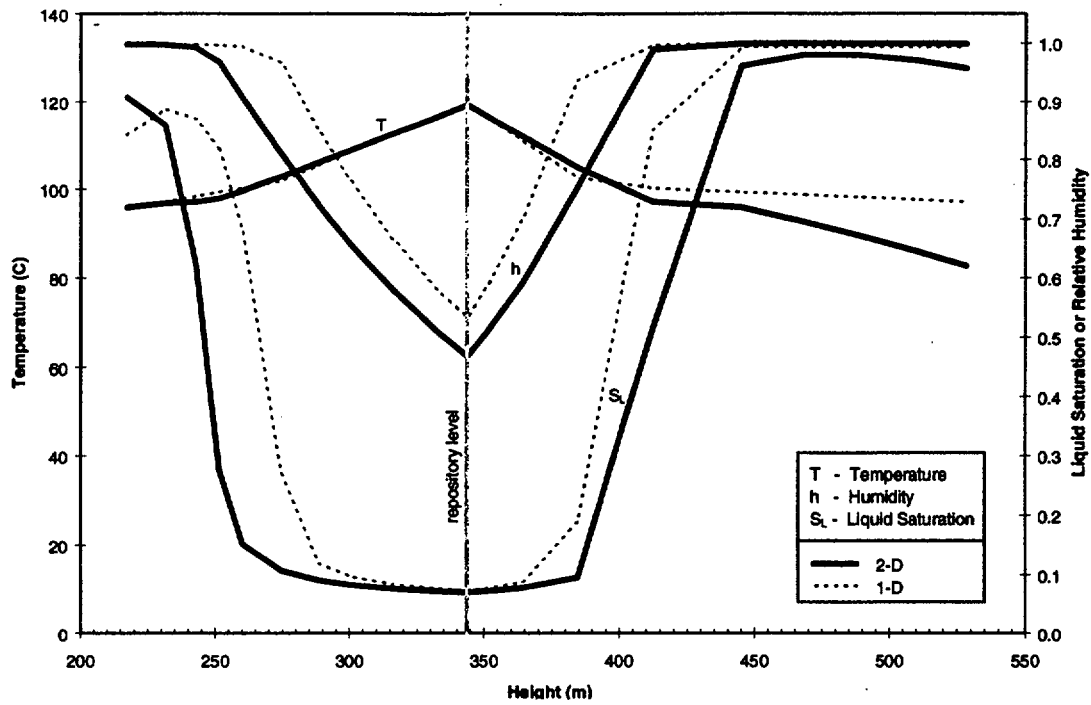
Figure 4.3-3   One- and Two-Dimensional Results at 1,000 years for Column 6 with a One-Dimensional Heat Loading of 92 MTU/acre, an Infiltration Rate of 0.1 mm/year, and Enhanced Vapor Diffusivity
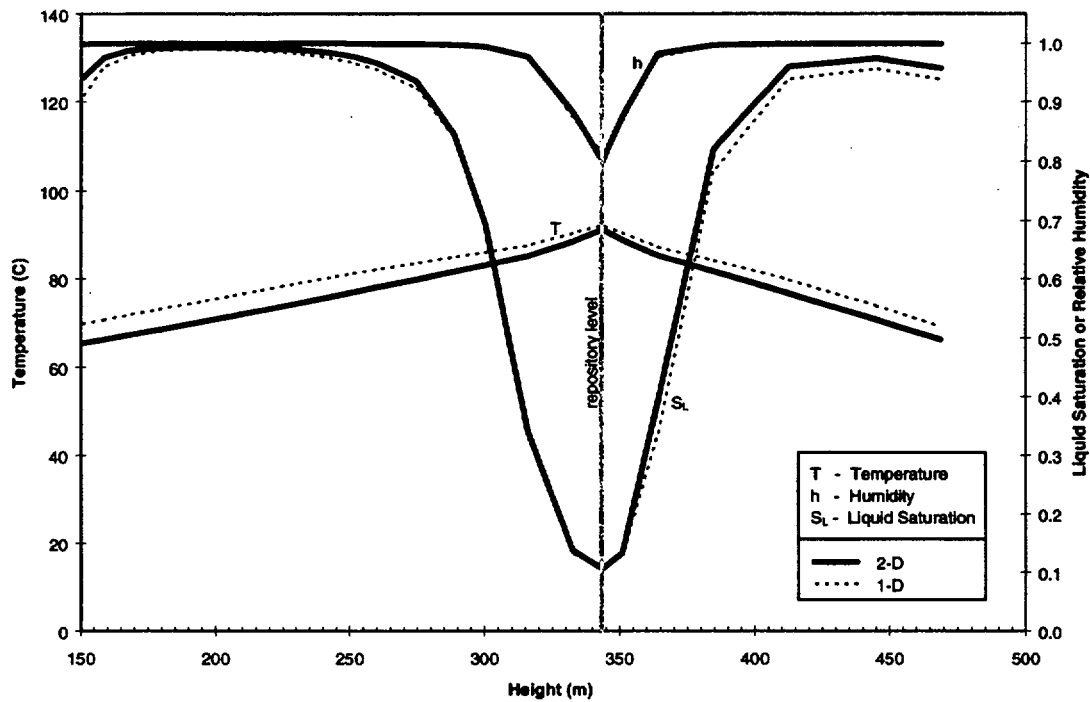
Figure 4.3-4   One- and Two-Dimensional Results at 1,000 Years for Column 11 with a One-Dimensional Heat Loading of 58 MTU/acre an Infiltration Rate of 0.1 mm/year and Enhanced Vapor Diffusity

4-39

5. WASTE PACKAGE DEGRADATION ABSTRACTION

Joon H. Lee and Joel E. Atkins

5.1   INTRODUCTION

The current design concept for a multi-barrier waste container provides the primary component of the engineered barrier system (EBS) for containment and isolation of spent fuel and vitrified defense high-level waste (DHLW) in the potential repository at Yucca Mountain. Fulfillment of the requirements for substantially complete containment and subsequent controlled release of radionuclides into the geosphere will rely upon a robust waste container design, among other EBS components. Failure of the waste container will most likely occur in the form of 'holes' created by localized corrosion of the container materials. An additional 'small' fraction of waste containers may fail prematurely due to material and/or manufacturing defects or damage during handling. Even if perforated with holes and cracks, the waste container should still be able to provide a substantial barrier to release (Pigford, 1993). Additional means to suppress and retard radionuclide release into the geosphere may be provided by introducing other engineered components in the immediate vicinity of the waste container. Such measures include placement of backfill around the waste container and/or absorbent materials underneath the waste container (DOE, 1995a).

Prior to any release of radionuclides from the waste packages, the waste package must be breached. Under the near-field environmental conditions expected in the unsaturated media at Yucca Mountain, the primary modes of waste package degradation are humid air and aqueous corrosion. As illustrated in Figure 5.1-1, this chapter presents the container material properties, their corrosion degradation models and the data on which they are based, and the model results which provide the waste package degradation histories to be abstracted into TSPA-1995.

Section 5.2 discusses the corrosion modes relevant to the candidate waste container barrier materials in the expected near-field environment. The technical basis for the humid-air corrosion models of the candidate corrosion-allowance material (CAM) is discussed in Section 5.3, and that for its aqueous corrosion models is discussed in Section 5.4. Section 5.5 describes the pitting corrosion model for the candidate corrosion-resistant material (CRM). Although for the nominal case, the potential positive attributes of cladding are not included in this TSPA iteration, Section 5.6 presents a conceptual basis for the incorporation of cladding performance in future TSPA analyses. Section 5.7 presents the predicted waste package degradation history resulting from the combination of the thermo-hydrologic modeling results presented in Chapter 4 and the corrosion degradation models presented in Sections 5.3 to 5.5.

The corrosion models presented in this chapter result from synthesis and analysis of literature data to capture and represent the major parameters in the corrosion degradation processes. The site-relevant corrosion testing and model development programs currently underway in this program should enable incorporation of detailed electrochemical and other physicochemical processes associated with waste container corrosion (Henshall, et al., 1993; McCright, 1994) for use in future TSPA analyses.

5.2   CORROSION MODES

This section discusses the corrosion modes expected for the candidate containment barrier materials (described in Section 3.5) in the near-field environment of the potential repository. The candidate barrier materials fall into two major categories: corrosion-resistant material (CRM) (Alloy 825) and corrosion-allowance material (CAM) (carbon steel). A third category of moderately corrosion resistant material (MCRM) (Monel 400 and 70Cu/30Ni alloy) has performance features between the two categories. Many factors influence the potential corrosion modes on the candidate materials. These include: 1) metallurgical factors (alloy composition and alloy microstructure); 2) physical factors (temperature); 3) chemical factors (pH and concentration of aggressive species such as chloride, sulfate, nitrate and carbonate); and 4) mechanical factors (stress) (McCright, 1994).

In general, the corrosion modes can be classified into five groups: 1) general corrosion; 2) localized corrosion (pitting and crevice corrosion); 3) environmentally induced cracking (stress corrosion cracking); 4) metallurgically influenced corrosion (intergranular corrosion); and 5) mechanically assisted degradation (erosion and corrosion fatigue) (Craig and Pohlman, 1987). A recent report discussed potentially important degradation modes for the candidate barrier materials in the potential repository near-field environment at Yucca Mountain (Van Konynenburg, et al., 1995). The potentially important degradation modes identified in the report include: 1) general corrosion; 2) pitting corrosion; 3) crevice corrosion; 4) stress corrosion cracking; 5) galvanic effects (galvanic corrosion and cathodic protection); 6) microbiologically influenced corrosion (MIC); 7) radiation induced corrosion; 8) corrosion in welded materials; and 9) low temperature oxidation. Each of these specific degradation modes is discussed below.

General corrosion normally results in a 'relatively' uniform thinning of materials without significant localized attack. The corrosion-allowance material would be affected mostly by this corrosion mode. Localized corrosion (pitting and crevice corrosion) is induced by local variations in electrochemical potential on a micro-scale over small regions. The variations in electrochemical potential may result from the local perturbations in the structure and composition of usually protective, passive films on metal surfaces and also in the electrolyte composition of the solution that contacts the metal (McCright, 1994; Henshall, et al., 1993).

Microbiologically influenced corrosion (MIC) results from the metabolic activity of micro-organisms. MIC may operate throughout the life of the repository, especially after the near-field temperature of the potential repository cools down. Microbial metabolism produces corrosive chemicals. For example, sulfate-reducing bacteria reduce sulfate (SO_4^{2-}) to sulfide (S^{2-}) which forms HS^-, a highly corrosive species (Van Konynenburg, et al., 1995). Because of the localized nature of MIC and associated electrochemical perturbations, the overall effects can be modeled probabilistically. Additionally, the biochemical variations surrounding microbial activity is expected to introduce a further probabilistic consideration (McCright, 1994). Although 300-series stainless steels are known to be susceptible to MIC, the nickel-based alloys such as Alloy 825 seem to be immune to MIC (Farmer, et al., 1988).

Stress corrosion cracking is a crack propagation process that results from the combined and synergistic interaction of mechanical stress and corrosion reactions. The distribution of mechanical strain is subject to local (micro-scale) perturbations in metals because of structural

5-2

inhomogeneities from one location to another on a similar scale to the electrochemical potential variations. Stress corrosion cracking can be represented probabilistically with a non-uniform electrochemical potential distribution and a non-uniform strain distribution (McCright, 1994). In many alloy systems, localized corrosion and stress corrosion cracking are interrelated because the sites of localized corrosion attack become the sources of initiation of stress corrosion (Farmer and McCright, 1989; Farmer, et al., 1988).

Radiation induced corrosion is another potentially important degradation process of waste packages in the repository. In the presence of a liquid phase irradiated under gamma radiation, the fixed nitrogen may exist in the liquid phase as nitrite and nitrate ions that are corrosive to metals. The total amount of nitrite and nitrate that can be formed in a liquid phase is limited by the gamma radiation dose rate and the volume of air irradiated. If a thin film of water on the waste package container is irradiated in the contact with a relatively thicker air space, it is possible to achieve a significant concentration of nitrate in the relatively small amount of water in the film (Van Konynenburg, et al., 1995).

Alloy microstructure, which can be thought of as the alloy composition at a very local level, may be an important parameter in many degradation modes. Since the alloy microstructure is most likely to vary in and around welds, differences in the behaviors are most likely to be with the welded materials (Strum, et al., 1988). The impact of oxidation of the candidate barrier materials in the potential repository condition is considered insignificant (Gdowski and Bullen, 1988).

Among the degradation modes discussed above, pitting corrosion is considered the primary degradation mode to impact waste container performance. In the simulation of the waste container degradation presented in this chapter, only general corrosion and pitting corrosion are considered.

5.3 HUMID-AIR CORROSION MODELS FOR CORROSION-ALLOWANCE MATERIALS

5.3.1 Introduction

Carbon steel, the candidate corrosion-allowance barrier material, undergoes active corrosion both in humid-air and aqueous environments (refer to Section 3.5 for the waste container barrier materials). In the potential repository, it is expected that the waste container will be exposed to humid-air and aqueous conditions at elevated temperatures for extended periods of time. In this report, the term "humid-air corrosion" is used to refer to corrosion which takes place under a 'thin' film of water that forms on the container surface above a certain critical humidity threshold. Such a water film is not thick enough to behave as bulk water. The term "aqueous corrosion" is used to refer to corrosion of metal in contact with bulk water.

This section outlines the development and abstraction of general and pitting corrosion models of the candidate corrosion-allowance barrier materials in humid-air, and presents results of these newly developed models. This section includes a comparison of the new model results with those from the existing McCoy model (McCoy, 1994).

5.3.2 Corrosion Data Compilation

A considerable amount of data for atmospheric general and pitting corrosion of commercial iron and steel has been accumulated by numerous testing programs over the past few decades in the U.S. and other countries. An average general corrosion depth at a given exposure time is determined from a weight loss measurement (after removing the corrosion products) of a specimen under testing. The pit depths are determined directly by measuring the depth of each pit with a device equipped with a microscope and a fine, measuring needle. A literature survey was conducted to collect data for atmospheric general and pitting corrosion for a suite of cast iron and carbon steel which are known to have corrosion behaviors similar to the candidate carbon steel. The atmospheric corrosion data include the effects of pollutants such as SO_2 and other chemicals in the atmosphere that interact with test specimens. The data also embed any effects of salts that may form on the surface of the corroding specimen due to cyclic wetting and drying. Data from marine sites were excluded because marine environments are much more corrosive (due mostly to the presence of chloride salts in a marine atmosphere) than the potential repository near-field environment considered in TSPA-1995. Future TSPA analyses may incorporate the effects of such corrosive environments for different conceptual models of near-field water chemistry, such as those that may result from salt precipitation in a moisture refluxing condition at elevated temperatures.

Important testing parameters that were considered in the data compilation included test duration, average exposure temperature and relative humidity, and average sulfur dioxide content in the test atmosphere. From the general corrosion data collected, a total of 166 data points that have the testing (exposure) parameters documented were included in the model abstraction. The test environments included rural, urban, and industrial sites. The following is the list of the data sources used in the model development.

1. Haynie, F.H., and J.B. Upham (1971)
2. Knotkova, D., P. Holler, and J. Vickova (1981)
3. Knotkova-Cermakova, D., J. Vickova, and J. Honzak (1982)
4. Komp, M.E. (1987)
5. Pereira D., O. Nobre, and E. Almeida (1993)
6. Southwell, C.R., and J.D. Bultman (1982)
7. Southwell, C.R., J.D. Bultman, and A.L. Alexander (1976)
8. Townsend, H.E., and J.C. Zoccola (1982)
9. Tri, N.Q., V.D. Huy, L.V. Cuong, P.Th. San (1993)
10. Wei, F.-I. (1991)

The longest-term data were from the 16-year corrosion test program conducted by the Naval Research Laboratory in a tropical environment in Panama (Southwell and Bultman, 1982; Southwell, et al., 1976). The exposure conditions for the entire set of data range from 5 to 27 °C average temperature, 63 to 85 % average relative humidity (RH), and an average SO_2 level of 2 to 406 µg SO_2/m^3.

5.3.3 Exposure Parameter Transformation

After the initial waste emplacement and subsequent heating to a peak temperature, the near-field environment of the potential repository is expected to be relatively steady-state (or quasi-steady state) during the gradual cooling periods in terms of temperature and relative humidity. However, the exposure conditions of the atmospheric corrosion data fluctuated over periods as short as a day. Therefore, in order to develop a model that is applicable to the potential repository environment, it was necessary to transform the collected corrosion data to testing periods, for which corrosion was active and also the exposure conditions were relatively steady.

In the data transformation, three generalized relationships were needed to transform the exposure conditions and corrosion data: (1) a relationship to estimate the fraction of the exposure time during which corrosion was active; (2) a relationship to estimate the average relative humidity during that fraction of the time; and (3) a relationship to estimate the average temperature during that fraction of the time. In an effort to develop the generalized relationships, hourly weather data for a 10-year period from 9 geographical areas were received from the Western Climatic Center in Reno, Nevada (Prowell, 1994). The areas were selected to cover a wide range of weather conditions from hot and dry (Las Vegas, NV, Albuquerque, NM, and Tucson, AZ) to warm and humid (Honolulu, HI, and Arcata, CA) to cold and humid (Great Falls, MT, Denver, CO, Cheyenne, WY, and Anchorage, AK).

Time Fraction for Relative Humidity Greater than 70 %

Numerous experimental results of iron specimens exposed to controlled humidity conditions have shown that at around 70 % RH their surfaces become covered with a 'thin' water film and 'active' corrosion initiates (Vernon, 1933; Phipps and Rice, 1979). Accordingly, 70 % RH was chosen as the threshold level at which 'active' humid-air corrosion initiates. Using the weather data, a relationship for estimating the fraction of time during which relative humidity is greater than or equal to 70 % was developed as a function of the average relative humidity and average temperature. For each year's hourly weather data, the time fraction with RH $\geq$ 70 % was calculated, and fitted as a function of the annual average relative humidity and temperature. The resulting functional form is expressed as:

$$f_{70} = \cfrac{1}{1 + \exp\left[1.0362 + \cfrac{27.8249(55.3159 - RH_{avg})}{T_{avg}}\right]} \qquad (5.3\text{-}1)$$

where f_{70} is the fraction of time during which RH $\geq$ 70 %, RH_{avg} is the annual average relative humidity (%), and T_{avg} is the annual average temperature (°C). RH_{avg} and T_{avg} are provided with the corrosion data. Estimates made with Equation (5.3-1) are compared with the weather data in Figure 5.3-1.

Reduction of Relative Humidity and Temperature

As discussed in Section 5.3.4, a 'new' exposure time of each corrosion data point was estimated by multiplying the actual exposure time with the time fraction during which RH ≥ 70 %, calculated with Equation (5.3-2), and it corresponds to the time fraction during which corrosion was active. The new exposure time is shorter than the actual exposure time because a portion of the actual exposure time during which the exposure condition was 'dry' or RH < 70 % is excluded. Accordingly, it was necessary to estimate a 'new' average relative humidity and 'new' average temperature of each corrosion data for that period of time during which RH ≥ 70 %. The weather data were utilized to develop relationships for estimating the 'new' average relative humidity and 'new' average temperature as follows: for each year's hourly weather data, the average relative humidity and average temperature were calculated for the periods with RH ≥ 70 %, and fitted as a function of the annual average relative humidity and average temperature. The relationship developed for the new average relative humidity is:

$$RH_{new} = 83.16 - 0.1383\,RH_{avg} - 0.1057\,T_{avg} + 0.002337\,RH_{avg}^2 \qquad (5.3\text{-}2)$$

where RH_{new} is the new average relative humidity (%). The new average temperature was estimated with the following equation:

$$T_{new} = -13.34 + 0.1514\,RH_{avg} + 1.017\,T_{avg} \qquad (5.3\text{-}3)$$

where T_{new} is the new average temperature (K). The new average relative humidity and temperature are assumed to be the representative exposure conditions for the transformed corrosion data discussed in the following section.

5.3.4 Development of General Corrosion Model

Corrosion Data Transformation

The corrosion data collected were transformed using Equations (5.3-1) to (5.3-3) as such: (1) the fraction of the exposure time, for each observation, during which RH ≥ 70 % (i.e. duration of active corrosion), was calculated with Equation (5.3-1), then a new exposure time was estimated by multiplying this time fraction and the actual exposure time; (2) a new average relative humidity for that time period (RH ≥ 70 %) was estimated with Equation (5.3-2); and (3) a new average temperature for that time period (RH ≥ 70 %) was estimated with Equation (5.3-3).

Conceptual Models

The following corrosion dependencies on exposure conditions in humid-air were incorporated into the model development.

$$D_g \propto A_1\,t^{A_2} \qquad (5.3\text{-}4)$$

$$\frac{dD_g}{dt} \propto B_1 e^{\frac{B_2}{RH}} \qquad\qquad (5.3\text{-}5)$$

$$\frac{dD_g}{dt} \propto C_1 e^{\frac{C_2}{T}} \qquad\qquad (5.3\text{-}6)$$

$$\frac{dD_g}{dt} \propto D_1 e^{D_2[SO_2]} \qquad\qquad (5.3\text{-}7)$$

D_g is general corrosion depth (μm), dD_g/dt is general corrosion rate (μm/yr), t is exposure time (years), RH is relative humidity (%), T is temperature (K), and $[SO_2]$ is sulfur dioxide content in the testing atmosphere (μg/m^3). A's, B's, C's, and D's are constants.

General Corrosion Model

Combining the conceptual relationships (Equations (5.3-4) to (5.3-7)), the corrosion model can be expressed as follows:

$$\ln D_g = a_0 + a_1 \ln t + \frac{a_2}{RH} + \frac{a_3}{T} + a_4 [SO_2] + \varepsilon , \qquad\qquad (5.3\text{-}8)$$

where a_0, a_1, a_2, a_3 and a_4 are constants to be determined from fitting Equation (5.3-8) to the transformed corrosion data, and ε is a term representing uncertainty not explained by the model. The variance of the model estimate was calculated as follows:

$$Var(\ln D_g) = \begin{bmatrix} 1 & \ln t & \dfrac{1}{RH} & \dfrac{1}{T} & [SO_2] \end{bmatrix} V \begin{bmatrix} 1 \\ \ln t \\ \dfrac{1}{RH} \\ \dfrac{1}{T} \\ [SO_2] \end{bmatrix} + \frac{RSS}{DF} , \qquad\qquad (5.3\text{-}9)$$

where $Var(\ln D_g)$ is the variance of the model estimate, V is the covariance matrix (5 x 5), RSS is the residual sum of squares of the model fit, and DF is the degrees of freedom in the model fitting.

Linear regression was used to fit the model in Equation (5.3-8), giving the following parameter values: $a_0 = 16.9865 \pm 2.8736$, $a_1 = 0.6113 \pm 0.0295$, $a_2 = -893.76 \pm 231.04$, $a_3 = -833.53 \pm 381.97$, and $a_4 = 0.002637 \pm 0.000377$.

The corrosion data used and the model estimate with its uncertainties (± 2 standard deviations) are shown in Figure 5.3-2. The input parameters (15 °C, 84 % R.H., and 90 μg SO_2/m^3) for the estimate in the figure are the averages of the data set. The atmospheric pollution level of 70 μg SO_2/m^3 was chosen arbitrarily to differentiate corrosion behaviors in heavily polluted areas from that in relatively clean atmospheric environments.

5.3.5 Results of the General Corrosion Model

Model predictions of the general corrosion rate as a function of exposure time at different humidities (80, 90 and 95 % RH) are shown in Figures 5.3-3a and 5.3-3b for exposure temperatures of 60 °C and 90 °C, respectively. The figures show that the general corrosion rate decreases rapidly with the exposure time. The rate reduction is due primarily to corrosion products formed on the bare metal, which act as a barrier to the transport of reacting species.

The model predictions for the effects of relative humidity on the general corrosion rate for different exposure times are shown in Figures 5.3-4a and 5.3-4b for exposure temperature of 30 °C and 90 °C, respectively. As discussed in Section 5.3.3, the figures show that the general corrosion rate of CAM is negligible at RH values less than about 60 %. The general corrosion rate starts to increase with humidity at about 65 % RH, and the rate of increase becomes greater with increasing relative humidity. However, the relative humidity effects on the general corrosion rate decrease with exposure time. The model predictions are consistent with the literature data discussed in Section 5.3.3.

Similar model predictions at different exposure temperatures showing the effects of relative humidity on the general corrosion rate are shown in Figure 5.3-5 for an exposure time of 1 year. It is shown in the figure that relative humidity has a greater effect on general corrosion than temperature. The model predictions for the effects of SO_2 levels in humid-air on the general corrosion of CAM are shown in Figure 5.3-6 for an exposure time of 1 year. The general corrosion rate at 200 μg SO_2/m^3, 90 % RH and 90 °C is about twice that of the general corrosion rate predicted at 90 % RH, 90 °C and no SO_2 pollution (shown in Figure 5.3-5). These corrosion behaviors predicted with the current model are consistent with numerous literature data (see Duncan and Spedding, 1973; Guttman, 1968; Guttman and Sereda, 1968; Haynie and Upham, 1974; Kucera and Mattson, 1974).

In Figures 5.3-7a to 5.3-7c, the predicted general corrosion of CAM as a function of exposure time in humid-air at different exposure conditions (i.e., humidity and temperature) is compared with that predicted by the aqueous general corrosion model (noted as "water" on the figures) which was developed for TSPA-1995 (discussed in Section 5.4). As shown in the figures, when humidity is in the range of 85 to 100 % RH, the humid-air general corrosion rates are close to the aqueous corrosion rates at the corresponding temperatures. These model predictions are consistent with an observation that the surface of a steel panel tested in a controlled humidity chamber was covered with moisture at about 85 % RH (visually detected) (Haynie, et al., 1978).

5.3.6 Development of Pitting Corrosion Model

In pitting corrosion models, pit initiation and pit growth rate are two major parameters that need to be quantified. However, these parameters are influenced by many factors including materials characteristics, exposure conditions, and aggressive species present. Additionally, complex electrochemical processes associated with the factors also strongly influence pit initiation and pit growth processes. In general, pitting of metal results from complicated interactions among many factors and appears to be random. As a result, stochastic approaches have been applied to represent and quantify pitting processes. .

Pitting of CAM is commonly represented with a pitting factor that is defined as the ratio of the maximum pit depth to the general corrosion depth at a given exposure time. Accordingly, the pitting factor has been utilized in developing a stochastic pitting corrosion model for the corrosion-allowance barrier in a humid-air condition. The range and distribution of the pitting factor were obtained from the literature.

The results from the extensive corrosion testing programs in inland tropical environments in Panama indicate that the pitting factor for carbon steels and cast irons exposed to 'normal' atmospheric conditions (i.e. in the absence of highly aggressive conditions such as in acidic or concentrated salt conditions) ranged from 2 to 6 (Southwell and Bultman, 1982; Southwell et al, 1976). The distribution may be considered as a normal distribution that is skewed to the right (or with a long tail to the right) (Marsh and Taylor, 1988; Marsh et al, 1988; Strutt et al, 1985). In the current stochastic pitting modeling, the pitting factor was assumed to be normally distributed with a mean at 4 and a standard deviation of 1. In addition, the pitting factor was constrained to be greater than or equal to 1, i.e. with the pitting factor equal to 1, the pit depth is equal to the general corrosion depth. The pitting factor was sampled randomly and used as a multiplier to the general corrosion depth. Thus, the pitting corrosion model of CAM in humid-air is expressed as follows:

$$D_p = f_p \cdot D_g = \begin{cases} normal(4,1) \cdot D_g & \text{if } normal(4,1) \geq 1 \\ D_g & \text{if } normal(4,1) < 1 \end{cases} \qquad (5.3\text{-}10)$$

D_p is pit depth (μm) in humid-air, D_g is general corrosion depth (μm) in humid-air, and f_p is the pitting factor.

In the stochastic pitting modeling, pit initiation was not explicitly considered. Instead, all the pits that can form on the waste container were assumed to start growing at the same time. The total number of pits that can form on the waste container was calculated from the pit density (about 10 pits/cm^2) obtained from literature (Marsh and Taylor, 1988; Marsh et al, 1988; Strutt et al, 1985) and the nominal surface area of the container discussed in Section 3.5.

5.3.7 Results of the Pitting Corrosion Model

The pitting corrosion model results for CAM in humid-air presented in this section are calculated using the expected values of the parameters in the humid-air general corrosion model in Equation (5.3-8). The predicted probability density functions (PDFs) of pit depth distribution for CAM at 60 °C and 80 and 90 % RH are shown in Figures 5.3-8a and 5.3-8b, respectively, for up to 3,000-year exposure times. Considering a CAM that is continuously exposed to the corresponding constant humid-air conditions, the deepest pit penetrates the CAM thickness within 3,000 years at 90 % RH and 60 °C, whereas it is only about 30-mm deep at 80 % RH and at the same temperature. Similar modeling results at 90 °C are given in Figure 5.3-9a for 80 % RH and Figure 5.3-8b for 90 % RH. For CAM exposed continuously to a humid-air at 90 % RH and 90 °C (Figure 5.3-9b), the deepest pit reaches about 70-mm after 1,000-year exposure and would penetrate up to about 130-mm deep after 3,000-year exposure. The corresponding cumulative probability density functions (CDFs) are shown in Figure 5.3-10a for the 1,000-year exposure case and in Figure 5.3-10b for the 3,000-year exposure case. As in general corrosion of CAM in humid-air discussed in Section 5.3.5, relative humidity has a greater effect in pitting corrosion of CAM than temperature.

5.3.8 Comparison with the McCoy Model

Recently, a model for general corrosion of CAM in humid-air environment has been suggested by McCoy (1994). The McCoy model was developed by combining the general corrosion model of CAM in brine and salt water developed by Westinghouse (1982; later recommended by Stahl (1993) for M&O TSPA-1993 (Andrews, et al., 1994)) with short-term corrosion current density data of pure iron foils exposed to controlled humid-air conditions (52, 64, 76 and 86 % RH) at 25 °C (Jones and Howryla, 1993). In the McCoy model the parameter value for the humid-air corrosion term was determined from only four data points of corrosion current density data, and the experimental technique employed to measure the data was semi-quantitative in nature. Inaccuracy of the electrochemical measurement technique used by Jones and Howryla (1993) was reported previously, and was attributed to the accumulation of corrosion products between electrodes, short-circuiting the corrosion current measurements (Kucera and Mattsson, 1974). Additionally, the data developed by Jones and Howryla (1993) do not account for potential uncertainties and variabilities of the humid-air corrosion rates anticipated in the potential repository environment.

Significant uncertainties also arise when extrapolating the McCoy model to a steam environment (humid-air at elevated temperatures), because the McCoy model uses the same value for the temperature-dependency parameter as the Westinghouse model, which was estimated from four data points collected from corrosion tests in brine and sea water. The temperature dependency of general corrosion in steam would be different from that in brine and sea water. Since the McCoy model is the only one currently available for CAM corrosion in humid air, it is desirable to compare the McCoy model to the current model.

Review of the McCoy Model

As discussed previously, the McCoy model is based on an aqueous general corrosion model for low carbon steels and cast irons, developed by Westinghouse (1982), and short-term corrosion

current density data of pure iron foils exposed to controlled humidity environments of 'static' and 'dynamic' air conditions at 25 °C (Jones and Howryla, 1993). The Westinghouse model is expressed as

$$D_g = 2525 \, t^{0.47} \, e^{\frac{-2850}{T}} \qquad (5.3\text{-}11)$$

where D_g is general corrosion depth (mm), t is exposure time (year), and T is exposure temperature (K). The temperature dependency term of the model (exp(-2850/T)) was evaluated from four corrosion data points in brine and sea water at temperatures up to 523 K (250 °C) (this was essentially two points as they were two data points at 298 K and another two data points at 523 K. The time dependency term was derived from the 16-year corrosion data in tropical lake water in Panama, developed by the Naval Research Laboratory (Southwell and Alexander, 1970; Southwell et al, 1976). This Westinghouse model was later suggested for the M&O TSPA-1993 (Stahl, 1993).

In the development of the McCoy model, Equation (5.3-11), expressed as $D_g = A \, t^c \exp(-B/T)$, was differentiated with respect to time to obtain the corrosion rate equation, and the explicit time dependence term was removed from the rate equation. The resulting equation is

$$\frac{dD_g}{dt} = cA^{\frac{1}{c}} D_g^{\frac{c-1}{c}} e^{\frac{-B}{cT}} + \frac{D_g B}{T^2} \frac{dT}{dt} \qquad (5.3\text{-}12)$$

The temperature-derivative term may be assumed to be negligible within a time step in which temperature is in a relatively steady-state or "quasi" steady-state. Dropping the temperature derivative term, Equation (5.3-12) becomes the corrosion rate expression of the McCoy model as follows

$$\frac{dD_g}{dt} = cA^{\frac{1}{c}} D_g^{\frac{c-1}{c}} e^{\frac{-B}{cT}} \qquad (5.3\text{-}13)$$

A humidity dependency term was added into Equation (5.3-13), giving:

$$\frac{dD_g}{dt} = cA^{\frac{1}{c}} D_g^{\frac{c-1}{c}} e^{(\frac{kh}{c} - \frac{B}{cT})} \qquad (5.3\text{-}14)$$

where h is defined as (RH - 100) where RH is relative humidity (%). The corrosion current density data of iron foils from Jones and Howryla (1993) were used to determine the constant k in Equation (5.3-14).

The corrosion current density data given in Table 5.3-1 were read directly from the graphs given by Jones and Howryla (1993). The data show that at the humidity conditions greater than 52 % RH, the corrosion current density in dynamic air-flow conditions is about two orders of magnitude larger than those in static air condition. From the data, McCoy obtained $k = 0.1908$ for the static air condition, and $k = 0.2$ for the dynamic air condition (McCoy, 1994). However, because smaller k values give higher corrosion rates, it is assumed in the following discussions that $k = 0.1908$ for the dynamic air condition, and $k = 0.20$ for the static air condition.

Being consistent with the Westinghouse aqueous corrosion model upon which it is based, the McCoy model can be rewritten as follows:

$$D_g = 2525000 \ t^{0.47} \ e^{(0.1908h - \frac{2850}{T})} \qquad (5.3\text{-}15)$$

where D_g has units of μm. A smaller value for constant k is used in the following discussions.

Evaluation of the McCoy Model

Using the electrochemical couple for dissolution reaction of iron (Equation (5.3-16)) which is applicable for general corrosion, and applying Faraday's law (Equation (5.3-17), the corrosion current density data in Table 5.3-1 can be converted to general corrosion rates.

$$Fe(m) \rightleftharpoons Fe^{2+}(aq) + 2e^- \qquad (5.3\text{-}16)$$

$$I_c = \frac{z_{Fe} F \rho_{Fe} R}{M_{Fe}} \qquad (5.3\text{-}17)$$

where I_c = corrosion current density (amp/cm^2 or coulombs/cm^2·sec),
z_{Fe} = number of electrons involved in the dissolution reaction (z_{Fe} = 2),
ρ_{Fe} = density of iron (7.86 g/cm^3),
M_{Fe} = molecular weight of iron (55.85 g/mol),
F = Faraday constant (96,485 coulombs/mole), and
R = general corrosion rate (cm/sec).

The calculated general corrosion rates at the corresponding humidities at 25 °C are shown in Table 5.3-1. Their range at humidities between 64 and 86 % RH is from 3 to 7 μm/yr. The data in the table indicate that the corrosion rate becomes negligible at humidities below about 60 % RH. In addition, the data agree qualitatively with the current model predictions (see Figures 5.3-4 to 5.3-6).

There is approximately two orders of magnitude difference in the corrosion rate between static and dynamic air conditions (Table 5.3-1). This difference was examined by varying the constant,

k, in the McCoy model within the range from k = 0.18 to k = 0.22. As shown in Figure 5.3-11, the McCoy model does not predict the corrosion rate changes indicated in Table 5.3-1.

The general corrosion depths calculated using the McCoy model are compared in Figure 5.3-12 with the atmospheric corrosion data used for the current model and also with the current model estimate (Equation (5.3-8)). The general corrosion depths calculated with the McCoy model and the current model are for the average exposure conditions (humidity and temperature) of the atmospheric corrosion data. As shown in the figure, the McCoy model underestimates general corrosion depth of CAM in humid air by a factor of about 10. Samples in atmospheric corrosion testing are likely to be exposed to cyclic wetting and drying conditions, which may cause a higher corrosion rate compared to testing in a constant condition. As such, the atmospheric corrosion data used in the current model development provide higher corrosion rates, which may be better representative of the humid-air corrosion environment expected in the potential repository (i.e., waste packages may be exposed to localized dripping fractures and consequent wetting and drying cycles).

Long-term general corrosion depths of CAM in humid-air calculated by the current model (Equation (5.3-8)) are compared with those by the McCoy model in Figure 5.3-13. As shown in the figure, the effect of the exposure temperature on the general corrosion depths predicted by the current model is less than those by the McCoy model. The differences between the two model predictions are smaller at higher humidities. When projected to 3,000-year exposure time at 70 % RH and 90 °C, the general corrosion depth predicted by the McCoy model is smaller than that by the current model by a factor of 7. This difference is reduced to a factor of 3 at 90 % RH and 90 °C.

5.4 AQUEOUS CORROSION MODELS FOR CORROSION-ALLOWANCE MATERIALS

5.4.1 Introduction

In addition to the effect on corrosion rate caused by the presence of corrosive species, the material characteristics, and other exposure conditions, corrosion rates of CAM in water are also strongly affected by temperature, exhibiting maximum corrosion rates at temperatures around 60 to 80 °C. Such corrosion behavior is commonly observed in corrosion processes governed by the reduction of dissolved oxygen. An increase in temperature enhances the diffusivity of oxygen molecules and reaction rates, but at the same time decreases the solubility of oxygen gas. The net mass transport of oxygen increases with temperature until a maximum is reached where the oxygen concentration begins to decrease approaching the boiling point. Thus, the corrosion rate attains a maximum and then decreases with further increase in temperature (Boden, 1994).

The Westinghouse aqueous general corrosion model (Equation 5.3-11) (Westinghouse, 1982) used in TSPA-1993 (Andrews et al, 1994) does not dictate properly the temperature-dependence. Thus, efforts to develop a more representative aqueous corrosion model for CAM take into account the temperature-dependent corrosion behavior.

5.4.2 Development of General Corrosion Model

Conceptual Models

The improved aqueous general corrosion model was developed using long-term corrosion data for a suite of carbon steel and cast iron, which were obtained from literature. The following aqueous general corrosion dependencies on exposure conditions were incorporated into the model development:

$$D_g \propto A_3 \, t^{A_4} \tag{5.4-1}$$

$$\frac{dD_g}{dt} \propto C_3 \, e^{(\frac{C_4}{T} + C_5 T^2)} \tag{5.4-2}$$

where D_g is general corrosion depth (μm), dD_g/dt is general corrosion rate (μm/yr), t is exposure time (years), T is temperature (K), and A's and C's are constants.

General Corrosion Model

By combining the above conceptual models (Equations (5.4-1) and (5.4-2)), the new aqueous general corrosion model is expressed as follows:

$$\ln D_g = b_0 + b_1 \ln t + \frac{b_2}{T} + b_3 T^2 + \varepsilon \;, \tag{5.4-3}$$

where b_0, b_1, b_2 and b_3 are constants to be determined from fitting Equation (5.4-3) to the aqueous general corrosion data, and ε is a term representing uncertainties not accounted for in the model. The variance of the model was calculated as follows:

$$Var(\ln D_g) = \begin{bmatrix} 1 & \ln t & \dfrac{1}{T} & T^2 \end{bmatrix} V \begin{bmatrix} 1 \\ \ln t \\ \dfrac{1}{T} \\ T^2 \end{bmatrix} + \frac{RSS}{DF} \;, \tag{5.4-4}$$

where $Var(\ln D_g)$ is the variance of the model estimate, V is the covariance matrix (4 x 4), RSS is the residual sum of squares of the model fitting, and DF is the degrees of freedom in the model fitting.

Parameter values for the corrosion rate constant (b_0) and the time-dependence term (b_1) were determined from long-term corrosion data (up to 16 years) in polluted river water (Larrabee, 1953; Coburn, 1978) and in tropical lake water (Southwell et al, 1970). The data include the potential effects of various chemical species dissolved and of microbial activity in the waters. Parameter values for the temperature dependence terms (b_2 and b_3) were determined from a set of short-term (100 days) corrosion data of mild steel in distilled water at temperatures from 5 to 90 °C (Brasher and Mercer, 1968; Mercer et al, 1968). The parameter values determined are: $b_0 = 111.506 \pm 10.804$, $b_1 = 0.532 \pm 0.0272$, $b_2 = -23303.2 \pm 2296.2$, and $b_3 = -3.193 \times 10^{-4} \pm 3.526 \times 10^{-5}$.

5.4.3 Results of the General Corrosion Modeling

Shown in Figure 5.4-1 are the long-term aqueous general corrosion data in lake water and (polluted) river water that were used for the model development, and the model estimate with its uncertainty envelope of two standard deviations. The temperature-dependent general corrosion data of mild steel in distilled water are shown in Figure 5.4-2 along with the model estimate with its uncertainty envelope of two standard deviations. The aqueous general corrosion rate of CAM is shown to have a maximum at temperatures between 60 and 70 °C.

Predictions of the aqueous general corrosion rate of CAM as a function of exposure time are shown in Figure 5.4-3 at three exposure temperatures (30, 60 and 90 °C). The calculations were made using the expected values of the model parameters of Equation (5.4-3). As shown in Figure 5.4-2, the general corrosion rates are about the same at 30 and 90 °C, and higher at 60 °C. Predictions of the temperature dependence of general corrosion rates at various exposure times shown in Figure 5.4-4 indicate the temperature dependence decreases with increasing exposure time. This is due to the increased thickness of the corrosion products forming on the bare metal over time.

The current model estimate is compared in Figure 5.4-5 with the general corrosion data of carbon steel and cast iron which were tested in a simulated (and possibly concentrated) J-13 water (McCright and Weiss, 1985). Even though the model was developed from a different set of data, the J-13 water corrosion depths are generally within two standard deviations of the model estimates. Compared to the greater temperature-dependence of mild steel corrosion in distilled water (Brasher and Mercer, 1968; Mercer, et al., 1968), the corrosion data in J-13 water given in the figure show a smaller temperature dependence.
In the corrosion of mild steel in distilled water, dissolved oxygen (O_2 (aq)) and, to a lesser extent, hydrogen ion (H^+ (aq)) in the water may have been the major species that participated in the corrosion reduction reactions (Mercer, et al., 1968). For the corrosion in the simulated (or possibly concentrated) J-13 water, other species (mostly carbonate ions and nitrate ions) in addition to dissolved oxygen and hydrogen ion may also have participated in the corrosion reduction reactions. This difference in the reduction reaction mechanisms would reduce the temperature dependence of the aqueous general corrosion (Beckmann and Mayne, 1960; Brasher and Mercer, 1968; Hersch, et al., 1961a and 1961b; Masamura and Matsushima, 1983; Mercer et al, 1968; Pryor and Cohen, 1953; Pyke and Cohen, 1948).

Aqueous general corrosion depths of CAM predicted with the current model for up to 3,000-year exposure time at three constant temperatures (30, 60 and 90 °C) are compared in Figure 5.4-6

with those from the Westinghouse model, Equation (5.3-11). The calculations were made using the expected values of the model parameters. As expected, the Westinghouse model predicts increased corrosion with increasing temperature, whereas the current model predicts the largest corrosion depth at 60 °C. From the simulation results shown in the figure, the mean general corrosion depth of CAM at 60 °C is about 30-mm after 3,000 years. This indicates that the 100-mm thick corrosion-allowance barrier should not fail by aqueous general corrosion at 3,000 years.

5.4.4 Development of Pitting Corrosion Model

As in humid-air pitting corrosion of CAM discussed in Section 5.3.6, aqueous pitting corrosion of CAM was modeled stochastically by assuming the pitting factor is normally distributed with a mean of 4 and a standard deviation of 1. The same approach discussed in Section 5.3.6 was taken in developing an aqueous pitting corrosion model of CAM, and the same equation (Equation (5.3-10)) is also employed to model aqueous pitting corrosion of CAM as follows

$$D_p = f_p \cdot D_g = \begin{cases} normal(4,1) \cdot D_g & if \quad normal(4,1) \geq 1 \\ D_g & if \quad normal(4,1) < 1 \end{cases} \qquad (5.4\text{-}5)$$

5.4.5 Results of Pitting Corrosion Modeling

Probability density functions (PDFs) of pit depths for CAM exposed to aqueous condition at three temperatures are shown in Figures 5.4-7a, 5.4-7b and 5.4-7c. The simulations were performed using the expected values of the parameters of the aqueous general corrosion model (Equation (5.4-3)). As for general corrosion, the simulation results show that aqueous pitting corrosion of CAM is most severe at temperatures around 60 °C. At the exposure temperatures of 30 and 90 °C, the deepest pit penetrates 100-mm thick CAM at about 3,000 years, whereas it takes only about 500 years at 60 °C. The modeling results indicate the 100-mm thick outer containment barrier may have the first pit penetration as early as 500 years if the near-field environment maintains aqueous conditions at about 60 °C.

5.5 CORROSION MODELING OF CORROSION RESISTANT MATERIALS

It has been shown that corrosion-resistant material (CRM) such as Alloy 825 (proposed as the inner barrier corrosion-resistant material) rarely corrodes under humid air conditions (Beavers and Durr, 1991). Thus, it was assumed CRM is not subjected to corrosion in humid-air conditions. Also, because general corrosion rates of CRM in 'normal' aqueous conditions are insignificant, only pitting corrosion was assumed to be active on CRM in aqueous conditions. Currently, no long-term pitting corrosion data for CRM are available, which may be utilized to develop a robust CRM pitting model. Although a limited number of short-term laboratory pitting data were reported previously (Beavers and Durr, 1991), only a few pits were observed on CRM in the short-term (about 90 days) tests, and those pits that formed were very shallow. Hence, the CRM

Since there has been no new development or improvement over the pitting corrosion model for Alloy 825 inner barrier which was developed from an expert elicitation and used in TSPA-1993 (Andrews, et al., 1994), the same pitting model (or expert elicitation) was utilized in TSPA-1995.

The elicitation (Table 5.5-1) provides a range of time-independent pit growth rates in aqueous conditions at 70 and 100 °C. In the elicitation, the pit growth rate ranges are presented as a median, a 95th percentile and a 5th percentile growth rates. For the pit growth rate ranges at other temperatures, these values were extrapolated as a function of temperature in an Arrhenius-type functional form. The resulting functional form for the median pit growth rate is given as follows:

$$\ln R_p = 50.373 - \frac{19655.85}{T} \qquad (5.5\text{-}1)$$

where R_p is the time-independent pit growth rate (mm/yr), and T is temperature (K). The median pit growth rates as a function of temperature are presented graphically in Figure 5.5-1 along with the 95th and 5th percentile growth ranges. As shown in the figure, the pit growth rate decreases exponentially with decreasing temperature, and the rate at room temperature is about 6 orders of magnitude less than the rate at 100 °C (373 K). The time-independent pit growth rates given in the elicitation are conservative because, in reality, the pit growth rate decreases with exposure time.

In TSPA-1995, pit growth rates for the Alloy 825 inner barrier were sampled randomly within the 95th and 5th percentile pit growth rate ranges given in the elicitation. For the 95th percentile value to be one order of magnitude larger than the mean value would require a very skewed distribution. Thus, the pit growth rate distribution in the mean growth rate column was used to generate the distribution of pitting rates. In the expert elicitation, the low and high growth rates were given as the 5th and 95th percentiles respectively. Thus, one order of magnitude, or 2.30 natural log units, is 1.645 standard deviations implying that a standard deviation is 1.40 natural log units. This was split equally between waste package to waste package variability and pit to pit variability. More details are discussed in Section 5.7.3.

Development of a defensible corrosion model for moderately corrosion resistant materials (MCRM) (Monel 400 and 70Cu/30Ni alloy) has been also hindered by the lack of long-term corrosion data. Since there are no adequate models available for the performance of these materials, it has been recommended that these materials not be included in any waste package performance analyses (Doering, 1995). Therefore, MCRM was not considered in TSPA-1995.

5.6   CLADDING DEGRADATION

5.6.1   Introduction

Previous iterations of total system performance assessment (Andrews, et al., 1994; M&O, 1993a; M&O, 1994a; Wilson, et al., 1994) did not take credit for spent fuel (SF) cladding as a potential barrier to radionuclide release after failure of the waste disposal container. In an additional

sensitivity study to TSPA-1993 (Andrews, et al., 1994), effects of cladding performance were simulated by progressively reducing SF wetted surface areas from 100 % to 0.01 % (M&O, 1994a). In addition, a preliminary analysis for cladding performance was recently reported (McCoy, 1995).

In an attempt to include more realism in studying the effects of cladding performance, initial efforts have been made to collect information and data for the dominant cladding failure modes expected during the containment period in the potential repository. In the following sections, brief descriptions are given for expected cladding degradation modes, conceptual models and approaches for cladding degradation modeling, and mechanistic models for the degradation modes. Additional data will be added as it becomes available. Utilizing the information and data available, continued efforts will be given to develop abstractions for cladding degradation that are suitable to be included into a TSPA code. In TSPA-1995, cladding performance was evaluated using approaches similar to those used in the additional sensitivity study to TSPA-1993 (M&O, 1994a).

5.6.2 Cladding Degradation Associated with Defective or Intact Fuel Rods

In view of the different types of cladding degradation modes, spent fuel rods placed in the waste package can be divided into two groups: 1) defective rods that have developed defects (or failures) on the cladding during the reactor operation and interim storage prior to permanent disposal; and 2) intact rods with intact cladding at the time of emplacement in the potential repository. Clads associated with the different fuel rods and their implications to cladding performance are discussed in the following subsections.

Defective Fuel Rods

A defective fuel rod is one that suffers cladding failure or becomes flawed through some physical or chemical damage. Fuel cladding can develop defects during service in reactor and/or interim (wet or dry) storage. Possible cladding failure modes leading to a defective fuel rod are listed below (DOE, 1987):

1. Pellet-clad interaction (PCI) is the differential movement of the fuel pellets and cladding following a rapid power transient during operation and can cause cladding breach;

2. Hydride embrittlement of cladding is caused by the reaction of zircaloy cladding with water vapor released from fuel pellets during service;

3. Gaseous fission products released into the gap between the fuel pellet and the cladding cause a decrease in the thermal conductivity of the initially helium-filled gap and generate stresses on the cladding by increasing the internal pressure;

4. Corrosion of cladding is caused by reactor water and the impurities it carries;

5. Deformation and bowing of fuel rods because of differential changes in dimension from nonuniform neutron fluxes;

6.   .   Other mechanical effects in service such as rubbing of metallic parts due to flow-induced vibrations, debris lodging in the fuel channels, or water jetting due to certain flow imbalances or blockages; and

7.   Welding defects, dropping, and excessive stress in handling.

The estimated fractional ranges of defective fuel rods for boiling water reactors (BWRs) and pressurized water reactors (PWRs) are summarized in the following table (DOE, 1987).

Reactor Type	Fraction of Defective Fuel Rods	
	Prior to 1981	1981 to 1985
BWR	0.06-1.13 %	0.03-0.55 %
PWR	0.02-0.28 %	0.02-0.17 %

In some extreme cases, 2.86 % of defective fuel cladding was reported for stainless steel clad fuels used in PWRs (Was, et al., 1985). The data may be used as a bounding estimate of defective fuel cladding prior to permanent emplacement in the repository.

Intact Fuel Rods

For intact fuel rods, an inert environment such as helium is maintained inside the cladding. Once spent fuel assemblies are placed inside the waste disposal container, the container is also filled with a similar inert environment before it is sealed off. Among various degradation modes of zircaloy cladding in an inert environment during storage and/or permanent disposal periods, creep rupture is the most dominant mechanism (Chin and Gilbert, 1989). Therefore, creep rupture of zircaloy cladding is considered the dominant degradation mode of intact fuel rods.

5.6.3 Conceptual Model and Approach for Cladding Degradation Modeling

In TSPA-1995, the waste container is assumed to undergo degradation by general and pitting corrosion. The current corrosion models predict general and pitting corrosion of the containment barriers as functions of emplacement time and the near-field environments (relative humidity and temperature). The models discussed in Sections 5.3 to 5.5 indicated failure of the waste container is likely to result from pitting corrosion, rather than by general corrosion. When the first pit penetrates the entire thickness of the waste container wall, the inert environment inside the waste container would be released immediately and replaced with the near-field moisture conditions. Following the waste container failure, the intact cladding and the spent fuel inside the "pre-failed" (relative to container failure time) cladding would begin degradation subject to the near-field environments.

In the simulation of degradation of cladding, fuel rods in a waste package are divided into two groups, fuel rods with intact cladding and those with "pre-failed" (relative to container failure

time) and defective cladding. The dominant degradation mechanism for intact cladding during disposal in the repository is creep rupture. Such failure is driven by stress caused by gas pressure buildup inside the cladding due to heating of the inert helium and fission gas released into the gap. Creep rupture is active during the entire disposal time span until cladding fails. Creep rupture is likely to produce "pin-hole"-type breaches, and, when cladding fails, the stress is relieved by releasing the gases from inside the fuel rod, and creep of the cladding will stop.

"Pre-failed" cladding at the time of waste container failure includes the cladding failed in reactor operation and interim storage (collectively referred to as defective cladding) and the cladding that fails during emplacement but prior to waste container failure. Cladding failure rates during emplacement are calculated from creep rupture models, and the fraction of defective cladding is given in the literature discussed previously. As soon as the first pit penetrates the waste container and the inert environment inside the waste container is lost, the spent fuel inside the breached cladding undergoes oxidation at a rate depending on the near-field environment (mostly temperature). Spent fuel oxidation results in volume expansion and surface area increase of the fuel matrix. The consequence is the splitting (or "unzipping") of cladding, which exposes a progressively greater amount of spent fuel to the near-field environment, making the spent fuel inside available for alteration and subsequent radionuclide release. After failure of the waste container, creep rupture still remains active on the intact cladding, and the cladding breaches continue. However, the failure rate by creep rupture will be reduced significantly as the cladding temperature decreases.

Another cladding degradation mode expected in a failed waste container is oxidation of cladding, which results in a gradual thinning of cladding. However, the oxidation rates are minimal at the near-field temperatures anticipated at the time of waste container failure, so cladding oxidation is not included in the cladding degradation models described below.

5.6.4 Cladding Degradation Models

As discussed above, failure of intact cladding by creep rupture, and splitting of the breached cladding due to oxidation of spent fuel inside are the dominant cladding degradation modes. Mechanistic models for these degradation modes are available from the literature, and are discussed in this section.

<u>Creep Rupture Models</u>

Zircaloy cladding creep rupture models developed by Santanam and others (1992) are considered to calculate failure of intact zircaloy cladding. The models for the different creep rupture modes are given as follows:

Transgranular Fracture:

$$\ln t_f^{tg} = -1.797 - \ln \dot{\varepsilon}$$

(5.6-1)

Triple-Point Cracking:

$$\ln t_f^{tp} = -5.655 - \ln \dot{\varepsilon} - \ln \frac{\sigma}{E} - \ln \frac{E}{10^4} \qquad (5.6\text{-}2)$$

Cavitation-Diffusional Growth:

$$\ln t_f^{cd} = 4.15 - \ln \dot{\varepsilon}_{gbs} + \ln \frac{\sigma}{E} \qquad (5.6\text{-}3)$$

Cavitation-Power Law Growth:

$$\ln t_f^{cp} = -1.587 - \ln \dot{\varepsilon} \qquad (5.6\text{-}4)$$

where t_f is time to fracture (years), $\dot{\varepsilon}$ is strain rate, σ is stress (MPa), and E is Young's modulus (MPa). Young's modulus is calculated as a function of temperature by

$$E = (11.81 - 13.0434577 \frac{T}{T_m}) \times 10^4 \quad for \quad \frac{T_m}{T} \ge 3.63 \qquad (5.6\text{-}5)$$

$$E = (11.09 - 10.3793382 \frac{T}{T_m}) \times 10^4 \quad for \quad \frac{T_m}{T} < 3.63 \qquad (5.6\text{-}6)$$

where T_m is zircaloy melting temperature (1900 K). Zircaloy cladding strain rates ($\dot{\varepsilon}$) used in Equations (5.6-1) to (5.6-4) are calculated using the following equations for different strain modes:

High-Temperature Climb:

$$\ln \dot{\varepsilon}_{HT} = 5 \ln \frac{\sigma}{E} + 55.862 - 15.828 \frac{T_m}{T} + \ln \frac{T_m}{T} + \ln \frac{E}{10^4} \qquad (5.6\text{-}7)$$

Low-Temperature Climb:

$$\ln \dot{\varepsilon}_{LT} = 7 \ln \frac{\sigma}{E} + 55.292 - 11.398 \frac{T_m}{T} + \ln \frac{T_m}{T} + \ln \frac{E}{10^4} \qquad (5.6\text{-}8)$$

Grain Boundary Sliding:

$$\ln \dot{\varepsilon}_{GBS} = 2 \ln \frac{\sigma}{E} + 20.852 - 11.078 \frac{T_m}{T} + \ln \frac{T_m}{T} + \ln \frac{E}{10^4} \qquad (5.6\text{-}9)$$

Nabarro-Herring:

$$\ln \dot{\varepsilon}_{NH} = \ln \frac{\sigma}{E} + 18.362 - 15.828 \frac{T_m}{T} + \ln \frac{T_m}{T} + \ln \frac{E}{10^4} \qquad (5.6\text{-}10)$$

5-21

Coble:

$$\ln \dot{\varepsilon}_{CO} = \ln \frac{\sigma}{E} + 11.142 - 11.078 \frac{T_m}{T} + \ln \frac{T_m}{T} + \ln \frac{E}{10^4} \qquad (5.6\text{-}11)$$

All the strain modes given in Equations (5.6-7) to (5.6-11) are considered at a given time period and cladding temperature, and the mode which gives the largest strain rate is taken as the dominant strain mode for that time period. Then, the dominant strain rate is used to calculate the time to fracture from the different fracture modes given in Equations (5.6-1) to (5.6-4), and the fracture mode giving the earliest fracture time is taken as the dominant fracture mode. The above equations are assumed to be applicable also to cladding of other materials such as stainless steel.

Cladding Splitting

All the cladding that fails prior to and following the container failure is subjected to another cladding degradation mechanism, i.e. cladding splitting resulting from oxidation of the spent fuel inside the clad. Cladding splitting grossly exposes the spent fuel, making it available for alteration and subsequent radionuclide release. Cladding splitting rate is largely dependent on the near-field temperature, and is divided into two stages: splitting initiation and propagation. The models for splitting initiation and splitting propagation developed by Einziger (1994) are:

$$t_{SI} = 9.8 \times 10^{-21} \exp(\frac{47.4\,Kcal}{RT}) \qquad (5.6\text{-}12)$$

$$t_{SP} = 1.14 \times 10^{-9} d \, \exp(\frac{18.4\,Kcal}{RT}) \qquad (5.6\text{-}13)$$

where t_{SI} is splitting initiation time (years) (i.e., time required to initiate cladding splitting relative to the time of waste container failure), t_{SP} is time required to split cladding a distance d (inches) relative to t_{SI}, R is the universal gas constant, and T is temperature (K). The models are also assumed to be applicable to cladding of other materials such as stainless steel.

The peak cladding temperature as a function of time after permanent disposal is available (Bahney, 1995). The peak cladding temperature may be used to conservatively represent the fuel clads in the waste package.

5.7 WASTE PACKAGE DEGRADATION HISTORY

5.7.1 Introduction

Incorporating the corrosion models discussed in Sections 5.3 to 5.5, and the temperature and humidity profiles at the waste package surface, which are provided from drift-scale thermal-hydrologic modeling (described in Section 4.2), a series of stochastic simulations for waste package degradation were performed.

The objectives of the simulations were to evaluate the effects of 1) repository designs, 2) scenarios for the near-field conditions, 3) corrosion initiation thresholds, and 4) corrosion mechanisms on the performance of the current design of the multi-barrier waste container (refer to Section 3.5). Different repository designs included alternative thermal loadings (25 MTU/acre and 83 MTU/acre) and the use of backfill. Different scenarios for the near-field conditions included the effects of alternative infiltration rates (0.05 mm/yr and 0.3 mm/yr) at the surface of the mountain for the potential repository. Corrosion initiation thresholds included using relative humidity (RH) only for the initiation of the outer barrier corrosion and using both temperature and relative humidity (RH) criteria. Different corrosion mechanisms included cases with and without cathodic protection of the Alloy 825 inner barrier by the carbon steel outer barrier.

General assumptions embedded in the stochastic waste package degradation simulations are discussed in the following section. A detailed description of the computing algorithms for the simulations is provided in Section 5.7.3. Analyses of the simulation results are presented in the following sections.

5.7.2 Major Assumptions in Waste Package Degradation Simulation

This section discusses the major assumptions made in the stochastic waste package degradation simulations. If not specifically indicated in each subsection, the assumptions are implicitly included.

1) Humid-air general and pitting corrosion of the carbon steel outer barrier initiate at a threshold RH which is uniformly distributed between 65 and 75 %. This threshold is independently chosen for each waste package. This assumption is based on numerous data found in the literature (see Haynie, et al, 1978; Phipps and Rice, 1979; Vernon, 1933).

2) Aqueous general and pitting corrosion of the carbon steel outer barrier initiate at a threshold RH which is uniformly distributed between 85 and 95 % RH. Visual observations indicating that steel coupon surfaces were covered with a thin film of water at about 85 % RH in a controlled environment chamber have been reported (Haynie, et al., 1978).

3) For each waste package, complete and positive correlation of the humid-air corrosion initiation threshold and the transition threshold from humid-air corrosion to aqueous corrosion is assumed. That is, if humid-air corrosion initiates at 65 % RH, aqueous corrosion initiates at 85 % RH.

4) Corrosion-allowance outer barrier material (carbon steel) is subjected to general and pitting corrosion both in humid-air and aqueous conditions. The uncertainties in the humid-air and aqueous general corrosion models (Equations (5.3-8) and (5.4-3)) were utilized to account for pit to pit variability and waste package to waste package variability. In the post-closure repository, about 10,000 waste packages will be spread over the repository area, and a local corrosion environment in one part of the repository may be different from that in another part. This variability of the local corrosion environment is referred to here as waste package to waste package variability. Also,

since a waste container has a relatively large surface area (37.26 m^2), the general corrosion rate on one part of the waste package may be different from that on another part of the waste package. This variability in corrosion rate on a waste package is referred to here as pit to pit variability. Because information on the degree of the variability among waste packages and among pits is not available currently, the variabilities are accounted for in TSPA-1995 by equally splitting the uncertainties in the humid-air and aqueous general corrosion models into the variability among waste packages and the variability among pits.

5) Corrosion resistant inner barrier material (Alloy 825) is subjected to aqueous pitting corrosion only (not to general corrosion). The time-independent pit growth rate distributions discussed in Section 5.5 (Equation (5.5-1)) were utilized to represent pit to pit variability and waste package to waste package variability. The same reasoning given in item (4) is applied also to account for the variability among waste packages and among pits.

6) When pits reach the inner barrier through the outer barrier, aqueous conditions are assumed there. This assumption is based on the observations that the capillary condensation of moisture by gel-like porous corrosion products of the outer barrier covering the inner barrier surface (Vernon, 1933) and the hygroscopic nature of many corrosion products (Fyfe, 1994; Haynie et al, 1978) would provide an aqueous corrosion condition at the surface of the inner barrier.

7) Pits form uniformly over the entire waste container surface. It is known that pits are most stable when growing in the direction of gravity because the dense, concentrated solution within a pit is necessary for its continuing activity (Fontana, 1986, pp. 64-69). Elongation of pits growing in the direction of gravity has been observed (Ruijini, et al, 1989). However, there is an uncertainty regarding crevice corrosion at the bottom of the waste container contacting the invert. Additionally, over the containment and isolation periods, rock may fall on the waste container, or backfill may be introduced. In these cases, there may be crevice corrosion occurring at the contact points between the rocks and waste container surface. Because of the uncertainty of the possibility of crevice corrosion at the side and bottom of waste containers, we assumed that pits form uniformly over the entire waste container surface.

8) All pits have a uniform area of 1 mm^2 which corresponds to a pit radius of 0.56 mm. This may be large for the pits forming in Alloy 825, which tend to be much narrower (Szklarska-Smialowska, 1986, pp. 127-141).

9) The waste container surface has a pit density of 10 pits/cm^2 (Marsh, and Taylor, 1988; Marsh, Taylor, and Sooi, 1988; Strutt, Nichols and Barbier, 1985), and the same pit density is also assumed for the inner barrier.

10) Taking the pit density (10 pits/cm^2), the uniform pit area (1 mm^2) and the nominal surface area (37.26 m^2) of the waste container for a typical large MPC, the total number of pits that can form on the waste container is about 4 million. This corresponds to about 10 % of the total surface area.

11)   All the pits on a waste package start to grow at the same time when the threshold humidity discussed in items (1) and (2) is reached. That is, pit initiation is not explicitly considered in TSPA-1995.

As discussed in Section 3.5, different moderately corrosion resistant materials (MCRM) were specified as candidate waste container barrier materials for spent fuel in a low-thermal load case (Monel 400 as the third layer) and for vitrified defense high-level waste in both a high-thermal load case (70/30 Cu-Ni alloy as the second layer) and a low-thermal load case (70/30 Cu-Ni alloy as the second layer and Monel 400 as the third layer). Since adequate corrosion models or data are not available for MCRM, it has been recommended that these materials not be included in any waste package performance analysis (Doering, 1995). Thus, in TSPA-1995, the waste containers for both spent fuel and defense high-level waste were treated equally as having two layers of containment barrier, i.e. Alloy 825 inner barrier and carbon steel outer barrier with the thicknesses given in Section 3.5.

5.7.3 Stochastic Simulation of Waste Package Degradation

<u>Corrosion Models for the Containment Barriers</u>

Since the sulfur dioxide level in the air of the potential repository is expected to be insignificant, the humid-air general corrosion model given in Equation (5.3-8) for the carbon steel outer barrier reduces to

$$\ln D_g = a_0 + a_1 \ln t + \frac{a_2}{RH} + \frac{a_3}{T} + \varepsilon \qquad (5.7\text{-}1)$$

The estimates of the model parameters are

$$E(CAM)_{air} \begin{bmatrix} a_0 \\ a_1 \\ a_2 \\ a_3 \end{bmatrix} = \begin{bmatrix} 16.984 \\ 0.6113 \\ -893.55 \\ -833.27 \end{bmatrix} \qquad (5.7\text{-}2)$$

and the covariance matrix of the model parameters is

$$V(CAM)_{air} = \begin{bmatrix} 8.257 & -0.03 & -591.0 & -365.0 \\ -0.03 & 8.68E\text{-}4 & 1.827 & 2.775 \\ -591.0 & 1.827 & 5.338E\text{+}4 & -1.173E\text{+}4 \\ -365.0 & 2.775 & -1.173E\text{+}4 & 1.459E\text{+}5 \end{bmatrix} \qquad (5.7\text{-}3)$$

The aqueous general corrosion model given in Equation (5.4-3) for the carbon steel outer barrier is re-written as

$$\ln D_g = b_0 + b_1 \ln t + \frac{b_2}{T} + b_3 T^2 + \varepsilon \tag{5.7-4}$$

The estimates of the model parameters are

$$E(CAM)_{aq} \begin{bmatrix} b_0 \\ b_1 \\ b_2 \\ b_3 \end{bmatrix} = \begin{bmatrix} 111.5 \\ 0.5320 \\ -2.330E+4 \\ -3.193E-4 \end{bmatrix} \tag{5.7-5}$$

and the covariance matrix of the model parameters is

$$V(CAM)_{aq} = \begin{bmatrix} 116.7 & -9.504E-4 & -2.480E+4 & -3.798E-4 \\ -9.504E-4 & 7.413E-4 & 1.777E-3 & 2.661E-11 \\ -2.480E+4 & 1.777E-3 & 5.272E+6 & 8.046E-2 \\ -3.798E-4 & 2.661E-11 & 8.046E-2 & 1.243E-9 \end{bmatrix} \tag{5.7-6}$$

Pitting corrosion of the corrosion resistant Alloy 825 inner barrier is modeled with the time independent pit growth rate model given by Equation (5.5-1) which is re-written here as

$$\ln R_p = c_0 - \frac{c_1}{T} \tag{5.7-7}$$

The elicitation for the time independent pit growth rate distributions (Table 5.5-1) used in TSPA-1993 (Andrews, et al., 1994) gave median pit growth rates of 0.001mm/yr at 70 °C and 0.1 m/yr at 100 °C. Using these values, c_0 in Equation (5.7-7) was estimated to be 50.37, and c_1 was estimated to be -19,656. The elicitation also suggested that for a given temperature, the pit growth rate would have a log-normal distribution with the given median and a standard deviation of 1.39975 in natural log space. To incorporate this variability, c_1 is set equal to -19,656 for every pit, and c_0 is allowed to vary among pits with a mean of 50.37 and a standard deviation of 1.39975. Therefore, the estimate of the model parameters is

$$E(CRM)_{aq} \begin{bmatrix} c_0 \\ c_1 \end{bmatrix} = \begin{bmatrix} 50.37 \\ -19656 \end{bmatrix} \tag{5.7-8}$$

and the covariance matrix of the model parameters is

$$V(CRM)_{aq} = \begin{bmatrix} 1.95929 & 0.0 \\ 0.0 & 0.0 \end{bmatrix}$$

(5.7-9)

The uncertainty in the parameters was equally divided between waste package to waste package variability and pit to pit variability, based on the reasoning discussed in Section 5.7.2. To do this, the covariance matrix, V, was divided by 2 to obtain a new covariance matrix, V_N. Then, V_N was used to select average values of the parameters for each waste package. These average values were used, again with V_N, to select parameters for each pit on that waste package. Thus, the average value of c_0 on a given waste package would be normally distributed with a mean of 50.43 and a standard deviation of 0.98977. For each pit on this waste package, c_0 would be normally distributed with the mean chosen above and a standard deviation of 0.98977. For example, 52.22 might be selected as the average value of c_0 for one waste package. In this case, the value of c_0 for each pit on this waste package would be chosen from a normal distribution with a mean of 52.22 and a standard deviation of 0.98977. Similarly, for each waste package, average values would be chosen for each of the parameters in the humid-air general corrosion model for the carbon steel outer barrier and each of the parameters in the aqueous general corrosion model for the outer barrier. These average values would be subsequently used to choose values for these parameters for each pit.

Waste Package Degradation Model Implementation

An overview of the stochastic waste package performance simulation model is shown in Figure 5.7-1. The humid-air and aqueous general and pitting corrosion models (with the uncertainties) for the carbon steel outer barrier, and the aqueous pitting corrosion model (with the uncertainties) for the Alloy 825 inner barrier are fed into the stochastic waste package degradation simulation module. The drift-scale temperature and humidity profiles at the waste package surface are incorporated into the waste package degradation simulation module as a lookup table. The waste package degradation simulation module calls on appropriate corrosion model(s) depending on the near-field environment and the waste package degradation at a given time step. The simulation module provides as output the "failure" time for each waste package, which corresponds to the time for the initiation of waste form alteration (or radionuclide mobilization) inside the waste package. "Failure" of waste package is defined as having at least one pit penetration. The simulation module also provides the pitting history of a "failed" waste package in terms of the number of pit penetrations as a function of time. A total number of pit penetrations at a given time gives an area on the waste package that is available for transport of mobilized radionuclides through the waste package. The waste package "failure" time and subsequent pitting history are fed into the EBS transport model.

The simulations were performed for up to 100,000 years, and the time steps were discretized such that within any time step, both the relative humidity and the temperature are relatively constant. The algorithm for the waste package degradation simulations is described in the flow chart shown in Figure 5.7-2. A total of 400 waste packages were simulated in each case. For each simulated waste package, random values were selected to represent the mean values on that particular waste

package of each of the parameters in the corrosion models. This selection process is represented by the second box in the flow chart in Figure 5.7-2.

A total of 250,000 pits per waste package were used in the simulations. The choice of this number is discussed in Section 5.7.4. Based on the mean values already selected for each waste package, random values were sampled for each pit to represent the parameters in the corrosion models. This is represented by the third box in the flow chart in Figure 5.7-2.

Once the parameter values for the corresponding corrosion model are known for a given pit, the depth of that pit is tracked through each time step. Within each time step, the average relative humidity and temperature are calculated. These are used to determine whether humid-air or aqueous corrosion is occurring, and at what rate corrosion is occurring. Based on this information, the model calculates how much corrosion occurs during that time step, and check if the pit penetrates the waste package. If the pit penetrates the waste package during that time step, the time when the pit penetrates the waste package is also calculated. This is illustrated in the fourth through seventh boxes of the flow chart in Figure 5.7-2.

5.7.4 General Descriptions for Waste Package Degradation Simulation

All the simulations discussed in the following sections were conducted for a total of 400 waste packages and 250,000 pits per waste package. Results for each case are presented with a sequence of three figures: 1) cumulative fraction of waste packages that have a first pit penetrated through the container wall; 2) representative pitting history as a function of time for each of 25 waste packages; and 3) abstraction of the pitting histories (based on 400 waste packages) into 6 groups of waste packages for implementation into the RIP code.

The simulations were conducted with a reduced number of waste packages (400 waste packages) and pits (250,000 pits per waste package) primarily because of constraints in computing resources. Considering various sources of uncertainties embedded in conceptual models and process-level models (thermal-hydrologic model, corrosion model, etc.), the results based on the smaller number of waste packages and pits should not be significant in light of the overall uncertainty range of the analyses. Also, test simulations were conducted with waste package numbers from 50 to 500 and pit numbers per waste package from 100,000 to 4,000,000 to evaluate the effect of using smaller values to represent the larger system. It was generally found that the number of waste packages used did not influence the results noticeably. For example, in the 83 MTU/acre case, when the number of pits was increased from 100,000 to 4,000,000 per waste package, the time for the first pit penetration was earlier by as much as 100 to 200 years than that for the runs with 100,000 pits. However, the differences are smeared out during the abstraction process in which the waste packages are divided into 6 groups. For each waste package group, an average of the first pit penetration times of individual waste packages in that group is used as the first pit penetration time for that group, and all the waste packages in the same group are assumed to have the same pitting history.

5.7.5 Corrosion Initiation with Humidity and Temperature

A set of simulations for a thermal loading of 83 MTU/acre was performed assuming that corrosion of the carbon steel outer barrier initiates only when the temperature at the waste

container surface becomes less than 100 °C and the relative humidity is above the threshold values defined in Section 5.7.2. Impacts of different infiltration rates (low infiltration rate with 0.05 mm/yr and high infiltration rate with 0.3 mm/yr) and backfill were also studied.

Effect of Infiltration Rate

The results for the case with low infiltration rate (0.05 mm/yr) and without backfill are shown in Figures 5.7-3a to 5.7-3c. As previously discussed for this case in Section 4.2, at about 2,000 years the waste container temperature cools to 100 °C, and RH is approaching about 85 %. Thus, some portion of the waste packages in the repository are exposed to an aqueous corrosion condition. The effects of this aqueous corrosion environment at elevated temperatures are illustrated in Figure 5.7-3a which presents the "failure" history (or "empirical" cumulative density function) for 400 waste packages. "Failure" of a waste package has been defined in Section 5.7.3 as having at least one pit penetration through the container. Waste packages start to fail (first pit penetration) at about 2200 years, and the number of failed waste packages increases rapidly before flattening out at about 6,000 years.

This result is expected from the temperature and humidity profiles at the waste container surface (refer to Section 4.2). After corrosion initiates at about 2,000 years, temperature steadily decreases from about 100 °C to about 70 °C at about 5,000 years, and RH is between 85 and 90 % during the time period. This indicates that the carbon steel outer barrier of a large portion of waste packages undergo aqueous corrosion at high corrosion rates. Additionally, at these temperature conditions, the time-independent pit growth rate for the inner barrier (Figure 5.5-1) is also high. It is also shown in the figure that about 8 % of the waste packages do not have a first pit penetration by 100,000 years.

Representative pitting histories for 25 waste packages, randomly selected from the waste packages that fail before 100,000 years, are shown in Figure 5.7-3b. The waste package with the 'highest pitting penetrations' has about 10 % of the total of 4 million pits penetrated at 10,000 years, and then the number of pit penetrations levels off. This is caused mainly by a very low pit growth rate for the inner barrier beyond 10,000 years, i.e. the waste container surface temperature is about 50 °C at 10,000 years. Other waste packages follow similar pitting histories. Shown in Figure 5.7-3c is the abstraction for implementation of the RIP of the six waste package groups.

As shown in Section 4.2, infiltration rate (high at 0.3 mm/yr or low at 0.05 mm/yr) does not have a significant effect on the temperature and humidity profiles at the waste container surface. The waste package degradation results for the high infiltration rate case are presented in Figures 5.7-4a to 5.7-4c, and are similar to those for the low infiltration rate case. In Figures 5.7-4b and 5.7-4c4, the number of pit penetrations steadily increase even after 10,000 years, and this contrasts with the low infiltration rate case for which the number of pit penetrations is virtually flat after about 10,000 years. This is mainly due to higher humidity for the high infiltration rate case.

Effect of Backfill

As described in the thermal-hydrologic modeling in Section 4.2, backfill is assumed to be emplaced after 100 years when most of the intense decay heat has dissipated from the waste package. The thermal-hydrologic modeling results showed that temperature and humidity profiles at the waste container surface are not affected greatly by the backfill emplacement.

Consequently, the waste package degradation histories (Figures 5.7-5a to 5.7-5c) for the case with backfill at the low infiltration rate are not much different from those without backfill at the same infiltration rate, except that the fraction of waste packages without a pit penetration at 10,000 years is about 20 % (Figure 5.7-5a) compared to about 10 % (Figure 5.7-3a). Similarly, in Figures 5.7-5b and 5.7-5c, the number of the pits penetrating the waste containers is lower, i.e. the maximum fraction is about 0.01 at 10,000 years compared to 0.1 at 10,000 years in the case without backfill. This was caused mainly by a lower humidity with the backfill case.

The simulation results for the case with backfill and at high infiltration rate are shown in Figures 5.7-6a to 5.7-6c. They are similar to those for the corresponding case at low infiltration rate, except the maximum fraction of pit penetrations is about 0.05 (Figures 5.7-6b and 5.7-6c) at 10,000 years compared to 0.01 at 10,000 years.

5.7.6   Corrosion Initiation with Humidity

It has been shown in the current drift-scale thermal-hydrologic modeling (see Section 4.2) that the waste container surface in a high thermal load case (83 MTU/acre) is predicted to have relatively high humidity profiles (above 60 % RH for most of time) while the temperature is predicted to be higher than 100 °C. Most of the uncertainties of the model prediction come from the assumptions in the humidity calculation, the uncertainty of the conceptual model of the drift-scale thermal-hydrology, and the uncertainty and variability of the thermal-hydrologic properties of the geologic materials. The simulations discussed in this subsection apply only to the high-thermal load case (83 MTU/acre); for a low-thermal load case (25 MTU/acre), the temperature profile at the waste package surface is below 100 °C almost all the time. A set of simulations in this subsection were performed to evaluate the impacts on the waste package performance by initiating the carbon steel outer barrier corrosion whenever humidity is greater than the threshold value (see Section 5.7.2) regardless of the temperature.

Effect of Infiltration Rate

The simulation results for the case with low infiltration rate and without backfill are shown in Figures 5.7-7a to 5.7-7c. As shown in Figure 5.7-7a, "failure" (first pit penetration) of waste packages begins at about 1,000 years, which is about 1,200 years earlier than the corresponding case using the RH and temperature switch for the corrosion initiation (Figure 5.7-3a). This earlier waste package penetration is caused mainly by an earlier initiation of corrosion (starting at about 400 years) while temperature is still high (about 120 °C). However, the rate of waste package failures (from the "slope" of the curve) is lower than the case using the RH and temperature switch. This is due mostly to the long duration of humid-air corrosion of the carbon steel outer barrier, which initiates at about 400 years and continues to about 2,000 years before it switches to an aqueous corrosion condition. As described in Sections 5.3 and 5.4, the humid-

air corrosion rate of the carbon steel outer barrier is lower than the aqueous corrosion rate. The pitting histories for 25 waste packages (Figure 5.7-7b) are similar to those using the RH and temperature switch, which are shown in Figure 5.7-3b.

The simulation results for the high infiltration rate (0.3 mm/yr) case are shown in Figures 5.7-8a to 5.7-8c. In this case, waste packages begin to fail at about 850 years (Figure 5.7-8a) compared to about 1,000 years in the low infiltration rate case shown in Figure 5.7-7a, and the waste package failure rate is about the same as in the low infiltration rate case. The number of pit penetrations steadily increase even after 10,000 years (Figure 5.7-8b), compared to the relatively steady-state at 10,000 years in the low infiltration rate case. A similar observation was made in the case with 83 MTU/acre, high infiltration, without backfill, and using RH and temperature switch (Figure 5.7-4a), and a similar explanation is offered, i.e. higher humidity in the high infiltration rate case.

Effect of Backfill

The simulation results for the case with backfill and low infiltration rate are presented in Figures 5.7-9a to 5.7-9c. Compared to the case without backfill (Figure 5.7-7a), the first waste package failure occurs at about 200 years later (Figure 5.7-9a), and the cumulative fraction of waste packages that have failed at 10,000 years is lower, i.e. about 75 % of waste packages failed compared to about 85 % for the case without backfill. Similar observations are made for the representative pitting histories of 25 waste packages shown in Figure 5.7-9b when compared to the case without backfill shown in Figure 5.7-7b.

The simulation results for the case with backfill and the high infiltration rate are shown in Figures 5.7-10a to 5.7-10c. As shown in Figure 5.7-10a, the time for the initiation of waste package failure is about the same as in the corresponding case without backfill (Figure 5.7-8a). However, the cumulative fraction of waste packages that have failed at 10,000 years is somewhat lower than the case without backfill. Additionally, for the backfill case, the number of failed waste packages is leveling off at 10,000 years (Figure 5.7-10a), and the number of pit penetrations in those waste packages beyond 10,000 years are relatively steady, i.e. fewer additional pit penetrations beyond 10,000 years (Figure 5.7-10b). These results contrast with those for the corresponding case without backfill, in which waste package failure continues beyond 10,000 years but at a significantly low rate (Figure 5.7-8a), and some waste packages have steadily increasing number of pit penetrations beyond 10,000 years (Figure 5.7-8b).

5.7.7 Alternative Thermal Load

A series of simulations were conducted for the low thermal load case (25 MTU/acre) to evaluate the effects of alternative thermal loadings (25 MTU/acre vs 83 MTU/acre) on waste package performance. These simulations were made using only the RH switch for the corrosion initiation of the carbon steel outer barrier because temperature at the waste container surface is below 100 °C all times except for the very early period during which humidity at the surface is below the threshold humidity (see Section 5.7.2). The effects of infiltration rate (low infiltration rate at 0.05 mm/yr or high infiltration rate at 0.3 mm/yr) and the presence of backfill were evaluated for the low thermal load case. The simulation results are compared with those of the

corresponding high thermal load cases using RH and temperature switch for the outer barrier corrosion initiation.

Effect of Infiltration Rate

The simulation results for the case of low infiltration rate and without backfill are shown in Figures 5.7-11a to 5.7-11c. As shown in Figure 5.7-11a, the time to the first waste package failure is about 2,000 years which is close to that (about 2,200 years) for the corresponding high thermal load case (Figure 5.7-3a). However, the waste package failure rate (or number of waste packages that fail at a given time) is substantially lower than the corresponding high-thermal load case, i.e. failure of about 10 % of the waste packages for this case compared to about 90 % for the corresponding high-thermal load case by 10,000 years, and failure of about 18 % of the waste packages for this case compared to about 92 % for the corresponding high-thermal load case by 100,000 years. The explanation below is offered for this marked difference in the waste package degradation histories.

In the low-thermal load case, the carbon steel outer barrier of the waste packages begins humid-air corrosion at very early time (starting at about 80 years), when humidity and temperature at the waste container surface reach about 65 to 75 % RH and 90 to 100 °C, respectively (refer to Section 4.2). At these conditions, the corrosion rates are very low (see Section 5.3.5), and the humid-air corrosion lasts about 700 years before switching to an aqueous corrosion condition (at between 85 and 95 % RH). Another important factor that contributes to the much reduced waste package failure rate in the low-thermal loading case is the lower pit growth rate of the corrosion-resistant inner barrier because of the lower waste container surface temperature. The waste container surface temperature cools to about 60 °C at 2,000 years to about 50 °C at 4,000 years and to about 40 °C at 6,000 years. In this temperature range, pit growth rates of the inner barrier are low (see Section 5.5).

Shown in Figures 5.7-12a to 5.7-12c are the simulation results for the case with the high infiltration rate and without backfill. Compared to the results for the low infiltration rate and without backfill case in the low-thermal loading (Figure 5.7-11a), the time for the first waste package failure is about the same (2,000 years as shown in Figure 5.7-12a). However, the waste package failure rate for the high infiltration rate case is about twice that of the failure rate for the low infiltration case, i.e. failure of about 20 % of the waste packages for the high infiltration rate case compared to about 10 % for the low infiltration rate case at 10,000 years, and failure of about 34 % of the waste packages for the high infiltration rate case compared to about 18 % for the low infiltration rate at 100,000 years. Also, the representative pitting histories for 25 waste packages presented in Figure 5.7-12b show higher pitting rate (greater number of pit penetrations) for the high infiltration rate case than that for the low infiltration rate case (Figure 5.7-11b). As in the low infiltration rate case, the waste package failure in the high infiltration rate case is significantly lower than the corresponding high-thermal loading case (Figures 5.7-4a to 5.7-4c), and explanations similar to those given above for the low infiltration rate case apply.

Effect of Backfill

The simulation results for the low thermal loading case with backfill and the low infiltration rate are shown in Figures 5.7-13a to 5.7-13c. Since there is no noticeable difference between the low

and high infiltration rate cases, only the results for the low infiltration rate case are discussed. As shown in Figure 5.7-13a, the time for the first waste package failure is the same as in the corresponding case without backfill (Figure 5.7-11a). The waste package failure rate for the case with backfill is somewhat lower than the corresponding case without backfill, i.e. failure of about 6 % of the waste packages for the case with the backfill compared to 10 % for the case without backfill by 10,000 years, and failure of about 13 % of the waste packages for the case with the backfill compared to about 18 % for the case without backfill by 100,000 years. The representative pitting histories for 25 waste packages for the case with backfill (Figure 5.7-13b) are very close to those for the case without backfill (Figure 5.7-11b).

5.7.8 Cathodic Protection

It is generally agreed that in the current waste package design, some degree of cathodic protection of the Alloy 825 corrosion-resistant inner barrier will be provided by the carbon steel outer barrier. The cathodic protection mechanism will become active when the outer barrier is breached and a galvanic couple is formed between the outer barrier and the inner barrier. Proper cathodic protection is ensured if the two metals maintain an intimate contact. However, no published data are available that are readily applicable to the current stochastic waste package degradation simulation. An elicitation was provided to account for the cathodic protection of the corrosion-resistant inner barrier in the waste package (McCright, 1995). The elicitation indicates the inner barrier would be protected cathodically by the outer barrier, and suggests the pitting corrosion of the inner barrier be delayed until the thickness of the carbon steel outer barrier is reduced by 75 %. Simulations were conducted to evaluate the effects of cathodic protection on the waste package performance by incorporating the elicitated cathodic protection measure.

High-Thermal Loading Case

A set of simulations were conducted for the case of high-thermal loading without backfill and at high infiltration rate, and the results are presented in Figures 5.7-14a to 5.7-14c. Compared to the simulation results for the corresponding case without cathodic protection (83 MTU/acre without backfill and with the high infiltration rate) shown in Figure 5.7-3a, the time for the initiation of waste package failure is delayed significantly from about 2,200 years to about 8,000 years (Figure 5.7-14a). With the current measure of cathodic protection, the fraction of failed waste packages (at least one pit penetration) is negligible at 10,000 years, compared to about 90 % without cathodic protection (Figure 5.7-4a). The waste package failure fraction is about 60 % by 100,000 years with cathodic protection compared to about 92 % without cathodic protection. Also shown in Figure 5.7-14a is the fraction of waste packages with their outer barrier thickness reduced by 75 %. Note that in the figure, the 'n-th' waste package to have its outer barrier thickness reduced by 75 % is not necessarily the same 'n-th' waste package to have its first pit penetrated. The representative pitting histories for 25 waste packages (shown in Figure 5.7-14b) are also reduced significantly, compared to those without cathodic protection (Figure 5.7-4b).

The waste package performance analyses indicate that the cathodic protection of the corrosion-resistant inner barrier by the carbon steel outer barrier may significantly improve the waste package performance and could be one most important mechanism that should be considered in developing a strategy for the waste isolation and containment in the potential repository.

However, the measure for cathodic protection provided by the elicitation, i.e. delaying the inner barrier pitting corrosion until the outer barrier thickness reduced by 75 %, was not developed from experimental data or detailed analysis, rather it is semi-quantitative in nature (McCright, 1995). To quantify better the cathodic protection effects in future waste package performance analysis, the current cathodic protection model should be improved and substantiated.

An additional uncertainty is the possibility of crevice corrosion that may occur by incomplete contacts between the corrosion-resistant inner barrier and the corrosion-allowance outer barrier materials. Crevice corrosion has an adverse effect to cathodic protection and is possible if there is a poor or incomplete contact between two metals with different corrosion potentials (such as between the inner barrier and outer barrier materials). In manufacturing the multi-barrier waste container which weighs about 70 tons with a dimension of 1.8 m diameter and 5.7 m length (M&O, 1995c), it may not be straightforward technically to maintain a complete contact between two barrier materials. A poor or incomplete contact between the barrier materials would make the cathodic protection of the inner barrier less effective and may introduce a large crevice region between the two metals that is detrimental to the performance (McCright, 1995). The effects of potential crevice corrosion should be addressed in future waste package performance analysis (Lee, 1995).

Low-Thermal Load Case

A similar set of simulations with the same cathodic protection measure implemented were run for the low-thermal loading case (25 MTU/acre) with the high infiltration rate and without backfill.

The number of waste package failures, i.e. waste packages with their first pit penetrated, is extremely low at 100,000 years (Figure 5.7-15). Also shown in the figure is the fraction of waste packages with their outer barrier thickness reduced by 75 %. Combined effects of the current measure of cathodic protection and the low pit growth rate in the inner barrier, caused by the low waste container surface temperature at the time for initiation of the inner barrier pitting, result in the very small number of waste package failures. Pitting rates of the waste packages are also very low. Other simulation results are not presented because of the insignificant waste package degradation for this case.

5.7.9 Time-Dependent Pit Growth Rate in Alloy 825 Inner Barrier

It is generally known that, like general corrosion rate (Sections 5.3 and 5.4), pitting corrosion rate decreases with exposure time. The time-independent pit growth rate for the corrosion-resistant inner barrier in the current stochastic waste package performance simulation (discussed in Section 5.5) may be conservative in light of the time-dependent pitting rate. To account for the time-dependency of pit growth rate, a sensitivity case study was performed which included the incorporation of a square root of exposure time term into Equation (5.5-1) as follows (Halsey, 1995).

$$\ln R_p = 50.373 - 0.5 \ln t - \frac{19655.85}{T} \qquad (5.7\text{-}10)$$

Since it would be more appropriate to use a distribution for the power of the time term instead of a single number (0.5), a set of simulations were conducted with the time power term being uniformly distributed between 0.3 and 0.5 (Lee, 1995). The simulations were run for the case of high-thermal loading (83 MTU/acre) with high infiltration rate, without backfill, and using the RH and temperature switch for the initiation of the outer barrier corrosion.

The simulation results for the fraction of waste packages with their first pit penetration are presented in Figure 5.7-16 which shows that only about 5 % of the waste packages have been penetrated by 100,000 years. Currently, no information is available for the validity of the time power term for the inner barrier pitting corrosion. This sensitivity study suggests that the inner barrier pitting corrosion model from the elicitation be improved and substantiated for future waste package performance analysis. Other simulation results are not presented because of negligible waste package degradation.

5.7.10 Alternative Thermal-Hydrologic Model

Alternate thermal-hydrologic models have been used for performance assessment calculations for the near-field (drift-scale) and far-field thermal hydrology for the potential repository: one by the M&O Performance Assessment (PA) Group which is being used in this study, and the other by Buscheck and coworkers at Lawrence Livermore National Laboratory (LLNL) (Buscheck, et al., 1995). Details of the alternative models are discussed in Section 4.2. Recently, selected simulation results for the temperature, humidity and saturation profiles in the drift, calculated with the alternative drift-scale thermal-hydrologic model by Buscheck and coworkers (hereafter referred to as Buscheck's model) were provided for comparison with the results from the M&O PA group (Buscheck, 1995). The results from Buscheck's model are for

1) 80 MTU/acre, no backfill, no infiltration;
2) 80 MTU/acre, backfill, no infiltration;
3) 24 MTU/acre, no backfill, no infiltration; and
4) 24 MTU/acre, backfill, no infiltration.

As noticed from the above list, all the results from Buscheck's model do not include the effects from the infiltration rate at the repository. Although this may not be a major factor, modeling results would indicate drier and hotter conditions than the case including the infiltration effects. Detailed comparisons of the drift-scale thermal-hydrologic modeling results (in terms of temperature, humidity and saturation) are discussed in Section 4.2. Using the temperature and humidity profiles at the waste package surface from Buscheck's model, a series of simulations were conducted for waste package performance in the different near-field environments. It may not be appropriate to compare directly the simulation results using the near-field conditions from Buscheck's model with those from this study, mainly because of the differences in the conceptual models and in the thermal and hydraulic properties of the materials employed in the two models. However, whenever reasonable, the results are compared with those from a similar case in this

study. As discussed below, the near-field conditions for the four cases calculated from Buscheck's model are hotter and drier than the results from this study, resulting in much lower waste package failure and degradation. Therefore, the waste package performance simulations for all the cases from Buscheck's model were run for up to 1,000,000 years, instead of 100,00 years as in the other cases in this study, assuming the waste packages maintain their structural integrity.

24 MTU/acre Case

Simulation results for the case of 24 MTU/acre without backfill and using the RH switch for the outer barrier corrosion initiation are presented in Figures 5.7-17a to 5.7-17c. Compared to the waste package failure rate results in this study for the low-thermal loading (25 MTU/acre) case at low infiltration rate and without backfill (Figure 5.7-11a), the time for the initiation of waste package failure at about 1,800 years (Figure 5.7-17a) is comparable. However, the waste package failure rates (about 4 % at 10,000 years and about 10 % at 100,000 years) are lower than the rate in this study (about 10 % at 10,000 years and about 18 % at 100,000 years). The pitting histories of the waste packages from Buscheck's model (Figure 5.7-17b) are also lower than the similar case in this study (Figure 5.7-11b).

The simulation results for the 24 MTU/acre case with backfill are shown in Figures 5.7-18a and 5.7-18b. As shown in Figure 5.7-18a, there is no waste package failure until about 50,000 years, and a very small number of waste package have failed at 100,000 years. The results are significantly different from those of the similar case in this study (25 MTU/acre at low infiltration rate and without backfill, shown in Figure 5.7-13a). Also, degradation of the waste packages by pitting corrosion with the Buscheck's model (Figure 5.7-18b) becomes significant only after about 200,000 years (compare to Figure 5.7-13b).

80 MTU/acre Case

The simulation results for the 80 MTU/acre case without backfill and using the RH and temperature switch for the outer barrier corrosion initiation are presented in Figures 5.7-19a and 5.7-19b. It is shown in Figure 5.7-19a that there is no waste package failure until 50,000 years, and only about 1 % of waste packages have their first pit penetration by 100,000 years. Also, pitting degradation of the waste packages becomes significant only after 100,000 years.

Figures 5.7-20a and 5.7-20b show the simulation results for the 80 MTU/acre case with backfill and using the RH and temperature switch for the outer barrier corrosion initiation. As shown in Figure 5.7-20a, the backfill further delays the time for the initiation of waste package failure to just beyond 100,000 years. As for the case without backfill, waste package degradation from pitting corrosion becomes significant only after about 200,000 years.

The alternative thermal-hydrologic models from the M&O PA Group and Buscheck provide very different (drift-scale) near-field environments in terms of temperature and relative humidity. Depending on the choice between the two models, the current stochastic waste package performance simulation predicts very different waste package performance. These comparative study results indicate there is a need to resolve the differences between the two thermal-hydrologic models in order to provide a consistent, more reliable and better representative

information of the near-field environment. Such reliability in the near-field environment is crucial to improve confidence in modeling the waste package and EBS performance and conducting a total system performance assessment for the potential repository.

5.7.11   Alternative Interpretation of the Elicitation for the Inner Barrier Pit Growth Rate

An alternative interpretation of the elicitation for the pit growth rate ranges given in Table 5.5-1 is that the pit growth rate given in the mean growth rate column should have been the median growth rate. If this were the case, it would be possible to assume that within each of the three rows, the growth rate follows a log-normal distribution. Then, it is possible to treat the variability between the rows as waste package to waste package variability, and the variability between the columns as pit to pit variability among the pits on the same waste package. This would provide a standard deviation of 1.40 natural log units for both the waste package to waste package variability and the pit to pit variability, thus effectively doubling the variability in the pit growth rate. Using this alternative interpretation, a set of simulations were run for the case of low thermal loading (25MTU/acre) without backfill, at high infiltration rate, and using the RH switch for the initiation of the outer barrier corrosion. Another set of simulations were run for the case of high thermal loading (83MTU/acre) without backfill, at high infiltration rate, and using the RH switch for the corrosion initiation.

The simulation results for the waste package failure rate (waste packages with at least one pit penetration) are presented in Figure 5.7-21 for the 25 MTU/acre case and in Figure 5.7-22 for the 83 MTU/acre case. Compared to the results for the corresponding low thermal loading cases using the earlier interpretation (Figure 5.7-12a), the time to initiation of waste package failure is about 1,000 years with this alternative interpretation (Figure 5.7-21), whereas the initiation time is about 2,000 years with the earlier interpretation. Also, although the cumulative fraction of waste packages with their first pit penetration is about 20 % at 10,000 years and about 34 % at 100,000 years with the earlier interpretation, these are about 70 % at 10,000 years and about 80 % at 100,000 years respectively with the alternate interpretation.

For the 83 MTU/acre case shown in Figure 5.7-22, the impact of the alternate interpretation is much less than the 25 MTU/acre case. The time for the initiation of waste package failure (first pit penetration) is about 900 years with the earlier interpretation (Figure 5.7-8a), whereas it is about 700 years with the alternative interpretation. The cumulative fraction of the failed waste packages is about 95 % at 10,000 years and about 98 % at 100,000 years with the alternate interpretation, and the fraction is about 85 % at 10,000 years and about 93 % at 100,000 years with the earlier interpretation.

5.8   SUMMARY AND RECOMMENDATION

Current design concept for the potential repository employs a robust waste package design and other defense-in-depth EBS components. The waste package is the primary EBS component and one of the major components in the current waste isolation and containment strategy (Younker, 1995). A detailed stochastic waste package performance simulation model has been developed for TSPA-1995, and the stochastic simulation model incorporates the following five individual corrosion models: 1) humid-air general corrosion model (including uncertainty) for the carbon steel corrosion-allowance outer barrier; 2) stochastic humid-air pitting corrosion model for the

carbon steel outer barrier; 3) aqueous general corrosion model (including uncertainty) for the carbon steel outer barrier; 4) stochastic aqueous pitting corrosion model for the carbon steel outer barrier; and 5) aqueous pitting corrosion model (including pit growth rate distribution) for the Alloy 825 corrosion-resistant inner barrier. The humid-air and aqueous corrosion models for the carbon steel outer barrier were developed for TSPA-1995 from the literature data. The same elicitation for time-independent pit growth rates for Alloy 825 as used in TSPA-1993 was utilized to model aqueous pitting corrosion of the corrosion-resistant inner barrier. The uncertainties in the individual corrosion models were incorporated to capture the variability in the corrosion degradation among waste packages and among pits in the same waste package.

Within the scope of assumptions employed in the simulations, the corrosion modes considered, and the near-field conditions from the drift-scale thermal-hydrologic model, the results of the waste package performance analyses show that the current waste package design appears to meet the 'controlled design assumption' requirement on waste package performance, which is currently defined as having less than 1 % of waste packages breached at 1,000 years (M&O, 1995c). Breach of waste package is defined here as having at least one pit penetration. Since a quantitative definition of the substantially complete containment requirement, as referred in the NRC subsystem requirement (10 CFR 60.113) has not been decided, the (tentative) 'controlled design assumption' requirement has been employed throughout the analyses of the waste package degradation simulations in this study.

Another important finding is the significant impact on waste package performance of cathodic protection of the corrosion-resistant Alloy 825 inner barrier by the corrosion-allowance carbon steel outer barrier. One reservation in interpreting the simulation results is that the measure used to account for the inner barrier cathodic protection in the current simulation model is semi-quantitative in nature. With the cathodic protection measure incorporated, it has been shown cathodic protection may be able to provide additional several thousand years in waste package performance, compared to the case without cathodic protection. The cathodic protection measure should be further improved and substantiated for future waste package performance analysis.

It has been pointed out throughout the analyses of the simulation results that pitting corrosion of the corrosion-resistant inner barrier is the major mechanism that controls the failure of waste packages and their subsequent degradation. The current aqueous pitting corrosion model for the inner barrier is from an expert elicitation, not based on a reasonably complete set of experimental data or detailed systematic analyses, and the model is expressed as a function of exposure temperature only. The inner barrier pitting corrosion model should be improved and substantiated in future waste package performance analyses. Other important parameters that need to be included in the inner barrier pitting corrosion model would be the effects of near-field chemical environments and exposure time. It has been reported that localized corrosion such as pitting and stress corrosion cracking are interrelated because the sites of localized corrosion attack become the sources of initiation of stress corrosion cracking (Farmer and McCright, 1989; Farmer, et al., 1989). Thus, synergistic effects of pitting and other localized corrosion combined with stress corrosion cracking need to be included in future waste package performance analyses. Additionally, the effects of microbiologically influenced corrosion on waste package performance should also be included.

Currently, alternative thermal-hydrologic models are being used by M&O Performance Assessment Group and Lawrence Livermore National Laboratory. It has been stressed that very different predictions of waste package performance are obtained depending on which drift-scale thermal-hydrologic model is chosen to calculate the near-field (drift-scale) conditions. Also, the two currently available thermal-hydrologic models have significant uncertainties in their conceptual models and the thermal-hydraulic properties of the geologic materials. Differences between the two models should be resolved, and the uncertainties in the thermal-hydraulic properties should be reduced, so that a more consistent representation on the near-field environments is provided for future waste package performance assessment.

Table 5.3-1 . Corrosion Current Density of Iron at Different Humidities at 25 °C in Static and Dynamic Air Conditions and General Corrosion Rates Calculated from the Corrosion Current Density Data.

Relative Humidity (%)	Corrosion Current Density[1] (amp/cm^2)		General Corrosion Rate[2] ($\times$ 10^{-6} m/yr or μm/yr)	
	Static Air	Dynamic Air	Static Air	Dynamic Air
52	3.0×10^{-10}	3.0×10^{-10}	0.0035	0.0035
64	1.3×10^{-9}	2.7×10^{-7}	0.0151	3.1350
76	3.4×10^{-9}	3.3×10^{-7}	0.0395	3.8320
86	6.7×10^{-9}	6.1×10^{-7}	0.0778	7.0840
100	8.7×10^{-6}	2.7×10^{-5}	101.0260	313.5300

[1] Read from graphs (Jones and Howryla, 1993).
[2] Calculated using Equation (5.3-16).

Table 5.5-1. Elicitation of 'Constant' Pit Growth Rate Distribution for the Alloy 825 Inner Barrier[1]

Growth Condition	Temperature = 70 °C		Temperature = 100 °C	
	Mean Growth Rate (mm/yr)	95th Percentile Growth Rate (mm/yr)	Mean Growth Rate (mm/yr)	95th Percentile Growth Rate (mm/yr)
Low Growth Rate	0.0001	0.001	0.01	0.1
Median Growth Rate	0.001	0.01	0.1	1.0
High Growth Rate	0.01	0.1	1.0	10.0

[1] Source: Andrews, et al (1994).

INFORMATION

Site Biosphere → 8

Site Geology → 7

Site Hydrology → 6

Site Geochemistry → 5

Repository Design → 4

Waste Package Design → 3

Material Properties → 2

Waste Form Properties → 1

5-42

PROCESS-LEVEL MODEL

7 → 6 → Saturated Zone Flow Model

7 → 6 → Unsaturated Zone Flow Model

7 → 6 → 4 → 3 → Drift-Scale Thermo-Hydrologic Model

3 → 2 → Waste Package Degradation Model

PROCESS-LEVEL MODEL ABSTRACTIONS

Response surface of saturated zone flux → E

Response surface of unsaturated zone flux
- fracture flux
- matrix flux
→ D

Response surface of drift-scale flux
- % packages with drips
- advective flux in drips
→ C

Response surface of
- temperature
- humidity
- liquid saturation
→ B

Response surface of
- first pit
- pit distribution
→ A

TOTAL SYSTEM PERFORMANCE ASSESMENT

Biosphere Transport -Dose

8

Geosphere Transport -Cumulative Release

D E 5 6 7

EBS Transport -Release Rate

B C 5 4 3 2 1

Waste Package Degradation -Containment

A

Figure 5.1-1   Relationship of Chapter 5 to the Overall Information Flow Diagram for TSPA 1995 (Figure 1.4-6)

Fraction Time for RH ≥ 70 % vs Average RH
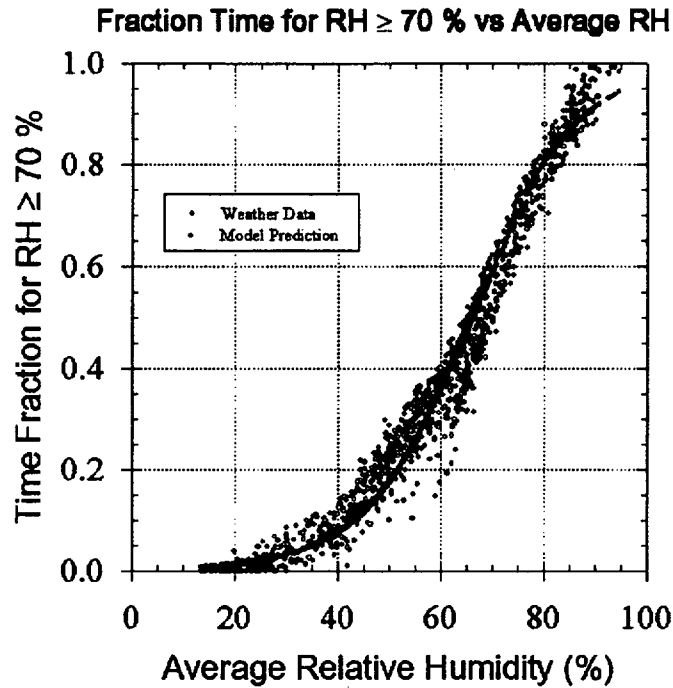
Figure 5.3-1 Weather data and model predictions of the fraction of time for RH ^{3} 70 % as a function of average relative humidity.

General Corrosion of CAM in Humid Air
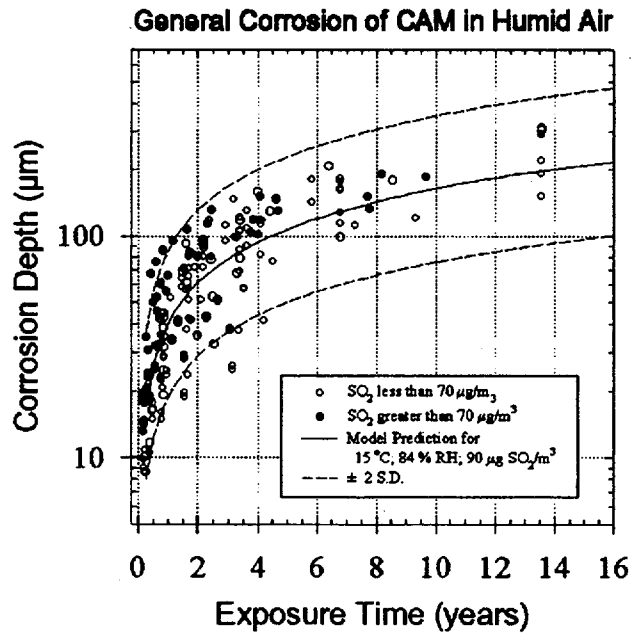
Figure 5.3-2 Atmospheric general corrosion data and the model prediction for corrosion allowance materials.
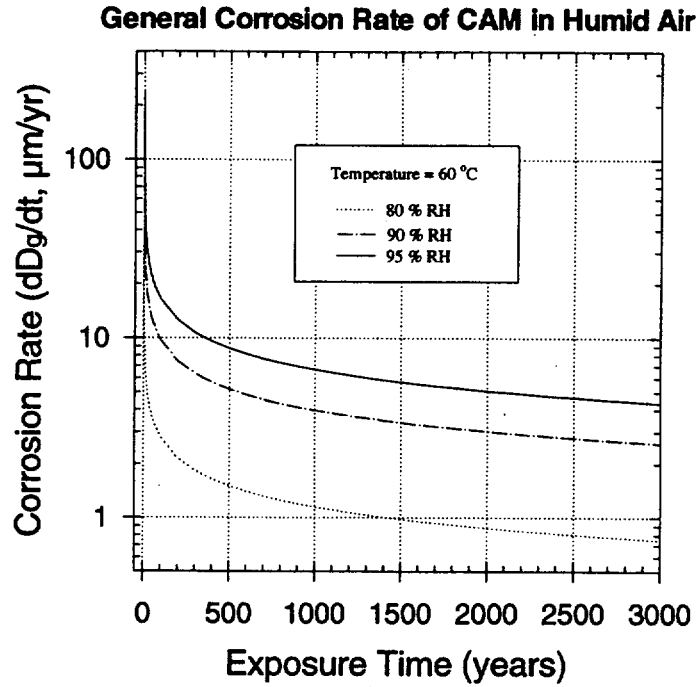
Figure 5.3-3a Model prediction of general corrosion rates of CAM in humid-air as a function of exposure time in humid-air at different humidities at 60 °C.
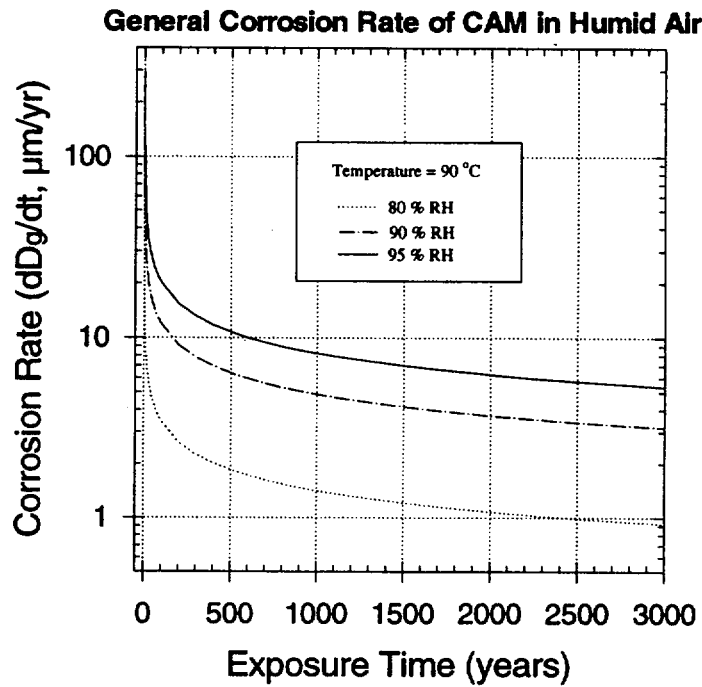
Figure 5.3-3b Model prediction of general corrosion rates of CAM in humid-air as a function of exposure time in humid-air at different humidities at 90 °C.

General Corrosion Rate of CAM in Humid Air
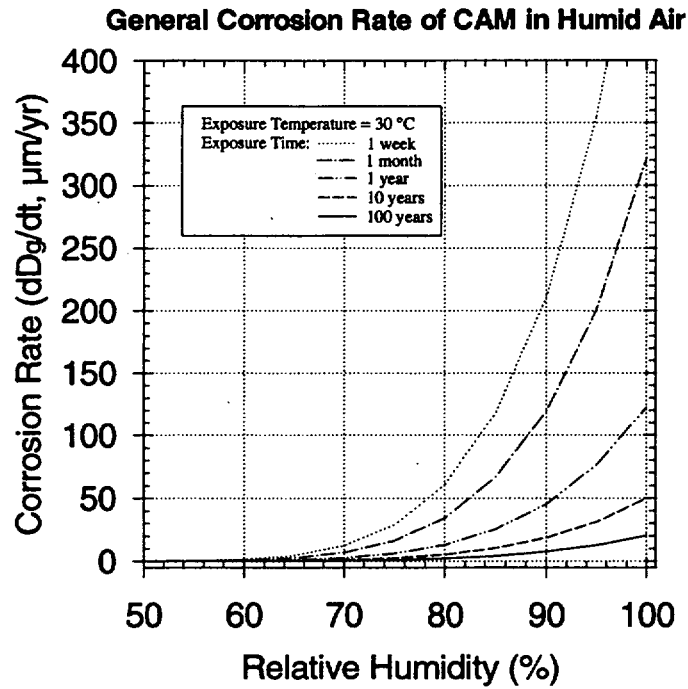
Figure 5.3-4a Model prediction of general corrosion rates of CAM in humid-air as a function of relative humidity at 30 °C and different exposure times. No SO_2 effect.

General Corrosion Rate of CAM in Humid Air
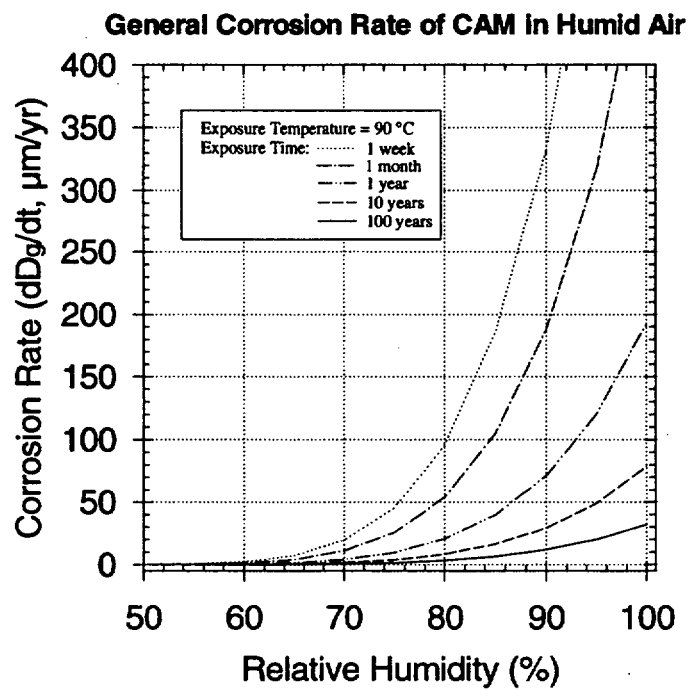
Figure 5.3-4b Model prediction of general corrosion rates of CAM in humid-air as a function of relative humidity at 90 °C and different exposure times. No SO_2 effect.

General Corrosion Rate of CAM in Humid Air
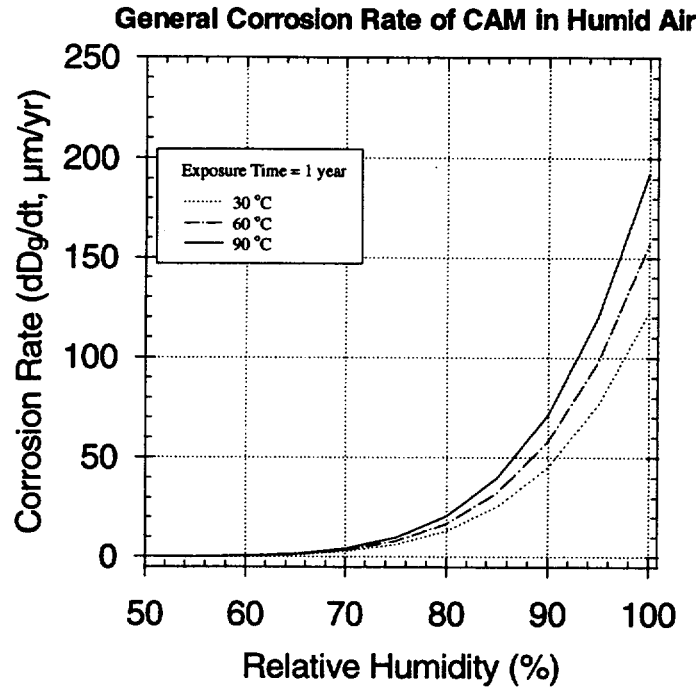
Figure 5.3-5 — Model prediction of general corrosion rate of CAM in humid-air as a function of relative humidity at different exposure temperatures after one year exposure.

General Corrosion Rate of CAM in Humid Air
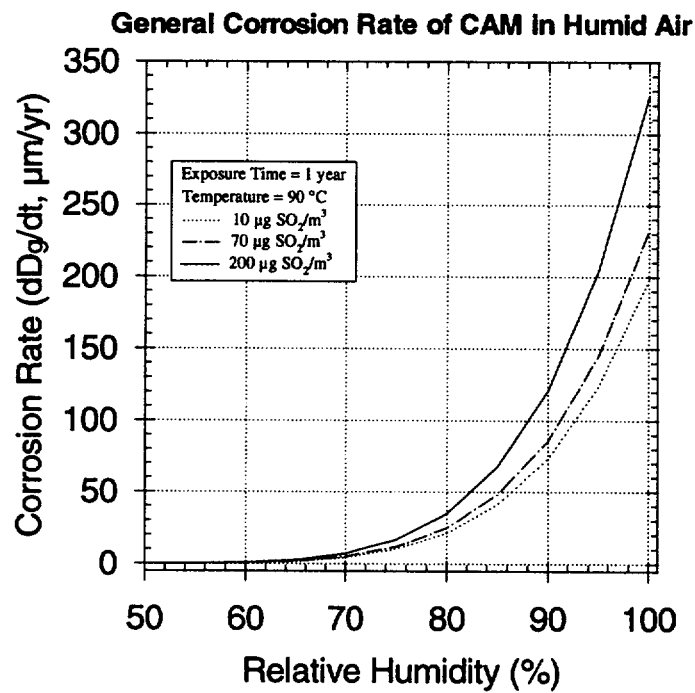
Figure 5.3-6 — Model prediction of general corrosion rates of CAM in humid-air as a function of relative humidity at different SO_2 levels in the air after one year exposure at 90 °C.

General Corrosion of CAM
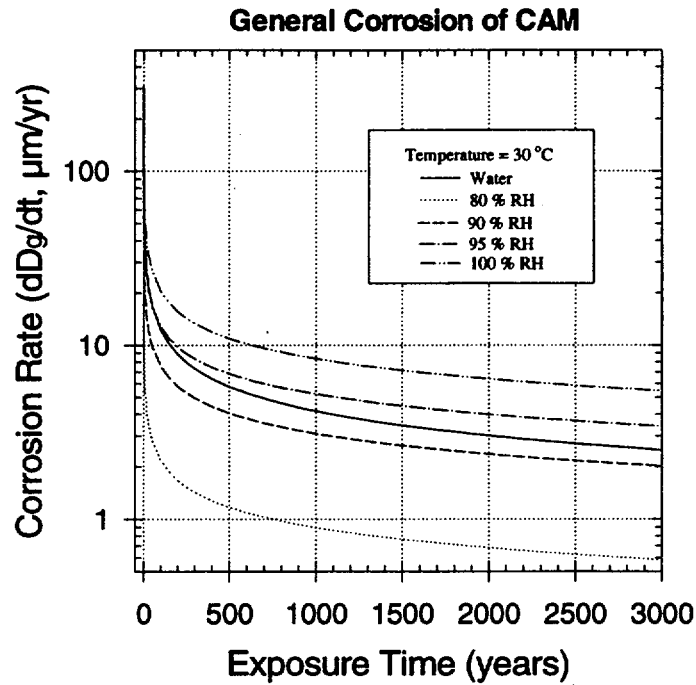
Figure 5.3-7a Comparison of model prediction of general corrosion rates of CAM in humid-air at different humidities and in water at 30 °C.

General Corrosion of CAM
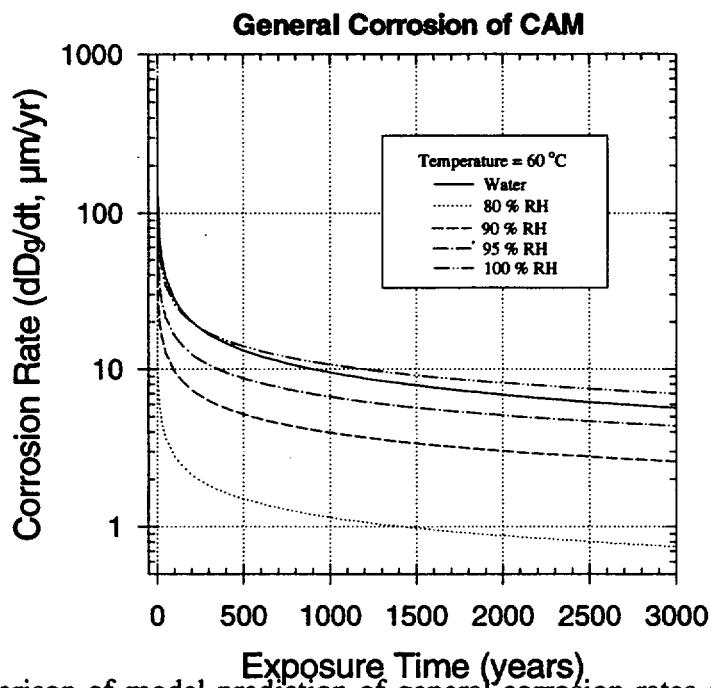
Figure 5.3-7b Comparison of model prediction of general corrosion rates of CAM in humid-air at different humidities and in water at 60 °C.

General Corrosion of CAM

Temperature = 90 °C
— Water
········ 80 % RH
--- 90 % RH
-·- 95 % RH
-··- 100 % RH
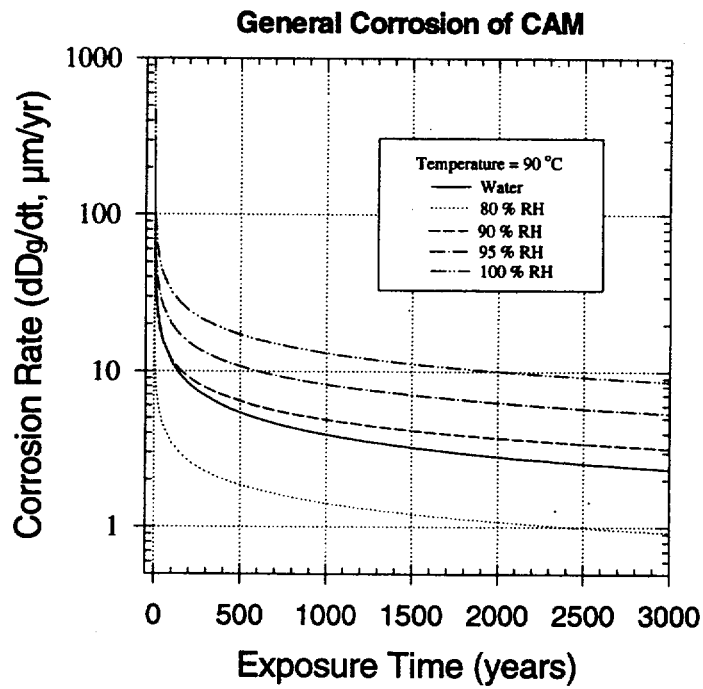
Figure 5.3-7c Comparison of model prediction of general corrosion rates of CAM in humid-air at different humidities and in water at 90 °C.
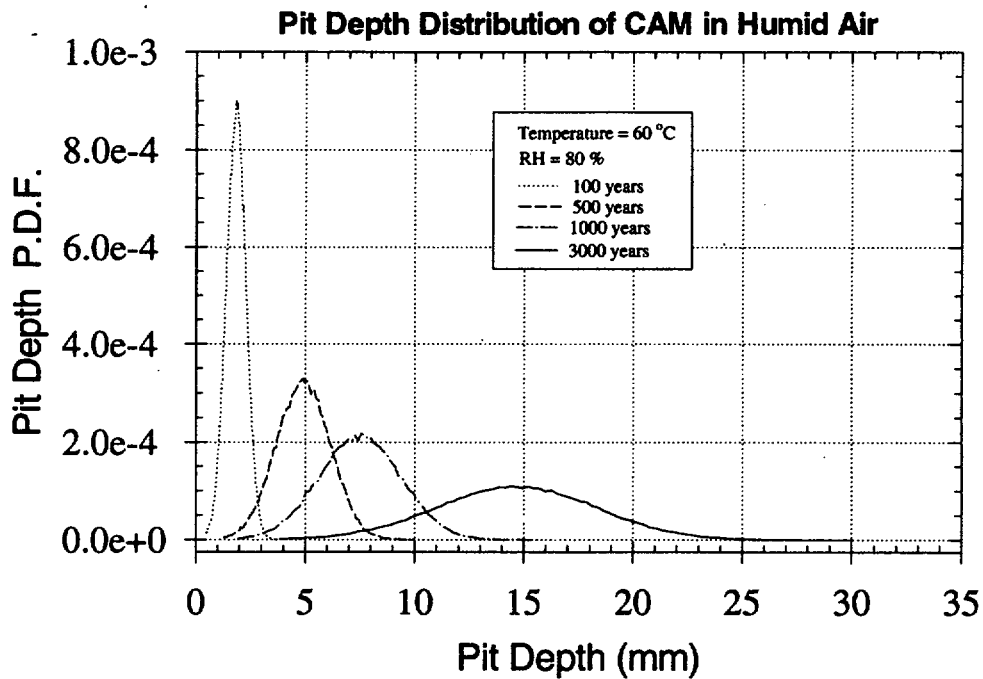
Figure 5.3-8a Model prediction of probability density functions (PDFs) of pit depth distribution of CAM in humid-air after different exposure times at 60 °C and 80 % RH.
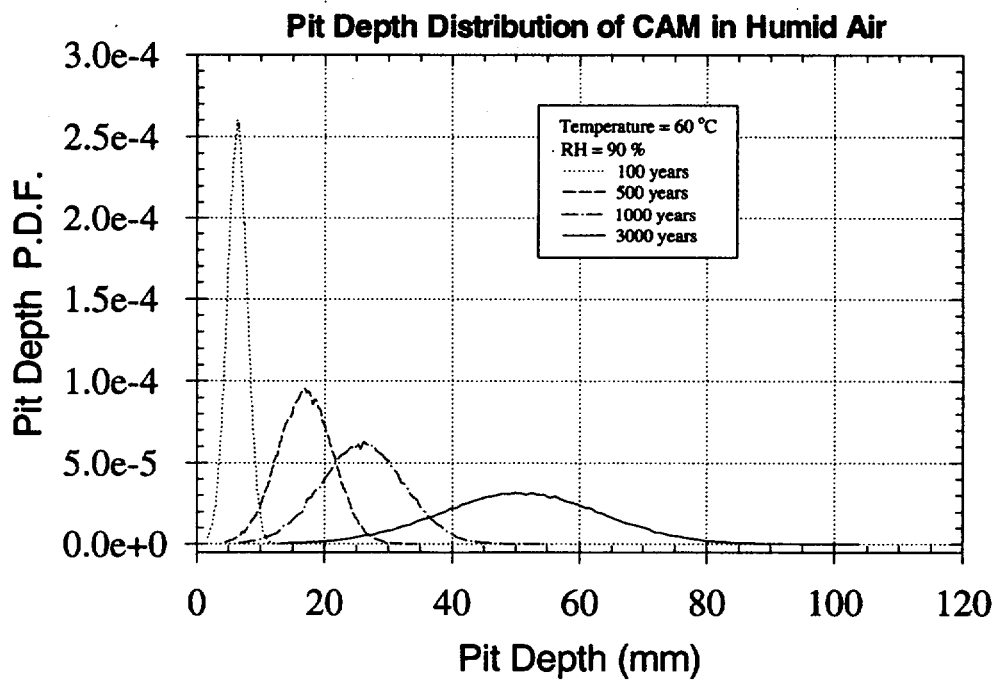
Figure 5.3-8b Model prediction of probability density functions (PDFs) of pit depth distribution of CAM in humid-air after different exposure times at 60 °C and 90 % RH.
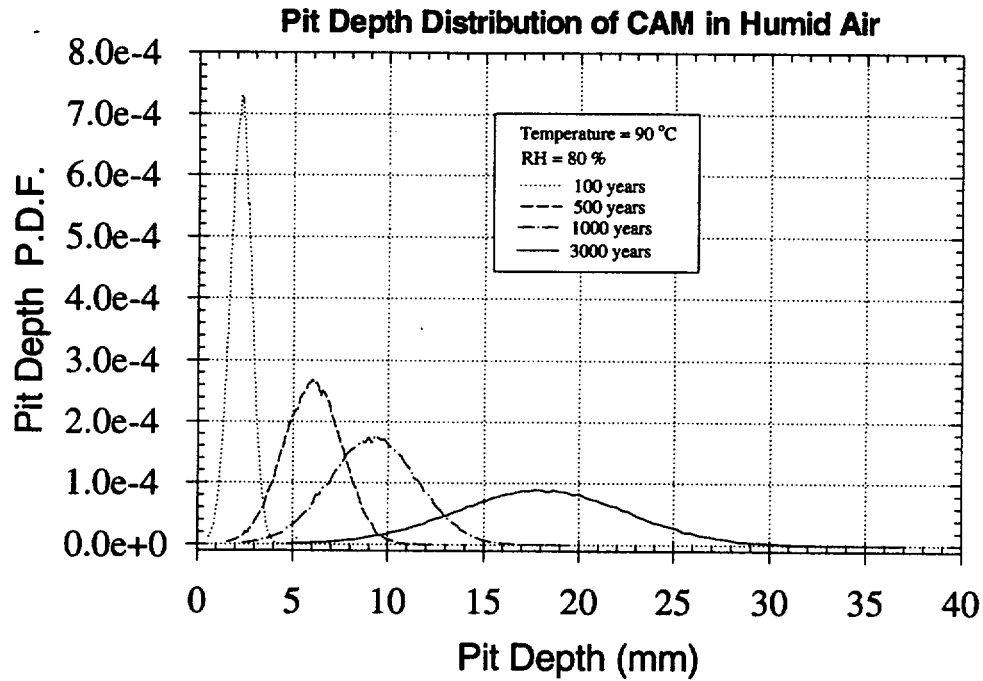
Figure 5.3-9a Model prediction of probability density functions (PDFs) of pit depth distribution of CAM in humid-air after different exposure times at 90 °C and 80 % RH.
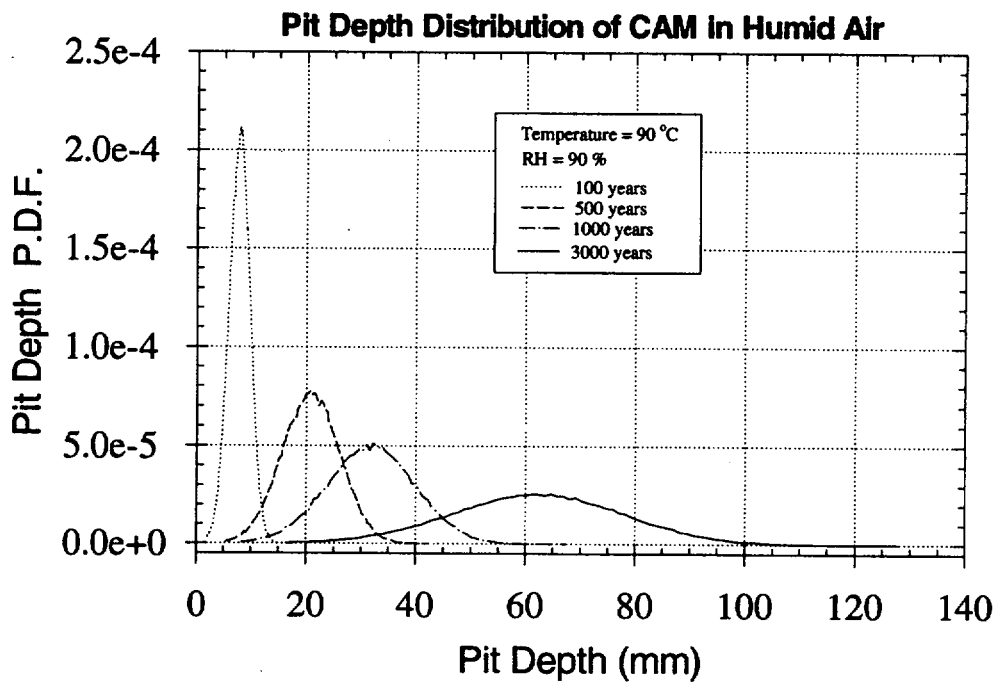
Figure 5.3-9b Model prediction of probability density functions (PDFs) of pit depth distribution of CAM in humid-air after different exposure times at 90 °C and 90 % RH.
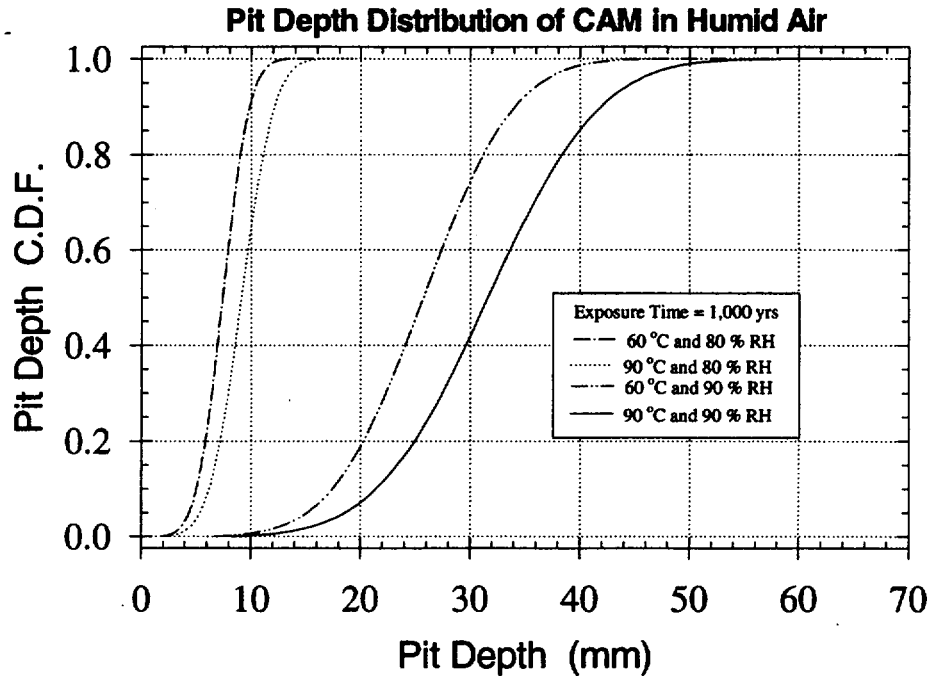
Figure 5.3-10a   Model prediction of cumulative density functions (CDFs) of pit depth distribution of CAM in humid-air at different temperatures and humidities after 1,000-year exposure.
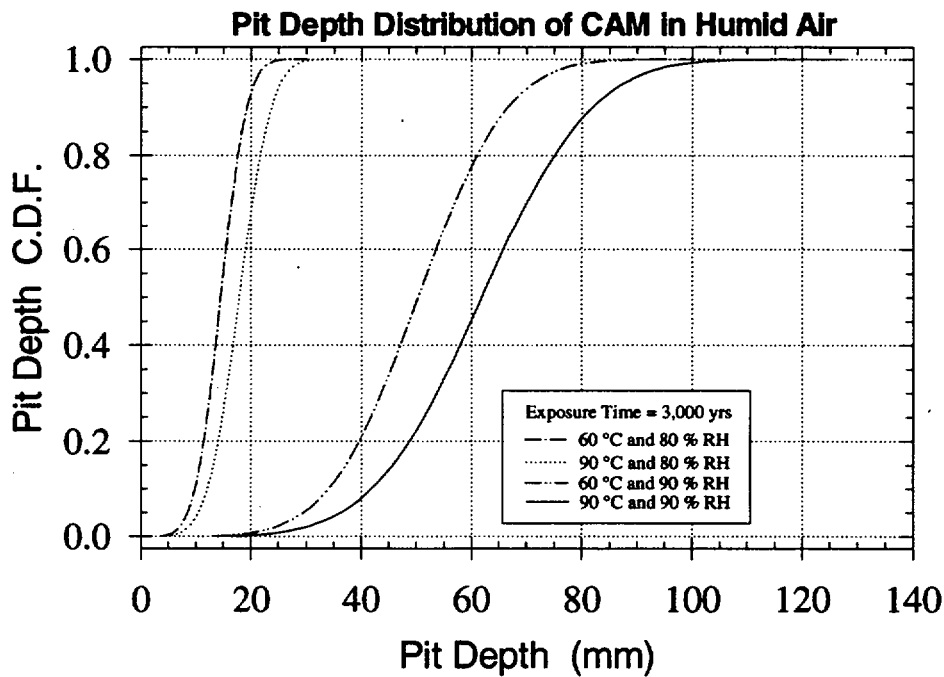
Figure 5.3-10b   Model prediction of cumulative density functions (CDFs) of pit depth distribution of CAM in humid-air at different temperatures and humidities after 3,000-year exposure.
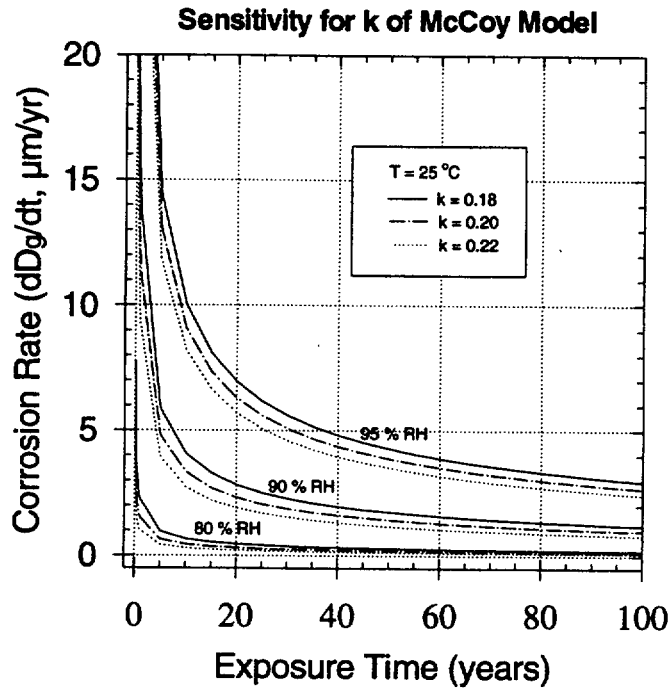
Figure 5.3-11 Sensitivity of constant k of the McCoy model in humid-air at 25 °C.
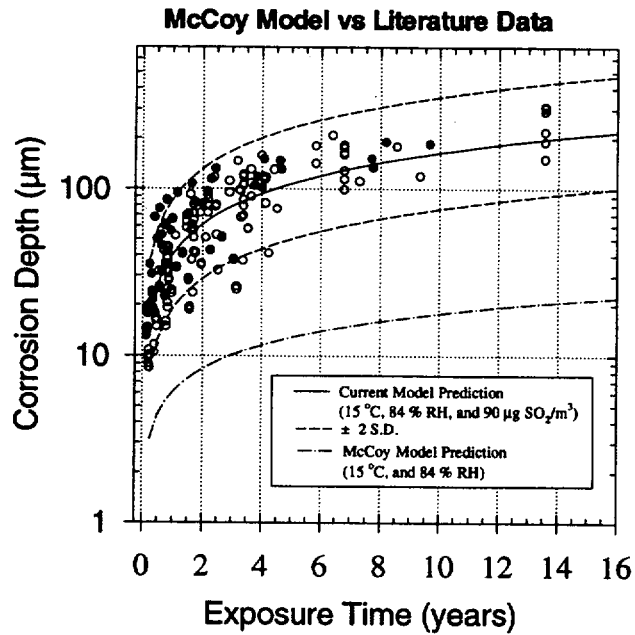
Figure 5.3-12 Comparison of the McCoy model prediction of general corrosion depth of
CAM in humid-air with the atmospheric corrosion data from literature.
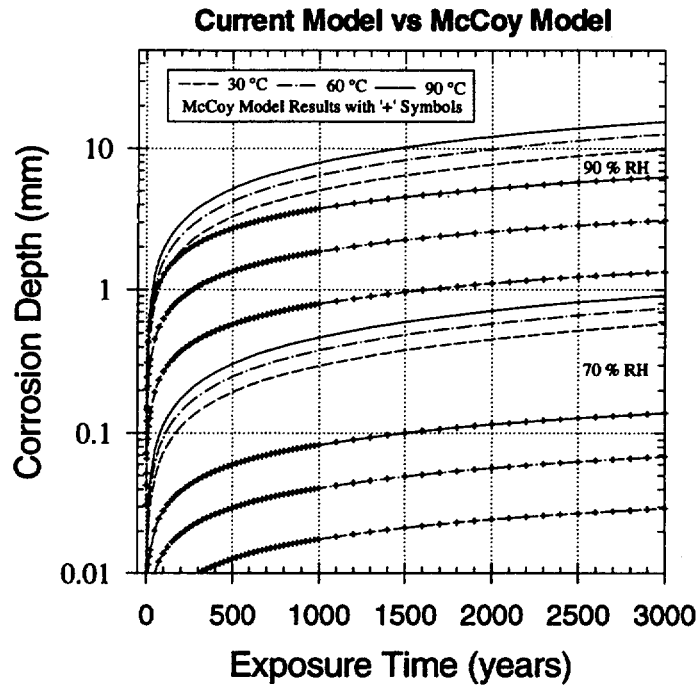
Figure 5.3-13 Comparison of the current model predictions for long-term general corrosion depth of CAM in humid-air with those of the McCoy model.
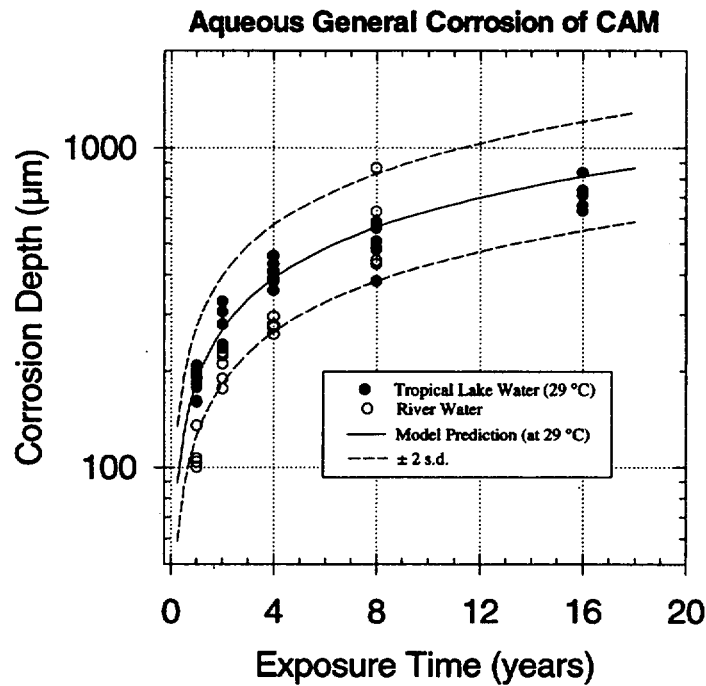
Figure 5.4-1 General corrosion data of CAM in tropical lake water and polluted river water, and the model prediction with the uncertainty.
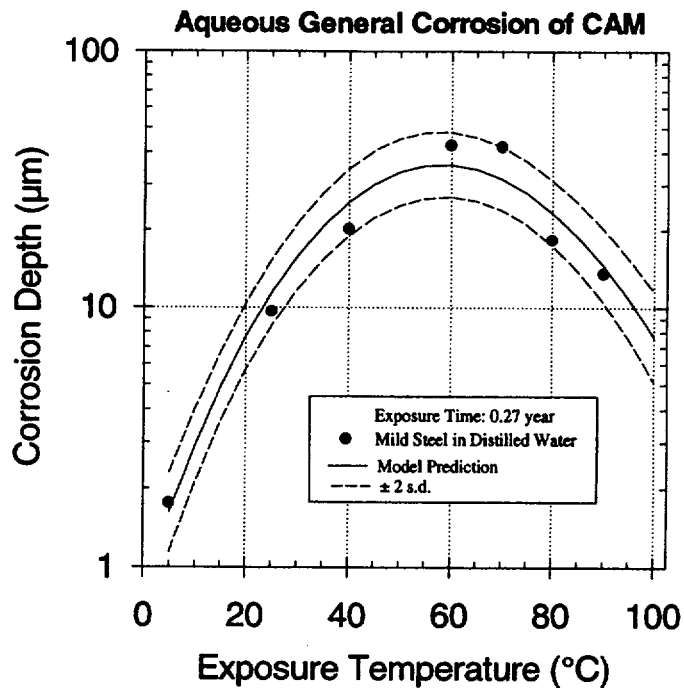
Figure 5.4-2 Temperature-dependent general corrosion data of mild steel in distilled water, and the model prediction with the uncertainty.
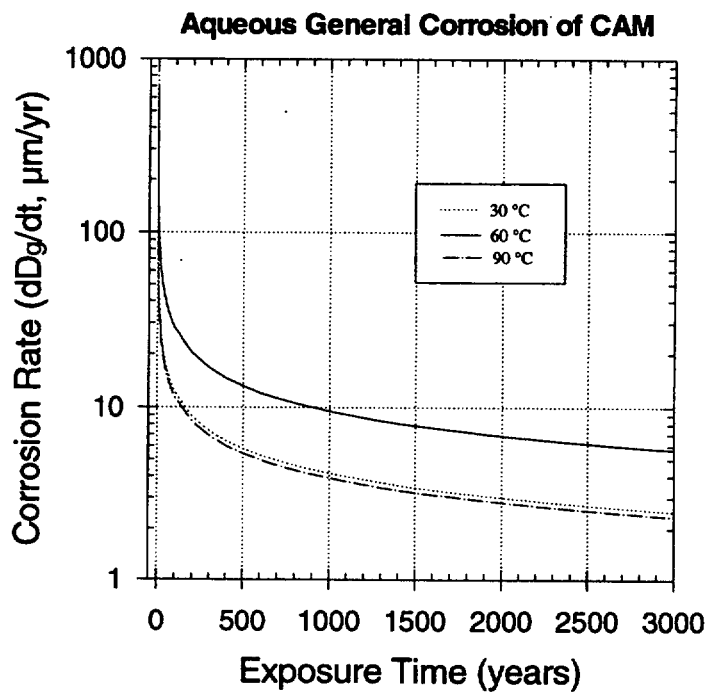
Figure 5.4-3 Model prediction of aqueous general corrosion rates as a function of exposure time at different temperatures.
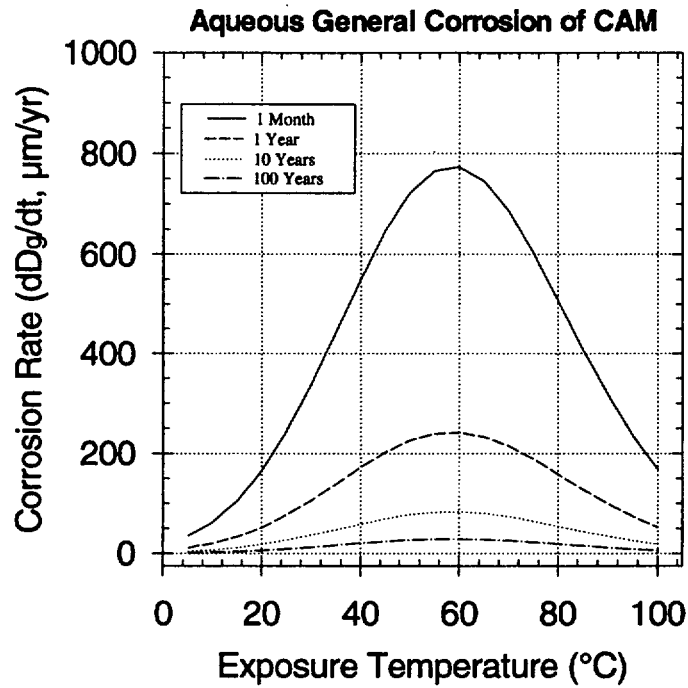
Figure 5.4-4 Model prediction of aqueous general corrosion rates as a function of temperature at different exposure times.
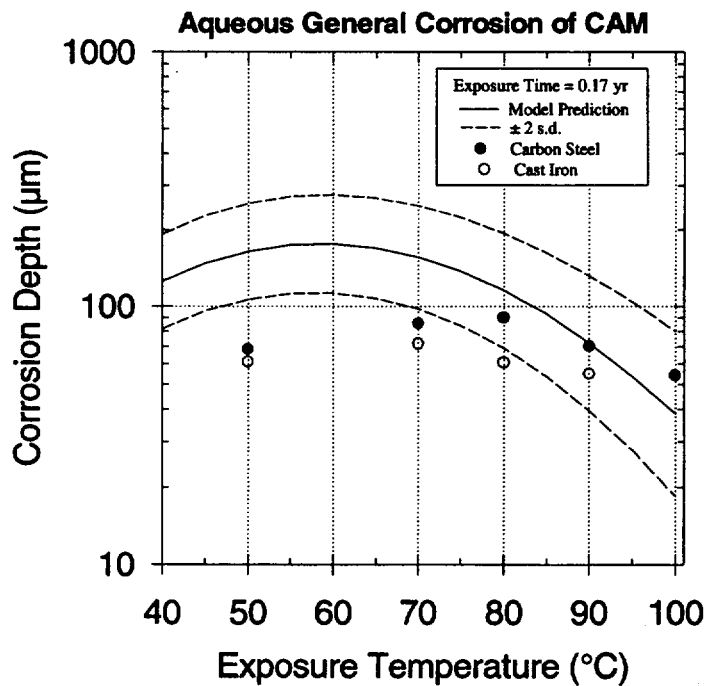
Figure 5.4-5 Comparison of model prediction of aqueous general corrosion of CAM at different temperatures with the data in J-13 water. The J-13 water data are from McCright and Weiss (1985).
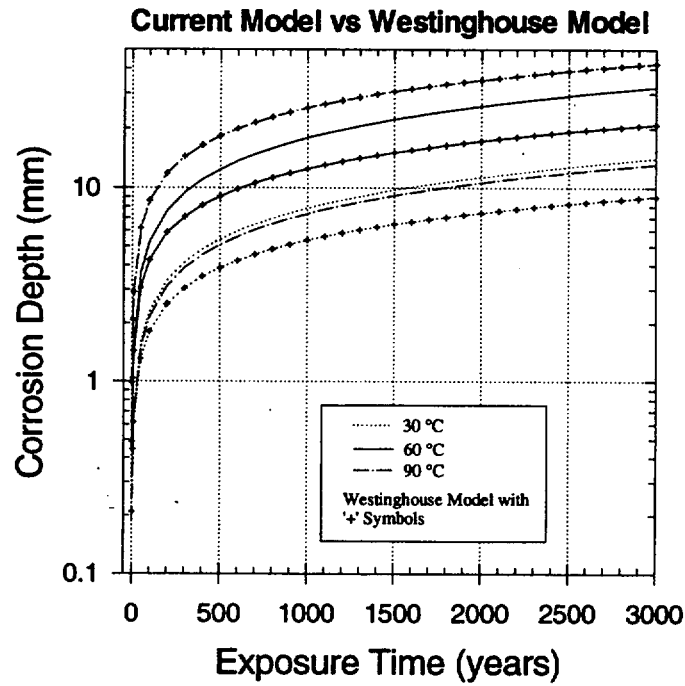
Figure 5.4-6 Comparison of the current model prediction of aqueous general corrosion of CAM with the Westinghouse model at different temperatures
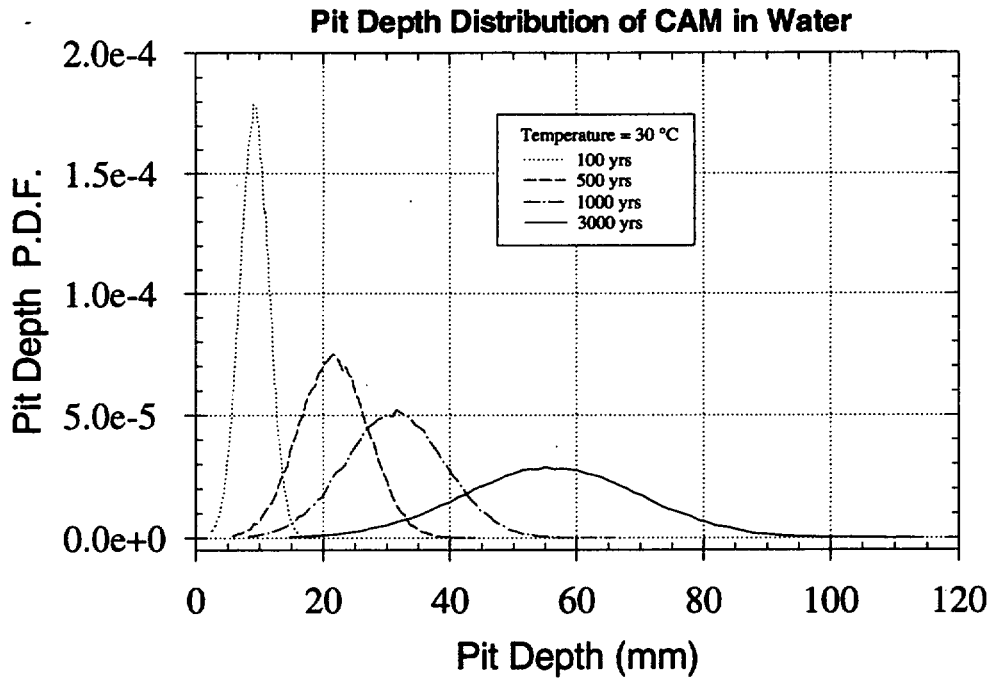
Figure 5.4-7a Model prediction of probability density functions (PDFs) of pit depth distribution of CAM in aqueous condition after different exposure times at 30 °C.
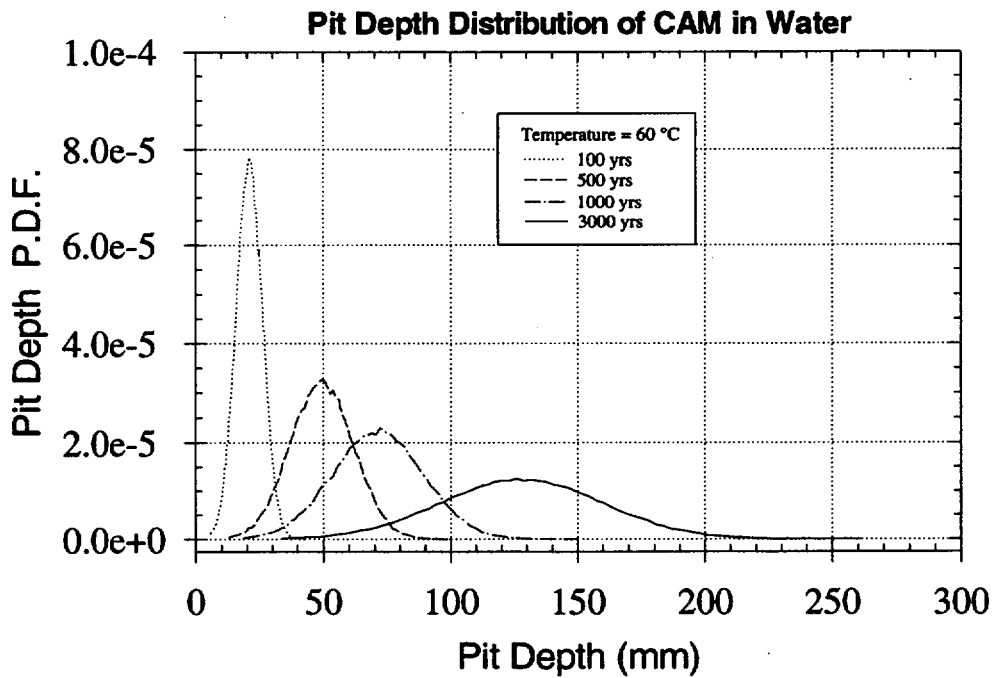
Figure 5.4-7b Model prediction of probability density functions (PDFs) of pit depth distribution of CAM in aqueous condition after different exposure times at 60 °C.

Pit Depth Distribution of CAM in Water
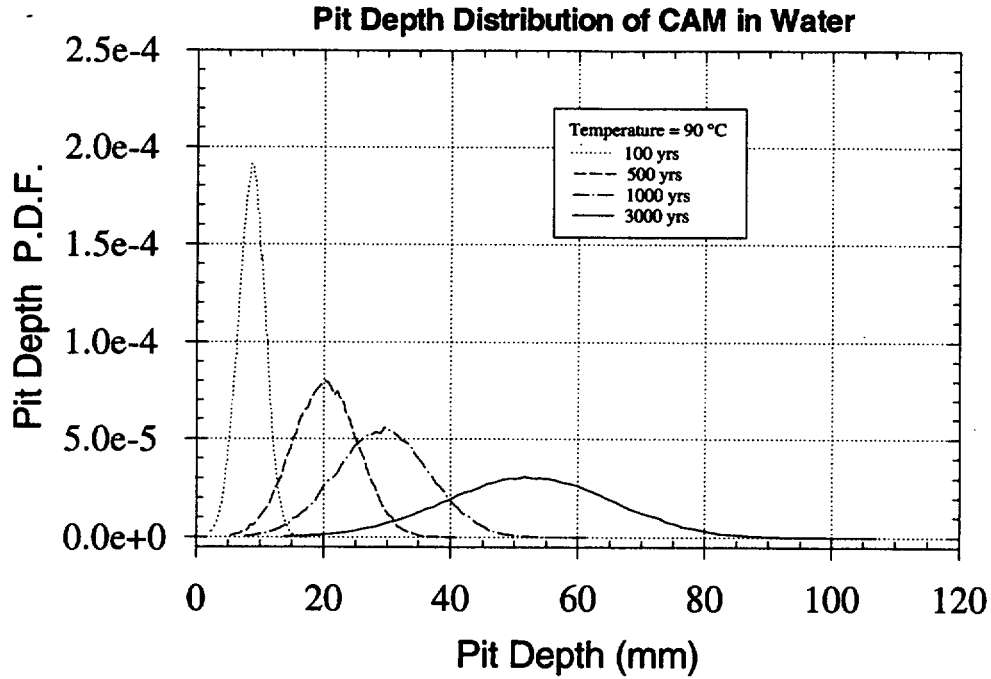
Figure 5.4-7c Model prediction of probability density functions (PDFs) of pit depth distribution of CAM in aqueous condition after different exposure times at 90 °C.

Pit Growth Rate vs Temperature
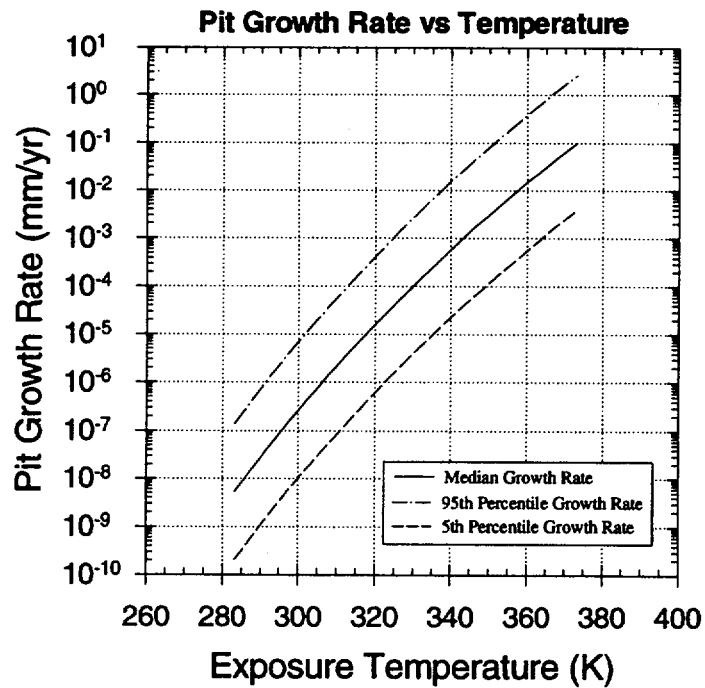
Figure 5.5-1 Elicitation for the distribution of 'constant' pit growth rate in Alloy 825 inner barrier as a function of temperature.

Stochastic Waste Package Performance Simulation Model
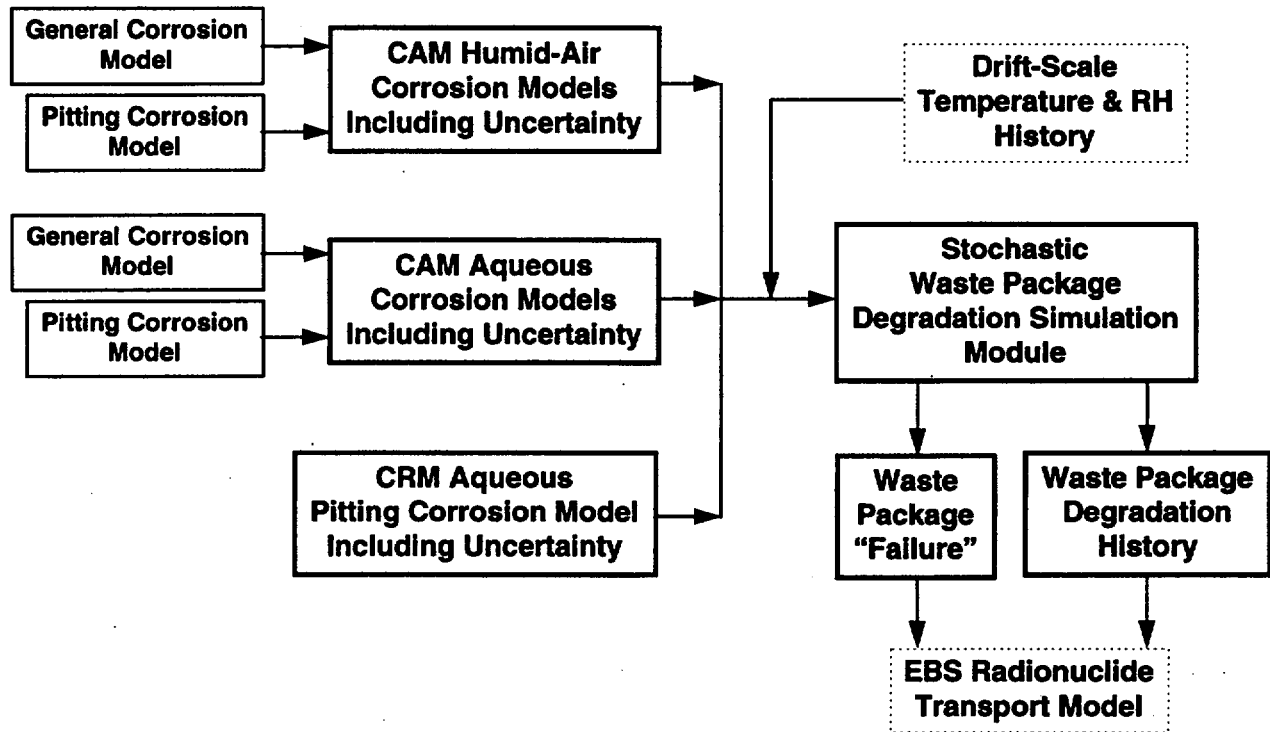
Figure 5.7-1   An overview of the stochastic waste package performance simulation model developed for TSPA-1995.

Select thermal load, backfill,
and infiltration rate.

i=1

**Select waste package
and pit parameters from
normal distributions,
based on estimates of
the model parameters
and their uncertainties**

Sample the expected values for each
parameter for the *i*th waste package

j=1

Sample all of the parameters for the *j*th pit
on the *i*th package.

k=1

**Determine corrosion
rates and when pits
penetrate the waste
package**

Determine corrosion rate and how much
corrosion will occur in the *j*th pit on the
*i*th waste package during the *k*th time step.
(*Go To A*)

B

Has the pit penetrated the package?

Yes

No

Are there more time steps?

Yes

No

Record the time when the pit penetrated the package

Are there more pits?

Yes

No

Are there more packages?

Yes

No

Stop

k=k+1   j=j+1   i=i+1

Figure 5.7-2a Flowchart of the stochastic waste package performance simulation model
developed for TSPA-1995.
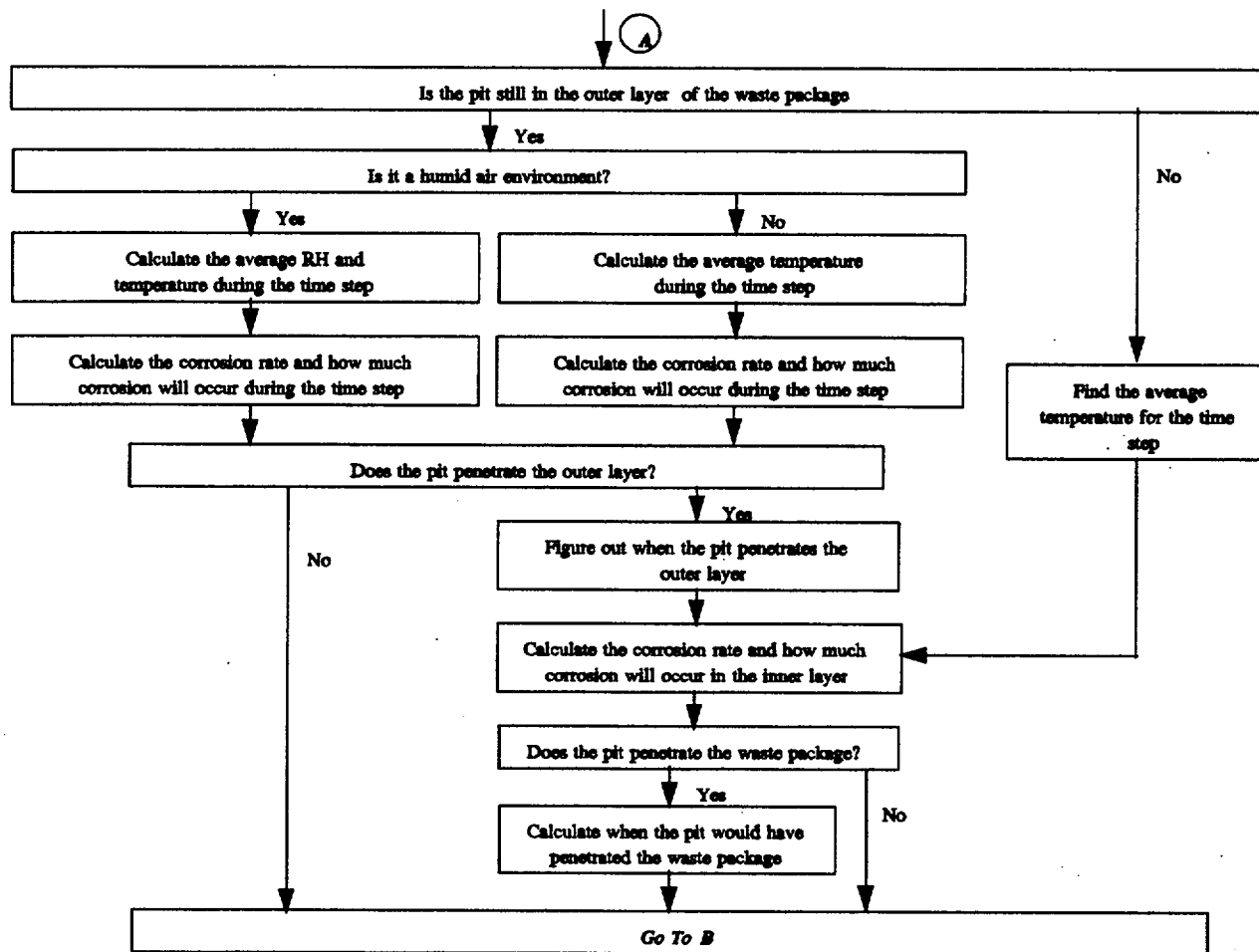
Figure 5.7-2b Flowchart of the stochastic waste package performansimulation model developed for TSPA-1995 (continued).

RH & T Switch; 83 MTU/acre; No Backfill; Low Infiltration
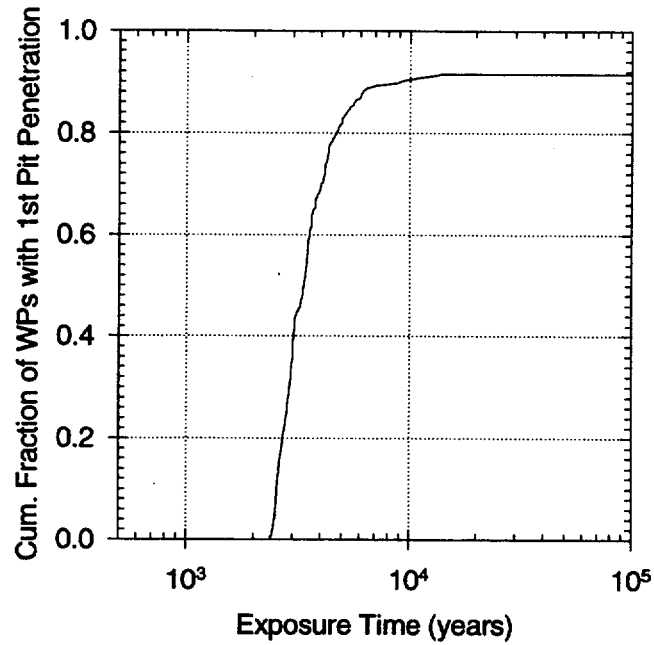
Figure 5.7-3a Waste package failure history for the case of 83 MTU/acre, low infiltration, and without backfill, using RH and temperature switch for corrosion initiation.

RH & T Switch; 83 MTU/acre; No Backfill; Low Infiltration
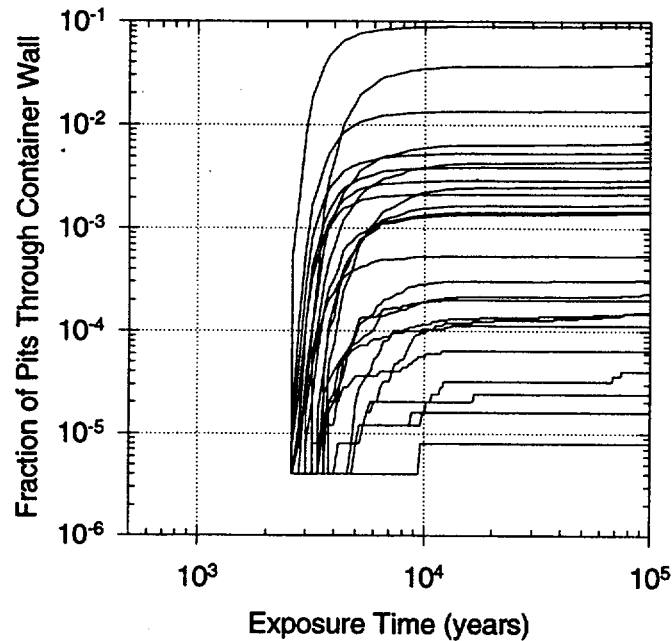
Figure 5.7-3b Representative pitting histories for 25 waste packages for the case of 83 MTU/acre, low infiltration, and without backfill, using RH and temperature switch for corrosion initiation.

RH & T Switch; 83 MTU/acre; No Backfill; Low Infiltration
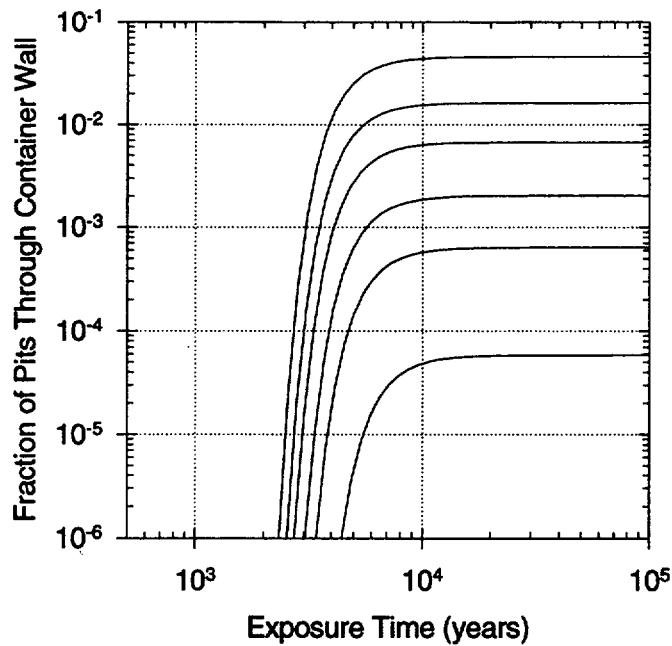
Figure 5.7-3c Abstractions for the RIP implementation for the case of 83 MTU/acre, low infiltration, and without backfill, using RH and temperature switch for corrosion initiation.

RH & T Switch; 83 MTU/acre; No Backfill; High Infiltration
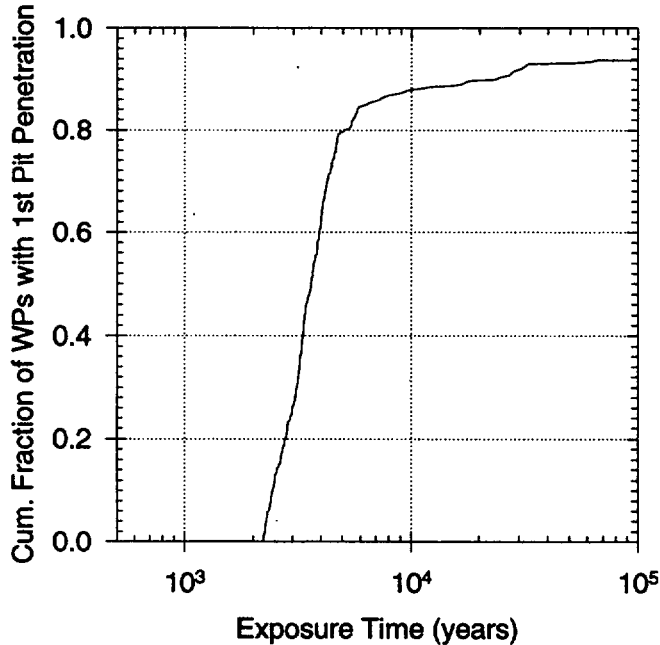
Figure 5.7-4a Waste package failure history for the case of 83 MTU/acre, high infiltration, and without backfill, using RH and temperature switch for corrosion initiation.

RH & T Switch; 83 MTU/acre; No Backfill; High Infiltration
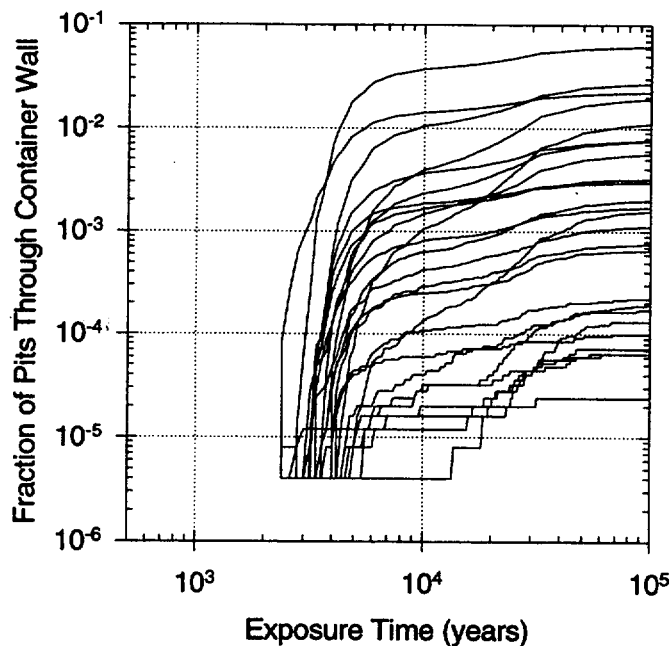
Figure 5.7-4b Representative pitting histories for 25 waste packages for the case of 83 MTU/acre, high infiltration, and without backfill, using RH and temperature switch for corrosion initiation.

RH and T Switch; 83 MTU/acre; No Backfill; High Infiltration
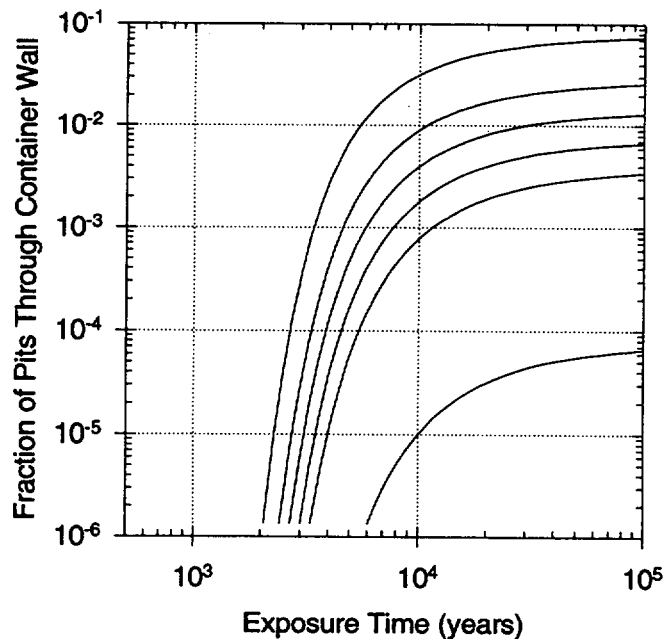
Figure 5.7-4c Abstractions for the RIP implementation for the case of 83 MTU/acre, high infiltration, and without backfill, using RH and temperature switch for corrosion initiation.

RH & T Switch; 83 MTU/acre; Backfill; Low Infiltration
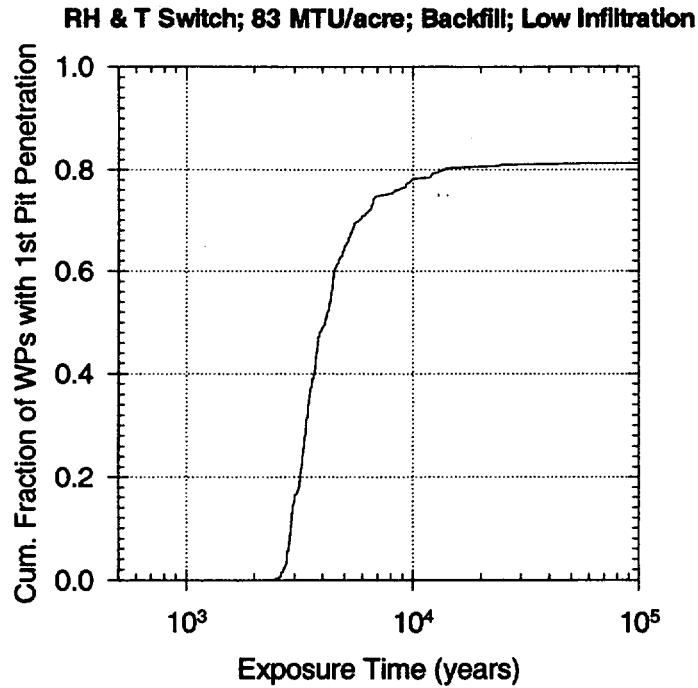
Figure 5.7-5a Waste package failure history for the case of 83 MTU/acre, low infiltration, and with backfill, using RH and temperature switch for corrosion initiation.

RH & T Switch; 83 MTU/acre; Backfill; Low Infiltration
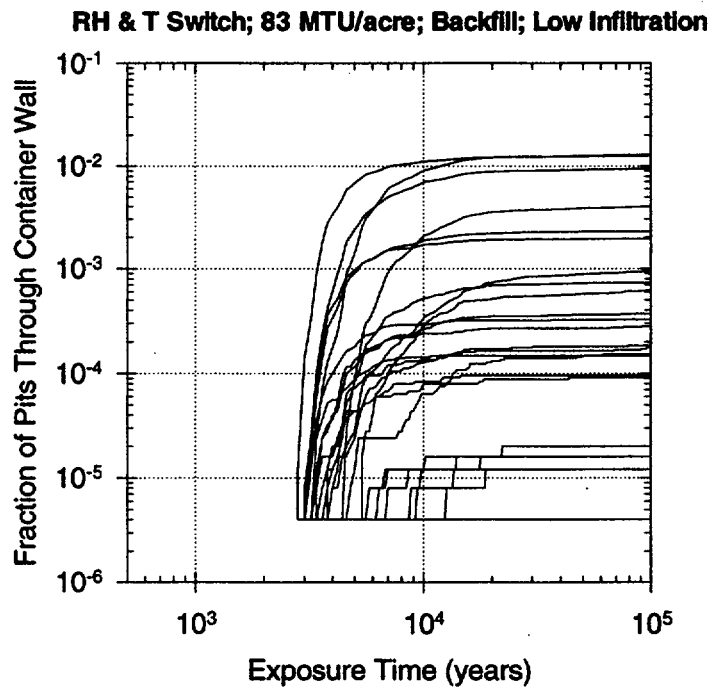
Figure 5.7-5b Representative pitting histories for 25 waste packages for the case of 83 MTU/acre, low infiltration, and with backfill, using RH and temperature switch for corrosion initiation.

RH & T Switch; 83 MTU/acre; Backfill; Low Infiltration
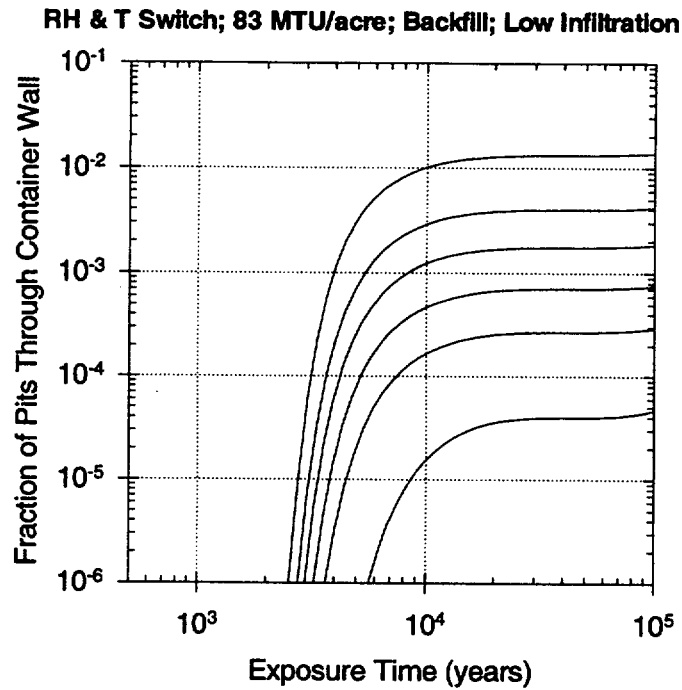
Figure 5.7-5c Abstractions for the RIP implementation for the case of 83 MTU/acre, low infiltration, and with backfill, using RH and temperature switch for corrosion initiation.

RH & T Switch; 83 MTU/acre; Backfill; High Infiltration
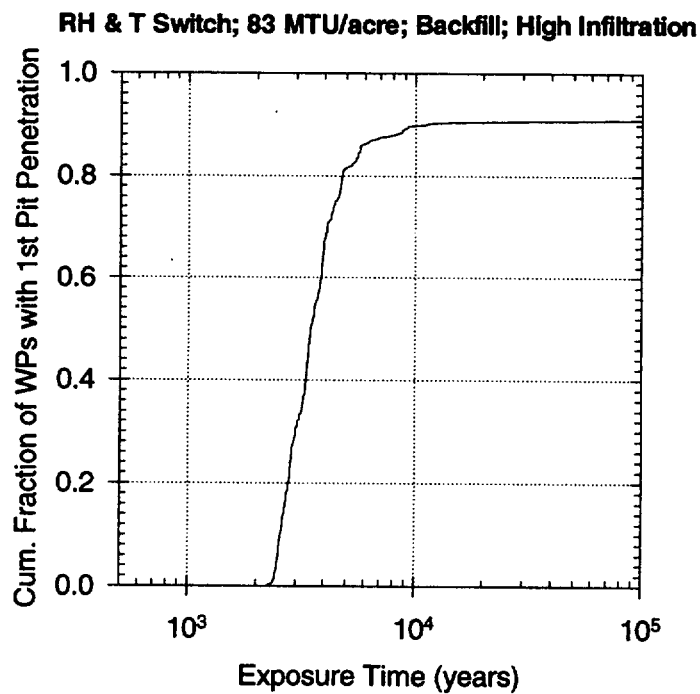
Figure 5.7-6a Waste package failure history for the case of 83 MTU/acre, high infiltration, and with backfill, using RH and temperature switch for corrosion initiation.

5-66

RH & T Switch; 83 MTU/acre; Backfill; High Infiltration
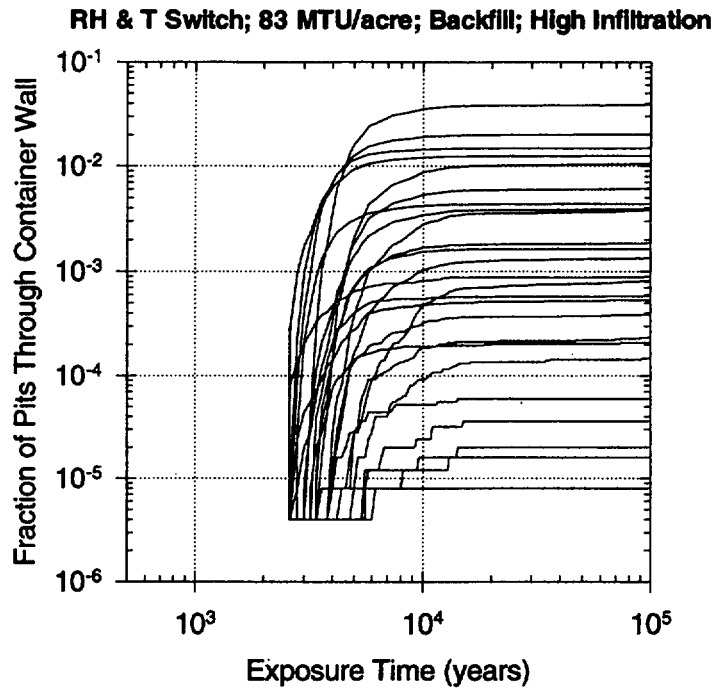
Figure 5.7-6b Representative pitting histories for 25 waste packages for the case of 83 MTU/acre, high infiltration, and with backfill, using RH and temperature switch for corrosion initiation

RH and T Switch; 83 MTU/acre; Backfill; High Infiltration
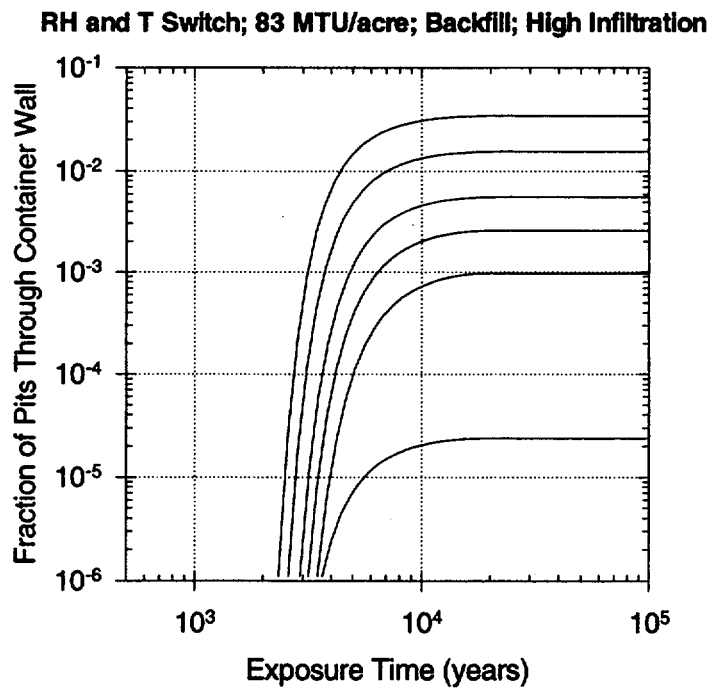
Figure 5.7-6c Abstractions for the RIP implementation for the case of 83 MTU/acre, high infiltration, and with backfill, using RH and temperature switch for corrosion initiation.

RH Switch; 83 MTU/acre; No Backfill; Low Infiltration
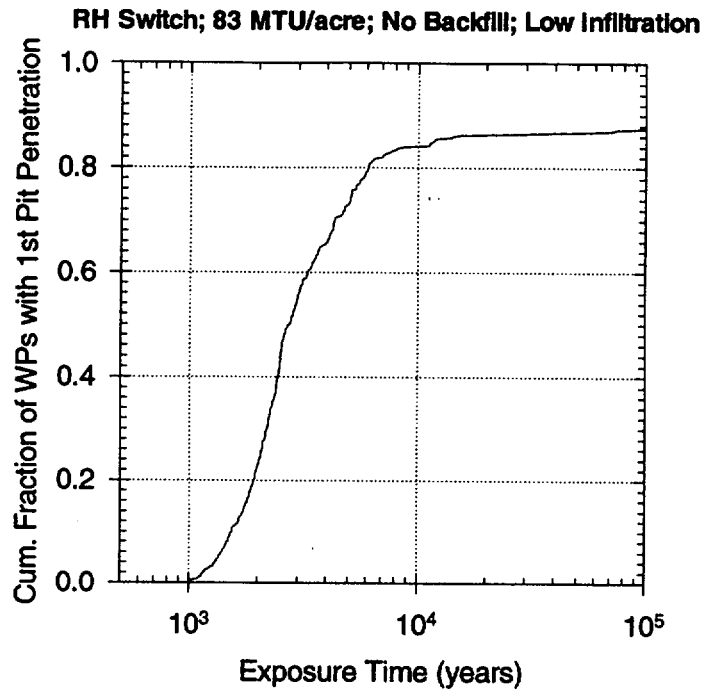
Figure 5.7-7a Waste package failure history for the case of 83 MTU/acre, low infiltration, and without backfill, using RH switch for corrosion initiation.

RH Switch; 83 MTU/acre; No Backfill; Low Infiltration
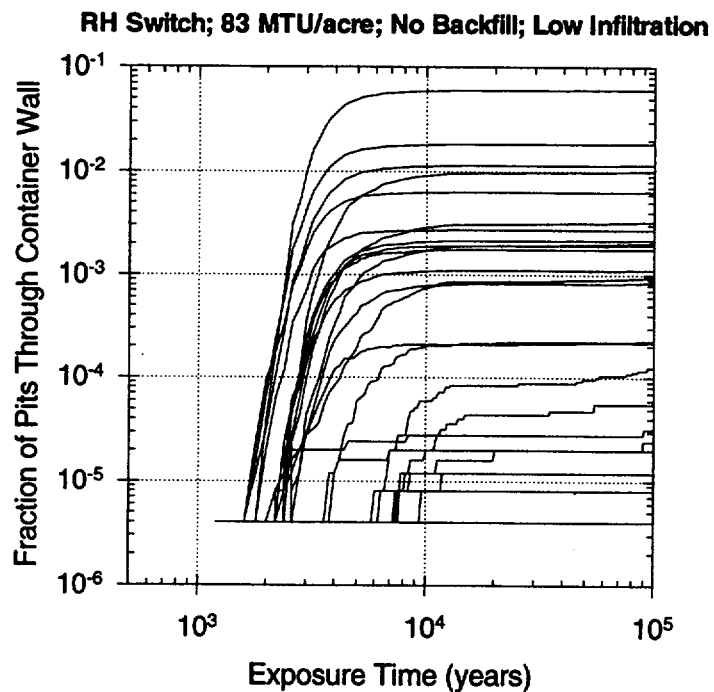
Figure 5.7-7b Representative pitting histories for 25 waste packages for the case of 83 MTU/acre, low infiltration, and without backfill, using RH switch for corrosion initiation.

5-68

RH Switch; 83 MTU/acre; No Backfill; Low Infiltration
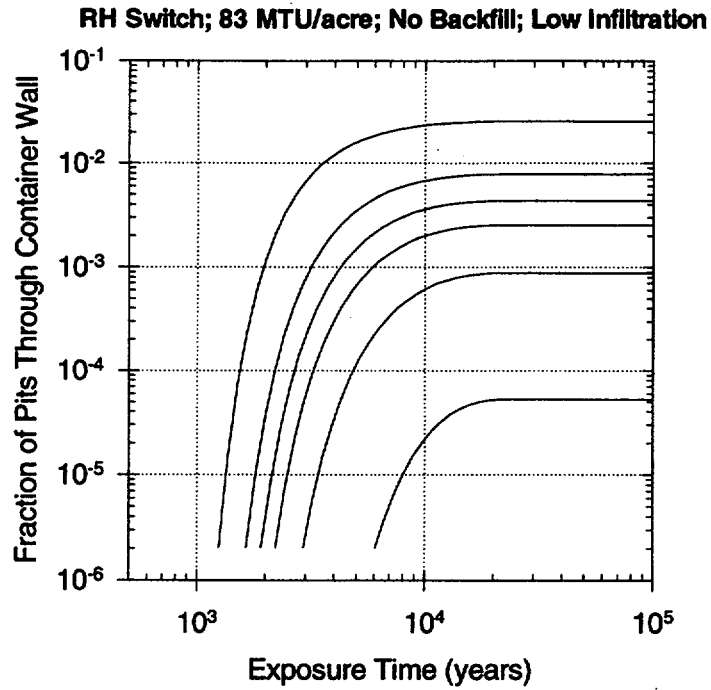
Figure 5.7-7c Abstractions for the RIP implementation for the case of 83 MTU/acre, low infiltration, and without backfill, using RH switch for corrosion initiation.

RH Switch; 83 MTU/acre; No Backfill; High Infiltration
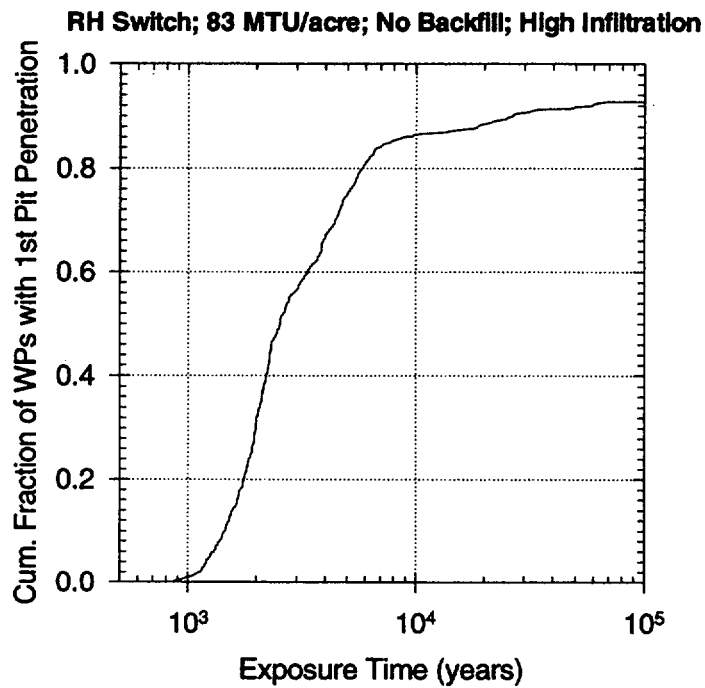
Figure 5.7-8a Waste package failure history for the case of 83 MTU/acre, high infiltration, and without backfill, using RH switch for corrosion initiation.

5-69

RH Switch; 83 MTU/acre; No Backfill; High Infiltration
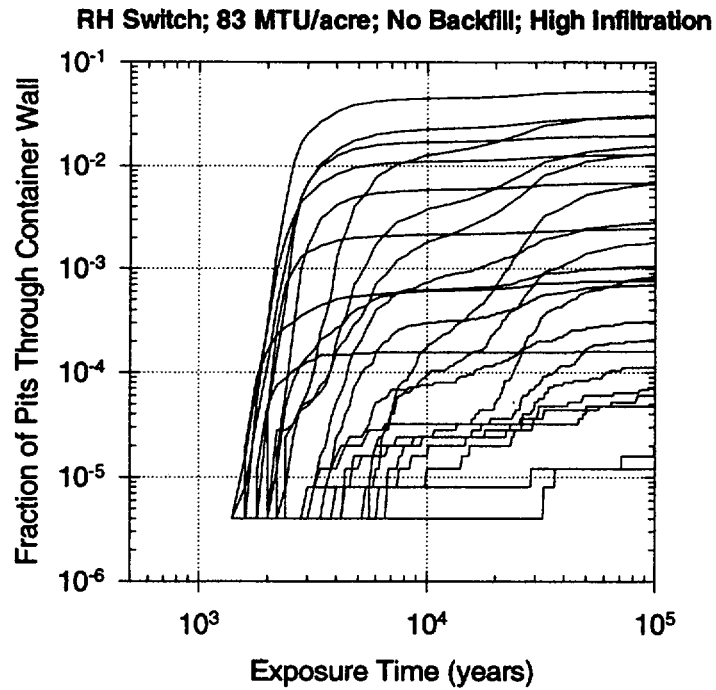
Figure 5.7-8b Representative pitting histories for 25 waste packages for the case of 83
MTU/acre, high infiltration, and without backfill, using RH switch for
corrosion initiation.

RH Switch; 83 MTU/acre; No Backfill; High Infiltration
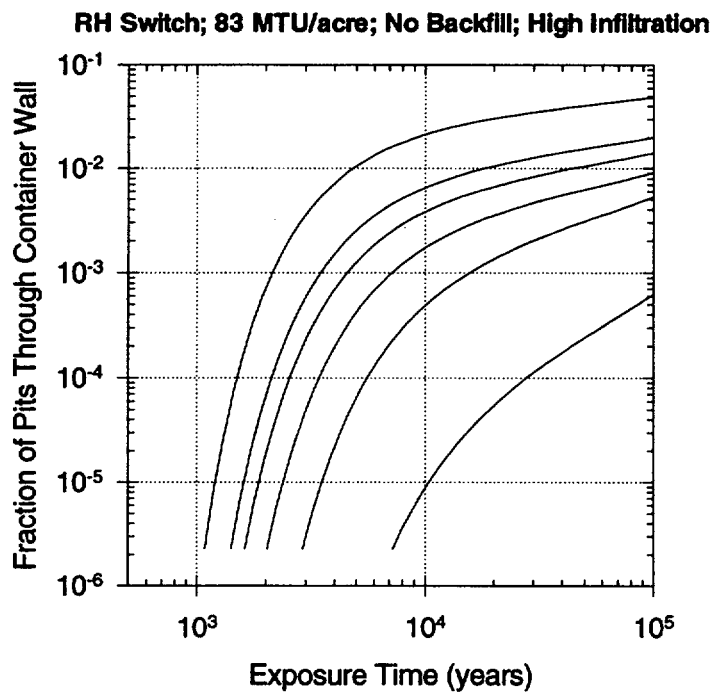
Figure 5.7-8c Abstractions for the RIP implementation for the case of 83 MTU/acre, high
infiltration, and without backfill, using RH switch for corrosion initiation.

RH Switch; 83 MTU/acre; Backfill; Low Infiltration
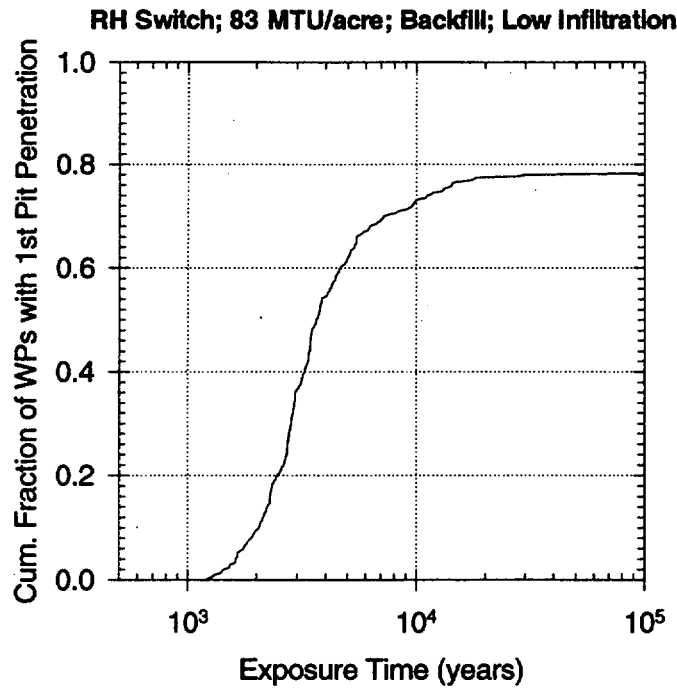
Figure 5.7-9a Waste package failure history for the case of 83 MTU/acre, low infiltration, and with backfill, using RH switch for corrosion initiation.

RH Switch; 83 MTU/acre; Backfill; Low Infiltration
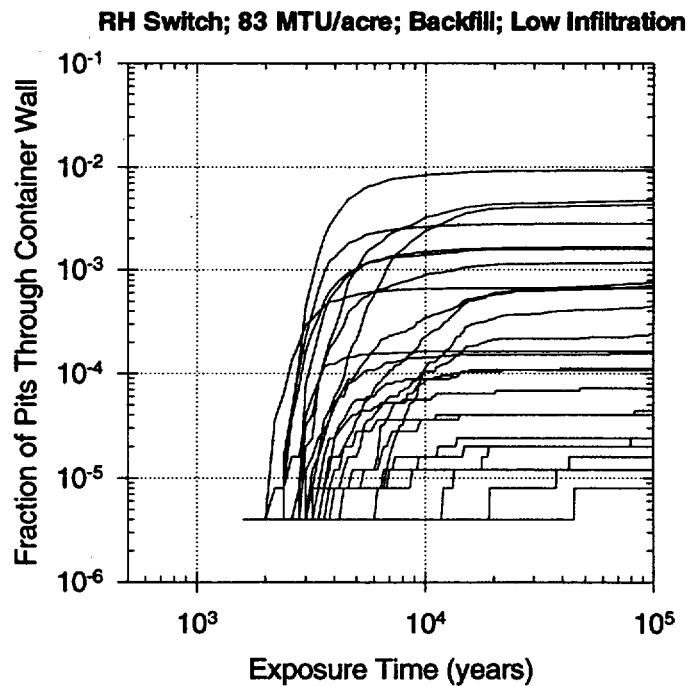
Figure 5.7-9b Representative pitting histories for 25 waste packages for the case of 83 MTU/acre, low infiltration, and with backfill, using RH switch for corrosion initiation.

5-71

RH Switch; 83 MTU/acre; Backfill; 0.05 mm/yr Infiltration
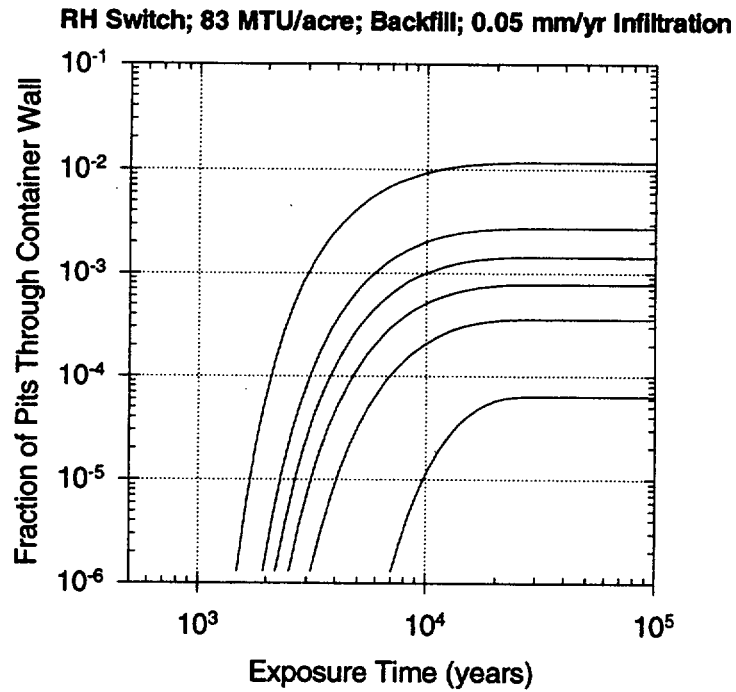
Figure 5.7-9c Abstractions for the RIP implementation for the case of 83 MTU/acre, low
infiltration, and with backfill, using RH switch for corrosion initiation.

RH Switch; 83 MTU/acre; Backfill; High Infiltration
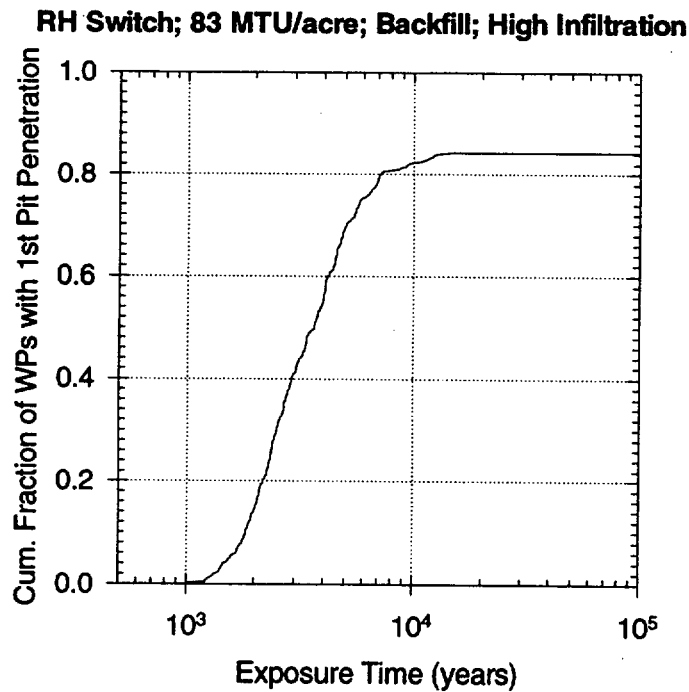
Figure 5.7-10a   Waste package failure history for the case of 83 MTU/acre, high
infiltration, and with backfill, using RH switch for corrosion initiation.

RH Switch; 83 MTU/acre; Backfill; High Infiltration
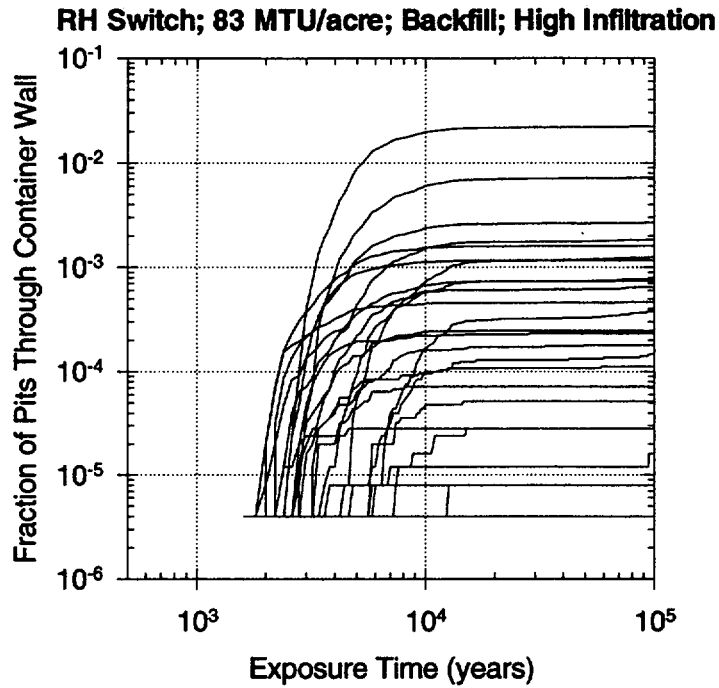
Figure 5.7-10b   Representative pitting histories for 25 waste packages for the case of 83 MTU/acre, high infiltration, and with backfill, using RH switch for corrosion initiation.

RH Switch; 83 MTU/acre; Backfill; High Infiltration
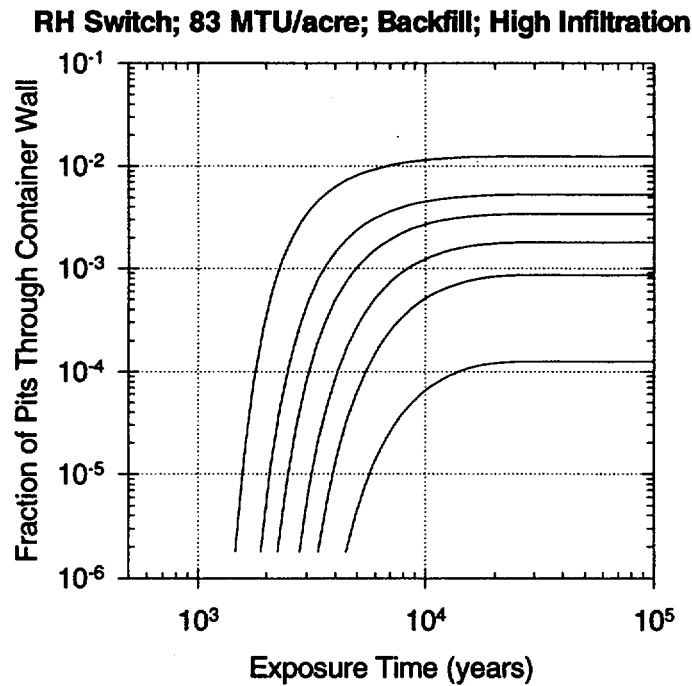
Figure 5.7-10c   Abstractions for the RIP implementation for the case of 83 MTU/acre, high infiltration, and with backfill, using RH switch for corrosion initiation.

RH Switch; 25 MTU/acre; No Backfill; Low Infiltration
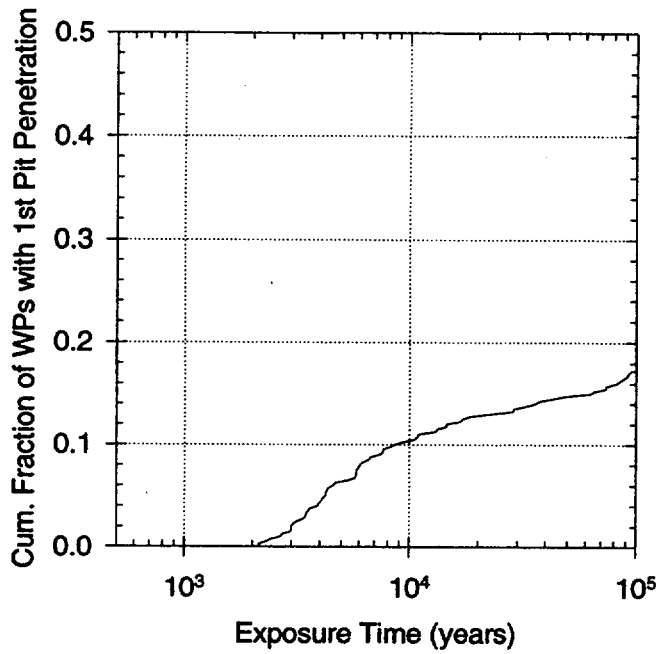
Figure 5.7-11a   Waste package failure history for the case of 25 MTU/acre, low infiltration, and without backfill, using RH switch for corrosion initiation.

RH Switch; 25 MTU/acre; No Backfill; Low Infiltration
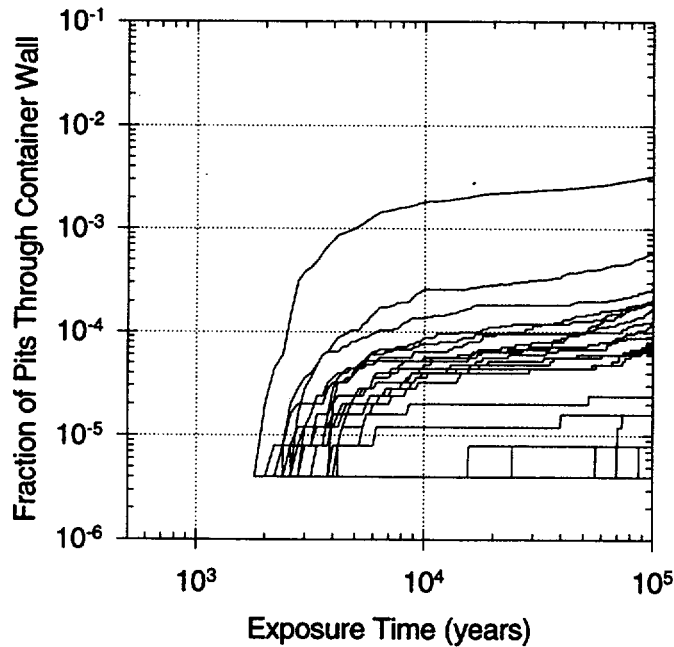
Figure 5.7-11b   Representative pitting histories for 25 waste packages for the case of 25 MTU/acre, low infiltration, and without backfill, using RH switch for corrosion initiation.

5-74

RH Switch; 25 MTU/acre; No Backfill; Low Infiltration
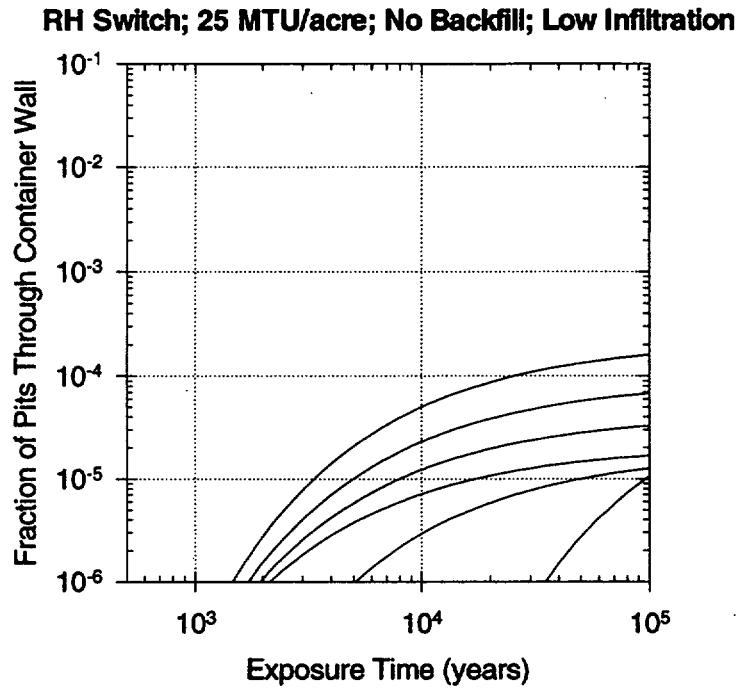
Figure 5.7-11c   Abstractions for the RIP implementation for the case of 25 MTU/acre, low infiltration, and without backfill, using RH switch for corrosion initiation.

RH Switch; 25 MTU/acre; No Backfill; High Infiltration
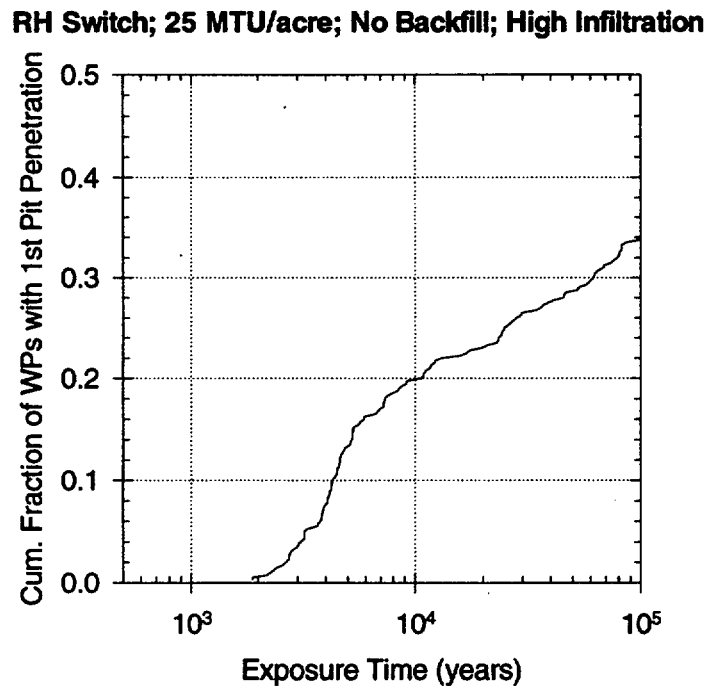
Figure 5.7-12a   Waste package failure history for the case of 25 MTU/acre, high infiltration, and without backfill, using RH switch for corrosion initiation.

RH Switch; 25 MTU/acre; No Backfill; High Infiltration
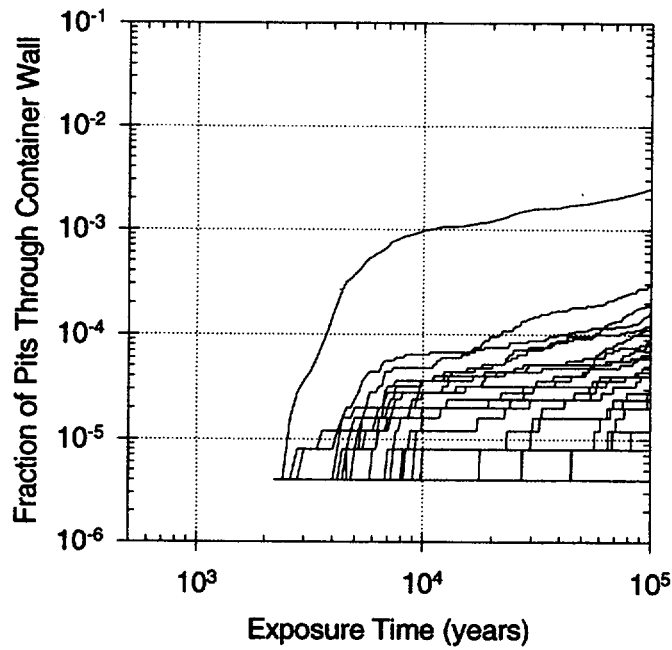
Figure 5.7-12b   Representative pitting histories for 25 waste packages for the case of 25 MTU/acre, high infiltration, and without backfill, using RH switch for corrosion initiation.

RH Switch; 25 MTU/acre; No Backfill; High Infiltration
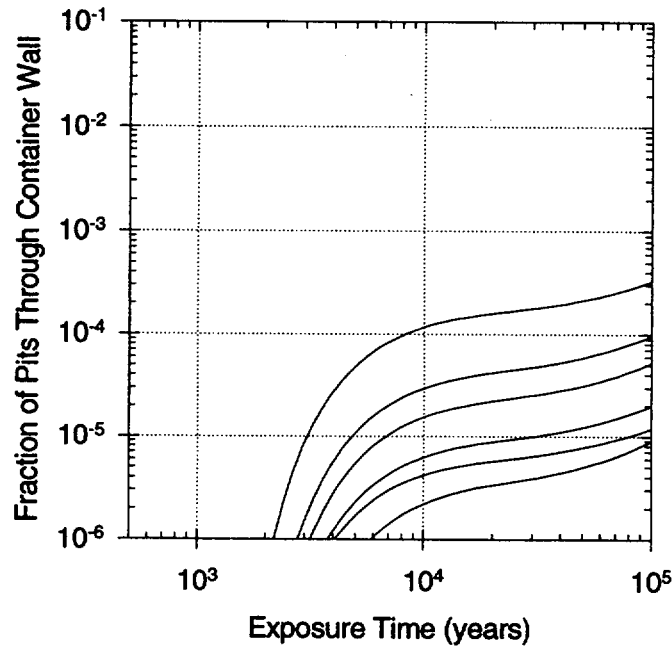
Figure 5.7-12c   Abstractions for the RIP implementation for the case of 25 MTU/acre, high infiltration, and without backfill, using RH switch for corrosion initiation.

RH Switch; 25 MTU/acre; Backfill; Low Infiltration
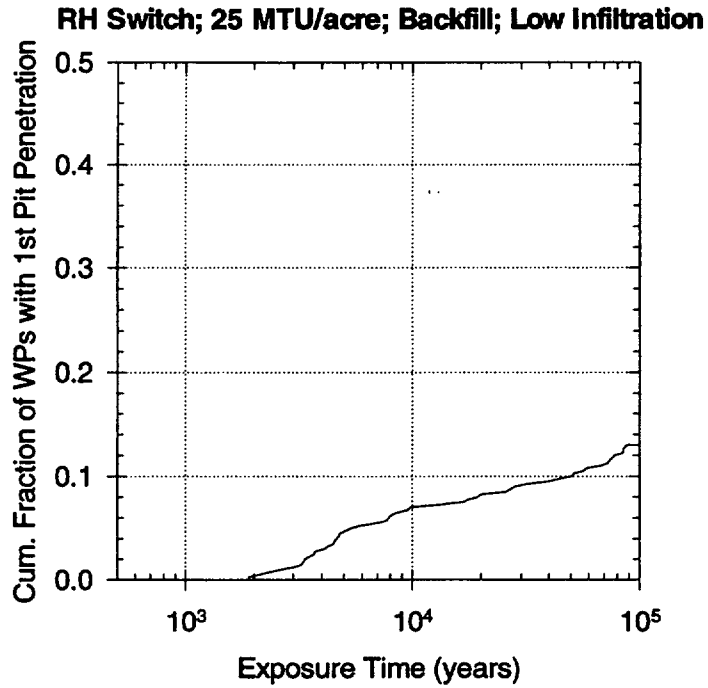
Figure 5.7-13a   Waste package failure history for the case of 25 MTU/acre, low infiltration, and with backfill, using RH switch for corrosion initiation.

RH Switch; 25 MTU/acre; Backfill; Low Infiltration
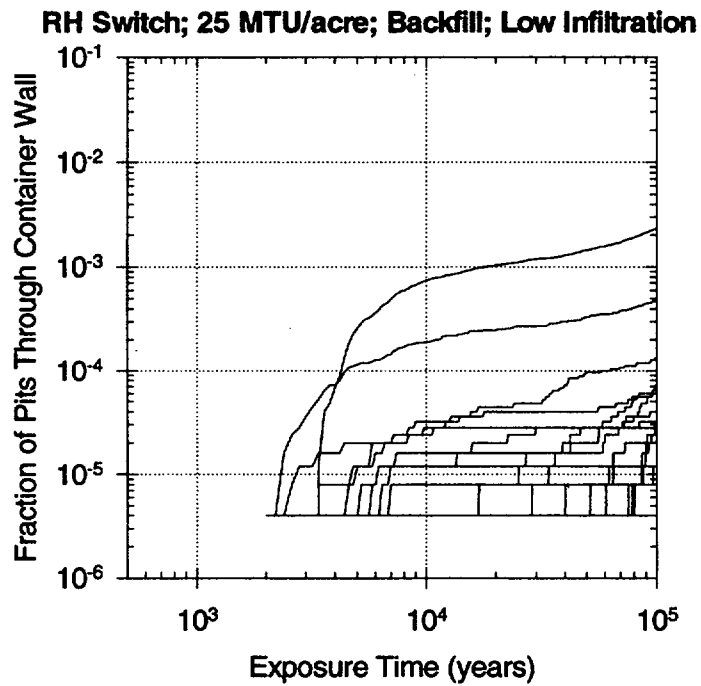
Figure 5.7-13b   Representative pitting histories for 25 waste packages for the case of 25 MTU/acre, low infiltration, and with backfill, using RH switch for corrosion initiation.

RH Switch; 25 MTU/acre; Backfill; Low Infiltration
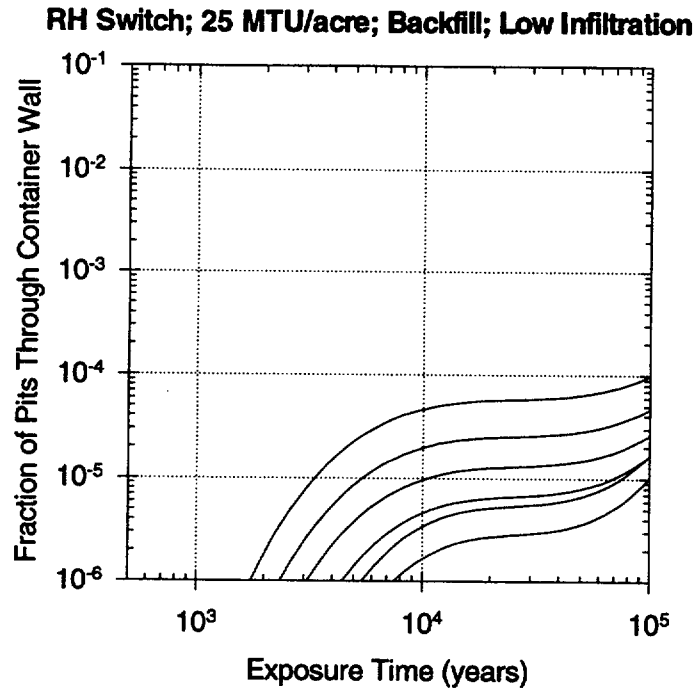
Figure 5.7-13c   Abstractions for the RIP implementation for the case of 25 MTU/acre, low infiltration, and with backfill, using RH switch for corrosion initiation.

Cathodic Protection; RH & T Switch
83 MTU/acre; No Backfill; High Infiltration
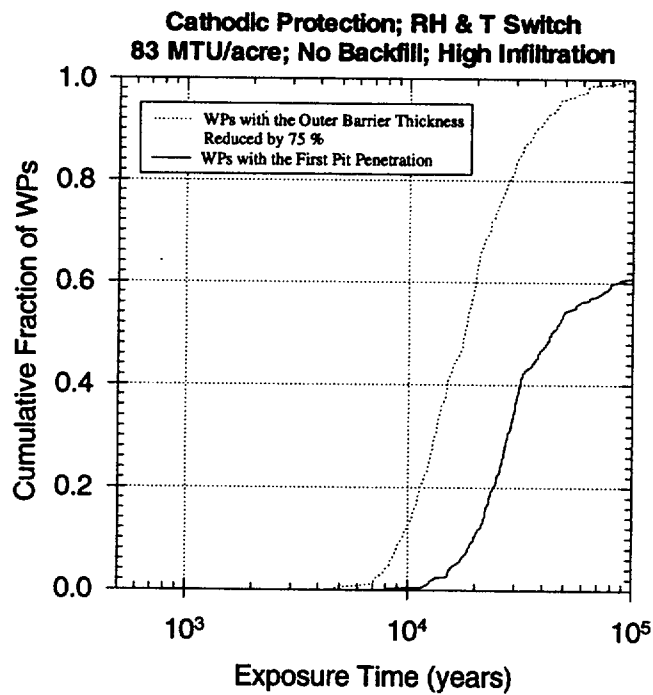
Figure 5.7-14a   Waste package failure history for the case of 83 MTU/acre, high infiltration, and without backfill, with cathodic protection of the inner barrier and using RH and temperature switch for corrosion initiation.
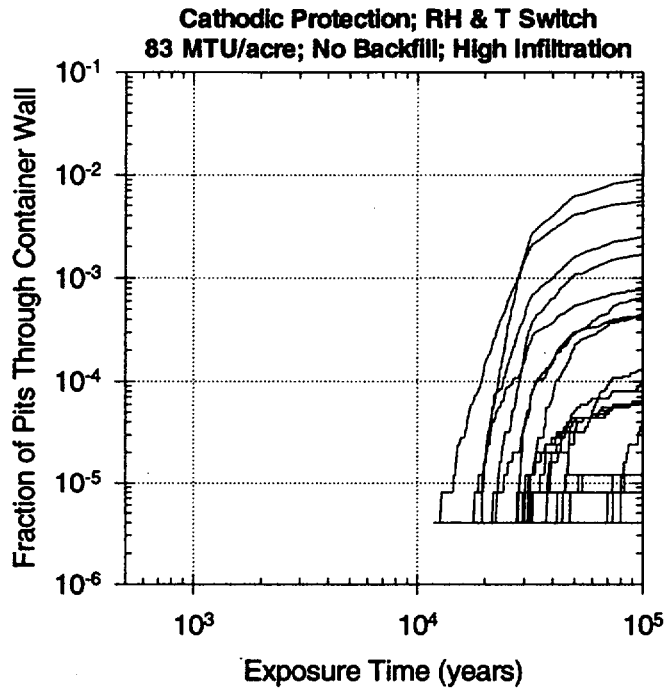
Figure 5.7-14b   Representative pitting histories for 25 waste packages for the case of 83 MTU/acre, high infiltration, and without backfill, with cathodic protection of the inner barrier and using RH and temperature switch for corrosion initiation.
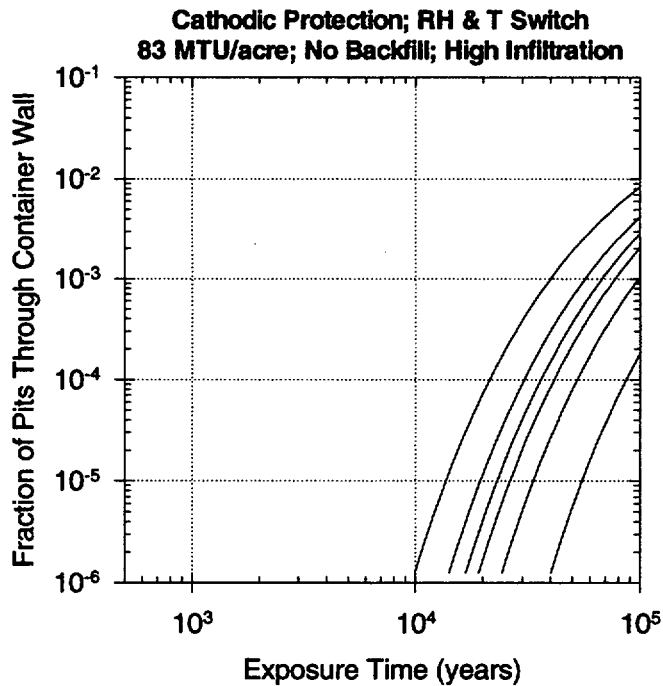
Figure 5.7-14c   Abstractions for the RIP implementation for the case of 83 MTU/acre, high infiltration, and without backfill, with cathodic protection of the inner barrier and using RH and temperature switch for corrosion initiation.

Cathodic Protection; RH & T Switch
25 MTU/acre; No Backfill; High Infiltration
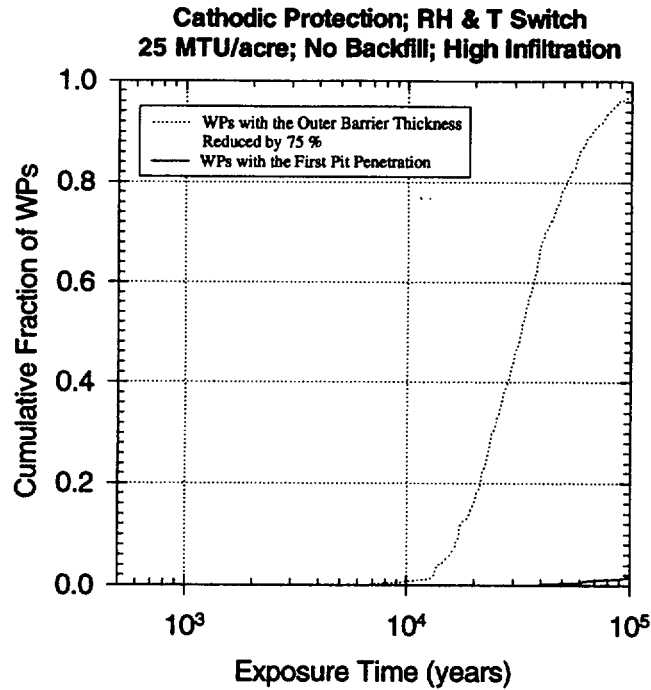
Figure 5.7-15 Waste package failure history for the case of 25 MTU/acre, high infiltration, and without backfill, with cathodic protection of the inner barrier and using RH switch for corrosion initiation.

Time-Dependent Pit Growth Rate; RH Switch
25 MTU/acre; No Backfill; High Infiltration
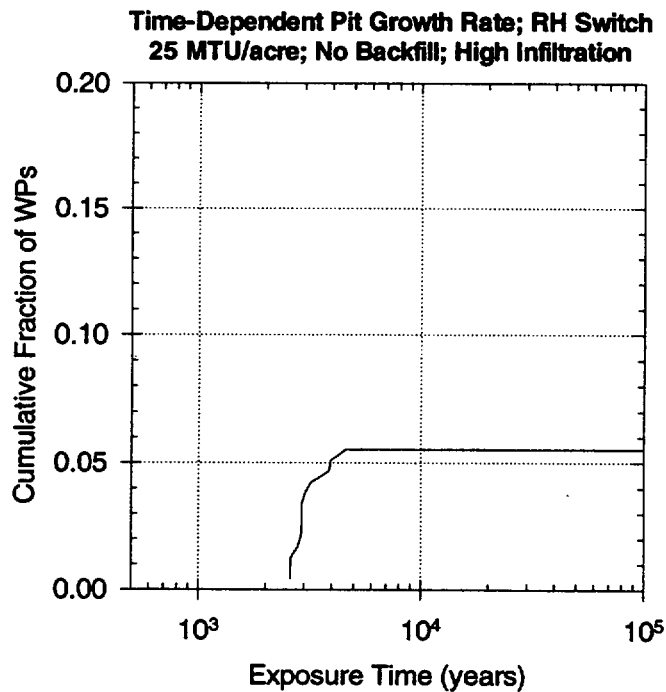
Figure 5.7-16 Waste package failure history for the case of 83 MTU/acre, high infiltration, and without backfill, with time-dependent pit growth rate in the inner barrier and using RH and temperature switch for corrosion initiation.

5-80

Buscheck's Model; RH Switch
24 MTU/acre; No Backfill; No Infiltration
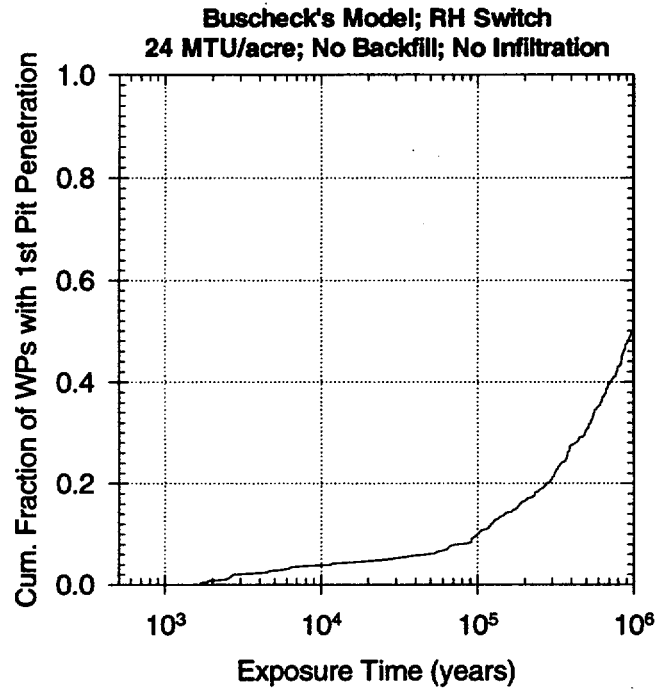
Figure 5.7-17a   Waste package failure history for the case of 24 MTU/acre, no infiltration, and without backfill, with the results from the Buscheck's model and using RH switch for corrosion initiation.

Buscheck's Model; RH Switch
24 MTU/acre; No Backfill; No Infiltration
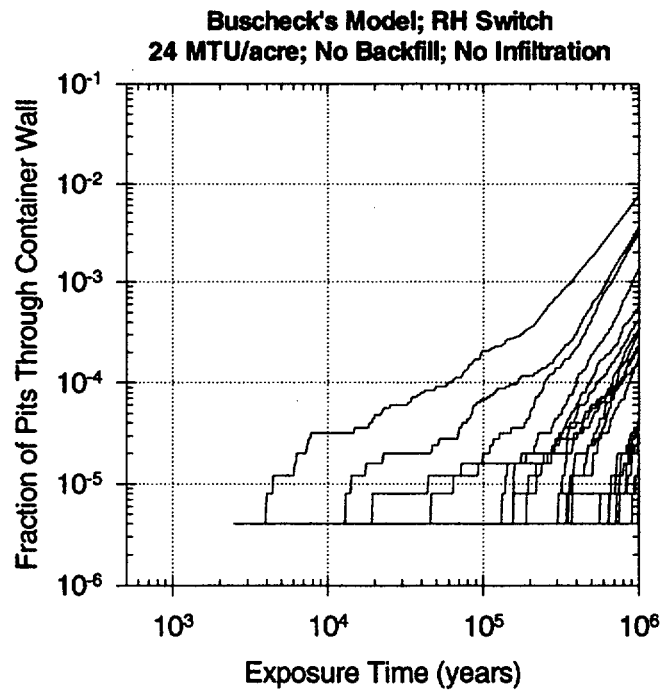
Figure 5.7-17b   Representative pitting histories for 25 waste packages for the case of 24 MTU/acre, no infiltration, and without backfill, with the results from the Buscheck's model and using RH switch for corrosion initiation.

Buschecks' Model; RH Switch
24 MTU/acre; No Backfill; No Infiltration
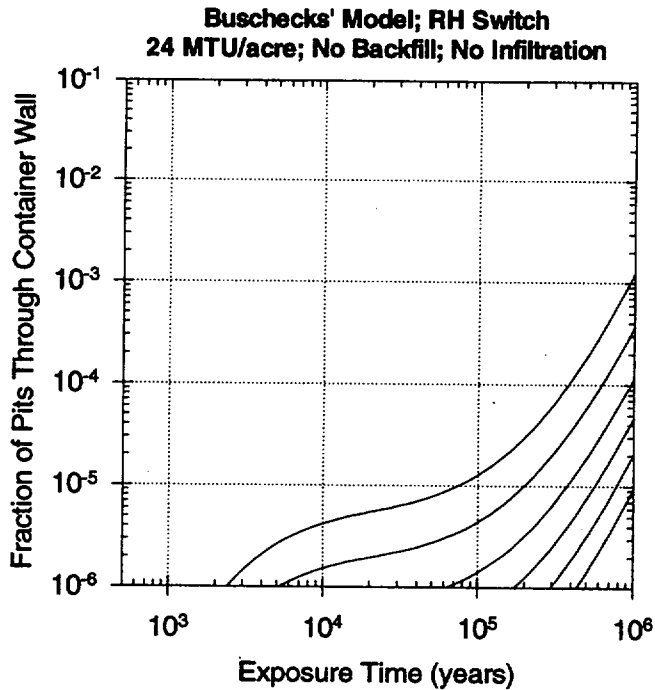
Figure 5.7-17c   Abstractions for the RIP implementation for the case of 24 MTU/acre, no infiltration, and without backfill, with the results from the Buscheck's model and using RH switch for corrosion initiation.

Buscheck's Model; RH Switch
24 MTU/acre; Backfill; No Infiltration
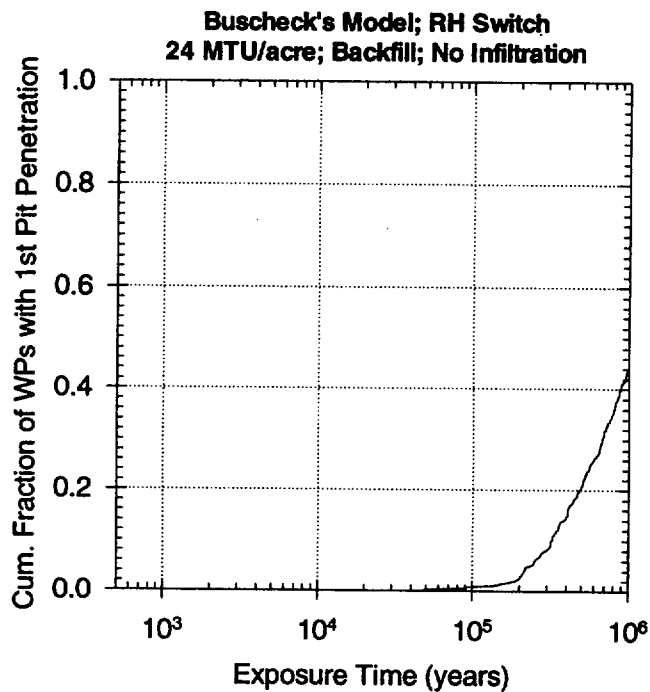
Figure 5.7-18a   Waste package failure history for the case of 24 MTU/acre, no infiltration, and with backfill, with the results from the Buscheck's model and using RH switch for corrosion initiation.

Buscheck's Model; RH Switch
24 MTU/acre; Backfill; No Infiltration
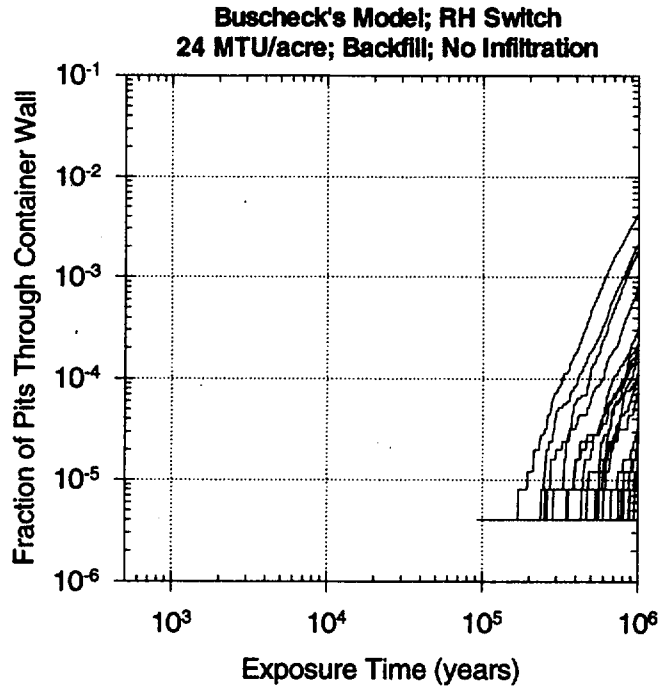
Figure 5.7-18b   Representative pitting histories for 25 waste packages for the case of 24 MTU/acre, no infiltration, and with backfill, with the results from the Buscheck's model and using RH switch for corrosion initiation.

Buscheck's Model; RH & T Switch
**80 MTU/acre; No Backfill; No Infiltration**
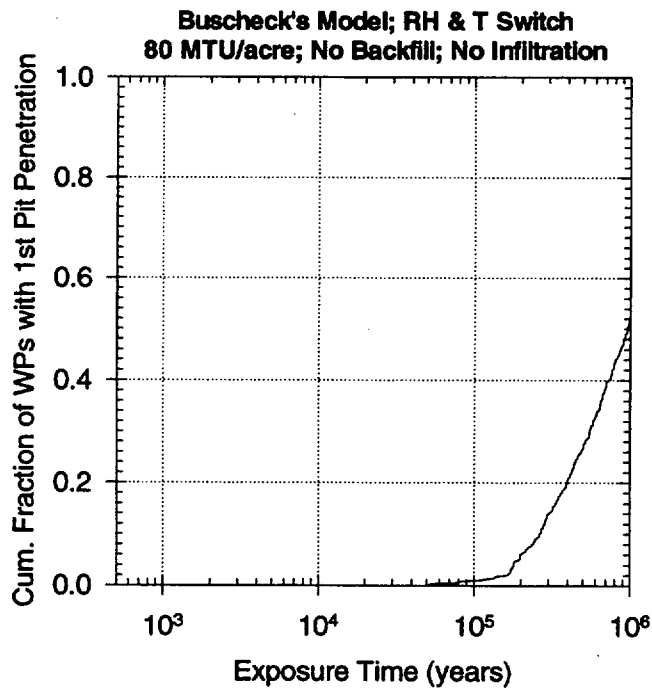
Figure 5.7-19a   Waste package failure history for the case of 80 MTU/acre, no infiltration, and without backfill, with the results from the Buscheck's model and using RH and temperature switch for corrosion initiation.

5-83

Buscheck's Model; RH & T Switch
80 MTU/acre; No Backfill; No Infiltration
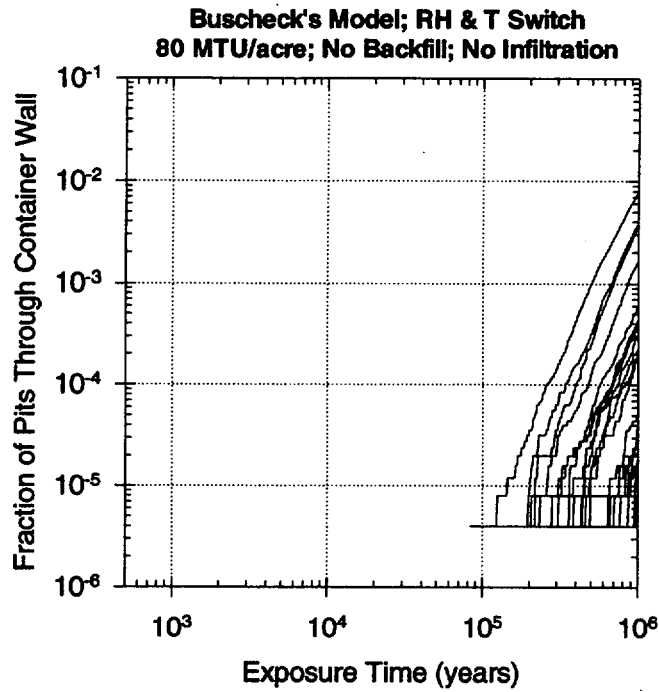
Figure 5.7-19b   Representative pitting histories for 25 waste packages for the case of 80 MTU/acre, no infiltration, and without backfill, with the results from the Buscheck's model and using RH and temperature switch for corrosion initiation

Buscheck's Model; RH & T Switch
80 MTU/acre; Backfill; No Infiltration
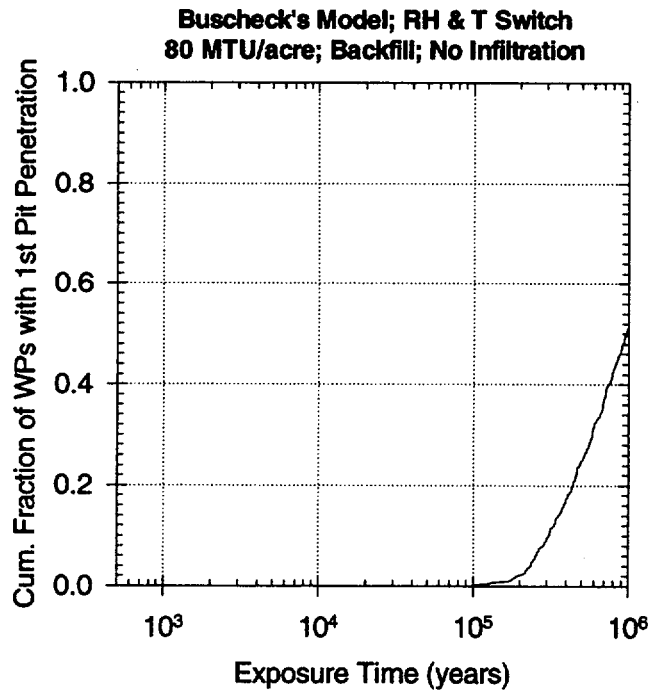
Figure 5.7-20a   Waste package failure history for the case of 80 MTU/acre, no infiltration, and with backfill, with the results from the Buscheck's model and using RH and temperature switch for corrosion initiation.

Buscheck's Model; RH & T Switch
80 MTU/acre; Backfill; No Infiltration
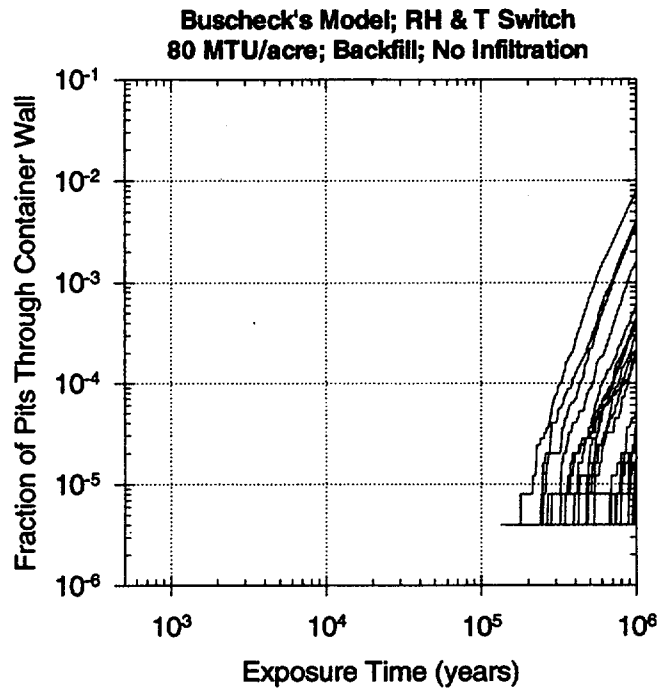
Figure 5.7-20b   Representative pitting histories for 25 waste packages for the case of 80 MTU/acre, no infiltration, and with backfill, with the results from the Buscheck's model and using RH and temperature switch for corrosion initiation

Alternative Interpretation; RH Switch
25 MTU/acre; No Backfill; High Infiltration
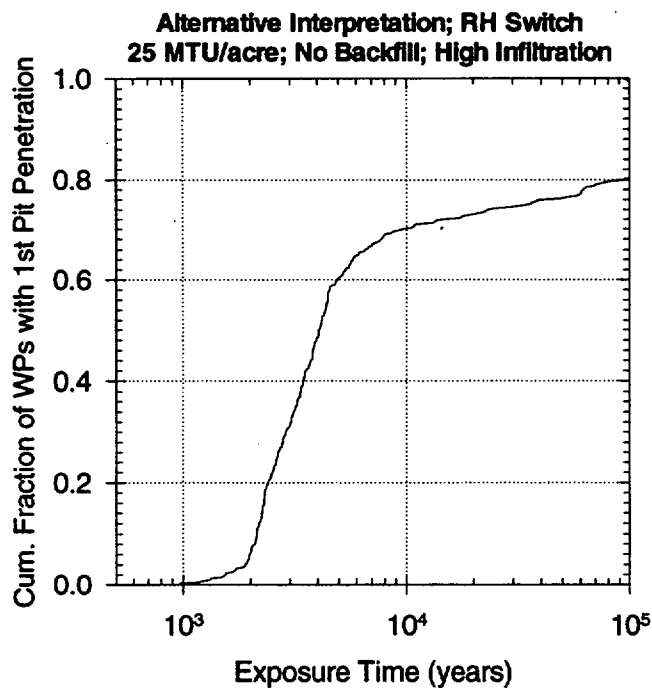
Figure 5.7-21 Waste package failure history for the case of 25 MTU/acre, high infiltration, and without backfill, with alternative interpretation of the elicitation for the inner barrier pit growth rate and using RH switch for corrosion initiation.

Alternative Interpretation; RH & T Switch
83 MTU/acre; No Backfill; High Infiltration
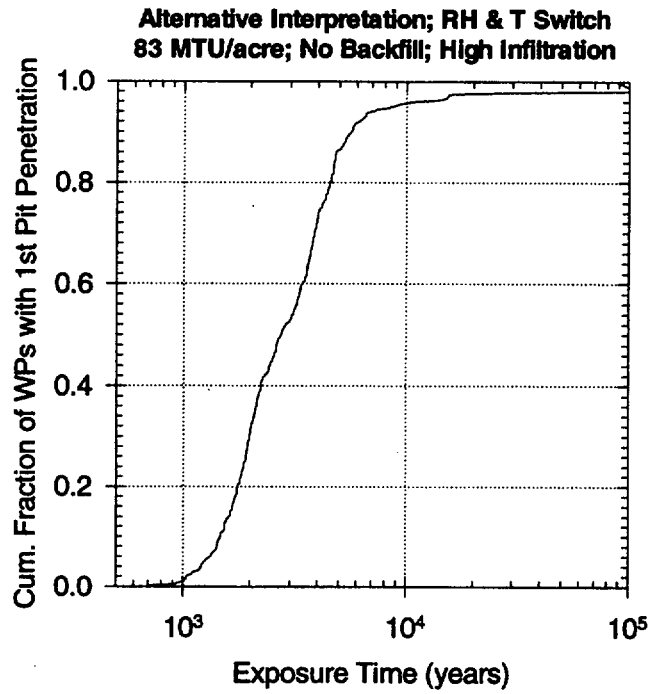
Figure 5.7-22 Waste package failure history for the case of 83 MTU/acre, high infiltration, and without backfill, with alternative interpretation of the elicitation for the inner barrier pit growth rate and using RH switch for corrosion initiation.

6. ENGINEERED BARRIER SYSTEM ABSTRACTION

David C. Sassani, Joon H. Lee, Joel E. Atkins

6.1 INTRODUCTION

For the engineered barrier system (EBS) analyses, it is assumed that the near-field environmental conditions exterior to a waste package are immediately transferred to the interior of the package after it is penetrated or "failed" by pitting corrosion. In calculating the release of radionuclides to the host rock from the engineered components of the system, the processes to be modeled include: waste form alteration/dissolution; solubility constraints on the concentration of dissolved radionuclide species; the potential for colloids to increase the source term and transport of radionuclides in the mobile phase; the effective diffusion of radionuclides through the degraded waste package and other engineered components; and the potential for advective transport in the localized flow intersecting the drift.

This chapter presents the abstraction of laboratory-derived information for use in the prediction of releases from the EBS. This information is used directly in the TSPA analyses as indicated in Figure 6.1-1. Section 6.2 presents information and its abstraction for the development of waste form alteration/dissolution model. Section 6.3 presents information on the solubility limits of radionuclides analyzed in TSPA-1995. Section 6.4 describes the potential effects of colloid formation and mobility, *although colloid formation/transport is not included in TSPA-1995 analyses.* Section 6.5 presents the EBS release models (diffusive and advective) used in TSPA-1995. In addition, the model abstractions constraining the percent of the waste package surface through which diffusive release can occur are presented. Also covered in Section 6.5 is the relation between the effective diffusion coefficient and the liquid saturation of drift materials.

6.2 WASTE FORM ALTERATION MODELING

After the modeled waste package container and cladding (for spent fuel) are calculated to fail (i.e., they are breached), the waste forms (spent fuel and vitrified defense high-level waste (DHLW) glass monolith) are assumed to be exposed to the near-field environment and to undergo alteration/dissolution before the radionuclides are released. It has been pointed out that a locally reducing environment may be possible in the vicinity of a corroding waste container and within a failed one, resulting in lower alteration/dissolution rates of the waste forms and lower solubility limits of species (Pigford, 1993). The baseline assumptions in this TSPA iteration are that the post-closure repository maintains a total pressure of one atmosphere (1 atm) and an oxygen partial pressure of 0.2 atm. These assumptions provide a conservatively oxidizing model environment for waste container corrosion and waste form degradation. This section outlines the TSPA-1995 approach for modeling spent fuel and glass waste form alteration/dissolution.

6.2.1 Alteration/Dissolution of Spent Fuel Waste Form

Conceptual Models and Approach

For radionuclide release from the spent fuel waste form (fuel pellets), two distinct release modes are considered: 1) instantaneous release; and 2) matrix release. The instantaneous release mode

consists of species in the gap between fuel pellets and cladding, and species on fuel grain boundaries. These species are referred to here as "gap-inventory species" and include ^{14}C, ^{135}Cs, ^{137}Cs, ^{129}I, ^{99}Tc, and ^{79}Se. The species are characteristically mobile and highly soluble in water. Typically, 1 to 2 % of their inventories are present in these regions of instantaneous release (Apted et al., 1989). The gap-inventory species and their gap fractions used in TSPA-1995 are given in Table 6.2-1. All other radionuclides listed in Table 3.7-1 are assumed to be located in the spent fuel matrix. The gap fractions of gap-inventory species are assumed to be available for immediate release as soon as both waste package container and cladding fail.

The distribution of the ^{14}C gap inventory in Table 6.2-1 represents the uncertainty of ^{14}C inventory in the gap and the oxidation layer on the cladding surface, and is the same as used in TSPA-1993 (Andrews et al., 1994). Van Konynenburg, et al., (1986) reported that about 65 % of the total ^{14}C inventory is present in cladding, crud and other fuel assembly hardware. However, only the ^{14}C in the gap and the grain boundary of the spent fuel matrix (about 1 %), and in an oxidation layer on the surface of the cladding is available for instantaneous release. The release rate for the rest of the ^{14}C is considerably slower (Barnard, et al., 1992). The release of ^{14}C is calculated assuming that all the ^{14}C available at a given simulation period migrates out of the EBS as a gas and then dissolves in the aqueous phase, i.e. no gaseous transport in the geosphere is considered.

The second release mode is matrix release in which the release rates of radionuclides are proportional to fuel matrix alteration/dissolution rate. Radionuclides released in this mode are referred to here as "matrix-release species", and may be grouped by their solubility limits into alteration/dissolution-limited species for highly soluble species and solubility-limited species for relatively insoluble species.

Spent Fuel Dissolution Model

A semi-empirical model for intrinsic dissolution (alteration) rate of the spent fuel matrix was developed from the experimental data reported by Gray, et al., (1992) and Steward and Gray (1994). In this TSPA, the post-closure environment inside the potential repository is assumed to maintain the atmospheric oxygen partial pressure of 0.2 atm. The model is expressed as a function of temperature, total carbonate concentration and pH of contacting water as follows

$$\log k_{SF} = a_0 + \frac{a_1}{T} + a_2 \log[CO_3] + a_3 pH + \varepsilon \quad , \quad \text{(6.2-1)}$$

where k_{SF} is the intrinsic dissolution rate of spent fuel (mg/m^2·day), T is temperature (K), [CO$_3$] is the total carbonate concentration of the contacting groundwater (in molarity units), and ε is a term representing uncertainty not included in the model. The parameter values determined for the functional form are: a_0 = 7.323 ± 0.957, a_1 = -1585.2 ± 303.3, a_2 = 0.2621 ± 0.0743, and a_3 = -0.1140 ± 0.0679. The dissolution rate strongly depends on temperature and total carbonate concentration, and is less influenced by pH.

The model prediction and the associated uncertainty of the dissolution rate as a function of temperature at total carbonate concentrations of 0.002 and 0.02 M are shown in Figures 6.2-1 and 6.2-2, respectively. The relevant experimental data are also presented in the figures. The spent fuel dissolution rate increases with temperature. The total carbonate concentration of the contacting water enhances the dissolution rate, but to a smaller extent than temperature. Figure 6.2-3 shows the dissolution rate as a function of the total carbonate concentration at a constant temperature of 296.15 K. The enhanced dissolution rate is due mostly to increased complexation of uranium and other actinides with carbonate ions. As shown in Figure 6.2-4, the values of dissolution rate predicted by Equation 6.2-1 are somewhat higher (about 2 to 4 times depending on temperature and the total carbonate concentration) than those used in TSPA-1993 (Andrews, et al., 1994). This difference is caused by the replacement of the TSPA-1993 temperature dependance term (exp (T)) with a more physically reasonable Arrhenius temperature dependence term (exp (1/T)) in TSPA-1995.

Potentially substantial increases in the alteration of spent fuel in steam environments have been indicated from the studies with unused (fresh) UO_2 fuels (Taylor, et al., 1989; Taylor, et al., 1992; Wasywich, et al., 1992) and with spent fuels (Finn, et al., 1995; Wasywich, et al., 1992). This potentially important observation and its effects on spent fuel alteration should be considered in future modeling.

Spent Fuel Surface Area

The actual spent fuel alteration rate is determined by multiplying the intrinsic dissolution rate from Equation 6.2-1 with the available surface area to be exposed (or wetted). To calculate the actual fuel matrix alteration rate in TSPA-1993 (Andrews, et al., 1994), the surface area of spent fuel available for dissolution was a function of the fraction of fuel that was wet. In TSPA-1995, assuming cladding fails at the same time as the waste container, the entire waste form surface area is assumed to be exposed to the near-field environment and covered with a "thin" water film once the waste container is pitted through its wall thickness. This conceptualization is based on the assumptions that, as soon as the waste container fails, the inert environment inside is quickly replaced with the near-field environment, and the moisture freely moves through the space inside the "failed" waste container to readily wet the waste form. This new approach provides higher degrees of dissolution than in TSPA-1993.

A recent report by Gray and Wilson (1995) provides an estimate of the specific surface area of non-oxidized spent fuel. From the measured spent fuel pellet surface area (150 mm^2 per millimeter of fuel rod length—Barner, 1985), a geometric specific surface area was calculated to be 2.2×10^{-4} m^2/g (Gray and Wilson, 1995). A factor of 18 was suggested for taking into consideration the surface area contributed from cracks that have formed during reactor operation and some penetration of the grain boundaries by water. The resulting specific surface area of 3.96×10^{-3} m^2/g was recommended as a reasonable minimum surface area for spent fuel (Gray and Wilson, 1995). A suggested maximum surface area derived from the Brunauer-Emmet-Teller (B.E.T.—Brunauer, 1961) surface area measurements is about 0.1 m^2/g (Gray and Wilson, 1995). The recommended minimum specific surface area of 3.96×10^{-3} m^2/g is used for the nominal case in TSPA-1995. An additional factor of 10 to 40 times the specific surface area was suggested for the spent fuel that has oxidized to U_3O_8 (Gray, 1995a). To account for these oxidation

effects, sensitivity analyses on cladding failure include a factor of 100 for the spent fuel surface area of those fuel rods which are exposed due to cladding rupture.

6.2.2 Alteration/Dissolution of DHLW Glass Waste Form

As in the spent fuel alteration/dissolution modeling discussed above, the entire surface area of DHLW glass waste form is assumed to be exposed to the near-field environment as soon as the first pit penetrates through the waste container. The waste form is then assumed to be covered by a "thin" water film, and alteration/dissolution processes are initiated.

DHLW Glass Dissolution Model

Since no new information has been developed for models for DHLW glass waste form dissolution, the same conservative rate equation used in TSPA-1993 (Andrews, et al., 1994) is used in TSPA-1995. The dissolution rate equation is written as follows (Knauss, et al, 1990; Bourcier, 1993)

$$R_{DHLW} = S\, k_{DHLW}\, (1 - \frac{Q}{K}) \ , \tag{6.2-2}$$

where R_{DHLW} the is dissolution rate of glass waste form (g/day), S is the surface area of the glass exposed to alteration solution (m^2), k_{DHLW} is the intrinsic dissolution rate constant for the glass ($g/m^2 \cdot day$) which is primarily a function of temperature and pH, Q is the concentration of dissolved silica in the contacting solution (M), and K is the equilibrium constant for amorphous silica dissolution (M).

It has been suggested that glass dissolution rates increase with temperature (Knauss, et al, 1990; Bourcier, 1993; Bourcier, et al, 1994). The temperature dependency of the empirical equation for the intrinsic glass dissolution rate constant (k_{DHLW}) used in TSPA-1993 was not properly represented at temperatures above 70 °C (i.e., the dissolution rates decreased at higher temperatures). Using the same glass dissolution rate data provided by Bourcier (1993), a new empirical equation was derived as

$$\log k_{DHLW} = a_0 + a_1 T + a_2 pH + a_3 pH^2 + a_4 pH^2 T + \varepsilon \tag{6.2-3}$$

where k_{DHLW} has the same units as in Equation 6.2-2, and T is in °C. The parameter values determined are: $a_0 = -0.442 \pm 0.290$, $a_1 = 0.0307 \pm 4.58 \times 10^{-3}$, $a_2 = -1.17 \pm 7.02 \times 10^{-2}$, $a_3 = 0.0793 \pm 6.38 \times 10^{-3}$, and $a_4 = 9.68 \times 10^{-5} \pm 6.95 \times 10^{-5}$. The ε term represents additional uncertainty not included in the model. This equation is valid from 10 to 100 °C and pH values from 1 to 12. The ratio Q/K in Equation 6.2-2 is estimated with the same empirical equation

used in TSPA-1993 which was derived from Bourcier's temperature dependent estimates of Q and K and is given as

$$\frac{Q}{K} = 0.1425 + 0.001878\,T \qquad (6.2\text{-}4)$$

where T is in °C.

The intrinsic glass dissolution rate model as a function of temperature and pH is presented in Figure 6.2-5 along with the rate data from Bourcier (1993). In Figure 6.2-6 the glass dissolution rate calculated using Equation 6.2-3 and the previous relation from TSPA-1993 are shown as functions of temperature at pH of 7. The figure shows that the current dissolution rate model predicts monotonically increasing dissolution rate with temperature.

The dissolution conceptualization presented here embodies several assumptions and limitations. The radionuclides are assumed to be released as fast as the glass structure breaks down, which is conservative because it does not account for solubility-limited radionuclides. No credit is taken for the fact that "experiments have shown that the actinides more commonly are included in alteration phases at the surface of the glass either as minor components of other phases or as phases made up predominantly of actinides" (Bourcier, 1993). The model does not include any solution chemistry other than pH and dissolved silica concentration. However, a variety of experiments show that species such as dissolved Mg and Fe can change glass dissolution rates by up to several orders of magnitude, with Mg decreasing the rate and Fe increasing the rate (Bourcier, 1993). The model also does not include vapor-phase alteration of the glass. Glass has been observed to undergo hydration in a humid-air environment and, upon subsequent contact with water, radionuclide releases from a hydrated glass layer were several orders of magnitude higher than those from an unhydrated (fresh) glass waste form (Bates, et al, 1990; Bourcier, 1993; Ebert and Bates, 1995; Bates, et al, 1995). These observations should be considered in future glass waste form performance modeling.

<u>DHLW Glass Surface Area</u>

Nominal surface area of a DHLW glass monolith (or log) is 5 m^2 per canister, and the surface area is increased by a factor of 10 to 30 per canister to account for the cracks that form during cooling following the glass pouring, leading to a glass surface area of 50 to 150 m^2 per canister (Bourcier, 1993). The current design concept calls for a DHLW disposal container with four-pour canisters; thus, the total surface area of DHLW glass waste form per waste-disposal container is from 200 to 600 m^2. As in TSPA-1993, the surface area range is assumed to be distributed uniformly.

6.3   SOLUBILITY-LIMITED AQUEOUS RADIONUCLIDE CONCENTRATIONS

6.3.1   Introduction

The term solubility refers to the equilibrium concentration of a solute (phase A) dissolved into a solvent (phase B) which produces a saturated solution of that solute at a fixed set of system conditions (e.g., temperature, pressure). The relation between solubility of a solute phase and

its constituent elemental concentrations in the saturated solution is given by the stoichiometry of the solute phase. At the solubility limit, the solution concentration of any particular solute element is dependent upon the solvent composition including pH, the initial concentration(s) of any other solute constituent(s), and complexing agents. The elemental solubility refers to the solution concentration of an element that is controlled by the equilibrium solubility of a saturated phase containing that element.

In TSPA-1995, calculated bounds on the aqueous concentration of radionuclides in ground water that has reacted with the waste form are derived initially from the waste form dissolution model. Subsequently another filter is applied which compares the dissolution-based aqueous radionuclide concentration with a solubility-limited value that is sampled from either a distribution of solubility limits for radionuclide-bearing minerals, or a functional form for the solubility limit for each radionuclide considered. If the sampled solubility-limited value is lower for a given radionuclide than its concentration derived from the waste form dissolution, then the aqueous concentration is set to the solubility-limited value and the difference in mass is calculated to "precipitate" out of solution. These solubility-limited values place constraints upon the aqueous concentration of the particular radionuclide *element* considered, with each isotope of that element present in proportion to its isotopic abundance.

This analysis does not include solubility limits with all their functional dependencies explicitly represented. These dependencies include temperature (and to a lesser extent pressure) and compositional parameters of both the concentration-limiting solid phase and the aqueous solution (e.g., pH, oxygen fugacity, concentrations of other metals and ligands). However, for some of the radionuclides (Np, Pu, and Am), experimental studies of their steady-state concentration limits in modified J-13 water compositions have been used to derive empirical relations describing the temperature and pH dependence for their aqueous concentrations. These results are used to evaluate the release of these radionuclides based on explicit dependence for both pH and temperature (based on thermal loading etc.), and to evaluate the sensitivities relative to using sampled distributions included in the nominal-case calculations. Both the nominal-case distributions and functional forms used in this analysis for radionuclide solubility limits are discussed below in detail.

6.3.2 Nominal-Case Distributions

The concentration of aqueous radionuclides in groundwater reacting with spent fuel or glass waste has a complex dependence on the composition and phase assemblage of the waste form, the composition of the aqueous phase (e.g., pH, dissolved carbonate, oxygen fugacity), and the conditions at which reaction occurs (e.g., temperature, pressure). For many of the radionuclides considered in this analysis, explicit representation of these dependencies is not currently possible in a comprehensive manner. In addition, constraints on the system conditions which would effect aqueous radionuclide concentrations are not currently fully defined/quantified. In order to account for these uncertainties, the ranges of possible radionuclide concentrations that would be controlled by radionuclide-bearing mineral equilibration with ground water (solubility-limited concentrations) are represented as probability distributions, in general. By randomly sampling these distributions of solubility-limited aqueous radionuclide concentrations in each realization, Performance Assessment can *implicitly* encompass a range of possible system conditions and assess the potential consequences of this variability. For the nominal-case analyses presented

below, distributions of solubility-limited concentrations for the radionuclides of Ac, Am, Cm, Cs, Nb, Ni, Np, Pa, Pb, Pd, Pu, Ra, Se, Sm, Sn, Tc, Th, U, and Zr are given in Table 6.3-1 and discussed in this section. Table 6.3-1 provides the radionuclide, the type of distribution used, the variable of the distribution as either concentration or log(concentration), the parameters for the distribution in units of g/m^3 and molarity, and the source of the information.

The distributions of concentration limits are based primarily on an elicitation of chemical/geochemical experts held at Sandia National Laboratories on April 13, 1993 (Elicitation—Gauthier, 1993). Judgement of the expert panel was based on both empirical studies and modeling results, but did not include consideration of distributions used in the 1991 TSPA (Barnard et al., 1992). The results of the expert elicitation were reviewed in 1993 by the Solubility Working Group (SolWoG is composed primarily of project scientists conducting actinide solubility/speciation studies) which recommended only two modifications to the distributions of Np and Pu as discussed below. The assumptions behind the Elicitation's development of the distributions are: (1) the unsaturated zone water composition is between the composition of J-13 well water and that of UE-25p#1; (2) the solubility-limits will be determined by the far-field ground-water environment; (3) the environment is oxidizing; and (4) future climate changes will cause ground-water compositional changes. As discussed below and shown in Table 6.3-1, a number of additional sources were used to further constrain distributions of solubility limits for the radionuclides used in this analysis.

C, Cl, and I

The Elicitation results (Gauthier, 1993) indicate that the solubility-limits on aqueous concentrations for these elements were all very high and would probably result in high dissolved concentrations. A reasonable value to use was given as 1 mole per liter (1 molar) for each of these which would place them into the dissolution-controlled regime. Each of these elements may form volatile species (e.g., Van Konynenberg, et al., 1987; Bullen, 1992). In the base case of this analysis, these elements are treated as gaseous, and hence their releases from waste packages are controlled by their presence in the gap-fraction and/or by waste form dissolution, not by solubility limits. The released "gases" are allowed to migrate *uninhibited* through the EBS, whereupon they are transferred into the aqueous phase. These radionuclides (^{14}C, ^{36}Cl, and ^{129}I) are then treated as unretarded dissolved species throughout the rest of the transport calculation and ultimately contribute to the calculated dose. The release of ^{14}C along gaseous pathways was evaluated in TSPA-1993 (Andrews et al., 1994), but because dose calculations were based on drinking of well water, that radionuclide did not contribute to those calculated doses. In a sensitivity study of the effects of a diffusive barrier on transport of Cl and I out of the EBS as dissolved components, the solubility-limiting values of 1 molar were applied. The results are discussed in Chapter 8.

Ac, Am, and Sm

A single uniform distribution is used for each of these elements as a result of the 1993 Elicitation (Gauthier, 1993). In the Elicitation, it was indicated that both Ac and Sm should be taken as analogous to Am. The distribution chosen was based on the range of values from the recent measurements of steady-state Am concentrations in both J-13 and UE-25p#1 ground waters (Nitsche et al., 1993; 1994). The distribution is shown in Figure 6.3-1 and the parameters are

given in Table 6.3-1. This uniform distribution of concentrations is shown in two ways. A linear representation (Figure 6.3-1A) emphasizes the uniform nature of the distribution, and a logarithmic representation (Figure 6.3-1B) emphasizes the range of values. Both of the views in Figure 6.3-1 indicate that ~90% of values sampled from this distribution would come from between concentrations of 1×10^{-7} and 1×10^{-6} molar.

Cm

As was done for Cm in TSPA-1993 (Andrews et al., 1994), the measured concentrations of Cm in J–13 ground water from Wilson's dissolution experiments (1.2×10^{-5} gm/m^3 at 25°C, and 1.5×10^{-9} gm/m^3 at 85°C—Jardine, 1991) were used in TSPA-1995. In the absence of any estimate of the error, a log–triangular distribution was assumed that extended one order of magnitude in each direction from each measured value. The temperature at which the solubility limit was switched from one distribution to the other was selected to be 55°C, the mid-point of the two temperatures. The parameters for these distributions are given in Table 6.3-1 and the distributions are shown in Figure 6.3-2.

Cs, Se, and Tc

For Cs, Se, and Tc, the solubility-limits were constrained by the Elicitation (Gauthier, 1993) to be large such that release of these radionuclides would probably be controlled by dissolution of the waste form. Therefore, log–triangular distributions for these elements (see Table 6.3–1 and Figures 6.3-3, 6.3-12, and 6.3-14 for Cs, Se, and Tc, respectively) were taken from the previous compilation of Golder (1993), which was based in part on the literature evaluation done by the Electric Power Research Institute (EPRI, 1992). These ranges of values allow this analysis to encompass implicitly a variety of possible conditions. Because these distributions encompass elemental concentrations controlled by highly soluble salts, they result in dissolution limited release for these radionuclides in general. It should be noted that very soluble salts have uncertain application to constraining dissolved elemental concentrations in natural systems, unless there is a large source of such salts, and it may therefore be possible in the future to constrain further the distributions of solubility-limits for these elements.

Nb

The Elicitation (Gauthier, 1993) based the log-uniform distribution for solubility-limited Nb concentration on the data given in Andersson (1988). This distribution is shown in Figure 6.3–4 and the parameters are given in Table 6.3-1.

Ni

The Elicitation (Gauthier, 1993) based the log-beta distribution for solubility-limited Ni concentrations on the data given in Andersson (1988) and data from the caisson experiment at Los Alamos National Laboratory (Siegel et al., 1993). The parameters for this distribution are given in Table 6.3-1. In TSPA-1993 (Andrews et al., 1994) this distribution was approximated by a log-normal distribution which has been replaced with the log-beta distribution for this analysis. As shown in Figure 6.3–5, the TSPA-1993 approximation is similar to the TSPA-1995 distribution.

Np

The distribution for solubility-limited Np concentrations used in this study represents a minor modification (as recommended by the Solubility Working Group-SolWoG) of the original distribution given by the Elicitation. The Elicitation (Gauthier, 1993) based the original log beta distribution on the range of values from the recent measurements of steady-state Np concentrations in both J-13 and UE-25p#1 ground waters (Nitsche et al., 1993; 1994) together with ongoing research at Los Alamos National Laboratory. In reviewing the proposed distributions, the SolWoG suggested that the minimum value be changed from 1×10^{-8} to 5×10^{-6} molar, but did not indicate how to adjust the coefficient of variation or the expected value (Dyer, 1993). It was decided for this study that a reasonable procedure was to adjust these values so that the shape of the modified distribution was similar to that of the original distribution, except for the lack of a tail at low values of log(Np concentrations). The original and modified log-beta distributions are shown in Figure 6.3-6 where it can be seen that the change makes the moderate values more probable at the expense of the probability of very low values of log(Np concentration). The parameters for the modified distribution are given in Table 6.3-1.

Pa

The Elicitation (Gauthier, 1993) based the range of the log-uniform distribution for solubility-limited Pa concentrations on the data given in Andersson (1988). A log-uniform distribution was assigned because the panel agreed that Pa should be less soluble than suggested by the range of values, and that the distribution should have a large variance and be skewed to low values. This distribution is shown in Figure 6.3-7 and the parameters are given in Table 6.3-1.

Pb

The Elicitation (Gauthier, 1993) based the log-beta distribution for solubility-limited Pb concentrations on the data range given in Andersson (1988) and other previous work on this element (Pei-Lin et al., 1985). It was noted also that the concentration of dissolved Pb is sensitive to the amount of dissolved carbonate. The parameters for this distribution are given in Table 6.3-1. In TSPA-1993 (Andrews et al., 1994) this distribution was approximated by a log normal distribution which has been replaced with the log beta distribution for this analysis. As shown in Figure 6.3-8, the TSPA-1993 approximation is similar to the TSPA-1995 distribution.

Pd

The distribution of solubility-limits for Pd given by Golder (1993) is a log-uniform distribution with a minimum of 1 g/m^3 and a maximum of 1×10^5 g/m^3. This was given as an estimated distribution to cover a large range of concentrations because there was a lack of readily available data. Because Pd is one of the noble metals and belongs to the platinum-group elements (PGE) (which as a group tend to have limits on their aqueous concentrations which are in general lower than many other metals- see Sassani, (1992) and references therein), this range of values appears to be extremely high. For this analysis, the maximum value for the Pd-distribution has been reduced to 1×10^4 g/m^3 (9.4×10^{-2} molar), a value which is still viewed as conservative. Additional justification that this lowered maximum is conservative comes from comparison

between the other estimated distributions given by Golder (1993) for Nb, Pa, and Pb, and the corresponding distributions given by the Elicitation (Gauthier, 1993) which are from 5 to 8 orders of magnitude lower. The modified distribution for Pd is shown in Figure 6.3-9 and the parameters are given in Table 6.3-1. Further refinement of the distribution of solubility-limits for Pd will probably lead to much lower values in future total system performance assessments.

Pu

The distribution for solubility-limited Pu concentrations used in this study represents a minor modification (as recommended by the Solubility Working Group-SolWoG) of the original distribution given by the Elicitation. The Elicitation (Gauthier, 1993) assigned the original uniform distribution as identical to that for Am and this was used in TSPA-1993 (Andrews et al., 1994). In reviewing the proposed distributions, the SolWoG suggested that the minimum value be changed from 1×10^{-10} to 1×10^{-8} molar (Dyer, 1993; Wilson et al., 1994), based on the range of values from the recent measurements of steady-state Pu concentrations in both J-13 and UE-25p#1 ground waters (Nitsche et al., 1993; 1994). Because the values below 1×10^{-8} molar would have represented only about 1% of the samples for the unmodified distribution, this change is not expected to substantially impact the results of this study. The modified distribution is shown in Figure 6.3-10 and the parameters are given in Table 6.3-1. This uniform distribution of Pu concentration is shown in two ways in Figure 6.3-10. A linear representation (Figure 6.3-10A) emphasizes the uniform nature of the distribution, and a logarithmic representation (Figure 6.3-10B) emphasizes the range of values. Both of the views in Figure 6.3-10 indicate that ~90% of values sampled from this distribution would come from between concentrations of 1×10^{-7} and 1×10^{-6} molar.

Ra

The Elicitation (Gauthier, 1993) based the log-beta distribution for solubility-limited Ra concentrations on the calculations done by Kerrisk (1984) noting that these limits should be similar to those for barium (Ba) and dependent upon the presence of sulfate in the ground water. It was noted in the Elicitation that Ra should only form a single cation and that the solubility limits should be relatively unaffected by compositional variations in the ground water. The elicited distribution is shown in Figure 6.3-11 and the parameters are given in Table 6.3-1.

Sn

The Elicitation (Gauthier, 1993) noted that the elemental solubility of Sn is very low and based the uniform distribution for solubility-limited Sn concentrations on the data range given in Andersson (1988) and the consensus that any value was equally likely. The elicited distribution is shown in Figure 6.3-13 and the parameters are given in Table 6.3-1. This uniform distribution of Sn concentration is shown in two ways in Figure 6.3-13. A linear representation (Figure 6.3-13A) emphasizes the uniform nature of the distribution, and a logarithmic representation (Figure 6.3-13B) emphasizes the range of values. Both of the views in Figure 6.3-13 indicate that ~90% of values sampled from this distribution would come from between concentrations of 1×10^{-8} and 1×10^{-7} molar.

Th

The Elicitation (Gauthier, 1993) noted that the elemental solubility of Th should be less in general than either Am or Pu making it relatively unimportant and that the range of values were well defined, similar to Am. The Elicitation also indicated that the distribution should make the lower values more probable and derived a log-uniform distribution for solubility-limited Th concentration. The elicited log uniform distribution is shown in Figure 6.3-15 and the parameters are given in Table 6.3-1.

U

The Elicitation (Gauthier, 1993) noted that the elemental solubility of U should be higher in general than either Am or Pu but also that it was not expected that solubility-limits for U would be a factor in release of U in Yucca Mountain even though the ground water contains dissolved silica which could cause uranium silicates to precipitate. The Elicitation panel indicated that the data for U (Wanner and Forest, 1992) have a wide range with a central tendency between 1×10^{-5} and 1×10^{-4} molar and about 1 order-of-magnitude spread (Gauthier, 1993; Wilson et al., 1994). Based on this information, the Elicitation resulted in a log-beta (skewed log-normal) distribution for solubility-limited U concentrations which is shown in Figure 6.3-16. The parameters for this distribution are given in Table 6.3-1.

Zr

The Elicitation (Gauthier, 1993) noted that the elemental solubility of Zr is very low and based the log-uniform distribution for solubility-limited Zr concentration on the data range given in Andersson (1988). The Elicitation panel selected a logarithmic distribution to emphasize the probability of the lower values which they concluded were more likely. The elicited log-uniform distribution is shown in Figure 6.3-17 and the parameters are given in Table 6.3-1.

6.3.3 Sensitivity Cases for Solubility-Limited Aqueous Radionuclide Concentrations

Although the distributions listed in Table 6.3-1 encompass implicitly a range of potential variation in system parameters, explicit incorporation of the major variables affecting the aqueous concentrations of radionuclides allows for more direct examination of parameters which impact the performance of the potential repository system. In addition, the distributions discussed above do not incorporate potential effects of near-field compositional variations which could result in fluids reacting with the waste form which are very different from those in the natural system. Such changes in the near-field fluid compositions should lead to changes in the constraints on the phases controlling the concentrations of dissolved radionuclides. Because the actual changes to the near-field environment are not yet well-defined, incorporation of such effects either into distributions such as those discussed above or into models for predicting the solubility-controlling phases for each radionuclide is not currently possible.

Experimental Studies of Steady-State Np, Pu, and Am Concentrations

A more-limited sensitivity study of the explicit temperature and pH dependencies of dissolved Np, Pu, and Am is developed in this analysis using the empirical measurements of Nitsche et al.

(1993) for the dissolved concentrations of these radionuclides in J-13 initial water. The experiments were conducted from oversaturation with temporal measurements of dissolved radionuclide concentrations to derive steady-state concentrations for Np, Pu, and Am as functions of both pH (~6, 7, and 8.5) and temperature (25°, 60°, and 90°C). As discussed below, these data are used here to derive empirical relations for the log(concentrations) of Np, Pu, and Am as functions of temperature and pH. Although there are a number of caveats as discussed below, these functions allow more explicit consideration of the effects of the variations in temperature and pH which is a first step in building a higher level of realism into the way Total System Performance Assessments constrain the aqueous concentrations of radionuclides.

An additional study which analyzed temperature and pH dependencies of dissolved Np, Pu, and Am in UE-25p#1 initial water (higher carbonate concentration than J-13 water) from oversaturation (Nitsche et al., 1994) indicates that, compared to the results for J-13 initial water, the steady-state concentrations for Np are lower, and for Pu are within one order of magnitude in all cases (pH ~6, 7, 8.5 and temperature 25°, 60°C). Measured steady-state concentrations of Am in UE-25p#1 initial water are 2 to 3 orders of magnitude as large as the J-13 study values at 25°C and all pH values, but are lower than those determined in J-13 initial water at 60°C. As a test of whether the experiments in these studies were approaching an equilibrium (metastable or stable) situation at the steady state, a set of experiments were conducted using the solid products of the previous oversaturation studies to approach the steady-state concentrations from undersaturation in UE-25p#1 initial water at 60°C (Nitsche et al., 1995). In general, the results of Nitsche et al. (1995) are similar to the oversaturation studies for Np at all pH values, but show some disagreement for Pu and Am oversaturation results, generally at high pH.

The measurements in J-13 initial water were fit empirically as functions of temperature and pH and used in an analysis of sensitivity for the following reasons: (1) the water from J-13 (tuff aquifer) is more likely to be representative of the water that will occur within the proposed repository horizon than the water from UE-25p#1 (deeper Paleozoic carbonate aquifer); (2) most of the previous solubility-limited studies assumed J-13 water (e.g., PNL's TSPA-91—Eslinger et al., 1993); (3) data are determined at more, and to higher, temperatures for J-13 water compared to UE-25p#1 water (Nitsche et al. 1993; 1994); and (4) the steady-state concentrations of Np and Pu vary by only about an order of magnitude between the two waters.

Functional Fits to the Steady-State Concentration Determinations

In TSPA-1993 (Andrews et al., 1994), the empirical data were fit with functions representing the temperature dependence for equilibrium thermochemical relations for a single solid-phase solubility reaction. However, the empirical determinations (Nitsche et al., 1993) do not meet all the criteria required to accurately apply such relations (e.g., demonstration of attainment of (stable or metastable) equilibrium between a single solid with the aqueous solution). Therefore this treatment is not used in TSPA-1995 and is replaced with an empirical fit of the data in order to reproduce the temperature and pH dependence of the measurements. Because it was decided to derive temperature- and pH-dependent functional forms for values of the log_{10}(radionuclide concentration) (i.e., $log(C_{RN})$), the original raw determinations reported in the Appendices of Nitsche et al. (1993) were reexamined in order to recast the observations as log-normal distributions.

The derived averages and standard deviations of $\log(C_{Np})$, $\log(C_{Pu})$, and $\log(C_{Am})$ are listed in Tables 6.3-2, 6.3-3, and 6.3-4, respectively, with the conditions and the range of samples (Nitsche et al., 1993) used to calculate the tabulated values for each determination. In addition, the last column of Tables 6.3-2, 6.3-3, and 6.3-4 contains the radionuclide concentration corresponding to the average $\log(C_{RN})$ (note that this value should always be smaller than the *average of the concentration*). Comparison of the these values with those reported in Nitsche et al. (1993) indicates that there is not a substantial difference introduced by this treatment. However, this treatment allows for direct inclusion of the uncertainties on the empirical values in the comparison of the functional fits for $\log(C_{Rn})$. During reexamination of the empirical determinations of the steady-state concentration measurements for Np, Pu, and Am (Nitsche et al., 1993) three of the determinations were not used. Because they appear to be increasing with time, the temporal measurements of Np concentration at 60°C and pH of ~7 were interpreted as not representative of an approach to steady-state. This was also the conclusion for the measurements of Am concentration at 60°C and pH of ~7 which show a general increase over the last half of the determinations. Also not used in this analysis was the determination of steady-state Am concentration at 60°C and pH of ~6 which, as discussed by Nitsche et al. (1993), appears to be controlled by metastable persistence of the orthorhombic solid causing grossly higher values relative to the rest of the Am determinations.

The empirical results for steady-state concentrations of Np, Pu, and Am (Nitsche et al., 1993) indicate that either different phases developed at different conditions in the experimental studies, each of which may or may not have been at equilibrium with the aqueous phase, or that there were mixtures of phases. Therefore, there are not many theoretical thermochemical constraints which can be readily used to guide the functional form to use for fitting the results. The two external guides for fitting the data that we applied were: (1) the pH dependence was represented as the difference between the pH of the determination and neutral pH at that temperature (ΔpH); and (2) the fits were constrained such that the isothermal sections of the functions were concave upwards along the ΔpH axis. The values used for neutral pH at temperatures from 10 to 100°C were calculated using SUPCRT92 (Johnson et al., 1992).

In order to obtain useful functional fits for the purpose of this analysis, least-squares regression was applied to the data in Tables 6.3-2, 6.3-3, and 6.3-4 using numerous polynomial functions constructed from combinations of inverse, linear, and quadratic temperature (T) terms, linear and quadratic ΔpH terms, and their interaction terms. A combination of goodness-of-fit and minimization of terms was used to guide the selection of the final fit functions without regard to obtaining the same form for each radionuclide. The temperature- and pH-dependent functions obtained to calculate the expected values are:

(1) for Neptunium

$$\text{Log}_{10}C_{Np} = -39.7 + 0.374(\Delta pH)^2 + 0.212T - 3.41\times10^{-3}T(\Delta pH) - 3.06\times10^{-4}T^2 \; ; \quad (6.3-1)$$

(2) for Plutonium

$$Log_{10}C_{Pu} = 0.124 - 0.876(\Delta pH)^2 - 0.0229T + 329.9\frac{(\Delta pH)^2}{T} \qquad (6.3-2)$$

and; (3) for Americium

$$Log_{10}C_{Am} = -9.02 + 0.0118T(\Delta pH) + 8.54 \times 10^{-4}T(\Delta pH)^2 - 3.96 \times 10^{-5}T^2(\Delta pH) \qquad (6.3-3)$$

where

$$(\Delta pH) = pH - pH_N \qquad (6.3-4)$$

and pH_N represents neutral pH and temperature is in Kelvin.

The temperature-dependent, iso-pH sections of these functions are shown as solid curves in Figures 6.3-18, 6.3-19, and 6.3-20 for Np, Pu, and Am, respectively, with their one standard deviation uncertainty envelopes shown by the dashed curves (note: for purposes of clarity, only the uncertainty envelope for the lowest pH curve is shown in Figures 6.3-19, and 6.3-20). Also shown in these figures are the corresponding empirical data points with error bars of two standard deviations (from Tables 6.3-2, 6.3-3, and 6.3-4, respectively) which are generally within the uncertainty envelopes of the fitted functions.

Comparisons of these functional fits with the concentration ranges of their corresponding TSPA-1995 distributions are shown in Figures 6.3-21, 6.3-22, and 6.3-23 for Np, Pu, and Am, respectively. The ranges of values given by the functional fits for Np and Pu are essentially equivalent to their distribution ranges. However, Figure 6.3-23 shows that the maximum of the Am distribution is about 2.5 orders of magnitude higher than the maximum for the corresponding functional fit. Because the distribution for Am is based on the empirical studies (Nitsche et al., 1993; 1994), this discrepancy reflects in part the metastable, high concentration in J-13 initial water measured for Am at 60°C and pH of 6, and the high Am concentrations measured at 25°C in UE-25p#1 initial water.

The functions represented by Equations 6.3-1, 6.3-2, and 6.3-3, and their uncertainties, are sampled for solubility-limits for Np, Pu, and Am, respectively, in order to conduct sensitivity analyses of explicit parameter dependencies versus random sampling of the distributions used in the base case (Table 6.3-1). The estimates of $log(C_{Rn})$ provided by these fits incorporate two sources of uncertainty. The first contribution to the uncertainty is that associated with each of the regressed parameters which results from fitting to a finite data set. As such, the parameters are represented as multivariate normal distributions which are based on the means and covariance matrix from the regression. The second source of uncertainty stems from the discrepancy between the form of the fit and the actual structure of the pH and temperature dependence, as well as the fact that other variables contribute to the observations of $log(C_{Rn})$ but have been

ignored in the regression. This uncertainty is represented as an additional error term (ε) to each of the functional relations given above. This term is sampled from a normal distribution with a mean of zero (0) and a standard deviation determined from the sum of the squares of the residuals of the fit. Within the sensitivity analysis, sets of fit parameters and values of ε are sampled for each realization to generate the three relations used to estimate $\log(C_{Rn})$ during the realization based on its temperature profile and pH.

There are a number of caveats for using the above functional fits to represent bounding estimates of the pH and temperature dependencies of solubility limits in J-13 water because the empirical studies may not reflect the actual solubility-controlling reactions over the range of conditions because of phase metastability and do not obtain the same solid phase at each condition. First, it cannot be demonstrated directly that the systems attained any equilibrium state, because the experiments were not conducted from both over- and undersaturation. Although attainment of equilibrium was not directly demonstrated (Nitsche et al., 1993), the approach from oversaturation makes it likely that any kinetic constraints on the system provide concentrations that are higher that one would expect had equilibrium be achieved.

Second, even if equilibrium (stable or metastable) had been achieved in the experiments, there are different solid phases at different conditions. This allows the possibility in the studies that metastable phases controlled dissolved concentrations at low temperatures, whereas at higher temperatures stable phases set concentrations to lower values. Fitting such data with a temperature-dependent function may lead to an empirical fit which is decreasing at high temperature, whereas the solubility of the stable phase could be actually increasing with temperature. Such a situation would lead to underestimation of the dissolved concentration of radionuclides at temperatures higher than the empirical data. This would be the most pronounced for estimating the Pu and Am concentrations from their functional fits because they are decreasing steeply at higher temperatures. Because the functional fits are extrapolated only 10°C (to 100°C), any underestimate of these values should be within the uncertainties of the functional fits.

Third, during the course of the experiments $HClO_4$ and NaOH added to the J-13 initial water to control pH (Nitsche et al., 1993) changed the composition from that of J-13 ground water. Initial process-level geochemical modeling of these experiments conducted at Los Alamos National Laboratory (Janecky et al., 1994) indicates that the added Na may have impacted (lowered) the measured dissolved Np concentration by changing the saturation state of the Na-neptunyl-carbonate-hydrate phase present in the system. Therefore using the above derived functional fits as representative of solubility constraints in J-13 water may not be bounding. However, the model calculations also indicate that the Na-neptunyl-carbonate-hydrate phase is approximately at metastable equilibrium, and that the stable equilibrium phase in this compositional system may be NpO_2, which would control dissolved Np concentrations to much lower values (at least a few orders of magnitude). This result, combined with consideration of the uncertainties on the above derived functional fits, allows that these fits can be used to represent a nearly J-13 fluid composition as a bounding sensitivity case. However, progress in thermochemical modeling of solubility-limited concentrations of these and other radionuclides may provide additional constraints on dissolved radionuclide concentrations and more explicit compositional dependencies to be incorporated into future total system performance analyses.

6.4 COLLOID CONTRIBUTIONS TO MOBILE MASS OF RADIONUCLIDES

6.4.1 Introduction

In addition to radionuclides dissolved in the aqueous phase, another potentially significant contribution to the mobile mass of radionuclides could come from colloids. Suspended in the aqueous phase, colloids are minute particles ranging in size from about 10^{-8} m (100 Å) up to about 10^{-5} m (10^5 Å); a range which includes viruses at the low end and bacteria at the high end (Stumm and Morgan, 1981). Field studies of saturated-system radionuclide migration associated with underground nuclear tests (Buddemeier and Hunt, 1988) or with actinide contaminant plumes (Penrose et al., 1990) indicate that those systems possess a highly mobile colloidal component. The degree to which colloids will impact the performance of a potential repository at Yucca Mountain is currently uncertain. The state of knowledge concerning this issue is summarized by Triay et al. (1995a), who propose a strategy to assess the importance of colloids for a potential repository by focussing on three aspects: (a) the presence of colloids at the potential repository; (b) the stability of the colloids in the ground-water system; and (3) the ability of the colloids to migrate through the unsaturated and saturated hydrogeologic system. Although it is not currently possible to constrain quantitatively these aspects comprehensively, a summary of how these issues may be incorporated into total system performance assessment calculations is presented below.

In a potential repository environment there are two general types of colloids: (a) *waste-form colloids* which contain radionuclides as part of their structural mass; and (b) *pseudocolloids* which are comprised of small particles of other materials which adsorb radionuclides and may act as a mobilizing agent. Waste-form colloids include *radiocolloids* ("true" or real colloids) produced by agglomeration of hydrolysed actinides (e.g., Hobart et al., 1989) which form during initial precipitation from supersaturated solutions, and *degradation colloids* formed by physical deterioration of the waste material (or alteration products) itself (e.g., Bates et al., 1992). Pseudocolloids generated from the natural system minerals or natural organic matter are *natural colloids*, and those generated from substances introduced to study the site or produce a potential repository are *introduced colloids*. For this discussion, the various colloids are sufficiently distinguished by their sources as waste-form colloids, natural colloids, and introduced colloids.

6.4.2 Assessment of Colloid Constraints

As pointed out by Triay et al., (1995a), the abundance, stability, and ability to migrate should determine the relative impact to the performance of a potential repository for each of these groups of colloids. In general, the detailed quantitative constraints and models for each of these aspects are not available, and it is therefore difficult to eliminate any of the potential colloid types from consideration or to develop a comprehensive Performance Assessment model of the effects of colloids (Ramsay, 1988; McCarthy and Zachara, 1989; Manaktala et al., 1995; Gauthier, 1995; Triay et al., 1995b).

Waste Form Colloids

For waste form colloids, it has been shown that degradation colloids form from high-level waste glass and can comprise over 99% of the mobile Am and Pu (Bates et al., 1992), but their long-

term stability is poorly understood. Studies by Feng et al. (1993) indicate that these types of colloids will agglomerate readily at high ionic strengths or low temperatures and settle out of the aqueous phase, but may resuspend if contacted by dilute fluids. Under acidic conditions stable Pu(IV) radiocolloids can form, but these may not be stable at higher pH (Hobart et al., 1989; Triay et al., 1991). Small-scale laboratory experiments on the transport of radiocolloids of both Pu(IV) and Am(III) through tuff columns indicate that most of the material was retained in the rock, but a minor portion moved through the system faster than a conservative tracer (Thompson, 1989).

Introduced Colloids

The major introduced substances in the potential repository environment that will be potential sources of introduced colloids include organic substances, steels, and cements leading to organic colloids, iron-oxy(hydroxy) colloids, and alumino-silicate colloids, respectively (Meike and Wittwer, 1993). Meike and Wittwer (1993) indicate that the ability of these colloids to migrate is dependent on a complex interrelation of many system variables including ionic strength, organic content, flow velocity, pH, temperature, and oxidation state. However, because the distribution and abundance of the these introduced materials is uncertain and the ability to quantify the generation and stability of colloids resulting from these materials is lacking, incorporation of the quantitative details of their effects into performance assessment models is not currently possible.

Natural Colloids

Natural colloids occurring at Yucca Mountain include inorganic colloids consisting essentially of clays, silica, and iron oxyhydroxides (Ogard 1987; Levy, 1992; Triay et al., 1995b) and organic colloids such as humic and fulvic acids (Minai et al., 1992). Such colloids may be able to enhance the transport of highly sorbing radionuclides such as Pu and Am. The abundance and stability of the inorganic colloids have been characterized in a manner which could facilitate incorporation into Performance Assessment models (Triay et al., 1995b). The mass concentration of natural colloids of size greater than 200 nm in J-13 water was measured to be about 23 ng/ml (Triay et al., 1995b), which was similar to the value of 27 ng/ml measured by Ogard (1987) for natural colloids greater than 400 nm. In order for these concentrations of natural colloids to account for 10% of a particular mobile radionuclide, Ogard (1987) calculated that a sorption distribution coefficient of greater than 4×10^6 ml/g was necessary for that radionuclide. This is much higher in general than the measured values or the values recommended to assess the effect of these colloids on trivalent and tetravalent actinides using an irreversible sorption assumption (Triay et al., 1995b).

Transport of natural colloids through the unsaturated zone may be affected by a number of processes including size/surface charge exclusion from matrix pores, agglomeration and sedimentation, and attachment of colloids to the rock wall, and is not well-modeled using filtration theory, particularly in systems with fractures (Triay et al., 1995a). The model calculations of unsaturated media effects on colloid transport by Nuttall et al. (1991) indicate that the hydrophobic colloids concentrate at the air/water interface and should move rapidly through the system at the highest flow velocity. In contrast, experimental work in unsaturated media by Wan and Wilson (1994) indicates that the hydrophobic colloids will be retarded and become

irreversibly immobilized at the air/water interfaces in the unsaturated system. Hydrophobic colloid transport is greatly reduced under these conditions unless the interface itself is moving. This reduced transport was observed even for continuous interfaces through the system and was less pronounced but still present for hydrophyllic colloids (Wan and Wilson, 1994).

Because these natural colloids are similar in composition to the host rock in the system, a simplified model for transport of natural colloids was presented by Gauthier (1995) assuming reversible sorption onto the colloids. The simplified model based on the work of Vilks (1994) accounts for the transport effects of natural colloids simply by reduction of the retardation factor which is justified because the colloids sorb radionuclides in the same manner that the rock itself does. In this model, the radionuclide retardation factor (R) is redefined by

$$R = 1 + \frac{\rho_b K_d}{\theta(1 + C_c F_A K_d)} \qquad (6.4\text{-}1)$$

where θ represents the fractional water content, ρ_b signifies the bulk rock density, K_d denotes the radionuclide distribution coefficient, C_c refers to the colloid concentration, and F_A indicates the adjustment factor for the K_d to account for the colloid surface area. In this treatment, the total mobile mass of radionuclides cannot be resolved into its component parts corresponding to those radionuclides dissolved in the aqueous phase and those radionuclides which are sorbed onto the colloids. In addition, Gauthier (1995) outlines a second model to consider irreversible sorption onto colloids which requires incorporation of an entire additional set of transport equations for the colloid component of the mobile mass of radionuclides. Although this second model is a more flexible representation of the system, it effectively doubles the amount of calculation required.

6.4.3 Incorporation of Colloids into Total System Performance Assessments

All of the uncertainties outlined above in both the colloid component source terms, and in the stability and transport of colloids make it difficult to assess quantitatively the colloid contribution to the mobile radionuclide mass in a Total System Performance Analysis. However, from the above discussion it also appears that a first step can be made in the construction of a performance assessment model for the effects of the natural colloids on highly-sorbing radionuclides that have solubility-limited releases (such as Pu and Am). Such a model would account for the effects of natural colloids on both the source term for the mobile mass of radionuclides and for the effects on transport of that mobile mass.

The conceptual representation of how the effects of natural colloids on the source term would be incorporated into current performance assessment models is shown in Figure 6.4-1. Figure 6.4-1 shows that for a mass of spent fuel (M_{sf}) the initial dissolved radionuclide mass (M_{dis}) is controlled by the dissolution rate (R_{dis}), the exposed area of spent fuel (A), and the length of the time step (t). This constrains the initial dissolved aqueous radionuclide concentration (C_{dis}) given the volume of water in contact with the waste form (V_w). At this point, a filter based on the sampled phase solubility-limit (S_i) is applied. If C_{dis} is less than S_i, then the mobile radionuclide concentration (C_{mobile}) is set equal to C_{dis}; otherwise the aqueous radionuclide concentration C_{aq} is set equal to S_i and the extra radionuclide mass is allowed to "precipitate" (M_p). At this point

the concentration of radionuclide on the natural colloids (C_{col}) can be calculated based on C_{aq}, the sorption distribution coefficient for the radionuclide on the natural colloid (K_p), and the mass concentration of the natural colloid ($[\overline{Coll}]_m$). In this case the C_{mobile} is equal to the summation of the two mobile components of C_{aq} and C_{col}. This would allow for calculation of the change in source term for actinides which have low solubility-limits and high sorption coefficients (e.g., Am and Pu). Constraints on the abundance of the natural colloids and values of K_P for trivalent and tetravalent actinides are presented in Triay et al. (1995b). For the first step in addressing the total mobile mass of Am and Pu in this system, the transport equations could be modified as recommended by Gauthier (1995) (Equation 6.4-1) to assess the sensitivity of Am and Pu releases to the natural colloid component in the system. In addition, future adaptations of more detailed approaches will be facilitated because the aqueous and colloidal radionuclide masses are kept explicitly separate in the source term.

6.5 RADIONUCLIDE RELEASE MODELING

6.5.1 Approaches for Radionuclide Release Modeling

Dominant cladding degradation mechanisms anticipated for given repository conditions (creep rupture and cladding splitting) were discussed in Section 5.6. The potential cladding degradation mechanisms and their effects on the performance of cladding as a barrier to radionuclide release have not been implemented in a detailed model in TSPA-1995. Thus, in the nominal case in TSPA-1995, performance credit for cladding is not included in the waste package and EBS release calculations discussed in Chapter 8. Additionally, potential performance credit for the stainless steel MPC shell as an additional barrier is not included in the nominal case in TSPA-1995. Similarly, for waste packages containing vitrified defense high-level waste (DHLW), the potential performance of the stainless steel pour canister as a barrier is not considered.

Accordingly, after a waste-disposal container failure, the waste forms contained inside (spent fuel pellets or monolithic glass log) are assumed to be exposed immediately to the near-field environment, making them available for alteration/dissolution. Then, radionuclides may be released and transported through the failed waste package and underlying gravel invert to the edge of the engineered barrier system (EBS).

6.5.2 Conceptual Models for Radionuclide Release

Depending on ground-water flux around or through the waste package and EBS, radionuclide release mechanisms are characterized as diffusive release, advective release, or a combination of both. As discussed in Chapter 5 for the waste-disposal container degradation modeling, waste containers are assumed to fail by pitting corrosion, not by general corrosion. The waste container degradation models developed for TSPA-1995 predict the number of pits penetrating the container wall as a function of the emplacement time, relative humidity and temperature. Therefore, release of radionuclides by diffusion, advection, or both is restricted by the number of perforations on the "partially failed" waste container, i.e. by the area available for the release. Discussed below are the conceptual models and model development approaches for diffusive and advective releases.

Figures 6.5-1 and 6.5-2 are the schematic diagrams for the cylindrical waste-disposal container in an emplacement drift viewed from the side and front respectively. The spent fuel assemblies and DHLW glass monolith are assumed to be distributed uniformly inside the waste container. To simplify the release calculation, the cylindrical waste container and the underlying invert are represented by an equivalent spherical configuration. Figure 6.5-3 shows the equivalent spherical configuration of the waste container with multiple perforations. The perforations are formed from pitting corrosion (see Chapter 5) and filled with fine, gel-like porous corrosion products. The perforations are assumed to be cylindrical holes of uniform radius. The perforations are also assumed to form uniformly over the entire surface. It is assumed conservatively that both downward and upward perforations are equally available for radionuclide release, and, once outside the waste container, all the radionuclides are immediately released into the underlying porous (crushed gravel or concrete) invert, and allowed to migrate toward the host rock.

Shown in Figure 6.5-4 is a cross-sectional view of the geometry of the cylindrical perforation, invert, and host rock in the equivalent 1-D conceptual release model. The contribution of each perforation to the radionuclide release is assumed to be independent of other near-by perforations, i.e. the release rates from each perforation are all the same. This assumption may be conservative in that the concentration gradients just inside adjacent perforations may be less than for the case in an isolated perforation. This assumption is supported by the finding that the concentration gradients near an aperture in a "thin" wall are very large (Chambre, et al, 1986). Although it is expected that the container wall becomes thinner with time due to wastage from general corrosion, the wall thickness is assumed to remain constant.

Because no data for the transport properties of radionuclides in the porous corrosion products filling the perforations (or pits) are currently available, it was assumed that the corrosion products have the same porosity and maintain the same water content (liquid saturation) at a given time as the invert material (either crushed gravel or concrete). In addition, whenever a waste package is under dripping water, the diffusion coefficient in the pits and the invert is assumed to be 10^{-7} cm^2/sec (Conca, 1990; Conca and Wright, 1992). In reality, the corrosion products normally have a "gel-like" structure which is much finer and has a higher surface area than the invert material, thus they would have a greater capacity for holding moisture. However, the uncertainty associated with the assumptions is small relative to the overall uncertainties associated with the conceptual models and assumptions given in this section and in the mathematical models discussed in the following sections.

6.5.3 Diffusive Release from Waste Package and EBS

Taking into account the approaches and the conceptual models for the release from the "partially failed" waste container discussed in the previous section, both steady-state and "quasi-transient" diffusive mass transport models were developed. In the simulations using the RIP code, the "quasi-transient" diffusive mass transfer model was used to calculate diffusive release of radionuclides at the EBS edge. Because steady-state diffusive mass transfer through the "failed" waste package is utilized in developing the "quasi-transient" diffusion model, derivation of the steady-state diffusive mass transfer relation is also discussed in detail.

Steady-State Diffusive Transport

The following is the derivation of an analytical solution for the radial steady-state diffusive mass transfer rate at the edge of EBS through the "partially failed" waste container and the underlying invert. The derivation is based on the equivalent spherical configuration of the waste package and other EBS components (Figure 6.5-3). Assuming that there are N uniformly distributed perforations on the surface of the spherical waste container (Figure 6.5-3), which represent non-interacting emitting sources, the steady-state diffusive mass transfer rate ($\dot{M}_{WP}$) through the waste package perforations can be expressed as follows (Chambre, 1995):

$$\dot{M}_{WP} = \frac{C_o - C_1'}{\dfrac{1}{N\pi\,\alpha^2}\left[\dfrac{\pi\,\alpha}{4}\left(\dfrac{1}{\sigma_0 D_0} + \dfrac{1}{\theta_2 D_2}\right) + \dfrac{l}{\theta_1 D_1}\right]} \qquad (6.5-1)$$

where C_0 = concentration of radionuclide at the surface of waste form;

C_1' = concentration of radionuclide just outside a perforation at the surface of the "failed" waste container;

σ_0 = porosity just inside the waste container (= 1.0);

θ_1 = fractional water content of the corrosion products filling the perforations;

θ_2 = fractional water content of the invert;

D_0 = diffusion coefficient just inside the waste container (= 10^{-5} cm^2/sec);

D_1 = diffusion coefficient in the corrosion products-filled perforations (function of liquid saturation);

D_2 = diffusion coefficient in the invert (function of liquid saturation);

l = thickness of the waste container wall;

α = radius of the perforation; and

N = number of perforations at a given exposure time.

The number of perforations (N) at a given exposure time is derived from the waste container degradation models (see Chapter 5). Assuming a spherical shell geometry for the invert surrounding the spherical waste container (Figure 6.5-3), the solution given by Crank (1975, pp. 89-90) was used to solve for the steady-state radial diffusive mass transfer rate from the surface of the waste package to the edge of EBS for a given set of boundary conditions. The boundary conditions used for the solution are

$$C = C_1 \qquad at \quad r = a \qquad (6.5-2)$$

$$C = 0 \qquad at \quad r = b \qquad (6.5-3)$$

where a is the distance from the center of the sphere to the edge of the waste container, and b is the distance from the center of the sphere to the edge of the EBS. The concentration at the boundary of the EBS (i.e., the edge of the invert) was conservatively set to zero (Equation 6.5-3) to yield the highest diffusive flux at the EBS boundary. The resulting equation for the steady-

state radial diffusive mass transfer rate from the surface of the waste package to the edge of EBS is

$$\dot{M}_{EBS} = \frac{4\pi a\,\theta_2 D_2\,C_1}{1 - \dfrac{a}{b}}$$ (6.5-4)

Using arguments essentially equivalent to the method of matched asymptotic expansion, C_1 in Equation 6.5-4 can be equated to $C_1{'}$ in Equation 6.5-1 (Chambre, 1995). Thus, equating $\dot{M}_{WP}$ (Equation 6.5-1) to $\dot{M}_{EBS}$ (Equation 6.5-4) and solving for C_1, an equation for the steady-state radial diffusive mass transfer at the edge of EBS is expressed as

$$\dot{M}_{EBS}^{ss} = \frac{4\pi\,\theta_2 D_2\,a\,C_o}{\dfrac{4}{N}\dfrac{a}{\alpha}\left[\dfrac{\pi}{4}\left(\dfrac{\theta_2 D_2}{\sigma_o D_o} + 1\right) + \dfrac{\theta_2 D_2}{\theta_1 D_1}\dfrac{l}{r}\right] + (1 - \dfrac{a}{b})}$$ (6.5-5)

Equation 6.5-5 shows that the diffusive mass transfer rate depends on the number of perforations (N) in the waste container, the container wall thickness (l), and the geometry of the waste container and invert (a and b). An equation for the steady-state radial diffusive mass transfer rate at the EBS edge from a *bare* spherical waste form can be obtained by setting N→∞, resulting in

$$\dot{M}_{EBS}^{WF} = \frac{4\pi\,\theta_2 D_2\,a\,C_o}{1 - \dfrac{a}{b}}$$ (6.5-6)

which lacks a dependence on the number of perforations. Figure 6.5-5 shows the steady-state diffusive release rate from the bare waste form (Equation 6.5-6) compared to the steady-state diffusive release rate at the EBS boundary from a perforated waste package as a function of the number of perforations. In the calculations, a volumetric water content of 0.1 was assumed for the crushed-tuff gravel invert. As shown in the figure, the steady-state diffusive release rate is strongly dependent on the number of perforations.

Transient Diffusive Transport

Using a similar approach to deriving the analytical solution for the steady-state diffusive mass transfer rate (Equation 6.5-5), an analytical solution for a "quasi-transient" diffusive mass-transfer rate at the EBS boundary (i.e., the edge of the invert) through the "partially failed" waste container was developed. This "quasi-transient" diffusive mass transfer rate equation was implemented into the RIP code to calculate the EBS diffusive release of radionuclides.

The term "quasi-transient" is used because the solution incorporates steady-state diffusive transfer through the perforations of the "failed" waste container (Equation 6.5-1) combined with transient diffusive mass transfer through the spherical shell of the invert (other EBS components) surrounding the waste container (see Figure 6.5-3). The approximation for steady-state diffusion

through the waste package should not result in a significant error because of the much shorter distance for diffusion (12 cm) through the waste container compared that for the invert (100 cm).

In developing an analytical solution for transient diffusive mass transfer through the spherical shell of the invert, the following boundary and initial conditions were considered:

$$C = C_1 \quad at \ r = a, \ t > 0 \qquad (6.5\text{-}7)$$

$$C = 0 \quad at \ r = b, \ t > 0 \qquad (6.5\text{-}8)$$

$$C = 0 \quad for \ a \leq r \leq b, \ t = 0 \qquad \cdot \qquad (6.5\text{-}9)$$

As in the steady-state diffusion case, the concentration at the EBS boundary was conservatively set to zero (Equation 6.5-8). Utilizing a solution given by Crank (1975, p. 98), the transient mass transfer rate at the EBS (or invert) edge is expressed as

$$\dot{M}_{EBS} = \frac{4 \pi a \theta_2 D_2 C_1}{b - a} \left[b + 2 \sum_{n=1}^{\infty} n \ \exp\left(-\frac{D_2 n^2 \pi^2 t}{R_2 (b-a)^2} \right) \right] \qquad (6.5\text{-}10)$$

where

$$R_2 = 1 + \frac{k_{d,2} \rho_2}{\theta_2} \qquad (6.5\text{-}11)$$

where t is time (years), R_2 is the retardation coefficient in the invert, $k_{d,2}$ is the distribution coefficient (cm^3/g) in the invert, and ρ_2 is the bulk density (g/cm^3) of the invert material. Other symbols are defined above. Following the same arguments as in the steady-state diffusive mass transfer case, equating $\dot{M}_{WP}$ (Equation 6.5-1) to $\dot{M}_{EBS}$ (Equation 6.5-10) and solving for C_1, the resulting equation for the "quasi-transient" diffusive mass transfer rate at the edge of EBS is expressed as follows:

$$\dot{M}_{EBS}^{tr} = \frac{P_3 C_o}{P_1 P_2 + 1} \qquad (6.5\text{-}12)$$

where

$$P_1 = \frac{1}{N \pi \alpha^2} \left[\frac{\pi \alpha}{4} \left(\frac{1}{\sigma_o D_o} + \frac{1}{\theta_2 D_2} \right) + \frac{l}{\theta_1 D_1} \right] \qquad (6.5\text{-}13)$$

$$P_2 = \frac{4 \pi a \theta_2 D_2}{b - a} \left[b + 2 \sum_{n=1}^{\infty} n \ \exp\left(-\frac{D_2 n^2 \pi^2 t}{R_2 (b-a)^2} \right) \right] \qquad (6.5\text{-}14)$$

and

$$P_3 = \frac{4 \pi a \theta_2 D_2}{b - a} \left[b + 2 \sum_{n=1}^{\infty} (-1)^n n \ \exp\left(-\frac{D_2 n^2 \pi^2 t}{R_2 (b-a)^2} \right) \right] \qquad \cdot \qquad (6.5\text{-}15)$$

Shown in Figure 6.5-6 is a representative pitting history (or the change in number of pits with time) of a waste container which has the first pit penetration at about 800 years. Using this pitting history, the transient diffusive release rates at the EBS boundary calculated using (Equations 6.5-12 through 6.5-15) with the distribution coefficients of 20, 200 and 1000 (cm³/g) are compared with the steady-state release rate in Figure 6.5-7. A volumetric water content of 0.1 was assumed for the invert. As shown in the figure, the difference between the steady-state and the transient diffusive release rates at any time is greater for larger values of the distribution coefficient, and the difference decreases with time.

6.5.4 Diffusion Coefficient in Unsaturated Porous Media

Using an unsaturated flow apparatus based on open-flow centrifugation, Conca and coworkers (Conca, 1990; Conca and Wright, 1990; Conca and Wright, 1992) measured aqueous diffusion coefficients in a wide spectrum of geologic materials at varying degrees of water saturation. It was suggested from their study that parameters such as diffusion coefficient and hydraulic conductivity are functions *primarily* of water content and not materials characteristics. The diffusion coefficient data for a wide variety of geologic materials were received from Conca (Engel, 1995) and were used to develop a relation for the diffusion coefficient in unsaturated porous media as a function of the volumetric water content. The functional form is expressed as

$$\log D_{p,i} = -8.255(\pm 0.0499) + 1.898(\pm 0.0464)\log \phi \qquad (6.5\text{-}16)$$

where $D_{p,i}$ is the diffusion coefficient (cm²/sec) (or "pore diffusivity") of diffusing species i within the pore-liquid phase (this parameter takes into account the tortuosity and constrictivity of the porous medium; Atkins and Nickerson, 1984; Brakel and Heertjes, 1974); and ϕ is the volumetric water content (in percent, i.e., $\phi = 100 \times \theta$). The data used and the model estimation with its uncertainty are shown in Figure 6.5-8. Equation 6.5-16 was implemented in the RIP code to calculate the diffusion coefficients used in the simulations of waste package and EBS diffusive releases.

As a point of clarification, the pore diffusivity can be related to the diffusion coefficient in bulk water ($D_{o,i}$) and the effective diffusion coefficient ($D_{eff,i}$) in a porous medium as follows (Brakel and Heertjes, 1974; Atkins and Nickerson, 1984)

$$D_{p,i} = D_{o,i}\left(\frac{\delta}{\tau^2}\right) = \frac{D_{eff,i}}{\theta} \qquad (6.5\text{-}17)$$

where τ is the tortuosity, δ is the constrictivity, and ε is the fractional volumetric water content of the material (which is equivalent to the porosity in saturated systems). The diffusion coefficient in aqueous solution decreases as ionic strength increases, and increases as temperature increases (Miller, 1982). However, these effects are minor compared to those from the degree of saturation in an unsaturated porous medium.

6.5.5 Advective Release from Waste Package and EBS

Advective releases from the waste package and EBS are analyzed using three different advective transport scenarios in TSPA-1995:

- Scenario 1: advective transport through both waste package and other EBS components;
- Scenario 2: no advective transport through the waste package, only through other EBS components;
- Scenario 3: no advective transport (capillary barrier effect).

In addition, diffusive transport through the waste package and other EBS components is active for each of these scenarios.

Advective flux into a drift (q_{drip} derived in Chapter 7) may result in advective flow across/through waste packages within the drift. In order to address the uncertainty concerning how fracture flow will distribute once it intersects the drift, an area larger than the waste package cross-section is defined as the region from which advective flux is "focussed" onto the waste package (i.e., the effective catchment area). In TSPA-1995, the effective catchment area is assumed (arbitrarily) to be four times the length times the diameter of the waste package (i.e., four times the waste-package maximum cross-sectional area perpendicular to flow). The product of the advective flux (q_{drip}) and the effective catchment area referred to in Chapter 7 as the total volumetric flow rate per package (Q_{drip}) and represents the advective flow for a given waste package.

Scenario 1. Advective Transport Through Both Waste Package and Other EBS Components

When there is ground water dripping onto a failed waste package, radionuclides from the waste package may be released by advection. In this scenario, once the waste package fails by pitting corrosion (i.e., at least one pit penetration) the dripping water is assumed to directly contact the waste form and the dissolved radionuclides may be released by advection. The advective release rate is calculated using the following conventional advective release rate equation

$$\dot{M}_{ad} = Q_{drip} \, C_o \qquad (6.5\text{-}18)$$

where $\dot{M}_{ad}$ is the advective mass transfer rate of species i (moles/yr), Q_{drip} is the total volumetric flow rate on the package (m³/yr—discussed above and derived in Chapter 7), and C_o is the radionuclide concentration at the waste form surface (moles/m³). Figure 6.5-9 presents a schematic of this conceptual model.

Scenario 2: No Advective Transport Through the Waste Package, Only Through Other EBS Components

The conceptual model for the advective release discussed in the previous section is conservative in that it does not include any potential performance credit for the "partially" failed (i.e., perforated) waste container as a barrier. The perforations in failed waste containers are filled with fine, gel-like porous corrosion products which may keep percolating ground water from flowing through the waste package and directly contacting the waste form. Therefore, in this

second scenario, percolating groundwater is assumed to be diverted around the waste container and the radionuclides are assumed to transport to the edge of the waste container solely by diffusion through the corrosion-product filled perforations. The diffusive release is calculated with Equation 6.5-1, assuming steady-state diffusion through the perforations.

From that point, the radionuclides transport advectively through the underlying invert and to the edge of the EBS. The advective release from the outside of the waste package and through the other EBS components is calculated with Equation 6.5-18. Thus, the release rate at the EBS boundary is controlled by the diffusive transport rate through the perforations and the rate of water dripping onto the waste package. This advective release scenario brings more realism to the performance of the waste container which, although perforated, may still providing waste isolation benefits through controlled release of radionuclides. A schematic of this conceptual model is presented in Figure 6.5-10. The sensitivity of the EBS release rate to this transport scenario is discussed in Chapter 8.

Scenario 3: No Advective Transport (Capillary Barrier Effect)

In addition to the backfill distributing any aqueous flux which may "drip" into the drifts above the waste package, it may be possible to design and implement a capillary barrier which diverts all inflowing water away from the waste package. The effectiveness of such barriers (which are commonly referred to as diversion barriers, capillary barriers, or Richard's barriers) in diverting water flow has been demonstrated under a wide range of conditions anticipated in different waste-disposal concepts as described in Conca (1990) and Conca and Wright (1992). The design of such a barrier requires at least two materials of different grain-size distributions (and therefore capillary characteristics). The finer-grained material (e.g., sand) is placed above the coarser-grained material (e.g., gravel), and the interface between the two is sloped slightly to allow the drainage of any water which seeps into the sand layer. Although a number of questions remain regarding the long-term stability and performance of such a barrier, as well as the issue of how such a barrier might be emplaced, sensitivity analyses have been conducted in Chapters 8 and 9 to evaluate the potential performance benefits of a capillary barrier. In this scenario, radionuclides are released only by diffusive transport through the entire EBS, and the release rate is calculated with Equation 6.5-12. A schematic of this scenario for waste package and EBS release is presented in Figure 6.5-11.

Table 6.2-1 . Fractional Distribution of Gap Inventory Species Used in TSPA-1995

Nuclide	Spent Fuel Matrix	Gap Inventory[1]
^{14}C	U(0.94, 0.99)[2]	U(0.01, 0.06)[2]
^{135}Cs	0.98	0.02
^{129}I	0.98	0.02
^{79}Se	0.98	0.02
^{99}Tc	0.98	0.02

[1] Includes the inventory in grain boundary.
[2] Uniformly distributed with the minimum and maximum given.

Table 6.3-1   Distributions of Solubility-Limited Aqueous Radionuclide Concentrations for Nominal Case in TSPA-1995

RN	Distribution Type	Distribution Variable	Minimum Value g/m³ & [mol/l]	Maximum Value g/m³ & [mol/l]	Mean or Peak g/m³ & [mol/l]	C.V.	Source
Ac	uniform	Concentration	2.3e−5 [1.0e−10]	2.3e−1 [1.0e−6]	1.2e−1 [5e−7]	---	Elicitation
Am	uniform	Concentration	2.4e−5 [1.0e−10]	2.4e−1 [1.0e−6]	1.2e−1 [5e−7]	---	Elicitation
Cm	triangular (two temperature ranges)	log(Concen.)	$T \leq 55°C$: log(1.2e−6) [log(4.9e−12)] $T > 55°C$: log(1.5e−10) [log(6.1e−16)]	$T \leq 55°C$: log(1.2e−4) [log(4.9e−10)] $T > 55°C$: log(1.5e−8) [log(6.1e−14)]	$T \leq 55°C$: log(1.2e−5) [log(4.9e−11)] $T > 55°C$: log(1.5e−9) [log(6.1e−15)]	---	Jardine (1991- from Wilson, 1987; 1990)
Cs	triangular	log(Concen.)	log(1.2) [log(9.0e−6)]	log(2.1e+3) [log(1.6e−2)]	log(3.9e+2) [log(2.9e−3)]	---	Golder (1993), EPRI (1992)
Nb	uniform	log(Concen.)	log(9.3e−5) [log(1.0e−9)]	log(9.3e−3) [log(1.0e−7)]	log(9.3e−4) [log(1.0e−8)]	---	Elicitation
Ni	beta	log(Concen.)	log(5.9e-2) [log(1.0e−6)]	log(5.9e+3) [log(1.0e−1)]	log(1.1e+2) [log(1.8e−3)]	0.34 [0.25]	Elicitation
Np	beta	log(Concen.)	log(1.2) [log(5e−6)]	log(2.4e+3) [log(1.0e−2)]	log(3.4e+1) [log(1.4e−4)]	0.37 [0.15]	Elicitation*
Pa	uniform	log(Concen.)	log(2.3e-5) [log(1.0e−10)]	log(2.3) [log(1.0e−5)]	log(7.3e−3) [log(3.2e−8)]	---	Elicitation

Table 6.3-1. Distributions of Solubility-Limited Aqueous Radionuclide Concentrations for Nominal Case in TSPA-1995
(Continued)

RN	Distribution Type	Distribution Variable	Minimum Value g/m^3 & [mol/l]	Maximum Value g/m^3 & [mol/l]	Mean or Peak g/m^3 & [mol/l]	C.V.	Source
Pb	beta	log(Concen.)	log(2.1e-3) [log(1.0e-8)]	log(2.1) [log(1.0e-5)]	log(6.6e-2) [log(3.2e-7)]	0.44 [0.08]	Elicitation
Pd	uniform	log(Concen.)	log(1.0) [log(9.4e-6)]	log(1.0e+4) [log(9.4e-2)]	log(1.0e+2) [log(9.4e-4)]	---	Golder (1993)*
Pu	uniform	Concentration	2.4e-3 [1.0e-8]	2.4e-1 [1.0e-6]	1.2e-1 [5.1e-7]	---	Elicitation*
Ra	beta	log(Concen.)	log(2.3e-4) [log(1.0e-9)]	log(2.3) [log(1.0e-5)]	log(2.3e-2) [log(1.0e-7)]	0.10 [0.43]	Elicitation
Se	triangular	log(Concen.)	log(7.9e+2) [log(1.0e-2)]	log(5.5e+5) [log(7.0)]	log(7.9e+3) [log(1.0e-1)]	---	Golder (1993), EPRI (1992)
Sm	uniform	Concentration	1.5e-5 [1.0e-10]	1.5e-1 [1.0e-6]	7.5e-2 [5.0e-7]	---	Elicitation
Sn	uniform	Concentration	1.2e-6 [1.0e-11]	1.2e-2 [1.0e-7]	6.0e-3 [5.0e-8]	---	Elicitation
Tc	triangular	log(Concen.)	log(3.5e-2) [log(3.6e-7)]	log(9.9e+5) [log(1.0e+1)]	log(1.0e+2) [log(1.0e-3)]	---	Golder (1993), EPRI (1992)
Th	uniform	log(Concen.)	log(2.3e-5) [log(1.0e-10)]	log(2.3e-2) [log(1.0e-7)]	log(7.3e-4) [log(3.2e-9)]	---	Elicitation
U	beta	log(Concen.)	log(2.4e-3) [log(1.0e-8)]	log(2.4e+3) [log(1.0e-2)]	log(7.6) [log(3.2e-5)]	1.02 [0.2]	Elicitation

Table 6.3-1. Distributions of Solubility-Limited Aqueous Radionuclide Concentrations for Nominal Case in TSPA-1995 (Continued)

RN	Distribution Type	Distribution Variable	Minimum Value g/m³ & [mol/l]	Maximum Value g/m³ & [mol/l]	Mean or Peak g/m³ & [mol/l]	C.V.	Source
Zr	uniform	log(Concen.)	log(9.1e-8) [log(1.0e-12)]	log(9.1e-3) [log(1.0e-7)]	log(2.9e-5) [log(3.2e-10)]	---	Elicitation

Table 6.3-1 Explanation:

log: refers everywhere in the table to the base 10 logarithm.

RN: stands for radionuclide.

Mean or Peak: The values listed are the Arithmetic Mean for all distributions *except* log triangular distributions where the values listed correspond to the Peak of the distributions. *NOTE*: For any Distribution of log(Concen.), the value of the Mean is *not equivalent* to the log(Mean) for the corresponding Distribution of Concentration.

C.V.: stands for Coefficient of Variation which equals the absolute value of the ratio of the Standard Deviation to the Mean. Values given only for log beta distributions.

e+: represents positive power(s) of ten.

e−: represents negative power(s) of ten.

Elicitation: Conducted at Sandia National Laboratory on April 13, 1993. Documented in draft report titled "Expert Elicitation of the Solubility Distributions to be used in TSPA#2 Calculations", June 1, 1993, from Jack Gauthier (SPECTRA Research).

*: indicates modifications to original source information—see text for discussion.

Table 6.3-2 Averages and Standard Deviations for log(Neptunium Steady-State Concentrations) Calculated Using the Measurements of Nitsche et al., (1993)

Conditions: T(°C); pH*	Data Points from Nitsche et al. (1993) Used in Derivation	Calculated Average of $\log_{10}$(Conc.)	Calculated Stnd. Deviation of $\log_{10}$(Conc.)	$10^{[\text{Avg. log(Conc.)}]}$
25; 5.94	last 4 of Appendix AI	−2.2760	0.2214E−01	0.5296E−02
25; 7.04	last 5 of Appendix AII	−3.9194	0.4839E−01	0.1204E−03
25; 8.48	last 10 of Appendix AIII	−4.3691	0.7026E−01	0.4275E−04
60; 5.92	last 5 of Appendix AIV	−2.1943	0.2942E−01	0.6393E−02
60; 8.47	last 3 of Appendix AVI	−4.0518	0.2514E−01	0.8876E−04
90; 5.93	last 3 of Appendix AVII	−2.9307	0.1603E−01	0.1173E−02
90; 7.02	last 5 of Appendix AVIII	−3.8256	0.5351E−01	0.1494E−03
90; 8.42	last 9 of Appendix AIX	−4.0510	0.1901E−01	0.8893E−04

* pH values are averages for measurements used to calculate values in the table.

Table 6.3-3 Averages and Standard Deviations for log(Plutonium Steady-State Concentrations) Calculated Using the Measurements of Nitsche et al., (1993)

Conditions: T(°C); pH*	Data Points from Nitsche et al. (1993) Used in Derivation	Calculated Average of $\log_{10}$(Conc.)	Calculated Stnd. Deviation of $\log_{10}$(Conc.)	$10^{[\text{Avg. log(Conc.)}]}$
25; 5.88	last 3 of Appendix BI	-6.2234	0.6596E-01	0.5978E-06
25; 6.9	last 13 of Appendix BII	-6.6756	0.1708E+00	0.2111E-06
25; 8.41	last 10 of Appendix BIII	-6.5138	0.1197E+00	0.3064E-06
60; 5.97	last 8 of Appendix BIV	-7.6786	0.9622E-01	0.2096E-07
60; 6.96	last 10 of Appendix BV	-7.4402	0.1210E+00	0.3629E-07
60; 8.46	last 5 of Appendix BVI	-6.9094	0.4434E-01	0.1232E-06
90; 5.96	last 4 of Appendix BVII	-8.2809	0.1220E+00	0.5237E-08
90; 7.00	last 4 of Appendix BVIII	-8.0382	0.1454E-01	0.9158E-08
90; 8.44	last 7 of Appendix BIX	-8.1363	0.2289E-01	0.7306E-08

* pH values are averages for measurements used to calculate values in the table.

Table 6.3-4 Averages and Standard Deviations for log(Americium Steady-State Concentrations) Calculated Using the Measurements of Nitsche et al., (1993)

Conditions: T(°C); pH*	Data Points from Nitsche et al. (1993) Used in Derivation	Calculated Average of $\log_{10}$(Conc.)	Calculated Stnd. Deviation of $\log_{10}$(Conc.)	$10^{[\text{Avg. log(Conc.)}]}$
25; 5.89	last 4 of Appendix CI	-8.7695	0.1926E+00	0.1778E-08
25; 6.97	last 3 of Appendix CII	-8.9290	0.1496E+00	0.1200E-08
25; 8.47	last 12[†] of Appendix CIII	-8.6777	0.1705E+00	0.2754E-08
60; 8.52	last 2 of Appendix CVIII	-8.5176	0.2041E+00	0.1217E-07
90; 6.05	last 12 of Appendix CX	-8.8267	0.2273E+00	0.1679E-08
90; 7.03	last 13 of Appendix CXI	-9.5950	0.3139E+00	0.3142E-09
90; 8.44	last 9 of Appendix CXII	-9.6369	0.2762E+00	0.3367E-09

* pH values are averages for measurements used to calculate values in the table.

† Note: Sample I.D. 9-11A1J2 was *not* used as it appears to be an incorrect entry from the data for Appendix CII; the pH for Sample I.D. 9-12A1J2 is listed as 7.63 but was taken to be 8.63 as pH variations for samples are only about ±0.1.

INFORMATION

Site Biosphere → 8

Site Geology → 7

Site Hydrology → 6

Site Geochemistry → 5

Repository Design → 4

Waste Package Design → 3

Material Properties → 2

Waste Form Properties → 1

PROCESS-LEVEL MODEL

7 → 6 → Saturated Zone Flow Model

7 → 6 → Unsaturated Zone Flow Model

7 → 6 → 4 → 3 → Drift-Scale Thermo-Hydrologic Model

3 → 2 → Waste Package Degradation Model

PROCESS-LEVEL MODEL ABSTRACTIONS

Response surface of saturated zone flux → E

Response surface of unsaturated zone flux
 - fracture flux
 - matrix flux → D

Response surface of drift-scale flux
 - % packages with drips
 - advective flux in drips → C

Response surface of
 - temperature
 - humidity
 - liquid saturation → B

Response surface of
 - first pit
 - pit distribution → A

TOTAL SYSTEM PERFORMANCE ASSESMENT

Biosphere Transport -Dose

↑ 8

Geosphere Transport -Cumulative Release

↑ D E 5 6 7

EBS Transport -Release Rate

↑ B C 5 4 3 2 1

Waste Package Degradation -Containment

↑ A

6-34

Figure 6.1-1   Relation of Chapter 6 to the Overall Information Flow Diagram for TSPA 1995 (Figure 1.4-6)

Spent Fuel Dissolution Rate vs Temperature
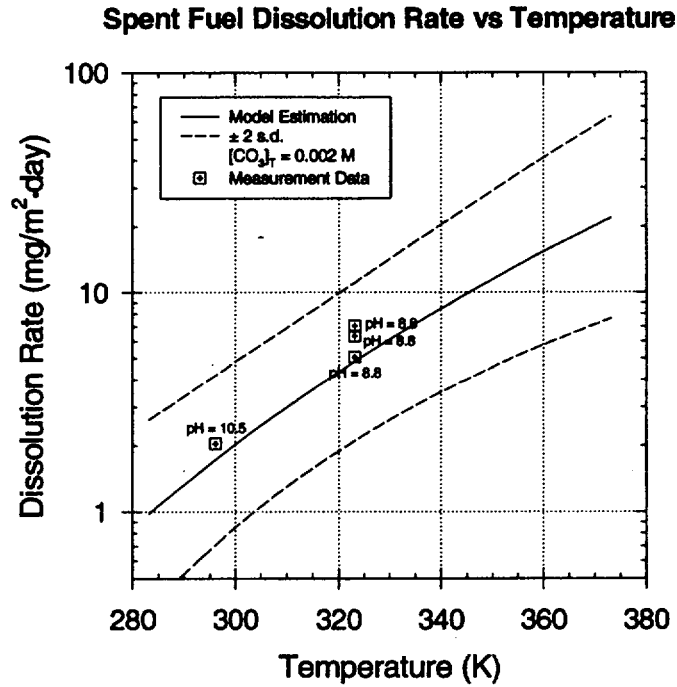
Figure 6.2-1   Model Prediction with the Uncertainty and Relevant Data of the Intrinsic Dissolution Rate of Spent Fuel Matrix as a Function of Temperature at a Total Carbonate Concentration of 0.002 M

Spent Fuel Dissolution Rate vs. Temperature
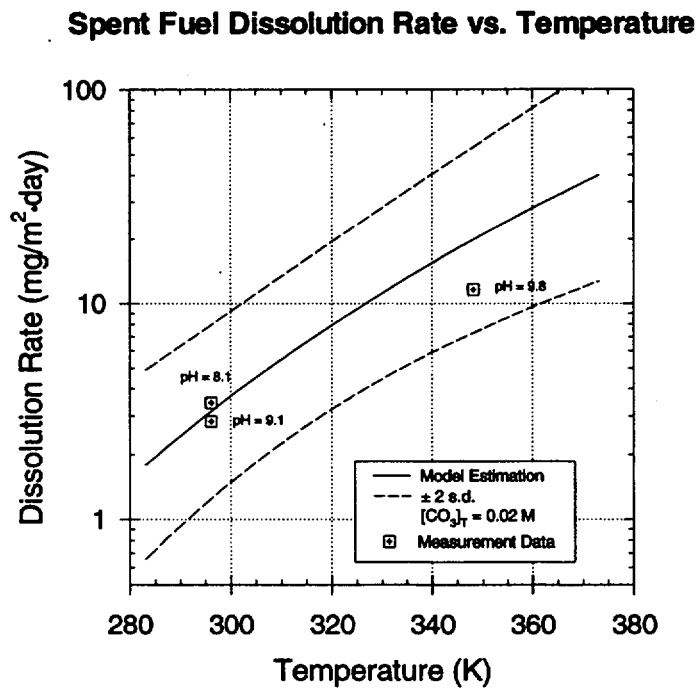
Figure 6.2-2   Model Prediction with the Uncertainty and Relevant Data of the Intrinsic Dissolution Rate of Spent Fuel Matrix as a Function of Temperature at a Total Carbonate Concentration of 0.02 M

Spent Fuel Dissolution Rate vs [CO₃]ₜ
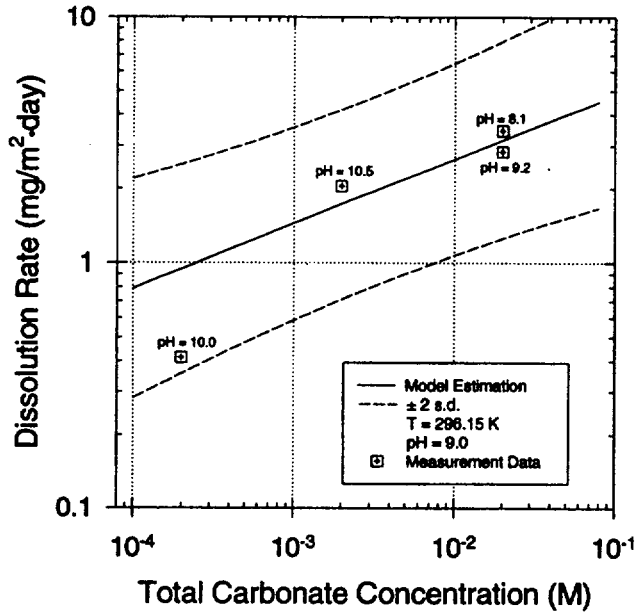
Figure 6.2-3   Model Prediction with the Uncertainty and Relevant Data of the Intrinsic Dissolution Rate of Spent Fuel Matrix as a Function of Total Carbonate Concentration at 296.15K.

Spent Fuel Dissolution vs Temperature and [CO₃]ₜ
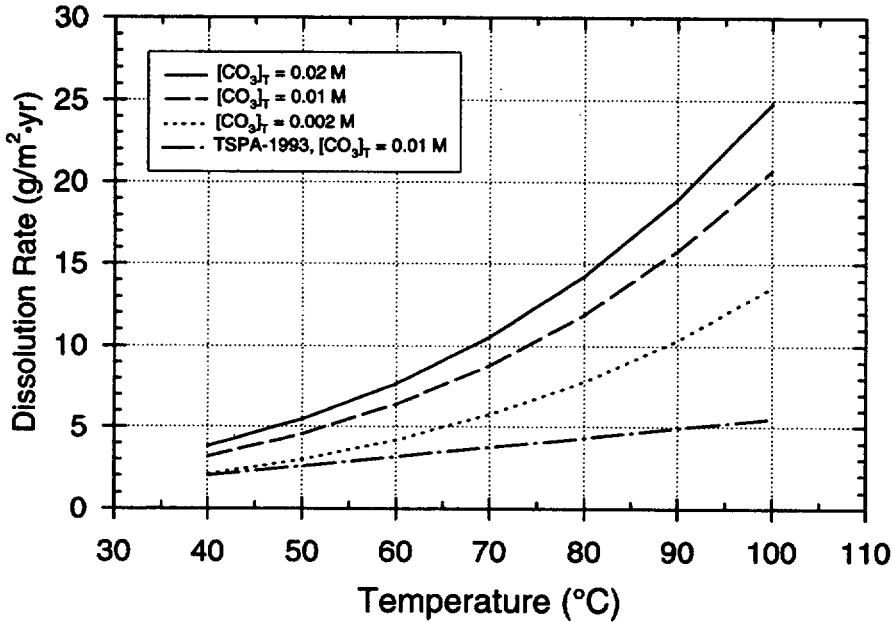
Figure 6.2-4   Comparison of Spent Fuel Dissolution Rates Calculated by the Current Model with the Model Used in TSPA-1993.

DHLW Glass Dissolution Rate vs pH and Temperature
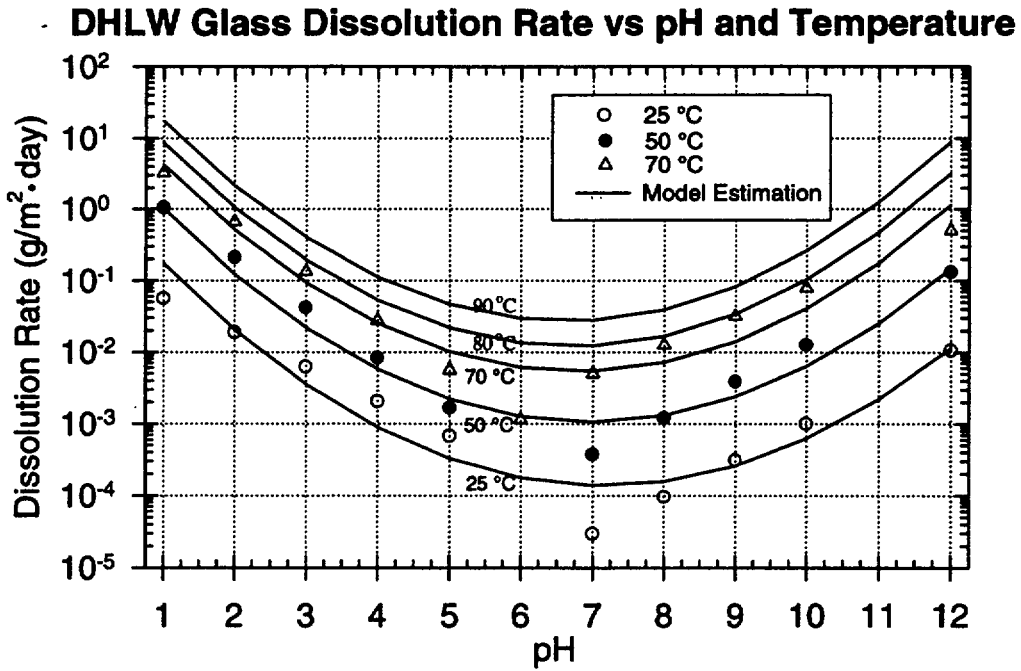
Figure 6.2-5   Prediction and the Data of the Intrinsic Dissolution Rates of DHLW Glass
Waste Form as a Function of pH and Temperature

DHLW Glass Dissolution Rate vs Temperature (pH=7)
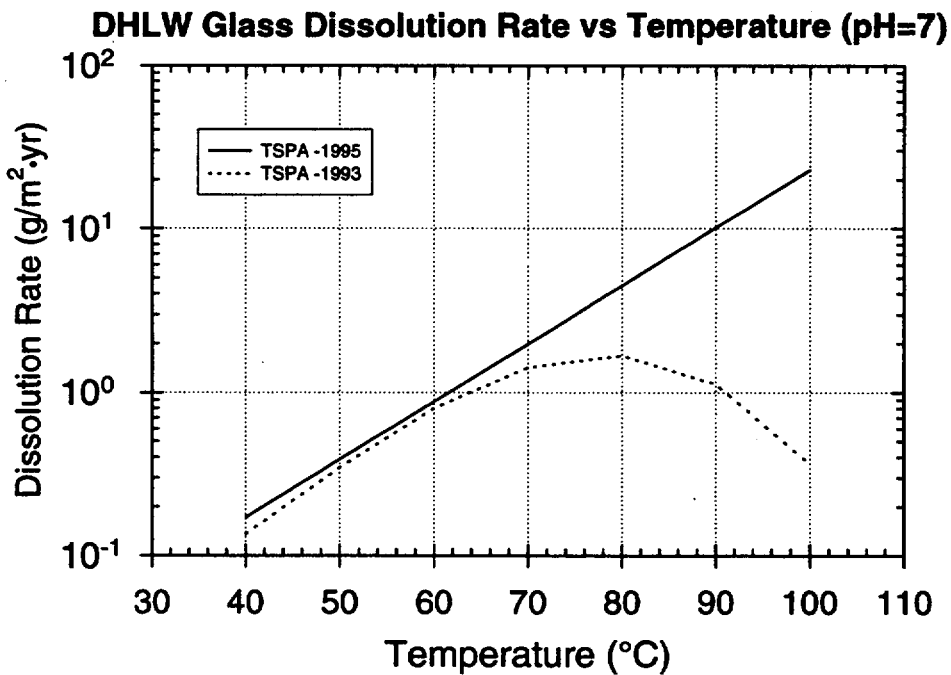
Figure 6.2-6   Comparison of the Prediction of the Intrinsic Glass Dissolution Rate as a
Function of Temperature at pH of 7 Calculated with the Current Model and the
Model Used in TSPA-1993

Probability Distribution Used to Represent Solubility-Limited Ac, Am, and Sm Concentrations
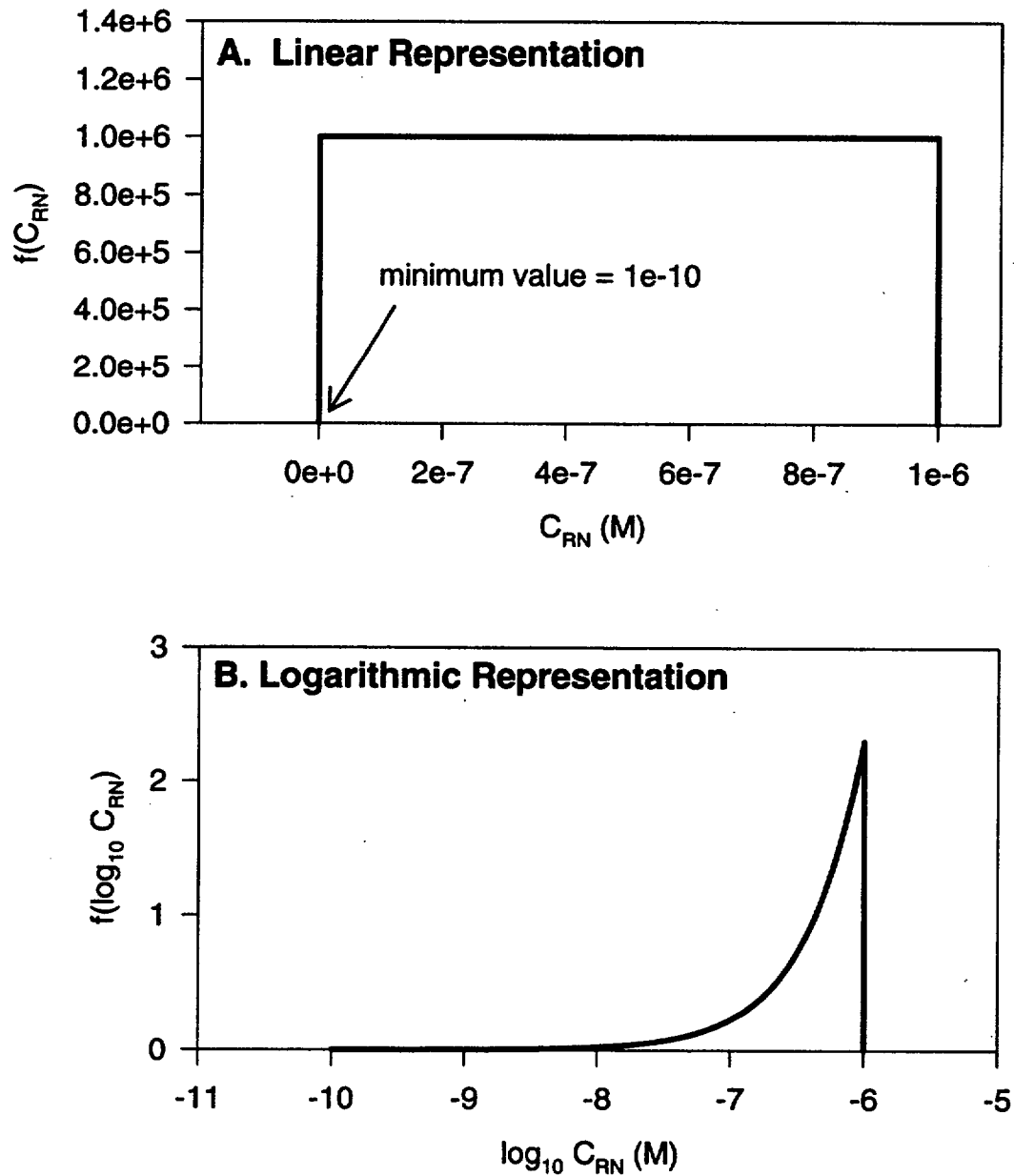
Figure 6.3-1   Plot of the Distribution Function for Solubility-Limited Concentrations of Ac, Am, and Sm. A. Linear representation. B. Logarithmic representation.
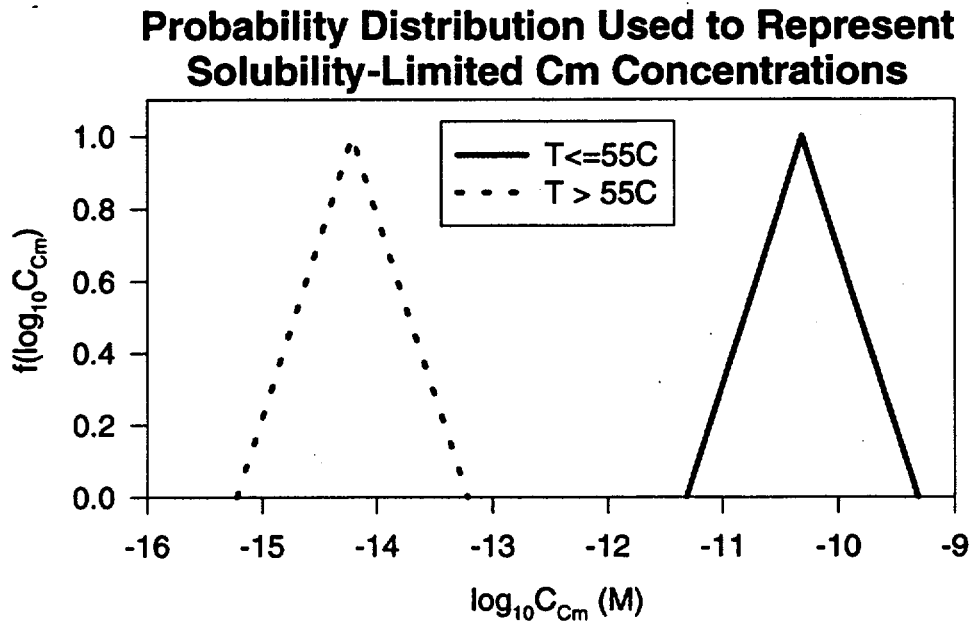
Figure 6.3-2 Plot of the Distribution Function for Solubility-Limited Concentrations of Cm.
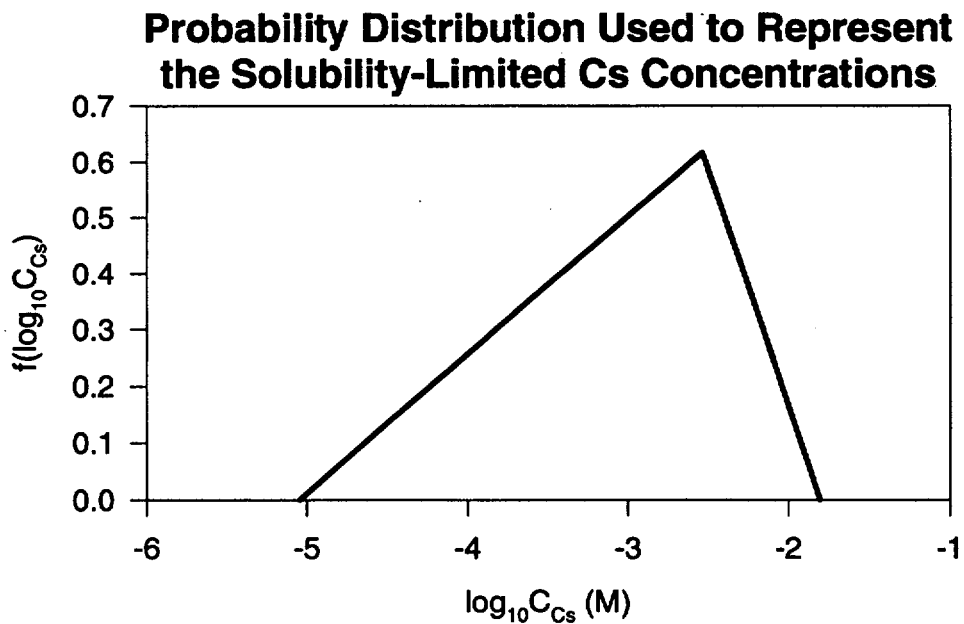
Figure 6.3-3 Plot of the Distribution Function for Solubility-Limited Concentrations of Cs.

**Probability Distribution Used to Represent Solubility-Limited Nb Concentrations**
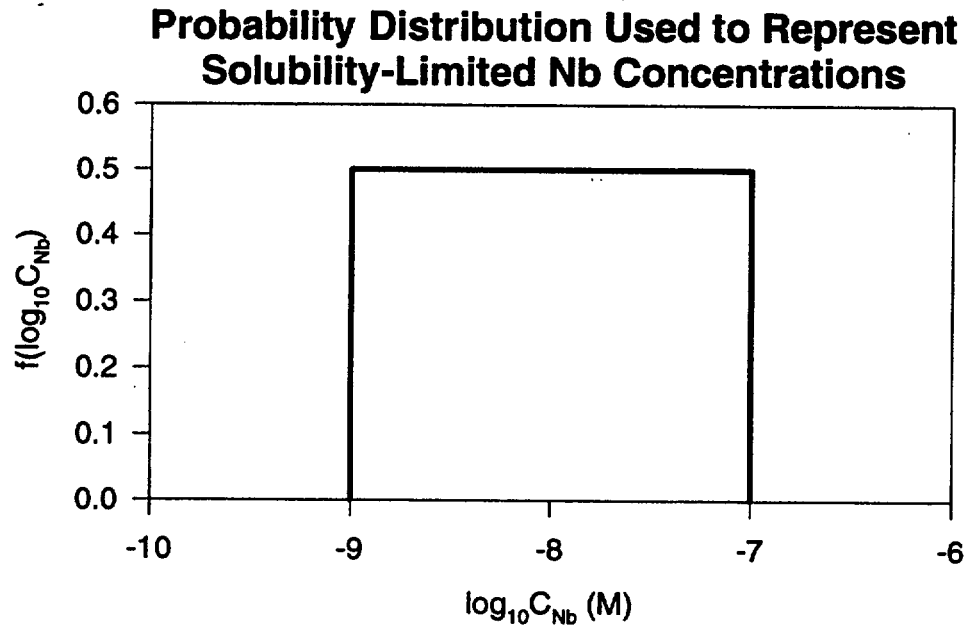
Figure 6.3-4 Plot of the Distribution Function for Solubility-Limited Concentrations of Nb.

Probability Distributions Used to Represent Solubility-Limited Ni Concentrations

TSPA-1995
TSPA-1993
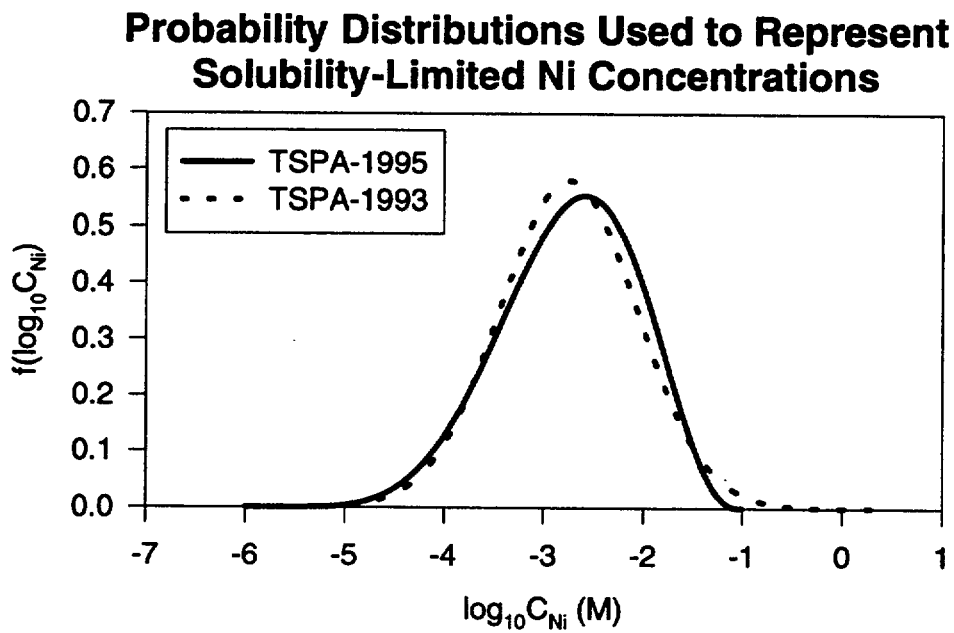
Figure 6.3-5 Plot of the Distribution Function for Solubility-Limited Concentrations of Ni.
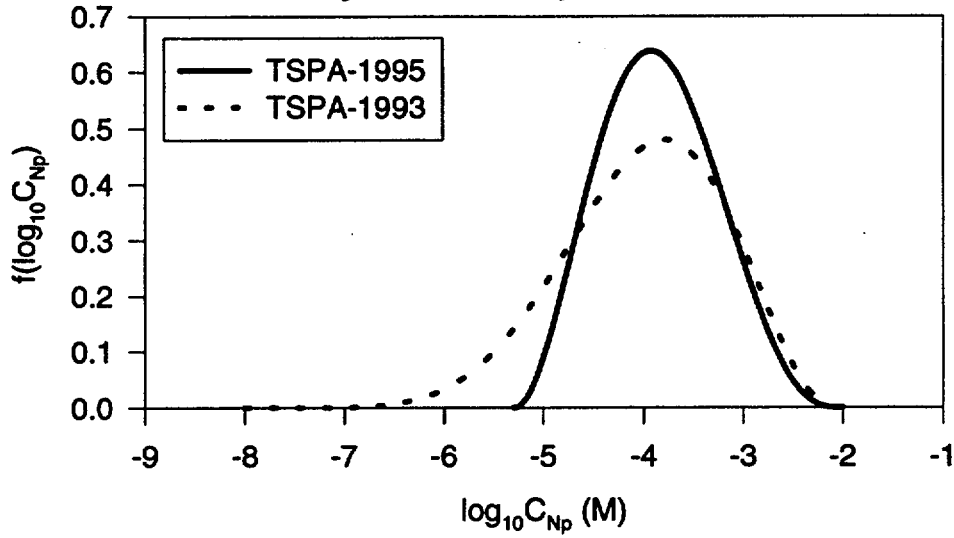
Figure 6.3-6 Plot of the Distribution Function for Solubility-Limited Concentrations of Np.
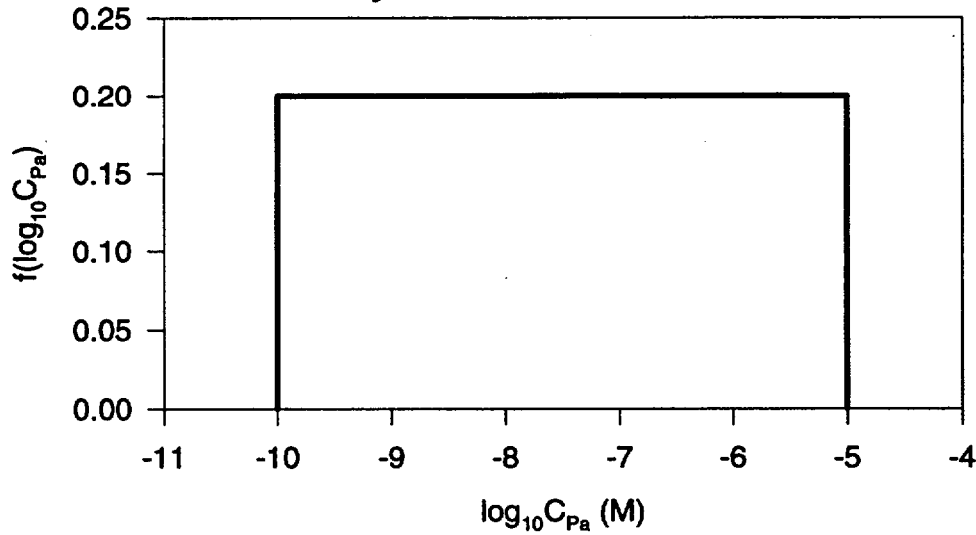
Figure 6.3-7 Plot of the Distribution Function for Solubility-Limited Concentrations of Pa.

Probability Distributions Used to Represent Solubility-Limited Pb Concentrations
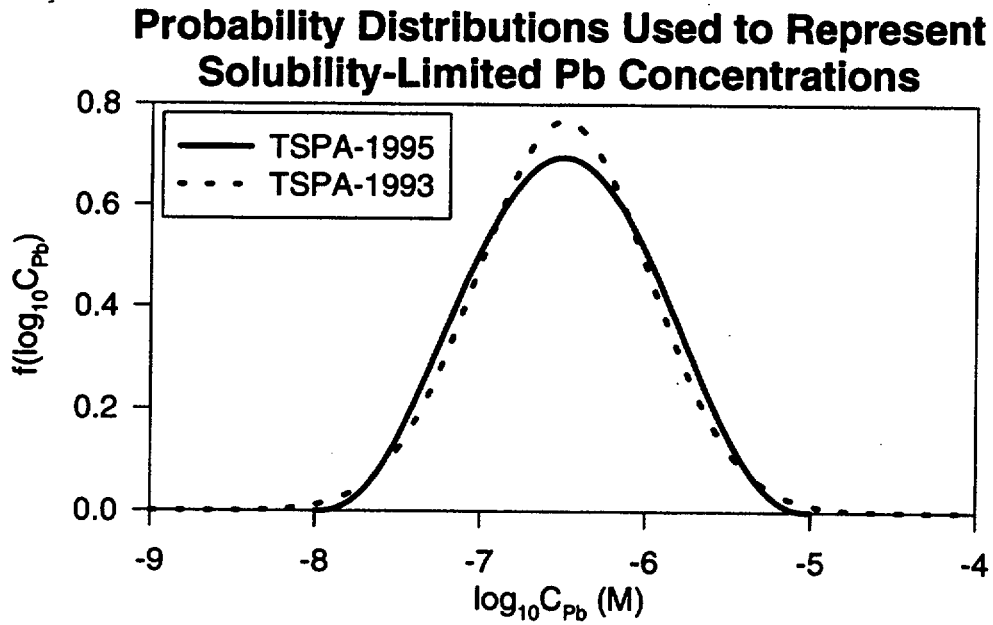
Figure 6.3-8 Plot of the Distribution Function for Solubility-Limited Concentrations of Pb.

Probability Distribution Used to Represent Solubility-Limited Pd Concentrations
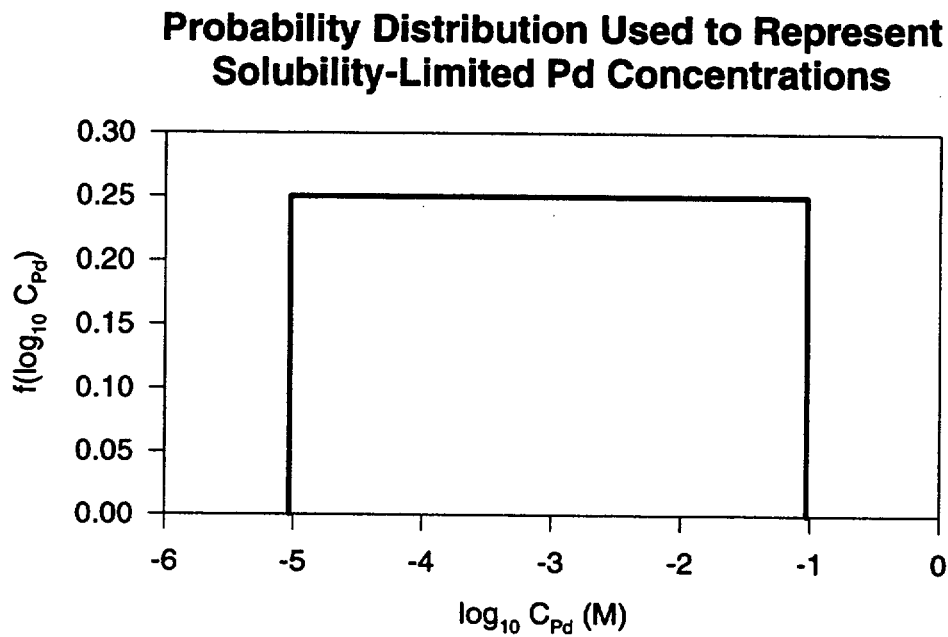
Figure 6.3-9 Plot of the Distribution Function for Solubility-Limited Concentrations of Pd.

Probability Distribution Used to Represent Solubility-Limited Pu Concentrations

A. Linear Representation

minimum value = 1e-8

B. Logarithmic Representation
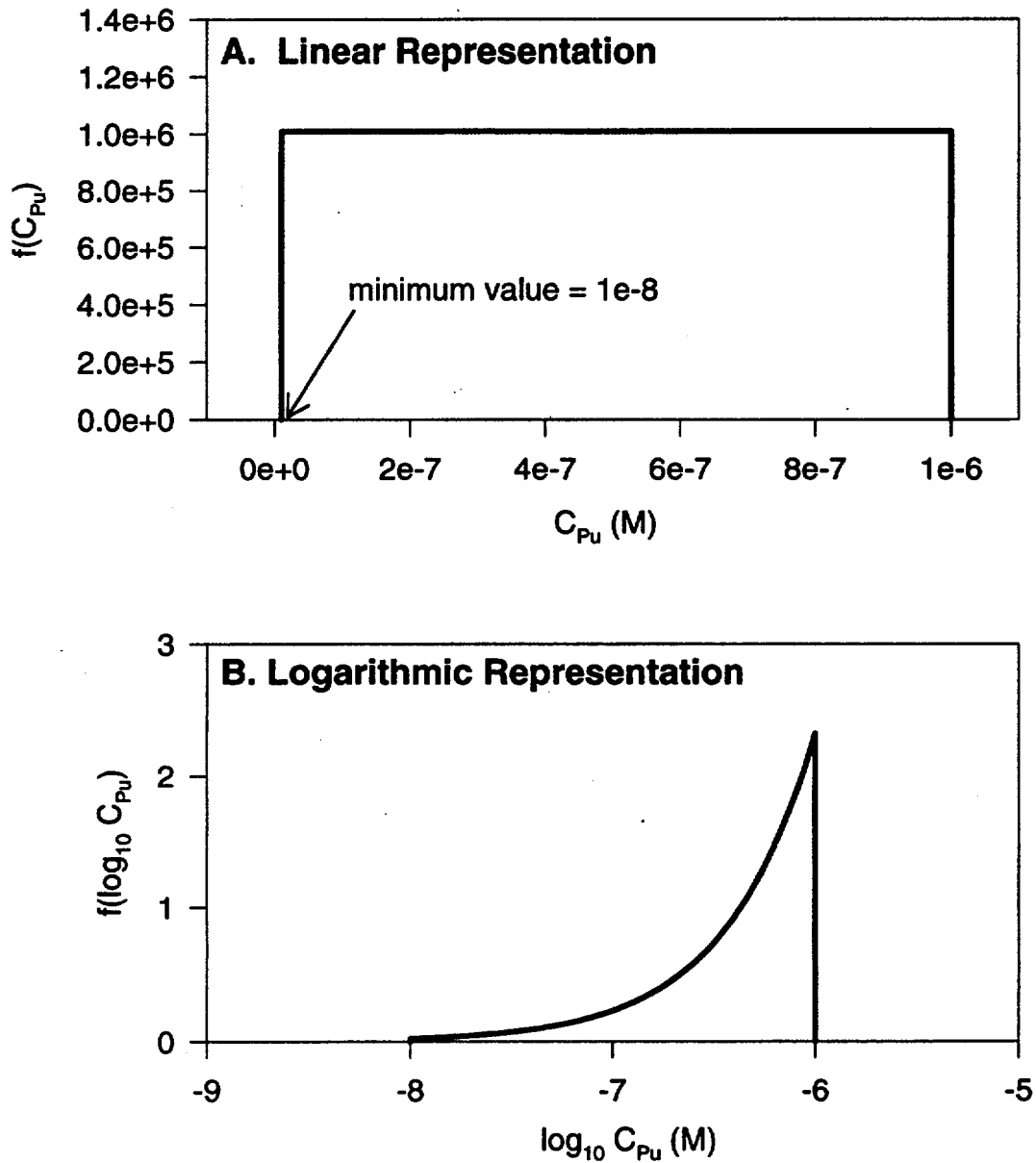
Figure 6.3–10 Plot of the Distribution Function for Solubility-Limited Concentrations of Pu.
A. Linear representation. B. Logarithmic representation.

Probability Distributions Used to Represent Solubility-Limited Ra Concentrations
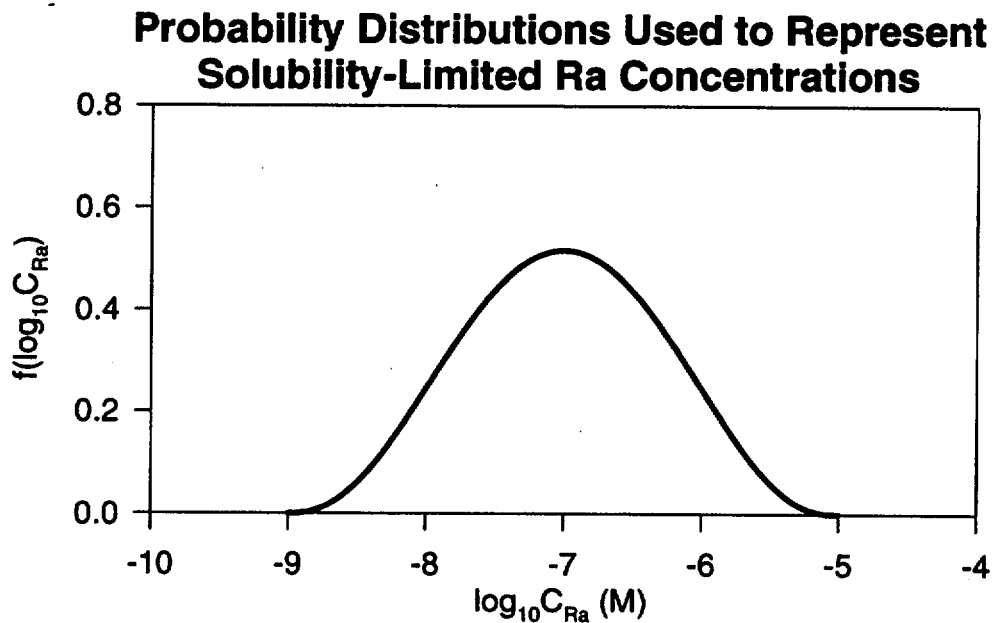
Figure 6.3-11 Plot of the Distribution Function for Solubility-Limited Concentrations of Ra.

Probability Distribution Used to Represent the Solubility-Limited Se Concentrations
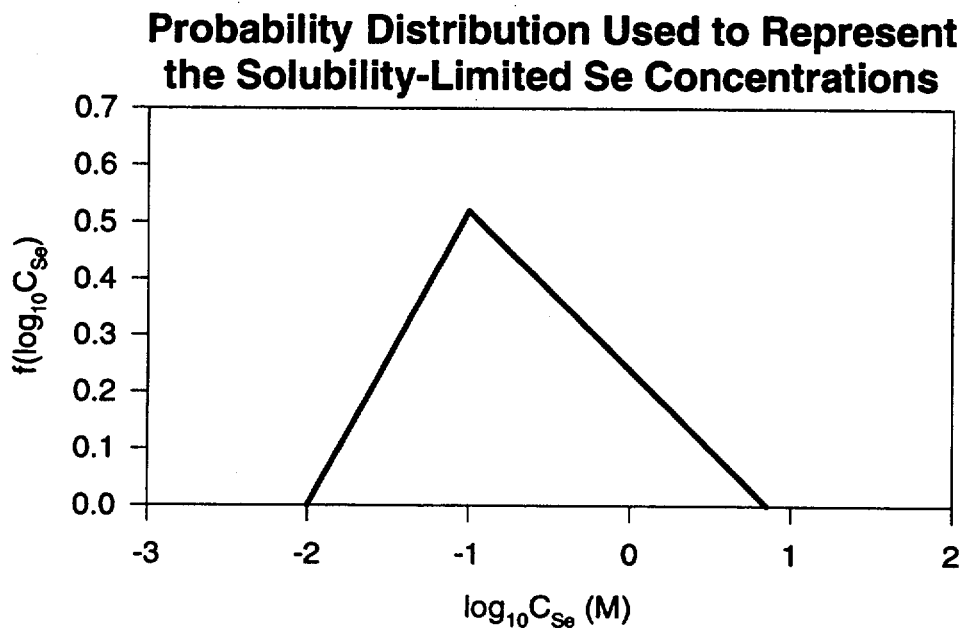
Figure 6.3-12 Plot of the Distribution Function for Solubility-Limited Concentrations of Se.

Probability Distribution Used to Represent Solubility-Limited Sn Concentrations
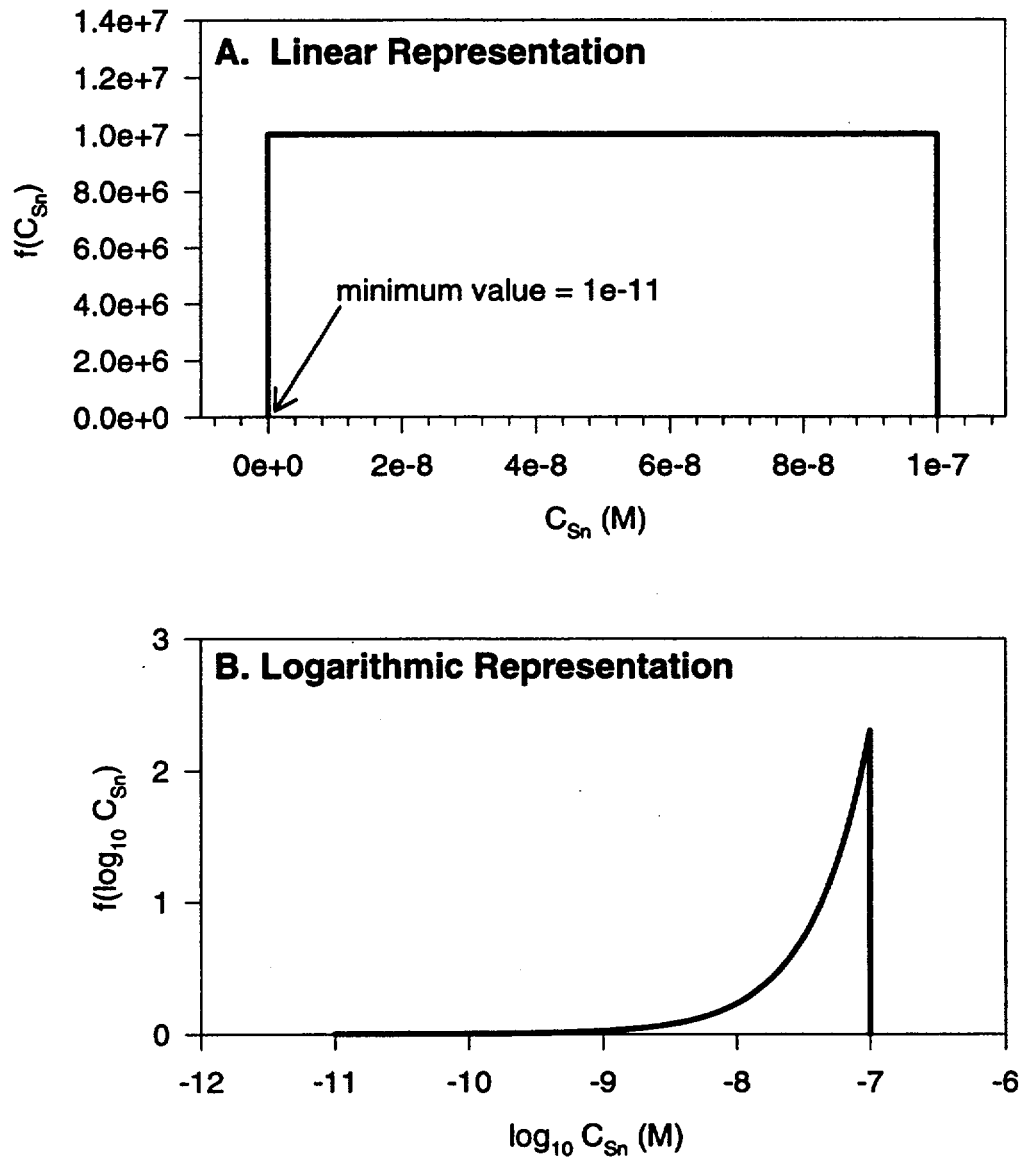
Figure 6.3−13 Plot of the Distribution Function for Solubility-Limited Concentrations of Sn. A. Linear representation. B. Logarithmic representation.

Probability Distribution Used to Represent the Solubility-Limited Tc Concentrations
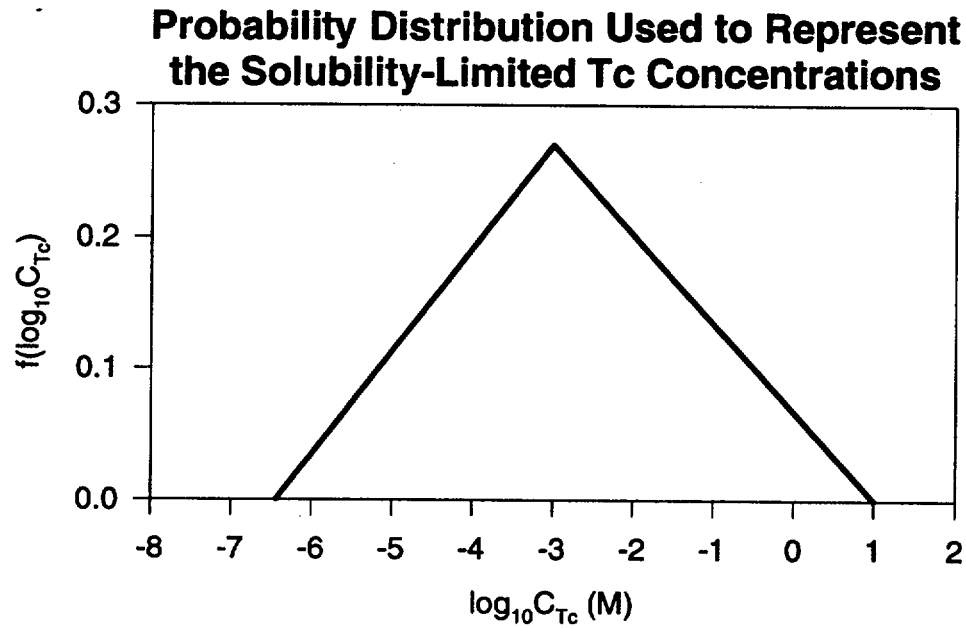
Figure 6.3-14 Plot of the Distribution Function for Solubility-Limited Concentrations of Tc.

Probability Distribution Used to Represent Solubility-Limited Th Concentrations
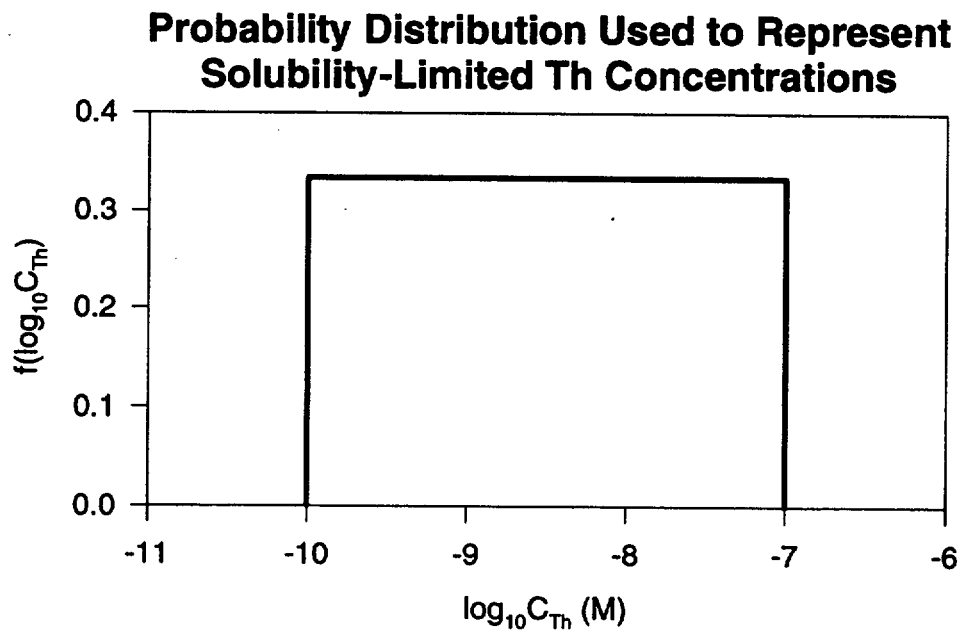
Figure 6.3-15 Plot of the Distribution Function for Solubility-Limited Concentrations of Th.

Probability Distributions Used to Represent Solubility-Limited U Concentrations
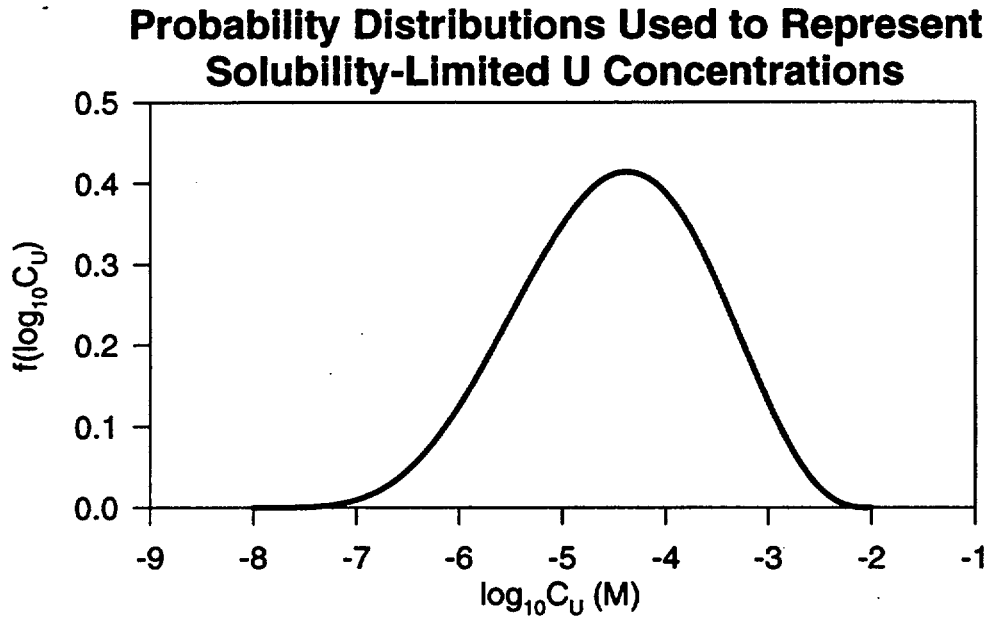
Figure 6.3-16 Plot of the Distribution Function for Solubility-Limited Concentrations of U.

Probability Distribution Used to Represent Solubility-Limited Zr Concentrations
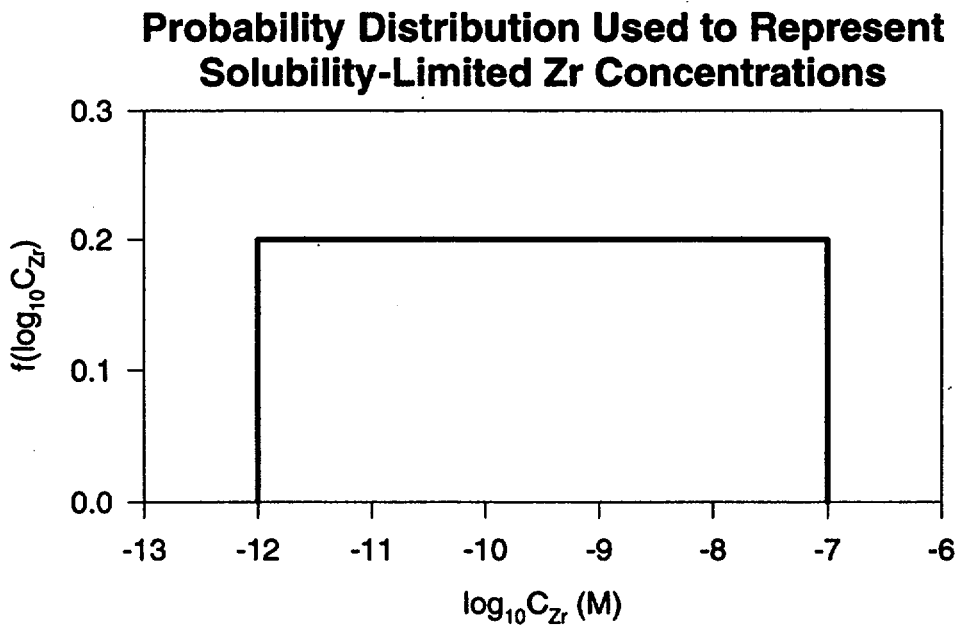
Figure 6.3-17 Plot of the Distribution Function for Solubility-Limited Concentrations of Zr.

Neptunium (Nitsche et al., 1993)
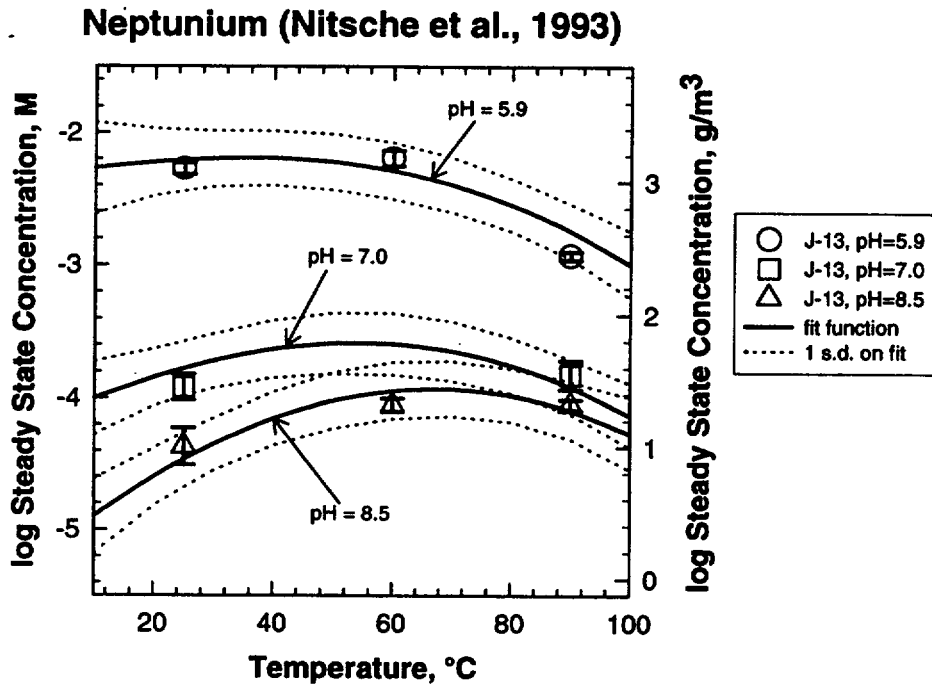
Figure 6.3-18   Temperature- and pH-Dependent Functional Fit to Nitsche et al. (1993) measurements of log(Steady-State Np Concentration) in J-13 Initial Water (Curves) Compared to Empirical Determinations Used (Symbols-Table 6.3-2). Two Standard Deviations from Analytical Uncertainties Shown on Data Points.


Plutonium (Nitsche et al., 1993)
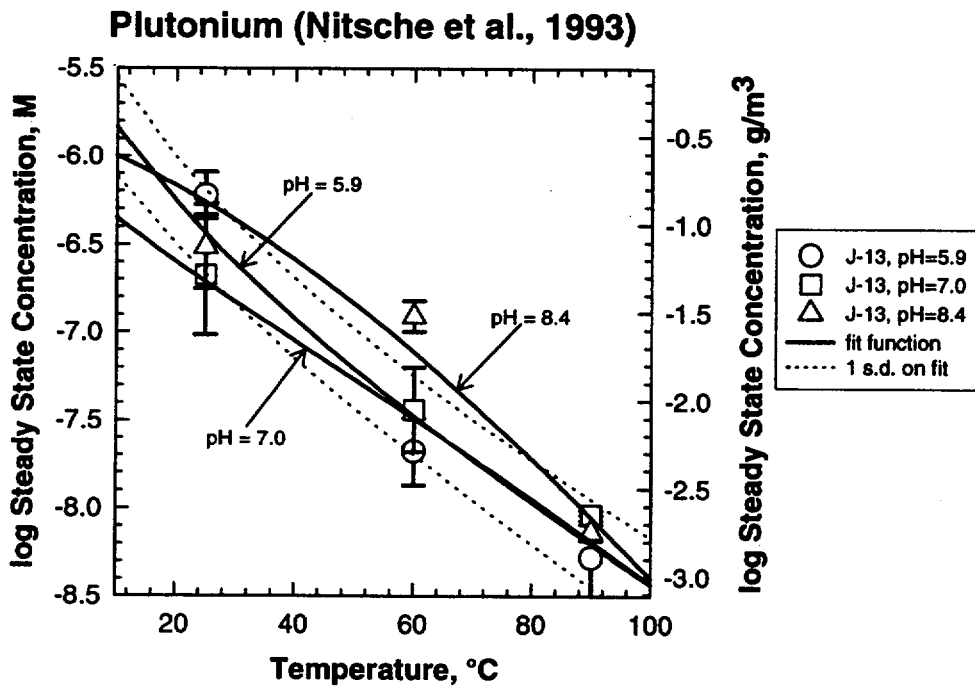
Figure 6.3-19   Temperature- and pH-Dependent Functional Fit to Nitsche et al. (1993) measurements of log(Steady-State Pu Concentration) in J-13 Initial Water (Curves) Compared to Empirical Determinations Used (Symbols-Table 6.3-3). Two Standard Deviations from Analytical Uncertainties Shown on Data Points.
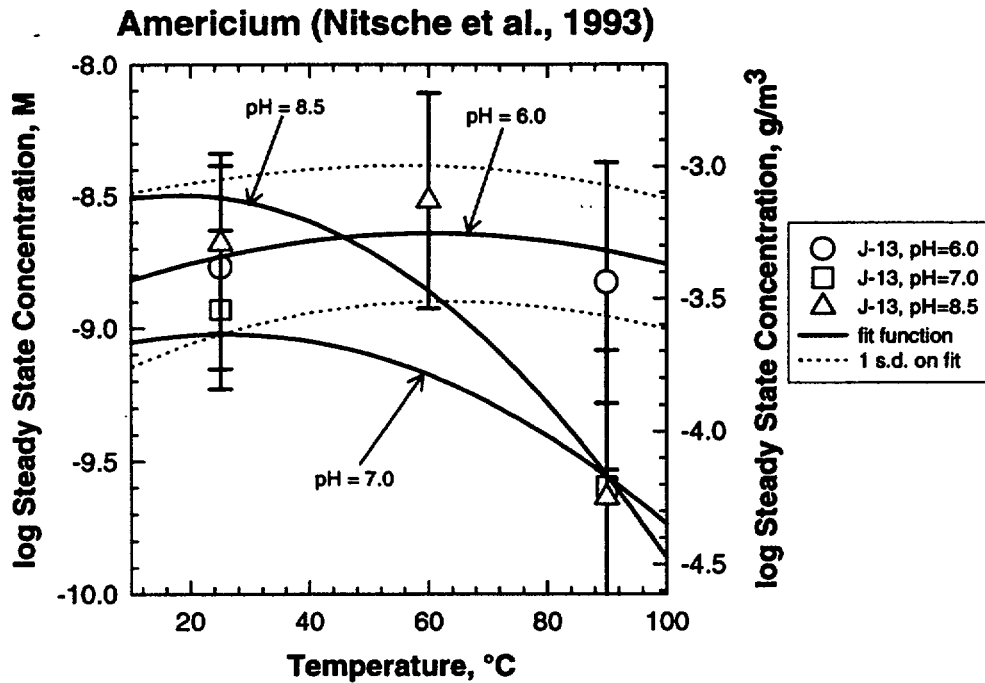
Figure 6.3-20 Temperature- and pH-Dependent Functional Fit to Nitsche et al. (1993)
measurements of log(Steady-State Am Concentration) in J-13 Initial Water (Curves)
Compared to Empirical Determinations Used (Symbols-Table 6.3-4). Two Standard
Deviations from Analytical Uncertainties Shown on Data Points.
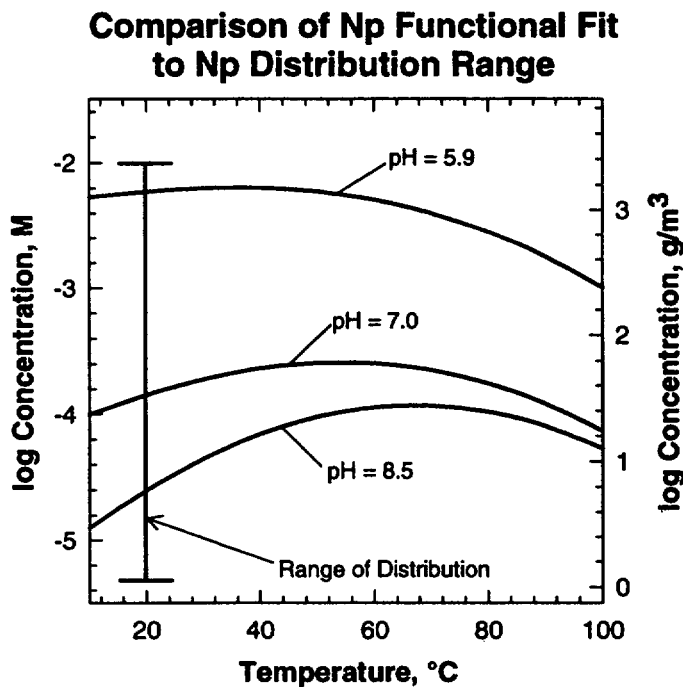
Figure 6.3-21 Comparison of Solubility-Limited log(Concentration) for Np as Function of
Temperature and pH in J-13 Initial Water with Np Distribution Function
Range.
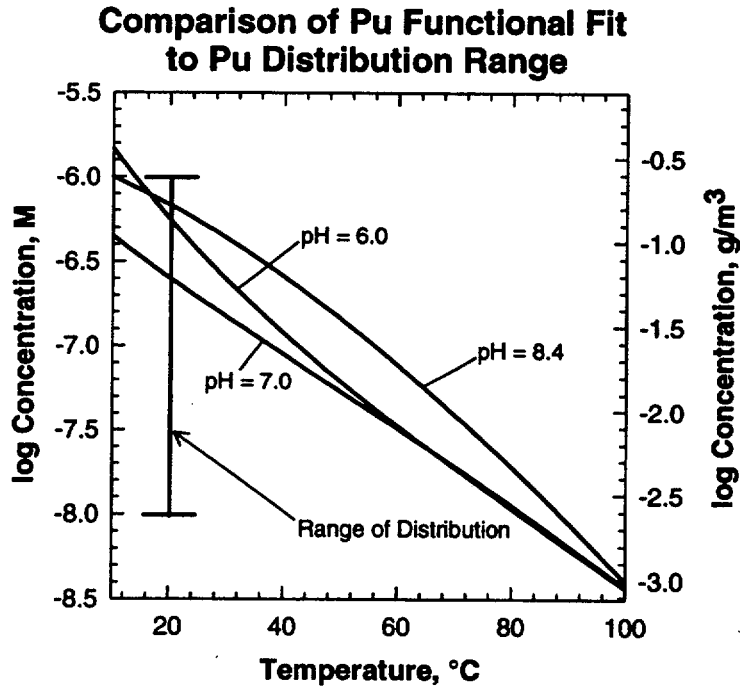
Figure 6.3-22 Comparison of Solubility-Limited log(Concentration) for Pu as Function of Temperature and pH in J-13 Initial Water to Pu Distribution Function Range.
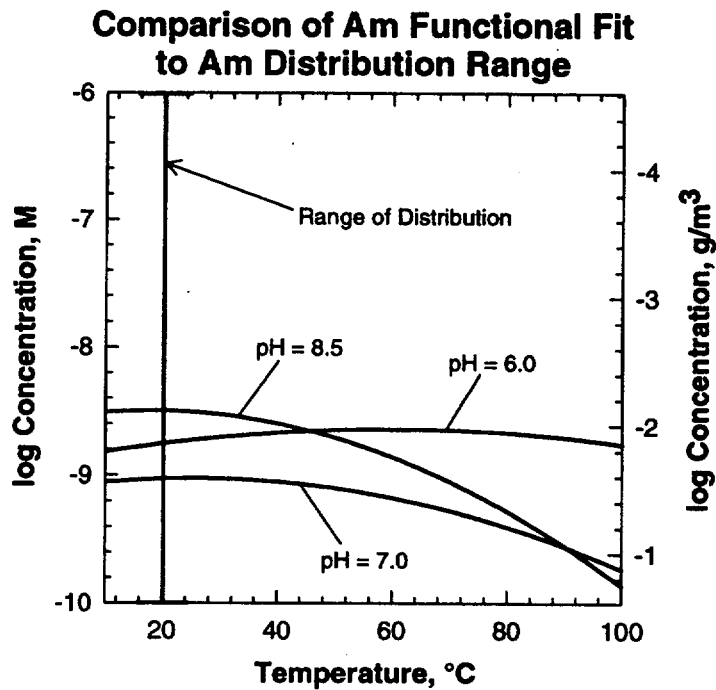

Figure 6.3-23 Comparison of Solubility-Limited log(Concentration) for Am as Function of Temperature and pH in J-13 Initial Water to Am Distribution Function Range.

6-50

$$M_{sf}$$

$$M_{dis} = R_{dis}(A)(t)$$

$$C_{dis} = (M_{dis})/(V_w)$$

$$S_i$$

No Limit

$$C_{mobile} = C_{dis}$$

Limited by Phase Saturation

$$C_{aq} = S_i$$

$$M_p = (C_{dis} - C_{aq})(V_w)$$

Add Colloids

$$C_{col} = ([\overline{Coll}]_m)(K_p)(C_{aq})$$

$$M_p = (C_{dis} - C_{aq} - C_{col})(V_w)$$

$$C_{mobile} = C_{aq} + C_{col}$$
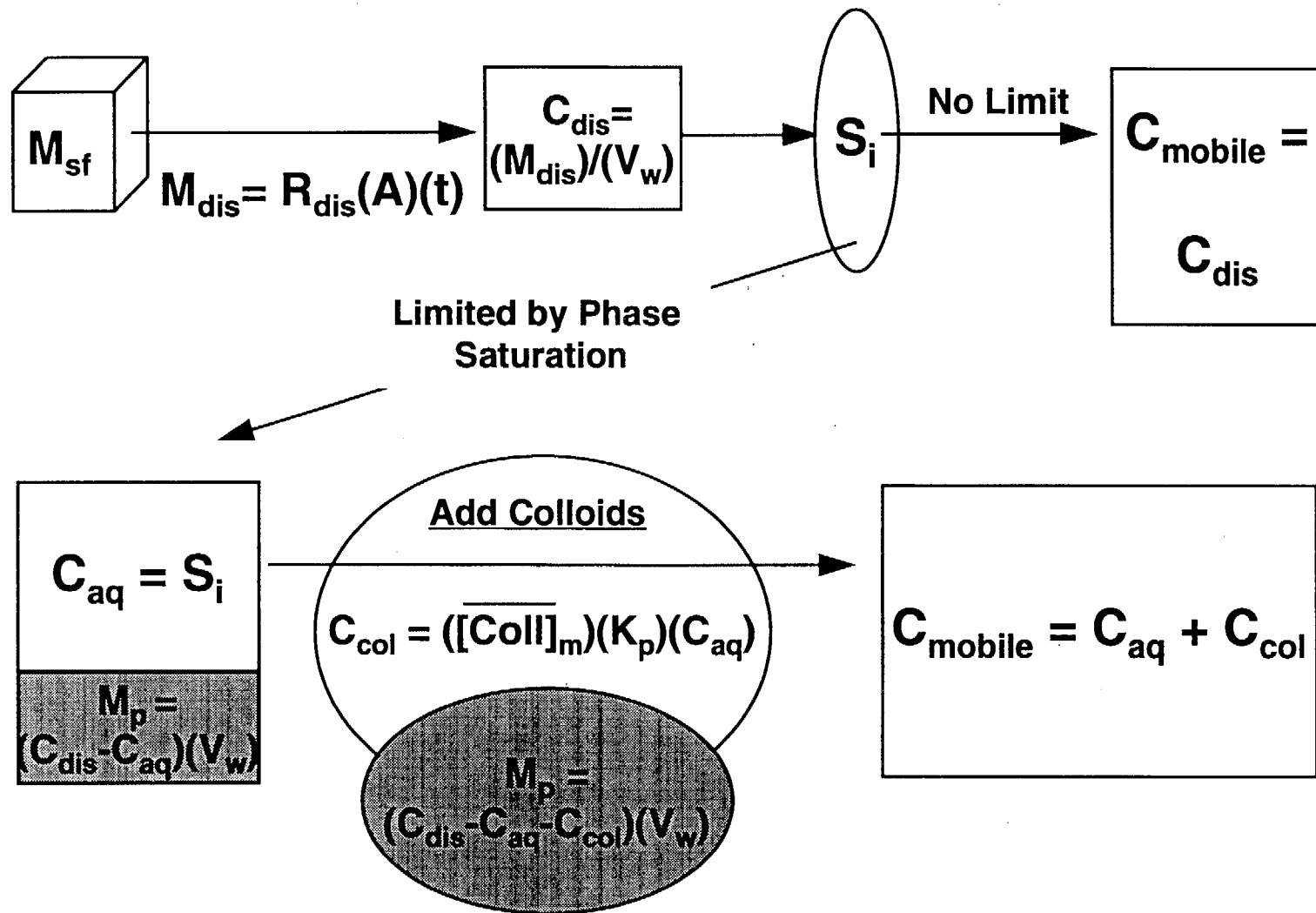
Figure 6.4-1   Incorporation of the Effects of Natural Colloids on the Source Term into TSPA
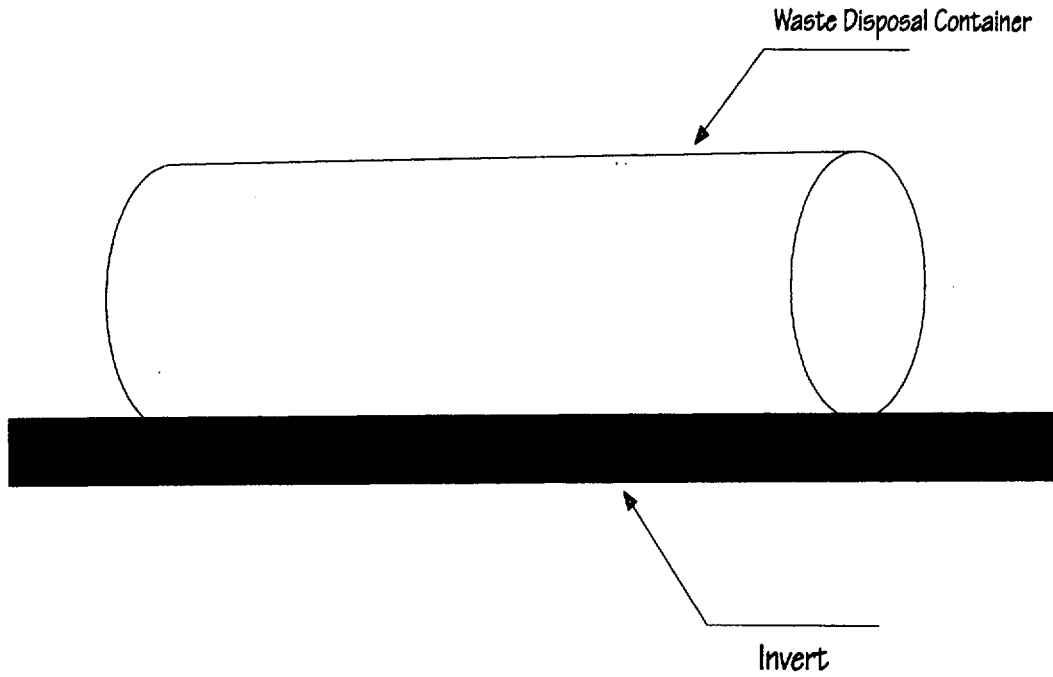
Figure 6.5-1 Schematic Drawing of Waste Disposal Container Placed on the Invert in an Emplacement Drift (side view)
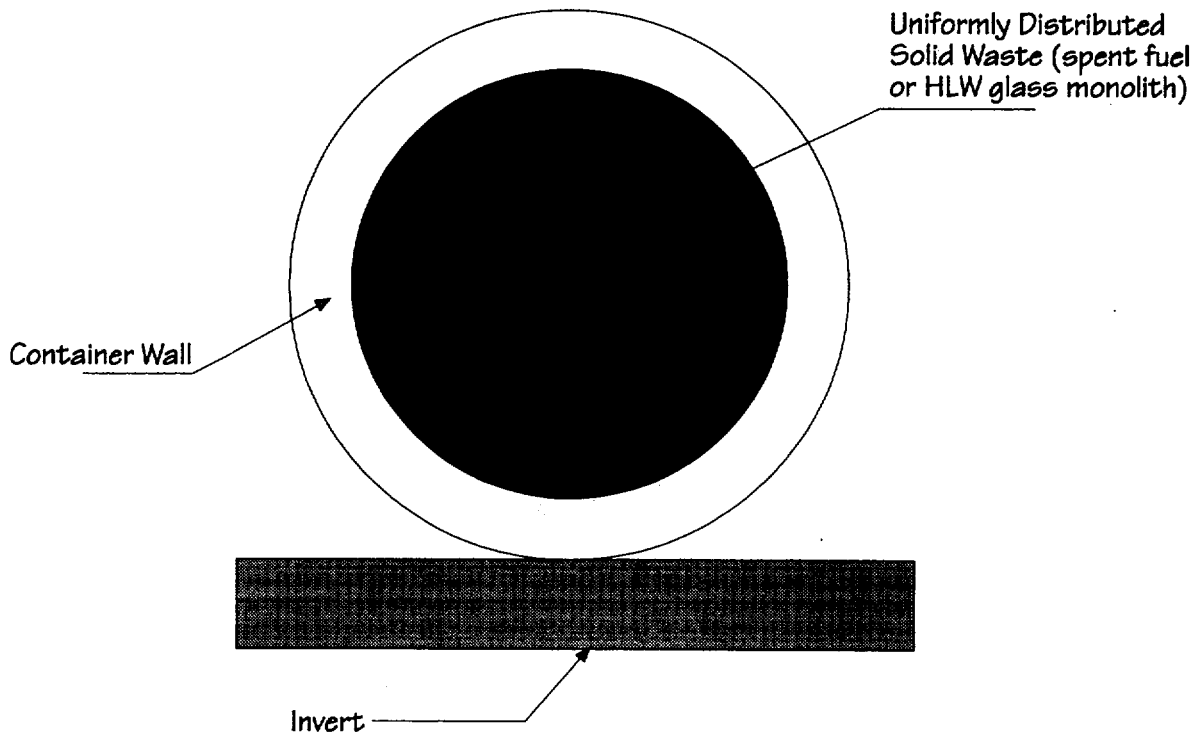

Figure 6.5-2 Schematic Drawing of Waste Disposal Container Placed on the Invert in an Emplacement Drift (front view)
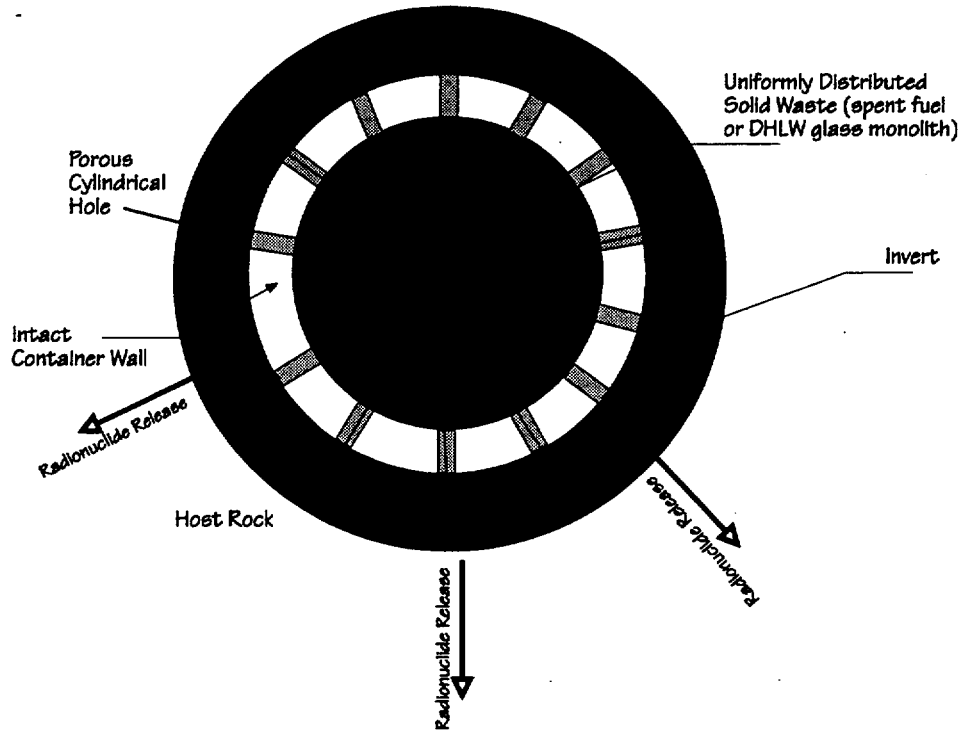
Figure 6.5-3   Schematic of Radionuclide Release Through Multiple Cylindrical Holes on the Waste Disposal Container for the Equivalent Spherical Configuration Approximation.
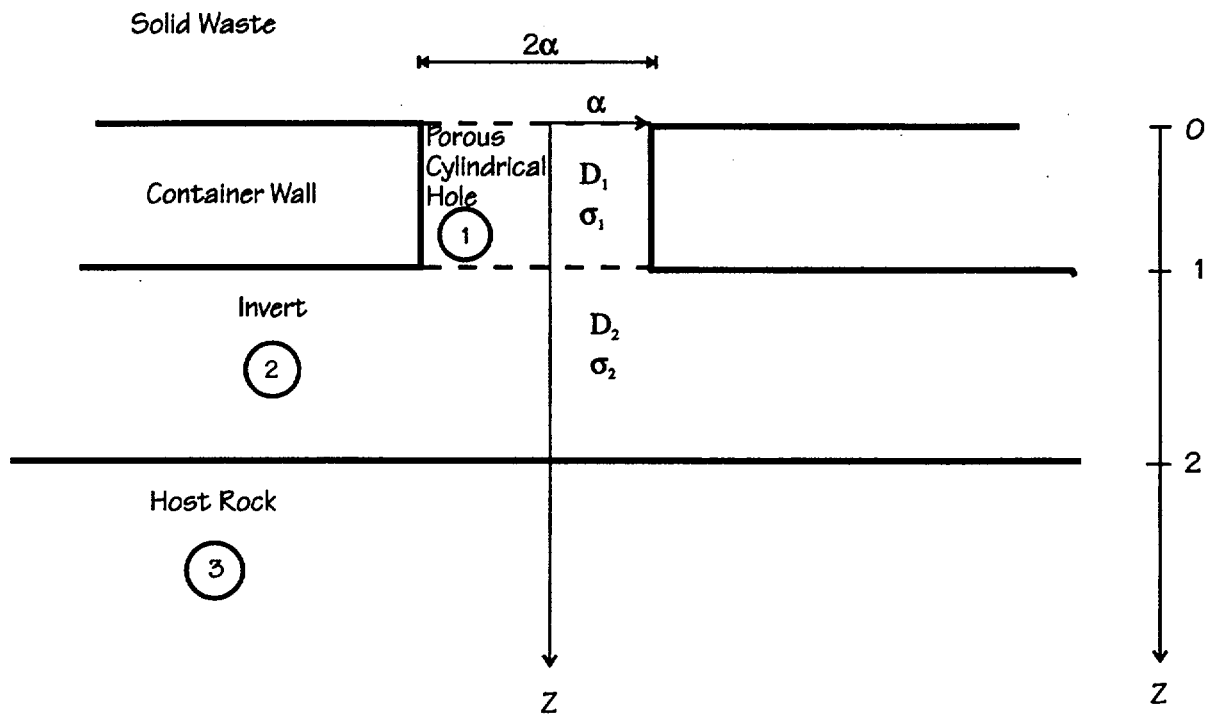
Figure 6.5-4   Conceptualization of Radionuclide Release Through a Cylindrical Hole in the Waste Disposal Container, the Invert, and the Host Rock.

**Steady-State Diffusive Release
at the Invert Boundary**
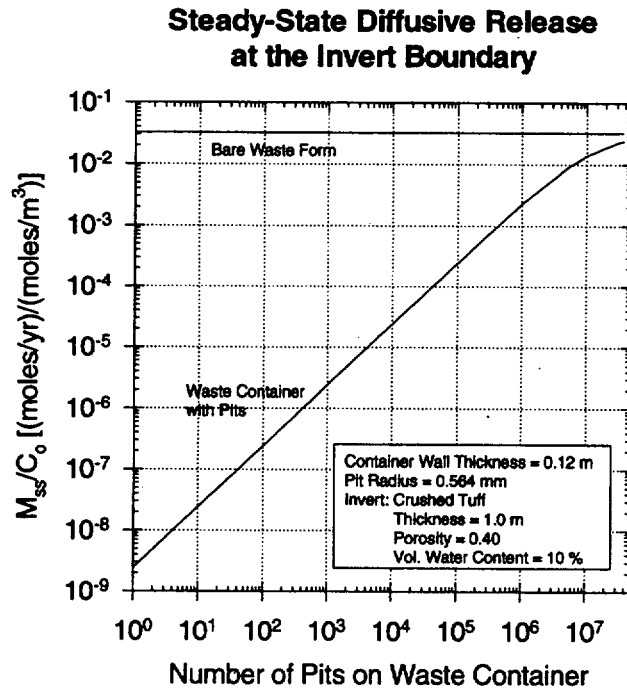
Figure 6.5-5   Comparison of Steady-State Diffusive Release at the EBS Boundary from A
Waste Container with Multiple Pits to the Release from the Bare Waste Form.

**A Representative Pitting Profile for
A Waste Container**
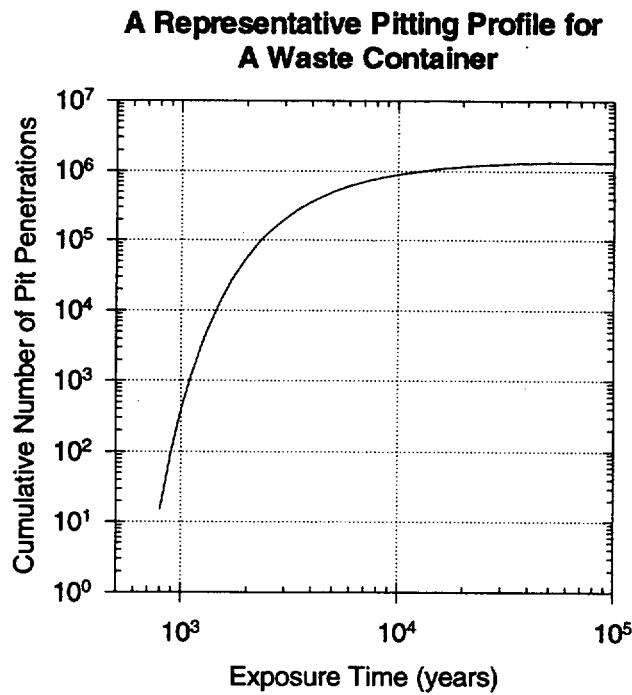
Figure 6.5-6   A Representative Pitting Profile of a Waste Container.

6-54

Diffusive Release at the EBS Boundary
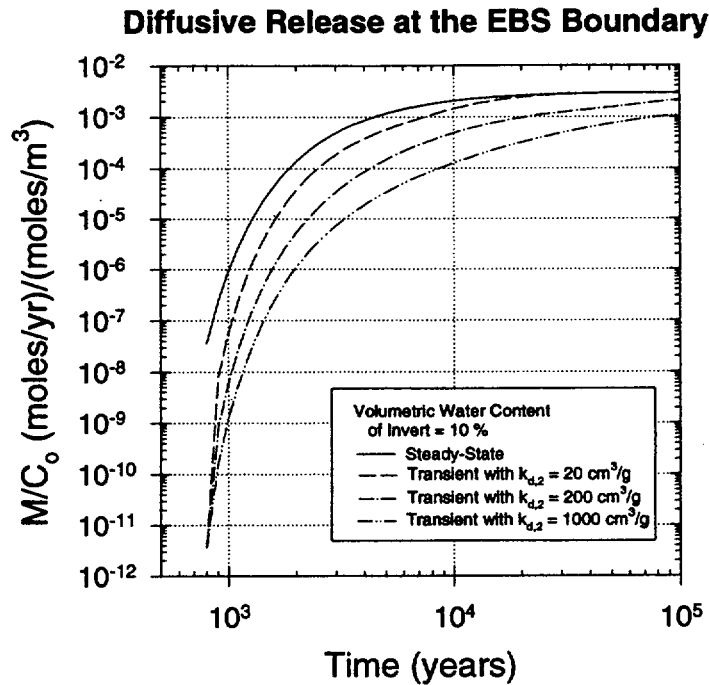
Figure 6.5-7   Transient and Steady-State Diffusive Releases at the EBS Boundary from A Waste Container with Multiple Pits.

Diffusion Coefficient vs Vol. Water Content
**(Ambient Room Temperature)**
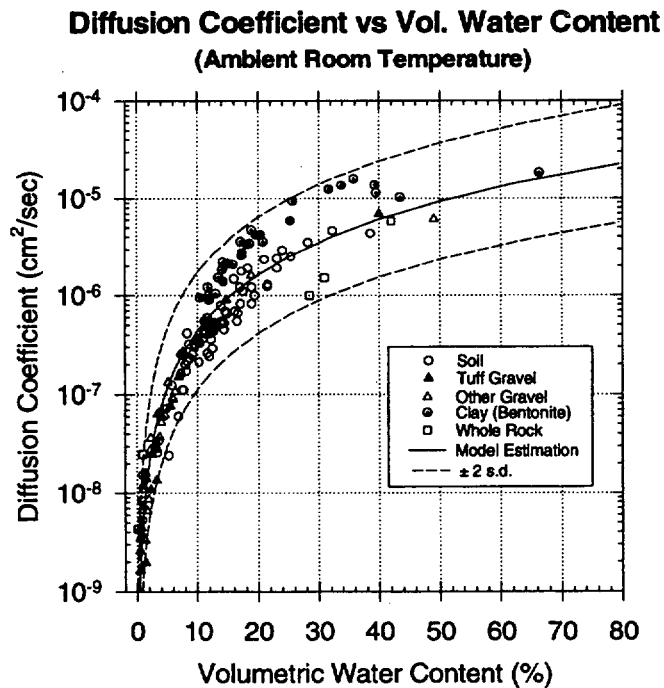
Figure 6.5-8   Model Estimation and the Uncertainty for the Diffusion Coefficient in Porous Geologic Media as a Function of the Volumetric Water Content. The raw data for a suite of geological materials were kindly provided by Jim Conca through David Engel at PNL (Engel, 1995).
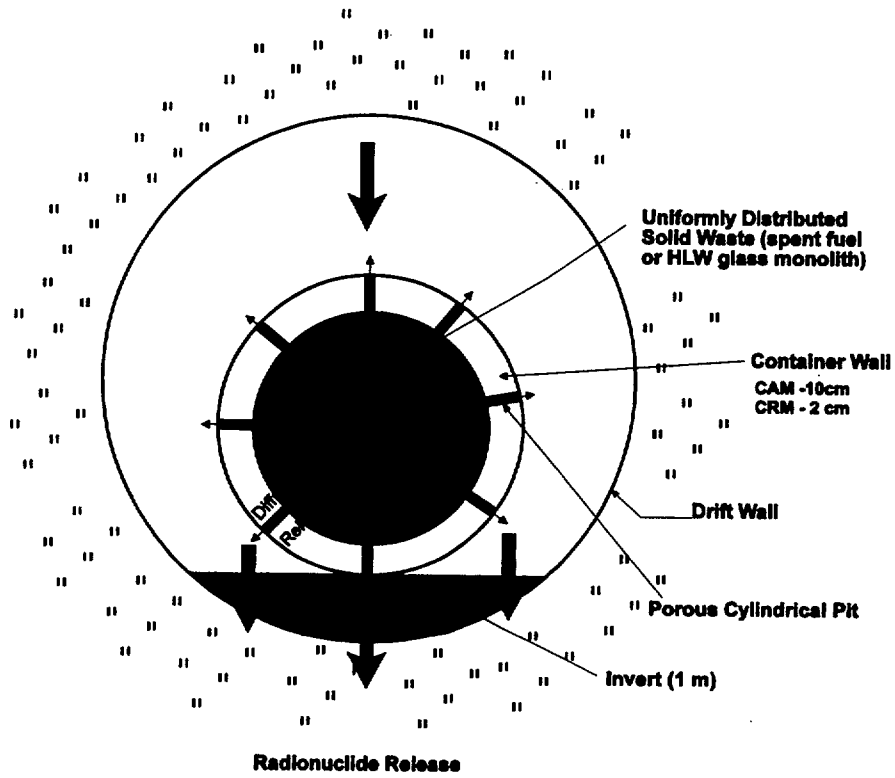
Figure 6.5-9 Conceptual Model for Diffusive Release and Advective Release from Both Waste Package and Other EBS Components.
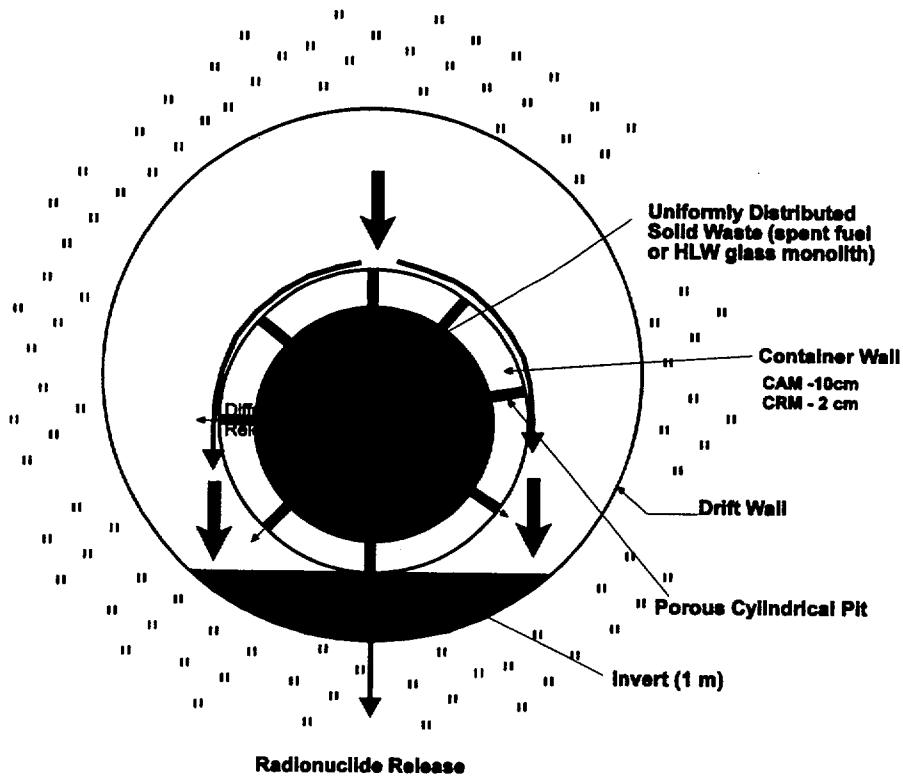

Figure 6.5-10 Conceptual Model for Diffusive Release from Waste Package and Diffusive Plus Advective Release from Other EBS Components.

6-56
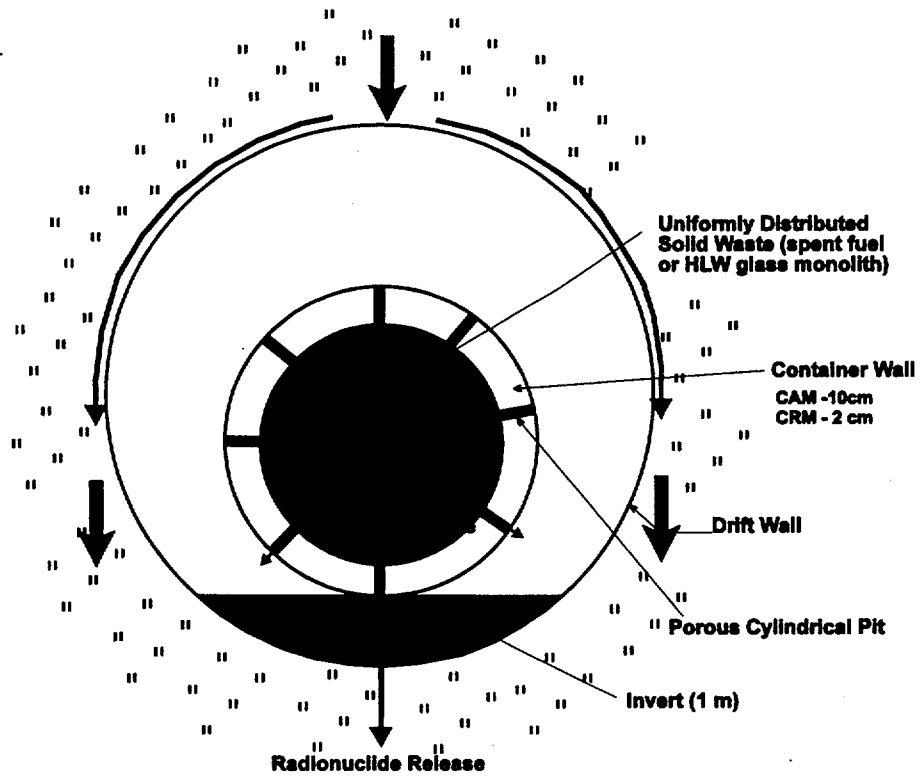
Figure 6.5-11 Conceptual Model for Only Diffusive Release from Both Waste Package and Other EBS Components (Capillary Barrier Effect).